

BULGARIAN CHEMICAL COMMUNICATIONS

2019 Volume 51 / Special Issue D

Selected papers presented on the 11th Chemistry Conference,
Plovdiv, Bulgaria, October 11-13, 2019

*Journal of the Chemical Institutes
of the Bulgarian Academy of Sciences
and of the Union of Chemists in Bulgaria*

BULGARIAN CHEMICAL COMMUNICATIONS

A quarterly published by

THE BULGARIAN ACADEMY OF SCIENCES

and

THE UNION OF CHEMISTS IN BULGARIA

Volume 51, Special Issue D

ИЗВЕСТИЯ ПО ХИМИЯ

Тримесечно издание на

БЪЛГАРСКА АКАДЕМИЯ НА НАУКИТЕ

и

СЪЮЗ НА ХИМИЦИТЕ В БЪЛГАРИЯ

Том 51, Специален брой D

2019

Editor-in-Chief:

V. Beschkov

Guest editor

V. Kmetov

EDITORIAL BOARD

Ch. Bonev, L. Boyadzhiev, I. Gutzow, I. Havezov, E. Ivanova, K. Petkov, K. Petrov, L. Petrov, I. Pojarlieff, S. Rakovsky, D. Stoychev, P. Petrov, D. Tsalev, D. Vladikova, D. Yankov, V. Kurteva

Members from abroad:

J. M. Albella (Spain), S. Berger (Germany), J. C. Breakman (Belgium), J. Etourneau (France), M. Farina (Italy), K. Friedrich (Germany), J. Gyenis (Hungary), A. J. Kirby (United Kingdom), T. Kowalska (Poland), K. Kutchitsu (Japan), A. Lasia (Canada), O. V. Mazurin (Russia), B. Mutaftshiev (France), E. Peter Kündig (Switzerland), S. De Rosa (Italy), T. F. Tadros (United Kingdom), K. Valko (Hungary)

The annual subscription (for 4 issues) for vol. 51 (2019) is € 160. – including postage, handling and packaging charge.

Payments should be delivered to:

*Editorial Board of Bulgarian Chemical Communications, Institute of Chemical Engineering,
UniCredit Bulbank, IBAN: BG65 UNCR 7630 3400 0017 48; SWIFT/BIC - UNCRBGSF (for Euro €).*

UniCredit Bulbank, IBAN: BG18 UNCR 9660 3119 9033 12; SWIFT/BIC - UNCRBGSF (for local currency BGN).

Dear reader,

Oxford Dictionaries named '*Toxic*' word of the year 2018. It is common to blame Chemistry for many global problems, but we do not share this point of view. The motto of the **11th Chemistry Conference (11CC)** organized by the Faculty of Chemistry at the University of Plovdiv 'Paisii Hilendarski' was „*Chemistry is not an evil*“.

<https://11cc.uni-plovdiv.net/>

The forum was held between 11-13 October 2018, in Park Hotel Sankt Peterburg, Plovdiv and received great response as one of the most significant events of the year for the chemical community in Bulgaria. It united **219** participants registered from **17** countries: Algeria, Austria, Bulgaria, France, Hungary, Kosovo, Macedonia, Monaco, Nigeria, India, Poland, Pakistan, Russia, Saudi Arabia, Spain, Turkey and United Kingdom. 431 names are listed into the **11CC** Book of abstracts author index.

The forum marked the passing away of Prof. Georgi Andreev (scientific committee member), and many of the speakers mentioned a memoriam of him.

All participants enjoyed the presentations of 12 invited plenary speakers: Prof. Dr. A. Canals and Prof. Dr. F. Alonso from University of Alicante, Spain; Prof. Dr. M. Moloney, from University of Oxford, UK; Prof. Dr. E. Rosenberg from Technical University of Vienna, Austria; Prof. Dr. E. Bulska from University of Warsaw, Poland; Dr. E. Vassileva from IAEA Environment Laboratories, Monaco; Prof. Dr. Paunović from University "Sts. Cyril and Methodius", Skopje, Macedonia; Prof. Dr. M. A. Tasdelen from Yalova University, Turkey and two corresponding members of the Bulgarian Academy of Science - Prof. DSc T. Spassov and Prof. DSc N. Denkov from University of Sofia "St. Kliment Ohridski", as well as the host representatives Prof. Dr. N. Dimcheva and Prof. Dr. P. Angelov. 26 oral presentations were delivered in five conference sections together with 129 posters presentations. The company exhibition during the **11CC** was very interesting and successful. It was attended by: ACM2 Ltd.; T.E.A.M. Ltd.; HROMA Ltd.; AQUACHIM JSC; Medical Technics Engineering Ltd. The event received a sponsorship from the NSFB with a grant № 01/17 23.08.2018; from University of Plovdiv, NEOCHIM PLC; KCM 2000 GROUP and ALIMENTI.

This special issue of the *Bulgarian Chemical Communications* contains 51 scientific papers (accepted after a peer review evaluation) of the studies presented during the **11CC** from the five sections: *i) Theoretical chemistry and Analytical chemistry; ii) Organic chemistry and New technological methods and materials; iii) Inorganic chemistry and Chemistry education; iv) Physical chemistry and v) Food chemistry.*

The Organizing Committee of the conference would like to thank this journal for the help in publishing the full text articles and for the chance given to the conference's participants to meet the wide audience.

Chair of the Organizing committee
Prof. Dr. G. Antova

Guest Editor
Assoc. Prof. Dr. V. Kmetov

Complex formation and liquid-liquid extraction of the ion-pair of molybdenum(VI) with 3,5-dinitrocatechol and 3-(4,5-dimethylthiazol-2-yl)-2,5-diphenyl-2H-tetrazolium bromide

K. T. Stojnova¹, V. V. Divarova², P. V. Racheva², K. G. Bozhinova³, V. D. Lekova^{1*}

¹University of Plovdiv, Faculty of Chemistry, Department of General and Inorganic Chemistry with Methodology of Chemistry Education, 24 Tsar Assen St., 4000 Plovdiv, Bulgaria

²Department of Chemical Sciences, Faculty of Pharmacy, Medical University-Plovdiv, 15A Vasil Aprilov Blvd., 4002 Plovdiv, Bulgaria

³Sage Technologies LTD, 17 Kuklensko chaussee St., 4000 Plovdiv, Bulgaria

Received October 26, 2018; Revised December 20, 2018

The complex formation and the ion-association of the ion-pair formed between the anionic chelate of molybdenum(VI)-3,5-dinitrocatechol (3,5-DNC) with the cation of 3-(4,5-dimethylthiazol-2-yl)-2,5-diphenyl-2H-tetrazolium bromide (MTT) in the liquid-liquid extraction system Mo(VI)-3,5-DNC-MTT-H₂O-CHCl₃ was studied by spectrophotometry. The optimum conditions for the chelate formation and extraction of the ion-associated complex Mo(VI)-3,5-DNC-MTT were established. The molar ratio of the components in the ion-associated complex Mo(VI)-3,5-DNC-MTT was determined by independent methods. The association process in aqueous phase and the extraction equilibria were investigated and quantitatively characterized. The following key constants of the processes were calculated: association constant, distribution constant, extraction constant and recovery factor. Based on this, a reaction scheme, a general formula and a structural formula of the complex were suggested.

Keywords: molybdenum(VI), ion-associated chelate, extraction equilibria, UV-Vis spectroscopy

INTRODUCTION

Molybdenum(VI) forms complexes with various organic ligands, such as polyphenols and their functional derivatives, polyhydroxycarboxylic acids, aminopolycarboxylic acids, hydroxamic acids, amines (primary, secondary and tertiary), 8-hydroxyquinoline and its derivatives, aldehyde hydrazones, oximes, β -diketones, fluorones, hydroxyazodyes, biomolecules (chitosan, chitin, D-glucosamine, L-alanine, L-phenylalanine) [1–9]. Molybdenum (VI) gives colored chelates with aromatic compounds, containing two or more hydroxyl groups in *o*-position relative to each other. The colored anionic chelates of molybdenum (VI) form ion-associated complexes with bulky organic cations, like methyltriethylammonium, cetylpyridinium, cetyltrimethylammonium, tetraphenylphosphonium [1, 10–12].

The structure and properties of tetrazolium salts determine their ability to form ion-associated complexes. The bulky hydrophobic organic substituents in the molecules of the tetrazolium salts increase the extractability of the ion associated complexes. The presence of a quaternary nitrogen atom in the molecules of the tetrazolium salts determines the ability to form ionic associates in the aqueous phase without protonation, as opposed to the amines [13–15]. Tetrazolium salts are used as

reagents for the preparation of various ion-associated complexes of metals, e.g. W(VI), Ge(IV), Ti(III), Nb(V), V(V), Ga(III), Co(II) [15–19].

The liquid-liquid extraction is a part of the chemistry of the solutions and the coordination compounds. It is applied to study the processes of complex formation and the extraction equilibria. The extraction spectrophotometry is a relatively simple, convenient, rapid to perform and inexpensive method for preparation and characterization of new complex compounds, as well as for their application in the chemical analysis [20–24].

The aim of this research was to study spectrophotometrically the extraction equilibria of the complex formation of the ion-pair formed between the anionic chelate of Mo(VI)-3,5-dinitrocatechol (3,5-DNC) and the cation of 3-(4,5-dimethylthiazol-2-yl)-2,5-diphenyl-2H-tetrazolium bromide (MTT) in the liquid-liquid system Mo(VI)-3,5-DNC-MTT-H₂O-CHCl₃.

EXPERIMENTAL

Reagents and apparatus

Na₂MoO₄•2H₂O (Fluka AG, p.a.): an aqueous 2.08×10⁻² mol dm⁻³ solution was prepared. 3,5-Dinitrocatechol (3,5-DNC) (Sigma-Aldrich, p.a.): 3,5-DNC was dissolved in CHCl₃ to give a

* To whom all correspondence should be sent.
E-mail: vanlek@uni-plovdiv.bg

1.0×10^{-3} mol dm⁻³ solution. 3-(4,5-Dimethylthiazol-2-yl)-2,5-diphenyl-2H-tetrazolium bromide (MTT) (Merck, Germany, p.a.): an aqueous 2.0×10^{-3} mol dm⁻³ solution was prepared. H₂SO₄ (95-97% for analysis, Merck): a 2 mol dm⁻³ solution was prepared. The concentration of H₂SO₄ was determined titrimetrically. A CamSpec M508 spectrophotometer (UK), equipped with 10 mm path length cells, was employed for measurement of the absorbance. The organic solvent CHCl₃ was additionally distilled.

Procedure for establishment of the optimum condition for complex formation

The required aliquots of the solutions of Mo(VI), MTT and H₂SO₄ were introduced into 250 cm³ separatory funnels. The resulting solutions were diluted with distilled water to a total volume of 10 cm³. A required aliquot of a chloroform solution of 3,5-DNC was added and then the organic phase was adjusted to a volume of 10 cm³ with chloroform. The funnels were shaken for a fixed time (up to 240 s). A portion of the organic extract was filtered through a filter paper into a 1 cm cell and the absorbance was measured against a blank. The blank extraction was performed in the same manner in the absence of molybdenum.

Procedure for determination of the distribution constant

The distribution constant (K_D) was determined from the ratio $K_D = A_1/(A_3 - A_1)$, where A_1 and A_3 are the absorbance (measured against blanks) obtained after a single and triple extraction, respectively. The single extraction and the first stage of the triple extraction were performed under the optimum conditions for complex formation (Table 1, column 1). The organic layers were transferred into 25 cm³ calibrated flasks and the flask from the single extraction was brought to volume with chloroform. The second stage of the triple extraction was performed by adding 7 cm³ of chloroform to the aqueous phase that remained after the first stage. After extraction, the obtained extract was added to this first stage of the triple extraction. The third stage of the triple extraction was performed in the same manner as for the second stage and the extract was added to those of the first two stages. The volume of the flask was brought to the mark with chloroform. The calibrated flasks were shaken before the spectrophotometric measurements [25].

RESULTS AND DISCUSSION

Optimum extraction-spectrophotometric conditions

The absorption spectrum of the extract of the studied ion-pair formed between the anionic chelate of Mo(VI) with 3,5-DNC and the tetrazolium cation

in CHCl₃ was characterized by an absorption maximum in the visible range ($\lambda_{\max} = 405$ nm) (Fig. 1).

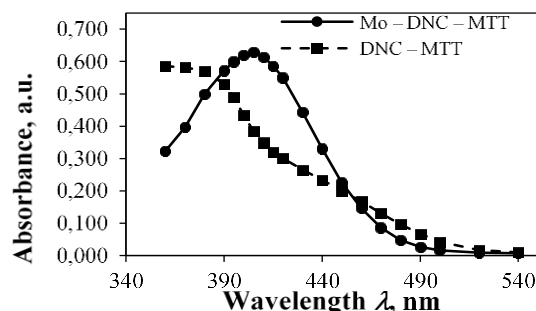


Fig. 1. Absorption spectra of the complex Mo(VI)-3,5-DNC-MTT and of the blank sample 3,5-DNC-MTT in CHCl₃. $C_{\text{Mo(VI)}} = 2.08 \times 10^{-5}$ mol dm⁻³; $C_{3,5\text{-DNC}} = 2.0 \times 10^{-4}$ mol dm⁻³; $C_{\text{MTT}} = 2.0 \times 10^{-4}$ mol dm⁻³; $C_{\text{H}_2\text{SO}_4} = 4.0 \times 10^{-1}$ mol dm⁻³; $\lambda = 405$ nm; $\tau = 2$ min.

The influence of the acidity of the aqueous phase on the extraction of the anionic chelate Mo(VI)-3,5-DNC into the organic phase in the form of an ion-pair with the tetrazolium cation was investigated. The maximum and constant extraction of the ion-associated complex is achieved in strongly acidic solution of (0.2–0.5) mol dm⁻³ H₂SO₄. The results showed that the extraction equilibrium is achieved for shaking time of not less than 90 s. A longer shaking time did not affect the absorbance. The experiments were performed for 2 min. The concentrations of the reagents are the most important factor influencing the extraction equilibria. The chelate formation of Mo(VI)-3,5-DNC requires 6.7-fold excess of 3,5-DNC ($C_{3,5\text{-DNC}} \geq 1.4 \times 10^{-4}$ mol dm⁻³) and 7.7-fold excess of MTT ($C_{\text{MTT}} \geq 1.6 \times 10^{-4}$ mol dm⁻³) for maximum association and extraction. The optimum experimental conditions for the extraction of the ion-associated complex are summarized in Table 1, column 1.

Beer's law, apparent molar absorptivity and other analytical characteristics

The range of obedience to Beer's law, i.e. the linear relationship between the molybdenum concentration in the aqueous phase ($C_{\text{Mo(VI)}}$, μg cm⁻³) and the absorbance of the ion-association complex in the organic phase after extraction was studied using regression analysis under the optimum conditions for complex formation. The equation of a straight line was found to be $Y = 0.3254 X - 0.0016$ with a correlation coefficient squared 0.9996. Further analytical characteristics, such as apparent molar absorptivity ϵ' , adherence to Beer's law, Sandell's sensitivity, limit of detection and limit of quantification, are shown in Table 1, column 2.

Table 1. Optimum extraction-spectrophotometric conditions and analytical characteristics of the system Mo(VI)–3,5-DNC–MTT–H₂O–CHCl₃

Optimum conditions	Analytical characteristic
Absorption maximum (λ_{\max}) 405 nm	Apparent molar absorptivity (ϵ') (3.13 ± 0.07) $\times 10^4$ dm ³ mol ⁻¹ cm ⁻¹
Volume of the aqueous phase 10 cm ³	True molar absorptivity (ϵ) (3.12 ± 0.04) $\times 10^4$ dm ³ mol ⁻¹ cm ⁻¹
Volume of the organic phase 10 cm ³	Sandell's sensitivity (SS) 3.07 ng cm ⁻²
Concentration of H ₂ SO ₄ in the aqueous phase 0.4 mol dm ⁻³ (0.2 ÷ 0.5)	Adherence to Beer's law up to 3.99 μ g cm ⁻³
Shaking time (τ) 2 min	Relative standard deviation (RSD) 1.84%
Concentration of 3,5-DNC $\geq 1.4 \times 10^{-4}$ mol dm ⁻³	Limit of detection (LOD) 0.0977 μ g cm ⁻³
Concentration of MTT $\geq 1.6 \times 10^{-4}$ mol dm ⁻³	Limit of quantification (LOQ) 0.3257 μ g cm ⁻³

Molar Ratios of the Complex, Reaction Scheme and Suggested General Formula

The mobile equilibrium method and the straight-line method of Asmus were applied to prove the molar ratios Mo(VI):3,5-DNC and Mo(VI):MTT [26]. The results from the application of these methods are shown in Figs. 2–4, respectively. On the basis of the results it can be concluded that Mo(VI), 3,5-DNC and MTT interact in molar ratio 1:2:2. The molar ratio was confirmed by an independent method – the method of Likussar-Boltz [27].

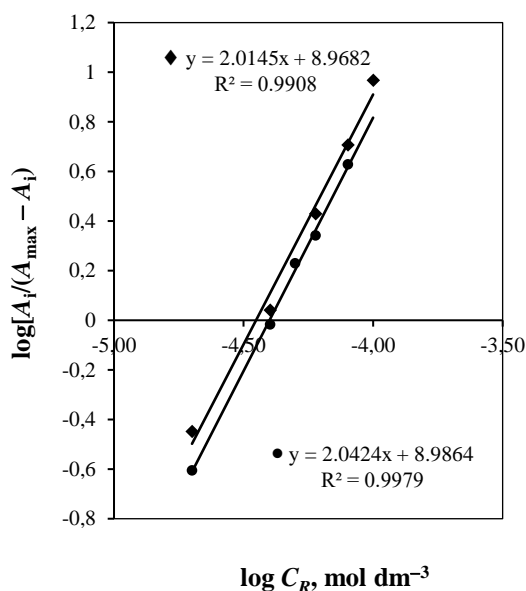


Fig. 2. Straight lines by the mobile equilibrium method for determination of the molar ratios Mo(VI) : 3,5-DNC and Mo(VI) : MTT. $C_{\text{Mo(VI)}} = 2.08 \times 10^{-5}$ mol dm⁻³; $C_{\text{H}_2\text{SO}_4} = 4.0 \times 10^{-1}$ mol dm⁻³; $\lambda = 405$ nm; $\tau = 2$ min
 ● Mo(VI) : 3,5-DNC, $C_{\text{MTT}} = 2.0 \times 10^{-4}$ mol dm⁻³;
 ■ Mo(VI) : MTT, $C_{3,5\text{-DNC}} = 2.0 \times 10^{-4}$ mol dm⁻³.

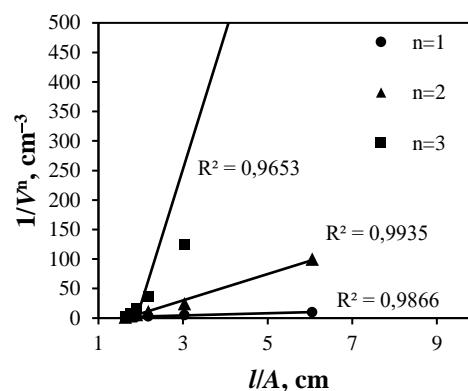


Fig. 3. Determination of the molar ratio (n) Mo(VI):MTT by the method of Asmus. $C_{\text{Mo(VI)}} = 2.08 \times 10^{-5}$ mol dm⁻³; $C_{3,5\text{-DNC}} = 2.0 \times 10^{-4}$ mol dm⁻³; $C_{\text{H}_2\text{SO}_4} = 4.0 \times 10^{-1}$ mol dm⁻³; V – volume of MTT, cm³; $\lambda = 405$ nm; $\tau = 2$ min.

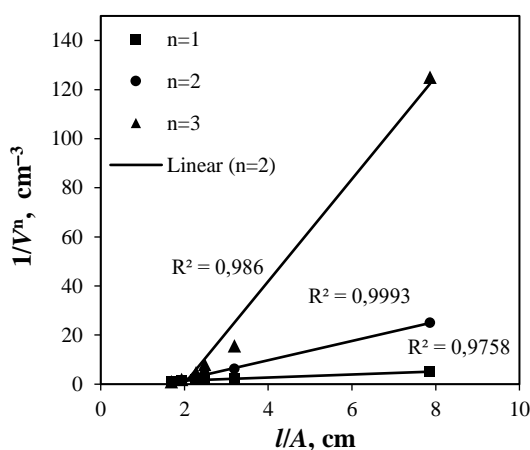
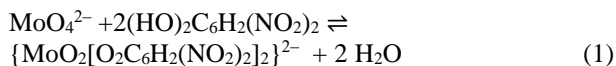
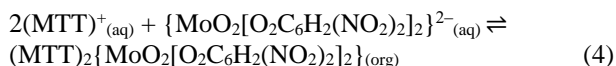
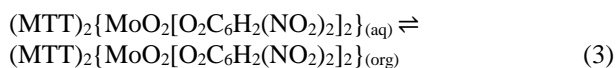
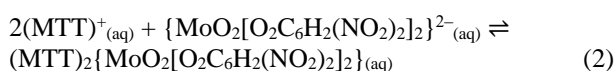


Fig. 4. Determination of molar ratio (n) Mo(VI) : 3,5-DNC by the method of Asmus. $C_{\text{Mo(VI)}} = 2.08 \times 10^{-5}$ mol dm⁻³; $C_{\text{MTT}} = 2.0 \times 10^{-4}$ mol dm⁻³; $C_{\text{H}_2\text{SO}_4} = 4.0 \times 10^{-1}$ mol dm⁻³; V – volume of 3,5-DNC, cm³; $\lambda = 405$ nm; $\tau = 2$ min.

The carried out experiments showed that the complex formation and the extraction of the ion-associated complex occurred in strongly acidic solution. Under these conditions, the complex formation of anionic chelate Mo(VI)-3,5-DNC is given by Eq. (1):



Having in mind the reaction of chelate formation of Mo(VI)-3,5-DNC and molar ratio indicated above, it can be suggested that the formation of the ion-associate in the aqueous phase, its distribution between the aqueous and the organic phases and its extraction in chloroform are given by the following Eqs. (2÷4).



Hence, the ion-pair formed between the anionic chelate of Mo(VI)-3,5-DNC with the tetrazolium cation can be represented by the general formula $(\text{MTT})_2\{\text{MoO}_2[\text{O}_2\text{C}_6\text{H}_2(\text{NO}_2)_2]_2\}$.

Equilibrium constants, True molar absorptivity and recovery factor

The values of the equilibrium constants and the recovery factor, describing quantitatively the equilibrium in the aqueous phase and the extraction of the ion-associated complex in the organic phase are presented in Table 2.

The association constant β and the true molar absorptivity ε were determined by the method of Komar-Tolmachev from Eq. (5) [26]:

$$\beta = (1/n)^n / [\varepsilon (\text{tg } \alpha)^{n+1}] \quad (5)$$

where l is the cuvette thickness ($l = 1 \text{ cm}$); n – the molar ratio between the components

independently determined (e.g. by the mobile equilibrium method or the straight-line method of Asmus) ($n = 2$); ε – the true molar absorptivity; $\text{tg } \alpha$ – angular coefficient of the straight line.

The true molar absorptivity ε was determined by the method of Komar-Tolmachev (Fig. 5) from the equation of a straight line $Y = 1.4805 X + 3.2075$ ($\varepsilon = 1 / (3.2075 \times 10^{-5})$) and its value is given in Table 1, column 2.

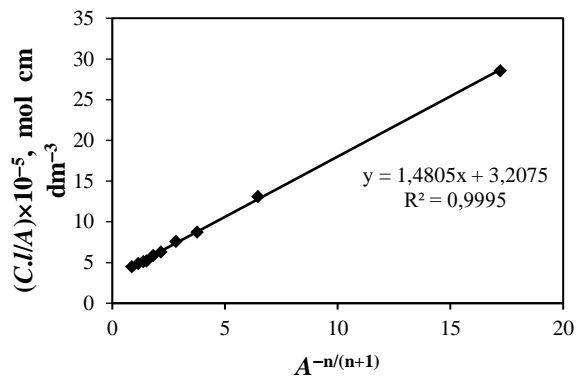


Fig. 5. Dependency of $(C.l/A)$ on $A^{-n/(n+1)}$ (method of Komar-Tolmachev); $C = C_{\text{Mo(VI)}} \text{ mol dm}^{-3}$; $C_{\text{MTT}} = 2 C_{\text{Mo(VI)}} \text{ mol dm}^{-3}$; $C_{3,5\text{-DNC}} = 2.0 \times 10^{-4} \text{ mol dm}^{-3}$; A – absorbance; l – cell thickness, $l = 1 \text{ cm}$; $n = 2$.

The distribution constant (K_D) was determined by Eq. (6), where A_I and A_3 are the absorbance (measured against blanks) obtained after a single and triple extraction, respectively.

$$K_D = \frac{\{(\text{MTT})_2\{\text{MoO}_2[\text{O}_2\text{C}_6\text{H}_2(\text{NO}_2)_2]_2\}\}_{\text{(org)}}}{\{(\text{MTT})_2\{\text{MoO}_2[\text{O}_2\text{C}_6\text{H}_2(\text{NO}_2)_2]_2\}\}_{\text{(aq)}}} = A_I / (A_3 - A_I) \quad (6)$$

The recovery factor $R\%$ and the extraction constant K_{ex} were determined from Eq. (7) and Eq. (8), respectively:

$$R\% = 100 K_D / (K_D + 1) \quad (7)$$

$$\log K_{ex} = \log K_D + \log \beta \quad (8)$$

where β was determined by the method of Komar-Tolmachev.

Table 2. Values of the equilibrium constants and the recovery factor

Equilibrium constant and recovery factor	Value
Equilibrium (Eq. 2) - Association constant β	
$\beta = (\text{MTT})_2\{\text{MoO}_2[\text{O}_2\text{C}_6\text{H}_2(\text{NO}_2)_2]_2\}_{\text{(aq)}} / \{[(\text{MTT})^+]_{\text{(aq)}}^2 \times \{\text{MoO}_2[\text{O}_2\text{C}_6\text{H}_2(\text{NO}_2)_2]_2\}^{2-}_{\text{(aq)}}\}$	$\log \beta = (9.39 \pm 1.07)^a$ $\log \beta = (9.54 \pm 0.21)^b$
Equilibrium (Eq. 3) - Distribution constant K_D	
$K_D = \{(\text{MTT})_2\{\text{MoO}_2[\text{O}_2\text{C}_6\text{H}_2(\text{NO}_2)_2]_2\}\}_{\text{(org)}} / \{(\text{MTT})_2\{\text{MoO}_2[\text{O}_2\text{C}_6\text{H}_2(\text{NO}_2)_2]_2\}\}_{\text{(aq)}}}$	$\log K_D = (1.25 \pm 0.01)^c$
Equilibrium (Eq. 4) - Extraction constant K_{ex}	
$K_{ex} = \{(\text{MTT})_2\{\text{MoO}_2[\text{O}_2\text{C}_6\text{H}_2(\text{NO}_2)_2]_2\}\}_{\text{(org)}} / \{[(\text{MTT})^+]_{\text{(aq)}}^2 \times \{\text{MoO}_2[\text{O}_2\text{C}_6\text{H}_2(\text{NO}_2)_2]_2\}^{2-}_{\text{(aq)}}\}$	$\log K_{ex} = (10.64 \pm 1.08)^d$ $\log K_{ex} = (9.89 \pm 0.04)^e$
Recovery factor $R\%$	$R = (94.65 \pm 0.14)\%^f$

^a Calculated by Komar-Tolmachev method (Eq.(5)); ^b Calculated by Holme-Lagmyhr method [28]; ^c Calculated by Eq. (6); ^d Calculated by Eq. (8), where β is determined by the Komar-Tolmachev method [26]; ^e Calculated by Likussar-Boltz method [27]; ^f Calculated by Eq. (7).

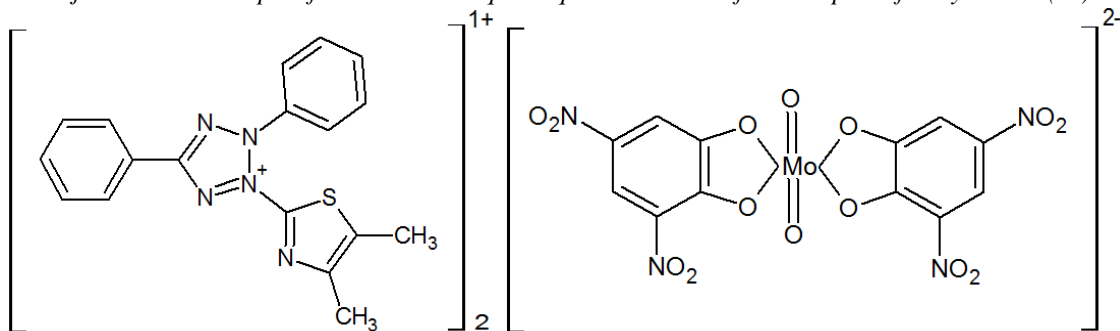


Fig. 6. Structural formula of the ion-associated complex Mo(VI)–3,5-DNC–MTT

The results obtained by independent methods are statistically similar and confirm the proposed scheme of the process of complex formation of the ion-pair in the aqueous phase, its distribution between the aqueous and the organic phases and its extraction in chloroform. Based on this, the proposed structure of the ion-associated complex is represented in Fig. 6.

The values of the equilibrium constants, the recovery factor and the analytical characteristics indicate that the ion-pair formed between the anionic chelate of Mo(VI) with 3,5-DNC and the tetrazolium cation is characterized by sufficiently high stability and good extraction. The presence of hydrophilic nitro groups in the molecule of the ion-associated complex stabilizes the ion-pair in the aqueous phase. The availability of the phenyl radicals in the tetrazolium salt increases the extractability of the ion-associated complex.

Acknowledgement: The authors would like to thank the Research Fund of the University of Plovdiv for the financial support of the current research.

REFERENCES

1. A. P. Vinogradov, Analytical Chemistry of Elements - Molybdenum, Nauka, Moscow, 1962.
2. V. M. Ivanov, G. A. Kochelaeva, *J. Anal. Chem.*, **58**, 31 (2003).
3. M. L. Harikumar Nair, Anju. S. Appukuttan, *J. Korean Chem. Soc.*, **56**, 217 (2012).
4. T. Nakamura, S. Nishihama, K. Yoshizuka, *Solvent Extr. Res. Dev.*, **16**, 47 (2009).
5. L. Xue, D. Deng, Y. Xu, Q. Wang, *Russ. J. Coord. Chem.*, **42**, 137 (2016).
6. V. M. Ivanov, G. A. Kochelaeva, G. V. Prokhorova, *J. Anal. Chem.*, **57**, 758 (2002).
7. P. A. Petrov, M. Yu. Afonin, D. Yu. Naumov, S. N. Konchenko, A. V. Piskunov, *Russ. J. Coord. Chem.*, **41**, 31 (2015).
8. W. X. Xu, W.H. Li, *Russ. J. Coord. Chem.*, **38**, 92 (2012).
9. S. Tascioglu, E. Kaki, S. Tascioglu, *J. Appl. Spectrosc.*, **79**, 540 (2012).
10. A. T. Pilipenko, M. M. Tananayko, Mixed Ligands and Mixed Metal Complexes and their Application in Analytical Chemistry, Khimiya, Moscow, 1983.
11. J. L. Martinez-Vidal, A. R. Fernandez-Alba, F. Salinas, *Analyst*, **3**, 329 (1990).
12. M. L. C. Passos, M. Lucia M. F. S. Saraiva, J. F. C. Lima, *Anal. Sci.*, **12**, 1509 (2005).
13. A. W. Nineham, *Chem. Rev.*, **55**, 355 (1955).
14. H. Şenöz, Hacettepe *J. Biol. & Chem.*, **40**, 293 (2012).
15. K. Gavazov, A. Dimitrov, V. Lekova, *Russ. Chem. Rev.*, **76**, 169 (2007).
16. V. Divarova, V. Lekova, P. Racheva, K. Stojnova, A. Dimitrov, *Acta Chim. Slov.*, **61**, 813 (2014).
17. V. V. Divarova, K. T. Stojnova P. V. Racheva, V. D. Lekova, *J. Appl. Spectrosc.*, **84**, 231 (2017).
18. V. Divarova, K. Stojnova, P. Racheva, V. Lekova, *Acta Chim. Slov.*, **63**, 97 (2016).
19. P. Racheva, K. Stojnova, V. Divarova, V. Lekova, *Acta Chim. Slov.*, **64**, 365 (2017).
20. A. K. Babko, A. T. Pilipenko, Photometric Analysis, Khimiya, Moscow, 1968.
21. J. Inczédy, Analytical Applications of Complex Equilibria, Mir, Moscow, Russia, 1979.
22. T. P. Rao, M. L. P. Reddy, A. R. Pillai, *Talanta*, **46**, 765 (1998).
23. A. N. Turanov, V. K. Karandashev, V. E. Baulin, E. V. Kirillov, S. V. Kirillov, V. N. Rychkov, A. Yu. Tsvadze, *Russ. J. Inorg. Chem.*, **61**, 1335 (2016).
24. A. N. Turanov, V. K. Karandashev, O. I. Artyushin, E. V. Sharova, *Solvent Extr. Ion Exch.*, **33**, 540 (2015).
25. K. Stojnova, V. Divarova, P. Racheva, K. Bozhinova, V. Lekova, *Acta Chim. Slov.*, **63**, 654 (2016).
26. M. I. Bulatov, I. P. Kalinkin, Practical Handbook on Photometric Methods of Analysis, Khimiya, Leningrad, 1986.
27. W. Likussar, D. F. Boltz, *Anal. Chem.*, **43**, 1265 (1971).
28. A. Holme, F. J. Langmyhr, *Anal. Chim. Acta*, **36**, 383 (1996).

Novel complexes of N-substituted-4,5-dimethoxy-phenylethyl-2-arylketoamides with metal ions

P. E. Marinova^{1*}, S. H. Tsoneva², S. A. Nikolova³, I. I. Ivanov³

¹University of Plovdiv "Paisii Hilendarski", Faculty of Chemistry, Department of General and Inorganic Chemistry with Methodology of Chemistry Education, 24 Tzar Asen Str., 4000 Plovdiv, Bulgaria

²University of Plovdiv "Paisii Hilendarski", Faculty of Chemistry, Department of Analytical Chemistry and Computer Chemistry, 24 Tzar Asen Str., 4000 Plovdiv, Bulgaria

³University of Plovdiv "Paisii Hilendarski", Faculty of Chemistry, Department of Organic Chemistry, 24 Tzar Asen Str., 4000 Plovdiv, Bulgaria

Received October 29, 2018; Revised December 20, 2018

The current work presented the synthesis and characterization of a new Pd(II) complex of N-(2-benzoyl-4,5-dimethoxyphenethyl)-2-phenylacetamide (L1) and Zn(II) complex of ethyl-(4,5-dimethoxy-2-(2-phenylacetyl)phenethyl) carbamate (L2). The complexes were analyzed using IR-, ¹H-NMR-, ¹³C-NMR-spectra and Raman spectroscopy. For Pd(II)L1 and Zn(II)L2 complexes we suppose that L1 was coordinated monodentate with NH group and L2 was coordinated as bidentate ligand with N- and O-atoms involved in complexation. The IR spectral data for Pd(II)L1 and Zn(II)L2 complexes showed presence of OH⁻ groups, most probably coordinated to the metal ion, thus forming square planar or octahedral geometry, respectively.

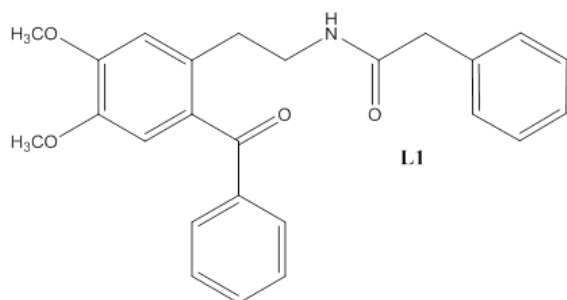
Keywords: metal complexes, ketoamides, synthesis

INTRODUCTION

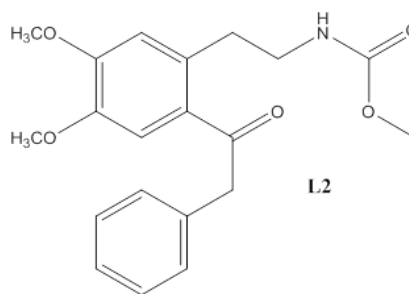
The pharmacological activity of tetrahydroisoquinolines has long been established. The tetrahydroisoquinoline motif is present in a variety of natural products, including cactus alkaloids (peyruvic acid), mammalian alkaloids (salsoline carboxylic acid), Esteinascidine family (ET743) and spiro-benzo-quinoline alkaloids (parfumine).

The biological activity of isoquinoline derivatives, as analogues of various drugs, has provided great deal of interest for the synthesis of new compounds. In our previous reports [1] we described ortho-acylation of 2-phenethylamines in polyphosphoric acid. The products were obtained after ortho-acylation of 2-phenethylamides in polyphosphoric acid (Figure 1).

The obtained ketoamides are interesting from the synthetic point of view as starting compounds for the synthesis of isoquinoline ring system. The construction of isoquinoline ring has been a popular area of research in natural product chemistry. The aim of the present study was the synthesis and structural elucidation of new complexes of palladium(II) and zinc(II) with N-(2-benzoyl-4,5-dimethoxyphenethyl)-2-phenylacetamide (L1) and ethyl-(4,5-dimethoxy-2-(2-phenylacetyl)phenethyl) carbamate (L2) as ligands. The Zn as transition metal was chosen because of its important biological role in enzyme system of animals and plants [2, 3], whereas Pd(II) coordinates differently with interesting site in amide ligands [4]. The structure of the obtained complexes was studied by means of experimental IR, Raman, ¹H- and ¹³C-NMR methods.



N-(2-benzoyl-4,5-dimethoxyphenethyl)-2-phenylacetamide



ethyl (4,5-dimethoxy-2-(2-phenylacetyl)phenethyl)carbamate

Figure 1. Structural formulas of the ketoamides

* To whom all correspondence should be sent.

E-mail: petia_marinova@abv.bg

EXPERIMENTAL

The metal salts $(\text{NH}_4)_2[\text{PdCl}_4]$ and $\text{Zn}(\text{CH}_3\text{COO})_2 \cdot 3\text{H}_2\text{O}$ - Sigma-Aldrich or Merck) and the solvents used for synthesis of the complexes were with p.a. qualification. The two organic ligands L1 and L2 were synthesized according to methods previously reported [1]. The IR spectra of all compounds were registered in KBr pellets on a Bruker FT-IR VERTEX 70 spectrometer from 4000 cm^{-1} to 400 cm^{-1} at resolution 2 cm^{-1} with 25 scans. The Raman spectra of the free ligands and the Pd(II)L1 and Zn(II)L2 complexes were measured on a spectrometer RAM II (Bruker Optics) with a focused laser beam of 20 mW and 200 mW power of Nd:YAG laser (1064 nm) from 4000 cm^{-1} to 50 cm^{-1} at resolution 2 cm^{-1} with 25 scans. The NMR spectra were taken on a Bruker Avance II+ 600MHz NMR spectrometer operating at 600.130 and 150.903 MHz for ^1H and ^{13}C , respectively, using the standard Bruker software. Chemical shifts were referenced to tetramethylsilane (TMS). Measurements were carried out at ambient temperature.

Synthesis of Pd(II) and Zn(II) complexes of N-(2-benzoyl-4,5-dimethoxyphenethyl)-2-phenylacetamide (L1) and ethyl-(4,5-dimethoxy-2-(2-phenylacetyl)phenethyl)carbamate (L2)-general procedure

5 mL NaOH (0.0004 mol (0.016 g) in 5 mL H_2O) was added slowly to the solution of L1 (0.0004 mol (0.1612 g) in 5 mL DMSO) or L2 (0.0004 mol (0.1484 g) in 5 mL DMSO). The solution of metal salts (0.0002 mol (0.05686 g) $(\text{NH}_4)_2[\text{PdCl}_4]$ in 10 mL H_2O or 0.0002 mol (0.0475 g) $\text{Zn}(\text{CH}_3\text{COO})_2 \cdot 3\text{H}_2\text{O}$ in 10 mL H_2O) was added dropwise from a burette during stirring with an electromagnetic stirrer. Non-charged complexes Pd(II)L1 and Zn(II)L2 were formed as orange-red or yellow amorphous precipitates, respectively. The precipitates were filtered off and washed with $\sim 2\text{ mL}$ H_2O . These were dried over CaCl_2 for 2 weeks. It was found that the all newly-synthesized complexes were soluble in DMSO and insoluble in water.

mp (L1) = $108\text{--}111^\circ\text{C}$, mp (PdL1) = $124\text{--}127^\circ\text{C}$; W(Pd)% = 11.2%;

mp (L2) = $93\text{--}95^\circ\text{C}$, mp (ZnL2) = $206\text{--}208^\circ\text{C}$; W(Zn)% = 7.8%.

RESULTS AND DISCUSSION

Complexation with Pd(II) and Zn(II) using metal salts, namely $(\text{NH}_4)_2[\text{PdCl}_4]$ and

$\text{Zn}(\text{CH}_3\text{COO})_2 \cdot 3\text{H}_2\text{O}$ at a molar ratio $\text{M:L:OH}^- = 1:2:2$ for all complexes were studied. All complexes were isolated as amorphous precipitates and have rather poor solubility in the most common organic solvents, except for strongly coordinating solvents such as DMSO.

The IR band at 3307 cm^{-1} of L1 that was observed may refer to the stretching vibrations of the N-H group of the ketoamide. In the IR spectrum of L1 the bands at 1662 cm^{-1} can be attributed to stretching vibrations of C=O group from the keto group and 1652 cm^{-1} to stretching vibrations of C=O group from the amide group. The first band in the Raman spectra of L1 and Pd(II)L1 complex appeared at 1670 cm^{-1} . The band at 1652 cm^{-1} missed in the Raman spectra of L1 and Pd(II)L1. Several bands in the Raman spectrum of the ligand L1 ($3058, 3004\text{ cm}^{-1}$) and in the IR spectrum ($3078, 3059, 3025, 3002\text{ cm}^{-1}$) were for stretching vibrations of CH in the benzene moiety. In the IR spectrum of the Pd(II)L1 complex a broad band was observed at $3500\text{--}3400\text{ cm}^{-1}$, confirming the presence of OH group. The $^1\text{H-NMR}$ data of the Pd(II)L1 complex showed that NH signal changes from 8.1 ppm (t, 1H, NH, $J=5.4\text{ Hz}$) in the ligand's NMR to 7.0 ppm (t, 1H, NH, $J=5.4\text{ Hz}$) in the $^1\text{H-NMR}$ of the complex. According to the NMR-data we can suggest that NH from the ketoamide is involved in the complex structure. The ^1H - and ^{13}C -NMR spectral data for L1 and its Pd(II) complex are given in Table 1.

The suggested structure of the metal complex of Pd(II) with N-(2-benzoyl-4,5-dimethoxyphenethyl)-2-phenylacetamide (L1) is presented in Figure 2. Shehata *et al.* reported palladium complexes with coordinated water molecules (OH group) [5-12].

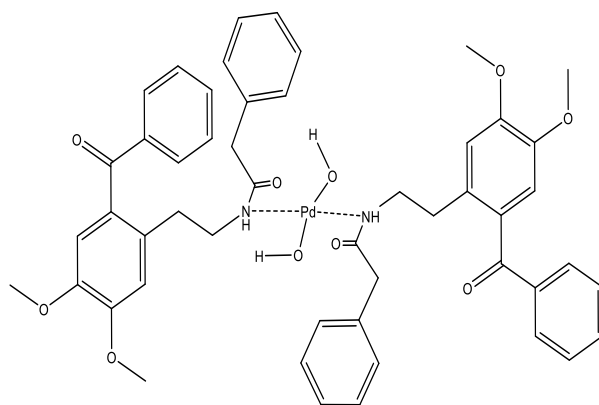


Figure 2. Suggested structure of the Pd(II)L1 complex

Table 1. ¹H and ¹³C NMR spectral data for N-(2-benzoyl-4,5-dimethoxyphenethyl)-2-phenylacetamide (L1) and Pd(II)L1[600.13 MHz (¹H) and 150.903 MHz (¹³C)]^a

Atom	δ (¹³ C) ppm	δ (¹ H) ppm	Multiplicity (J, Hz)	δ (¹³ C) ppm Pd(II)L1	δ (¹ H) ppm Pd(II)L1	Multiplicity (J, Hz) Pd(II)L1
CH ₂	32.7	2.5	(q, 2H, CH ₂ , J ₁ =2.4; J ₂ =3)	32.7	2.3	(t, 2H, J=6.6)
CH ₂ NH	40.4	2.7	(t, 2H, CH ₂ , J=7.2)	40.4	1.0	(t, 2H, J=7.2)
(NH)	-	8.1	(t, 1H, NH, J=5.4)	-	7.0	(t, 1H, NH, J=5.4)
COPh	197.3	-	-	197.3	-	-
COBn	150.8	-	-	150.8	-	-
2×OCH ₃	56.0	3.7; 3.8	(s, 3H, OCH ₃); (s, 3H, OCH ₃)	56.0	3.6; 3.8	(s, 3H, OCH ₃) (s, 3H, OCH ₃)
Ar	150.8	6.8	(s, 1H, o-Ar)	150.8	6.8	(s, 1H, o-Ar)
	138.3	7.0	(s, 1H, o-Ar)	138.3	6.9	(s, 1H, o-Ar)
	133.6	7.2-7.3	(m, 5H, Ar)	133.6	7.4-7.5	(m, 2H, Ar)
	130.3	7.5-7.7	(m, 5H, Ar)	130.3	7.6	(m, 1H, Ar)
	129.4			129.4	7.6-7.7	(m, 2H, Ar)
	129.1			129.1		
	128.6			128.6		
	126.7			126.7		
	114.3			114.3		
	113.2			113.2		

a) In DMSO-*d*₆ solution.

On the other hand the IR-spectra of L2 showed a band at 3339 cm⁻¹ that may refer to the stretching vibrations of the N-H group of the ketoamide. The vibrational stretching modes did not appear in the Raman spectrum of L2 and Zn(II)L2. In the IR spectrum of the Zn(II)L2 complex a broad band was observed at 3500-3400 cm⁻¹, confirming the presence of OH group. The C=O stretching vibration gives rise to strong IR bands and weak Raman bands [13]. The carbonyl C=O stretching band was easily identified in the IR spectrum because of its intensity and its lack of interference from most other group frequencies. In the IR spectrum of L2 the bands at 1691 cm⁻¹ can be attributed to stretching vibrations of C=O group from the keto group and at 1656 cm⁻¹ to C=O from the carbamate group. The first vibrational stretching modes did not appear in the Raman spectrum of the free ligand and the second appeared at 1652 cm⁻¹. The same bands in the Raman spectrum of the Zn(II)L2 complex appeared at 1689 cm⁻¹ and 1652 cm⁻¹. Unfortunately, there is a little difference in the stretching vibration of the CO from the ester COOCH₂CH₃ group. The cleavage of the intramolecular hydrogen bond is probably observed. According to that presuming it would be difficult to handle the characteristic bands and the observed changes in the complex spectra would be insignificant. Several bands in the Raman spectrum of the ligand L2 (3065, 3014 cm⁻¹) and in the IR spectrum (3082, 3065, 3055, 3026, 3011 cm⁻¹) were for stretching vibrations of CH in the benzene moiety.

The Raman data of the free ligands L1 and L2 and their metal complexes with Zn(II) and Pd(II) are presented in Table 2.

Table 2. Raman data of the free ligands L1 and L2 and their metal complexes with Zn(II) and Pd(II)

Raman data of free ligand L1	Pd(II)L1 complex
3058, 3004, 2936, 1670, 1598, 1574, 1449, 1347, 1268, 1240, 1173, 1103, 1061, 1031, 1000, 878, 830, 749, 721, 616, 552, 475, 408, 371, 349, 241.	3059, 2935, 1670, 1598, 1574, 1448, 1341, 1031, 1000, 760, 720.
Raman data of free ligand L2	Zn(II)L2 complex
3065, 3014, 2939, 2606, 1652, 1599, 1571, 1452, 1391, 1362, 1346, 1332, 1298, 1268, 1218, 1176, 1104, 1062, 1031, 1002, 971, 950, 888, 852, 818, 751, 721, 688, 617, 578, 552, 496, 476, 411, 379, 345, 304, 278, 248, 229.	3065, 2935, 1689, 1652, 1599, 1571, 1444, 1362, 1345, 1332, 1268, 1176, 1104, 1062, 1031, 1002, 888, 751, 721, 617, 552, 496, 410, 381, 345, 228.

The ¹H-NMR data of the Zn(II)L2 complex showed that NH signal changes from 7.06 ppm (t, 1H, NH, J=6 Hz) in the ligand's NMR to 8.02 ppm (t, 1H, NH, J=5.4 Hz) in the complex NMR. The ¹³C-NMR spectral data showed that the signal for C-atom from keto group (COOC₂H₅) was observed at 156.5 ppm in the ligand L2, while that in the Zn(II) complex at 170.4 ppm. The observed chemical shifts (14 ppm) clearly indicate

P.E. Marinova *et al.*: Novel complexes of *N*-substituted-4,5-dimethoxy-phenylethyl-2-arylketoamides with metal ions coordination of keto group to the metal center. According to the NMR-data we can suggest that NH and CO group from the carbamate are involved in complexation with the Zn(II) ion. The signal for the carbonyl group (from the ketone) in the ^{13}C -NMR spectrum of the complex and ligand was observed at 197.3 ppm and did not change.

The most probable structure of the Zn(II)L2 complex was suggested with two ligand molecules coordinated in a bidentate fashion and two OH groups coordinated to the metal centre (octahedral geometry for metal ion) (Figure 3). The structure of the obtained Zn(II)L2 complex was similar to those presented by Bhagwan *et al.* for *N*-(pyridyl)-3-carboxypropanamide and *N*-(pyridyl)-3-carboxybenzamide with Zn(II) [13].

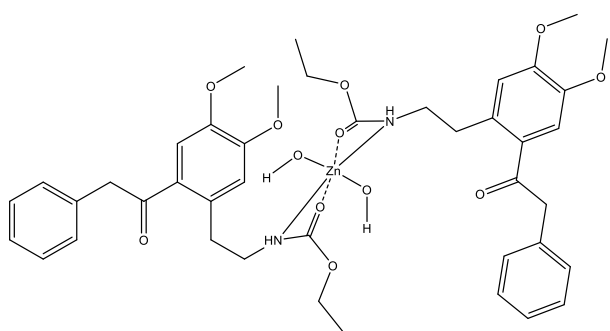


Figure 3. Suggested structure for the Zn(II) complex

CONCLUSIONS

The synthesis of new Pd(II) and Zn(II) complexes with ketoamide and ketoester, respectively have been described. The IR and ^1H - ^{13}C -NMR data showed, that in Pd(II)L1 complex the ligand behaves as a monodentate with N-atom from NH group. For Zn(II)L2 complex we suggested that L2 coordinates as a bidentate ligand

with N- and O-atoms involved in complexation and formed the chelate structure. The IR data for both complexes showed presence of OH group, most probably coordinated to the metal center, thus forming square planar (Pd(II)L1) and octahedral geometry (Zn(II)L2).

Acknowledgment: We acknowledge the financial support from the Fund for Scientific Research of the University of Plovdiv, project FPI7-HF-013.

REFERENCES

1. I. Ivanov, S. Nikolova, D. Aladjov, I. Stefanova, P. Zagorchev, *Molecules*, **16**, 7019 (2011).
2. R. G. Ball, R. S. Brown J. L. Cocho, *Inorg. Chem.*, **23**, 2315 (1984).
3. E. Kimura, S. Tabeshi, K. Tohr, S. Motto, K. Mutsuo, *J. Am. Chem. Soc.*, **112**, 5805 (1990).
4. H. Sigel, R. B. Martin, *Chem. Rev.*, **82**, 385 (1982).
5. M. M. Shoukry, M.R. Shehata, A. Abdel-Razik, A.T. Abdel-Karim, *Monatsh. für Chem.*, **130**, 409, (1999).
6. M. R. Shehata, *Transition Met. Chem.*, **26**, 198 (2001).
7. M. C. Lim, *J. Chem. Soc. Dalton Trans*, 726 (1978).
8. A. A. El-Sherif, M. M. Shoukry and R. van Eldik, *J. Chem Soc Dalton Trans*, 1425 (2003).
9. M. R. Shehata, M. M. Shoukry, A.A. Osman, A.T. AbdelKarim, *Spectrochim. Acta A*, **79**, 1226 (2011).
10. M.R. Shehata, Ragab M.S. Shoukry, *Cent. Eur. J. Chem.*, **10** (4), 1253 (2012).
11. M. R. Shehata, *Arabian Journal of Chemistry*, (2014). <https://doi.org/10.1016/j.arabjc.2014.11.017>
12. G. W. Bushnell, K. R. Dixon, R. G. Hunter, J. J. Mcfarlan, *Canad. J. Chem.*, **50**, 3694 (1972).
13. P. Larkin, *Infrared and Raman Spectroscopy. Principles and Spectral Interpretation*, 1st edn., Elsevier, 2011, p.126, ISBN: 9780123869845.
14. S. G. Bhagwan, V. Kumar, M. J. Reddy, *Indian J. Chemistry*, **35**, 598 (1996).

Kinetic analysis of ultrasound leaching of nickel laterite ore

P. Paunović*, G. Načevski, A. Petrovski, A. Tomova, A. Grozdanov, A. T. Dimitrov

*Faculty of Technology and Metallurgy, University “Sts. Cyril and Methodius”
Ruger Bošković Str., 16, 1000 Skopje, R. Macedonia*

Received October 30, 2018; Revised January 10, 2019

The subject of this study is the ultrasound leaching process of nickel-bearing laterite ore from Ržanovo, R. Macedonia. The studied ore was characterized by means of X-ray fluorescence method (XRF), X-ray diffraction method (XRD), thermal analysis (TGA, DTA, DTG) and optical microscopy. The influence of sulfuric acid concentration (1, 2 and 3 M H₂SO₄) on the extracted Ni (% wt.) was investigated. Further, ultrasound leaching at different temperatures (298, 313, 323 and 348 K) was performed. These results were used for kinetic analysis of the process. It was found that for 3 M H₂SO₄, the best fitting has shown the Ginstling-Braunshtein model, which points out that the limiting step of the process is diffusion. Activation energy was calculated to be 33.1 kJ·mol⁻¹, which confirms the diffusion controlled process.

Keywords: nickel-bearing laterite ore, ore characterization, ultrasonic leaching, kinetic models, activation energy.

INTRODUCTION

Nickel and its alloys have important role in modern life for variety of applications [1]. Industrial production of nickel is based on sulfide and laterite (oxide) ores. Although laterite ores are more abundant (about 70 % of the land reserves), with lower negative impact to environment and lower mining cost, their contribution in the world's nickel production is only 40 % [2-4]. The present technological processes for nickel production from laterite ores are based on both pyro- and hydrometallurgical routes [5, 6]. The pyrometallurgical ones include ferronickel smelting *via* the rotary kiln-electric furnace (RKEF) process and nickel matte smelting, while the hydrometallurgical techniques include high-pressure acid leaching (HPAL) and the Caron process. HPAL procedure requires expensive aggregates – autoclaves, while in the Caron process, pyrometallurgical reduction roasting is included before the ammonia leaching.

In finding new cheaper and ecologically friendly technologies for nickel extraction from laterite ores, the research work was focused on development of leaching under atmospheric pressure or atmospheric leaching, AL. The research studies of AL are directed to the use of different acid solvents such as sulfuric acid [7], hydrochloric acid [8], nitric acid [9], citric acid, acetic acid and oxalic acid [10,11]. With an appropriate optimization of the AL process, i.e. with overcoming the usual problems such as high acid consumption, high content of iron content in the solution and high residual acid concentration, AL could reach the effectiveness of

HPAL process [12].

The aim of this work was to investigate the LA process using sulfuric acid, intensified by ultrasound. Also, kinetic analysis of the ultrasound atmospheric leaching was done, determining both, the rate-limiting step and the activation energy of the leaching process.

EXPERIMENTAL

Ore

The subject of study was low-grade nickel-bearing laterite ore from Ržanovo mining area near the ferronickel smelting plant FENI INDUSTRI, Kavadarci in R. Macedonia. It belongs to intermediate type Saprolitic ores classified in the class C, due to increased content of MgO (12–16 %, wt.) and Fe (25–33 %, wt.). Mechanical preparation of the ore was performed within the production line of the FENI INDUSTRI, Kavadarci. The set of different sieves (0.200 mm, 0.104 mm, 0.074 mm, 0.043 mm and 0.037 mm) was used for determination of the granulometric composition. The dominant fraction with the highest content of Ni was chosen for further study. Before the leaching, magnetic separation was done in order to reduce the amount of Fe, and to increase the Ni content.

The composition of the ore was measured by X-ray fluorescence spectroscopy, using XRF ARL 9900 spectrometer. Thermal analysis was performed by TGA/DTA/DTG technique, using Perkin Elmer Diamond instrumentation. The sample was heated from 25 to 1000 °C, with a heating rate of 20 °C·min⁻¹. XRD measurements were carried out by X-ray powder diffractometer

* To whom all correspondence should be sent.

Philips APD 15, with CuK α radiation. The diffraction data were collected at a constant rate of 0.02 deg \cdot s $^{-1}$ over an angle range of 2 θ from 5 deg to 80 deg. Microscopic observation of the ore morphology was performed by Jeol Superprobe 737 microscope.

Ultrasonic leaching

Experimental setup for ultrasonic leaching of Ni-bearing ore is shown in Fig. 1. Glass reactor (1) is immersed into ultrasound bath (2) filled with water. The ultrasound bath has a system for temperature regulation. The aqueous cooler (3) connected with a tap through rubber hose (4) provides cooling of the reactor and avoiding evaporation of the solvent, thereby increasing the pressure in the reactor. The temperature is measured with a mercury thermometer (5).



Figure 1. Experimental setup for ultrasound leaching.

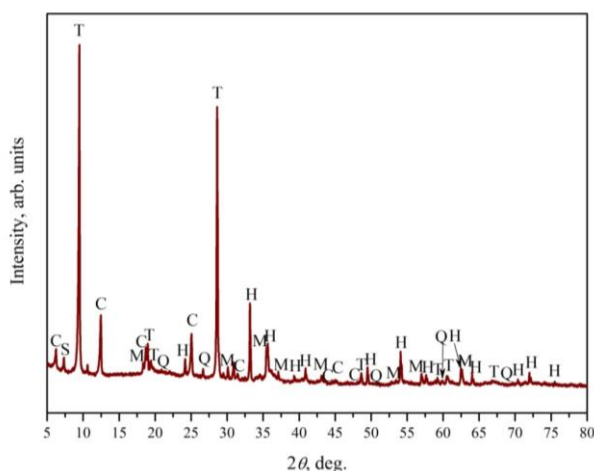


Figure 2. XRD spectrum of the Ržanovo's ore: H - hematite (Fe $_2$ O $_3$, rhombohedral), C - clinochlore ((Mg $_5$ Al)(Al,Si) $_4$ O $_{10}$ (OH) $_8$, triclinic), T - talc (Mg $_3$ Si $_4$ O $_{10}$ (OH) $_2$, monoclinic), Q - quartz (SiO $_2$, hexagonal), S - stilpnomelane (Fe $_2$ (Si $_3$ O $_9$), triclinic), M - magnetite (Fe $_3$ O $_4$, cubic).

As a solvent, H $_2$ SO $_4$ with different concentrations (1, 2 and 3M) was used. The ratio of solid vs. liquid phase was 1:50 (5g ore in 250 ml aqueous solution of H $_2$ SO $_4$). The leaching was performed under atmospheric pressure at different temperatures: 25, 40, 50 and 75 °C (298, 313, 323 and 348 K). For each leaching experiment, samples of 5 ml were taken at the following time interval: 5, 15, 30, 60, 90, 120 and 150 min.

Concentration of leached Ni was determined by atomic absorption spectrometry (AAS) using a spectrometer model PinAAcle 900F (PINAACLE900F).

RESULTS AND DISCUSSION

Preparation and characterization of ore

Chemical composition of the raw ore is shown in Table 1. It can be seen that Ržanovo's ore belongs to the low-grade nickeliferrous laterite ores with Ni content of 0.85 %, wt., moderate content of Fe (27.7 %, wt.) and increased content of magnesia (14.3 %, wt.) and silica (32.3 %, wt.). Present minerals within the studied lateritic ore were detected by XRD analysis, the corresponding spectrum is shown in Figure 2. According to the XRD spectrum, dominant mineral is hematite (Fe $_2$ O $_3$), while less, but considerable amount have shown talc (Mg $_3$ Si $_4$ O $_{10}$ (OH) $_2$) and clinochlore ((Mg $_5$ Al)(Al,Si) $_4$ O $_{10}$ (OH) $_8$). Quartz (SiO $_2$), magnetite (Fe $_3$ O $_4$) and stilpnomelane (Fe $_2$ (Si $_3$ O $_9$)) are shown as minor phases.

After mechanical preparation (crushing and milling), the granulometric composition was determined by sieve analysis. Corresponding composition of different granulometric fractions and corresponding distribution of the ore's components within each fraction is shown in Table 2. The finest fraction (below 0.037 mm) has shown to be the dominant one (67.2%), containing increased amount of Ni (up to 0.92%) and it was selected for further treatment. Before the leaching, magnetic separation was performed in order to reduce the amount of Fe. Ni mostly remains in the non-magnetic fraction, while Fe turns to magnetic one. As can be seen in Table 3, non-magnetic fraction contains a considerably decreased amount of Fe, up to 16.76 %, while the Ni content increased to 1.03%. This fraction was further submitted to the leaching study.

The results of thermal analysis of the ore are shown in Fig. 3. The first DTG maximum is less pronounced and appears at 85 °C. It is followed by low weight loss of 0.15 % (TG curve) and corresponds to removal of the physically adsorbed moisture of the previously dried ore.

Table 1. Composition of raw Ržanovo's ore

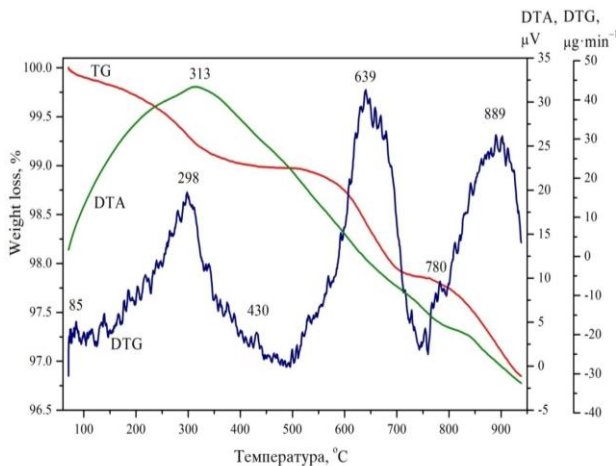
Components	Fe	Ni	Co	Cr	CaO	MgO	Al ₂ O ₃	SiO ₂
%, wt.	27.70	0.85	0.04	1.90	1.70	14.30	1.50	32.30

Table 2. Granulometric composition after mechanical preparation of the ore

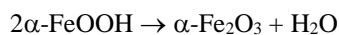
Granulometric fraction, mm	Granulometric composition, %, wt.	Contribution of the components in each fraction, %, wt.							
		Fe	Ni	Co	Cr	CaO	MgO	Al ₂ O ₃	SiO ₂
-0.200 + 0.104	11.5	33.09	0.75	0.04	2.0	1.7	13.1	1.4	25.6
-0.104 + 0.074	11.0	34.28	0.75	0.04	1.9	1.6	12.9	1.4	23.9
-0.074 + 0.043	7.3	32.59	0.8	0.04	1.9	1.8	13.1	1.6	25.4
-0.043 + 0.037	3.0	30.00	0.85	0.04	1.9	1.8	13.2	1.5	27.2
-0.037	67.2	24.75	0.92	0.04	1.9	1.7	14.7	1.6	35.8

Table 3. Composition after magnetic separation of the ore fraction -0.037 mm

Fraction	Contribution, %, wt.	Fe	Ni	CaO	MgO	SiO ₂
Magnetic	5.70	48.11	0.35	1.14	10.55	9.25
Non-magnetic	94.30	16.76	1.04	1.73	15.26	44.26

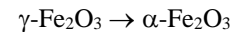
**Figure 3.** TGA-DTA-DTG spectra of the Ržanovo's ore.

The next DTG maximum at 297 °C is followed with weight loss of near 1 % and corresponds to removal of hydroxylic water (dehydration). It is likely that the hydroxylic water in the ore is present in the goethite, α -FeOOH, and this peak corresponds to the transformation of the goethite to hematite by the releasing of hydroxylic water [13,14]:



The relatively low temperature of this transformation indicates that the hematite is amorphous or is poorly crystalline with a very small size of crystalline grains [13,15]. This is a logical explanation why the goethite was not detected by the XRD analysis. According to the literature, a highly crystalline goethite transforms at 385 °C, showing strongly shaped peak [16,17]. Also, the dehydration occurs directly without the

formation of intermediary phases [18], or a small amount of magnetite can appear as an intermediate [19]. Also, during the transformation, there may be a significant change in the porosity and morphology of the ore particles [20]. Less pronounced DTG maximum is recorded at 430 °C. This maximum can be attributed to the partial transformation of the maghemite (γ -FeOOH) to hematite:



Maghemite was previously detected by XRD analysis. At 640 °C a more pronounced DTG peak is positioned, followed by a loss of mass of about 2%. This peak corresponds to a complete transformation of the maghemite to hematite [21]. A less intense peak was recorded at 720 °C [13], with a small additional weight of 0.3% (total 2.3%). According to the literature, in this temperature range there is increased mobility of the atoms, which leads to an increase of activation energy, to loss of the anisotropy of the oblique of the hematite grains and to interstitial sintering which means beginning of agglomeration of the grains, and further reduction of the real surface of the material. The DTG peak appearing at 890 °C corresponds to transformations in nickel-iron serpentines [22].

Microscopic images of the ore morphology are shown in Fig. 4. In Fig. 4a one can see a matrix of clay-based minerals intimately mixed with iron oxides formed by erosion. In some cases, small polygonal grains of corroded magnetite with gray color and good reflection ability are observed (Fig. 4b).

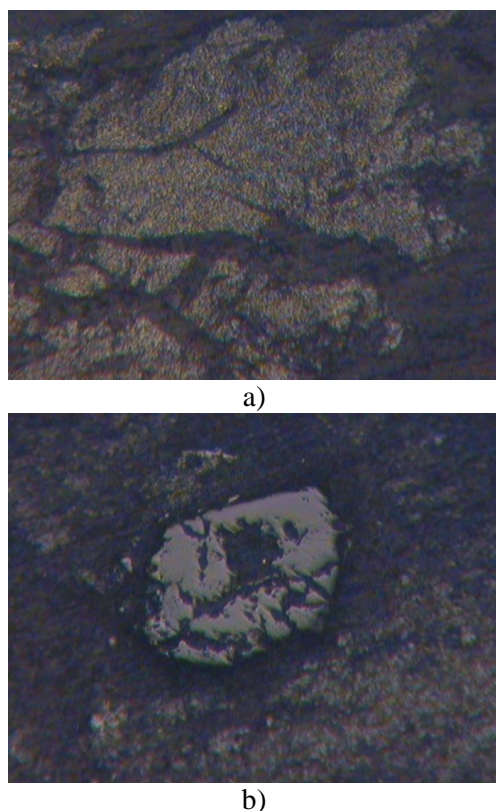


Figure 4. Microscopic images of the Ržanovo's ore.

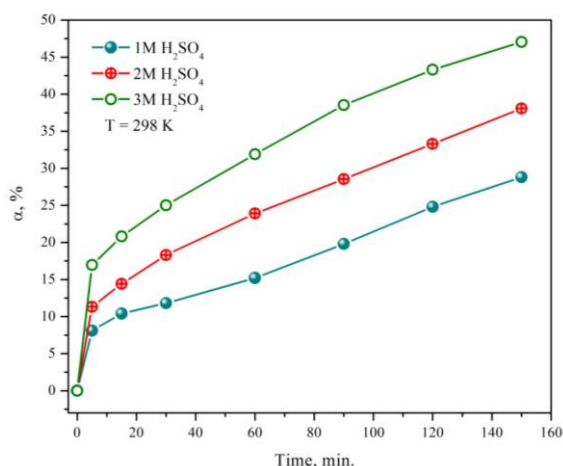
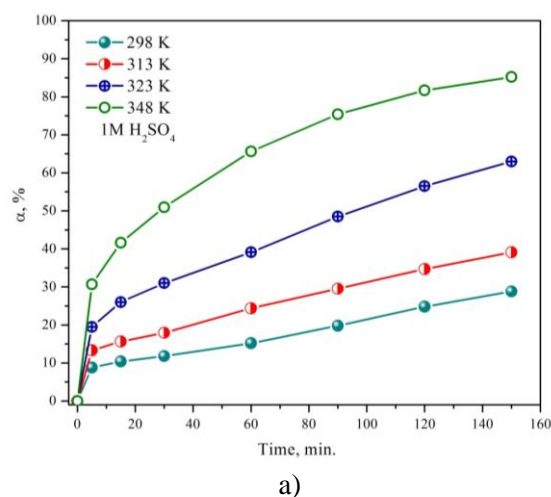


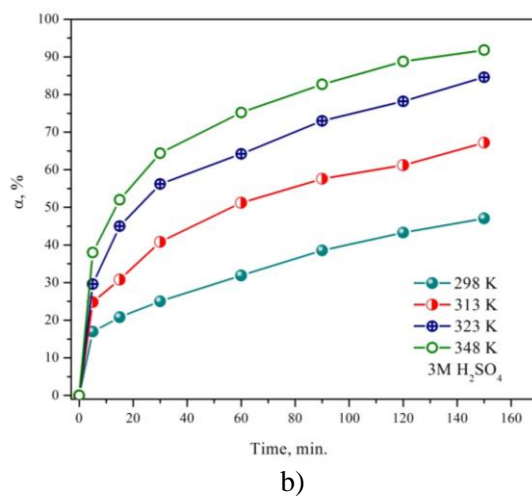
Figure 5. Diagram of yield of leached fraction α – time dependence for different concentrations of H_2SO_4 at ambient temperature.

Ultrasound leaching

The first step in the study of the ultrasound leaching of nickel laterite ore was the determination of the influence of solvent (H_2SO_4) concentration at ambient temperature (298 K). In Fig. 5 is shown the change of the yield of the leached fraction (α) during the leaching process. As can be seen, the yield of the leached fraction increases with time. Within the experimental time, the diffusion region of the curve is not reached. Also, with increasing of the solvent (H_2SO_4) concentration, the yield of the leached fraction increased, from 28.8 % in 1M H_2SO_4 , to 47.06 % in 3M H_2SO_4 .



a)



b)

Figure 6. Diagram of yield of leached fraction α – time dependence for different temperatures in a) 1 M H_2SO_4 and b) 3 M H_2SO_4 .

In Fig. 6, the change of the yield of the leached fraction at different temperatures is shown, for 1 and 3 M H_2SO_4 . It is obvious that the temperature considerably intensifies the leaching process. After 150 min leaching in 1 H_2SO_4 , the yield of the leached fraction increased from 28.8 % at ambient temperature (298 K) to 85.2 % at 75 °C (348 K). In 3 M H_2SO_4 , the rise of α ranged from 47.06 % at ambient temperature (298 K) to even 91.8 % at 75 °C (348 K). In Table 4, the comparison of the yield of leached fraction of ultrasound leaching and leaching with magnetic stirrer [23] after 120 min at 75 °C (348 K) is given. As can be seen, the ultrasound considerably increases the leaching process. In 3 M H_2SO_4 , the maximal yield of the leached fraction is 70.3 %, while in 1 M H_2SO_4 with ultrasound leaching this yield is 81.68 %, by almost 10 % higher. In 3 M H_2SO_4 with ultrasound leaching the yield of the leached fraction is 88.8 %, almost 20 % higher. Under the action of ultrasound, ultrasonic flows and cavitation occur in the solution, where the fluid intensively mixes and penetrates into the pores and cracks of the ore

particles. At more intense ultrasound regimes, one can come to cavitation destruction of solid particles and surface films. This increases the reaction surface of the solid ore particles, decreases the diffusion layer, and all this contributes to considerable intensifying the leaching process.

Table 4. The yield of leached fraction α (%), obtained at different leaching regimes after 120 min at 75 °C (348 K)

	Leaching regimes		
	Magnetic stirrer 3 M H ₂ SO ₄	Ultrasound 1 M H ₂ SO ₄	Ultrasound 3 M H ₂ SO ₄
α , %	70.32	81.68	88.8

Kinetic analysis of the ultrasound leaching

In general, leaching of nickel laterite ores can be described by the shrinking core model (Fig. 7), where the chemical reaction on the core surface or diffusion can be rate-determining step of the process [24,25].

If the leaching process is controlled by a chemical reaction, it can be described by the Spenser-Topley-Kewan model [26]:

$$1 - (1 - \alpha)^{\frac{1}{3}} = k_S \cdot t, \tag{1}$$

$$k_S = \frac{k \cdot C}{r_0 \cdot \rho}, \tag{2}$$

where α is yield of reacted fraction, k_S is Spenser-Topley-Kewan rate constant, k reaction rate constant, C is concentration of the solid reactant (ore particle), r_0 is radius of the solid reactant, ρ is density of the solid reactant and t is duration of the chemical reaction.

If the leaching process is controlled by the diffusion, it can be described by the Ginstling-Braunshstein model [27]:

$$1 - \frac{2}{3} \cdot \alpha - (1 - \alpha)^{\frac{2}{3}} = k_G \cdot t \tag{3}$$

$$k_G = \frac{2 \cdot M \cdot D \cdot C}{a \cdot \rho \cdot r_0^2} \tag{4}$$

where k_G is Ginstling-Braunshstein rate constant, M is molecular weight of the solid reactant, D is diffusion coefficient and a is a stoichiometric coefficient.

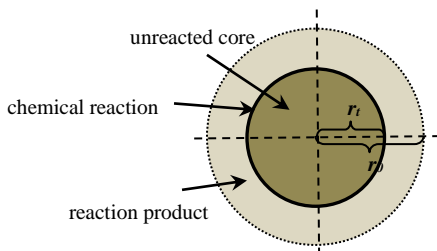
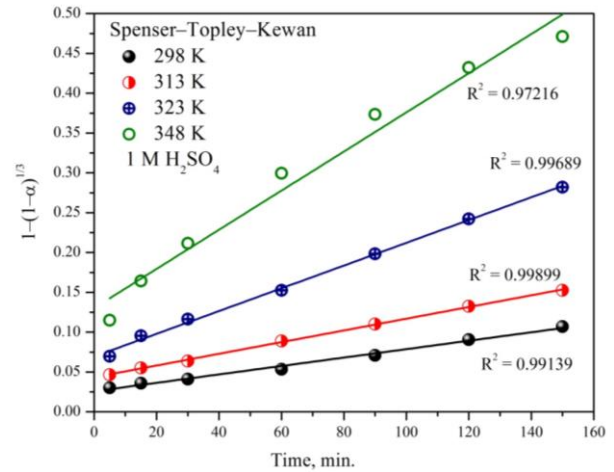


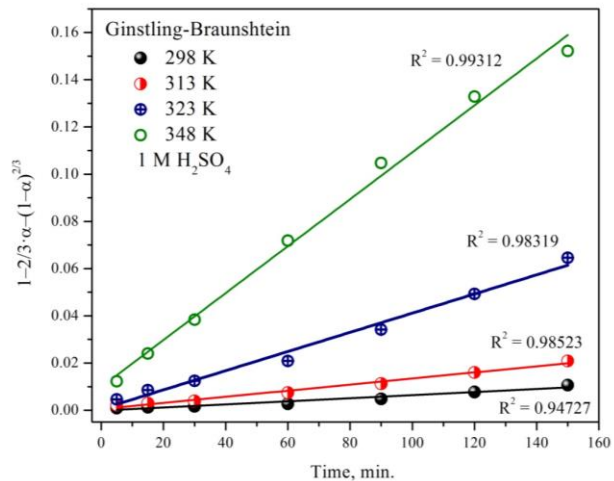
Figure 7. Schematic view of the shrinking core model: r_0 - starting radius of the reacting ore article; r_1 -

radius of the reacting ore article after some time t .

The data from the diagrams in Figs. 8 and 9 were replaced in the model equations (1) and (3), and the corresponding straight-lines are shown in Figs. 10 and 11 for 1 and 3 M H₂SO₄, respectively. The leaching process in 1 M H₂SO₄, at lower temperatures (from 25 to 50 °C) was described by the Spenser-Topley-Kewan equation, which means that in this temperature region the rate-determining step of the process is the chemical reaction. At higher temperatures, Ginstling-Braunshstein model describes the process better and the rate-determining step of the process is diffusion. The leaching process in 3 M H₂SO₄ in the whole temperature region is better described by the Ginstling-Braunshstein model. This points out diffusion as rate-determining step of the ultrasound leaching process.

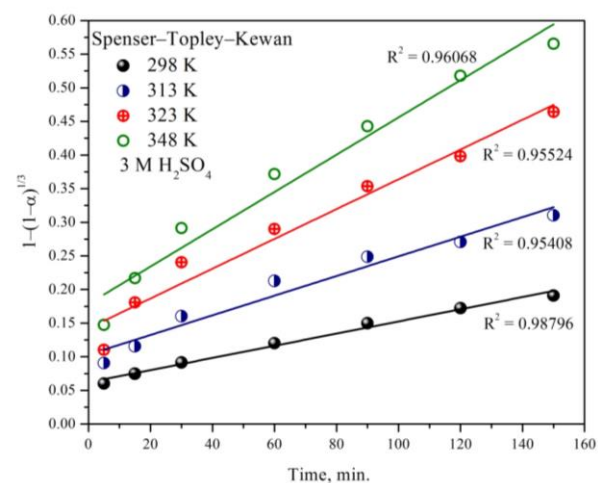


(a)

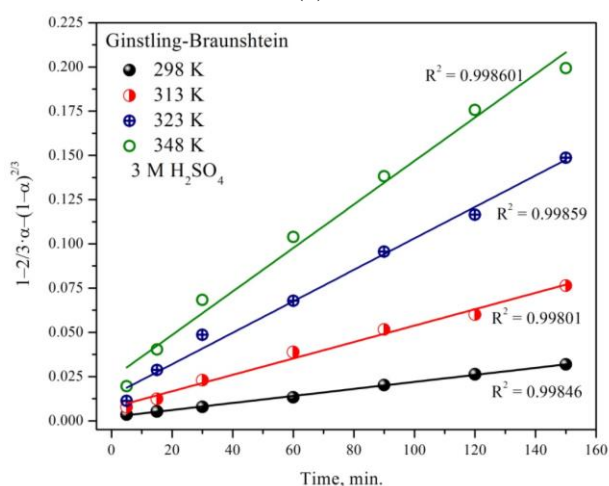


(b)

Figure 8. Linear fit of nickel leaching process in 1 M H₂SO₄ described by a) Spenser-Topley-Kewan model and b) Ginstling-Braunshstein model.



(a)



(b)

Figure 9. Linear fit of nickel leaching process in 3 M H₂SO₄ described by a) Spenser-Topley-Kewan model and b) Ginstling-Braunshtein model.

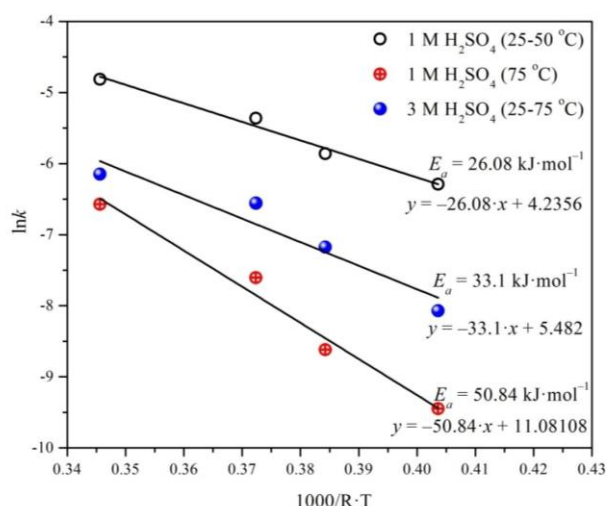


Figure 10. Arrhenius plots of nickel leaching process.

Using the Arrhenius equation:

$$\ln k = -\frac{E_a}{R \cdot T} + \ln A \quad (5)$$

where k can be Spenser-Topley-Kewan (k_S) or Ginstling-Braunshtein (k_G) rate constant, R is universal gas constant, T is temperature and A is the Arrhenius constant, the activation energy, E_a of the leaching process can be determined by further derivation of the previous experimental data and results. In Fig. 10, constructed straight-lines of Arrhenius equation and determined values of activation energy for the leaching process are shown. At lower temperature range to 50 °C in 1 M H₂SO₄, activation energy was determined using the temperature dependence of the Spenser-Topley-Kewan rate constant (k_S) and showed a value of 26.08 kJ·mol⁻¹·K⁻¹. Corresponding value of E_a for higher temperature region, determined using temperature dependence of the Ginstling-Braunshtein rate constant (k_G), is 50.84 kJ·mol⁻¹·K⁻¹. These values are in agreement with the literature data. Activation energy for leaching process in 3 M H₂SO₄, using k_G , in whole temperature region was determined to be 33.1 kJ·mol⁻¹·K⁻¹.

CONCLUSIONS

According to the above presented results, we can draw the following conclusions:

1. Ržanovo's ore belongs to the low-grade nickel-ferrous laterite ores with low Ni content of 0.85 %, wt., moderate content of Fe (27.7 %, wt.) and increased content of magnesia (14.3 %, wt.) and silica (32.3 %, wt.). Dominant compound in the ore is hematite, α -Fe₂O₃, but there is also a considerable amount of talc, Mg₃Si₄O₁₀(OH)₂ and clinoclhor, (Mg₅Al)(SiAl)₄O₁₀(OH)₈ and less of quartzit, SiO₂, magnetite, Fe₃O₄, maghemite, γ -Fe₂O₃ and stilpomelan, Fe₂(Si₃O₉).

2. According to granulometric analysis, the richest fraction with Ni (0.92 %, wt.) is -0,037 mm. After magnetic separation, the content of Ni in the non-magnetic fraction increases to 1.03%.

3. Maximal nickel extraction of 91.8 % was achieved by ultrasound leaching in 3M H₂SO₄ at 75 °C.

4. Ultrasound significantly intensifies the leaching process compared to the magnetic stirrer. Ultrasound causes ultrasonic flows and cavitation in the solution, where the fluid intensively mixes and penetrates into the pores and cracks the ore particles. As a result, there is an increase of the reaction surface of the solid ore particles, decrease of the diffusion layer, contributing to considerable intensifying the leaching process.

5. The leaching process in 1M H₂SO₄ at lower temperatures is best described by the Spenser-Topley-Kewan model (chemically controlled), while at higher temperatures - by the Ginstling-Braunshstein model (diffusion controlled). The leaching process in 3 M H₂SO₄ in the whole experimental temperature region is best described by the Ginstling-Braunshstein model (diffusion controlled). Activation energy for the leaching in 1M H₂SO₄ was determined to be 26.08 kJ·mol⁻¹·K⁻¹ for chemically controlled and 50.84 kJ·mol⁻¹·K⁻¹ for diffusion controlled process. Activation energy in 3 M H₂SO₄ was determined to be 33.1 kJ·mol⁻¹·K⁻¹ in the whole temperature region.

REFERENCES

1. F. Crundwell, M. Moats, V. Ramachandran, T. Robinson, W.G. Davenport, Extractive Metallurgy of Nickel, Cobalt and Platinum Group Metals, Elsevier, 2011.
2. A. D. Dalvi, W. Gordon Bacon, R. C. Osborne, The Past and the Future of Nickel Laterites, PDAC 2004 International Convention, Trade Show & Investors, Exchange, Toronto, March 7-10, 2004.
3. N. D. H. Munroe, *Metallurgical and Materials Transactions B*, **28**, 995 (1997).
4. USGS Bureau of Mines Yearly Statistics 1950-2003.
5. E. Ozberk, A. S. Gendron, G. H. Kaiura, Review of Nickel Smelters, Proceedings- Nickel Metallurgy, Vol. I: Extraction and Refining of Nickel, E. Ozberk and S. W. Marcuson (eds.), Met Soc. CIM and NiDI, Montreal (1986), p. 304.
6. S. R. Stopić, B. G. Friedrich, *Military Technical Courier*, **64**, 1033 (2016).
7. R.G. McDonald, B.I. Whittington, *Hydrometallurgy*, **91**, 35 (2008).
8. R.G. McDonald, B.I. Whittington, *Hydrometallurgy*, **91**, 56 (2008).
9. B. Ma, C. Wang, W. Yang, B. Yang, Y. Zhang, *Miner. Eng.*, **45** 151 (2013).
10. S. Sahu, N. C. Kavuri, M. Kundu, *Braz. J. Chem. Eng.*, **28**, 251 (2011).
11. A. Pawlowska, Z. Sadowski, *Physicochem. Probl. Miner. Process.*, **53**, 869 (2017).
12. E. Büyükakinci, Y.A. Topkaya, *Hidrometallurgy*, **97**, 33 (2009).
13. F. A. López, M. C. Ramirez, J. A. Pons, A. López-Delgado, F. J. Alguacil, *J. Therm. Anal. Calorim.*, **94**, 517 (2008).
14. Y.V. Swamy, B.B. Kar, J.K. Mohanty, *Hydrometallurgy*, **69**, 89 (2003).
15. H. Liu, T. Chen, X. Zou, C. Qing, R. L. Frost, Thermal treatment of natural goethite: Thermal transformation and physical properties, *Thermochim. Acta*, **568**, 115 (2013).
16. R. Derie, D. M. Ghodsi, C. Calvo-Roche, *J. Therm. Anal. Calorim.*, **9**, 435 (1976).
17. U. Schwertmann, *Thermochim. Acta*, **78**, 39 (1984).
18. C. J. Goss, *Mineral. Mag.*, **51**, 437 (1987).
19. Ö. Özdemir, D. J. Dunlop, *Earth Planet. Sci. Lett.*, **177**, 59 (2000).
20. V. Balek, V. J. Šubr, *Pure Appl. Chem.*, **67** 1839 (1995).
21. X. Song, J-F. Boily, *J. Phys. Chem. A*, **120**, 6249 (2016).
22. S. Stopić, B. Friedrich, R. Fuchs, *Erzmetall*, **56**, 198 (2003).
23. G. Načevski, P. Paunović, A. Petrovski, A. Grozdanov and A. T. Dimitrov, Leaching of nickel from Ržanovo's lateritic ore, Book of Abstracts, 3rd Metallurgical & Materials Engineering Congress of South-East Europe, MME SEE 2017, Belgrade, 1-3 June, 2017, p. 53.
24. O. Levenspiel, Chemical Reaction Engineering, John Wiley & Sons, Inc., New York, 1999.
25. F. Habashi (ed.), Handbook of extractive metallurgy, Volume I, WILEY-VCH, Weinheim, 1997.
26. W. D. Spenser, B. Topley, *J. Chem. Soc.*, **27**, 2633 (1929).
27. A. M. Ginstling, B. I. Braunshstein, *J. Appl. Chem. USSR*, **23**, 1327 (1950).

Palladium complexes containing dithiocycloheptanespiro-5'-hydantoin ligand. Synthesis, characterization, theoretical analysis and cytotoxic activity

E. Cherneva^{1,2*}, R. Buyukliev¹, A. Bakalova¹

¹ Department of Chemistry, Faculty of Pharmacy, Medical University - Sofia, 2 Dunav Str., 1000 Sofia, Bulgaria

² Laboratory of Structural Organic Analysis, Institute of Organic Chemistry with Centre of Phytochemistry, Bulgarian Academy of Sciences, Sofia, Bulgaria

Received November 01, 2018; Revised December 17, 2018

A new palladium complexes with dithiocycloheptanespiro-5'-hydantoin as ligand were synthesized and characterized. Elemental analyses, IR and NMR spectral measurements were used to verify the structures of the ligand and its complexes. The results of spectroscopic characterization confirm the S-coordination modes of the ligand. The coordination geometries around the palladium atoms and vibration frequencies were evaluated by DFT method. The metal complexes were screened *in vitro* for their anticancer activity

Keywords: palladium complexes, anticancer activity, DFT calculations

INTRODUCTION

Antitumor drugs like cisplatin, carboplatin, oxaliplatin and other platinum complexes play a significant role in the treatment of solid tumors [1,2]. However, the above mention platinum-based antitumor drugs have several serious disadvantages such as nephrotoxicity, renal and cervical problems, allergy, elevated blood pressure and others [3]. Because of side effects, scientists have used another strategy to design new cancer drugs similar to cisplatin, changing the nature of a metal ion. Palladium ion is often selected because of its structural similarity to platinum ion and its coordination pattern, i. e. it also forms square planar complexes [4-6]. There are a numerous cases in which palladium complexes have demonstrated higher anticancer activity *in vitro* than their platinum counterparts [7,8]. On the other hand the appropriate choice of ligand plays a crucial role in modifying biological properties [1]. Sulfur-containing ligands could improve the cytotoxicity *in vitro* and *in vivo* of the metal complexes [3].

Herein we describe the synthesis and spectral investigation of new palladium complexes with dithiocycloheptanespiro-5'-hydantoin as ligand. In order to get more information about their molecular structures, the newly synthesized compounds were studied by theoretical methods

EXPERIMENTAL

General information

All chemicals were purchased from Fluka (UK) and Sigma-Aldrich. The newly synthesized Pd (II)

and Pd (IV) complexes were characterized by elemental analyses, melting points, IR and NMR spectra. The elemental analyses were carried out on a "EuroEA 3000 – Single", EuroVectorSpA apparatus (Milan, Italy). Corrected melting points were determined, using a Buchi 535 apparatus (BuchiLabortechnik AG, Flawil, Switzerland). The IR spectra were recorded on Thermo Scientific Nicolet iS10 spectrophotometer (Thermo Scientific, USA) in the range of 4000-400 cm⁻¹ as Attenuated Total Reflection Fourier Transform Infrared Spectroscopy (ATR-FTIR). The ¹H and ¹³C NMR spectra were recorded on a Bruker WM 500 (500 MHz) spectrometer. All theoretical calculations were performed using the Gaussian 09 package [9] of programs. Optimization of the structures of the ligand and Pd complexes were carried out by DFT calculations, employing the B3LYP (Becke's three-parameter non-local exchange [10]) and Lee et al. correlation [11] hybrid functional and 6-311++G** set for all non-metal atoms and LANL2DZ basis set for the palladium atom.

Synthesis of 1,4-Dithiepan-6-one

The starting ketone was synthesized according to procedure described by Cook and Bergesen [12] with small modifications.

A solution prepared from sodium (6 g) and ethane-1,2-dithiol (11.3 mL) in absolute ethanol (100 mL), were added dropwise to a solution of 1,3-dichloroacetone (15.2 g) in anhydrous diethyl ether (100 mL). The mixture was stirred for 3 hours at room temperature, poured with stirring into a mixture of diethyl ether (100 ml), 3% NaOH

* To whom all correspondence should be sent.
E-mail: e.d.cherneva@gmail.com

(250 mL) and powdered ice (100 g). The organic layer was separated and the aqueous layer extracted with diethyl ether (3 x 100 mL). The organic solutions were combined, filtrated, dried (MgSO₄) and the ether was evaporated with rotary evaporator. The crude ketone (7 g, 53%) was distilled at 94-98°C at 0.4 mmHg.

Synthesis of 3,6-dithiocycloheptanespiro-5'-hydantoin

1,4-dithiacycloheptan-6-one (2.96 g, 20 mmol) was dissolved in 60 mL aqueous ethanol. To the solution was added 2 g (40 mmol) NaCN and 6 g (60 mmol) (NH₄)₂CO₃. The mixture was stirred and heated at 65°C for 24 hours. After that the solution was acidified with conc. HCl in a strong ventilation hood to pH = 5. The precipitate was filtered off and recrystallized from aqueous ethanol. Yield 2.22 g (51%), m.p. 288-289°C.

Elemental analyses: C₇H₁₀N₂O₂S₂ (%), Calcd.: C 38.53; H 4.59; N 12.84; S 29.36. Found: C 38.71; H 4.71; N 12.35; S 28.98. ¹H NMR (250 MHz, DMSO-d₆): 10.63 (s, 1H, NH-3'); 8.23 (s, 1H, NH-1'); 3.27, 2.98 (AB quartet, 4H, J = 15 Hz, CH₂-5 + CH₂-7); 2.96-2.88 (m, 4H, CH₂-4 + CH₂-5). ¹³C NMR (62.5 MHz, DMSO-d₆): 177.1 (C=O - 4'); 156.5 (C=O - 2'); 67.8 (C - 5'); 40.3 (C-5 + C-7); 39.1 (C-2 + C-3).

Synthesis of Pd(II) complex with 3,6-dithiacycloheptanespiro-5'-hydantoin

An aqueous ethanol solution of the ligand (**4**) (0.10 g, 0.45 mmol) was added to the aqueous solution of K₂PdCl₄ (0.10 g, 0.30 mmol) and stirred for 6 hours at ambient temperature. The yellow-brown crystals were filtered off and dried under KOH and P₂O₅. The new Pd(II) complex was dissolved in DMSO. The purity was checked by thin-layer chromatography with the eluent CH₃COOC₂H₅/C₂H₅OH - 2:1, and elemental analyses.

Yield: 43%; mp. 307°C.

Elemental analyses: C₁₄H₂₀N₄O₄S₄Cl₂Pd (%). Calcd.: C 27.39; H 3.26; N 9.13. Found: C 27.08; H 2.97; N 8.87. ¹H NMR (500 MHz, DMSO-d₆): 10.23 (s, 1H, NH-3'); 8.25 (s, 1H, NH-1'); 3.44 (m, 1H); 3.25 (m, 1H); 3.19 (m, 1H), 3.12 (m, 1H); (CH₂-5 + CH₂-7); 3.08, 2.96, 2.94, 2.83 (four multiplets, 4H, CH₂-2 + CH₂-4).

¹³C NMR (125 MHz, DMSO-d₆): 177.2 (C=O - 4'); 156.2 (C=O - 2'); 80.1 (C-5 + C-7); 67.8 (C - 5'); 39.1 (C-4 + C-5).

Synthesis of Pd(IV) complex with 3,6-dithiacycloheptanespiro-5'-hydantoin

An aqueous ethanol solution of the ligand (**4**) (0.10 g, 0.46 mmol) and aqueous solution of K₂PdCl₆ (0.09 g, 0.23 mmol) were mixed and stirred

for 6 hours at ambient temperature. The obtained yellow-brown crystals were filtered off and dried under KOH and P₂O₅. The new Pd(IV) complex was dissolved in DMSO. The purity was checked by thin-layer chromatography with the eluent CH₃COOC₂H₅/C₂H₅OH - 2:1, and elemental analyses.

Yield: 31%; mp. 312°C (dec.).

Elemental analyses: C₁₄H₂₀N₄O₄S₄Cl₄Pd (%), Calcd.: C 24.55; H 2.92; N 8.18. Found: C 24.46; H 2.65; N 7.89. ¹H NMR (500 MHz, DMSO-d₆): 10.25 (s, 1H, NH-3'); 8.27 (s, 1H, NH-1'); 3.52 (m, 1H); 3.27 (m, 1H); 3.25 (m, 1H), 3.12 (m, 1H), (CH₂-5 + CH₂-7); 3.10, 2.98, 2.90, 2.82 (four multiplets, 4H, CH₂-2 + CH₂-4).

¹³C NMR (125 MHz, DMSO-d₆): 177.6 (C=O - 4'); 160.1 (C=O - 2'); 84.1 (C-5 + C-7); 68.1 (C - 5'); 41.1 (C-4 + C-5).

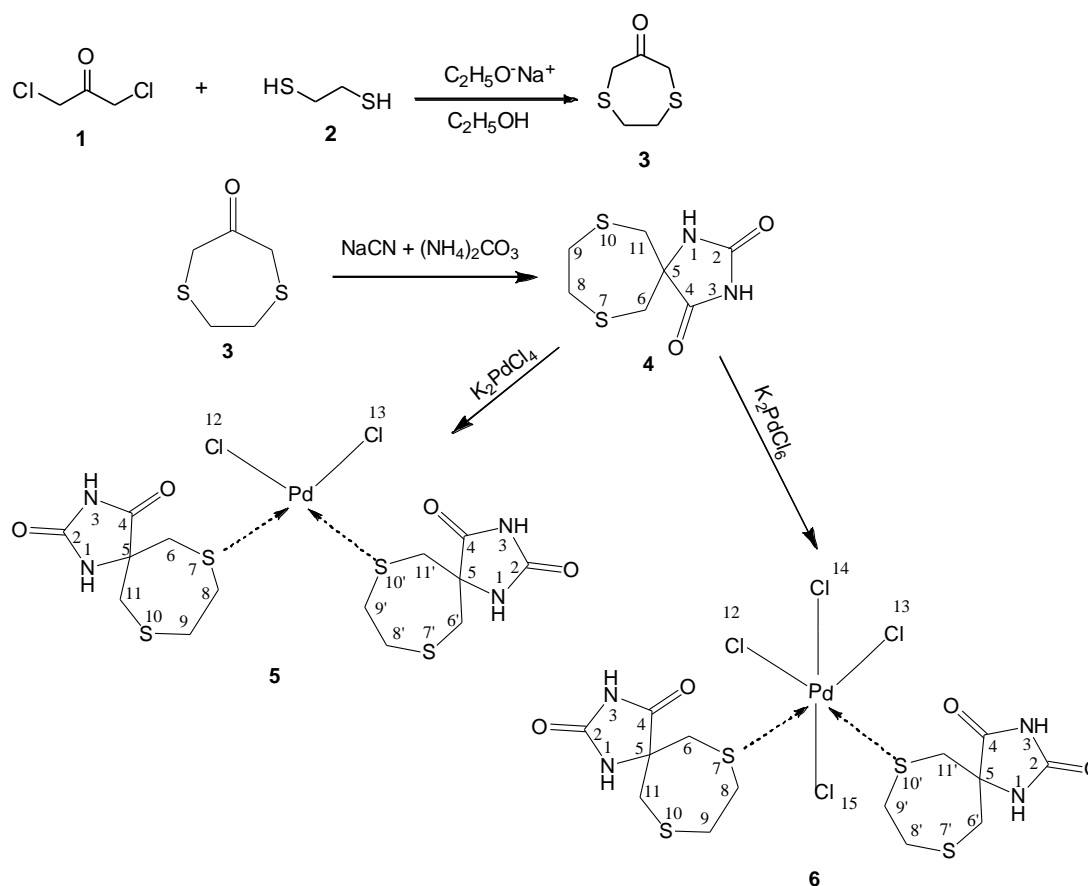
Cytotoxicity assessment

Cytotoxicity of the compounds was assessed using the MTT [3-(4,5-dimethylthiazol-2-yl)-2,5-diphenyltetrazolium bromide] dye reduction assay as described by Mossman [13] with some modifications [14]. Exponentially growing cells were seeded in 96-well microplates (100 μL/well at a density of 3.5 x 10⁵ cells/mL for the adherent and 1 x 10⁵ cells/mL for the suspension cell lines) and allowed to grow for 24 h prior the exposure to the studied compounds. Stock solutions of the investigated Pd(II) and Pd(IV) complexes were freshly dissolved in DMSO and then promptly diluted in RMPI-1640 growth medium, immediately before treatment of cells. At the final dilutions the solvent concentration never exceeded 0.5 %. Cells were exposed to the tested compounds for 72 h, whereby for each concentration a set of 8 separate wells was used. Every test was run in triplicate, i.e. in three separate microplates. After incubation with the tested compounds MTT solution (10 mg/mL in PBS) aliquots were added to each well. The plates were further incubated for 4 h at 37°C and the formazan crystals formed were dissolved by adding 110 μL of 5 % HCOOH in 2-propanol. Absorption of the samples was measured by an ELISA reader (UniscanTitertec) at 580 nm. Survival fraction was calculated as percentage of the untreated control. In addition IC₅₀ values were calculated from the concentration-response curves. The experimental data was processed using GraphPadPrizm software and was fitted to sigmoidal concentration/response curves *via* non-linear regression.

The structures of the synthesized compounds were confirmed by IR, NMR spectra and elemental analyses. The results were consistent with the assigned structures.

RESULTS AND DISCUSSION

Synthetic pathway to obtain the new ligand and its Pd complexes are illustrated on the Scheme 1.



Scheme 1. Synthesis of 3,6-dithiocycloheptanespiro-5'-hydantoin (4) and its Pd complexes (5,6)

Vibrational analysis

The most important vibrational frequencies for the investigated ligand and its Pd complexes are stretching vibrations of secondary amino groups, $\nu_{C=O}$ and C-S bonds. Broad bands for N-H stretching vibration are observed at 3237 cm^{-1} for the ligand and 3232 cm^{-1} , 3229 cm^{-1} for the complexes. The vibrations of the C=O bonds appear as two very strong bands at 1754 cm^{-1} and 1673 cm^{-1} for the ligand. In the complexes carbonyl stretching modes are observed around 1746 cm^{-1} and 1660 cm^{-1} . The bands for stretching vibrations of C-S bond of Pd complexes are shifted to lower frequency in comparison with ligand. They are measured at 644 cm^{-1} (theor.: 651 cm^{-1}) in the ligand and 623 cm^{-1} (theor.: 625 cm^{-1}) and 616 cm^{-1} (theor.: 625 cm^{-1}) in the complexes. The shifting of the frequencies characteristic for C-S bonds of 21 and 28 cm^{-1} in the complexes shows that the sulfur atom is coordinated with palladium ion.

NMR analysis

We assume that in the complexes only one sulfur atom is bonded. In the 1H NMR spectrum of the Pd(II) complex, there is a splitting of two AB

quartets for the two methylene groups at C-5 and C-7. The chemical shifts for the four protons of two methylene groups are 3.44 (axial) and 3.21 ppm (equatorial) of CH_2-7 and at 3.25(a) and 3.17(e) ppm of CH_2-5 while in the free ligand these values are 3.27(a) and 2.98(e) for CH_2-7 (increasing with 0.17 and 0.23 ppm), 2.95(a) and 2.88(e) for CH_2-5 (increasing with 0.30 and 0.29 ppm). This indicates the bonding between the metal ion and one of the sulfur atoms in the ring. The shifting of the C-2 and C-4 methylene groups are not influenced in the Pd(II) complex. All signals are simplified in comparison of the CH_2 signals in the free ligand, due to the fact, that cycloheptane ring has fixed conformation in the metal complex.

In the 1H NMR spectrum of Pd(IV) complex, the same differences of the chemical shifts of the CH_2-5 and CH_2-7 are observed: 0.25(a) and 0.27 (e) for CH_2-7 , respectively 0.29(a) and 0.25(e) for CH_2-5 .

Computational analysis

Due to the difficulties to obtain the crystals suitable for X-ray analysis we studied the structure of the ligand and its complexes mainly by theoretical methods. All the structures were

optimized at the DFT level with the B3LYP functional and the 6-311++G** basis set for all non-metal atoms and LANL2DZ basis set for the palladium atom. The calculations were used to obtain the important information about coordination

modes, geometrical parameters and spectroscopic properties of ligand (4) and complexes (5, 6). The optimized structures of the compounds (4,5,6) are presented in Figure 1.

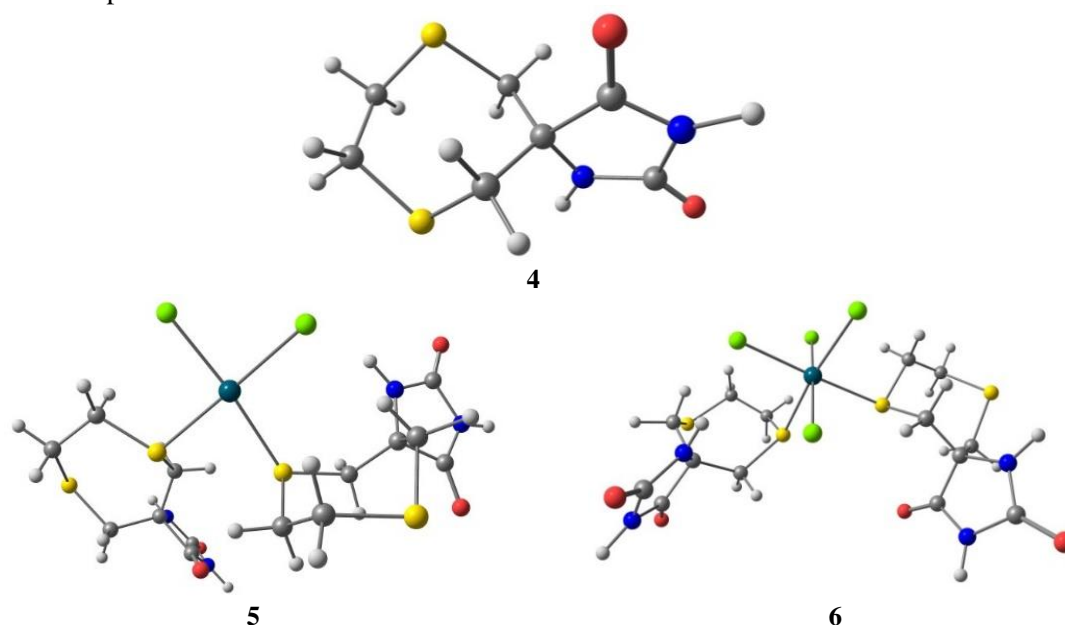


Figure 1. Optimized structures of ligand (4) and palladium complexes (5, 6)

Table 1. Selected calculated geometry parameters

Parameters	Ligand	[PdL ₂ Cl ₂]	[PdL ₂ Cl ₄]
$\mu(D)$	3.3	10.18	9.74
Bond lengths (Å)			
Pd-Cl ₁₂	-	2.36	2.39
Pd-Cl ₁₃	-	2.37	2.40
Pd-Cl ₁₄	-	-	2.42
Pd-Cl ₁₅	-	-	2.42
Pd-S ₇	-	2.50	2.53
Pd-S ₁₀	-	2.51	2.54
C ₆ -S ₇	1.83	1.90	1.91
C ₈ -S ₇	1.83	1.91	1.91
Angles (°)			
C ₆ -S ₇ -C ₈	100.4	99.9	99.2
C ₉ '-S ₁₀ '-C ₁₁ '	-	104.2	106.1
C ₆ -S ₇ -Pd	-	127.5	105.5
C ₈ -S ₇ -Pd	-	108.1	105.6
C ₉ '-S ₁₀ '-Pd	-	110.7	119.5
C ₁₁ '-S ₁₀ '-Pd	-	106.4	113.3
S ₇ -Pd-Cl ₁₂	-	97.4	95.9
S ₁₀ '-Pd-Cl ₁₃	-	90.2	87.6

The S-C bonds length becomes slightly longer than those in the ligand. There is small deviation in the calculated C-S-C bond angles in the complexes than those in the ligand by 3.8° and 0.5° in the complex (5) and 5.7° and 1.2° in the complex (6).

The Pd-S bond distance in the PdL₂Cl₂ complex is slightly shorter than that in the PdL₂Cl₄ complex by 0.03 Å. The Pd-S bond lengths are similar to those found in the literature for other optimized Pd complexes [15,16].

Table 2. *In vitro* evaluation of cytotoxicity of the ligand (4) and its palladium complexes (5,6) in comparison with referent drug cisplatin in three human tumour cell lines.

Compound	IC ₅₀ (μ M)		
	HL-60 ^a	REH ^b	LAMA-84 ^c
Ligand	132.5 \pm 6.6	n.d. ^d	142.2 \pm 6.9
Complex 5	98.6 \pm 6.8	48.7 \pm 5.1	60.0 \pm 6.2
Complex 6	123.1 \pm 11.5	29.4 \pm 3.7	33.1 \pm 4.1
Cisplatin	8.7	1.07	16.9

^aAcute myeloid leukemia; ^bAcute lymphoblastic leukemia^cHuman chronic myeloid leukemia; ^d n.d. - not detected*In vitro cytotoxicity*

The complexes (5,6) were tested for cytotoxic activity on a panel of human tumor cell lines - acute myeloid leukemia - HL-60, acute lymphoblastic leukemia - REH and Human chronic myeloid leukemia - LAMA-84. The results are summarized in Table 2.

In all cellular test systems, the organic compound (4) and complexes (5) and (6) showed dose-dependent anticancer activity in the tested concentration range following 72 h exposure time, whereby chemosensitivity of the different cell lines varied within a wide range. As evident from the presented data, complex (6), proved to be more active analogue then the complex (5) on the leukemic models REH and LAMA-84.

CONCLUSIONS

The structures of the synthesized compounds are confirmed by IR, NMR spectra and elemental analyses. Spectral analyses confirm that the ligand coordinates with metal ions through its S-atom indicating the monodentate nature of the ligand. The geometry of the ligand and its palladium complexes are optimized, using the DFT method. A good correlation between theoretical calculations and experimental results is observed.

REFERENCES

- P. A. S. Oliveira, L. M. Sartori, N. A. Rey, H. F. Dos Santos, M. A. L. De Oliveira, L. Antônio S. Costa, *J. Braz. Chem. Soc.*, **24**, 1732 (2013)
- M. Gaber, H. A. El-Ghamry, M. A. Mansour, *Journal of Photochemistry and Photobiology A: Chemistry*, **354**, 163 (2018)
- L. Yan, X. Wang, Y. Wang, Y. Zhang, Y. Li, Z. Guo, *Journal of Inorganic Biochemistry*, **106**, 46 (2012)
- N. T. Abdel Ghani, A. M. Mansour, *J. Mol. Struct.*, **991**, 108 (2011)
- S. Rubino, R. Busà, A. Attanzio, R. Alduina, Vita Di Stefano, M. A. Girasolo, S. Orecchio, L. Tesoriere, *Bioorg. Med. Chem.*, **25**, 2378 (2017)
- A. R. Kapdi, I. J. S. Fairlam, *Chem. Soc. Rev.*, **43**, 4751 (2014)
- A. A. El-Sherif, *Stoichiometry and Research - The Importance of Quantity in Biomedicine* book, Intech publisher, Ch. 4, 80, 2012.
- A. R. Kapdi, I. J. S. Fairlamb, *Chem. Soc. Rev.*, **43**, 4751 (2014)
- M. J. Frisch, G. W. Trucks, H. B. Schlegel, G. E. Scuseria, M. A. Robb, J. R. Cheeseman, G. Scalmani, V. Barone, B. Mennucci, G. A. Petersson, H. Nakatsuji, M. Caricato, X. Li, H. P. Hratchian, A. F. Izmaylov, J. Bloino, G. Zheng, J. L. Sonnenberg, M. Hada, M. Ehara, K. Toyota, R. Fukuda, J. Hasegawa, M. Ishida, T. Nakajima, Y. Honda, O. Kitao, H. Nakai, T. Vreven, J. A. Montgomery, Jr., J. E. Peralta, F. Ogliaro, M. Bearpark, J. J. Heyd, E. Brothers, K. N. Kudin, V. N. Staroverov, R. Kobayashi, J. Normand, K. Raghavachari, A. Rendell, J. C. Burant, S. S. Iyengar, J. Tomasi, M. Cossi, N. Rega, J. M. Millam, M. Klene, J. E. Knox, J. B. Cross, V. Bakken, C. Adamo, J. Jaramillo, R. Gomperts, R. E. Stratmann, O. Yazyev, A. J. Austin, R. Cammi, C. Pomelli, J. W. Ochterski, R. L. Martin, K. Morokuma, V. G. Zakrzewski, G. A. Voth, P. Salvador, J. J. Dannenberg, S. Dapprich, A. D. Daniels, O. Farkas, J. B. Foresman, J. V. Ortiz, J. Cioslowski, and D. J. Fox, Gaussian 09, Revision A.1, Gaussian Inc., Wallingford CT, 2009.
- P. J. Stephens, F. J. Devlin, C. F. Chabalowski, M. J. Frisch, *J. Phys. Chem.*, **98**, 11623 (1994).
- C. T. Lee, W.T. Yang, R.G. Parr, *Phys. Rev., B*, **37**, 785 (1988)
- M. J. Cook, K. Bergesen, *Org. Magn. Reson.*, **21**, (1983)
- T. Mosmann, *J. Immunol. Methods*, **65**, 55 (1983).
- S. Konstantinov, H. Eibl, M. Berger, *Br. J. Haemat.*, **107**, 365 (1999).
- S. Ahmad, Sh. Nadeem, A. Anwar, A. Hameed, S. A. Tirmizi, W. Zierkiewicz, A. A. Abbas, A. Isab, M. A. Alotaibi, *J. Mol. Str.*, **1141**, 204 (2017)
- S. Mukherjee, B. V. Reddy, I. Mitra, S. Ch. Moi, *Polyhedron*, **124**, 251 (2017).

Elemental composition and some optical characteristics of Bulgarian beers

K. Nikolova^{1*}, G. Gentsheva^{2,3}, S. Minkova¹, C. Tzvetkova³

¹Medical University–Varna, Department of Physics and Biophysics, BG-9000, Bulgaria

²Medical University–Pleven, Department of Chemistry and Biochemistry, BG-5800, Bulgaria

³Institute of General and Inorganic Chemistry, Bulgarian Academy of Sciences, BG-1113, Sofia, Bulgaria

Received October 17, 2018; Revised December 17, 2018

In this study, the concentrations of 14 elements in two brands of Bulgarian (three products of each) and a Romanian beer were determined. As a low alcoholic beverage, beer is often consumed in large quantities, therefore the concentration of the elements is compared with the rules for their content in drinking water. The fluorescence spectra for investigated samples are obtained at excitation wavelengths 250 nm, 300 nm, 350 nm, 400 nm, 450 nm and 500 nm. The zone of excitation at 450 nm gives emission between 500 nm - 600 nm. This zone is characteristic for vitamin B2 (riboflavin) emission and it can be attributed to flavins present in beer.

Keywords: beer, essential elements, toxic elements, fluorescence spectra

INTRODUCTION

The determination of heavy metals in beer is important for consumers. Relatively low concentrations of toxic elements affect human health. Elements such as Ni, Cd, As, Cr, Sb and Pb can lead to serious side effects. Although the content of Cd and Pb in drinks and food is usually low, we should not forget that can accumulate in biological systems, and have a long half-life. Arsenic occurs naturally in the environment or as a result of pollution caused by industrialisation. Most often, the environmental pollution with lead originates from anthropogenic activity. Content of lead, cadmium, mercury and arsenic in foods and beverages in most cases is regulated. The authors have never found mercury as a contaminant of food and drink home-produced in Bulgaria,

Beer is a complex mixture consisting mainly of water and ethanol with about 0.5% of dissolved solids [1]. Beer analysis is important for evaluation of its organoleptic characteristics, quality, nutritional aspects, and safety. The majority of methods require pre-treatment of samples and chemical reagents. The usefulness of optical methods is recognized, because their non-invasiveness, rapidity, sensitivity. They do not require chemical reagents.

The aim of this work is to determine the chemical composition and explore the possibilities of using fluorescence spectroscopy for further characterization of different brands of beer during storage.

EXPERIMENTAL

Samples:

Romanian beer (can)

Beer 1

-unfiltered (glass bottle)

-gold edge (glass bottle)

-can (1)

Beer 2

-unpasteurized (glass bottle)

-special (glass bottle)

-can (2)

Apparatus:

Inductively coupled plasma-mass spectrometer “X SERIES 2” – Thermo Scientific with 3 channel peristaltic pump; concentric nebulizer; Peltier-cooled spray chamber (4°C); Xt interface option; Ni cones and forward plasma power of 1400 W was used for the determination of Al, Mn, Fe, Zn, Cu, Co, Pb, Cd, As, Cr, Ni, Mo, Sb and Rb.

Content of the Fe, Cu, Mn and Zn in beers was further confirmed with a Prodigy 7 ICP-AES spectrometer (Teledyne Leeman).

Fluorescence measurements were made by the HORIBA Jobin Yvon Fluorolog-3 spectrofluorometer. The instrument is fully-computerized and uses a Xenon lamp as an excitation source. The wavelength range was set at 220-800 nm in excitation and emission. The slits were set at 3 nm and the increment was set at 1 nm for both excitation and emission measurements.

Reagents

Multi-element standard solution V for ICP (Fluka, Sigma-Aldrich) and 1000 mg L⁻¹ As (Fluka, Sigma-Aldrich) were used for the preparation of diluted working standard solutions for calibration for ICP-MS measurements. Stock standard solutions of Fe, Cu, Mn and Zn (1.000 g L⁻¹ (Merck)) were used for the preparation of diluted working standards for

* To whom all correspondence should be sent.

E-mail: kr.nikolova@abv.bg

calibration for ICP-AES. Nitric acid (65%), (Suprapur, Merck) were used for sample digestions.

Method for digestion of samples

10 ml of sample was treated with 1 ml HNO₃ to remove the organic portion of the beer on a sand bath, and then again brought to 10 ml with distilled water. The same procedure is used to prepare a blank.

RESULTS AND DISCUSSION

The fluorescence spectra of two famous types of Bulgarian beers were investigated and were compared with the spectrum of Romanian beer. For this purpose the excitation-emission matrix were obtained in the region 290 nm - 750 nm.

The fluorescence spectra for investigated samples are obtained at excitation wavelengths 250 nm, 300 nm, 350 nm, 400 nm, 450 nm and 500nm. The ratio $I_{\text{emission}}/I_{\text{excitation}}$ is over 1 for short wavelength - 250 nm, 300 nm and 350 nm, for the other wavelengths the ratio is under 1.

The ratios for short wavelength 250 nm, 300 and 350 nm are very different, while for 400nm, 450 nm and 500nm $I_{\text{emission}}/I_{\text{excitation}}$ have close values. Hence, it can be concluded that short wavelengths are appropriate for investigation of different types of beer.

The fluorescence emission spectra for excitation wavelength 300 nm are presented on the figure 1.

The short-wavelength fluorescence, with excitation at 250 nm, 300 nm and 350 nm and emission between 420 nm and 520 nm, tentatively attributed to aromatic amino acids. The emission in region 420 nm - 450 nm may originate from components of the vitamin B group [2]. There is a difference in fluorescent spectra in the range 500-600 nm and excitation at 450 nm. That zone is characteristic for vitamin B2 (riboflavin) emission and can be attributed to flavins present in beer. This emission disappears in beer exposed to light, in accordance with the well-known photoinstability of flavins [3].

The fluorescence intensities at 520 nm were presented on the figure 2 at excitation wavelength 450 nm. The Bulgarian beers in cans demonstrated higher fluorescence intensity than the samples in glass bottles. Lower intensity of the Romanian beer most probably is determined by the lower content of determined components in raw materials.

Considering that beer contains about 90% water, the main source of microelements are barley, hops and yeast, as the water in use should follow regulations for drinking water. During the brewing process, the metal content of beer could be also affected by the components of the brewery

equipment involved [4]. Beer is a low alcoholic beverage, usually consumed over 250 ml per drink, therefore the concentration of Cd, Cu, Cr, Ni, and As in the analyzed beers are tested against the permitted norms in water in Bulgarian regulations (Cu - 2000 µg L⁻¹, Fe - 200 µg L⁻¹, Mn - 50 µg L⁻¹, Cr - 50 µg L⁻¹, Ni - 20 µg L⁻¹, Pb - 10 µg L⁻¹, As - 10 µg L⁻¹ and Cd - 5 µg L⁻¹). The permitted amount of Pb in low alcoholic beverages and wines is 0.20 mg kg⁻¹.

As seen in Table 1, there aren't major differences in Al concentration between glass bottles and cans, neither between the two brands of beer; as a reference concentration of Al in Spanish beers is around 36.5 - 795.2 µg L⁻¹ [5]. Chromium concentration is below the recommendation for drinking water, and can be compared to what we can find in Italian beers [6]. Concentrations of Cu, Zn and Mn in the two brands are very similar, as copper concentration is close to the one found in the Spanish beers [7]. The only difference is Mn in unfiltered beer, which is 1.7 times higher than in other beers. The contents of Co, Mo, Fe, Sb and Rb do not differ in the two brands. Main differences with the Romanian beer are the concentrations of Cr, Cu, Mo and Rb.

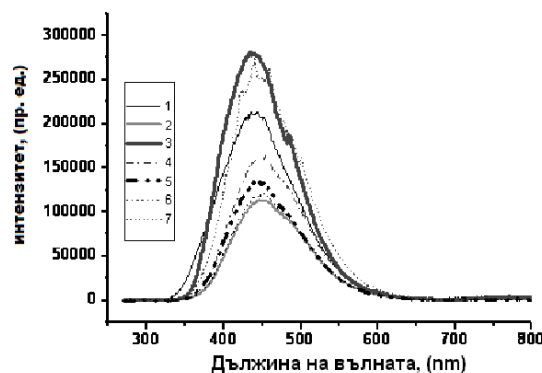


Fig. 1. Fluorescence spectra of beer samples for excitation wavelength 300 nm 1. Romanian beer - can, 2. gold edge, 3. unfiltered, 4. can (1), 5. unpasteurized, 6. special, 7. can (2)

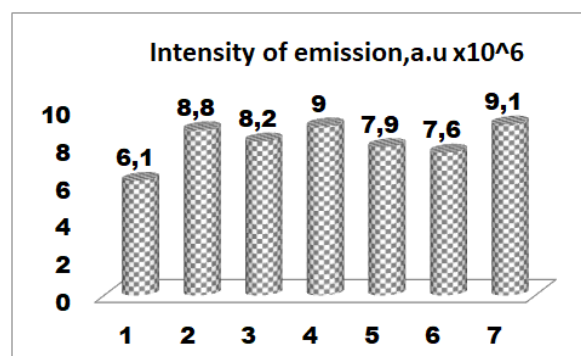


Fig. 2. Intensity of emission at 520 nm for beer samples at excitation at 450 nm.

Table 1. Concentration range of some elements in beer (RSD=1-7%)

Sample		Elements				
		Al, $\mu\text{g L}^{-1}$	Cr, $\mu\text{g L}^{-1}$	Cu, $\mu\text{g L}^{-1}$	Zn, $\mu\text{g L}^{-1}$	Mn, $\mu\text{g L}^{-1}$
Romanian		70-81	3-6	8-12	72-80	28-33
Beer 1	unfiltered	50-57	15-20	31-37	60-72	74-89
	gold edge	45-48	12-14	33-37	44-46	44-52
Beer 2	(1)	45-49	10-13	46-52	83-103	47-53
	unpasteurized	44-51	10-12	42-47	115-219	43-53
	special	52-66	8-12	50-58	48-68	44-57
	(2)	50-55	10-17	45-54	65-77	52-63
water - norm			50	2000		50

Table 1. (continue)

Sample		Elements				
		Co, $\mu\text{g L}^{-1}$	Mo, $\mu\text{g L}^{-1}$	Fe, $\mu\text{g L}^{-1}$	Sb, $\mu\text{g L}^{-1}$	Rb, $\mu\text{g L}^{-1}$
Romanian		0.1-0.2	10-13	112-127	0.3-0.5	61-69
Beer 1	unfiltered	0.2-0.3	4-5	81-92	0.3-0.6	104-112
	gold edge	0.2-0.4	3-4	104-153	0.4-0.6	112-120
Beer 2	(1)	0.2-0.3	2-4	87-101	0.8-1.1	137-142
	unpasteurized	0.1-0.2	1-3	83-112	0.6-1.0	112-128
	special	0.1-0.2	2-3	80-94	0.8-1.3	98-114
	(2)	0.1-0.3	3-4	86-90	1.2-1.4	125-150
water - norm				200		

Table 2. Concentration range of toxic elements in beer (RSD=3-7%)

Sample		Elements			
		As, $\mu\text{g L}^{-1}$	Cd, $\mu\text{g L}^{-1}$	Pb, $\mu\text{g L}^{-1}$	Ni, $\mu\text{g L}^{-1}$
Romanian		4-5	0.14-0.16	22-26	1-3
Beer 1	unfiltered	5-6	0.06-0.09	12-14	8-10
	gold edge	8-10	0.15-0.19	20-23	6-7
Beer 2	(1)	5-7	0.05-0.06	17-20	8-9
	unpasteurized	2-3	0.03-0.05	15-17	5-6
	special	2-4	0.06-0.08	13-15	5-6
	(2)	4-6	0.07-0.12	17-20	7-8
water - norm		10	5	10	20

Table 2 shows the concentrations of toxic elements in the beers. Only Pb concentrations are actually higher than the established norms for drinking water with beer having twice as much. The measured values of Pb in Bulgarian beers is close to or less than the reported values of Brazilian beers [8], but higher than different European ones [9]. As concentrations levels are close to what can be found in water, matching the reported values for Italian, Spanish and other beers [9, 10]. The Romanian beer is identical when it comes to the toxic elements, excluding Ni which has lower values.

CONCLUSIONS

Bulgarian beers are safe for consumption with concentrations of the determined elements mostly matching the norms for drinking water.

Can packages preserve beer's organic components better than glass bottle.

In the following investigations model can be obtained, which will correctly predict riboflavin and amino acids in beers. Fluorescence method may become a suitable alternative, giving accurate, rapid and less expensive results.

It would be interesting to identify correlations between fluorescent constituents and other components such as association of changes in Flavin with development of light struck flavor in beers upon exposure to light.

REFERENCES

1. S. Cortacero-Ramirez, A. Segura-Carretero, C. Cruces-Blanco, Fernandez- A. Gutierrez, *TrAC*, **22**, 440 (2003).
2. E. Sikorska, J. Chmielewski Koziol, I.V. Khmelinskii, R. Herance, J. L. Bourdelande, M. Sikorski, *Pol J Food Nutr Sci*, **53**, 113 (2003).
3. P. F. Heelis, *Chem Soc Rev*, **11**, 15 (1982).
4. P. Pohl, *Food Additi Contam*, **25**, 693 (2008).
5. F. F. Lopez, C. Cabrera, M. L. Lorenzo, M. C. Lopez, *Sci Total Environ*, **220**, 1 (1998).
6. P. Passaghe, S. Bertoli, F. Tubaro, S. Buiatti, *Eur Food Res Technol*, **241**, 199 (2015).
7. P. Viñas, N. Aguinaga, I. López-García, M. Hernandez-Córdoba, *JAOAC Int*, **85**, 736 (2002).
8. L.M.V. Soares, A.M.M. de Moraes, *Cienc Tecnol Aliment Campinas*, **23**, 285 (2003).
9. G. Donadini, S. Spalla, G.M. Beone, *J Inst Brew*, **114**, 283 (2008).
10. N. Mahmood, N. Petraco, Y. He, *Anal Bioanal Chem*, **402**, 861 (2012).

Chemical reagents for immunodetection of fluoroquinolones with determinable specificity

I.A. Shanin^{1,2}, E.A. Zvereva³, A.V. Zherdev³, T. Godjevargova⁴, S.A. Eremin^{1,3,*}

¹*M.V. Lomonosov Moscow State University, Faculty of Chemistry, Leninskie Gory 1, Moscow 119991, Russia*

²*XEMA Company Limited, Ninth Parkovaya street 48, Moscow 105264, Russia*

³*A.N. Bach Institute of Biochemistry, Research Centre of Biotechnology of the Russian Academy of Sciences, Leninsky prospect 33, Moscow 119071, Russia*

⁴*Department of Biotechnology, University Prof. Dr. Assen Zlatarov, Burgas 8010, Bulgaria*

Received October 30, 2018; Revised December 12, 2018

A new approach is proposed to obtain specific immunoreagents for detection of fluoroquinolones (FQs) that have a cyclopropyl radical in the 1st position of the quinolone core. The recommended immunogens should use coupling to a protein carrier via a carboxyl group in the 3rd position of the FQs, whereas solid-phase antigens for immunoassay should be obtained using the active groups of the radical in the 7th position. The given approach was applied to produce polyclonal antibodies against 3 FQs, danofloxacin (DAN), clinafloxacin (CLI), and moxifloxacin (MOX). The developed enzyme immunoassays based on their use are characterized by detection limits of 0.5 ng/mL for DAN, 1.0 ng/mL for CLI, and 0.5 ng/mL for MOX. Interactions of the antibodies with 25 representatives of FQs were studied, and the possibility of using the obtained reagents for immunodetection of FQs with broad cross-reactivity was shown.

Keywords: antibodies, fluoroquinolones, 3D structures, enzyme immunoassay, cross-reactivity

INTRODUCTION

Fluoroquinolones (FQs) are a class of antibiotics now widely used in veterinary medicine [1]. Consequently, the systematic intake of antibiotic-containing food may be accompanied by a number of undesirable effects such as disbacterioses, allergy, metabolic disorders, and selection of antibiotic-resistant strains [2]. Therefore, monitoring of FQs along food chains is an extremely important task. Immunoassays are among the leading approaches to antibiotics detection due to their simplicity, productivity, and relatively low cost [3, 4]. Antibodies are key reactants for immunoassays that determine sensitivity and specificity of analyte detection. Immunogens of different structures can be used to generate anti-FQ antibodies, and their structure may lead to narrow [5, 6] or broad [7-9] specificity of the obtained antibodies. Therefore, the choice of immunogens and protein-hapten conjugates for competitive assays needs detailed consideration to reach desirable immunoassay parameters.

The molecular structure of all FQs (Fig. 1) contains a carboxyl group, which is most often used for conjugation by carbodiimide activation or method of mixed anhydrides [10-14]. The carbodiimide syntheses may be realized in several

ways depending on the presence or absence of the primary or secondary amino groups in the radical in the 7th position of the quinolone nucleus. The most common practices are FQ modification at the secondary nitrogen atom of the piperazine radical in the 7th position of the quinolone core [7-9], or obtaining recombinant antibodies [13, 15].

One of the promising approaches for studying the influence of the structure of the FQ derivatives on the specificity of antibodies is 3-dimensional (3D) modeling of chemical structures, and the FQ class is especially convenient for this in view of its vastness. Special software (HyperChem, Sybyl, etc.) allows not only building 3D models of compounds and optimizing them in space, but also identifying the structure-property correlations, and even simulating the structure of the immunogen to produce antibodies with the desired specificity [16]. In addition, the analysis of cross-reactions of antibodies to several structurally close compounds provides the possibility of determining the properties of the active center of antibodies to predict their specificity to other, not-experimentally-characterized compounds [17].

* To whom all correspondence should be sent.
E-mail: eremin_sergei@hotmail.com

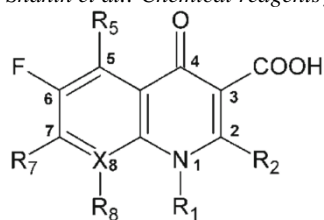


Fig. 1. General structure of fluoroquinolones.

The purpose of this work is to obtain reagents for immune detection of FQs with determinable specificity.

EXPERIMENTAL

Reactants

We used danofloxacin (DAN), clinafloxacin hydrochloride (CLI), moxifloxacin (MOX), ofloxacin (OFL), R-ofloxacin (R-OFL), garenoxacin (GAR), pefloxacin (PEF), gatifloxacin (GAT), sarafloxacin hydrochloride (SAR), lomefloxacin (LOM), sparfloxacin (SPA), difloxacin (DIF), pazufloxacin (PAZ), marbofloxacin (MAR), rufloxacin (RUF), norfloxacin (NOR), ciprofloxacin (CIP), enrofloxacin (ENR), pipemidic acid (PIP), nalidixic acid (NAL), oxinic acid (OXI), orbifloxacin (ORB), enoxacin (ENO), nadifloxacin (NAD), flumequin (FLU), bovine serum albumin (BSA), ovalbumin (OVA), casein, 1-ethyl-3-(3-dimethylaminopropyl) carbodiimide hydrochloride (EDC), N-hydroxysuccinimide (HSI), 3,3',5,5'-tetramethyl benzydine (TMB), and N,N-dimethylformamide (DMF) from Sigma-Aldrich Chemical (St. Louis, MO, USA) plus horseradish peroxidase-labeled antibodies against rabbit IgG (H+L) from the N.F. Gamaleya Research Institute of Epidemiology and Microbiology (Moscow, Russia). All auxiliary reagents (salts, acids, alkalis, and organic solvents) were of analytical or chemical purity.

Synthesis of FQ conjugates by carbodiimide activation

FQ conjugates with carrier proteins were synthesized according to procedures [12, 18] with some modifications. 14.7 μmol of a FQ, 5.7 mg (30 μmol) of EDC, and 3.5 mg (30 μmol) of HSI were dissolved in 1.0 mL of DMF. The mixture was incubated for 2 hours with stirring. A solution of 10 mg of a protein was prepared in 8 mL of 100 mM sodium carbonate buffer, pH 9.5, with 50 μL of triethylamine, and the mixture was incubated for 1 h at +4°C. A solution of a FQ with an activated carboxyl group was added dropwise with constant slow stirring to the protein solution. Then the mixture was incubated with stirring for 5 h at room temperature in the dark. The synthesized conjugate was purified from low-molecular-weight substances

against 0.01 M K-phosphate buffer, pH 7.4. Thus, the conjugates MOX-BSA, DAN-BSA, and CLI-BSA were obtained.

Synthesis of FQ conjugates using glutaraldehyde

The synthesis was carried out in accordance with previously published procedure [7] with some modifications. Five milligrams (0.11 μmol) of OVA and 2.2 mg (5.6 μmol) of CLI were dissolved in 8 mL of distilled water, and 20 μL of triethylamine was added. With vigorous stirring, 23 μL (5.6 μmol) of 2.5% glutaraldehyde was added. The solution was incubated for 1 h in the dark with constant vigorous stirring at room temperature. Five hundred microliters (30 μmol) of a 0.22% sodium borohydride solution in distilled water was added and the obtained mixture was incubated for 30 min. The synthesized conjugate was purified from low-molecular-weight substances by dialysis with an 0.01 M K-phosphate buffer, pH 7.4. Thus, the conjugate CLI-NH-C5-NH-OVA was synthesized.

Enzyme-linked immunosorbent assay (ELISA)

The conjugate KLI-NH-C5-NH-OVA (100 μL , 0.5 $\mu\text{g}/\text{mL}$) in 50 mM K-phosphate buffer, pH 7.4, containing 0.1 M NaCl (phosphate-buffered saline [PBS]), was immobilized in microplate wells overnight at 4°C. The wells were then washed 4 times with PBS containing 0.05% Triton X-100 (PBST). For analysis, 50 μL of a FQ solution in PBST (from 0.1 to 1000 ng/mL) and 50 μL of antibody solution (1:2000) were added to the wells. The mixture was incubated for 1 h at 37°C; then the wells were washed by PBST 4 times. One hundred microliters of the immunoperoxidase conjugate (1:6000 dilution in PBST) was added to the wells and incubated for 1 h at 37°C. After washing (3 times with PBST and once with distilled water), the activity of peroxidase bound to the carrier was determined. To do this, 100 μL of a 0.4 mM solution of TMB in 40 mM Na-citrate buffer, pH 4.0, containing 3 mM H_2O_2 , were added to the wells and incubated for 15 min at room temperature. The reaction was stopped by the addition of 50 μL of 1 M H_2SO_4 per well. The optical density (D_{450}) of the reaction product was measured at 450 nm on a Zenyth 3100 microplate photometer.

Estimation of specificity

Cross-reactivity of the assay was evaluated as the percentage of cross-reaction with other compounds in comparison with the target analyte:

$$CR(X)\% = IC_{50}(\text{target analyte})/IC_{50}(X) * 100\%$$

where $IC_{50}(\text{target analyte})$ is the concentration of the target substance at which the value of the analytical signal decreases by 50% from the

difference between the maximum and minimum signals, and $IC_{50}(X)$ is the concentration of the cross-reacting substance causing the same 50% decrease.

3D modeling

To calculate the conformation of FQ molecules in a vacuum, the Polak-Ribière algorithm was used. The chosen criterion for termination of the approximation cycles was a mean square gradient equal to 5 cal/(Å × mol). Then the conformations of the molecules in the solvated form were calculated. The obtained structures were compared using superposition between them.

RESULTS AND DISCUSSION

Structural analysis of FQs

Selectivity of immunoassays for FQs is connected to the following feature of the molecular structure of substances from this class (Fig. 1). For FQs, the carboxyl group in the 3rd position, the keto group in the 4th position, and the fluorine atom in the 6th position are constant structural compounds. Radicals in the 1st, 7th, and 8th positions form the variable region, being individual for different FQs.

Therefore, for selective immunoassays of individual compounds, it is necessary to synthesize immunogens and protein conjugates using groups of the constant region (most often the carboxyl group in the 3rd position). To ensure group specificity of FQ immunoassays, it is necessary to use the conjugates synthesized via groups from the variable region. Most often [7-9], the radical with the primary or secondary amino group in the 7th position or the newly introduced carboxyl or amino groups are used for this purpose.

The combination of existing methods has allowed us to develop a new approach for immune detection of FQs with a certain radical in the 1st position. The approach consists of the use of immunogens synthesized via the carboxyl group in the 3rd position, and solid-phase antigens synthesized via active groups of the radical in the 7th position. The proposed approach was implemented to obtain antibodies and develop enzyme immunoassays of FQs with a cyclopropyl radical in the 1st position of the quinolone core (Fig. 2).

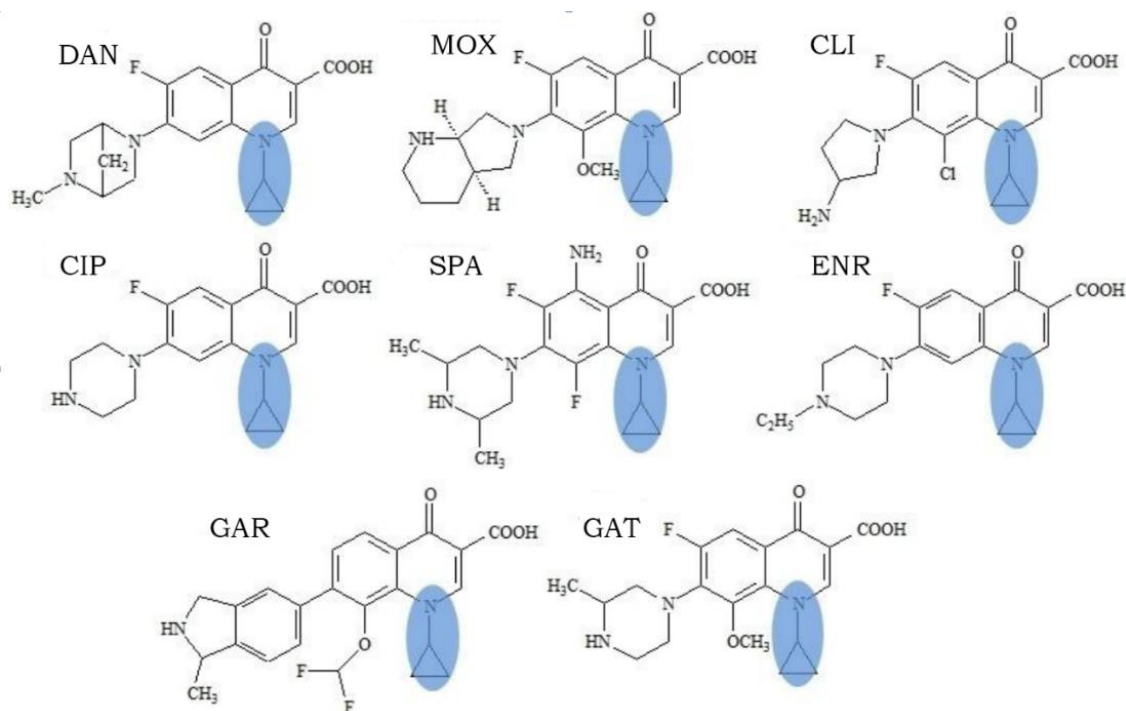


Fig. 2. Fluoroquinolones with a cyclopropyl radical in the 1st position of the quinolone core.

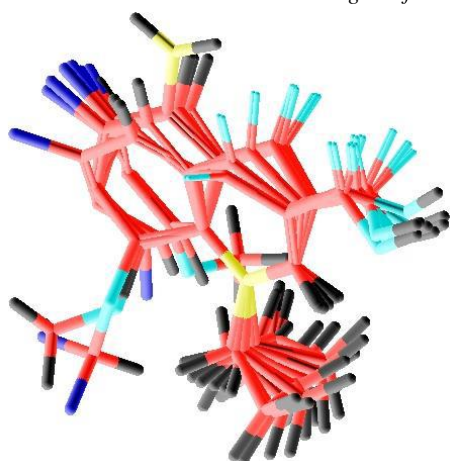


Fig. 3. Three-dimensional structures of 8 fluoroquinolones (danofloxacin, moxifloxacin, clinafloxacin, sparfloxacin, enrofloxacin, garenoxacin, and gatifloxacin) with a cyclopropyl radical in the 1st position of the quinolone core.

Using the HyperChem software and methods of molecular mechanics, the 3D structures of molecules in solvated form were optimized. After that, superposition on the nitrogen atom in the first position and 2 adjacent carbon atoms of the quinolone nucleus was applied, and the conformations of the FQs were combined, excluding the radicals in the 7th position (Fig. 3).

As you can see, the conformations of the FQ molecules with a cyclopropyl radical in the 1st position of the quinolone nucleus are variable, which can affect the specificity of their immunodetection. Note that even the constant region is characterized by a certain variation, for example, the spatial orientation of the keto group in the 4th position. The carboxyl group in the 3rd position and the fluorine atom in the 6th position have the most constant conformation, which suggests the absence of the influence of these radicals on specificity of immune recognition.

Production of antibodies to FQ

In the development of ELISA techniques, anti-DAN antibodies (obtained and characterized previously [19]), anti-MOX, and anti-CLI antibodies were used. CLI-NH-C5-NH-OVA was used as a solid-phase conjugate, in which the primary amino group of clinafloxacin at the 7th position of the quinolone core was conjugated with OVA via glutaraldehyde. Thus, the target fragments for antibodies are radicals in the 1st and 8th positions of the quinolone core.

Using these reagents, the conditions of the ELISAs were optimized to ensure maximum sensitivity of FQ detection. The calibration curves obtained under optimized conditions were characterized by the limits of detection of 0.5 ng/mL

for DAN, 0.5 ng/mL for MOX, and 1 ng/mL for CLI (Fig. 4a-c).

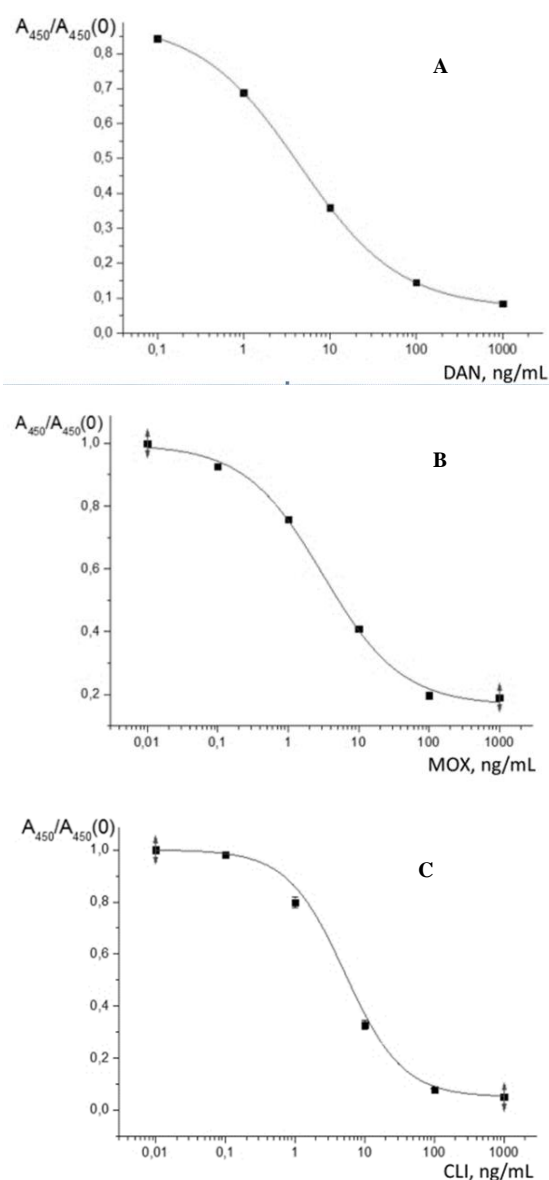


Fig. 4. Calibration curves for enzyme-linked immunosorbent assay (ELISA) of danofloxacin (a), moxifloxacin (b), and clinafloxacin (c).

Characterization of the specificity of antibodies to FQs

Evaluation of the specificity of the developed ELISA techniques was carried out using 25 compounds from the FQ class. Anti-DAN, anti-MOX, and anti-CLI antibodies are not cross-reactive with PEF, OFL, R-OFL, SAR, DIF, PAZ, MAR, RUF, NOR, PIP, NAL, OXI, and FLU. These 3 antibodies are all characterized by cross-reactivity with 12 other FQs (the cross-reactivity is more than 1%), 8 of which have a cyclopropyl radical in the structure and are characterized by maximum values of the cross-reactivity (Table 1).

Table 1. Data on the specificity of anti-DAN, anti-MOX, and anti-CLI antibodies in ELISA with the solid phase antigen CLI-NH-C5-NH-OVA.

Antigen	anti-DAN	Antibodies	
		anti-MOX	anti-CLI
Cross-reactivity, %			
DAN	100	48	63
MOX	<1	100	10
CLI	15	120	100
CIP	38	20	73
SPA	5	5	10
ENR	25	10	33
GAR	5	100	92
GAT	5	27	20
NAD	130	67	90
ENO	5	40	5
LOM	5	80	<1
ORB	2	<1	10

CONCLUSIONS

The results obtained confirm the proposed approach for reactants obtained for immunodetection of FQs with a certain radical in the 1st position. The antibodies and conjugates obtained provide a wide selectivity and are the basis for the development of various formats of immunoassay systems for FQs.

Acknowledgment This work was partially supported by the Russian Foundation for Basic Research (Grant 18-53-18013).

REFERENCES

- G. F. Zhang, S. Zhang, B. F. Pan, X. F. Liu, L. S. Feng, *Eur J Med Chem*, **143**, 710 (2018).
- C. Manyi-Loh, S. Mamphweli, E. Meyer, A. Okoh, *Molecules*, **23**(4), pii: E795 (2018).
- Y. F. Li, Y. M. Sun, R.C. Beier, H. T. Lei, S. Gee, B. D. Hammock, H. Wang, Z. H. Wang, X. L. Sun, Y. D. Shen, J. Y. Yang, Z. L. Xu, *TrAC Trends Anal Chem.*, **88**, 25 (2017).
- B. B. Dzantiev, N. A. Byzova, A. E. Urusov, A. V. Zherdev, *TrAC Trends Anal Chem*, **55**, 81 (2014).
- M. Chusri, P. Wongphanit, T. Palaga, S. Puthong, S. Sooksai, K. Komolpis, *J Microbiol Biotechnol*, **23**, 69 (2013).
- H. Watanabe, A. Satake, Y. Kido, A. Tsuji, *Analyst*, **127**, 98 (2002).
- Y. Z. Liu, G. X. Zhao, P. Wang, J. Liu, H. C. Zhang, J. P. Wang, *J Environ Sci Heal B*, **48**, 139 (2013).
- S. A. Tittlemier, J. M. Gelinas, G. Dufresne, M. Haria, J. Querry, C. Cleroux, C. Menard, P. Delahaut, G. Singh, N. Fischer-Durand, S.B. Godefroy, *Food Analytical Methods*, **1**, 28 (2008).
- A. C. Huet, C. Charlier, S. A. Tittlemier, G. Singh, S. Benrejeb, P. Delahaut, *J Agric Food Chem*, **54**, 2822 (2006).
- S. Bucknall, J. Silverlight, N. Coldham, L. Thorne, R. Jackman, *Food Additives Contaminants*, **20**, 221 (2003).
- S. X. Lu, Y. L. Zhang, J. T. Liu, C. B. Zhao, W. Liu, R. M. Xi, *J Agric Food Chem*, **54**, 6995 (2006).
- W. Sheng, X. F. Xia, K. Y. Wei, J. Li, Q. X. Li, T. Xu, *J Agric Food Chem*, **57**, 5971 (2009).
- K. Wen, G. Nolke, S. Schillberg, Z. H. Wang, S. X. Zhang, C. M. Wu, H. Y. Jiang, H. Meng, J. Z. Shen, *Anal Bioanal Chem*, **403**, 2771 (2012).
- S. Suryoprabowo, L. Q. Liu, J. Peng, H. Kuang, C. L. Xu, *Food Agricul Immunol*, **26**, 317 (2015).
- X. Q. Tao, M. Chen, H. Y. Jiang, J. Z. Shen, Z. H. Wang, X. Wang, X. P. Wu, K. Wen, *Anal Bioanal Chem*, **405**, 7477 (2013).
- D. G. Pinacho, F. Sanchez-Baeza, M. P. Marco, *Analyt Chem*, **84**, 4527 (2012).
- Z. H. Wang, Y. Zhu, S. Y. Ding, F. Y. He, R. C. Beier, J. C. Li, H. Y. Jiang, C. W. Feng, Y. P. Wan, S.X. Zhang, *Anal Chem*, **79**, 4471 (2007).
- Z. Q. Liu, S. X. Lu, C. H. Zhao, K. Ding, Z. Z. Cao, J. H. Zhan, C. Ma, J. T. Liu, R. M. Xi, *J Sc Food Agriculture*, **89**, 1115 (2009).
- I. A. Shanin, E. A. Zvereva, A. V. Zherdev, S. A. Eremin, B. B. Dzantiev, *Int J Chem Sciences*, **14**, 283 (2016).

Analytically confirmed synthetic cannabinoid 5F-ADB sprayed on “herbal mixture”

I. D. Ivanov^{1,2,*}, S. S. Stoykova^{1,2}, N. T. Burdzhiev³, I. N. Pantcheva¹, V. N. Atanasov^{1,2}

¹ Sofia University “St. Kliment Ohridski”, Faculty of Chemistry and Pharmacy, Department of Analytical Chemistry, 1, J. Bourchier Blvd., 1164 Sofia, Bulgaria

² Military Medical Academy, Department of Toxicology, Analytical Toxicology Laboratory, 3, St. G. Sofiiski Str., 1606 Sofia, Bulgaria

³ Sofia University “St. Kliment Ohridski”, Faculty of Chemistry and Pharmacy, Department of Organic Chemistry and Pharmacognosy, 1, J. Bourchier Blvd., 1164 Sofia, Bulgaria

Received October 30, 2018; Revised January 9, 2019

Synthetic cannabinoids (SCs) are new psychoactive substances, called “legal” alternative to cannabis. Their structures differ from that of Δ^9 -tetrahydrocannabinol (THC), but mimic its biological effect. On the “black” market, SCs appear sprayed on “herbal mixtures” intended for smoking. It is well known that SCs are more potent cannabinoid receptors (CB_1/CB_2) agonists in human body than THC and possess wide and severe toxicity pattern. Pharmacokinetics, pharmacodynamics and toxicity profile of most of SCs are not well studied although it is already known that they may pose a risk to human health.

In the present study we report five cases of seized “herbal mixtures” containing synthetic cannabinoid 5F-ADB (5F-MDMB-PINACA) which was identified by gas chromatography-mass spectrometry (GC-MS) and confirmed by nuclear magnetic resonance (NMR).

Keywords: “herbal mixture”, synthetic cannabinoids, 5F-ADB, GC-MS, NMR

INTRODUCTION

Synthetic cannabinoids (SCs) are chemical compounds which when inhaled, imitate pharmacological effects of Δ^9 -tetrahydrocannabinol (Δ^9 -THC) – the main psychoactive ingredient in marijuana. Firstly, SCs appear on drug market in 2008 [1, 2], and since then hundreds different products containing various synthetic cannabinoids are annually sold. Therefore, these substances became the biggest part of the family of new psychoactive drugs [3]. Typically, the products containing SCs, are traded as powders, “herbal mixtures” or cigarettes [4, 5]. Identification of new synthetic cannabinoids is a challenge for national and international drug control due to their structural diversity (a large assortment of chemical structures which is difficult to properly identify) and unpredictable risk to human health (most of SCs are pharmacologically uncharacterized).

Generally, chemical structure of SCs consists of four major fragments – heterocyclic nucleus (core), side chain (tail), linker and lipophilic substituent (Fig. 1). In most cases heterocyclic nucleus is an indole or azaindole (indazole, benzimidazole, pyrrolopyridine), although pyrroles, naphthalenes,

and thiazoles have been also reported. The core is bound *via* N-atom to the side chain built by alkyl, alicyclic, heterocyclic, aromatic, or heteroaromatic moieties [6-9]. The heterocyclic nucleus and lipophilic substituent are connected through a linker, which is ketone, ester or amide group, and in some cases - alkyl ether or thiazole. A large number of lipophilic substituents exists as 8-hydroxyquinoline, naphthalene, amino acid ester, etc. [7, 10-12].

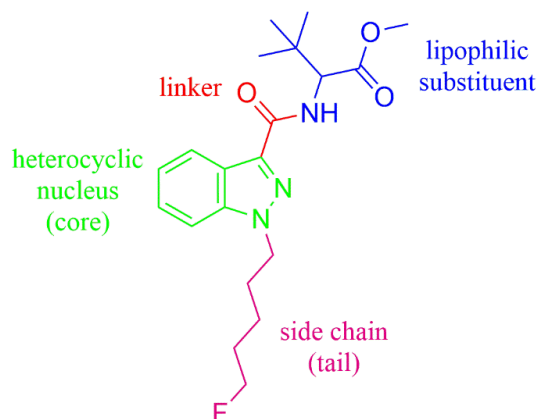


Fig. 1. Chemical structure of 5F-ADB (the four major fragments are colored differently).

The current study presents five cases of seized “herbal mixtures” in Bulgaria within two-year

* To whom all correspondence should be sent.

E-mail: ahidi@chem.uni-sofia.bg

period (2017-2018). The synthetic cannabinoid 5F-ADB (5F-MDMB-PINACA; methyl-S-2-[1-(5-fluoropentyl)-1H-indazole-3-carboxamido]-3,3-dimethyl butanoate, Fig. 1) was identified and analytically confirmed as an active component of the dried plant materials. It belongs to the indazole-3-carboxamide family of SCs and first appeared in Europe in Hungary (January 2015) [13]. 5F-ADB shows strong agonistic activity at both human cannabinoid receptors (CB₁ and CB₂) and may significantly threaten the human health. Recently it was banned for usage and added to List I of Regulation on Classification of plants and substances as narcotics in Bulgaria.

EXPERIMENTAL

Reagents

Chromatographic grade methanol (MeOH) and ethyl acetate (EtOAc), as well as chloroform-d (CDCl₃) were purchased from Sigma-Aldrich (Germany).

Herbal mixtures

Herbal products seized in course of criminal investigation (five different cases) were provided for forensic study of drugs and toxic chemicals to the Analytical Toxicology Laboratory (Military Medical Academy, Sofia). “Herbal mixtures” represent unknown greenish, brownish or yellowish dried crushed plant materials with pungent smell.

GC-MS identification of active ingredients of herbal mixtures

Due to inhomogeneous distribution of possible physiologically active ingredients on “herbal mixtures”, in each case a composite sample (50 mg) from different sampling points was prepared. Then MeOH (2 mL) was added, mixture was vortexed for 1 min and sonicated for 20 min. After centrifugation (3000 rpm / 5 min), the organic layer was filtered off through syringe filter (0.45 µm pore size, Millex-FH, Merck-Millipore, Germany) into a test-tube and evaporated to dryness under nitrogen. The dried extract was dissolved in EtOAc at final volume of 100 µL. 1 µL of the solution was analyzed by GC-MS (Agilent 7890B/5977A, a DB-1701 capillary column with 30 m length, 0.25 mm i.d., and 0.25 µm film thicknesses, Agilent Technologies, USA). The injector was operated in splitless mode at 270 °C. Helium gas was used as a carrier gas at a flow rate of 1.5 mL/min. The oven temperature was held at 50 °C for 5 min, ramped to 290 °C at a rate of 30 °C/min and held for 30 min. The MS detector temperature was set to 230 °C and electron energy was 70 eV. Data were collected at scan mode (50-550 m/z) and analyzed with Agilent MassHunter Workstation software (Agilent Technologies, USA).

The compounds were identified by mass spectral library search (Cayman Spectral Library 2016 [14]).

NMR confirmation of sprayed ingredient on herbal mixtures

The presence and the structure of the synthetic cannabinoid identified by GC-MS analysis were additionally confirmed by NMR spectroscopy (Avance III HD 500 MHz; Bruker, Germany). Each composite sample (250 mg) was extracted in scale as described above. The resulting dried extract was reconstituted with 600 µL CDCl₃, filtered off through syringe filter (0.45 µm pore size) and transferred into an NMR tube. ¹H- (500 MHz) and ¹³C-NMR (125 MHz) spectra were recorded. Chemical shifts were adjusted to the CDCl₃ residual signals at δ = 7.26 ppm (¹H) and at δ = 77.16 ppm (¹³C), respectively [15, 16]. Full band shape analysis of ¹H-NMR spectra was performed using TopSpin 3.5pl7 package (Bruker, Germany).

RESULTS AND DISCUSSION

Identification of SCs in “herbal mixtures” represents a major challenge for forensic chemists and toxicologists due to rapid change of their structures and dynamic appearance of new synthesized compounds. In the present study, five different herbal products were submitted for forensic expertise.

At first, a GC-MS screening of MeOH extracts from each of the provided “herbal mixtures” was performed. In each of the resulting total ion chromatograms, a peak with retention time at 16.1 min was detected. The compound was identified by comparison of the obtained mass spectral data with reference data from Cayman Spectral Library. Thus, the active substance in the five herbal products seized was identified as 5F-ADB. It should be mentioned that the identified SC possesses temperature-stable core skeleton and does not undergo thermal degradation during GC-MS analysis to produce analytical artifacts like 1H-indole-3-carboxylate compounds [17, 18]. Representative total ion chromatogram of “herbal mixture” and corresponding mass spectrum are shown on Fig. 2 and Fig. 3, respectively.

The presence of 5F-ADB in “herbal mixtures” and its chemical structure were confirmed by ¹H- and ¹³C-NMR spectroscopy. Both spectra contain also additional signals due to water-insoluble compounds derived from the plant materials. However, all chemical shifts and multiplicities assigned to SC correspond to those previously reported in the literature [8, 9]. Representative ¹H-NMR spectrum (Fig. 4) clearly confirms the presence of the synthetic cannabinoid 5F-ADB

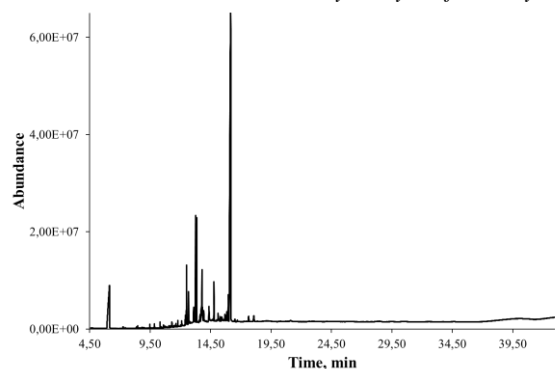


Fig. 2. Representative total ion chromatogram of methanol extract of “herbal mixture”.

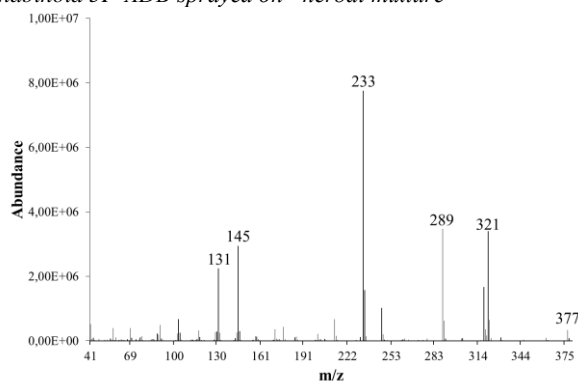


Fig. 3. The mass spectrum of the peak eluted at $R_t = 16.1$ min.

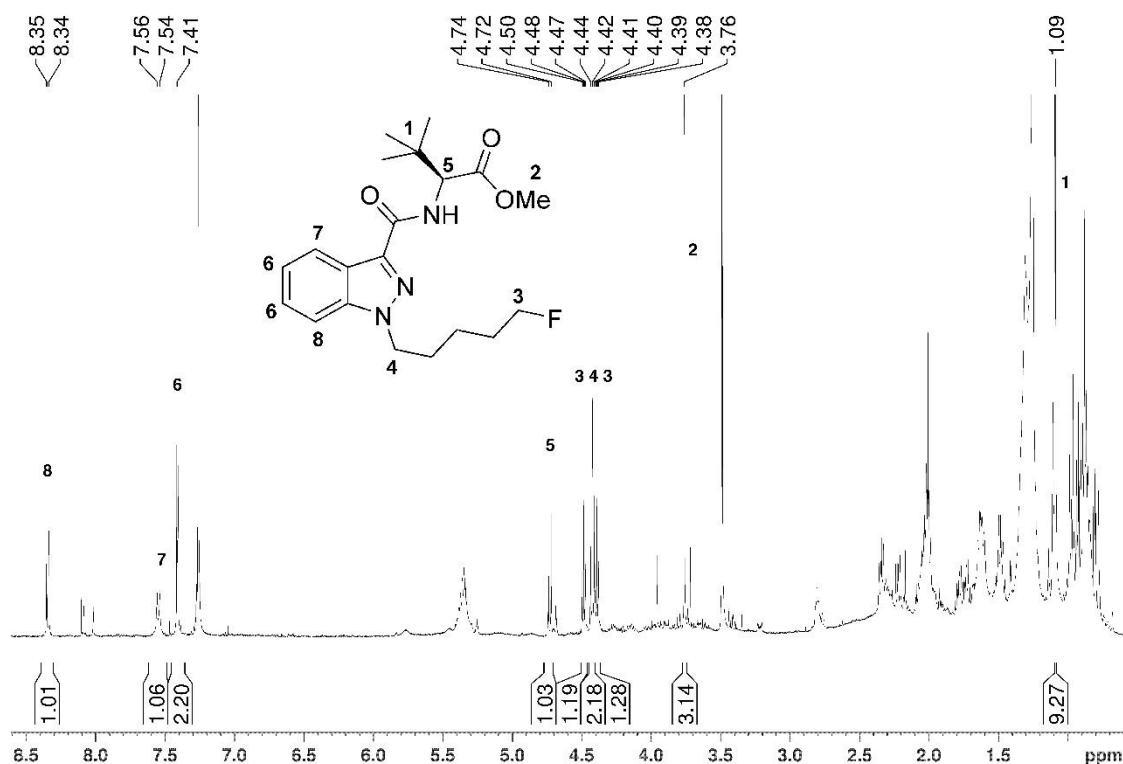


Fig. 4. $^1\text{H-NMR}$ spectrum of “herbal mixture” extract.

The singlets for protons belonging to methyl and ester methyl groups in lipophilic substituent were observed at 1.09 ppm and 3.76 ppm, respectively. The signals for protons of CH_2F group were recorded as doublet of triplets (4.43 ppm) due to the spin coupling of fluorine. The doublet at 4.73 ppm was assigned to the α -hydrogen of the amino acid moiety. Protons of indole heterocycle were observed at 7.42 ppm (singlet), 7.54 ppm and 8.35 ppm (doublets), respectively.

On the other hand, the $^{13}\text{C-NMR}$ spectra of herbal extracts are not informative as corresponding $^1\text{H-NMR}$ data due to the presence of a number of signals attributed to the carbon atoms of unknown ingredients of the plant materials, small amount of

provided “herbal mixtures” and low concentration of sprayed synthetic cannabinoid.

In the all five cases studied, identification of 5F-ADB using GC-MS and confirmation of its structure by $^1\text{H-NMR}$ spectroscopy were efficient for the purposes of toxicological expertise. GC-MS is an analytical method, which provides chromatographic and mass spectral data for identification and characterization of unknown compounds. In addition, the data obtained by second independent analytical method (NMR spectroscopy) corroborate well with the findings achieved by GC-MS technique. Combination of these two methods is a powerful tool for identification and characterization of unidentified substances, as well as for

confirmation of presence of already known chemical compounds.

CONCLUSIONS

Five different “herbal mixtures” seized as criminal evidence in the country were analyzed for the presence of drugs, presumably sprayed on plant materials. In all cases plant materials contained the synthetic cannabinoid 5F-ADB. Identification and structural characterization of SCs are important stages in the case of analysis of new synthesized physiologically active substances in herbal blends intended for smoking.

Acknowledgment: Authors acknowledge the financial support from Sofia University “St. Kliment Ohridski” (Grant № 80-10-23/2018).

REFERENCES

1. R. Lindigkeit, A. Boehme, I. Eiserloh, M. Luebbecke, M. Wiggermann, L. Ernst, T. Beuerle, *Forensic Sci. Intern.*, **191**, 58 (2009).
2. V. Auwärter, S. Dresen, W. Weinmann, M. Müller, M. Pütz, N. Ferreirós, *J. Mass Spectrom.*, **44**, 832 (2009).
3. UNODC. World Drug Report 2017, Drug markets (2017).
4. K. Seely, A. Patton, C. Moran, M. Womack, P. Prather, W. Fantegrossi, A. Radominska-Pandya, G. Endres, K. Channell, N. Smith, K. McCain, L. James, J. Moran, *Forensic Sci. Intern.*, **233**, 416 (2013).
5. S. Brandt, L. King, M. Evans-Brown, *Drug Test. Anal.*, **6**, 587 (2014).
6. B. Logan, L. Reinhold, A. Xu, F. Diamond, *J. Forensic Sci.*, **57**, 1168 (2012).
7. N. Uchiyama, S. Matsuda, M. Kawamura, R. Kikura-Hanajiri, Y. Goda, *Forensic Toxicol.*, **31**, 223 (2013).
8. V. Shevyrin, V. Melkozerov, A. Nevero, O. Eltsov, Y. Shafran, *Forensic Sci. Intern.*, **323**, 1 (2013).
9. N. Langer, R. Lindigkeit, H.M. Schiebel, U. Papke, L. Ernst T. Beuerle, *Forensic Toxicol.*, **34**, 94 (2016).
10. B. Atwood, J. Huffman, A. Straiker, K. Mackie, *Br. J. Pharmacol.*, **160**, 585 (2010).
11. K. Hasegawa, A. Wurita, K. Minakata, K. Gonmori, I. Yamagishi, H. Nozawa, K. Watanabe, O. Suzuki, *Forensic Toxicol.*, **33**, 112 (2014).
12. S. Akamatsu, M. Yoshida, *J. Mass Spectrom.*, **51**, 28 (2016).
13. EMCDDA, Forensic Toxicology Department University Medical Center Freiburg, Lisbon, (2015).
14. Cayman Chemical, <https://www.caymanchem.com/forensics/csl> (2016).
15. H. Gottlieb, V. Kotlyar, A. Nudelman. *J. Org. Chem.*, **62**, 7512 (1997).
16. G. Fulmer, A. Miller, N. Sherden, H. Gottlieb, A. Nudelman, B. Stoltz, J. Bercaw, K. Goldberg. *Organometallics*, **29**, 2176 (2010).
17. K. Tsujikawa, T. Yamamuro, K. Kuwayama, T. Kanamori, Y. T. Iwata, H. Inoue. *Forensic Toxicol.*, **32**, 201 (2013).
18. B. Tomas, T. Lefever, R. Cortes, A. Kovach, A. Cox, P. Patel, G. Pollard, J. Marusich, R. Kevin, T. Gamage, J. Wiley. *J. Pharmacol. Exper. Therap.*, **361**, 162 (2017).

Spectroscopic study of nanocomposites based on PANI and carbon nanostructures for pH sensors

Anita Grozdanov¹, Aleksandar Petrovski¹, Maurizio Avella², Perica Paunović^{1*}, Maria E. Errico², Roberto Avolio², Gennaro Gentile², Francesca De Falco², Aleksandar T. Dimitrov¹

¹ Faculty of Technology and Metallurgy, SS Cyril and Methodius University, RudjerBošković, 16, 1000 Skopje, R. Macedonia

² Institute for Polymers, Composites and Biomaterials, National Research Council, Via Campi Flegrei 34, 80078 Pozzuoli, Italy

Received October 30, 2018; Revised January 7, 2019

Nanocomposites of polyaniline (PANI) and two carbon nanostructures – multiwall carbon nanotubes (MWCNTs) and graphene (G) were obtained by electrochemical polymerization. PANI based nanocomposites with different concentration of carbon nanostructures (CNS:1, 2 and 3wt%) as well as with different methods for CNS dispersion in the electrolyte, were synthesized. The interactions among the CNS nanostructures and polyaniline matrix were studied and the results confirmed strong interactions among the quinoidal structure of PANI and both CNS. In order to design nanocomposite sensors, PANI/CNS nanocomposites were directly electro-polymerized on gold wires of screen printed electrodes. Their sensing activity was evaluated through the resistivity changes at different pH.

Keywords: polyaniline, nanocomposites, carbon nanostructures

INTRODUCTION

Conductive organic polymers capable of conducting electricity due to the partial oxidation or reduction (i.e., doping), were proved as a prospective class of materials in many technological applications [1-3]. They possess an extended π -conjugation along the polymer backbone and exhibit semiconducting behavior [4]. Special attention was given to the polyaniline (PANI) due to its good environmental stability, interesting redox behavior, unique electrical and electrochemical properties, low cost/easy synthesis [4-7]. Depending on the oxidation state, polyaniline can be found in five different states, from which the most important is the so called “emeraldine base” as the most conductive form of neat polyaniline. To achieve conductive polyaniline, emeraldine base must be transformed to emeraldine salt. This can be achieved by doping the emeraldine base with some protonic acids [9]. The choice of the dopant depends on the PANI application [5]. In most of the recent studies, it was shown that hydrochloric and sulphuric acids were the best dopants in terms of stability and conductivity of PANI [10, 11].

PANI application was restricted by its poor mechanical properties and low processability. Because of that, scientists worked to find new ways to improve these properties. One of the approaches is the preparation of PANI-based nanocomposites

with carbon nanostructures (CNS). Recently, it was confirmed that PANI mixed with nanoparticles have emerged as a new class of composites, as the resulting materials demonstrated unique synergistic properties [12]. Among the various nanoparticles, carbon based nanomaterials such as multi-walled carbon nanotubes (MWCNT) and graphene (G) are of particular interest because of their exceptional structural and electronic properties [4, 5]. One of the main reason for application of CNS in nanocomposites is their large surface area to volume ratio, their sp^2 hybridized structure able to give the advantage of π - π interactions with electron rich molecules and their high electrical conductivity. Aromatic structures, in general are known to strongly interact with the basal plane of graphitic surfaces via π -stacking [13, 14].

Several publications have been recently focused on PANI/CNS nanocomposites. Zhou *et al.* demonstrated strong interactions in conjugated systems and greatly improved charge-transfer reaction between polyaniline and carbon nanotubes [14]. Kondawar *et al.* discussed the electrical transport properties of PANI/MWCNT nanocomposites [4]. Kim and Huh [15] prepared PANI/MWCNT-polystyrene composite films with increased electrical conductivity over pure PANI. The enhanced conductivity effect was attributed to carbon nanotubes that may act as conducting bridges between PANI (emeraldine salt) domains due to their large aspect ratio and surface area [16, 17]. As

* To whom all correspondence should be sent.

E-mail: pericap@tmf.ukim.edu.mk

concerning graphene, enhanced electrochemical performances of PANI/G nanocomposites over pristine PANI was reported even if in some cases using modified graphene, these performances decreased. Electrical properties and cycling stability were also improved by the obtainment of graphene chemically grafted with PANI. This was attributed to the increased specific surface area and improved electrical conductivity of graphene [18-21]. Also, amine functionalization of graphene induced improvements of the electrical conductivity and the thermal stability of PANI/G composites [19, 22]. These properties were also found dependent on the particle size and morphology of graphene [5]. Regarding the use of PANI based materials and composites for sensor applications, several work have been reported in the last years to elucidate the chemisorption behavior of PANI and the application of PANI composites in sensors, based on various techniques [23-28]. In a previous work, we have reported the electrochemical polymerization of PANI/CNS nanocomposites and the results obtained on their thermal and morphological characterization in view of the use of these materials for the realization of pH sensors [12]. Preliminary sensing activity of PANI/CNS tablets for pH determination was evaluated using the 4 probe method and interesting results were obtained.

The aim of this work was to obtain a detail characterization of the polymer matrix/CNS-interactions in PANI based nanocomposites containing MWCNT and graphene in order to optimize the properties and the stability of the realized systems.

EXPERIMENTAL

PANI/MWCNT and PANI/G nanocomposites were prepared by electrochemical synthesis described elsewhere [12]. The pristine MWCNTs (code 732, purity ~ 95%, external diameter 10 - 40 nm) were used as received from JRC (ISPRA). Graphene was produced in the laboratories of Faculty of Technology and Metallurgy by molten salt electrolysis using highly oriented graphite electrodes [29]. Before the electrolysis, graphene was purified in 10 wt% solution of H₂O₂ for 2 h and further, in concentrated solution of HF (40 wt%) for 1 h. For some compositions (3wt% of MWCNT and 1,2, and 3 wt% of graphene) further samples were obtained by preliminary deposition of the appropriate amount of CNS on the electrode followed by electro-polymerization. The produced composites were doped in 0.1 M HCl for 24 h. Pure PANI was also synthesized in the same experimental conditions.

Direct electro-polymerization of PANI/CNS nanocomposites on gold wires of screen printed electrodes (SPE) was performed using the same experimental conditions described in reference 12.

Characterization of the prepared nanocomposites was performed by Fourier transform infrared (FTIR) spectroscopy in attenuated total reflectance (ATR) mode, UV-VIS and Raman spectroscopy. FTIR-ATR measurements were carried out on a Perkin Elmer – Spectrum 100 machine using 64 scans. UV-VIS absorption spectra were collected using a JASCO V-570 UV-VIS spectrometer, in the range from 200 to 900 nm with scan speed of 200 nm/min. SEM analysis was done using FEI Quanta 200 system at acceleration voltage of 30 kV.

RESULTS AND DISCUSSION

FTIR-ATR spectra of the prepared PANI/MWCNT nanocomposites are shown in Fig. 1, while FTIR-ATR spectra of PANI/G nanocomposites are shown in Fig. 2.

Due to the incorporation of MWCNT and graphene in the PANI polymer matrix, FTIR-ATR spectra showed the shift of different typical adsorption bands [2,3]. The C=C stretching of quinonoid and benzenoid absorptions of the emeraldine salt in PANI and PANI based nanocomposites were observed at about 1570 cm⁻¹ and ~1480cm⁻¹, respectively [3,4].

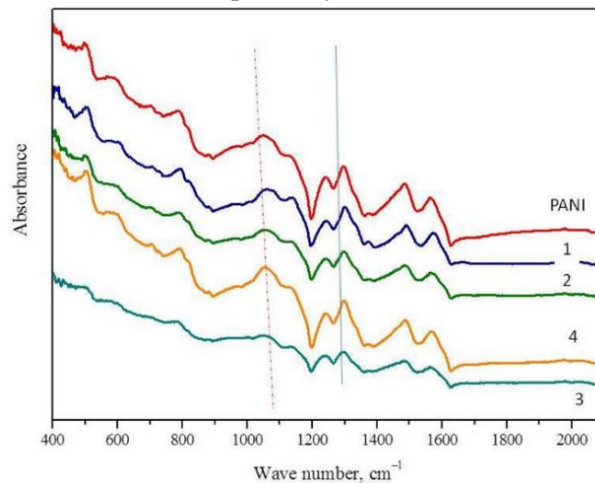


Figure 1. FTIR-ATR spectra of PANI/MWCNT nanocomposites at different MWCNT concentrations: 1) PANI/1 wt% MWCNT; 2) PANI/2 wt% MWCNT; 3) PANI/3 wt% MWCNT, all obtained by preliminary dispersion of MWCNT in the electrolyte; 4) PANI/3 wt% MWCNT obtained after preliminary MWCNT deposition on the electrode. All nanocomposites were obtained with electro-polymerization time of 40 min. FTIR-ATR spectrum of PANI electropolymerized for 40 min is reported for comparison.

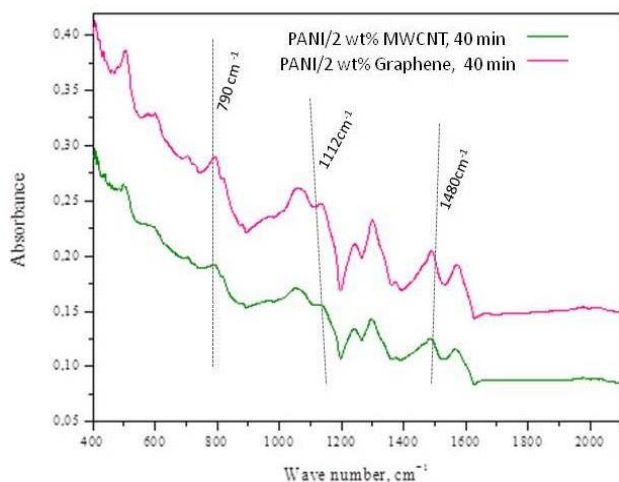


Figure 2. FTIR-ATR spectra of PANI/graphene nanocomposites with different carbon nanostructures (Graphene and MWCNT) with 2 wt% concentrations, all obtained by dispersion of carbon nanostructure in the electrolyte and electropolymerization time of 40 min.

Actually, the characteristic peak at 1560-1630 cm^{-1} attributed to the C=C stretching vibrations of graphite domains of graphene and nanotubes were not clearly detected because of the relatively low amount of CNS and of the overlapping of these absorption bands with the C=C stretching of quinonoid rings of PANI [5]. The C-N stretching and C-H in plane and out-of-plane bending absorption, typical for PANI, were also observed for all the samples at $\sim 1300 \text{ cm}^{-1}$, 1112 cm^{-1} and 790 cm^{-1} , respectively. For all the nanocomposites, either those obtained by dispersion of CNS in the electrolyte, either those obtained by preliminary deposition of the CNS on Pt electrode, the absorption band centered at about 1570 cm^{-1} was shifted to higher wave number values with respect to neat PANI. Moreover, for all the nanocomposite samples, by increasing the concentration of nanostructures from 1 to 3 wt%, the C-N stretching absorption band centered at about 1300 cm^{-1} was shifted to lower values, close to 1290 cm^{-1} [3]. Structural changes obtained by adding CNS to PANI were also evidenced by UV-VIS spectroscopy. Fig. 3 shows the UV-VIS spectra of PANI/MWCNT nanocomposites and Fig. 4 the UV-VIS spectra of PANI/graphene nanocomposites.

The emeraldine form of PANI polymer matrix exhibited two peaks with maxima at about 320 nm, corresponding to $\pi-\pi^*$ transition centered on the benzenoid unit, and about 620 nm, corresponding to the quinonoid excitation band [2]. A shoulder at 272 nm in the PANI spectrum corresponded to $\pi-\pi^*$ transitions of aromatic C-C bonds. A comparison of the effect of the addition of graphene and MWCNT to plain PANI is summarized in Table 1 for nanocomposites containing 2 and 3 wt% of

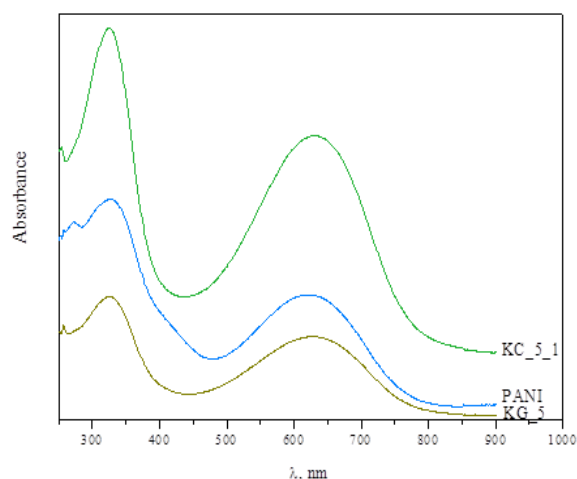


Figure 3. UV-VIS spectra of PANI/3 wt% MWCNT(KC5) and PANI/3 wt% Graphene (KG5) nanocomposites. All nanocomposites were obtained with electro-polymerization time of 40 min. UV-VIS spectrum of PANI electro-polymerized for 40 min is reported for comparison.

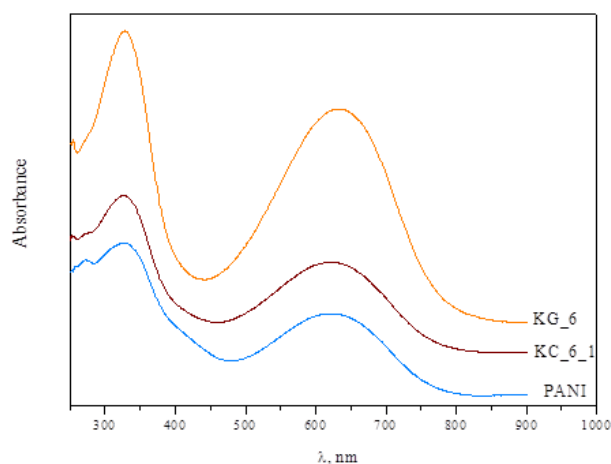


Figure 4. UV-VIS spectra of PANI/2 wt% MWCNT and PANI/2 wt% Graphene nanocomposites. All nanocomposites were obtained with electro-polymerization time of 40 min. UV-VIS spectrum of PANI electro-polymerized for 40 min is reported for comparison.

Table 1. UV-VIS data for the prepared PANI based nanocomposites

Sample	λ , nm	λ , nm	$A_{\text{quin}}/A_{\text{benz}}$
PANI	328	621	0,57
PANI/2wt%MWCNT*	326	630	0,74
PANI/2wt%Graphene	329	635	1,00
PANI/3wt%MWCNT*	325	622	0,4233
PANI/3wt%Graphene	328	634	0,9868

*-Nanocomposites obtained by CNS dispersion in the electrolyte followed by electro-polymerization for 40 min

nanofillers obtained by dispersion of CNS in the electrolyte followed by electro-polymerization. For

almost all nanocomposites, in presence of CNS, the characteristic peak at 620 nm was shifted to higher wavelengths values due to the electronic transition between quinonoid and benzenoid of PANI structures [3]. This effect was always recorded for nanocomposites containing graphene, whereas for nanocomposites containing MWCNT in some cases the shift was negligible (see for instance PANI/3 wt% MWCNT in Table 1). CNS and graphene in particular, also induced a relative increase of the intensity of the absorption band centered at 630 nm with respect to the band centered at about 320 nm. As it can be observed in Table 1, for PANI/2 wt% MWCNT and for PANI/2wt% graphene, the intensity ratio of $A_{\text{quin}}/A_{\text{benz}}$ was found 0.74 to 1.00 respectively and these values are significantly higher than $A_{\text{quin}}/A_{\text{benz}}$ of 0.57 recorded for PANI. Lower increase was recorded at higher CNS loading. For PANI/3 wt% MWCNT the $A_{\text{quin}}/A_{\text{benz}}$ ratio was found comparable to that recorded for PANI, whereas for PANI/3 wt% graphene the $A_{\text{quin}}/A_{\text{benz}}$ ratio was about 0.75. This effect can be attributed to possible agglomeration phenomena of the nanofillers, occurring at higher CNS loadings that reduce PANI/CNS interactions. Comparable effects were also recorded for nanocomposites realized by preliminary deposition of CNS on the electrode followed by PANI electro-polymerization. No significant differences were recorded amongst nanocomposites realized by electro-polymerization lasting 40 min or 60 min.

The characteristic morphology of PANI based nanocomposites is shown in Fig. 5 (for PANI/3 wt% MWCNT system) and Fig. 6 (for PANI/3 wt% Graphene system). It is evident that fibrous and porous morphology was found in both nanocomposite systems which is typical for PANI based nanocomposites.

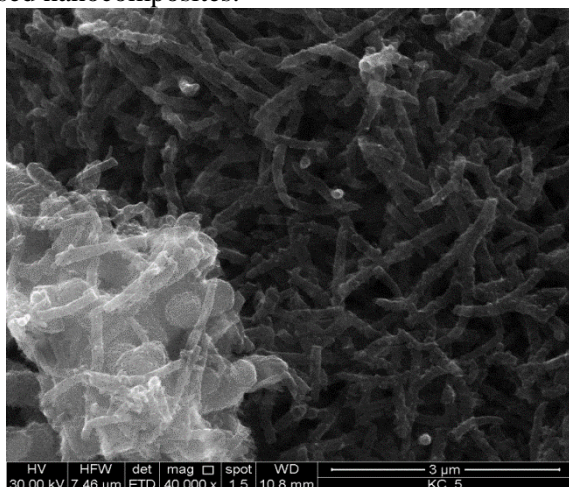


Figure 5. SEM microphotographs of PANI/3 wt% MWCNT.

The high level of interactions established by PANI and CNS in the nanocomposites, confirmed by FTIR, UV-VIS and Raman spectroscopy (Raman analysis published in ref.32), let us suppose a possible significant effect of the nanofillers on the redox properties of PANI in the nanocomposites. Therefore, selected PANI/CNS nanocomposites (PANI/3wt%MWCNT and PANI/3wt%graphene obtained by dispersion of the nanofillers within the electrolyte) were applied on gold SPE by 40 min electro-polymerization. The SPE coated with PANI/MWCNT is exemplificatively shown in the insert in Fig. 7.

Electrical conductivity of these SPE-nanocomposites was measured in different aqueous buffers at various pH values, in order to check the possible suitability of these sensors for pH determination. Interesting, a non linear response was recorded for both MWCNT and graphene nanocomposites coated SPE, with huge electrical resistivity differences recorded at different pH. For instance, the gold SPE coated with PANI/3wt%graphene showed resistivity of 4.60 kΩ.cm at pH=4.5; 360 kΩ.cm at pH=7, and 2430 kΩ.cm at pH=10. A similar trend was also recorded for the gold SPE coated with PANI/3wt%MWCNT. The effect of pH variation on the electrical conductivity of PANI nanocomposites was explained on the basis of different degree of protonation of the imine nitrogen atoms of the polymer chain in the presence of the nanofillers. Starting from these results, further researches are in progress to optimize the composition and the response of the SPE/nanocomposite electrodes.

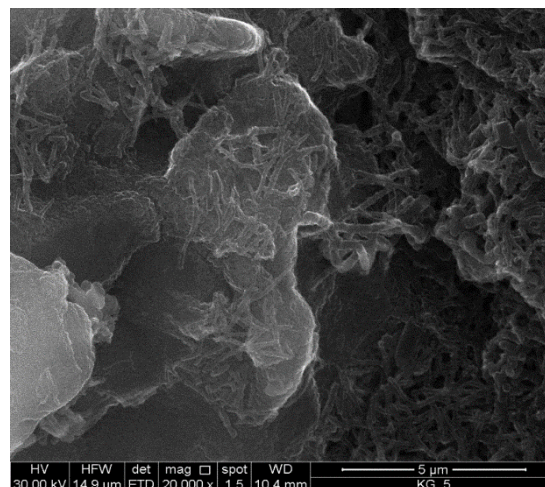


Figure 6. SEM microphotographs of PANI/3 wt% Graphene.

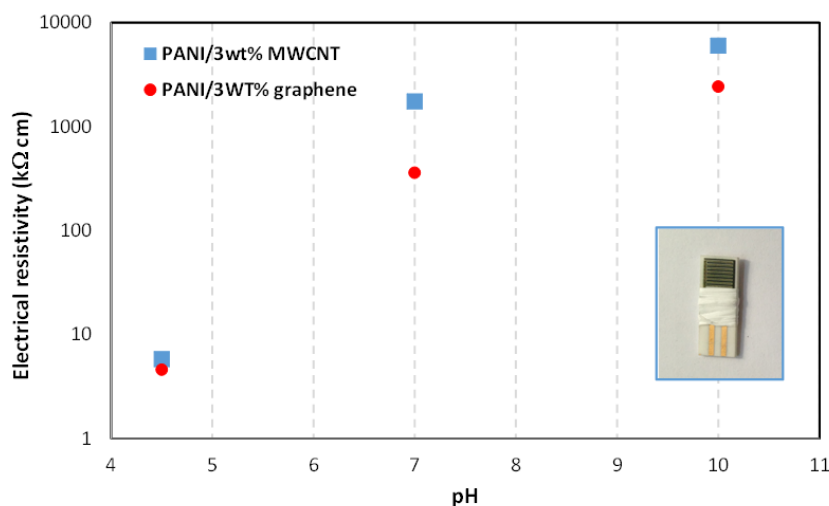


Figure 7. Electrical resistivity of SPE/nanocomposite sensors as a function of pH of aqueous buffer solutions. In the insert, the SPE electropolymerized with PANI/3 wt% MWCNT is shown.

CONCLUSIONS

Characterization of PANI/MWCNT and PANI/graphene nanocomposites prepared by electropolymerization was performed by spectroscopic techniques such as FTIR-ATR, Raman and UV-VIS. The realized nanocomposites were also applied by electro-polymerization on gold SPE and the electrical resistivity of these SPE/nanocomposites was evaluated as a function of the pH of aqueous buffers. Based on the obtained results, the following conclusions were drawn:

Due to the incorporation of pristine MWCNT and graphene nanostructures in the PANI polymer matrix, all spectroscopic analyses indicated strong interactions between the carbon nanostructures and the polymer matrix. In particular, FTIR-ATR spectra showed that for nanocomposites and in particular, for those obtained by preliminary deposition of CNS on the Pt electrode followed by PANI electropolymerization, the typical band of PANI centered at 1571 cm^{-1} was shifted to higher wave number values. The same trend was also the peak attributed to the C–N stretching, centered at about 1300 cm^{-1} , shifted to lower values, down to about $1290\text{--}1294\text{ cm}^{-1}$ by increasing the CNS content in the nanocomposites. Raman spectra of the studied nanocomposites have shown that characteristic bands at 1586 cm^{-1} and 1346 cm^{-1} are due to D peaks and G peaks, respectively, indicating the lattice distortions of the graphene due to the presence of the polyaniline in the network. Also, UV-VIS of nanocomposites were significantly influenced by the presence of CNS, with significant shifts recorded for the peak in comparison to that centered at about 330 nm , in particular in presence of graphene. Raman spectroscopy further confirmed the high

levels of interactions between CNS and PANI, with the significant shift of the position of typical PANI absorption bands and the change of their relative intensity, also in this case more significant for graphene nanocomposites. The electrical behavior of SPE/nanocomposites as a function of the pH of aqueous buffers was evaluated by electrical resistivity measurements. Results were very interesting indicating a non linear dependence of the electrical resistivity with pH, indicating the possible use of these systems for pH determination.

Acknowledgments: This research was performed under the FP7 Project COMMON SENS - "Cost-effective sensors, interoperable with international existing ocean observing systems to meet EU policies requirements" (Project reference 614155).

REFERENCES

1. J. Huang, S. Virji, B. Weiller, R. B. Kaner, *Chem. Eur. J.*, **10**, 1314 (2004)
2. B. J. Gallon, R. W. Kojima, R. B. Kaner, P. L. Diaconescu, *Angew Chem Int Ed Engl.*, **46**, 7251 (2007)
3. V. Gupta, N. Miura, *Mater. Lett.*, **60**, 1466 (2006)
4. S. B. Kondawar, M. D. Deshpande, S. P. Agrawal, *Int. J. Compos. Mater.*, **2**, 32 (2012)
5. R. Arora, A. Srivastav, U. K. Mandal, *Int. J. Mod. Eng. Res. (IJMER)*, **2**, 2384 (2012)
6. H. Shirakawa, E. J. Louis, A. G. MacDiarmid, C. K. Chiang, A. J. Heeger, *J. Chem. Soc., Chem. Commun.*, **16**, 578 (1977)
7. E. Hermelin, J. Petitjean, S. Aeiyaeh, J. C. Lacroix, P. C. Lacaze, *J. Appl. Electrochem.*, **31**, 905 (2001)
8. Y. Wei, G. W. Jang, K. F. Hsueh, E. M. Scherr, A. G. MacDiarmid, A. J. Epstein, *Polymer*, **33**, 314 (1992)
9. D. D. Borole, U. R. Kapadi, P. P. Kumbhar, D. G. Hundiware, *Mater. Lett.*, **57**, 844 (2002)
10. S. H. Kim, J. H. Seong, K. W. Oh, *J. Appl. Polym. Sci.*, **83**, 2245 (2002)

11. A. Pron, J-E. Osterholm, P. Smith, A. J. Heeger, J. Laska, M. Zagorska, *Synth. Met.*, **57** 3520 (1993)
12. A. Petrovski, P. Paunović, R. Avolio, M. E. Errico, M. C. Cocca, G. Gentile, A. Grozdanov, M. Avella, J. Barton, A. T. Dimitrov, *Mater. Chem. Phys.*, **185**, 83 (2017)
13. X-L. Xie, Y-W Mai, X-P. Zhou, *Mater. Sci. Eng. R*, **49**, 89 (2005)
14. Y. Zhou, Z-Y. Qin, L. Li, Y. Zhang, Y-L. Wei, L-F. Wang, M-F. Zhu, *Electrochim. Acta*, **55**, 3904 (2010)
15. W. J. Kim, D. S. Huh, *Bull. Korean Chem. Soc.*, **33**, 2345 (2012)
16. T. M. Wu, Y. W. Lin, *Polymer*, **47**, 3576 (2006)
17. D. K. Kim, K. W. Oh, S. H. Kim, *J. Polym. Sci. Part B Polym. Phys.*, **46**, 2255 (2008)
18. H. K. Hassan, N. F. Atta, A. Galal, *Int. J. Electrochem. Sci.*, **7**, 11161 (2012)
19. S. Sahoo, G. Karthikeyan, G. C. Nayak, C. K. Das, *Macromol. Res.*, **20**, 415 (2012)
20. Z. Gao, F. Wang, J. Chang, D. Wu, X. Wang, X. Wang, F. Xu, S. Gao, K. Jiang, *Electrochim. Acta*, **133**, 325 (2014)
21. J. Li, H. Xie, Y. Li, J. Liu, Z. Li, *J. Power Sources*, **196**, 10775 (2011)
22. S. Sahoo, P. Bhattacharya, G. Hatui, D. Ghosh, C. K. Das, *J. Appl. Polym. Sci.*, **128**, 1476 (2013)
23. Z-F. Li, F. D. Blum, M. F. Bertino, C-S. Kim, *Sens. Actuators B*, **183**, 419 (2013)
24. S. Srivastava, S. S. Sharma, S. Kumar, S. Agrawal, M. Singh, Y. K. Vijay, *Int. J. Hydrogen Energy*, **34**, 8444 (2009)
25. B. Ding, M. Wang, J. Yu, G. Sun, *Sensors*, **9**, 1609 (2009)
26. K. J. Loh, J. P. Lynch, N. A. Kotov, *J. Intell. Mater. Syst. Struct.*, **19**, 747 (2008)
27. Alamusi, N. Hu, H. Fukunaga, S. Atobe, Y. Liu, J. Li, *Sensors*, **11**, 10691 (2011)
28. B. Lakard, G. Herlem, S. Lakard, R. Guyetant, B. Fahys, *Polymer*, **46**, 12233 (2005)
29. A. T. Dimitrov, A. Tomova, A. Grozdanov, O. Popovski, P. Paunović, *J. Solid State Electrochem.*, **17**, 399 (2013)
30. V. Ambrogì, G. Gentile, C. Ducati, M. C. Oliva, C. Carfagna, *Polymer*, **53**, 291 (2012)
31. R. Beams, L. G. Cancado, L. Novotny, *J. Phys. Condens. Mater.*, **27**, 083002 (2015)
32. A. Grozdanov, A. Petrovski, P. Paunovik, A. T. Dimitrov, M. Avella, "MWCNT/Polyaniline Nanocomposites used for pH Nanosensors of Marine waters", pp.231-238, Springer International Publishing AG 2018, M.Cocca et al.(eds.), Proceedings of the International Conference on Microplastic Pollution in the Mediteranean Sea, Springer Water, (2018)https://doi.org/10.1007/978-3-319-71279-6_32

A static headspace GC-FID method for trace analysis of volatile organic compounds (VOCs) in waters

Z. A. Mustafa*, R. S. Milina

Central Research Laboratory, Prof. Assen Zlatarov University – Burgas, Bulgaria

Received October 31, 2018; Revised December 20, 2018

The possibility of trace levels volatile organic compounds in water was investigated. Headspace was employed for isolation/preconcentration of the samples. Gas Chromatography with flame ionization detector followed. Some HS parameters were experimentally considered to maximizing the signal and sensitivity and minimizing the relative standard deviation of the results. Optimization of conditions was carried out using a lot of experiments combining different parameters. The optimized HS–GC–FID method was validated in terms of linearity, limit of detection, limit of quantitation and relative standard deviation.

Keywords: volatile organic compounds, gas chromatography, headspace

INTRODUCTION

Volatile organic compounds (VOCs) are organic chemical compounds that have high enough pressures under normal conditions to significantly vaporize and enter the atmosphere. Benzene, toluene, ethyl benzene, mixture of xylenes, isopropylbenzene and 4-ethyltoluene are among the volatile monoaromatic organic hydrocarbons found in petroleum derivatives [1]. Water contamination by monoaromatic compounds is a very serious problem as these compounds are toxic and classified as carcinogens for humans, especially benzene, which is a leukemic agent in humans and has a very low tolerance standard [2] and because they can change the taste and odour of drinking water. The chronic health effects to the general public from ingestion of VOCs at low concentrations in drinking water are less well understood but health values are well above offensive taste/odour thresholds and contain significant safety margins. The US environmental protection agency (EPA) has included these compounds on the list of national primary drinking water standards and established a maximum contaminant level (MCL) of 5.0 µg/L for benzene, for toluene 1000 µg/L, for ethyl benzene 700 µg/L and for xylenes 10,000 µg/L in drinking water [2, 3]. The presence of these compounds in both ground- and surface water are related to fuel spills, leaking underground storage tanks, and the release of unburned fuel directly into the atmosphere and surface waters [4, 5].

Analytical methods for investigation and determination of water contaminated with compounds of low concentrations is a complex problem that can be solved by using isolation and

pre-concentration procedures. VOCs concentration levels found in drinking and natural water samples are typically in the order of ng/L to µg/L. There are many techniques that can be used for the isolation and pre-concentration of the considered pollutants [6]. Conventional liquid-liquid extraction (LLE) [7], dispersive liquid-liquid microextraction [8], headspace (HS) techniques [9, 10], solid-phase extraction (SPE) [9, 11, 12] and solid-phase microextraction (SPME) [9, 12, 13] have all been used for isolation and pre-concentration of volatile organic compounds from water. Gas chromatography has commonly been used as a final step to obtain qualitative and quantitative results. The reason for this status is because chromatography combines the separation power of the method with the selectivity and sensitivity of detectors, able to fast qualitative and quantitative determination.

Head-space gas chromatography (HS-GC) indirectly determines the volatile constituent in liquid and solid samples by analyzing the vapor phased that is in thermodynamic equilibrium with the sample in a closed system. This technique is relatively simple and can provide sensitivity similar to dynamic purge and trap analysis. Complex sample matrices, which may be difficult to analyze directly or would require sample extraction or preparation can be placed in the vial with little or no preparation. Recently HS-GC is widely used in environmental analysis because of its advantages: economy of efforts and the attainment of a sample which is relatively free from the problems associated with the chromatographic properties of the matrix. As a gas extraction procedure it replaces a solvent extraction, thus avoiding the many problems with solvents.

Head-space extraction technique is classified into two types: static and dynamic. The theoretical

* To whom all correspondence should be sent.

E-mail: zmustafa@abv.bg

Mustafa & Milina: A static headspace GC-FID method for trace analysis of volatile organic compounds (VOCs) in waters principles and quantification by two types headspace have been clearly described in several papers [14-17]. For routine analysis static headspace GC is the method of choice because it is rapid and requires no cleaning between samples while dynamic headspace is a much slower method because the sample tube and trapping column are difficult to clean and often require purging of the system to completely remove some volatile compounds.

It is known that different parameters affect headspace extraction. Optimization of this procedure requires consideration of parameters including vial equilibration time, extraction temperature and sample volume.

In this work possibility of trace levels volatile organic compounds in water was investigated. The influence of the different conditions for headspace analysis was investigated in order to reach low concentrations of the determinable compounds. A method using HS-GC-FID was validated.

EXPERIMENTAL

Chemicals and standard solutions

All chemicals used were of the highest available purity purchased from Sigma – Aldrich (Switzerland) and Supelco. A stock standard solution of benzene, toluene, ethylbenzene, o-xylene, p-xylene, iso-propylbenzene and 4-ethyltoluene was prepared in methanol. The vial was sealed, mixed and were stored in a refrigerator at 4°C. Working standard solutions of lower concentrations were prepared by dilution of the stock standard solution with deionized water to the required concentration.

GC analysis

GC analyses were carried out on a GC system Agilent Technologies 7890A equipped with flame ionization detector (FID) and split/splitless injector. The fused silica column used was HP-5, 30 m x 0.320 mm I.D. film thickness 0.25 µm. Temperature program of the oven: initial temperature 50°C for 2 minutes, rate 5 °C/min to 120°C, 2 minutes. Detector temperature: 300°C,

injector temperature: 250°C. Carrier gas: He, column flow 1.2 ml/min. Hydrogen flow 40 ml/min, air flow 400 ml/min, make-up gas (nitrogen) 40 ml/min. ChemStation for GC was used for instrument control, data acquisition and data analysis.

Static headspace GC analyses were carried out using Agilent 7694 Headspace Sampler.

Optimization

Different parameters that influence the extraction efficiency in a headspace experiment of the VOCs were optimized, selecting peak areas as response. Optimization of conditions was carried out using experiments combining 5 sample volumes in the headspace vial, 5 sample equilibration times and 4 temperatures of the oven and triplicate analyses.

RESULTS AND DISCUSSION

Optimization of Headspace parameters

The most important parameters affecting extraction efficiency in a headspace experiment are sample volume, sample equilibration time and temperature of the sample in oven [14].

Different parameters that influence the extraction efficiency in a headspace experiment of the VOCs were optimized. All parameters which may influence benzene, toluene, ethylbenzene, o-xylene, p-xylene, iso-propylbenzene and 4-ethyltoluene analysis are discussed below.

Selection of optimal sample volume

Headspace sample vials are typically in 10 ml and 20 ml sizes. We used 20 ml vials in order to have more possibilities to vary the sample weight.

The analytical chemist would increase the concentration of the sample or inject more samples onto a column to get a better signal. With headspace, more sample volume does not always provide the expected increase in peaks areas. We changed the sample volume from 5 to 16 ml at two different temperatures but the same time. Five samples with analytes concentration (160 µg/l) and sample volumes: 5, 10, 12, 14 and 16 ml were investigated. The other parameters were sample equilibration time 15 minutes, oven temperature 75°C and 85°C.

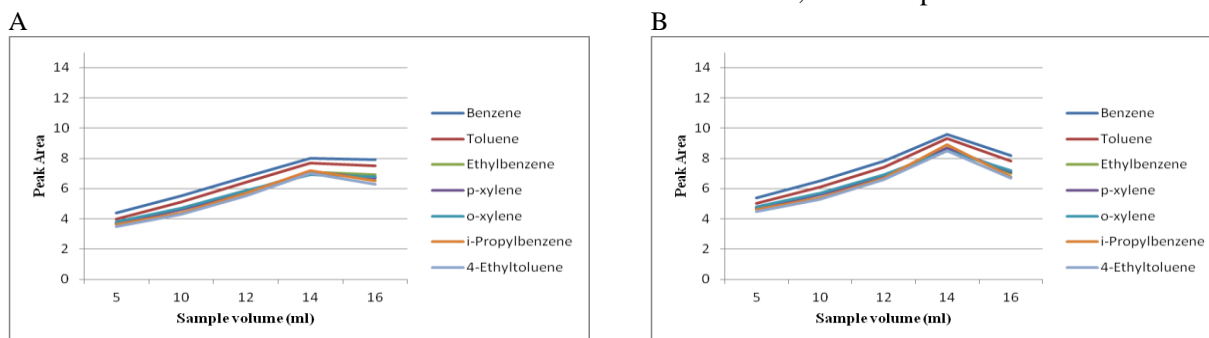
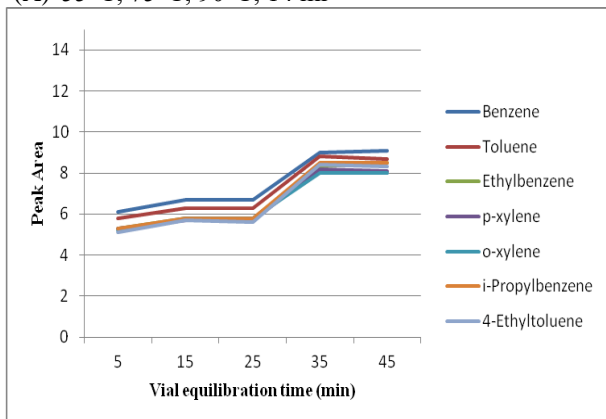
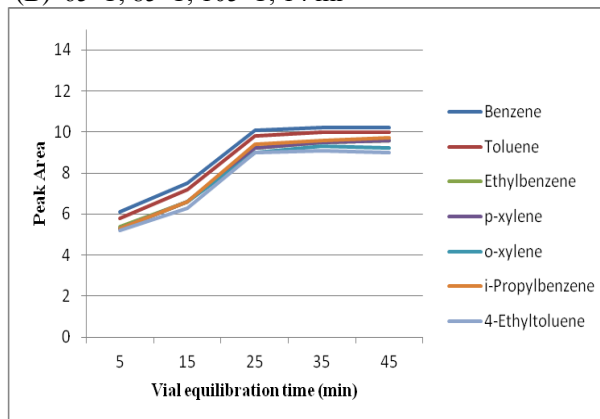


Fig. 1 The effect of sample volume on a detector response (peak area) of the VOCs. Extraction conditions: analytes concentration 160µg/L, sample equilibration time 15 minutes, oven temperature 75°C (A) and 85°C (B).

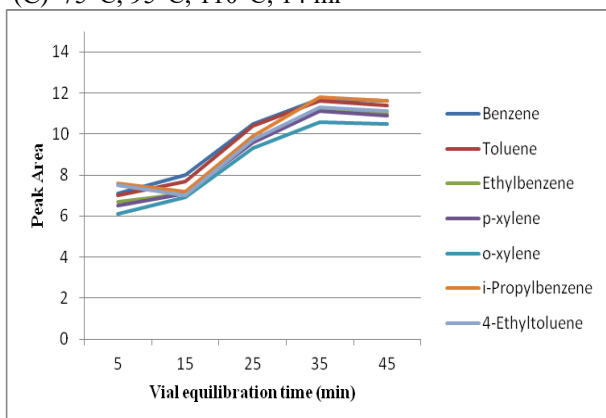
(A) 55°C, 75°C, 90°C, 14 ml



(B) 65°C, 85°C, 105°C, 14 ml



(C) 75°C, 95°C, 110°C, 14 ml



(D) 85°C, 100°C, 120°C, 14 ml

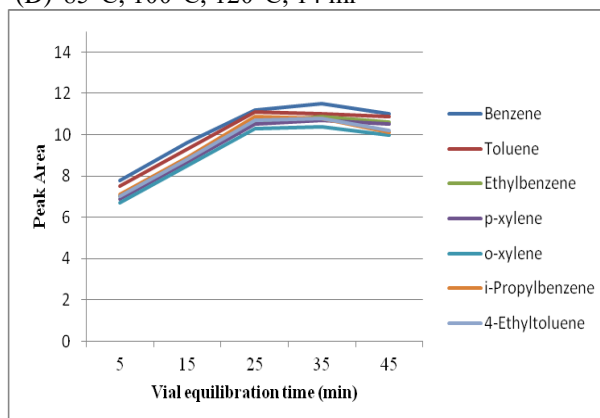


Fig. 2 The effect of sample equilibration time and temperature on a detector response (peak area) of the VOCs. Extraction conditions: analyte concentration 160 μ g/L, sample equilibration time 5 – 45 minutes, oven temperature 55°C (A), 65°C (B), 75°C (C), 85°C (D).

The results shown in Fig.1 A and B indicates that for all analytes the analytical signal increases with sample volume in the range of 5–14 ml and after 14 ml the rate of increase slows down (75°C) or even decreases (85°C). Hence, a sample volume of 14 ml was applied to subsequent experiments.

Selection of Sample equilibration time and temperature

Other two factors that should be considered at this point are the equilibration time and temperature. Higher temperatures lead to higher vapor pressure of the analyte and hence its concentration in the headspace increases. The effect of temperature and time on the extraction was investigated at 4 different temperatures 55°C, 65°C, 75°C, 85°C for five different equilibration times 5, 15, 25, 35 and 45 min respectively. It was not possible to apply a higher temperature than 85°C because would be introduced a higher amount of water (as vapor) during the headspace injection and this would lead to an increase in background level.

As shown in Fig. 2 the highest detector response was obtained when the thermostat was kept at 75°C (C) and 85°C (D), but the equilibration time at 75°C

was ten minutes longer. It can be also seen that the difference in detector response between the lowest (55°C) (A) and the highest (85°C) (D) temperature is two orders of magnitude. Therefore, an equilibration time of 25 min and equilibration temperature of 85°C were selected for further experiments.

Method validation

After analyzing all experimental results, the following conditions have been selected to evaluate the performance of the method: 14 ml water samples, equilibration time of 25 min and equilibration (oven) temperature 85°C. The method of external standard was used for quantitation.

Typical validation characteristics which should be considered are Accuracy, Precision (Repeatability, Intermediate Precision), Specificity, Limit of detection (LOD), Limit of quantitation (LOQ), Linearity, Range [18-20].

The optimized HS-GC-FID method was validated in terms of linearity, precision, limit of detection (LOD), limit of quantitation (LOQ) and relative standard deviation RSD (%).

To evaluate the linearity of the method, a calibration curve was performed with working aqueous standards containing concentrations in the range from 5 - 200 µg/L for all analytes. Three replicate samples for each point were made. The calibration curve constructed was evaluated by its correlation coefficient. All the analytes exhibited good linearity over the range studied with correlation coefficients (r^2) between 0.9951 and 0.9974 (Table 1).

LOD of an analytical method refers to the lowest amount of analyte that can be detected which is not necessarily quantified as an exact value. Meanwhile, LOQ is the lowest concentration of an analyte that can be quantitatively determined with appropriate precision. In a GC measurement, both LOD and LOQ are important. The LOD and LOQ were

calculated as 3 SD and 10 SD respectively [18-21]. The results obtained are show Table 1.

Precision as relative standard deviation RSD (%) and accuracy as recovery (%) were measured by spiking the sample with two known concentrations (5 and 100 µg/L) of each aromatic hydrocarbon. The spiked sample was analyzed five times following the described procedure.

The spiked concentrations and standard deviation values for the precision and accuracy also are given in Table 1. For five independent determinations at 5 and 100 µg/L, precision (RSD) was between 4.90 % to 9.13 % for the low level and 1.80 % to 4.71 % for the high level. Accuracy from spiked water was between 79.41 and 98.82 % for the low level and 93.00 and 99.98 % for the high level.

Table 1. Parameters of calibration curves for investigated VOCs in water, precision, accuracy results for the analysis of VOCs in spiked water, LOD and LOQ

Compound	Linear range (µg/L)	Correlation coefficient (r^2)	Spiked Conc. (µg/L)	RSD (%)	Accuracy (%)	LOD µg/L	LOQ µg/L																																																													
Benzene	5.19 – 207.60	0.9958	5.19	6.57	93.83	0.96	3.20																																																													
			96.90	2.31	99.98			Toluene	5.13 – 205.20	0.9964	5.13	6.80	93.90	0.96	3.20	95.80	2.04	99.50	Ethylbenzene	5.13 – 205.20	0.9967	5.13	4.90	95.51	0.72	2.40	95.80	1.80	97.34	p-xylene	5.10 – 204.00	0.9966	5.10	6.76	95.68	0.99	3.30	95.20	2.97	99.02	o-xylene	5.22 – 208.80	0.9970	5.22	7.54	98.82	1.14	3.80	97.50	2.96	97.10	iso-Propylbenzene	5.10 – 204.00	0.9974	5.10	9.13	79.41	1.11	3.70	95.20	4.71	93.50	4-Ethyltoluene	5.10 – 204.00	0.9951	5.10	8.40	79.60
Toluene	5.13 – 205.20	0.9964	5.13	6.80	93.90	0.96	3.20																																																													
			95.80	2.04	99.50			Ethylbenzene	5.13 – 205.20	0.9967	5.13	4.90	95.51	0.72	2.40	95.80	1.80	97.34	p-xylene	5.10 – 204.00	0.9966	5.10	6.76	95.68	0.99	3.30	95.20	2.97	99.02	o-xylene	5.22 – 208.80	0.9970	5.22	7.54	98.82	1.14	3.80	97.50	2.96	97.10	iso-Propylbenzene	5.10 – 204.00	0.9974	5.10	9.13	79.41	1.11	3.70	95.20	4.71	93.50	4-Ethyltoluene	5.10 – 204.00	0.9951	5.10	8.40	79.60	1.02	3.40	95.20	3.43	93.00						
Ethylbenzene	5.13 – 205.20	0.9967	5.13	4.90	95.51	0.72	2.40																																																													
			95.80	1.80	97.34			p-xylene	5.10 – 204.00	0.9966	5.10	6.76	95.68	0.99	3.30	95.20	2.97	99.02	o-xylene	5.22 – 208.80	0.9970	5.22	7.54	98.82	1.14	3.80	97.50	2.96	97.10	iso-Propylbenzene	5.10 – 204.00	0.9974	5.10	9.13	79.41	1.11	3.70	95.20	4.71	93.50	4-Ethyltoluene	5.10 – 204.00	0.9951	5.10	8.40	79.60	1.02	3.40	95.20	3.43	93.00																	
p-xylene	5.10 – 204.00	0.9966	5.10	6.76	95.68	0.99	3.30																																																													
			95.20	2.97	99.02			o-xylene	5.22 – 208.80	0.9970	5.22	7.54	98.82	1.14	3.80	97.50	2.96	97.10	iso-Propylbenzene	5.10 – 204.00	0.9974	5.10	9.13	79.41	1.11	3.70	95.20	4.71	93.50	4-Ethyltoluene	5.10 – 204.00	0.9951	5.10	8.40	79.60	1.02	3.40	95.20	3.43	93.00																												
o-xylene	5.22 – 208.80	0.9970	5.22	7.54	98.82	1.14	3.80																																																													
			97.50	2.96	97.10			iso-Propylbenzene	5.10 – 204.00	0.9974	5.10	9.13	79.41	1.11	3.70	95.20	4.71	93.50	4-Ethyltoluene	5.10 – 204.00	0.9951	5.10	8.40	79.60	1.02	3.40	95.20	3.43	93.00																																							
iso-Propylbenzene	5.10 – 204.00	0.9974	5.10	9.13	79.41	1.11	3.70																																																													
			95.20	4.71	93.50			4-Ethyltoluene	5.10 – 204.00	0.9951	5.10	8.40	79.60	1.02	3.40	95.20	3.43	93.00																																																		
4-Ethyltoluene	5.10 – 204.00	0.9951	5.10	8.40	79.60	1.02	3.40																																																													
			95.20	3.43	93.00																																																															

CONCLUSIONS

The possibility of trace levels volatile organic compounds in water using static head-space was investigated. Capillary gas chromatography with flame ionization detector was used for resolution and quantitation. The most important parameters affecting extraction efficiency in a headspace experiment of the VOCs were optimized. The optimized HS-GC-FID method was validated in terms of linearity, limit of detection (LOD), limit of quantitation (LOQ) and relative standard deviation RSD (%). All the analytes exhibited good linearity over the range studied (5 - 200 µg/L) with correlation coefficients (r^2) between 0.9951 and 0.9974. LODs and LOQs varied from 0.72 to 1.14 µg/L and from 2.4 to 3.8 µg/L, respectively.

REFERENCES

1. A. Sarafraz-Yazdi, A. Amiri, Z. Eshaghi, *Chemosphere*, **71**, 671 (2008).
2. Y. AlSalka, F. Karabet, S. Hashem, *Anal. Methods*, **2**, 1026, (2010).
3. USEPA, List of Contaminants & their Maximum Contaminant Level (MCLs) in drinking water, <http://www.epa.gov/safewater/mcl.html#organ ic>.
4. I. Arambarri, M. Lasa, R. Garcia, E. Millan, *J. Chromatography A*, **1033**, 193 (2004).
5. M. Rosell, S. Lacorte, A. Ginebreda, D. Barcelo, *Journal of Chromatography A*, **995**, 171 (2003).
6. K. Demeestere, J. Dewulf, B. De Witte, H. Van Langenhove, *J. Chromatography A*, **1153**, 130 (2007).
7. D. Peroni, W. Egmond, W. Kok, H. Janssen, *J. Chromatography A*, **1226**, 77 (2012).
8. Y. Assadi, F. Ahmadi, M. Reza, M. Hossieni, *Chromatographia*, **71**, 1137 (2010).

9. J. Menendez, M. Sanchez, J. Uria, E. Martinez, A. Sanz-Medel, *Anal. Chim. Acta*, **415**, 9 (2000).
10. A. Serrano, M. Gallego, *Journal of Chromatography A*, **1045**, 181 (2004).
11. C. Erger, T. Schmidt, *Trends Anal. Chem.*, **61**, 74 (2014).
12. P. Castells, F.J. Santos, M.T. Galceran, *J. Chromatography A*, **1025**, 157 (2004).
13. H. Piri-Moghadam, F. Ahmadi, J. Pawliszyn, *Trends Anal. Chem.* **85**, 133 (2016).
14. A.C.Soria, M.J.Garcia-Sarrio, M.L.Sanz, *Trends Anal. Chem.* **71**, 85 (2015).
15. C. Bicchi, C. Cordero, E. Liberto, B. Sgorbini, P. Rubiolo, *J. Chromatography A*, **1184**, 220 (2008).
16. N.H. Snow, G.P. Bullock, *J. Chromatography A*, **1217**, 2726 (2010).
17. B. Kolb, *J. Chromatography A*, **842**, 163, (1999).
18. I. Taverniers, M. De Loose, E. Van Bockstaele, *Trends Anal. Chem.*, **23**, 535 (2004).
19. B. Magnusson, U. Örnemark (eds.) Eurachem Guide: The Fitness for Purpose of Analytical Methods – A Laboratory Guide to Method Validation and Related Topics, (2nd ed. 2014).
20. ICH-Q2A, Guideline for Industry: Text on Validation of Analytical Procedures, 1995.
21. A. Shrivastava, V. Gupta, *Chron. Young Sci.*, **2**, 21 (2011).

Determination of brodifacoum, bromadiolone and difenacoum in commercial rodenticides by using high-performance liquid chromatography with UV detection

E. S. Belyaev¹, S. V. Andreev^{*1}, A. O. Ivanova¹, A. A. Ischenko²

¹Department of Chemistry, Scientific Research Disinfectology Institute, 18 Nauchniy proezd, Moscow, 117246, Russia

²Department of Analytical Chemistry, Russian University of Technology-MIREA, Vernadskogo ave., 86, Moscow, 119571, Russia

Received October 31, 2018; Revised January 8, 2019

Small vertebrates are carriers of infectious diseases. Recently, brodifacoum, bromadiolone, difenacoum are used in rodenticides more often. This work describes simple methods for determination of brodifacoum, bromadiolone and difenacoum in all types of rodenticide baits. For analysis of wheat-based and grain baits, about 10 g of the sample is sonicated in acetone for 3 hours. Then, the grain or flour is separated. Then the acetone is evaporated, the residue is dissolved in acetonitrile. Solid briquettes are a mixture of paraffin, poison and filler, which can be used as grain, flour and the like. Extraction in the hexane-acetonitrile system solves the problem of difficult analysis of baits containing paraffin. Paraffin dissolves in hexane, while brodifacoum, bromadiolone and difenacoum are not. If the bait contains any filler, it is filtered and the poison is extracted from it as described above. The resulting extract was examined using reversed phase HPLC with a diode array detector. The best separation of the components was achieved using a Thermo Acclaim Surfactant 5 μ m (4.6 \times 250 mm) column with a mobile phase consisting of acetonitrile and 0.1 M aqueous ammonium acetate solution (pH 5.4) in a gradient elution mode. Linearity for considered rodenticides varies from 0.00067 to 0.010 %. Depending on the type of bait limits of detection for bromadiolone was from 0.000102 to 0.000143 %, for brodifacoum from 0.000101 to 0.000255 % and for difenacoum from 0.000156 to 0.000313 %. The recovery of bromadiolone was 94 %, for brodifacoum – 98 %, for difenacoum – 90 %.

Keywords: brodifacoum, bromadiolone, difenacoum, rodenticides, HPLC

INTRODUCTION

Infectious diseases are caused by various pathogens, such as fungi, viruses, bacteria, helminths, etc. Rodents carry about 60 infectious diseases, many of which pose a serious threat to human health [1]. Such diseases include hemorrhagic fevers, Born's disease, Lassa fever, hepatitis E, plague, tularemia, salmonellosis, and others [2-5]. In addition, rodents disrupt human activities causing damage to communications and foodstuffs.

Recently, the total number of rodents and the number of rats in particular have been increasing [2,6]. Chemical rodenticides are most commonly used to control rodent numbers [7].

Rodenticide bait has several main components - poison, attractant, preservative, as well as an additive that protects the bait from environmental exposure. There are grain baits, as well as hard (paraffin briquettes) and soft briquettes (wheat-based baits). As active ingredients use poisons of acute action (zinc phosphide) or chronic action (blood anticoagulants) [8]. Anticoagulants of blood are divided into first and second generation. The first generation includes: warfarin, diphacinone,

coumatetralyl, ethylphenacin, chlorophacinone etc. To achieve efficiency, the bait, including anticoagulants of the first generation, must be eaten by mouse-like rodents many times. The second generation anticoagulants include: difenacoum, brodifacoum, difethialone, flocoumafen, bromadiolone, isoindane. Anticoagulants of the second generation cause death of rodents for 3-5 days, which is faster than from anticoagulants of the first generation [9].

Recently, the majority of new rodenticides as active substances contain anticoagulants of the second generation - bromadiolone, brodifacoum or difenacoum (Fig. 1).

To extract bromadiolone from baits in the form of granules in [10] it was proposed to use a 2% solution of formic acid in methanol. A sample of the product was ground in a mortar, then 50 mg was taken, 2 ml of formic acid solution was added and placed in an ultrasonic bath for 15 minutes. Then the sample is centrifuged and chromatographed on a C18 column using a mixture of acetonitrile, methanol and water as eluents. To increase the sensitivity a fluorescent detector was used. The detection limit of bromadiolone was 0.004 mg, the recovery rate was from 86 to 99 %.

* To whom all correspondence should be sent.
E-mail: svandreev.niid@gmail.com

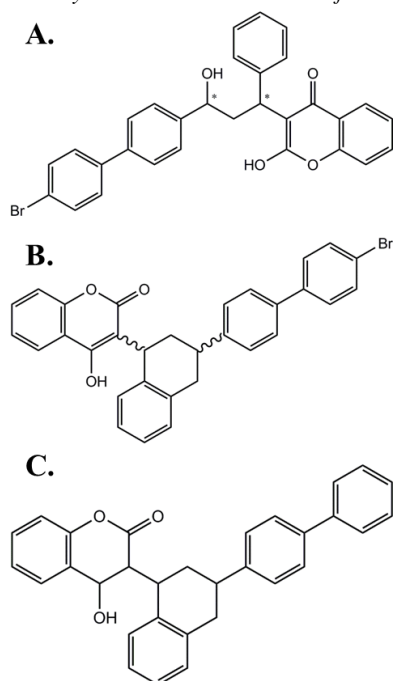


Figure 1. Bromadiolone (A), brodifacoum (B) and difenacoum (C)

Later, the same group of authors used similar conditions for the extraction of chlorphacinone and diphacinone from paraffin briquettes [11]. To prepare model samples, a solution of the active substance in ethyl acetate was added to the molten wax, then the solvent was removed at 70 °C under a nitrogen atmosphere. The detection limit of both substances was about 20 ng, which was achieved through the use of a mass spectrometric detector.

However, no universal method has been proposed for the determination of poisons in rodenticides. In this paper, a universal method is proposed for the determination of second-generation anticoagulants in grain baits and soft briquettes. A new method for extracting bromadiolone, brodifacoum and difenacoum from paraffin briquettes has also been proposed.

EXPERIMENTAL

Materials

Bromadiolone, brodifacoum and difenacoum (Pestanal®, Sigma-Aldrich), acetonitrile HPLC-grade (Merck, Germany), sodium acetate HPLC-grade (Acros Organics, USA), hexane (analytical grade, Russia), deionized water with resistance less than 18.2 MOM × cm. Other reagents used were analytical grade or higher. Commercial reagents were used without further purification.

Instrumentation and chromatographic conditions.

The HPLC system used was a Thermo ULTIMATE 3000 equipped with a DAD-3000 diode array detector. This device is also supplied with

column thermostat, auto-sampler with a 20 µL loop and gradient pump with mixing on the low pressure side for 4-component gradient with a built-in degassing device. The separation was conducted using Thermo Acclaim Surfactant column, 5 µm (4.6 × 250 mm).

The mobile phase consisted of acetonitrile (A) and 0.1 M ammonium acetate solution pH 5.4 (B) in a gradient elution programmed as follows: 0–5.0 min, linear gradient from 50% to 40% B; 5.0–10.0 min, linear gradient from 40% to 5% B, maintain at 5% B until 10.0 min.

The solvent flow rate was 1.0 ml·min⁻¹ and the temperature of the column oven was 25 °C. The analysis was carried out within the wavelength interval of 190–400 nm and the optimal wavelength value for the detection of rodenticides is 264 nm.

Identification of substances was carried out according to the retention time comparing with reference sample.

Preparation of stock solution.

A 0.500% stock standards of brodifacoum, bromadiolone, and difenacoum in acetonitrile were prepared. Working standards for a five-point calibration curve were prepared from the stock standards by making appropriate dilutions with acetonitrile.

Preparation of model baits.

For the preparation of grain baits to the grain (about 9 g), 1 g of a 0.050% solution of poison in ethylene glycol was added. The mixture was thoroughly mixed and dried at 60 °C. Similarly, prepared and wheat-based bait.

For the preparation of solid briquettes 1 g of a 0.050% solution of poison in ethylene glycol was added to molten paraffin (about 9 g). Then ethylene glycol was evaporated at 60 °C and the bait was cooled.

Calculations and data processing.

Collection and processing of chromatographic data were conducted using Chromeleon 6 software (Thermo Fischer Scientific, USA). Excel 2016 (Microsoft Corporation) was used for detailed calculation.

The limit of detection LOD was set at the three times the noise level of the baseline in the chromatogram, while the limit of quantification LOQ was set at three times the LOD.

RESULTS AND DISCUSSION

Fig. 2 shows a chromatograms of standard solutions contained brodifacoum, bromadiolone and difenacoum, obtained using the ternary mobile phase

for the separation. The cis and trans forms of brodifacoum and difenacoum are well resolved.

Five sets of each form were analysed to determine methods validity. The standard of brodifacoum was assumed to consist of 56.3 % of the cis isomer and 43.7 % of the trans isomer. As the response factors for the two isomers are different, the levels for the two isomers were quantitated separately and added together for total brodifacoum in the sample. The same situation was with difenacoum. Quantification was done by using a five-point calibration curves.

Based on previous studies, we have suggested that extraction in an ultrasonic bath is the most suitable and simplest method for baits based on grain and flour. Optimization of extraction conditions was determined by the extraction coefficient. Acetonitrile, acetone and chloroform were used as solvents. To determine the recovery at each point, five baits of each type were prepared. Table 1 shows the dependence of recovery on extraction time and solvent.

Despite the different structure and properties of the matrix, it was found that extraction of acetone in an ultrasonic bath is best suited for the analysis of grain and wheat-based baits. The 3 h sonication is enough for recover more than 90 % of active substance. For better recovery from the wheat-based baits they have been previously grinded up.

Analysis of paraffin containing baits is very difficult because paraffin with incomplete removal from a solution can precipitate, which leads to contamination of the analytical column. Usually to remove the paraffin using a difficult and long-lasting filtration. We suggest a two-phase hexane-acetonitrile extraction system. In this case, the paraffin solves into hexane, while the poison remains in acetonitrile. After stirring for 12 hours, the system is placed in a separatory funnel and the acetonitrile fraction is separated. If the bait contains any filler, it is filtered and sonicated for 3 h in acetone as described above.

Percentage recoveries for each substance in each form and the associated RSD are given in Tables 2-4.

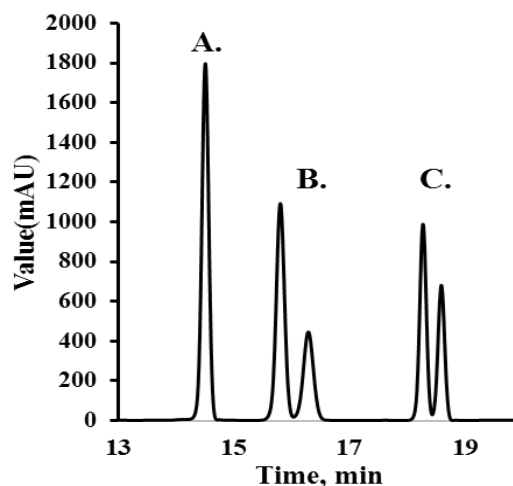


Figure 2. Chromatograms of bromadiolone (A), brodifacoum (B) and difenacoum (C) standard solutions

Table 1. The dependence of the recovery (%) from the solvent and sonicating time (calculated for five samples)

		Sonicating time, h		
		1	2	3
Bromadiolone				
Acetone	Wheat-based baits	55.5	80.0	97.7
	Grain baits	58.9	81.2	95.2
Acetonitrile	Wheat-based baits	55.4	69.1	85.2
	Grain baits	58.3	74.3	87.6
Chloroform	Wheat-based baits	60.2	71.3	84.2
	Grain baits	63.5	77.4	88.8
Brodifacoum				
		1	2	3
Acetone	Wheat-based baits	64.5	84.6	99.8
	Grain baits	67.2	89.0	98.0
Acetonitrile	Wheat-based baits	62.1	72.3	84.3
	Grain baits	64.7	75.8	90.1
Chloroform	Wheat-based baits	65.8	84.3	93.6
	Grain baits	67.2	85.3	94.5
Difenacoum				
		1	2	3
Acetone	Wheat-based baits	56.1	78.2	94.2
	Grain baits	57.2	77.6	90.0
Acetonitrile	Wheat-based baits	49.9	67.9	82.3
	Grain baits	50.1	68.4	84.6
Chloroform	Wheat-based baits	52.4	71.9	86.9
	Grain baits	53.8	72.3	88.6

Table 2. Recovery of brodifacoum, bromadiolone and difenacoum from the grain baits (calculated for five samples and three injections)

Object	Range, %	Recovery, %	RSD, %
Brodifacoum	0.00067 – 0.010	98.0	0.073
Bromadiolone	0.00067 – 0.010	95.2	0.073
Difenacoum	0.00067 – 0.010	90.0	0.147

Table 3. Recovery of brodifacoum, bromadiolone and difenacoum from the soft baits (calculated for five samples and three injections)

Object	Range, %	Recovery, %	RSD, %
Brodifacoum	0.00067 – 0.010	99.8	0.147
Bromadiolone	0.00067 – 0.010	97.7	0.058
Difenacoum	0.00067 – 0.010	94.2	0.214

Table 4. Recovery of brodifacoum, bromadiolone and difenacoum from the block baits (calculated for five samples and three injections)

Object	Range, %	Recovery, %	RSD, %
Brodifacoum	0.00067 – 0.010	98.5	0.058
Bromadiolone	0.00067 – 0.010	94.0	0.081
Difenacoum	0.00067 – 0.010	90.0	0.107

We have been found that recoveries from unshredded wheat-based baits are lower than for grain baits or hard briquette. This is due to the fact that the solvent does not completely penetrate the bait under the action of ultrasound. This problem disappears when the sample was grinded. It does not occur when analyzing grain and paraffin baits, since in the first case the poison is on the surface of the grain, and in the second, the bait is completely dissolved. The method showed satisfactory results in the analysis of real samples (Figures 3-5).

The results of chromatographic study showed that the peaks of the poisons and the other components of real rodenticide baits were clearly separated. This is why we conclude that this method is selective and it is appropriate for identification and quantitative analysis of brodifacoum, bromadiolone and difenacoum in wheat-based, grain and paraffin baits.

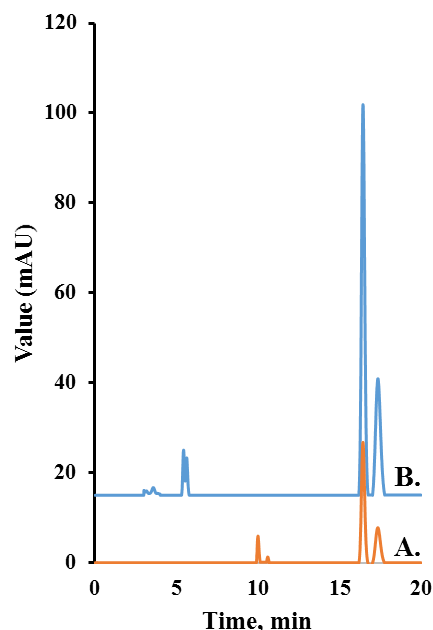


Figure 3. Chromatograms of commercial brodifacoum wheat-based (B) and paraffin (A) baits

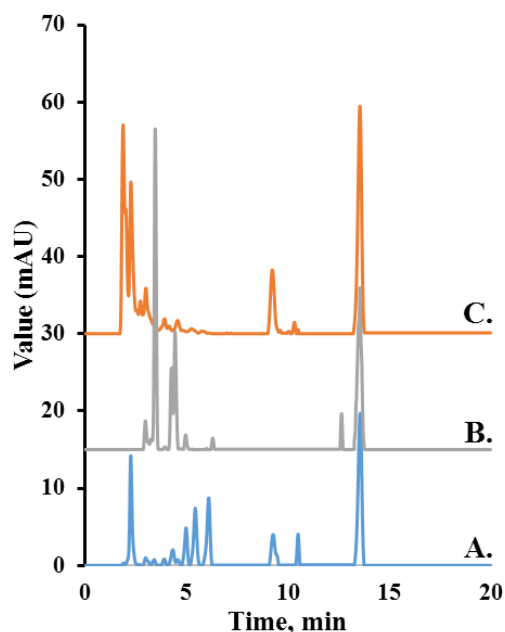


Figure 4. Chromatograms of commercial bromadiolone wheat-based (A) and grain (B) baits and solid briquettes (C)

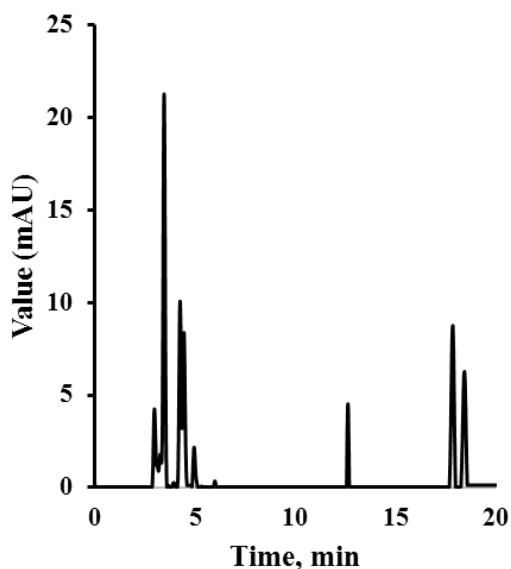


Figure 5. Chromatogram of commercial difenacoum wheat-based bait

CONCLUSIONS

The described methods provide a simple and sensitive procedure for the determination of brodifacoum, bromadiolone and difenacoum in different preparative forms of rodenticides. The methods can be recommended for routine analysis.

REFERENCES

1. S. Morand, S. Jittapalpong, M. Kosoy, *Vector Borne Zoonotic Dis.*, **15**, 1 (2015).
2. N. Gratz, *Vector- and rodent-borne diseases in Europe and North America: Distribution, public health burden, and control*, Cambridge University Press, New York, 2006.
3. W. C. Pitt, L. C. Driscoll, R. T. Sugihara, *Arch. Environ. Contam. Toxicol.*, **60**, 533 (2011).
4. E. Schmolz, *Integr Zool*, **5**, 44 (2010).
5. B. G. Meerburg, G. R. Singleton, A. Kijlstra, *Crit Rev Microbiol.* **35**, 221 (2009).
6. V. A. Ryl'nikov, A. V. Bogacheva, in: *Proceedings of the Ninth International Conference on Urban Pests (Birmingham, 2017)*, M. P. Davies, C. Pfeiffer, W. H. Robinson (eds.), Pureprint Group, Uckfield, 2017, P. 147-152.
7. E. M. Roper, G. Buczkowski, in: *Proceedings of the Ninth International Conference on Urban Pests (Birmingham, 2017)*, M. P. Davies, C. Pfeiffer, W. H. Robinson (eds.), Pureprint Group, Uckfield, 2017, P. 157-160.
8. V. V. Shkarin, M. S. Shafeev, *Disinfectology*, NGMA, Nizhniy Novgorod, 2003.
9. P. Fisher, C. O'Connor, G. Wright, C. T. Eason, *DOC Science Internal Series.* **188** (2004).
10. M. Z. Mesmer, R. D. Satzger, *Analyst*, **120**, 2195 (1995).
11. M. Z. Mesmer, R. A. Flurer, *J Chromatogr A*, **891**, 249 (2000). V. 891.

Sample preparation and calibration optimization for ICP-MS analysis of copper, zinc, selenium, rubidium, strontium, magnesium, iron, molybdenum and barium in human serum

D. M. Davcheva^{1,2,5*}, G. K. Kirova^{2,3}, T. Z. Tsvetkova², D. D. Terzieva^{1,5},

M. T. Kiryakova⁴, V. J. Kmetov⁴

¹Department of Clinical Laboratory, Medical University of Plovdiv, Plovdiv, Bulgaria

²Technological Center for Emergency Medicine, 120 Brothers Buxton Blvd., Plovdiv, Bulgaria

³Department of Chemical Sciences, Medical University of Plovdiv, Plovdiv, Bulgaria

⁴Department of Analytical Chemistry and Computer Chemistry, University of Plovdiv "Paisii Hilendarski", Plovdiv, Bulgaria

⁵University Hospital "St George", Plovdiv, Bulgaria

Received November 12, 2018; Revised December 19, 2018

An optimized sample preparation and calibration approach for inductively coupled plasma mass spectrometry (ICP-MS) for multielement determination of Cu, Zn, Se, Rb, Sr, Mg, Fe, Mo, Ba in human serum is proposed. Four microwave-assisted digestion methods were tested. The chosen method (0.3 mL of sample mixed with 1.5 mL of HNO₃ and 1.5 mL of water, digested for 25 min at 190°C) provides complete digestion of the serum matrix with acceptable residual carbon content. Internal Standard (IS) Rh was introduced through an online IS kit. For introduction stability, the acid content in the IS and calibration standard solutions was equalized. It was observed that the high Na content in serum sample solutions causes two opposite effects on the analyte signals: suppression of ionization efficiency into the ICP and gradual enhancement of the ion transmission. For overcoming this matrix interference all calibration solutions and blanks were prepared in 15% v/v HNO₃ with 130 mg/L Na, as a matrix-match component. The proposed method for sample preparation and calibration strategy was found adequate for human serum ICP-MS analysis, with very good recoveries of the aforementioned elements, determined in two certified reference materials, *Seronorm Trace Elements Serum Level I and Level II, SERO AS, Norway*.

Keywords: ICP-MS, multielement analysis, trace elements, human serum, matrix-matched calibration, sensitivity drift

INTRODUCTION

Simultaneous determination of multiple elements in human biological materials is of growing interest, due to the accumulated scientific evidence of their pleiotropic effects on the human body, as well as their key importance for the environmental and occupational health. Multielemental quantification of elements in several orders of concentration magnitude (mg/L, µg/L, ng/L) is a challenging task, which requires robust, reliable, high-throughput analytical methods, with wide working range. Inductively coupled plasma mass spectrometry (ICP-MS) covers these requirements, therefore in the recent years it has been increasingly used for multielemental analysis in a large variety of biological samples, such as serum [1–8], plasma [4, 9, 10], whole blood [2, 3, 5, 9–12], urine [3, 9, 13], tissues [14, 15], hair [9, 10], etc. However, ICP-MS is not free from some drawbacks, as occurrence of spectral and non-spectral interferences [4, 16].

For reducing spectral interferences, it is of great

importance to select the appropriate isotope for the analyte measurement [3, 14]. One of the most common approaches for coping with spectral overlap is using a collision cell. Working in kinetic energy discrimination mode (KED) overcomes polyatomic interferences, though it compromises sensitivity [16–18].

As opposed to spectral, the nonspectral interferences are most commonly caused by matrix effects (ME) of multiplicative kind [3, 4, 19]. An internal standard (IS) approach is effective for handling ME, if the interference effects over the signals of the analyte and IS are matched [3, 4, 19]. Multiple ISs are usually preferred for multielemental analysis [3, 4, 19]. However, previous studies [20, 21] demonstrate that if a mixture of NaCl and CaCl₂ was added to the calibration standards, any IS [Ge, Rh, Re, Ir] could be used for any analyte in blood samples.

There are different approaches for alignment of biological matrix diversity, described in literature, such as acid digestion or alkali dilution [1, 5, 9, 10,

* To whom all correspondence should be sent.
E-mail: d.davcheva@hotmail.com

14, 15]. One of the most widely recommended methods is microwave assisted acid mineralization (MW) with different acid mixtures. After MW treatment some nonspectral interferences could still be observed, such as signal suppression or enhancement, as well as signal instability or drift [4, 20, 22, 23]. Owing to the interindividual diversity of the serum samples, ME occur to a greater extent if the so-called “dilute and shoot” approach for direct sample introduction is preferred [4, 7, 24]. According to several authors [4, 25, 26] the enhancement of the analyte signals is due to the presence of concomitant elements, such as Cl and S in the samples, or to the charge transfer from C^+ ions to elements with a FIP from 9 to 11 eV. Suppression of ionization efficiency is associated with changes in ion-atom equilibrium in the ICP, or the space charge effect, taking place beyond the cones. This phenomenon is often attributed to easily ionizable elements (EIE), i.e. macroelements K, Na, Mg, Ca, typical for human serum. Elevated levels of EIE in serum samples potentially cause bias in analytical results, in particular, in case of external calibration with aqueous standards [4, 20, 23, 27, 28]. An easy to use matrix-matching approach is adding Na, or mixed salts, containing EIE to the standard solutions [4].

In the following study we aimed to propose a fast and effective acid digestion procedure for human serum, with limited sample volume, acceptable residual carbon content (RCC) and appropriate dilution factor. An optimized calibration for ICP-MS determination of Cu, Zn, Se, Rb, Sr, Mg, Fe, Mo, Ba is suggested, with online IS introduction and Na as a matrix-match component.

EXPERIMENTAL

Blood sampling

Thirty venous blood samples were collected from healthy adult human volunteers in the Central Laboratory of the University Hospital St. George in Plovdiv. Blood sampling was performed under fasting conditions, following the standard procedure for collection of blood specimens. Furthermore, the guidelines of Helsinki Declaration, regarding informed consent of human volunteers were duly met. The blood samples were let to clot for 20 min at room temperature. After centrifugation at 3000 rpm for 10 min, serum subsamples were separated and stored at $-70^{\circ}C$ until analysis. For collection and storage of the samples serum blood tubes (Kabe Labor Technik, Primavette V Serum, 2.6 mL) and cryotubes (Biosigma CL2ARBEP5 CRYOGEN, 1.8 mL) were used.

All elemental standards used for preparation of the calibration standard solutions were NIST-traceable. Multielement standard (Etalon multi element ICP, 100 mg/L) was purchased from VWR Chemicals (Leuven, Belgium), ICP-MS monoelement Zn 100 mg/L, Cu 100 mg/L, Fe 100 mg/L, and Mg (CRM 6 components: Mg 60 mg/L, P 100 mg/L, Ca 300 mg/L, K 500 mg/L, Na 10000 mg/L) and NaCl (10161 mg/L) were from CPAchem Ltd. (Stara Zagora, Bulgaria). Rhodium (10 mg/L), was provided by Merck (Darmstadt, Germany). All solutions were prepared with ultra-pure water ($18.2 M\Omega cm$) from ELGALabWater (PURELAB Chorus 2+) and nitric acid (suprapur) from Fisher Scientific UK Limited. The reference materials (Seronorm Trace Elements Serum Level I and Level II, SERO AS, Norway) were prepared according to the supplier's instructions.

External multielement aqueous standards were prepared in 15% HNO_3 at concentrations of 0.02, 0.1, 0.2, 1.0, 2.0, 4.0 and 6.0 $\mu g/L$ for Se, Rb, Sr, Mo and Ba; 20.0, 40.0, 60.0, 80.0 $\mu g/L$ for Cu, Zn and Fe; 0.5, 0.6 and 0.9 $\mu g/L$ for Mg. A second group of calibration solutions was prepared in the same concentration ranges in 15% HNO_3 , with a 130 mg/L Na content. Rh was used as IS in concentration of 2 $\mu g/L$.

All labware used for blood sampling, storage and analysis was previously tested for contamination with the elements of interest, following a procedure, previously described [29].

Digestion method

After thawing at room temperature, the serum samples were thoroughly vortexed for 10 min and immediately pipetted into a microwave digestion vessel. The MW was performed by Multiwave GO Microwave Digestion system with closed vessels (Anton Paar, Graz, Austria). Two levels of serum reference materials (SeronormTM, Norway) were digested and analyzed in four batches to test four digestion modes with variation of the sample and reagents quantity, the MW program and the dilution factor. The RCC in each digested sample was evaluated by means of MP-AES (Agilent 4500) at the spectral line 193.027 nm. Reagent blanks were prepared by addition of deionized water in the place of the sample. Mineralizates were cooled to room temperature and transferred to 15 mL polypropylene tubes. Deionized water was added to provide a final volume of 10 mL (dilution factor, DF=33.3).

Instrumentation

Multielement determination was carried out by Thermo Scientific iCAP Qc ICP-MS (Thermo Scientific, Germany). The mass spectrometer is equipped with a collision cell, working in Kinetic Energy Discrimination (KED) mode, with helium as collision gas. The iCAP Qc sample introduction system consists of a perfluoroalkoxy (PFA) nebulizer, quartz glass Peltier-cooled cyclonic spray chamber and quartz injector, nickel interface cones. The IS was added *via* a kit for online introduction (Thermo Scientific) to the sample solutions. For better precision relatively long dwell times were selected. Thermo Scientific QTegra Software was used for calculations of the analytical results. ICP-MS operating conditions are summarized in Table 1. Instrument settings for the analytes of interest and corresponding Instrumental detection limits (IDL) obtained are presented in Table 2.

Table 1. ICP-MS operating conditions

Plasma conditions	
RF-power	1550 W
Nebulizer gas flow	1.03 L min ⁻¹
Auxilliary gas flow	0.80 L min ⁻¹
Plasma gas flow	14.00 L min ⁻¹
He gas flow	4.4 mL min ⁻¹
Mass Spectrometer Settings	
Sweeps	15
Replicates	3
Survey run amu	22.39 – 245

Table 2. ICP-MS iCAP Qc instrument settings for target analytes and obtained instrumental detection limits (IDL).

Isotope	Dwell time, s	Resolution	IDL, µg/L
²⁴ Mg	0.02	High	1.00
⁵⁶ Fe	0.05	High	0.009
⁶³ Cu	0.05	High	0.011
⁶⁶ Zn	0.02	High	0.067
⁷⁸ Se	0.2	Norm	0.022
⁸⁵ Rb	0.05	Norm	0.004
⁸⁸ Sr	0.05	Norm	0.013
⁹⁵ Mo	0.1	Norm	0.001
¹³⁷ Ba	0.5	Norm	0.007

Prior to each analytical run a performance check procedure for interferences and sensitivity levels was routinely accomplished (¹⁴⁰Ce.¹⁶O/¹⁴⁰Ce < 0.01; ⁵⁹Co/³⁵Cl.¹⁶O > 17, ⁵⁹Co and ¹¹⁵In > 30000 cps, ²³⁸U > 80000 cps). All blanks, serum and QC samples were analyzed in duplicate. Continuing calibration verifications were performed after every ten serum samples. Continuing calibration blanks were inserted after calibration standards.

Table 3. Human serum acid mineralization – hot plate HCl and four microwave assisted methods (MW I-IV), final dilution factor (DF), residual carbon content (RCC, %) and internal standard shift.

	Hot HCl	MW I	MW II	MW III	MW IV
Serum, mL	0.5	0.5	0.5	0.3	0.3
HNO ₃ , mL	-	3.0	2.0	1.5	2.0
H ₂ O ₂ , mL	-	1.0	0	0	0
T, °C	-	180	160	190	180
DF	20	30	20	33.3	33.3
RCC, %	16	0.01	0.09	0.03	0.06
Rh IS shift	-	78 %	83 %	86 %	86%

RESULTS AND DISCUSSION

Digestion

Four methods (MW I-IV) for MW mineralization were tested to optimize digestion efficiency. Four batches of CRM samples (Seronorm Trace Elements Serum Level I and Level II) and blanks were prepared, with variable MW program temperature, DF and quantities of samples and reagents used. Every batch consisted of 2 blanks, prepared with deionized water and equal to the samples acid content, 5 serum CRM Level I and 5 serum CRM Level II. Thereafter the RCC in the digested samples was determined, as a relevant parameter for digestion efficiency. The lowest RCC was observed in the samples, digested at 180°C with 3 mL of HNO₃ and 1 mL of H₂O₂ (MW I). However, in the presence of H₂O₂ in ICP-MS measurement, the recorded blank signals for the elements of interest were significantly high. It was found unacceptable to work with the same HNO₃/H₂O₂ mixture at higher temperature, because of the risk of excessive pressure and explosion of the vessels. Digestion procedure MW III was found appropriate: 0.3 mL of sample, 1.5 mL of HNO₃ and 1.5 mL of deionized water, maximum temperature 190°C, ramp-time 15 min, hold-time 10 min. Compared to the other three programmes (MW I, II, IV) it provides complete digestion of the serum matrix, with minimum sample and acid volume, acceptable RCC and IS shift (Table 3). The results obtained from the ICP-MS analysis of the reference materials, mineralized by the aforementioned conditions, were in good agreement with the CRM values, as discussed later. The proposed method is characterized by minimized sample handling steps, requiring microvolumes of serum and only HNO₃ reagent for mineralization. The relatively high dilution factor provides improved nebulization, as well as reduced maintenance of the sample introduction system.

IS Rh was introduced through an online IS kit to calibrators and samples. The online IS merge system is crucial for eliminating of human error, associated with manual spiking of IS to each sample, standard and blank. It was experimentally proved that the precision is worsening if aqueous IS solution merges with samples containing 15% HNO₃. Merging of streams with the same acid media, prevents bubble formation in the capillaries of the inlet system. Therefore it was found beneficial if IS is also prepared in 15% HNO₃.

The IS recovery remained relatively stable, while measuring signals in blanks and calibration solutions in 15% HNO₃, with low sodium content (0.02-6.0 µg/L). But if standards with high sodium content (80-150 mg/L) are subsequently introduced, initial 15-20% drop of all signals (IS and analytes) is observed. Then in a series of 10 consecutive samples (Fig 1A) the drop is followed by a gradual enhancement of the signals, reflecting in a 15% positive shift of the IS recovery. Obviously, the ME was not effectively compensated by a single IS and leads to mass-dependent bias of CRM results (see Table 4). As previously commented by other authors [4, 20, 23, 27, 28] the sensitivity drifts could be explained by the presence of EIE, coexisting in significant levels in serum (Na, Mg, Ca and K). This presence provokes two opposite phenomena: i) loading plasma with EIE influences ion-atom equilibrium and causes suppression of the

analyte signals; ii) saturation of mass spectrometer interface and vacuum system with EIE improves ion transport, due to a protective effect of EIE ions and reduction of mass-discrimination. Both effects are displayed in Fig 1A. For overcoming these MEs all calibration solutions and blanks were prepared in 15% HNO₃ with 130 mg/L Na as EIE. The Na content in the calibrators was calculated to match the serum sample mineralizates. Applying such pseudomatrix-matching calibration overcomes the ionization suppression of the IS (Fig.1B) and nine target analytes (Table 4). Our observations confirmed the opinion [4], that addition of Na to the calibration standards provides a successful matrix-match.

In case of a large set of human serum analyses a positive drift up to 10% of the IS was observed (Fig 1B). This sensitivity drift was effectively compensated by correction with IS (¹⁰³Rh). Continuing calibration verifications were performed after every ten serum samples, with a very good within-run precision. Continuing calibration blanks were inserted after calibration standards with insignificant carryover. Comparison of the analytical results of Seronorm Trace Elements Serum Level I and II is presented in Table 4. The corresponding recoveries were as follows: before optimization of the calibration recoveries (R) were in the range from 98 to 131% and after optimization recoveries (R*) were in the range from 98 to 113%.

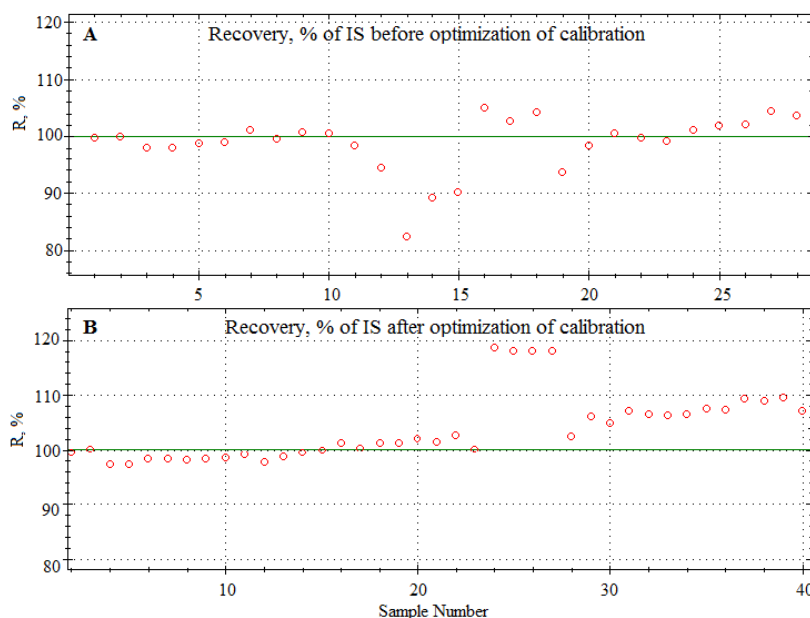


Fig. 1. Recovery of Internal standard Rh (2 µg/L) in consecutive measurements as follows: **A.** Sample numbers: (1-10) Calibration standards in 15% HNO₃ with low Na content; (11-15) Calibration standards in 15% HNO₃ with increasing Na content; (16-18) 15% HNO₃; (19-28) serum samples; **B.** Sample numbers: (2-23) Calibration standards in 15% HNO₃ with 130 mg/L Na content; (24-27) 15% HNO₃; (28-40) serum samples.

Table 4. Analytical results of certified reference materials Seronorm™ -CRM Certified values (Cert/ref); ICP-MS measured values (Found), relative standard deviation (RSD, %), n=6.

	Mg, mg/mL	Fe, mg/mL	Cu, mg/mL	Zn, mg/mL	Se, µg/L	Rb, µg/L	Sr, µg/L	Mo, µg/L	Ba, µg/L
Seronorm™ Trace Elements Serum L-1									
Cert/ref	16.8	1.47	1.09	1.10	86	4.4	99	0.76	189
Found	21.1	1.85	1.34	1.35	106	4.9	117	0.82	204
RSD, %	10.7	0.20	5.0	5.7	3.6	15	5.3	13	4.6
R, %	126	126	126	128	123	111	118	108	108
Found*	17.6	1.49	1.04	1.20	87.1	5.1	99	0.80	186
RSD*, %	0.7	0.40	0.50	0.80	3.4	3.7	0.60	1.9	1.4
R*, %	105	101	98	113	101	116	100	106	98
Seronorm™ Trace Elements Serum L-2									
Cert/ref	33.9	2.15	1.93	1.53	136	8.7	110	1.21	139
Found	43.1	2.60	2.28	2.01	164	9.9	130	1.2	163
RSD, %	11.2	1.4	6.8	4.1	1.9	6.8	1.0	6.7	5.0
R, %	127	121	119	131	119	114	118	98	117
Found*	36.9	2.18	1.93	1.71	147	9.8	119	1.3	145
RSD*, %	2.0	1.6	2.8	0.70	2.2	2.4	0.90	1.7	0.70
R*, %	109	101	100	111	106	113	108	106	104

* Values obtained after applying the optimized pseudo-matrix matched calibration (see in the text).

CONCLUSIONS

The proposed approach for microwave-assisted acid mineralization provides fast and effective digestion with microvolumes of human serum required for multielement ICP-MS analysis. The following digestion method was found appropriate: 0.3 mL sample, 1.5 mL HNO₃, 1.5 mL H₂O maximum temperature 190°C, ramp-time 15 min, hold-time 10 min, DF (33.3). The proposed calibration strategy (calibrators in 15% HNO₃, 130 mg/L Na and Rh as IS in 15% HNO₃) provides a satisfactory matrix-match, assuring determinations of analytes with good analytical recoveries. We recommend this sample preparation and calibration as “fit for purpose” for ICP-MS determination of Cu, Zn, Se, Rb, Sr, Mg, Fe, Mo, Ba in human serum for medical and biomonitoring studies.

Acknowledgement: Medical University of Plovdiv – project HO-01/2017.

REFERENCES

- S. Meyer, M. Markova, G. Pohl, T. A. Marschall, O. Pivovarova, A. F. H. Pfeiffer, T. Schwerdtle, *J. Trace Elem. Med. Biol.*, **49**, 157 (2018).
- J. M. Harrington, D. J. Young, A. S. Essader, S. J. Sumner, K. E. Levine, *Biol. Trace Elem. Res.*, **160**(1), 132 (2014).
- F. Ruggieri, A. Alimonti, B. Bocca, *TrAC Trends Anal. Chem.*, **80**, 471 (2016).
- R. Gajek, K.-Y. Choe, *J. Anal. At. Spectrom.*, **30**, 1142 (2015).
- Y. Lu, M. Kippler, F. Harari, M. Grander, B. Palm, H. Nordqvist, M. Vahter, *Clin. Biochem.*, **48**, 140 (2015).
- R. Alis, A. Santos-Lozano, F. Sanchis-Gomar, H. Pareja-Galeano, C. Fiuza-Luces, N. Garatachea, A. L. E. Emanuele, *J. Trace Elem. Med. Biol.*, **35**, 103 (2016).
- O. Paz-Tal, A. Canfi, R. Marko, E. Katorza, Z. Karpas, D. Schwarzfuchs, I. Shai, E. K. Sheiner, *ESPEN J.*, **8**, e100 (2013).
- A. V. Skalny, N. V. Simashkova, T. P. Klyushnik, A. R. Grabeklis, I. V. Radysh, M. G. Skalnaya, A. A. Nikonorov, A. A. Tinkov, *J. Trace Elem. Med. Biol.*, **43**, 9 (2017).
- J.-P. Goullé, L. Mahieu, J. Castermant, N. Neveu, L. Bonneau, G. Lainé, D. Bouige, C. Lacroix, *Forensic Sci. Int.* **153**, 39 (2005).
- J. L. Rodrigues, B. L. Batista, J. A. Nunes, C. J. S. Passos, F. Barbosa Jr., *Sci. Total Environ.*, **405**, 370 (2008).
- D. R. Jones, J. M. Jarrett, D. S. Tevis, M. Franklin, N. J. Mullinix, K. L. Wallon, C. D. Quarles Jr, K. L. Caldwell, R. L. Jones, *Talanta*, **162**, 114 (2017).
- C. S. Kira, A. M. Sakuma, N. da Cruz Gouveia, *J. Appl. Pharm. Sci.*, **4** (05), 39 (2014).
- P. Heitland, H. D. Köster, *Clin. Chim. Acta.*, **365**, 310 (2006).
- B. L. Batista, D. Grotto, J. L. Rodrigues, V. C. de Oliveira Souza, F. Barbosa, *Anal. Chim. Acta*, **646**, 23 (2009).

15. Y. Takasaki, K. Inagaki, A. Sabarudin, S.-I. Fujii, D. Iwahata, A. Takatsu, K. Chiba, T. Umemura, *Talanta*, **87**, 24 (2011).
16. L. Balcaen, E. Bolea-Fernandez, M. Resano, F. Vanhaecke, *Anal. Chim. Acta*, **894**, 7 (2015).
17. N. Yamada, *Spectrochim. Acta Part B At. Spectrosc.*, **110**, 31 (2015).
18. S. D. Tanner, V. I. Baranov, D. R. Bandura, *Spectrochim. Acta Part B At. Spectrosc.* **57**, 1361 (2002).
19. C. Agatemor, D. Beauchemin, *Anal. Chim. Acta*, **706**, 66 (2011).
20. C. Bonnefoy, A. Menudier, C. Moesch, G. Lachatre, J. M. Mermet, *Anal. Bioanal. Chem.*, **383**, 167 (2005).
21. R. Gajek, F. Barley, J. She, *Anal. Methods*, **5**, 2193 (2013).
22. G. H. Floor, R. Millot, M. Iglesias, P. Negrel, *J. Mass. Spectrom.*, **46**, 182 (2011).
23. C. Mariet, F. Carrot, M. Moskura, *Am. J. Anal. Chem.*, **02**, 739 (2011).
24. B. Cai, Y. Wang, X. H. Zhao, Z. S. Gong, *Anal. Lett.*, **50**, 554 (2017).
25. Z. Hu, S. Hu, S. Gao, Y. Liu, S. Lin, *Spectrochim. Acta, Part B*, **59**, 1463 (2004).
26. Z. C. Hu, S. Gao, S. H. Hu, Y. C. Liu, H. H. Chen, *Chin. Chem. Lett.*, **18**, 1297 (2007).
27. A. Cesbron, E. Sausseureau, L. Mahieu, I. Couland, M. Guerbet, J. P. Goulle, *J. Anal. Toxicol.*, **37**, 401 (2013).
28. C. Richardson, E. Roberts, S. Nelms, N. B. Roberts, *Clin. Chem. Lab. Med.*, **50**, 317 (2012).
29. D. Davcheva, G. Kirova, T. Tsvetkova, V. Kmetov, <http://publisher.mu-plovdiv.bg/books/sbornik-statii-nacionalna-nauchna-konferencia-15g-farmacia-mu-plovdiv/>.

Nanoparticles-assisted MSIS-MP-AES hydride generation determination of As and Sb

M. T. Kiryakova, E. K. Varbanova, K. K. Simitchiev, V. J. Kmetov*

*Department of Analytical Chemistry and Computer Chemistry,
University of Plovdiv "Paisii Hilendarski", 24 Tzar Assen Str.4000 Plovdiv, Bulgaria*

Received November 16, 2018; Revised December 17, 2018

For the first time hydride generation (HG) in the presence of silica-coated $\text{MnFe}_2\text{O}_4@\text{SiO}_2$ magnetic nanoparticles (MNPs) was tested. A benefit of adding inert and easily recyclable (collected from the waste by a permanent magnet) MNPs into the reaction cell - Multi Mode Sample Introduction System (MSIS®) was expected, namely by providing expanded contact surface and improving the gas-liquid separation, to extend the potential of microwave plasma atomic emission spectrometry (MP-AES) to determine As and Sb at sub-ppb levels. It was found that the suggested approach does not contribute to sensitivity changes for As or for Sb, but more than twice improves the measurement precision for both elements. The addition of 1.6 mg ml^{-1} MNPs into the 1.5 % NaBH_4 leads to smooth and steady reagent flow supply due to a diminishing of hydrogen bubbles formation in the delivery tubing. Therefore, a stable equilibrium of the input-output analyte mass transfer can be maintained, even working at extremely high for MSIS sample and hydride reagent flows (15 ml min^{-1} and 7.5 ml min^{-1} , respectively). A sensitivity enhancement for As in presence of alcohols was found and attributed to a carbon-related matrix effect, therefore 2% ethanol was added to the NaBH_4 . The proposed nanoparticles assisted hydride generation approach extends the ability of MSIS-MP-AES and allows determination of As and Sb with instrumental LODs of 0.17 ppb and 0.05 ppb respectively, which are much lower than those in other recently published works.

Keywords: microwave plasma atomic emission spectrometry (MP-AES), nanoparticles, hydride generation, MSIS, As, Sb, trace elements analysis

INTRODUCTION

Microwave Plasma Atomic Emission Spectrometry (MP-AES) is a relatively new technique, which works with nitrogen sustained plasma (N_2 gas could be extracted from the air) and does not require flammable or expensive gases. The method provides several analytical benefits as: fast multielement consecutive measurements in a large linear dynamic range. The microwave plasma is cooler than the widely used inductively coupled plasma (ICP), which works with argon gas flows. Another difference is that the microwave applied power in MP-AES instruments is fixed (i.e. 1000 W) and cannot be changed. For that reason, the temperature of MP discharge cannot be instrumentally controlled, hence the sensitivity of the recorded emission signals could be optimised only by variations of N_2 nebulization gas flow, sample flow and the viewing position of the plasma [1, 2]. It was proved [3, 4] that the MP-AES detection limits (LOD) are compatible to those of Flame Atomic Absorption Spectrometry (FAAS), but are not so low as in ICP-OES. The limitation of MP-AES to detect trace elements at low concentrations in environmental samples have been

reported in [5]. European legislation postulates maximum acceptable concentrations (MAC) of total Sb and As of 5 and $10 \mu\text{g L}^{-1}$, respectively, for waters for human consumption and natural waters [6, 7]. These levels are much below the detection limits of MP-AES if conventional nebulisation is used [5].

A well-known approach for improving the analytical potential of atomic spectrometry analysis is the so called *hydride generation technique* (HG), applicable for elements such as As, Se, Sb, Bi, Te, Sn, Ge, Pb, which can form volatile hydrides by chemical reaction with a hydride donor reagent (most often NaBH_4). The important advantages of HG are: i) fast separation of the analytes in gaseous form from the liquid, allowing complex matrix analyses, i.e. high dissolved solids sample solutions and even suspensions (which cannot be nebulized); ii) the generated volatile hydrides can be easily and efficiently transported to the plasma by a carrier gas; iii) less solvent is loaded in the plasma source, which prevents its cooling; iv) enables work with much higher sample flows compared to the nebulization mode, ensuring significantly higher mass transfer of the analytes.

In a specially dedicated monography [8], Dedina

* To whom all correspondence should be sent.

E-mail: kmetov@uni-plovdiv.bg

M. T. Kiryakova et al.: Nanoparticles-assisted MSIS-MP-AES hydride generation determination of As and Sb and Tsalev describe the instrumental and chemical parameters that have to be considered for HG procedure optimisation. The important ones are: sample acidity; sample volume and amount/concentration of NaBH_4 ; analyte oxidation state/pre-reduction; carrier gas flows; chemical reaction temperature; reaction/collection time. In HG, the total mass fraction of the analyte delivered in the atomizer depends on two major parameters - sample flow rate and carrier gas flow rate and these variables are specific for individual instrumental setup [9].

The use of a new commercial Multi Mode Sample Introduction System (MSIS®) in HG mode enables up to 100 times lowering of LODs for the target hydride-forming elements in comparison to conventional nebulisation [10, 11]. In MSIS® the sample solution and hydride generation reagent (HGR) react in a thin film onto a rough – surfaced cone, which provides good reagents mixing and fast gas-liquid separation. The advantages of using MSIS® in HG mode are described in [12].

The combination MSIS-HG-MP-AES is quite new and still not enough explored. Very recent papers about the analytical applications of this instrumental setup are given in [13-15]. Total As analysis in Californian wines is presented in [13]; multielemental determination of As, Bi, Ge, Sb, and Sn in agricultural samples is reported in [14]; determination of As and Se in mineral waters is described in [15].

Nanoparticles can be used as a trapping sorbent, for selective separation and preconcentration of analytes prior to spectrometric determination [16, 17]. Silica-coated $\text{MnFe}_2\text{O}_4@\text{SiO}_2$ magnetic nanoparticles synthesized in our laboratory showed good magnetic properties and have been used for magnetic supported micro dispersive solid phase extraction [18]. The MNPs protected by silica coating are stable and could be reused several times [18].

The present work aims to explore the possibility of the above-mentioned relatively inert MNPs to act as surface expansion and gas-liquid separation supporting media in combination with MSIS-HG-MP-AES. The goal was, working with this combination, to extend the potential of the method to determine As and Sb in sub-ppb levels. To the best of our knowledge, this is the first time when such approach is used.

EXPERIMENTAL

Instrumentation

All analyses were performed with an Agilent 4200 MP-AES spectrometer equipped with Agilent

4107 nitrogen generator; Agilent MSIS® was used only in HG mode (the unused sample line to the nebulizer was blocked). Other used equipment was as follows: External peristaltic pump – Gilson, Minipuls 2; ER10 stirrer; delivery tubing: purple/black 2.29 mm i.d, connected to the top of the MSIS® for hydride generation reagent; blue/blue 1.65 mm i.d, attached to the MSIS® bottom for sample solution delivery tubing; black/white 3.18 mm i.d. for waste tubing; permanent magnet: Disc magnet S-45-30-N, \varnothing 45 mm, height 30 mm, Supermagnete (Uster, Switzerland)

Reagents and standard solutions

All reagents and solvents were of analytical grade. $\text{MnFe}_2\text{O}_4@\text{SiO}_2$ nanoparticles were synthesized in our laboratory according to the procedure described in [18]. The used reagents in the study were: L-cysteine powder 98%, Acros Organics; sodium borohydride powder 98%, Acros Organics; CH_3OH 99.8%, Merck; $\text{C}_2\text{H}_5\text{OH}$ 99.9%, Rai-him; $i\text{-C}_3\text{H}_7\text{OH}$, Chimtex Ltd, Dimitrovgrad; Na_2CO_3 95.8%, Valerus; standard solutions: As (III) 100 mg L^{-1} in 0.5% NaOH 0.1% NaCl, CPAchem; As(V) 100 mg L^{-1} in H_2O , CPAchem; Sb 100 mg L^{-1} 99.99% in 2% HNO_3 , 0.5% HF CPAchem, HCl 35.9%, Rai-him; double distilled water (BDW).

Sample preparation

Stock standard solutions of As or Sb 100 mg L^{-1} were diluted with 0.1 mol L^{-1} HCl to desired working concentrations. L-cysteine was added to a final concentration of 0.5% m/v. The solution was incubated for 60 min (room temperature). Hydride generation reagent (HGR) contains 1.5% NaBH_4 and 0.1% NaOH, prepared by dissolving NaBH_4 in appropriate BDW volume, followed by addition of NaOH to 0.1% final concentration. Stirrer was used to maintain the homogeneity in the case of MNPs addition.

RESULTS AND DISCUSSION

Optimisation of the operating conditions

The MSIS-MP-AES instrumental setup was optimised for HG determination of As and Sb by using model solutions. A set of characteristic emission lines for both analytes (Table 1) was tested in order to select free from spectral interference wavelengths with best sensitivity and good precision.

The MP-AES instrumental parameters were optimised in respect of maximum signal-to-noise ratio. The working parameters are given in Table 2.

L-cysteine was used as non-toxic pre-reducing agent, which was found efficient to increase

M. T.Kiryakova et al.: Nanoparticles-assisted MSIS-MP-AES hydride generation determination of As and Sb sensitivity at low acid concentration [19, 20]. Hydrochloric acid was used as acidic medium, in which the oxidation states of As(III) and Sb(III) are sustained. Experimentally it was proved that working with 0.5% of L-cysteine in the presence of HCl with concentration (0.06 - 0.2 mol L⁻¹) leads to equalization of HG sensitivity for both As(III) and As(V).

Table 1. MP-AES tested emission lines

Analyte	Line, nm	Type	Relative intensity
As	188.979	I	582
As	193.695	I	1307
As	228.812 ^a	I	1731
Sb	206.833	I	1487
Sb	217.581	I	2827
Sb	231.147	I	3841

^a Spectral interference from Cd was observed

Table 2. MP-AES working parameters

Plasma viewing position	0
Integrated pump speed, (rpm)	80
Read time, s	5
Sample uptake time, s	10
Stabilization time, s	20
Number of replicates	5
Background correction	Off-peak, left + right

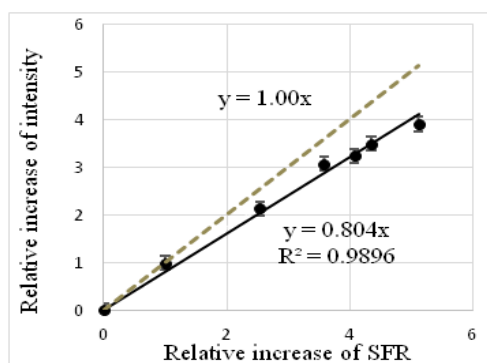


Fig. 1. Relative enhancement of emission intensity (50 ppb As 193.695 nm) vs relative increase of SFR.

The effect of sample and carrier gas flow rates on the emission intensity of As (193.695 nm) was studied, and it was found that there is no interaction between the two variables. It was proved that the sample flow rate (SFR) has much greater effect than that of the N₂ carrier with optimal gas flow rate of 0.6 L min⁻¹. Using further multivariate optimization by central composite design, the following optimal values for MSIS working conditions were found: i) NaBH₄ concentration - 1.5 % m/m; ii) SFR - 15 mL min⁻¹; and iii) ratio of

reagent (NaBH₄)-to-sample flow rates - 1:2 i.e. NaBH₄ flow rate - 7.5 mL min⁻¹.

In order to facilitate the work with SFR above 11 mL min⁻¹ the original MSIS chamber was modified by widening the diameter of the sample entrance aperture to 1.2 mm. For efficient draining of the huge volume of liquid phase entering the chamber (15 mL min⁻¹ SFR + 7.5 mL min⁻¹ HGR), it was necessary to use two channels of the integrated peristaltic pump and to install two waste tubings (3.18 mm i.d.) connected with T-junction to the drainage orifice of the MSIS chamber. In order to ensure independent variation of HGR flow rate, an external Gilson peristaltic pump was used with separate control.

Close to straight line relationship between the recorded emission intensities and the sample amount pumped into the MSIS cell was derived for SFR in the range 2 - 15 mL min⁻¹. This indicates that the efficiency of signal production is not deteriorated at higher sample flow rates, despite of working with flows much higher than recommended by the manufacturer. From Fig. 1, obtained by plotting the calculated relative enhancements of emission intensities vs the relative SFR increases, it is evident that some part (~20%) of the analyte introduced into the MSIS chamber is not utilised (the slope in Fig. 1 is 0.804 instead of the optimal 1.00). The reason for this could be an incomplete hydride formation chemical reaction, due to ineffective mixing of sample and HGR or other kinetic limitations.

Effect of MNPs

It is worthwhile to investigate whether the addition of MNPs to the HGR could increase the efficiency of the chemical reaction by providing higher contact surface into the MSIS cell and improving gas-liquid separation. For this purpose, a mixture of HGR solution with silica-coated magnetic nanoparticles (MnFe₂O₄@SiO₂) was pumped from the top of MSIS. Emission signals for As (193.695, 188.979 and 228.812 nm) and Sb (217.581, 231.147 nm) were measured, varying the MNPs concentrations into the HGR. The results were compared with those without addition of MNPs. The first tests showed no effect in sensitivity for Sb lines and a prominent sensitivity enhancement (13-25%) in emission signals for all As lines in the presence of freshly prepared MNPs (~2 mg ml⁻¹). The used MNPs were collected from the waste by means of a permanent magnet, rinsed by BDW and reused with no memory effect observed. Surprisingly, the commented enhancement effect on As signals was lost working with recycled MNPs. Repetitive experiments

showed restored sensitivity enhancement only if MNPs were previously washed with ethanol. The explanation for this unexpected behavior could be that the signal enhancement is a result of the presence of alcohol, carried by freshly synthesized nanoparticles (see the synthetic procedure in [18]). This explanation was afterwards proved by the same results obtained from both experiments - using recycled MNPs (~2 mg ml⁻¹) rinsed with ethanol and by working without MNPs, but adding 2% ethanol in HGR instead. An important conclusion is that introduction of MNPs in the MSIS reaction cell does not contribute to sensitivity changes neither for As nor for Sb. Evidently, the hydride generation procedure in the MSIS reactor design runs with enough efficiency, hence provision of extra surface or better mixing is not required even at these extremely high sample and reagent flows.

On the other hand, it was visually observed that the presence of MNPs into the HGR solution reduces bubbles formation in delivery tubing and significantly improves the stability of NaBH₄. This phenomenon resulted in smooth and steady reagent flow supply and is beneficial for maintaining a dynamic equilibrium of the input-output mass transfer into the reaction chamber. The use of easily recyclable MNPs could be appointed as a green analytical approach. The commented stabilization effect of MNPs reflects in improving the precision of MSIS-HG-MP-AES measurements of both hydride forming elements tested. This is proved by the results presented in Table 3 which summarises the pooled standard deviation for signals of As and Sb. The MNPs supported HG shows more than twice improvement in the precision irrespective from the alcohol presence.

Table 3. Improvement of the measurement precision of the registered intensities of As (193.695 nm) and Sb (217.581 nm)

No of consec. measurement	As				Sb			
	HGR ^a		HGR/MNPs/ C ₂ H ₅ OH ^b		HGR ^a		HGR/MNPs ^c	
	I, c s ⁻¹	(SD), c s ⁻¹	I, c s ⁻¹	(SD), c s ⁻¹	I, c s ⁻¹	(SD), c s ⁻¹	I, c s ⁻¹	(SD), c s ⁻¹
1	248	(11)	302	(6)	759	(33)	779	(11)
2	241	(23)	303	(11)	767	(47)	778	(17)
3	254	(15)	296	(14)	763	(16)	770	(25)
4	240	(8)	294	(5)	797	(55)	772	(9)
5	239	(22)	292	(6)	774	(21)	780	(14)
6	265	(19)	299	(10)	789	(45)	769	(9)
7	241	(24)	299	(10)	804	(64)	755	(10)
8	243	(14)	298	(10)	757	(13)	757	(5)
9	229	(14)	297	(5)	799	(45)	754	(13)
10	241	(16)	294	(5)	760	(15)	772	(6)
Sum	2441	(164)	2974	(82)	7769	(353)	7687	(118)
pooled RSD	7%		2.8%		5%		1.5%	

Conditions: 2 ppb As or 1 ppb Sb in 0.1 mol L⁻¹ HCl and 0.5% L-cysteine.

^a Only HGR (solution of 1.5% NaBH₄/0.1% NaOH) was used; ^b HGR with addition of 1.6 mg ml⁻¹ MNPs and 2% C₂H₅OH; ^c HGR with addition of 1.6 mg ml⁻¹ MNPs.

By varying MNPs concentration from 0.4 to 6 mg ml⁻¹ in HGR with 2% C₂H₅OH, a robust stabilisation effect was found if the content of MNPs is kept between 1 - 2 mg ml⁻¹. For HGR solution with above 3 mg ml⁻¹ MNPs the precision was deteriorated because of the increased viscosity of the HGR solution. All further experiments have been performed with 1.6 mg ml⁻¹ MNPs. Effect of carbon-containing compounds.

The commented above sensitivity enhancement for As in presence of alcohol could be explained by a carbon-related matrix effect, which has been already confirmed for ICP-AES and ICP-MS

measurements of As in the presence of C [21– 23]. Despite this the effect of the carbon in HG-MSIS-MP-AES analysis has not been reported in the literature before. The mass fraction of carbon transported to the excitation source can be monitored by C emission signal at λ=193.045 nm. This spectral line is close to the emission of As at 193.695 nm, and both lines can be recorded by MP-AES in the same spectral window. Additional experiments performed by us showed signal enhancement for As depending on the physico-chemical characteristics of the carbon containing

M. T. Kiryakova et al.: Nanoparticles-assisted MSIS-MP-AES hydride generation determination of As and Sb solutions used in combination with MSIS-HG-AES. The results are presented in Table 4.

Table 4. Carbon emission intensity and signal enhancement for 10 ppb As for HGR with additives

HGR + additives	C _{193.045nm} , I c s ⁻¹	AS 193.695 nm signal enhancement, %
Non	-	-
CH ₃ OH	23269	13±1.1
C ₂ H ₅ OH	39682	20±2
i-C ₃ H ₇ OH ^a	86561	11±2
i-C ₃ H ₇ OH+NPs	89275	20±1.8
0.05% NaCO ₃	4881	7±0.6
0.1% NaCO ₃	7816	8±0.5
0.6% NaCO ₃	25062	9±0.7
1.2% NaCO ₃	64166	6±0.9

^a Visual observation of foam generation

Table 5. Instrumental detection limits compared to those from recent papers.

	LOD, ppb, MSIS-MP-AES-HG	
	From the literature	Modified MSIS HGR/MNPs/C ₂ H ₅ OH (current work)
As	0.38 [13]	0.17
	0.48 [14]	
	10 [15]	
Sb	0.48 [14]	0.05

The sensitivity gain was greater for C₂H₅OH and it could be preferred as a less toxic agent. The gas-liquid separation in the MSIS chamber could be troubled if the viscosity of the reaction mixture is increased. In the case of i-C₃H₇OH, foam generation in the MSIS cell arises, but by adding 1.6 mg ml⁻¹ of MNPs less foaming is observed and as a result a gain in sensitivity for As was found (Table 4). Additional studies are required to explain these observations and to investigate the application of MNPs as an antifoaming agent in HG.

CONCLUSIONS

An effective technique for generation of hydrides of As, Sb by using a commercial (MSIS®) cell combined with nitrogen microwave plasma atomic emission spectrometry (MP-AES) was developed. A modification in (MSIS®) enables work with high reagents flow rates. At this conditions the addition of inert and easily recyclable magnetic nanoparticles to the hydride reagent do not improve the HG reaction efficiency, but leads to significant stabilization effect of the hydride generation reagent delivery and more than twice precision improvement. Sensitivity enhancement for As was confirmed in a presence of carbon carrying agents.

The proposed nanoparticles assisted hydride generation approach extends the ability of MSIS-MP-AES to determine sub-ppb levels of As and Sb.

Acknowledgment: The work was supported by NSF Project DN19/9 2018-2020 (INISA). The authors would like to thank T.E.A.M. Ltd. and Agilent Technologies for kindly providing Agilent 4200 MP-AES instrumentation to the Department of Analytical Chemistry and Computer Chemistry at University of Plovdiv "P. Hilendarski".

REFERENCES

- D. Gonçalves, T. McSweeney, G. Donati, *J. Anal. At. Spectrom.*, **31**, 24, (2016).
- N. Chalyavi, P. S. Doidge, R. J. S. Morrison, G. B. Partridge, *J. Anal. At. Spectrom.*, **32**, 1988, (2017).
- M. Wiedenbeck, L. Bedard, R. Bugoi, M. Horan, K. Linge, S. Merchel, L. Morales, D. Savard, A. Souders, P. Sylvester, DOI: 10.1111/j.1751-908X.2014.00347.x, *Geostand. Geoanalytical Res.*, **38**, 467, (2014).
- Agilent Technologies, Application eHandbook, 2016, p. 5
- S. Karlsson, V. Sjöberg, A. Ogar, *Talanta*, **135**, 124, (2015).
- COMMISSION DIRECTIVE 2003/40/EC, *Regulation*, **2**, 30 (2003).
- "COUNCIL DIRECTIVE 98/83/EC," (1998).
- J. Dedina, D. Tsalev, Hydride Generation Atomic Absorption Spectrometry, John Wiley & Sons Ltd., Chichester, 1995.
- J. Dedina, Generation of Volatile Compounds for Analytical Atomic Spectroscopy, R.A. Meyers (ed.), *Encyclopedia of Analytical Chemistry*, **S1-S3**, 897, John Wiley & Sons Ltd., Chichester, 2011.
- A. Asfaw, G. Wibetoe, *J. Anal. At. Spectrom.*, **21**, 1027, (2006).
- M. Ślachciński, *Appl. Spectrosc. Rev.*, **49**, 271, (2014).
- I. D. Brindle, *Patent*, US 2003 / 0230712 A1, **1**, (2003).
- C. K. Tanabe, H. Hopfer, G. Gilleland, A. Liba, S. E. Ebeler, J. Nelson, *J. Anal. At. Spectrom.*, **31**, 1223, (2016).
- R. C. Machado, C. D. B. Amaral, J. A. Nóbrega, A. R. Araujo Nogueira, *J. Agric. Food Chem.*, **65**, 4839, (2017).
- I. V. Mikheev, E. A. Karpukhina, L. O. Usol'tseva, T. O. Samarina, D. S. Volkov, M. A. Proskurnin, *Inorg. Mater.*, **53**, 1422, (2017).
- H. Ahmad, A. Ahmad, S. S. Islam, *Microchim. Acta*, **184**, 2007, (2017).
- A. Dados, E. Papparizou, P. Eleftheriou, C. Papastefanou, C. D. Stalikas, *Talanta*, **121**, 127, (2014).

18. D. Georgieva, V. Stefanova, V. Kmetov, I. Roman, N. Kovachev, A. Canals, *Univ. Plovdiv „Paisii Hilendarski“ – Bulg. Sci. Pap.*, **38**, 7, (2011), https://blogs.uni-plovdiv.net/argon/files/2011/09/001_NT38_2011.pdf
19. H. Chen, I. D. Brindle, X. chun Le, *Anal. Chem.*, **64**, 667, (1992).
20. B. Welz, M. Sucmanova, *Analyst*, **118**, 1425, (1993).
21. H. Wiltsche, M. Winkler, P. Tirk, *J. Anal. At. Spectrom.*, **30**, 2223, (2015).
22. G. Grindlay, L. Gras, J. Mora, M. T. C. De Loos-Vollebregt, *Spectrochim. Acta Part B At. Spectrosc.*, **115**, 8, (2016).
23. T. Nakazawa, D. Suzuki, H. Sakuma, N. Furuta, *J. Anal. At. Spectrom.*, **29**, 1299, (2014).

Assessment of different approaches for background correction in microwave plasma atomic emission spectrometry – case study for analysis of Cd, Cr, Cu, Ni, Pb and Zn in treated bio-waste

V. Y. Markova^{1,2*}, K. K. Simitchiev¹

¹Department of Analytical Chemistry and Computer Chemistry, University of Plovdiv “Paisii Hilendarski”,
24 Tzar Assen Str., 4000 Plovdiv, Bulgaria

²Laboratory for Testing of Solid Biofuels and Compost, Energy Agency of Plovdiv, 139 Ruski Blvd, office 403,
4000 Plovdiv, Bulgaria

Received November 14, 2018; Revised December 6, 2018

Several approaches for background correction were studied when nitrogen microwave plasma atomic emission spectrometry (MP-AES) was applied for analysis of Cd, Cr, Cu, Ni, Pb and Zn in treated bio-waste (compost and stabilized organic fraction samples). Since the temperature of the microwave plasma is relatively lower than that of the argon operated inductively coupled plasma, the former excitation source is more prone to the occurrence of structured background emission, as well as matrix-induced shifts at the background level. Indeed, these two effects were observed when sample solutions of the treated bio-waste were subjected to measurements by MP-AES and led to the need to investigate the adequateness of the implemented background correction algorithm. A comparison of the “on-peak”, two-sided “off-peak” and one-sided “off-peak” correction approaches was made for the following emission lines: Cd I 228.802; Cd II 226.502; Cr I 427.480; Cr I 520.844; Cu I 324.754; Cu I 327.395; Ni I 341.476; Ni I 305.082; Pb I 405.781; Pb I 363.957; Zn I 213.857; Zn I 481.053. Furthermore, the spread of wavelengths (1 or 3 CCD pixels) used for intensity integration was also evaluated. The tested correction algorithms led to different results only in the case of Ni I 305.082 and Pb I 363.957. Nevertheless, it was found that the one-sided/off-peak/3 pixels approach was adequate for all studied analyte lines. In addition, it was proved that the measurement repeatability was not influenced by the used mathematical model for background correction.

Keywords: background correction, microwave plasma atomic emission spectrometry (MP-AES), compost, stabilized organic fraction, bio-waste

INTRODUCTION

The microwave induced plasma is well known concept [1] used in elemental analysis. Commercial microwave induced plasma atomic emission spectrometer (MP-AES) has been introduced on the market since 2011 [2]. The plasma is sustained using microwave magnetic field and nitrogen, which can be extracted from the ambient air. MP-AES has been applied for the quantification of B, P and Mo in biosludge [2], trace elements in fusel oil [3], sunflower [4], leather and fur [5], gasoline and ethanol [6], animal feed and fertilizer [7], trace and macro elements in geochemical samples [8] and environmental samples [9], macro elements in soils [10], lanthanides in environmental samples [11].

The microwave plasma has different properties than the inductively coupled argon plasma, two of which are the lower temperature (around 5000 K) and the operation on nitrogen [12]. The background of the microwave plasma is reported to be highly structured due to the emission of radical species

such as NO⁺, NO, N₂, N₂⁺, NH, OH [12], which impact on the analytical signal that must be assessed. Three approaches for background correction are provided by the MP Expert software of Agilent 4200 MP-AES spectrometer: “automatic” correction, “off-peak” two-sided correction, “off-peak” one-sided correction [13]. The “automatic” correction is defined as linear regression method [12], but no information is supplied if this algorithm is able to correct a shift in the background level caused by any difference of the matrices of the standard solutions and the analysed samples. The concept of the “off-peak” correction is well known [13], but the adequateness of this approach is usually strongly dependent on the choice of the “off-peak” wavelengths, as well as the number of pixels used for integration of the signal (for spectrometers with CCD or CID).

In our previous investigations we have found that MP-AES has sufficient detection power for the determination of Cd, Cr, Cu, Ni, Pb and Zn in compost [14]. However, no detailed investigation

* To whom all correspondence should be sent.
E-mail: vzapryanova@uni-plovdiv.net

V.Y. Markova, K.K. Simitchiev: Assessment of different approaches for background correction in microwave plasma ... of the different approaches for background correction has been made. The aim of the current study was to compare and select the most appropriate algorithm for background correction needed for MP-AES analysis of Cd, Cr, Cu, Ni, Pb and Zn in treated bio-waste such as compost and stabilized organic fraction (SOF).

EXPERIMENTAL

Nitric acid ($\text{HNO}_3 \geq 65\%$, Fluka, p.a. grade) was used for extraction of soluble fractions of elements from compost and stabilized organic fraction (SOF). Ultrapure water with $2 \mu\text{S cm}^{-1}$ electroconductivity (Ultrapure Water System Adjarov Technology Ltd.) was used throughout this work for preparation of solutions and rinsing the vessels. Standard solutions were prepared from a multi-element standard solution (ICP Multi-element Standard Solution IV 1000 mg L^{-1} - Ag, Al, B, Ba, Bi, Ca, Cd, Co, Cr, Cu, Fe, Ga, In, K, Li, Mg, Mn, Na, Ni, Pb, Sr, Tl, Zn, Merck KGaA) by dilution with acidified ultrapure water (1% v/v HNO_3).

The analysed samples – compost and SOF were produced by one of the regional waste management systems in Bulgaria treating biodegradable waste. The samples were dried in an oven at 40°C for 16 hours, after that they were quartered to provide about 500 g sub-sample which was homogenized with a cutting mill Retsch SM 200.

A microwave digestion system (MARS 6, CEM Corporation) with closed vessels was used to perform the microwave-assisted extraction. The samples were proceeded in accordance with the EN 16173 [15]. The samples passed through the extraction procedure were diluted with factor 50 or 100 and blank sample was proceeded.

A nitrogen microwave induced plasma optical emission spectrometer MP-AES 4200 Agilent Technologies was used. The measured emission lines were Cd I 228.802; Cd II 226.502; Cr I 427.480; Cr I 520.844; Cu I 324.754; Cu I 327.395; Ni I 341.476; Ni I 305.082; Pb I 405.781; Pb I 363.957; Zn I 213.857; Zn I 481.053.

Multivariate optimization of the operating parameters (sample flow rate, nebulizer gas flow rate and optical view point) was carried out by using central composite design as a tool for experimental planning. The MP-AES operating parameters are presented in Table 1.

All calculations for background correction were carried out by spreadsheet program (MS Excel) using “raw” data (registered intensities at defined wavelengths), exported from the MP Expert software of the 4200 Agilent MP-AES.

Table 1. MP-AES 4200 Agilent operating parameters

Magnetron, MHz	2450
Plasma gas, L.min^{-1}	20
Auxiliary gas, L.min^{-1}	1.5
Nebulizer type	OneNeb®
Optics viewing position	axial
Integration (read) time, s	1
Number of readings	5
Nebulizer gas flow rate, L.min^{-1}	0.65
Sample flow rate, mL.min^{-1}	1.43
Optical view point	0

RESULTS AND DISCUSSION

The instrumental set-up of Agilent 4200 MP-AES allows the registration of each analyte line within a spectral window of approximately 0.6 nm consisting of *ca.* 40 measurement pixels (Fig. 1). This allows the operator to assess the background near the spectral line of interest, as well as the appearance of other lines generated from interfering elements. An evaluation of the background emission within the registered spectral windows for selected wavelengths of the studied elements (Cd, Cr, Cu, Ni, Pb, Zn) have shown the structured nitrogen plasma background (Fig. 1). The latter phenomenon is due to the emission of radical species which are present in the low temperature microwave plasma [12]. In general, the existence of structured background near the analyte line is a potential obstacle for the application of the conventional “off-peak” correction approach since it becomes more sophisticated to make an adequate background subtraction. An alternative correction not influenced from the structured background is the “on-peak” approach. However, the latter mathematical method suffers from shifts of the background level among the analysed samples, e.g. the blank and the real-matrix sample. In our study, it was observed that for all studied analytical lines the background level registered for compost or SOF samples substantially drops or increases in respect to the blank solution (Fig. 1). The listed above facts show that for adequate determination of Cd, Cr, Cu, Ni, Pb and Zn in compost and SOF the applicability of the “off-peak” and “on-peak” correction approaches needs to be checked for each analyte line.

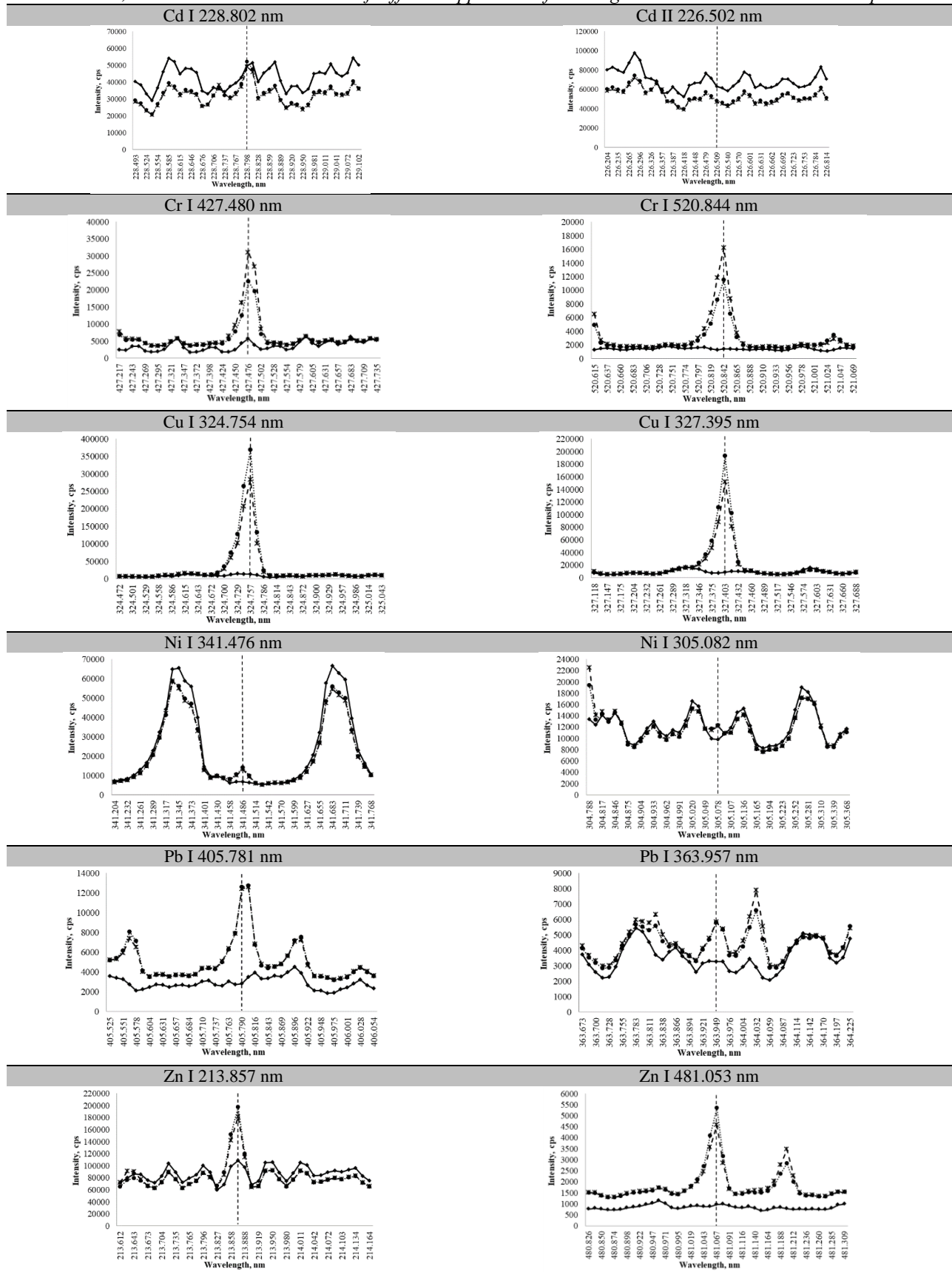


Figure 1. Profiles of the studied emission lines of elements: \rightarrow blank sample; $-*$ - compost sample with DF=100 for emission lines of Cr, Cu, Ni, Pb and Zn, and compost sample with DF=50 + 0.5 mg.L⁻¹ addition of Cd; \cdots SOF sample with DF=100 for emission lines of Cr, Cu, Ni, Pb and Zn, and SOF sample with DF=50 + 0.5 mg.L⁻¹ addition of Cd. With vertical dashed line is presented the position of WP wavelength used in eqs. 1-3.

In the current work we have studied the following algorithms for background correction: i) “on-peak” using intensities derived from bins of 1 registered pixel (Eq. 1); ii) two-sided “off-peak” using bins of 1 pixel (2 sided/off-peak/1 pixel) (Eq. 2); iii) two-sided “off-peak” using bins of 3 pixels (2 sided/off-peak/3 pixels) (Eq. 2); iv) one-sided “off-peak” using bins of 1 pixel (1 sided/off-peak/1 pixel) (Eq. 3); and v) one-sided “off-peak” using bins of 3 pixels (1 sided/off-peak/3 pixels) (Eq. 3). The “on-peak” correction was applied according to Equation 1. This approach requires the initial registration of the spectrum of the blank solution (1% v/v nitric acid) and was based on the assumption that the magnitude of any matrix-induced shift in the background level will have the same value at the analyte wavelength, as well as in the neighbor region around the spectral line of interest. At the two-sided “off-peak” correction a linear interpolation was performed between two background points (one on either side of the analyte peak) to predict the background intensity at the analyte wavelength, which is then subtracted from the analyte signal (Eq. 2). The one-sided “off-peak” correction was carried out by subtraction of the emission signal at the analyte wavelength and the intensity at selected background point located in the left or right side of the analyte peak (Eq. 3).

$$I_{corrected}^{on-peak} = I_S^{WP} - \left(\frac{I_S^{LP} + I_S^{RP}}{2} - \frac{I_B^{LP} + I_B^{RP}}{2} \right) \quad \text{Eq. 1}$$

$$I_{corrected}^{2\ sided/off-peak} = I_S^{WP} - [slope(I_S^{LP}:I_S^{RP}; LP:RP) \times WP + intercept(I_S^{LP}:I_S^{RP}; LP:RP)] \quad \text{Eq. 2}$$

$$I_{corrected}^{1\ sided/off-peak} = I_S^{WP} - I_S^{LP\ or\ RP} \quad \text{Eq. 3}$$

I_S^{WP} - the emission intensity registered at a wavelength pixel closest to the maximum of the analyte spectral peak (for on-peak; 2 sided/off-peak/1 pixel and 1 sided/off-peak/1 pixel correction) or average of a bin of 3 pixels enclosing the peak maximum (for 2 sided/off-peak/3 pixels and 1 sided/off-peak/ 3 pixels correction);

I_S^{LP} - the corresponding intensities registered for a sample solution at a pixel (for on-peak; 2 sided/off-peak/1 pixel and 1 sided/off-peak/1 pixel correction) or average of a bin of 3 pixels (for 2 sided/off-peak/3 pixels and 1 sided/off-peak/ 3 pixels correction) located in the left side of the analyte spectral peak;

I_S^{RP} - the corresponding intensities registered for a sample solution at a pixel (for on-peak; 2 sided/off-peak/1 pixel and 1 sided/off-peak/1 pixel correction) or average of a bin of 3 pixels (for 2 sided/off-peak/3 pixels and 1 sided/off-peak/ 3 pixels correction) located in the right side of the analyte spectral peak;

I_B^{LP} - the corresponding intensities registered for the blank solution at a wavelength pixel located in the left side of the analyte spectral peak (for “on-peak” correction);

I_B^{RP} - the corresponding intensities registered for the blank solution at a wavelength pixel located in the right side of the analyte spectral peak (for “on-peak” correction);

WP - the wavelength (nm) at a pixel, closest to the maximum of the analyte spectral peak;

LP - the wavelength (nm) at a pixel located in the left side of the analyte spectral peak;

RP - the wavelength (nm) at a pixel located in the right side of the analyte spectral peak.

The wavelengths at which the corresponding intensities were taken for calculation of the “on-peak”, the two-sided “off-peak” and the one-sided “off-peak” correction of the studied analyte lines are given in Table 2.

Table 2. Wavelengths at which the corresponding intensities were used for calculation of the “on-peak”, two-sided “off-peak” and one-sided “off-peak” correction using bins of 1 pixel or 3 pixels

WP, nm	Bins of 1 pixel			Bins of 3 pixels				
	LP, nm	RP, nm	LP1, nm	LP2, nm	LP3, nm	RP1, nm	RP2, nm	RP3, nm
228.802 (Cd)	228.630	228.859	228.615	228.630	228.646	228.844	228.859	228.874
427.480 (Cr)	427.398	427.528	427.385	427.398	427.411	427.515	427.528	427.541
520.844 (Cr)	520.774	520.888	520.763	520.774	520.785	520.876	520.888	520.899
324.754 (Cu)	324.629	324.943	324.615	324.629	324.643	324.929	324.943	324.957
327.395 (Cu)	327.246	327.517	327.232	327.246	327.261	327.503	327.517	327.531
341.476 (Ni)	341.458	341.528	341.444	341.458	341.472	341.514	341.528	341.542
305.082 (Ni)	304.890	305.180	304.875	304.890	304.904	305.165	305.180	305.194
405.781 (Pb)	405.697	405.935	405.684	405.697	405.710	405.922	405.935	405.948
363.957 (Pb)	363.907	363.990	363.894	363.907	363.921	363.976	363.990	364.007
213.857 (Zn)	213.796	213.950	213.781	213.796	213.811	213.934	213.950	213.965
481.053 (Zn)	480.995	481.116	480.983	480.995	481.007	481.104	481.116	481.128

Table 3. Comparison of the results obtained by “on-peak”, two-sided “off-peak” and one-sided “off-peak” background correction for a) compost and b) SOF sample

Line	LOQ, mg L ⁻¹	on-peak		2 sided/off-peak/1 pixel		2 sided/off-peak/3 pixels		1 sided/off-peak/1 pixel		1 sided/off-peak/3 pixels	
		Conc., mg L ⁻¹	SD, mg L ⁻¹	Conc., mg L ⁻¹	SD, mg L ⁻¹	Conc., mg L ⁻¹	SD, mg L ⁻¹	Conc., mg L ⁻¹	SD, mg L ⁻¹	Conc., mg L ⁻¹	SD, mg L ⁻¹
a) Compost											
Cd I 228.802	0.02 ^f	0.498 ^a	0.001	0.495 ^a	0.003	0.508 ^a	0.002	0.497 ^{a,d}	0.003	0.498 ^{a,d}	0.002
Cr I 427.480	0.02 ^f	0.518 ^b	0.004	0.518 ^b	0.004	0.515 ^b	0.004	0.515 ^{b,d}	0.004	0.511 ^{b,d}	0.004
Cr I 520.844	0.03 ^f	0.491 ^b	0.010	0.491 ^b	0.011	0.509 ^b	0.011	0.492 ^{b,e}	0.011	0.509 ^{b,e}	0.011
Cu I 324.754	0.007 ^f	1.27 ^b	0.02	1.27 ^b	0.02	1.28 ^b	0.02	1.27 ^{b,e}	0.02	1.28 ^{b,e}	0.02
Cu I 327.395	0.009 ^f	1.32 ^b	0.01	1.32 ^b	0.01	1.31 ^b	0.01	1.32 ^{b,e}	0.01	1.32 ^{b,e}	0.02
Ni I 341.476	0.05 ^f	0.207 ^b	0.001	0.207 ^b	0.002	0.214 ^b	0.001	0.207 ^{b,e}	0.001	0.207 ^{b,e}	0.002
		1.19 ^c	0.02	1.19 ^c	0.02	1.21 ^c	0.02	1.19 ^{c,e}	0.02	1.19 ^{c,e}	0.02
Ni I 305.082	0.08 ^f	0.222 ^b	0.001	0.225 ^b	0.003	0.205 ^b	0.002	0.234 ^{b,e}	0.003	0.216 ^{b,e}	0.003
		1.23 ^c	0.01	1.24 ^c	0.01	1.21 ^c	0.01	1.25 ^{c,e}	0.01	1.23 ^{c,e}	0.01
Pb I 405.781	0.07 ^f	1.07 ^b	0.02	1.08 ^b	0.02	1.06 ^b	0.02	1.09 ^{b,d}	0.02	1.09 ^{b,d}	0.02
Pb I 363.957	0.11 ^g	0.85 ^b	0.01	0.85 ^b	0.01	0.77 ^b	0.01	1.05 ^{b,d}	0.02	1.07 ^{b,d}	0.01
Zn I 213.857	0.08 ^f	5.55 ^b	0.02	5.55 ^b	0.03	5.54 ^b	0.03	5.50 ^{b,d}	0.03	5.53 ^{b,d}	0.03
Zn I 481.053	0.90 ^f	5.52 ^b	0.03	5.51 ^b	0.03	5.57 ^b	0.03	5.52 ^{b,d}	0.02	5.51 ^{b,d}	0.03
b) SOF											
Cd I 228.802	0.02 ^f	0.552 ^a	0.001	0.549 ^a	0.003	0.561 ^a	0.002	0.550 ^{a,d}	0.003	0.554 ^{a,d}	0.002
Cr I 427.480	0.02 ^f	0.326 ^b	0.005	0.326 ^b	0.006	0.325 ^b	0.006	0.323 ^{b,d}	0.006	0.321 ^{b,d}	0.006
Cr I 520.844	0.03 ^f	0.327 ^b	0.004	0.327 ^b	0.005	0.341 ^b	0.005	0.328 ^{b,e}	0.005	0.341 ^{b,e}	0.005
Cu I 324.754	0.007 ^f	1.66 ^b	0.02	1.66 ^b	0.03	1.66 ^b	0.03	1.65 ^{b,e}	0.03	1.65 ^{b,e}	0.03
Cu I 327.395	0.009 ^f	1.61 ^b	0.01	1.61 ^b	0.03	1.61 ^b	0.01	1.61 ^{b,e}	0.01	1.61 ^{b,e}	0.01
Ni I 341.476	0.05 ^f	0.235 ^b	0.001	0.234 ^b	0.001	0.238 ^b	0.002	0.236 ^{b,e}	0.002	0.234 ^{b,e}	0.002
		1.21 ^c	0.01	1.21 ^c	0.01	1.22 ^c	0.01	1.22 ^{c,e}	0.01	1.22 ^{c,e}	0.01
Ni I 305.082	0.08 ^f	0.215 ^b	0.001	0.218 ^b	0.002	0.213 ^b	0.002	0.224 ^{b,e}	0.001	0.221 ^{b,e}	0.001
		1.20 ^c	0.01	1.20 ^c	0.01	1.20 ^c	0.01	1.20 ^{c,e}	0.01	1.21 ^{c,e}	0.01
Pb I 405.781	0.07 ^f	1.09 ^b	0.02	1.09 ^b	0.03	1.07 ^b	0.03	1.11 ^{b,d}	0.03	1.10 ^{b,d}	0.03
Pb I 363.957	0.11 ^g	0.81 ^b	0.01	0.81 ^b	0.02	0.78 ^b	0.02	0.95 ^{b,d}	0.03	1.00 ^{b,d}	0.02
Zn I 213.857	0.08 ^f	6.83 ^b	0.02	6.83 ^b	0.03	6.89 ^b	0.03	6.75 ^{b,d}	0.03	6.86 ^{b,d}	0.03
Zn I 481.053	0.90 ^f	7.04 ^b	0.03	7.03 ^b	0.03	6.89 ^b	0.05	7.05 ^{b,d}	0.04	6.79 ^{b,d}	0.05

^a sample with DF=50 + 0.5 mg.L⁻¹ Cd; ^b sample with DF=100; ^c sample with DF=100 + 1.0 mg.L⁻¹ Ni; ^d left one-sided “off-peak” correction; ^e right one-sided “off-peak” correction; ^f calculated LOQ using two-sided/off-peak/1 pixel correction; ^g calculated LOQ using left one-sided/off-peak/1 pixel correction .

The five approaches for background correction were compared for registered spectra of compost and SOF samples (Table 3). Several emission lines of elements were studied. For each element were selected two lines – one priority and one alternative, except for Cd, for which only one spectral line was reasonable to be used in view of achieving the lowest possible detection limit. However, the content of Cd in both analysed sample matrices was below the established instrumental quantification limit of 0.02 mg L⁻¹. So in order to assess the different background correction approaches (Eqs. 1-3) for this element the compost and SOF sample solutions were spiked with 0.5 mg.L⁻¹ of Cd in order to produce a measurable signal for the analyte. Another element which was present in the real samples at levels close to the established LOQs (Table 3) was Ni - the found concentrations were approximately 3 times (for Ni 305.082) and 4 times (for Ni 341.476) higher than the corresponding LOQs. Even though the detection power of MP-AES was sufficient to register the native signals of Ni in the compost and SOF the adequateness of the different background correction approaches (Eqs. 1-3) was also tested for spiked samples with 1 mg L⁻¹ Ni. The latter was done aiming to assure that the measured emission intensities at the analyte WPs are with improved signal-to-noise ratio.

In the current study a tolerance limit of 5% deviation, among the analyte concentrations achieved by different approaches for background correction, as well as by using alternative spectral lines for the target elements, was accepted. Any result, which exceeds this limit, was regarded as significantly different.

For both sample types (compost and SOF) it was found that the application of all studied approaches for background correction resulted in identical concentrations when the following analyte lines were used: Cd I 228.802, Cr I 427.480, Cr I 520.844, Cu I 324.754, Cu I 327.395, Ni I 341.476, Pb I 405.781, Zn I 213.857 and Zn I 481.053 (Table 3). Furthermore, the obtained concentrations of Cr, Cu and Zn by using the listed above spectral lines (two for each element) were within the specified tolerance limit of 5%. The correction algorithms led to different results in the case of Ni I 305.082 and Pb I 363.957. It was found that only the one-sided/off-peak/3 pixels approach gives adequate results for Ni and Pb measured respectively at 305.082 and 363.957 nm in compost and SOF samples. The evident reason for the incorrect results when “two-sided” correction was used for Pb I 363.957 is the

existence of closely located line of Fe I 364.039 nm (Fig. 1). The analysis of the treated bio-waste samples spiked with 1 mg.L⁻¹ Ni showed that all algorithms for background correction applied for the line 305.082 nm lead to identical results when the analyte concentration exceeds at least 10 times the corresponding limit of quantification (Table 3).

The measurement repeatability, as a component of the comparison among the applied background corrections, was also assessed. For the purpose, the standard deviation of five instrumental readings was calculated considering that each reading was individually proceeded using a particular background correction. The obtained results are presented in Table 3. For all studied spectral lines it was found that the derived standard deviations do not depend on the chosen approach for background correction and for every single analyte line the achieved SD values were statistically identical (Table 3).

CONCLUSIONS

Summarizing the results above it can be concluded that for all studied analyte lines adequate results can be achieved if one-sided/off-peak/3 pixels correction of the background is applied. However, all investigated algorithms for assessing the background level (Eqs. 1-3) are interchangeable applicable for the regarded set of spectral lines except for Ni I 305.082 and Pb I 363.957. It is important to be mentioned that the suggested “on-peak” approach (Eq. 1) is not integrated in the MP Expert software [13] of the 4200 Agilent MP-AES and hence it must be done by an alternative spreadsheet program (e.g. MS Excel) after an export of the registered data. The latter makes difficult to apply the “on-peak” correction for routine analysis. Since the other four “off-peak” correction algorithms (Eqs. 2 and 3) can be proceeded by the MP Expert software, the readers are suggested to use them setting the corresponding WP, LP and/or RP wavelength values as depicted in Table 2.

Acknowledgements: VM and KS are grateful for financial support of Project Number DN19/9 2018 - 2020 (INISA), financed by NSF of Bulgaria. The authors also acknowledge Dr. Violeta Stefanova for the fruitful discussions and given advices, as well as T.E.A.M. Ltd. for the complimentary supplied spectrometer Agilent 4200 MP-AES at Faculty of Chemistry, University of Plovdiv.

REFERENCES

1. A.E. Croslyn, B.W. Smith, J.D. Winefordner, *Crit. Rev. Anal. Chem.*, **27**, 199 (1997)

- V.Y. Markova, K.K. Simitchiev: Assessment of different approaches for background correction in microwave plasma ...
2. V. Sreenivasulu, N. S. Kumar, V. Dharmendra, M. Asif, V. Balaram, H. Zhengxu, Z. Zhen, *Appl. Sci.*, **7**, 264 (2017).
 3. D. Araujo, T. Mcsweeney, M. Cristina, M. A. Utrera, *Curr. Anal. Chem.*, **13** 474 (2017).
 4. S. Karlsson, V. Sjöberg, A. Ogar, *Talanta*, **135**, 124 (2015).
 5. Y. Zhao, Z. Li, A. Ross, Z. Huang, W. Chang, K. Ou-Yang, Y. Chen, C. Wu, *Spectrochim. Acta - Part B, At. Spectrosc.*, **112**, 6 (2015).
 6. G. L. Donati, R. S. Amais, D. Schiavo, J. A. Nóbrega, *J. Anal. At. Spectrom.*, **28**, 755 (2013)
 7. W. Li, P. Simmons, D. Shrader, T. J. Herrman, S.Y. Dai, *Talanta*, **112**, 43 (2013).
 8. B. Vysetti, D. Vummiti, P. Roy, C. Taylor, C. T. Kamala, M. Satyanarayanan, P. Kar, K. S. V. Subramanyam, A. K. Raju, K. Abburi, *At. Spectrosc.*, **35**, 65 (2014).
 9. C. T. Kamala, V. Balaram, M. Dharmendra, V. Satyanarayanan, K. S. V. Subramanyam, A. Krishnaiah, *Environ. Monit. Assess.*, **186**, 7097 (2014).
 10. P. Niedzielski, L. Kozak, K. Jakubowski, W. Wachowiak, J. Wybieralska, *Plant Soil Environ.*, **62**, 215 (2016).
 11. E. Varbanova, V. Stefanova, *Ecology & Safety*, **9**, 362 (2015).
 12. G. B. Partridge, *J. Anal. At. Spectrom.*, **32**, 1988 (2017).
 13. MP Expert Help, Software version 1.4.0.4317, Agilent Technologies.
 14. V. Y. Zapryanova, K. K. Simitchiev, *Bulg. Chem. Commun.*, **49 G**, 10 (2017).
 15. EN 16173 Sludge, treated biowaste and soil - Digestion of nitric acid soluble fractions of elements, 2012.

Determination of silver in cosmetic products by microwave plasma - atomic emission spectrometry

E. K. Varbanova, V. M. Stefanova*

*Department of Analytical Chemistry and Computer Chemistry,
University of Plovdiv "Paisii Hilendarski", 24 Tzar Asen str., Plovdiv, Bulgaria*

Received November 14, 2018; Revised January 8, 2019

The potential of a new spectral method, namely, microwave plasma atomic emission spectrometry (MP-AES), for determination of silver in various types of cosmetic products was studied. Instrumental operating parameters as nebulizer flow rate of nitrogen (L min^{-1}) and viewing position are optimized.

Three types of cosmetic products are tested, i.e. face cream, body lotion and tooth paste. All samples were digested with HNO_3 and H_2O_2 by hot plate heating ($\text{DF}=50$) and then face cream and body lotion were diluted prior analysis by an additional factor of 40. Tooth paste was analyzed directly after digestion because of the lower content of Ag in the sample.

The four available wavelengths of silver in the MP-AES library (328.068, 338.289, 520.907 and 546.549 nm) were explored and the following instrumental limits of detection were obtained: 1.9, 2.3, 81, 98 $\mu\text{g L}^{-1}$, respectively. The study of spectral interferences in presence of sample matrix shows that only in the toothpaste there is a risk of interference due to neighbor titanium lines on 338.377 and 521.038 nm.

It was shown that all sample matrices did not cause a significant non-spectral effect on emission signals of Ag (<5%), at the specified above dissolution procedure and the proposed dilution factors. All measurements were done by external calibration with aqueous standard solutions.

The recovery of spikes of analyte to real samples is in the range 95-105%. The accuracy of the measurement is verified by independent ICP-MS determination. Obtained limit of quantification for the most sensitive emission line 328.068 nm is 0.32 mg kg^{-1} , which allows successful application of microwave plasma atomic emission spectrometry for determination of silver content in different cosmetics. The developed method is a fast, accurate and cheaper alternative to ICP-MS for controlling the silver levels in a variety of personal care products.

Keywords: MP-AES, ICP-MS, silver, cosmetics, analysis.

INTRODUCTION

Silver is a common addition in a variety of cosmetic products due to its well known antibacterial, antimicrobial and antifungal properties [1, 2]. Since silver is one of the most expensive metals, the cosmetic manufacturers often speculate on the exact content of Ag in their products. The most frequently used methods for quantification and control of the metal content in personal care products manufacture are fast, multi-element and generally very expensive [3, 4].

Microwave induced plasmas as alternative sources for atomic emission spectrometry have been rarely used in the last decade for determination of silver [5, 6] because of the lower detection power in comparison to ICP-OES [7].

Microwave induced nitrogen-based plasma working at atmospheric pressure was successfully interfaced to an atomic emission spectrophotometer (MP-AES) resulting in a next generation of spectral instrumentation for simultaneous determination of major and minor elements in a variety of environmental and industrial objects.

As MP-AES combines the multi-elemental

capabilities of an emission source with eliminating the need of expensive gases to support plasma, it is often defined as a cheaper alternative to FAAS and ICP-OES. Since 2012, when the instrument was first released by Agilent, the method has received a variety of practical applications. Ozbek and co-authors developed methods for determination of different elements in wines [8], cheese [9], bread [10] and rice samples [11]. MP-AES was also applied for analysis of waters [12], soils [13], plants [14], leather [15] and compost [16]. Besides the typically explored trace and alkaline elements, the method was also used for determination of rare-earth elements in waters, plants [17] and ores [18]. A few articles cope with the use of hydride generation MP-AES for determination of As and Se [19–22]. The vast variety of explored matrices and elements shows the potential of MP-AES to become a cheaper multi-element alternative to FAAS in the analytical laboratory. Furthermore, the method is often compared to ICP-OES [16, 17] and even ICP-MS [14].

The aim of the present study is to show the applicability of MP-AES for fast, cheap and

* To whom all correspondence should be sent.
E-mail: stefanova@uni-plovdiv.net

E.K. Varbanova, V.M. Stefanova: Determination of silver in cosmetic products by microwave plasma - atomic ... reliable determination of Ag in different cosmetic products.

EXPERIMENTAL

MP-AES 4200, Agilent and ICP-MS 7700, Agilent are used for all measurements after external calibration. ICP-MS determination is done under standard measurement conditions on isotopes ^{107}Ag and ^{109}Ag . ^{103}Rh is used for internal standard.

Samples are prepared as follows: approximately 0.5 g of the samples (face cream, body lotion and tooth paste) were treated on a hot plate with 10 mL of concentrated nitric acid (Fluka™) and 2 mL of 30 % H_2O_2 (Valerus Ltd). After digestion the solutions were left to cool down and diluted to 25 mL with doubly distilled water (BDW). Blank samples were prepared as well. Tooth paste was measured directly by MP-AES and with additional dilution factor 20 for ICP-MS. Face cream and body lotion were measured respectively with additional DF=40 for MP-AES and DF=100 for ICP-MS. Silver standard 1000 mg L^{-1} is purchased from Merck. An aliquot of IS Rh (CPA-spectr™) was added to the samples and standards prior to ICP-MS determination. All of the used stock standards are traceable to NIST. Calibration and working solutions are prepared with BDW and acidified with 0.5% p.a. nitric acid where necessary.

RESULTS AND DISCUSSION

Instrumental optimization

The Agilent MP-AES 4200 instrument allows the operator to optimize working parameters as nebulizer flow rate and plasma view position in such manner as to achieve the best sensitivity for a particular case. Optimization of both parameters was done in order to establish the best conditions for silver analysis using all wavelengths available in the spectral library of the instrument (Table 1).

Nebulizer flow rate affects both the size of aerosol droplets, the amount of analyte entering the plasma and the time that the analyte spends in the source. For this reason, nebulizer flow rate is an essential parameter that influences sensitivity. Optimization of N_2 flow rate was done for all wavelengths in the interval $0.3 - 1 \text{ L min}^{-1}$. Results for two of the studied Ag lines are presented on Figures 1 A and B for 328.068 and 546.549 nm.

View position was also optimized using the software option. The results for all tested lines were

very similar with optimum at the zero point – standard view position which is located coaxially to the central axis of the plasma discharge (Fig. 2).

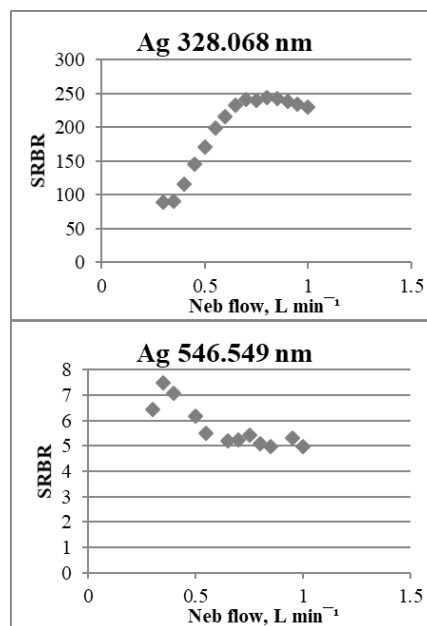


Figure 1. Influence of nebulizer flow rate on the corresponding signal-ratio-to- background-ratio (SRBR) for two Ag lines – 328.068 nm and 546.549 nm.

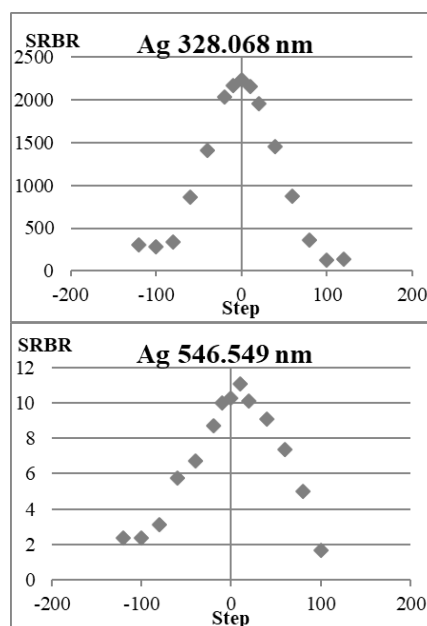
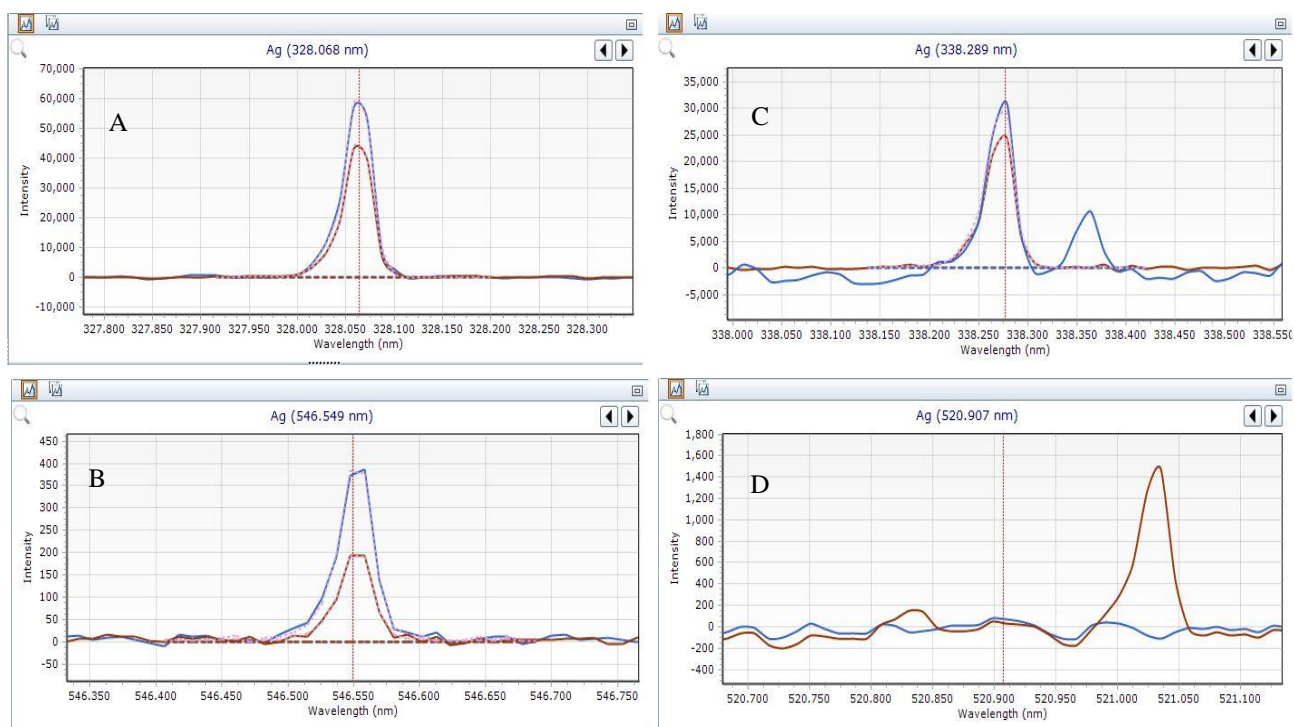


Figure 2. Influence of view position on the corresponding signal-ratio-to- background-ratio (SRBR) for two Ag lines – 328.068 nm and 546.549 nm.

Table 1. Emission lines of silver, type of emitting particle, relative intensity, order in spectral library and close lines of titanium.

Ag				Ti			
Wave-length, nm	Type of line	Relative Intensity	Transition energy (eV)	Wave-length, nm	Type of line	Relative Intensity	Transition energy (eV)
328.068	I	461836	3.78				
338.289	I	257077	3.66	338.377	II	76893	3.66
546.549	I	2361	6.04				
520.907	I	1440	6.04	521.038	I	13189	2.43

**Figure 3.** A-D Spectral profiles of Ag emission lines obtained for acidified water solution of Ag^+ 0.5 mg L^{-1} (red line) and toothpaste sample solution.

The influence of nebulizer gas flow rate on the sensitivity is much more pronounced than the viewing position. Optimum of 0.8 L min^{-1} is obtained for lines 328 and 338 and $0.3\text{-}0.35 \text{ L min}^{-1}$ for lines 546 and 520 nm. The behavior of the emission signals is consistent with what is expected in terms of their excitation energy. As the first couple (328 and 338 nm) belongs to the “soft” atomic lines (see Table 1) with low transition energy, increasing the nebulizer flow rate will stimulate production of finer aerosol droplets and corresponding enhancement of transport efficiency. Therefore, for these lines higher nitrogen flow rates are preferable. The second couple of lines (520 and 546 nm) are “hard” lines and for them lower nebulizer flow rate will ensure longer residence time in the hot plasma region needed for effective excitation.

Spectral interferences

A review of the MP-AES library showed that there are only four wavelengths for measuring silver. All of the lines are atomic with significant

differences in relative intensities (Table 1). The available lines were studied for potential spectral interferences from matrix components in the studied cosmetic products. There are strict requirements for cosmetic products that are commercially available. They concern both their purity (i.e. ensuring low levels of metal concentrations in them) and the declaration of all the main ingredients. After comparing information on the composition of the tested samples with the spectral library of the MP-AES instrument, we assumed that the only potential risk of spectral interference in silver analysis could be caused by the presence of titanium. As this element is a major component in a variety of products, its presence should be taken into consideration during development of the analytical method.

Library data showed that two of the Ag lines could be possibly overlapped by highly intensive neighbor lines of Ti.

For evaluation of spectral interferences on the lines of Ag two solutions were compared – acidified standard of silver and dissolved sample

E.K. Varbanova, V.M. Stefanova: Determination of silver in cosmetic products by microwave plasma - atomic ...
with appropriate dilution factor. No spectral interferences were observed for face cream and body lotion – measured concentration of silver on all wavelengths in these samples is practically identical. In contrast, tooth paste showed different behavior most probably because of the high content of TiO₂ in the sample. On Figures 3 A-D are presented signals obtained by measuring samples (tooth paste – blue line) and acidified water

solution of silver 0.5 mg L⁻¹ (red line). Results show that sample matrix does not lead to spectral interferences for lines 328 and 546 nm. In the case of the other two wavelengths it could be seen that neighbor emission lines of Ti emerge. Besides this it could be noted that the sample matrix changes the background which could lead to serious mistakes in calculating analyte concentration.

Table 2. Measured concentration of silver in tooth paste sample on different lines (n=3).

	328.068 nm	338.289 nm	520.907 nm	546.549 nm
Conc., mg L ⁻¹	0.15 ± 0.003	0.19 ± 0.003 0.15 ± 0.02*	< LOD	0.15 ± 0.018

* The given result is obtained after mathematical correction of Ti spectral interference.

Table 3. Threshold concentration of Ti in solution, mg L⁻¹

Ag	328.068 nm	338.289 nm	520.907 nm	546.549 nm
C _{threshold} , mg L ⁻¹	No	0.22	0.46	No

Table 4. Recovery of standard additions of Ag to samples (n=3)

Spike concentration	328.068 nm		338.289 nm		Spike concentration	328.068 nm
	R, %		R%			
	Face cream	Body lotion	Face cream	Body lotion		
0.50 mg L ⁻¹	106±7	102±3	106±7	101±3	0.05 mg L ⁻¹	104±5
1.0 mg L ⁻¹	102±4	103±5	101±4	102±4	0.10 mg L ⁻¹	101±4
2.0 mg L ⁻¹	100±5	100±4	101±3	101±5	0.20 mg L ⁻¹	103±6
	DF=2000					DF=50

Measured concentration of silver in the sample on different lines is presented on Table 2. The result obtained at a measurement of 338 nm is by about 40% lower compared to the free spectral lines of Ag, which can be caused by an improper background correction due to the nearby titanium line. The severe matrix interference in combination with the low sensitivity of the line at 520 nm resulted in a negative signal value for toothpaste solution after automatic background correction. For the interfered spectral lines of Ag, automatic background correction is inappropriate, hence only a left side correction at 338.15 nm and 520.694 is recommended. This leads to 25% higher concentration of Ag measured on 338 nm. Even in this case the contribution of Ti as interfering element should be additionally estimated.

It could be concluded that all emission lines are appropriate for determination of silver in the tested face cream and body lotion. Ag in samples with high content of Ti could be measured on line 328 nm or if the concentration of the analyte is higher, the less sensitive line (546 nm) could be also used.

Threshold concentration of Ti was determined to specify the limitation of measuring silver in the presence of the interference. Threshold levels are calculated as Ti concentration that gives a

statistically distinct signal at the respective analyte wavelength (i.e., the interfering signal is equal to 3×standard deviation of background). Results are presented in Table 3. The measured concentration of Ti in the sample with DF=50 is 0.35 mg L⁻¹. This means that for the spectral line of 338.289 nm there is a real strong interference effect that requires additional correction. The interference factor of Ti on this line was estimated as 1800 and after mathematical correction the estimated concentration of in tooth paste on this Ag line (338 nm) is statistically identical to the ones for free spectral lines (see table 2). It should be noted that additional correction of Ti interference on 338 nm reflects in increased uncertainty. Concerning the latter line at 520 nm the presence of Ti is below the threshold concentration, but the weak sensitivity makes this line impractical when measuring real samples with a low silver content.

Non-spectral matrix effect

The three tested samples were examined for non-spectral matrix effect with appropriate dilution factor. The concentration of Ag in the samples could be measured with dilution factor 2000 for face cream and body lotion and 50 for tooth paste. As cosmetic products consist of a comparatively

E.K. Varbanova, V.M. Stefanova: Determination of silver in cosmetic products by microwave plasma - atomic ...
 “light” matrix, severe non-spectral effects were not expected. In order to investigate if there is some matrix influence on emission signals, real samples were spiked with known amount of silver. Concentration of spikes is selected accordingly to the concentration of silver in the real samples. The recoveries of three spikes to each of the studied

cosmetic samples are presented on Table 4. For face and body lotion results are identical for all wavelengths. Quantitative recovery shows that the matrix does not lead to suppression or enhancement of the analyte signal in real samples, hence a simple external calibration by water standards of Ag is adequate strategy.

Table 5. Comparison of MP-AES and ICP-MS results for Ag in cosmetic products.

	MP-AES (n=3)	ICP-MS (n=5)
	conc., %	conc., %
Face cream	0.35±0.005	0.34±0.014
Body lotion	0.45±0.006	0.45±0.009
	conc., mg kg ⁻¹	conc., mg kg ⁻¹
Tooth paste	7.76±0.2	7.80±0.12

Table 6. MP-AES limits of quantification (10×stand. deviation) for Ag (DF=50).

Ag, wavelength	328.068 nm	338.289 nm	520.907 nm	546.549 nm
MLOQ, mg kg ⁻¹	0.32	0.38	13.4	16.2

The concentration of silver in tooth paste and corresponding standard additions are above LODs only for 2 lines, 328 and 338 nm, but for the second one an additional correction of spectral interference is needed. Therefore, the free line is recommended for real samples analysis as less problematic. The recoveries of the standard additions measured on this line are in the interval 101-104 %. Results show that DF=50 allows measuring Ag without a risk of non-spectral matrix effect. Further attempts to decrease the dilution factor to 25 lead to significant change in the background even for line 328 nm and made the analysis impossible.

Analytical characteristics of the MP-AES method

Due to the lack of an appropriate certified reference material for the determination of silver in cosmetic products, the accuracy of the proposed MP-AES method was demonstrated by comparison with an alternative ICP-MS analysis (Table 5). Ag content in the three samples is measured by mass spectrometry with appropriate dilution factors (see Experimental).

Concentrations of the analyte obtained by both methods are statistically identical which demonstrates the applicability of MP-AES for determination of silver in a variety of cosmetic products.

The intra-laboratory reproducibility was assessed by repeating the analytical procedure described above for determination of Ag in all studied objects in three different days. The obtained relative standard deviations (RSD, %) were as follows: 1.96, 2.8 and 3.7 for face cream, body

lotion and tooth paste, respectively. The target reproducibility of the method was calculated according to the Horwitz model [23], taking into account the correction factor of 2/3 for intra-laboratory comparison. As the silver content of the tested products significantly differs, the target reproducibility for *face cream* and *body lotion* was estimated as 3.1% RSD, while for trace levels of Ag in the *tooth paste* the corresponding target RSD was 7.7%. As it can be seen from the above results, the internal laboratory reproducibility of the method is better than that predicted by the Horwitz model.

Method detection limits are presented on Table 6. Obtained results show that the method is sufficiently sensitive for quantification of Ag in different cosmetic products.

CONCLUSIONS

The performed investigations proved that the new instrumental technique MP-AES is an adequate alternative to ICP-MS for determination of silver in a variety of cosmetic products. The analytical performance is easy, cheap and fast, allows quantifying Ag content by simple external calibration with limits of determination between 0.3-16 mg kg⁻¹. Two emission lines at 328.068 and 546.549 nm are recommended, since they are free from spectral interferences, while for the next two lines 338.289 and 520.907 nm the presence of Ti in toothpastes or sunscreen creams should be taken into consideration because of the risk of spectral interferences originated by neighbor emission lines. The estimated threshold concentrations of

E.K. Varbanova, V.M. Stefanova: Determination of silver in cosmetic products by microwave plasma - atomic ...
interfering element give fast and reliable information about the need of additional mathematic correction of real interference effects.

REFERENCES

1. A. B. G. Lansdown, *Current Problems in Dermatology*, **33**, 17 (2006).
2. H. I. Adawi, M. A. Newbold, J. M. Reed, M. E. Vance, I. L. Feitshans, L. R. Bickford, N. A. Lewinski, *Nanoimpact*, **11** 170 (2018).
3. B. V. Santos, J. M. Oliveira, W. Bonventi, V. M Hanai-Yoshida, *X-ray Spectrometr.*, **47**, 242 (2018).
4. N. Wasukan, S. Srisung, M. Kuno, K. Kulthong, R. Maniratanachote, *Spectrochim. Acta A, Mol. Biomol. Spectrosc.*, **8**, 149 (2015).
5. P. Pohl, P. Jamroz, *J. Anal. At. Spectrom.*, **26**, 1317, (2011).
6. H. Matusiewicz, M. Ślacheński, *Spectrosc. Lett.*, **43**, 172 (2010).
7. B. Mansouri, A. Maleli, M. Mahmoodi, B. Davari, S. Shahsavari, *Scientific Journal of Kurdistan University of Medical Sciences*, **22**, 31 (2017).
8. N. Ozbek, S. Akman, *LWT - Food Sci. Technol.*, **61**, 532, (2015).
9. N. Ozbek, S. Akman, *Food Chem.*, **192**, 295 (2016).
10. N. Ozbek, S. Akman, *Food Chem.*, **200**, 245 (2016).
11. N. Ozbek, H. Tinas, E. Atespare, *Microchem. J.*, 3393, (2018).
12. S. V Smirnova, T. O. Samarina, D. V Ilin, and I. V Pletnev, *Anal. Chem.*, **90**, 6323, (2018).
13. A. Baysal, H. Saygin, *Chem. Ecol.*, **34**, 713 (2018)
14. S. Karlsson, V. Sjöberg, A. Ogar, *Talanta*, **135**, 124 (2015).
15. Y. Zhao, Z. Li, A. Ross, Zh. Huang, W. Chang, K. Ou-yang, Y. Chen, Ch. Wu, *Spectrochim. Acta Part B At. Spectrosc.*, **112**, 6, (2015).
16. V. Y. Zapryanova, K. K. Simitchiev, E. N. Piskova, *Bulg. Chem. Commun.* **49**, 10 (2017).
17. E. K. Varbanova, V. M. Stefanova., *Int. Sci. Pub. - Ecology and Safety*, **9**, 362 (2015).
18. E. Helmecci, Y. Wang, I. D. Brindle, *Talanta*, **160**, 521 (2016).
19. E. Y. Barrientos, E. A. Karpukhina, L. O. Usol'tseva, T. O. Samarina, D. S. Volkov, M. A. Proskurnin, *J. Anal. At. Spectrom.*, **31**, 203, (2015).
20. C. K. Tanabe, H. Hopfer, G. Gilleland, A. Liba, S. E. Ebeler, J. Nelson, *J. Anal. At. Spectrom.*, **31**, 1223 (2016).
21. M. G. Esperanza, E. Y. Barrientos, K. Wrobel, Fr. J. A. Aguilar, A. R. C. Escobosa, K. Wrobel, *Anal. Methods*, **9**, 2059 (2017).
22. V. Mikheev, E. A. Karpukhina, L. O. Usol'tseva, T. O. Samarina, D. S. Volkov, M. A. Proskurnin, *Inorganic Materials*, **53**, 1422 (2017).
23. M. Thompson (ed.) AMC Technical Brief No.17, Royal Society of Chemistry, 2004.

General characteristics of silver nanoparticles analysis by single particle inductively coupled plasma mass spectrometry

V. M. Stefanova*, L. I. Kaynarova, D. L. Georgieva

University of Plovdiv "Paisii Hilendarski"; Department of Analytical Chemistry and Computer Chemistry,
24 Tzar Assen Str., 4000 Plovdiv, Bulgaria

Received December 10, 2018; Revised January 18, 2019

Single particle inductively coupled plasma mass spectrometry (spICP-MS) is a new powerful and sensitive technique for detecting, characterizing, and quantifying nanoparticles in suspension. The possibility to detect in a single run the presence of both dissolved and particulate forms of an element is promising in the context of nanotoxicology studies. In order to obtain adequate information, the recorded peak must be produced by a single nanoparticle, which automatically leads to several challenges – appropriate dilution providing separation of the signals generated from the individual particles, stabilization of the introduced nanocolloidal suspension, and recording of fast peak signals.

In the current study a model for theoretical calculation of the dilution factor of AgNPs with different size is applied ensuring optimal peak frequency. Various reagents and washing solutions such as non-ionic surfactants (TX-100, TX-114), buffers and acid solutions were tested for stabilization of the sample introduction of Ag nanocolloidal suspension, aiming to decrease transport losses and “memory effect”. Some general characteristics of AgNPs analysis by spICP-MS as: particle number concentration (#Particles L⁻¹), separate evaluation of mass concentration of NPs and ionic silver and corresponding % fraction of nanoparticles in suspension were estimated. The method was applied for analysis of three nanocolloidal suspensions - one synthesized in our lab and two commercial products.

Keywords: Silver nanoparticles; Single particles; Inductively coupled plasma mass spectrometry; Characterization

INTRODUCTION

The rapid development of nanoscience and nanotechnology in the last decade leads to intensive use of nanosized materials in different fields of human life. According to the statistics of the Emerging nanotechnologies program, up to 2014 there are more than 1800 products with engineered nanomaterials, released on the markets in 32 countries, and more than 440 (24%) of them contain silver nanoparticles (AgNPs) [1, 2]. Due to their unique properties they find application in drug delivery, cosmetics, water purification systems and other products [2, 3]. The everyday use of products which contain silver nanoparticles leads to their release in the environmental system. A good understanding of their ecological cycle and assessment of human health risk requires not only detection and quantification but also physicochemical characterization as shape, size, diameter, surface charge [4].

Different types of techniques such as: i) electron microscopy - transmission electron microscopy (TEM) and scanning electron microscopy (SEM); ii) optical spectroscopy - UV-visible spectroscopy (UV-vis), dynamic light scattering (DLS); iii) atomic spectroscopy methods and electrochemical methods are exploited for characterization of AgNPs [5, 6]. A powerful

technique for nanoparticles characterization, evolved recently, is the single particle inductively coupled plasma mass spectrometry (spICP-MS) which combines the low limits of detection (ng L⁻¹) and the high sensitivity of ICP-MS with a new single particle detection mode [7–10]. The theoretical principle of this method was developed by Degueldre *et al.* [11] who demonstrated the capability of ICP-MS for single particle analysis of colloids in water. According to the theory of the method it is expected that each particle produces in the plasma a flash of ions originating a fast transient signal that can be measured. The fundamental prerequisites for registration of single particle events are: sufficiently large dilution that provides separation of the peaks generated by individual nanoparticles and fast detection system working with short dwell times (10 ms or less). If the number of particles in suspension is low enough, then only one particle will reach the plasma at a time, producing a spike with intensity above the background which represents the ionic concentration of “dissolved” material in solution. Thus, the frequency of the pulse is directly related to the number concentration of particles. Degueldre *et al.* relate the frequency of the particle events (N_p), to the particle number concentration (C_{NPs} , #Particles L⁻¹). For suspensions of nanoparticles measured by the spICP-MS method, C_{NPs} can be

* To whom all correspondence should be sent.
E-mail: stefanova@uni-plovdiv.net

expressed as:

$$C_{\text{NPs}} = N_{\text{p}} \times \frac{1}{\eta_{\text{n}}} \times \frac{1}{V} \times \frac{1}{T} \times 10^3, \quad (1)$$

where: N_{p} – nanoparticle events measured; η_{n} – transport efficiency; V – sample uptake flow rate, (ml min^{-1}); T – total acquisition time, (min).

The transport efficiency can be calculated in several ways [12]: i) as the ratio of sample uptake and drain flow rates; ii) by the certified diameter of a reference material; iii) by the mass concentration of a reference material. Correct determination of η_{n} is necessary for calculation of particle number concentration.

The intensities of registered peaks are proportional to the mass of NPs and are therefore related to their size. So the smallest detectable size of nanoparticles is element specific and will depend on both instrument sensitivity and background level. An approximate estimation of the background signal contribution can be made by calculating the Background Equivalent Diameter (BED) which represents the average continuous signal (originating from ionic concentration), over which the peaks should be statistically distinguished. The BED is an estimate analogous to the Background Equivalent Concentration (BEC) used in the optical spectral methods.

As the spICP-MS method is capable of measuring nanoparticles mass concentration together with the ionic concentration of the carrier solution, the mass distribution between both phases (NPs and ionic) can also be evaluated.

Despite the growing number of recent publications devoted to AgNPs characterization by spICP-MS some general issues are still under investigation such as: stabilization of working solutions containing NPs; memory effect and protocols of washing; validation of methods for estimation of particle number concentration and distribution of Ag between solid and liquid phases of a nanocolloidal system. Last but not least, controlling the dilution of nanocolloids is crucial to ensure both the registration of single particle events together with the accumulation of a sufficiently large data set for subsequent statistical processing that allows a reliable interpretation of the results. The aim of this work was to characterize suspensions of silver nanoparticles with different size (RM AgNPs 60 nm, RM AgNPs 40 nm and AgNPs synthesized by us with unknown size). For this purpose, we proposed a model for theoretical calculation of the dilution factor of silver nanoparticles ensuring an optimal peak frequency. The model allows predicting the number of nanoparticles expected to be recorded, depending

on the input data for the size and mass concentration of the samples, together with instrumental parameters of the measurement itself.

EXPERIMENTAL

Instrumentation and reagents

ICP-MS 7700 Agilent spectrometer with MicroMist™ nebulizer and Peltier cooled double pass spray chamber was used for silver nanoparticles determination at a mass of 107 amu. The ICP-MS operating parameters are as follow: RF power - 1.55 kW; sample flow rate - 0.342 mL min^{-1} ; carrier Ar gas flow rate - 1.1 L min^{-1} . Data were collected at time resolved analysis (TRA) acquisition mode with 5 ms integration time for 60 s acquisition time.

UV-vis spectra were recorded using a ONDA spectrophotometer UV-30 SCAN in absorbance mode within the wavelength range 200 – 600 nm with a scanning step of 2 nm.

For sonication of silver colloids an ultrasonic bath (Kerry US) was used.

Certified reference materials of AgNPs suspensions with two different sizes (40 $\text{nm} \pm 4 \text{ nm}$, and 60 $\text{nm} \pm 8 \text{ nm}$) and mass concentration 0.02 mg mL^{-1} were purchased from Sigma-Aldrich. Two commercial products “Silver water” with declared presence of Ag NPs and mass concentration of silver 10 mg L^{-1} were purchased from local pharmacies.

AgNO_3 (Merck, p.a.), H_2O_2 (30%, Valerus, p.a.), NaBH_4 (Acros Organics- Fisher-Scientific, 98+%) and sodium citrate tribasic monohydrate – TSC (Chemsnab Dimitrovgrad, p.a.) were used for synthesis of silver nanoparticles. Single standard solution of Ag 1000 mg L^{-1} was purchased from Merck. Nitric acid HNO_3 (65% Fluka p.a.), nonionic surfactants TX-114 (Fluka AG, p.a.), TX-100 (Fisher-Scientific, p.a.) and citrate buffer (0.1 mol L^{-1}) prepared in our lab were tested as washing and stabilization agents. All suspensions and solutions were prepared by dilution with double distilled water (BDW).

The raw data obtained from spICP-MS measurements were statistically evaluated by MassHunter Workstation Single Nanoparticle Application (Rev. A, June 2017; Agilent Technologies) and Excel (Microsoft).

Sample preparation

Synthesis of silver nanoparticles. Methodology for synthesis of AgNPs was taken from [13]. Briefly, 50 μl of AgNO_3 (0.05 mol L^{-1}), 0.5 ml of TSC (75 mmol L^{-1}), 60 μl of 30% H_2O_2 , and 250 μl of NaBH_4 (100 mmol L^{-1}) were added

into 24.14 ml of BDW at room temperature under vigorous stirring for 30 min.

Sample preparation for quantitative analysis. All dilute samples, as well as intermediate standards were daily prepared. Based on our theoretical model, samples for spICP-MS analysis were prepared with different dilution factors (DF) as follows: i) RM AgNPs 60 nm, DFs 8×10^4 and 1.6×10^5 ; RM AgNPs 40 nm, DFs in the interval $2.7 \times 10^5 \div 1 \times 10^6$; iii) Ag NPs synthesized in the lab, DF 1×10^5 ; and iv) commercial products, DF 5×10^4 . These factors were achieved with two-step dilution. All samples and RMs were treated in an ultrasonic bath for 30 min before and after dilution to guarantee homogeneous distribution of AgNPs in solution. Ionic standard solution of Ag ($1 \mu\text{g L}^{-1}$) was used to assess instrument signal response for silver and as calibrator for mass concentration determination. RM AgNPs 40 nm was used as a reference material for calibration by size. The other materials were measured only as samples. Transport efficiency was evaluated by the size of reference material. In order to decrease transport losses and memory effect, a comparison of a variety of washing and stabilization reagents was made: 5% solution of HNO_3 , 0.1 mol L^{-1} citrate buffer, 0.5% solutions of non-ionic surfactants (TX-114 and TX-100).

For UV-vis detection all samples were diluted by a DF=10.

RESULTS AND DISCUSSION

Theoretical calculation model for dilution of NPs prior to spICP-MS measurement

Appropriate dilution of the nanoparticulate suspension is a key parameter which affects both the possibility of separate registration of the individual particle events and the accumulation of sufficient data for adequate statistical processing of the measured signals. The basic assumption of spICP-MS that each recorded signal represents a single NP motivated us to develop a model for theoretical calculation of the dilution factor of AgNPs, to guarantee optimal peak frequency (table 1).

This model represents the quantitative relation between size, mass and number of atoms of one nanoparticle (Eq. 2) which allows us to calculate the expected number of nanoparticles (NP) in 1 ml of solution with a given mass concentration (assigned to NPs content) (Eq. 3):

$$No_{atoms}/NP = \frac{\frac{1}{6} \times \pi \times d^3 \times \rho \times f \times 6.02214 \times 10^{23}}{A_m} \quad (2)$$

$$\# \text{ Particles/ml} = \frac{C_{\text{sample}} \times 6.02214 \times 10^{23}}{A_m \times No_{atoms}/NP} \quad (3)$$

where: d is diameter of NPs in nm; ρ is NPs material density in g cm^{-3} ; f is mass fraction of analyte; A_m is atomic mass of analyte in g mol^{-1} ; C_{sample} is mass concentration of NPs in suspension in mg L^{-1}

The model incorporates the current instrumental parameters influencing both sample transport through the nebulization system (i.e. sample flow rate and nebulization efficiency) and timing. Time parameters of the measurement - single measurement time (integration time - t_d) and whole time for data collection (acquisition time - t_{acq}) determine the total number of measurements to be recorded for the sample.

To ensure effective separation of the signals generated by nanoparticles from the baseline produced by dissolved analyte in the carrier solution, we set the condition to have a ratio of approximately 1:10. The latter provides an optimal frequency of nanoparticle events together with accurate measurement of the baseline.

Hence, the desired number of particles corresponding to the commented above condition could be defined before analysis. In the case of the current study, with time parameters given in table 1, 12000 data points were measured per single replicate. Thus, 1200 is the number of desired nanoparticles in sample solution. The dilution factor was calculated as a ratio of expected and desired number of peaks (Eq. 4):

$$DF = \frac{No \text{ peaks}_{exp}}{No \text{ peaks}_{des}} = \frac{\# \text{ Particles/ml} \times \eta_t \times V \times t_d}{t_{acq} \times 10^2} \quad (4)$$

where: η_t is transport efficiency; V is sample flow rate in ml min^{-1} ; t_d is integration time in ms; t_{acq} is acquisition time in sec.

The theoretical model includes preliminary data, such as the diameter and mass concentration of nanoparticles, which are commonly available for certified reference materials or engineered NPs. For unknown samples the application of the described model requires some preliminary measurements. The tentative size of silver nanoparticles could be obtained from the UV-vis spectrum, while mass concentration could be determined by spectrochemical analysis of digested sample.

Table 1. An example for application of the calculation model for NPs suspension dilution of RM AgNPs 40 nm before spICP-MS determination

NPs Characteristics			
Analyte	Ag	Density (g cm ⁻³)	10.49
Atomic mass - A _m (g mol ⁻¹)	107.8682	Analyte mass fraction	1
Preliminary data		Calculations	
Diameter - d (nm)	40	No of atoms/NPs	1.96×10 ⁶
Conc sample (mg L ⁻¹)	20	NPs conc (# Particles mL ⁻¹)	5.69×10 ¹⁰
SP-ICP-MS parameters		Expected No of peaks	1.28×10 ⁹
Sample flow rate – V (mL min ⁻¹)	0.342	No of data points for acquisition	12000
Transport efficiency	0.066		
Integration Time (ms)	5	Desired No of peaks	1200
Acquisition Time (s)	60	Dilution Factor	1.07×10 ⁶

UV-vis spectral characterization of AgNPs

As is well known, Ag colloids show a strong plasmon resonance band in which the maximum wavelength depends on particle size and shape [14, 15]. In the current work this specific behavior was used to obtain preliminary information about the mean size of a sample of AgNPs synthesized by us according to the procedure described by Yan *et al.* [13] and for comparison the two RM AgNPs, 60 nm and 40 nm were measured as well. The registered UV-spectra are presented on fig. 1.

The wavelengths of the maxima of plasmon resonance peaks for AgNPs in the tested RMs are in agreement with the spectral data provided by the manufacturer (i.e. λ_{\max} in the range of 405-425 nm and 425-450 nm for AgNPs with diameter 40 and 60 nm, respectively) with well distinguished “blue” shift typical for NPs with smaller size [14]. The lowest wavelength of the maximum ($\lambda_{\max}=390$ nm), recorded for the AgNPs synthesized by us, corresponds to a mean diameter of ~ 20 nm [16]. The clear shift of the peak maxima over the diameter of the silver nanoparticles allows a rapid preliminary estimation of the particle size in an unknown sample and thus a correct dilution of the sample for spICP-MS measurement could be calculated.

In addition, the UV-spectra of AgNPs can be used for evaluation of the stability of nanocolloidal systems.

Using the above described information the following DFs were calculated for NPs measured in the current study: 3.2×10^5 for RM AgNPs 60 nm; 1.1×10^6 for RM AgNPs 40 nm; 2.1×10^5 for AgNPs synthesized in the lab ($d \sim 20$ nm; mass concentration - 5 mg L^{-1}); 1.3×10^6 for the commercial products.

Study of memory effect and stabilization of AgNPs

In the numerous articles published in the scientific journals on spICP-MS no comments were found regarding the memory effect during the introduction of highly diluted nanocolloidal systems. However, some authors draw attention to the need for a relatively long stabilization time prior to measuring the sample. Our experiments showed a strong memory effect, i.e., when measuring a blank immediately after the sample many peaks originated by NPs remaining along the transport path were observed. Thus a variety of washing solvents were tested - nitric acid; citrate buffer and two surfactants, TX-100 and TX-114. For evaluation of the washing ability of the tested solvents, the measurement was performed after introduction of a sample containing Ag NPs and 2 min washing. The total signals acquired (counts for Ag) for washing solvents were compared to that obtained for a blank sample (St0) measured before introduction of NPs. The best washing properties shows nitric acid, where the overall Ag signal was ~ 30% higher than in the blank sample and only 5 NPs peaks were identified. For the other tested washing solutions (citrate buffer, TX-100 and TX-114) the signals exceeded the background by factors of 9, 11 and 14, respectively, and the number of identified peaks increased in the same order (150, 170 and 440). The ability of HNO₃ to dissolve AgNPs left on the capillary walls is probably the reason of the best washing effect. Therefore, it was used in all subsequent studies.

The carrier solvent composition affects two factors, on the one hand it stabilizes the nanocolloidal system and, on the other hand, it determines the equilibrium between solid and liquid phases (i.e., AgNPs/Ag⁺). The first effect is important for the precision of NPs concentration

determination, while the second one is crucial for the baseline Ag^+ signal over which the peaks of NPs appeared and determined the corresponding Background Equivalent Diameter (BED) of a running measurement. Four carrier solutions of diluted AgNPs were tested: pure water (BDW); citrate buffer and non-ionic surfactants, TX-100 and TX-114.

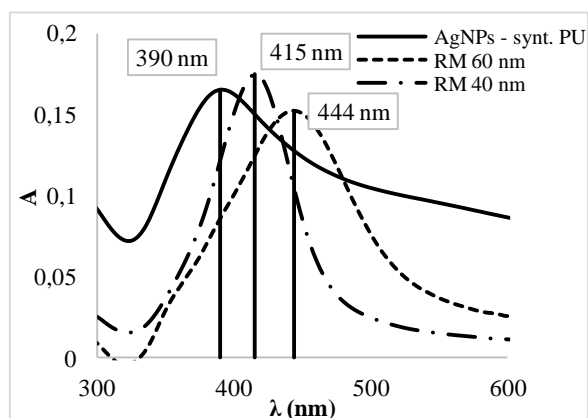


Fig. 1. UV-vis spectra of nanocolloidal suspensions from two RMs of AgNPs 60nm and 40nm and AgNPs synthesized in our lab.

As can be seen from the stability tests (figure 2), non-ionic surfactants are not suitable carriers for AgNPs for two reasons: the number of registered peaks is by about 25% lower than the corresponding one in pure water or citrate buffer; in addition, a gradual decrease of peak numbers in successively measured replicas was observed. The commented effect may be due to modification of the walls of the sample introduction tubing with a surfactant that can capture AgNPs and thereby increase transport losses. The latter is in agreement with our previous studies demonstrating that surfactants are not effective as washing solvents.

Concerning the second effect – the concentration of ionic silver that determines the baseline signal and could be assessed by BED, the obtained values were as follows: 18 nm for citrate buffer; 13 nm for BDW and 10 nm for TX-100 and TX-114. Probably, both surfactants are able to prevent silver nanoparticles from dissolving by creating a micellar environment, thus resulting in minimal silver ion signals which are preferable in determination of particles with a smaller size. But in this case the problem with transport losses still has to be overcome. The best compromise between maximum particle counting capabilities while maintaining a minimum level of background signal is the use of BDW as a carrier solvent. Under the established protocol the RM AgNPs 40 nm diluted by BDW was measured 3 consecutive times with intermediate washing by 5% HNO_3 . The relative

standard deviation (RSD%) of the number of NPs measured was 7.5%. In order to check the stability of the peaks appearance within the time of a single measurement, the total acquisition time (60 s) was divided into three segments (0-20 s; 20-40 s and 40-60 s) and the relative standard deviation within the mentioned segments was compared.

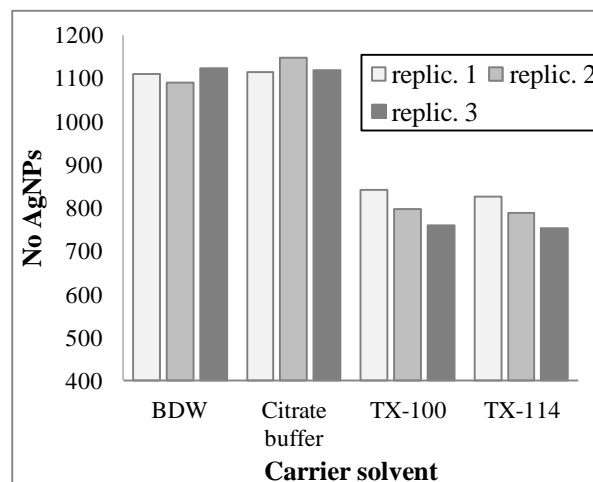


Fig. 2. Effect of the carrier solvent on the number of registered particles in three consecutive replicates upon introduction of RM AgNPs 60nm at a concentration of 125 ng L^{-1}

The results showed that the reproducibility of peaks appearance within the time segments of a single acquisition cycle is much better (RSD in the range of 2.5-4.9%) than that between parallel measurements. An attempt was made to improve the NPs counting repeatability by removing the washing step between parallel replicates. As a result, for 3 consecutive measurements of diluted RM 60 nm with a mass concentration of 250 ng L^{-1} the RSD (of number of peaks counted) was reduced down to 2.6%. Therefore, it is recommended that the washing cycle (to remove the memory effect by 5% HNO_3) be performed only between different samples, then the next measurements to be carried out on prolonged (up to 2-3 min) stabilization time without intermediate washing.

Estimation of nanoparticles mass fraction in dilute Ag NPs suspensions

One of the undisputed advantages of spICP-MS methodology is the possibility of simultaneous observation of signals generated by nanoparticles and ions in the carrier solution, on the basis of which it is possible to assess the distribution of nanoparticulate components between the two phases of the colloid system. The special software package for single particle mode of operation of ICP-MS instruments offers an option together with statistical evaluation of NPs peaks the ionic

concentration of target element to be reported by single point calibration using an ionic standard (usually at a concentration of $1 \mu\text{g L}^{-1}$). As discussed above, good separation of peaks from single nanoparticles is achieved at very low mass concentrations of the colloids (ng L^{-1}). Unfortunately, because of the huge dilution factors in combination with the very short measurement time, in most of the optimization studies it was impossible to estimate the concentration of silver ions. Therefore, we propose a new approach to assessing the distribution of silver between solid and liquid phases from a single measurement. The percent mass fraction of AgNPs was evaluated by the ratio of the summarized signals for all

registered NPs peaks to the total signal measured for the specific replicate. It should be noted that blank subtraction is applied before calculation. The results obtained for both tested RMs of citrate stabilized AgNPs are presented in Table 2.

The possibility to estimate the mass fraction of NPs in reference materials for particles characterization is an important issue, because most of the manufacturers include in the certificate the total mass concentration of the material together with the data about mean diameter with corresponding size uncertainty. This hampers the validation of analytical procedures for determination of particle number concentration.

Table 2. Percent mass fraction of Ag incorporated in NPs in two reference materials (Sigma Aldrich) with different particle diameters

Type of RM Replicate No	AgNPs 40 nm ($75 \mu\text{g L}^{-1}$)			AgNPs 60 nm ($250 \mu\text{g.L}^{-1}$)		
	1	2	3	1	2	3
Sum of NPs peaks (counts)*	91050	96938	103709	274489	265295	256551
Sum of all signals (counts)*	104621	112292	121818	377564	367024	364639
% mass fraction of AgNPs	87.0	86.3	85.1	72.7	72.3	70.4
	Average	SD	RSD %	Average	SD	RSD %
% AgNPs	86.2	1.0	1.1	71.8	1.2	1.7

*The corresponding blank signals are previously subtracted

Table 3. Detected number of particles in two reference materials with different diameters and dilution factors

Type of RM	Total mass concentration RM (ng L^{-1})	Corrected mass concentration (ng L^{-1})*	Detected number of particles		Calculated number of particles**	Recovery %
			Average number (n=3)	RSD %		
Ag NPs 40 nm	50	43	2437	0.7	2762	88
	20	17	1053	2.1	1106	95
Ag NPs 60 nm	250	180	2175	2.6	2597	84
	125	90	1209	2.7	1295	93

* The total mass concentration of RM was corrected taking into account the corresponding mass fractions of AgNPs listed in table 2. ** The specified number of nanoparticles was calculated by the proposed above theoretical model taking into account the transport efficiency of the current measurement.

Determination of Ag nanoparticle number concentration

Under the optimized measurement protocols discussed above the diluted solutions of two RMs for AgNPs with certified size and total mass concentration were subjected to spICP-MS analysis and the data are presented in table 3.

For each test material, two samples with different DFs were measured. The average values of the number of NPs of 3 consecutive measurements, as well as the relative standard deviation in %, are presented. It is clear that the number of identified nanoparticles decreases in

proportion to the mass concentration of silver in the diluted solutions for both RMs.

In order to validate the applicability of the developed spICP-MS method for correct determination of particle number concentration, the experimental results were compared to the calculated ones obtained by the theoretical model. In this calculation the total mass concentration of Ag in the samples was corrected by the % fraction of AgNPs, determined experimentally (see Table 2) also including the transport efficiency of the current measurement. The presented evaluation demonstrates that recoveries $> 84\%$ are obtained in all cases. It is noted that for both materials the

recovery decreases as the number of recorded peaks increases, which can be caused by simultaneous reading of the signals from two NPs. In the investigated range of particle concentrations, this effect is not very pronounced, but confirms our hypothesis that the dilution factor for an individual nanocolloid is essential to the accuracy of the data obtained through the spICP-MS methodology.

The developed spICP-MS method was applied for determination of particle number concentration in AgNPs suspension synthesized in our lab and in two commercial products containing silver nanoparticles according to the manufacturer's declaration ("Silver water"). The RM AgNPs 40 nm was used for estimation of transport efficiency and as a standard for nanoparticles size determination. The instrument response factor and calibration for mass concentration were calculated by measurement of an ionic standard of Ag ($1 \mu\text{g L}^{-1}$). The obtained results for particle number concentration, mass concentration of nanoparticles and Ag ions in samples with corresponding percent mass fraction of silver NPs are summarized in table 4. In both commercial products, the presence of silver nanoparticles with mean size around 30 nm and concentration in the range of $10^8 - 10^9$ NPs per mL was proven. The percent fraction of AgNPs was determined in two of the analysed samples – AgNPs synthesized in our lab and "Silver water" #1. To ensure an optimal peak frequency in the samples containing a low percentage of nanoparticle fraction (5% and 40.2% for the commercial product and for the NPs synthesized in our lab), the dilution factor was reduced in comparison to the one predicted by the theoretical model (the applied dilutions are noted in table 4).

The data from the analysis show significant differences between the tested two commercial products "Silver Water", both in terms of concentration of AgNPs and of the content of silver ions. This indicates that the developed spICP-MS method is suitable for assessing both the total silver content and silver nanoparticles in commercially available products.

The size distribution diagrams for the two tested RM AgNPs (40 nm and 60 nm) and for Silver water #1 are presented on figure 3. The estimated mean sizes, as well as the corresponding size distribution for both reference materials are consistent with the certified values (i.e, $40 \text{ nm} \pm 4 \text{ nm}$, and $60 \text{ nm} \pm 8 \text{ nm}$) which prove the reliability of the spICP-MS for characterization of silver nanoparticles. The mean size of NPs in Silver water #1 was determined to 30 nm with asymmetric size distribution (fig. 3C), while high concentration of ionic silver leads to increasing of steady-state signal shown on the time-resolved graph (fig. 3D) and corresponding rise of the BED diameter (see table 4).

CONCLUSIONS

The proposed model for calculating the dilution factor of samples containing silver nanoparticles allows reliable control of the desired detection rate of single nanoparticles for materials of known diameter and mass concentration. The preliminary information on size and total mass concentration of real samples subjected to the characterization of silver nanoparticles can be provided by successful combination of two spectral methods - UV-vis spectra and preliminary ICP-MS analysis. Optimized protocols for washing and stabilization of nanoparticles in the carrier solutions allow an adequate determination of AgNPs concentration with recoveries between 84 and 95%. The developed spICP-MS method is capable of estimating AgNPs concentration, as well as the distribution of silver between solid and liquid phases in real samples.

Acknowledgements: The current work has been developed as a part of project DN19/9 2018 – 2020 (INISA) financed from the National Science Fund of Bulgaria. D. Georgieva is thankful to the National Program of Ministry of education and science "Young Scientists and Postdoctoral Students" (PMC 577/2018) for financial support.

Table 4. Results from spICP-MS analysis of two commercial products and AgNPs synthesized in our lab.

Sample Name	# of Particles	Particle Conc. (#particles mL ⁻¹)	Mass Conc. (mg L ⁻¹)	Ionic Conc. (mg L ⁻¹)	BED (nm)	Mean Size (nm)	AgNPs (%)
*Silver Water #1	867 ± 49	$2.10^9 \pm 1.10^8$	0.40 ± 0.02	7.6 ± 0.7	36.5 ± 0.9	30.4 ± 0.3	5.0 ± 0.2
*Silver Water #2	153 ± 14	$3.10^8 \pm 3.10^7$	0.12 ± 0.02	< 0.1	10.7 ± 0.4	29±2	-
**AgNPs PU	730 ± 28	$3.10^9 \pm 1.10^8$	1.8 ± 0.2	2.8 ± 0.3	10.9 ± 0.4	23±1	40.2 ± 1.6

*DFs for „Silver water“ samples were 5×10^4 . **DF for AgNPs PU was 1×10^5

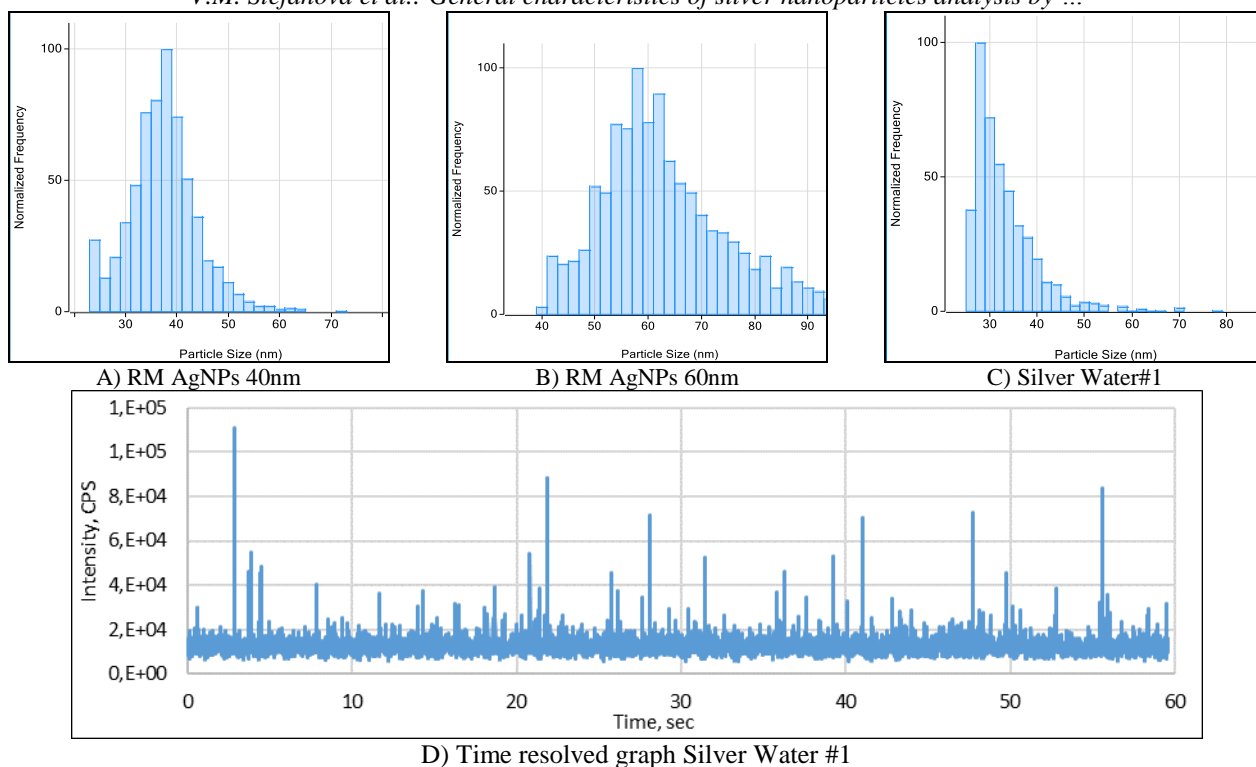


Fig. 3. Size distribution diagram of A) RM AgNPs 40 nm; B) RM AgNPs 60 nm; C) Silver water#1 and D) time-resolved data record for Silver water #1

REFERENCES

- Consumer Products Inventory, [Online], Available: <http://www.nanotechproject.org/cpi/>. [Accessed: 13-Nov-2018].
- M. E. Vance, T. Kuiken, E.P. Vejerano, S.P. McGinnis, M.F. Hochella Jr., D. Rejeski, M.S. Hill, *Beilstein J. Nanotechnology*, **6**, 1769, (2015).
- A. Kaphle, P. N. Navya, A. Umaphathi, H. K. Daima, *Environ. Chem. Lett.*, **1**, (2017).
- M. Bundschuh, J. Filser, S. Lüderwald, M.S. McKee, G. Metreveli, G.E. Schaumann, R. Schulz, S. Wagner, Nanoparticles in the environment: where do we come from, where do we go to?, *Environmental Sciences Europe*, **30**, 1. (2018).
- F. Laborda, E. Bolea, G. Cepriá, M.T. Gómez, M.S. Jiménez, J. Pérez-Arantegui, J.R. Castillo, *Anal. Chim. Acta*, **904**, 10, (2016).
- S. Palchoudhury, M. Baalousha, J. R. Lead, Characterization of nanomaterials in complex environmental and biological media, 8. Elsevier, 2015.
- F. Laborda, E. Bolea, J. Jimenez-Lamana, J. Jiménez-Lamana, *Anal. Chem.*, **86**, 2270, (2014).
- M. D. Montaña, J. W. Olesik, A. G. Barber, K. Challis, J. F. Ranville, *Anal. Bioanal. Chem.*, **408**, 5053 (2016).
- F. Laborda, E. Bolea, J. Jiménez-Lamana, *Trends Environ. Anal. Chem.*, **9**, 15 (2016).
- K. E. Murphy, J. Liu, A. R. M. Bustos, M. E. Johnson, M. R. Winchester, *NIST Spec. Publ. 1200-21*, (2015).
- C. Degueldre P. Y. Favarger, *Colloids Surfaces A Physicochem. Eng. Asp.*, **217**, 137 (2003).
- H. E. Pace, N. J. Rogers, C. Jarolimek, V. A. Coleman, C. P. Higgins, J. F. Ranville, *Anal. Chem.*, **83**, 9361 (2011).
- Y. Yan, K. Bin Chen, H. R. Li, W. Hong, X. Bin Hu, Z. Xu, *Trans. Nonferrous Met. Soc. China (English Edn.)*, **24**, 3732 (2014).
- E. Saion, E. Gharibshahi, K. Naghavi, E. Saion, E. Gharibshahi, K. Naghavi, *Int. J. Mol. Sci.*, **14**, 7880 (2013).
- J. Krajczewski, K. Kołataj, A. Kudelski, *RSC Adv.*, **7**, 17559, (2017).
- SIGMA ALDRICH Product specification N 730793. [Online], Available: https://www.sigmaaldrich.com/Graphics/COFAInfo/SigmaSAPQM/SPEC/73/730793/730793-BULK_ALDRICH.pdf. [Accessed: 13-Nov-2018].

Magnetic assisted solid phase extraction of trace elements by APDC impregnated silica coated manganese-ferrite nanoparticles

D. Georgieva^{1*}, A. Ivancheva¹, Ts. Lazarova², V. Stefanova¹

¹Department of Analytical Chemistry and Computer Chemistry, University of Plovdiv "Paisii Hilendarski"
24 Tzar Assen Str., Plovdiv 4000, Bulgaria

²Institute of General and Inorganic Chemistry, Bulgarian Academy of Sciences,
Acad. G. Bonchev str., Bl 11, Sofia-1113, Bulgaria

Received December 21, 2018; Revised January 14, 2019

Magnetic nanoparticles (MNPs) are widely used as solid phase extraction (SPE) sorbents. In present work the sorption efficiency of manganese-ferrite nanoparticles synthesized by two methods (co-precipitation and solution combustion) were compared. The investigated nanoparticles have a different size distribution i) mono-modal with average size ~13 nm for MNPs synthesized by solution combustion and ii) bi-modal for NPs produced by co-precipitation with sizes 2 nm and 25 nm. These physical parameters presume a difference in surface area which could reflect on effectiveness of SPE.

The application of MNPs for the purpose of elemental analysis often requires improvement of selectivity and stability in an acid media. Two steps modification of magnetic core, which includes: i) covering with silica in order to prevent its dissolution in acidic media and ii) impregnation with complexing agent – ammonium pyrrolidine dithiocarbamate (APDC) for selectivity improvement is proposed.

Modified manganese-ferrite magnetic nanoparticles (MnFe₂O₄@SiO₂-APDC NPs) were tested as a sorbent for solid phase extraction of Co, Cu, Zn, Mo, Cd, Tl, Pb and Bi prior their determination by ICP-MS. The experimental conditions influencing on sorption efficiency of tested elements on the MnFe₂O₄@SiO₂-APDC NPs surface as pH of solution and mass of sorbent were optimized. A selectivity of the extraction system can be improved by variation of the media acidity. For group solid phase extraction of all tested elements, the following compromise conditions were selected: pH = 5; 30 mg NPs; elution with 1 mol L⁻¹ HNO₃ at elevated temperature for 15 minutes.

It has been proven that solid phase extraction of Co, Cu, Zn, Mo, Cd, Tl, Pb and Bi on MnFe₂O₄@SiO₂-APDC NPs is reproducible and applicable for analysis by ICP-MS.

Keywords: magnetic nanoparticles, solid phase extraction, APDC modification

INTRODUCTION

Iron oxides (magnetite and hematite) or mixed ferrites with general formula MFe₂O₄ (where M = Mn, Co, Ni, Zn, etc.) are the most often used magnetic nanoparticles for SPE [1]. Undisputable advantages of these materials for dispersive SPE are their large contact surface, possibility for modification and easy separation of the sorbent by external magnetic field.

Various synthetic methods for preparing nanoparticles of mixed ferrites are described in the scientific literature. Among them the co-precipitation from Mn²⁺/Fe³⁺ aqueous solutions by adding a base under an inert atmosphere at room (or elevated) temperature is one of most often used method, because it is fast and easy for implementation. The size, shape and composition of magnetic nanoparticles depend on the type of salts used, ratio of Mn²⁺/Fe³⁺, temperature, pH and ionic strength of the solution [2]. This method offers high yields, but poor size control, and therefore the

resulting NPs have a relatively broad size distribution.

Another well-known approach to obtaining nanomaterials is a solution combustion synthesis (SCS) [3-5]. It is based on self-sustained redox exothermic reactions between hydrated metal nitrates and fuel(s). Hydrated metal nitrates are typically used as oxidizer precursors, while the fuels represent a broad range of compounds including urea, glycine, citric acid, etc. The combustion reaction usually is initiated by preheating until a self-sustaining exothermic reaction arises, generating heat and releasing combustion gases. This leads to self-ignition, and in the certain parts of system, local temperatures reach from 500 to 3000 °C, depending on the combination of metal salts and fuel [5].

In most cases, a modification of NPs surface is necessary, when they are intended to SPE of elements. The construction of a surface protective layer of NPs is accomplished by using various inorganic components (such as silica or carbon), organic molecules, surfactants or polymers. Silica

* To whom all correspondence should be sent.
E-mail: georgieva@uni-plovdiv.net

coating is most often used because of its acidic stability and thermal resistance [6, 7]. Modifications to improve selectivity are related to incorporation of functional groups on the NPs surface. For this purpose, S and N containing organic substances are preferred because of their ability to form stable complexes with various transition metals such as Cd, Cu, Hg, Pb, Ag, Zn, Cr, etc. [8].

Ammonium pyrrolidine dithiocarbamate (APDC) is a complexing agent, well-known in analytical practice, that acts as bidentate ligand and forms hydrophobic chelate complexes with more than 40 elements [9]. The metal-APDC complexes are stable over a wide pH range (2 ÷ 14), making this reagent suitable for developing variety of separation - concentration methods such as co-precipitation [9, 10] liquid-liquid [11, 12], solid phase [13, 14] or cloud point [15, 16] extraction. The established methods are successfully combined with atomic spectroscopy techniques as: ICP-MS [9], ICP-OES [10], FAAS [12, 14, 15].

Different nano-sized sorbents such as carbon nanotubes [17] and unmodified magnetite and manganese-ferrite nanoparticles [18, 19] are used for sorption of Me-APDC chelates preliminary formed in sample solution. Recently Meng *et al* [20] proposed silica coated magnetite nanoparticles modified with APDC for SPE of Cu and Ni prior their FAAS determination. Despite APDC modification procedure, authors reported insufficient recovery of both analytes, without further addition of ligand to the extraction system.

In present investigation comparative study of two steps modification procedure and extraction abilities of MnFe₂O₄ NPs synthesized by different methods is proposed. An indirect experimental approach was used to evaluate the effectiveness of building a protective layer (MnFe₂O₄@SiO₂) over magnetic core in conducting a modification of magnetic nanoparticles prepared by co-precipitation and solution combustion methods. Protected nanoparticles are impregnated with a second layer of APDC, which facilitates the retention of metal ions by complexing reaction on the surface itself. The resulting MnFe₂O₄@SiO₂-APDC nanoparticles were applied for group solid phase extraction of Co, Cu, Zn, Mo, Cd, Tl, Pb and Bi prior to ICP-MS determination.

EXPERIMENTAL

Instrumentation

Quadruple Inductive Coupled Plasma Mass Spectrometer ICP-MS Agilent 7700 (Tokyo, Japan) with octopole reaction system (ORS) and helium as collision gas was used for SPE optimization and for final studies as well. Thirteen isotopes: ⁵⁹Co, ^{63,65}Cu,

^{66,68}Zn, ⁹⁵Mo, ^{111,114}Cd, ²⁰⁵Tl, ^{206,208}Pb, ²⁰⁹Bi and ¹⁰³Rh (as internal standard) were monitored at 1 point per mass peak with 100 ms integration time with five replicates for each measurement.

ICP-OES - iCAP 6300 Duo Thermo (Thermo Fisher Scientific Inc.) with axial and radial plasma observation, equipped with a CID detector was used for estimation of silica modification efficiency. For this purpose, two emission lines of iron (Fe II 259.940 nm and Fe II 259.837 nm) were monitored.

High Resolution Transmitting Electron Microscope (HR-TEM) JEOL JEM-2010 equipped with an energy dispersion micro-analysis system (EDS) Inca Energy TEM100 Oxford Instruments (Marlow, United Kingdom) working with accelerating voltage 200 kV and resolution up to 0.20 nm was used for size characterization of studied MnFe₂O₄ NPs

Ultrasonic system with a UP 100H ultrasonic processor (Dr. Hielscher GmbH, Teltow, Germany) with a 24 kHz operating frequency and a maximum output of 100 W, equipped with a S7 titanium sonotrode (7 mm diameter, 100 mm long) was used in silica coating of magnetic NPs.

A permanent Fe-Nd-B magnet S-45-30-N (45 mm diameter and 30 mm height) from Supermagnete (Uster, Switzerland) was used to separate the solid phase from the solution during SPE experiments.

Reagents and standard solutions

The precursors used for the synthesis of magnetic nanoparticles by the precipitation method - iron trichloride hexahydrate (FeCl₃·6H₂O), manganese dichloride tetrahydrate (MnCl₂·4H₂O) were purchased from Sigma-Aldrich Company Milwaukee, WI, USA and NaOH p.a (HIMTEKS LTD -Dimitrovgrad). Ammonia solution NH₄OH (25% p.a., d = 0.91 g cm⁻³ RAY-HIM product EOOD) and; HNO₃ (65% p.a., d = 1.40 g cm⁻³ Merck Darmstadt, Germany) were used for pH adjustment. Ammonium pyrrolidine dithiocarbamate (APDC), (Sigma Aldrich); Tetraethoxysilane (TEOS, Sigma-Aldrich) and ethanol (RAY-HIM product EOOD) were used in surface modification of nanoparticles.

A multi-element standard solution ICP: MU28: N; 100 mg L⁻¹ (CPA Chem, Stara Zagora Bulgaria) was used for preparation of model solutions and calibrators, after appropriate dilution. The final concentration of all elements in model solutions for SPE optimization was 10 µg L⁻¹. A standard solution of Rh - 100 mg L⁻¹ (CPA Chem, Stara Zagora Bulgaria) was used in all studies as

internal standard for correction for instrumental drift and non-spectral matrix effect.

The surface water reference material SPS-SW1 - Level 1 (Spectrapure Standards as, Oslo, Norway) was used for validation of SPE procedure

Synthesis and modification of manganese-ferrite nanoparticles

The co-precipitation method was described elsewhere [19]. Briefly, as the precursor solution mixture containing metal ions of Mn^{2+} and Fe^{3+} in a molar ratio of 1: 2 at a total molar concentration of both ions 0.05 mol L^{-1} , was used. To 500 mL of pre-heated (50°C) precursor solution, was added 100 ml of 0.25 mol L^{-1} NaOH. The reaction mixture was heated up to 80°C for 3 hours with continuous homogenization. The resulting nanoparticles were separated by a magnet and washed repeatedly with double distilled water (BDW) until $\text{pH} = 7$ of washed solution was reached, then once with ethyl alcohol. The nanoparticles are stored as slurry in BDW.

The magnetic nanoparticles synthesized by solution combustion method with which the study was conducted were obtained according to the procedure described in [5]. For synthesis, $Mn(NO_3)_2 \cdot 4H_2O$ (Sigma Aldrich), $Fe(NO_3)_3 \cdot 9H_2O$ (Sigma Aldrich) and glycerol as a reducing agent and subsequent thermal treatment at 400°C for 2 hours were used.

Modification of nanoparticles. Modification of $MnFe_2O_4$ nanoparticles with SiO_2

The core-shell type surface modification with the protective SiO_2 layer by was made by the Ströber method, by hydrolysis of TEOS in a basic medium and ultrasonic (US) treatment. To 5 g of manganese-ferrite nanoparticles, 450 ml of ethyl alcohol was added and the suspension is sonicated for ~ 30 min. To the ethanol suspension was added 140 ml of an ammonia solution (1 mol L^{-1}) cooled (for 10 minutes at -18°C), and the US treatment is continued for 15 min. As a next step, 125 ml of a cooled solution of TEOS in ethyl alcohol ($42.2\% \text{ m m}^{-1}$) was added dropwise and US treatment continued for 1 hour. The modified nanoparticles are separated by a magnet and washed with BDW and ethyl alcohol.

Impregnation of silica-coated nanoparticles $MnFe_2O_4@SiO_2@APDC$

Silica-coated nanoparticles were treated twice with 3 ml of 1 mol L^{-1} HNO_3 in boiling water bath for 45 min in order to remove unmodified fraction before modification.

For impregnation ~ 0.1 g of $MnFe_2O_4@SiO_2$ nanoparticles are suspended in 20 ml of BDW, the pH of the solution is adjusted to $\text{pH} = 3$ (by adding 1 mol L^{-1} HNO_3 or NH_4OH) and the suspension is homogenized for 10 min on shredder. Impregnation procedure was performed with 20 ml of APDC solution ($2\% \text{ m/v}$) for 2 hours at continuous stirring. The resulting $MnFe_2O_4@SiO_2@APDC$ nanoparticles are washed twice with BDW.

Procedure of solid phase extraction

The extraction is carried out by adding of 30 mg nanoparticles to 50 ml model solution of the elements and the pH is brought to the desired value. The extraction was carried out by shaking for 30 min. A solid phase is separated by a magnet for 5 minutes. The supernatant solution was then poured out and solid phase was washed with BDW. Elution of elements is performed with 3 ml of 1 mol L^{-1} HNO_3 by heating in a boiling water bath for 15 min. After removing of MNPs (by a magnet), the concentration of the target elements was determined by ICP-MS.

RESULTS AND DISCUSSION

Characterization of magnetic nanoparticles

The shape and size of the obtained nanomaterials is characterized by a transmission electron microscope (TEM) (Fig.1). From the images depicted, it is obvious that nanoparticles with approximately spherical shape were obtained in both synthetic procedures but by the SCS (Figure 1A), the MNPs have a narrower size distribution (mean size 13 nm), whereas in co-precipitation method (Figure 1B) the size distribution is bimodal, with two major fractions with diameters of ~ 2 nm and ~ 20 nm respectively. This implies different behaviour of the materials in both surface modification and their use as sorbents in SPE.

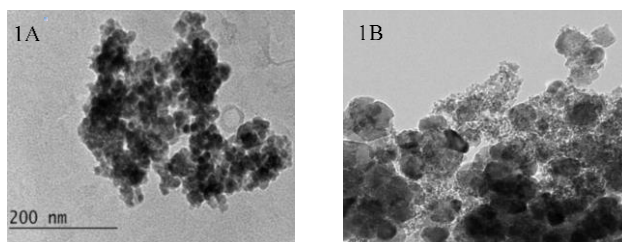


Fig. 1. TEM images of $MnFe_2O_4$ NPs synthesized by SCS (A) and co-precipitation (B)

Determining the efficiency of modification with SiO₂ shell on the magnetic core

The difference in size (surface) of MNPs obtained by both synthetic procedures assumes that a different amount of TEOS will be needed for effective covering of magnetic core with silica layer. The quantity of TEOS was varied at two levels 4.5 g and 9 g per gram MnFe₂O₄ NPs. The efficiency of the core-shell modification was indirectly evaluated by treating the resulting MnFe₂O₄@SiO₂ nanoparticles with nitric acid (1 mol L⁻¹) at elevated temperature for 15 minutes. The concentration of dissolved Fe was determined by ICP-OES and the obtained results are summarized in Table 1.

Table 1. Amount of dissolved Fe (expressed as mg Fe per g of MnFe₂O₄@SiO₂ NPs) at different amounts of TEOS used for silica layer formation

Type of nanoparticles	Quantity TEOS g for modification of 1g MnFe ₂ O ₄	mg Fe dissolved per 1g MnFe ₂ O ₄ @SiO ₂
MnFe ₂ O ₄ @SiO ₂ – co-precipitation	4.5	0.85
MnFe ₂ O ₄ @SiO ₂ – SCS	4.5	9.84
MnFe ₂ O ₄ @SiO ₂ – SCS	9	3.86

As can be seen from the presented results 4.5 g of TEOS are sufficient to form the SiO₂ protective layer on MnFe₂O₄ nanoparticles synthesized by the co-precipitation method. When NPs produced by SCS are modified with the same amount of TEOS, the dissolved Fe is almost 11 times higher, which is an indication for ineffective formation of a protective shell over magnetic core, probably due to a larger surface area. Double amount of TEOS leads to decreasing of the dissolved Fe by a factor of ~3. Unfortunately, this still is higher than results for NPs obtained by co-precipitation, i.e. unprotected fraction remains after the procedure. In order to remove the unmodified MNPs before impregnation, we propose a preliminary treatment of the material synthesized by SCS with 1 mol L⁻¹ HNO₃ at elevated temperature for 45 min. After “washing” step, the residual amount of Fe was decreased to 1.2 mg per 1g of NPs, which is comparable to the one for MNPs obtained by co-precipitation.

The impregnation process with ammonium pyrrolidine dithiocarbamate (APDC)

The acidity of medium greatly impacts the efficiency of MnFe₂O₄@SiO₂ modification with APDC. On the one hand, the surface charge of the siliconized nanoparticles depends on pH – it is a positive at pH <3, zero at pH ~3 and negative at

higher pH of solution. Surface charge determines the possibility of ligand retention on the nanoparticles. On the other hand, the speciation of ligand also directly depends on the pH (pK_a (HPDC) = 3.300 ± 0.002). Preliminary studies on the effect of pH on impregnation efficiency have shown that the best results are obtained in an acid medium (pH ~2-3). Under these conditions, the surface charge of MnFe₂O₄@SiO₂ is ~ 0 or slightly positive, and the ligand presents in a predominant neutral form of pyrrolidine dithiocarbamic acid, which imply its physical adsorption on the MNPs surface.

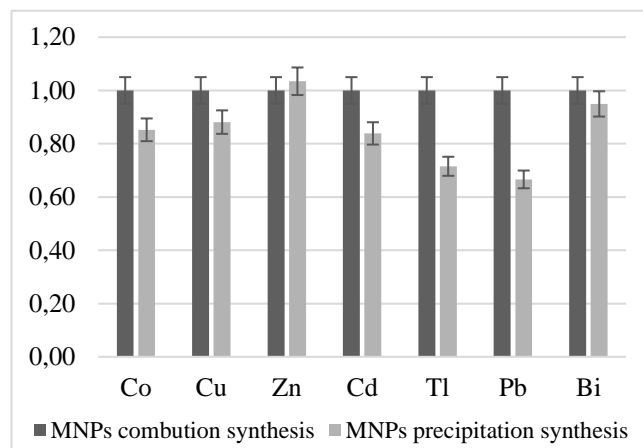


Fig. 2. Comparison of normalized signals for Co, Cu, Zn, Cd, Tl, Pb and Bi after MSPE with MnFe₂O₄@SiO₂-APDC synthesized by both approaches

In the present study, impregnation of MNPs with APDC is carried out at ambient temperature, unlike the conditions suggested by Meng *et al.*, [20] where the authors carry out the process for the same time at 60° C. In our opinion the heating will lead to thermal decomposition of the APDC. The last is also supported by the fact that in order to increase extraction of Cu and Ni, the authors recommend introduction of an additional amount of ligand during SPE.

Optimization of solid phase extraction procedure

The parameters influencing sorption of Co, Cu, Zn, Mo, Cd, Tl, Pb and Bi on the MnFe₂O₄@SiO₂-APDC NPs such as solution acidity and amount of the solid phase were evaluated by extraction degree (E%), based on ICP-MS determination of residual elements concentrations in aqueous phase after performing the SPE.

Comparison of the sorption properties of both types modified MNPs for group extraction of 7 elements from model solutions (10 µg L⁻¹) is presented on figure 2. The measured signals for tested elements in solution after extraction were normalized and used for estimation of sorption efficiency.

For all tested elements, except Zn and Bi, higher sorption efficiency was achieved using $MnFe_2O_4$ MNPs produced by the solution combustion method. The observed effect is probably due to the smaller size of these nanoparticles, which reflects on a larger sorption surface. Therefore, all subsequent studies were conducted with these nanoparticles.

The acidity of aqueous phase affects the stability of the metal-ligand complex formation. The extraction efficiency was studied in pH range of 3-8 (Fig.3). In a strongly acidic environment, the ligand may decompose to thiourea, whereas at $pH > 9$, it may be expected that the hydroxide-forming reactions of the target elements will compete.

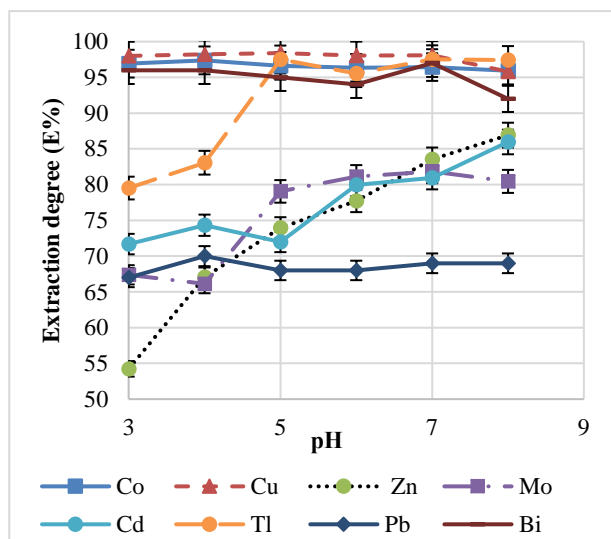


Fig. 3. Influence of the acidity of the aqueous phase on extraction
 Conditions: 30 mg sorbent, $C_A = 10 \mu g L^{-1}$; $V_A = 50 mL$; $t_{extr} = 30 min$

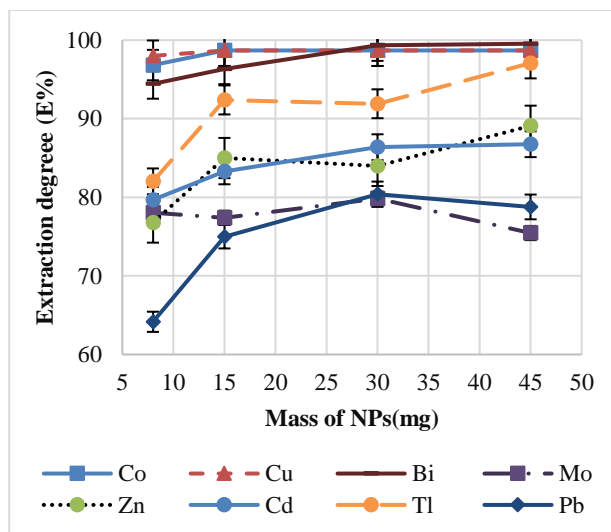


Fig. 4. Influence of the MNPs amount on extraction efficiency. Conditions: $pH=5$, $C_A = 10 \mu g L^{-1}$; $V_A = 50 mL$; $t_{extr} = 30 min$

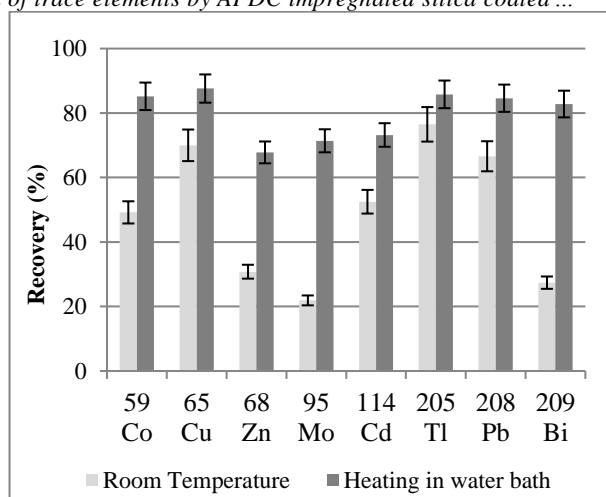


Fig. 5. Influence of the temperature on recoveries of tested elements using $1 mol L^{-1}$ nitric acid as eluent

Three groups of elements could be distinguished according to their behavior at variation of pH. Three elements (i.e., Co, Cu, Bi) are extracted completely ($E > 95\%$) regardless of the pH. Lead may also be added to this group, the extraction of which is also constant to the pH range tested, but does not exceed 70%. For Tl and Mo the extraction degree increases until $pH = 5$, then remains constant. The third group includes Zn and Cd and shows an increase in extraction efficiency across the whole range examined; hence for them is more beneficial to conduct extraction in basic medium. The commented above indicates that selectivity of sorbent could be improved by performing extraction at different pH but for the purpose of group solid phase extraction of all tested elements, $pH = 5$ was chosen as a compromise acidity for further experiments.

Optimization of the quantity of sorbent $MnFe_2O_4@SiO_2@APDC$

The amount of nanoparticles used for SPE determined the contact surface between phases, as well as the amount of ligand introduced into the system. The influence of quantity of sorbent on solid phase extraction efficiency is studied varying the amount of NPs in the range of 8 mg to 45 mg (Figure 4).

Efficient extraction with $E\% \geq 95\%$ for Co, Cu and Bi and 78% for Mo could be achieved using only 8 mg modified NPs. For Tl, Cd, Zn and Pb, a raise in the extraction degree (by 8-14%) with a sorbent mass increase up to 30 mg was observed. For a group extraction 30 mg $MnFe_2O_4@SiO_2-APDC$ was chosen as optimum.

Desorption studies

The process of desorption of the analytes with a suitable solvent is estimated by their recovery (R%). In this case, a concentration of the elements in final

solution, after performing of SPE and elution was measured.

In most of published investigations using APDC as complexing agent for SPE extraction, as best eluent an organic solvent (i.e acetonitrile [20]) or combination of acid and organic solvent i.e nitric acid and acetone [21] are proposed. In our case the organic eluents are inappropriate, considering the stability of inductively coupled plasma used for final measurement (namely ICP-MS). For this reason, dilute nitric acid with a volume of 3 ml and a concentration of 1 mol L⁻¹ was used to dissolve the APDC complexes of tested elements. The influence of temperature on the desorption process was studied, and the results from comparison of elution at room temperature for 30 minutes at continuous stirring and heating in boiling water bath for 15 minutes are presented on figure 5.

For all tested elements recovery is increased if the elution was performed at elevated temperature. The most affected by the elution temperature are results for Co, Zn, Mo and Bi. In order to achieve higher recovery and shorten the overall time for solid phase extraction, it was chosen to carry out desorption of the analytes by heating in boiling water bath for 15 minutes. Recoveries in the range of 68% (Zn) and 88% (Cu) were achieved for all studied elements.

Analytical characteristics of the developed (MnFe₂O₄@SiO₂-APDC)-ICP-MS method

The analytical characteristics of the combined (MnFe₂O₄@SiO₂-APDC) - ICP-MS method were evaluated by analysis of the tested elements in calibration solutions passed through SPE on modified nanoparticles under optimized conditions (SPEcalib). The concentration of elements varied in the range of 5 to 20 µg L⁻¹ at three levels (5, 10 and 20 µg L⁻¹). The obtained coefficients of the calibration equations with their statistical evaluations as well as the achieved method limits of detection are presented in Table 2. The enrichment factors (EF) are calculated as the ratio of slopes for two calibration curves – the ones obtained when standard solutions were subjected to the SPE procedure (SPE calib) and when standards were prepared by spiking of aliquots in the 1 mol L⁻¹ nitric acid. Considering the concentration factor, calculated as the ratio of volumes of sample and eluent, is 16.6 the obtained EF confirmed that the optimized SPE procedure provides sustainable recoveries in studied concentration range. By using SPE calib as a calibration approach the losses due to the incomplete recoveries commented above can be adequately corrected.

During the ICP-MS measurement it was observed that signals measured in the final solution after

extraction revealed a non-spectral matrix effect expressed in ~ 5 ÷ 10% suppression compared to the corresponding solutions prepared directly in dilute nitric acid (1 mol L⁻¹). The suppression obtained here is lower in comparison to the one reported in a previous work, where unmodified NPs were used for extraction of Me-APDC complexes, preliminary formed in solution (matrix suppression ~30%) [18]. The alleviation of matrix effect is due to a protective silica layer, which prevents the dissolution of magnetic core (containing Fe and Mn) during elution. For correction of the commented matrix impact as well as instrumental drift, only one internal standard (Rh) was added to the eluting acid.

The obtained high correlation coefficients (> 0.99 for all tested elements except for Zn and Mo), presented in table 2, proved that SPE of tested elements on APDC-impregnated silica modified magnetic nanoparticles is reproducible and applicable in studied concentration range. The intercept values of the regression equations for Co, Cu, and Pb are statistically distinguishable from zero because of the signals registered in blank sample, due to the presence of these elements in the precursor salts used for nanoparticle synthesis.

For validation of the combined (MnFe₂O₄@SiO₂-APDC)-SPE-ICP-MS method a surface water reference material SPS-SW1 was analysed with both MNPs used as a solid phase. The extraction was performed under optimized conditions and SPE-calib approach was used for calibration and Rh as IS. The obtained results with corresponding uncertainties and certified values are presented on table 3.

The measured concentrations for Co, Cu, Cd, Tl and Pb are in good agreement with the certified values for both studied sorbents, which proves proved the reliability of the proposed magnetic NPs-SPE-ICP-MS procedure.

CONCLUSIONS

The modified MnFe₂O₄@SiO₂-APDC nanoparticles are promising sorbent for SPE of trace elements. Core – shell modification with silica prevents the magnetic core from dissolution in acidic medium, which reduces non-spectral matrix effect in ICP-MS analysis.

A higher amount of silica reagent is necessary for modification in case of MNPs synthesized by SCS and preliminary treatment with nitric acid for eliminating unmodified fraction before impregnation is recommended. By proposed procedure for impregnation with APDC a successful extraction of Co, Cu, Zn, Cd, Tl, Pb and Bi could be performed without necessity of additional introduction of ligand during extraction.

Table 2. Analytical characteristics achieved with (MnFe₂O₄@SiO₂-APDC)-SPE-ICP-MS

Isotope	slope IS ratio x L x μg ⁻¹	±SD IS ratio x L x μg ⁻¹	Intercept IS ratio	±SD IS ratio	Correlation coefficient	Enrichment factor (EF)	MLOD* μg L ⁻¹
⁵⁹ Co	3.5	± 0.1	7.9	± 1.5	0.999	14.2	0.05
⁶⁵ Cu	1.04	± 0.01	6.9	± 0.1	1.000	14.6	0.18
⁶⁸ Zn	0.42	± 0.07	2.3	± 0.9	0.985	11.2	0.30
⁹⁵ Mo	0.18	± 0.03	3.0	± 0.3	0.972	11.9	0.35
¹¹⁴ Cd	1.42	± 0.07	-0.8	± 0.8	0.998	12.2	0.01
²⁰⁵ Tl	9.0	± 0.2	2.4	±2.7	0.999	14.3	0.01
²⁰⁸ Pb	3.4	± 0.3	57	± 3	0.995	14.1	0.67
²⁰⁹ Bi	5.9	± 0.2	-0.3	± 2.8	0.998	13.8	0.02

*MLOD is calculated according to 3σ criteria using standard deviation of 5 independent measurements of blank and regression parameters obtained by SPE calib

Table 3. Results from (MnFe₂O₄@SiO₂-APDC)-SPE-ICP-MS analysis of surface water reference material SPS-SW1 with both modified MNPs

Element	Reference material SPS_SW 1 Measured concentration		Certified value μg L ⁻¹ ±U
	MnFe ₂ O ₄ @SiO ₂ -APDC (co-precipitation)	MnFe ₂ O ₄ @SiO ₂ -APDC (solution combustion)	
	μg L ⁻¹ ±U	μg L ⁻¹ ±U	
Co	1.84 ±0.18	2.0 ±0.2	2 ±0.02
Cu	21.2 ±1.7	18.5 ±1.6	20 ±1
Cd	0.52 ±0.09	0.46 ±0.06	0.5 ±0.01
Tl	0.47 ±0.02	0.47 ±0.02	0.5 ±0.01
Pb	4.79 ±0.16	4.79 ±0.15	5 ±0.1

The elution at elevated temperatures improves obtained recoveries for all tested elements. The combined MnFe₂O₄ NPs-SPE-ICP-MS method proved to be effective for group determination of trace elements in water using SPE-calib approach and Rh as internal standards.

Acknowledgements: D. Georgieva is thankful to a National Program of Ministry of education and science "Young Scientists and Postdoctoral Students" (PMC 577/2018) for financial support.

REFERENCES

- M. Wierucka, M. Bizziuk, *TrAC - Trends Anal. Chem.*, **59**, 50, (2014).
- A.-H. H. Lu, E. L. L. Salabas, F. Schüth, *Angew. Chemie Int. Ed.*, **46**, 1222, (2007).
- A. S. Mukasyan, P. Epstein, P. Dinka, *Proc. Combust. Inst.*, **31** II, 1789, (2007).
- A. Varma, A. S. Mukasyan, A. S. Rogachev, K. V. Manukyan, *Chem. Rev.*, **116**, 14493, (2016).
- T. Lazarova, D. Kovacheva, G. Tyuliev, *Bulg. Chem. Commun.*, **49**, no. G, 217, (2017).
- L. Chen, T. Wang, J. Tong, *TrAC - Trends Anal. Chem.*, **30**, 1095, (2011).
- L. Xie, R. Jiang, F. Zhu, H. Liu, and G. Ouyang, *Anal. Bioanal. Chem.*, **406**, 377, (2014).
- M. H. Mashhadizadeh, Z. Karami, *J. Hazard. Mater.*, **190**, 1023 (2011).
- Y. Sun and M. Sun, *Anal. Lett.*, **40**, 2391, (2007).
- D. M. M. Hopkins, *J. Geochem. Explor.*, **41**, 349 (1991).
- M. Satyanarayanan et al., *Indian J. Mar. Sci.*, **36**, 71, (2007).
- R. R. Brooks, B. J. Presley, I. R. Kaplan, *Talanta*, **14**, 809, (1967).
- V. Camel, *Spectrochim. Acta Part B*, **58**, 1177, (2003).
- T. Aydemir, S. Güçer, *Anal. Lett.*, **29**, 351, (1996).
- Z. Li, J. Chen, M. Liu, Y. Yang, *Anal. Methods*, **6**, 3241, (2014).
- D. L. Giokas, E. K. Paleologos, S. M. Tzouwara-Karayanni, M. I. Karayannis, *J. Anal. Atom. Spectrom.*, **16**, 521, (2001).
- M. Tuzen and M. Soylak, *J. Hazard. Mater.*, **147**, 219, (2007).
- V. Stefanova, D. Georgieva, V. Kmetov, I. Roman, A. Canals, *J. Anal. At. Spectrom.*, **27**, 1743, (2012).
- D. Georgieva, V. Stefanova, V. Kmetov, I. Roman, N. Kovachev, A. Canals, *Univ. Plovdiv „Paisii Hilendarski“ -Bulg. Sci. Pap.*, **38**, 7 (2011).
- D. Meng, S. Ju, Q. Hu, and X. Li, *Int. J. Environ. Anal. Chem.*, **95**, 1435, (2015).
- M. Tuzen, K. O. Saygi, M. Soylak, *J. Hazard. Mater.*, **152**, 632, (2008).

Amino acids in edible wild mushroom from the Batak mountain, Bulgaria

L. Dospatliev^{1*}, V. Lozanov², M. Ivanova³, P. Papazov⁴, P. Sugareva²

¹Department of Pharmacology, Animal Physiology and Physiological Chemistry,
Trakia University, 6000 Stara Zagora, Bulgaria

²Department of Chemistry and Biochemistry, Medical University Sofia, 2 Zdrave Str., 1431 Sofia, Bulgaria

³Department of Informatics and Mathematics, Trakia University, 6000 Stara Zagora, Bulgaria

⁴Department of Organic Chemistry and Inorganic Chemistry, University of Food Technology - Plovdiv,
4000 Plovdiv, Bulgaria

Received October 23, 2018; Revised December 30, 2018

The samples were collected from the Batak mountain, Bulgaria. Three popular wild edible mushroom species *Boletus pinophilus*, *Cantharellus cibarius* and *Craterellus cornucopioides* were analyzed for their free amino acid compositions by Q Exactive mass analyzer equipped with TurboFlow LC system and IonMax II electrospray ionization module (ThermoScientific Co, USA). Data acquisition and processing were carried out with XCalibur 4.2 software package. Twenty free amino acids: histidine, arginine, asparagine, glutamine, serine, aspartic acid, glutamic acid, threonine, glycine, proline, tyrosine, valine, methionine, leucine/isoleucine, phenylalanine, ornithine dihydrochloride, tryptophane, lysine, 4-hydroxyproline and γ -amino butyric acid, were determined. The total free amino acid (TAA) contents were from 26.46 mg kg⁻¹ in *Cantharellus cibarius* to 44.18 mg kg⁻¹ in *Boletus pinophilus*. The ratio of EAA to TAA were from 0.04 mg kg⁻¹ in *Cantharellus cibarius* to 0.14 mg kg⁻¹ in *Craterellus cornucopioides*. Glutamine, arginine, ornithine, and serine were among the most abundant amino acids present in all species. The results showed that the analyzed mushrooms contained a significant amount of free amino acids which may be important compounds contributing to the typical mushroom taste, nutritional value, and potent antioxidant properties of these wild edible mushrooms. Furthermore, the principal component analysis (PCA) showed that the accumulative variance contribution rate of the first two principal components reached 90.57%.

Keywords: Amino acid composition, Wild edible mushroom, LC/MS/MS analysis

INTRODUCTION

Mushrooms have long been favored as highly tasty, nutritive, and health-promoting foods [1–5]. While preferred to cultivated fungi, wild growing mushrooms are collected and consumed as a delicacy worldwide for their specific aroma and texture [6,7]. They are also an attractive source of food flavoring materials in soups and sauces due to their umami or palatable taste [8–10]. Moreover, a vast body of evidence indicates that wild edible mushrooms contain many biologically active compounds disclosing antioxidant, antibacterial, hepatoprotective, antiradical, antihyperglycemic, antiangiogenic, and even anti-inflammatory, antitumor, antiallergic, antiatherogenic, and hematological properties [11–15].

Amino acid composition is a reliable indicator of the nutritional value of food. Free amino acids are the main constituents of functionally essential compounds that are found in mushrooms. The most typical mushroom taste can be given by the nonvolatile compounds, such as free amino acids and soluble sugars [16–18]. No literature data on wild edible mushrooms in Bulgaria have been

reported, nor data on free amino acid compositions. Therefore, the aim of this study was to determine the free amino acid compositions of the species *Boletus pinophilus*, *Cantharellus cibarius* and *Craterellus cornucopioides* from the Batak mountain.

EXPERIMENTAL

Mushroom samples

The Batak mountain is located in the western Rhodopes. Its western border is defined by the Chepinska river, the southern border – by Dospatska river and Dospat dam, the eastern border – by Vacha river and the northern border – by the Thracian Plane (GPS41°46'02.6"N 24°08'48.4"E) (Fig. 1). The region is industry-free and is characterised with forests, land and low buildings. Mushroom samples from the species *Boletus pinophilus*, *Cantharellus cibarius* and *Craterellus cornucopioides* were collected in 2014 and 2018 from the Batak mountain by the authors themselves. Mushroom samples were washed with distilled water and dried at 65°C in a fan oven to constant weight.

* To whom all correspondence should be sent.

E-mail lkd@abv.bg:

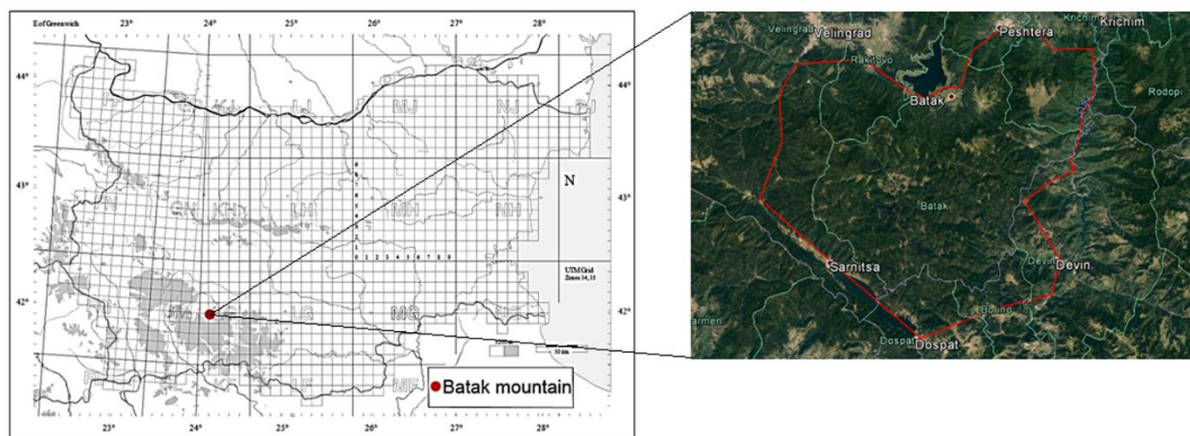


Fig. 1. Location of the sampling sites.

The dried samples were ground, then homogenized and stored in polyethylene bottles until analysis.

Reagents

All chemicals were at least of analytical-reagent grade. Water was de-ionized in a Milli-Q system (Millipore, Bedford, MA, USA) to a resistivity of 18.2 MΩ cm. All plastic and glassware were cleaned by soaking in dilute HNO₃ (1/9, v/v) and were rinsed with distilled water prior to use.

Determination of free amino acid composition

Instrumentation

Analyses were carried out on Q Exactive[®] mass analyzer equipped with TurboFlow[®] LC system and IonMax II[®] electrospray ionization module (ThermoScientific Co, USA). Data acquisition and processing were carried out with XCalibur[®] 4.2 software package.

Chromatographic conditions

Column: Synchronis C18, 1.7 μm (50 × 2.1 mm) (ThermoScientific Co, USA); Mobile phase: A= 0.1 % formic acid in water; B= 0.1 % formic acid in acetonitrile; Flow rate: 300 μL min⁻¹; Gradient: 10 % B for 1 min; 10 - 90% B for 6 min; 90 % B for 2 min; 90 – 10 % B for 1 min and 10% B for 3 min. Injection volume: 10.0 μL.

Mass spectrometric conditions

Full-scan spectra over the m/z range 200-2000 were acquired in positive ion mode at resolution settings of 70 000. All MS parameters were optimized for sensitivity to the target analytes using the instrument control software program. Q Exactive parameters were - spray voltage 4.0 kV, sheath gas flow rate 32, auxiliary gas flow rate 10, spare gas flow rate 3, capillary temperature 280 °C, probe heater temperature 300 °C and S-lens RF level 50. Parallel reaction monitoring (PRM) mode was used for quantitation of the amino acids, biogenic amines and polyamines. The selected ions

used in PMT for quantitative analyses are presented in the table below. Data acquisition and processing were carried out with Xcalibur 2.4[®] software package (ThermoScientific Co, USA). The calibration curves for each of the analyzed compounds were constructed using external standards in the range 0.1 – 1000 ng mL⁻¹.

Table 1. Detected ions and their most abundant MS2 fragments of amino acids in positive ionization mode.

No	Compound	[M+H] ⁺	MS/MS ion used for quantitation
1	Histidine	439.1431	110.0719
2	Arginine	458.1853	185.0927
3	Asparagine	416.1269	202.0717
4	Glutamine	430.1427	355.1090
5	Serine	389.1159	130.0504
6	Aspartic acid	417.1109	186.0402
7	Glutamic acid	431.1268	218.0666
8	Threonine	403.1317	121.1017
9	Glycine	559.1050	146.0449
10	Proline	399.1367	186.0765
11	Tyrosine	465.1476	206.0819
12	Valine	401.1523	188.0920
13	Methionine	433.1246	133.0322
14	Leucine/Isoleucine	415.1679	156.1023
15	Phenylalanine	449.1524	190.0868
16	Orn dihydrochloride	699.2285	442.1425
17	Tryptophane	488.1633	188.0711
18	Lysine	713.2444	243.0981
19	4-Hydroxyproline	415.1316	351.1149
20	γ-Amino butyric acid	387.1365	174.0766

Statistical analysis

All analyses were carried out in triplicate and the data were reported as means ± standard deviation (SD). Statistical analysis and all chartings

were performed within the R program version 3.4.4 (2018-03-15). The results were analyzed through one-way analysis of variance (ANOVA) followed by Duncan's test with $p < 0.05$. Particular effects between mushroom species and their amino acids were examined using a principal component analysis.

RESULTS AND DISCUSSION

The three wild edible mushroom species studied in this paper, such as *Boletus pinophilus*, *Cantharellus cibarius* and *Craterellus cornucopioides*, are considered the most delicious mushrooms by indigenous peoples for soup or fried with excess oil and salt for long-term consumption. These mushroom species are difficult for storage and transportation due to their crisp and tender texture. Therefore, they are commercially popular for the local markets. On the other hand, they are very important economic species for domestic and foreign trade.

As shown in Table 2 in almost all of the species it was possible to determine 20 free amino acids:

histidine, arginine, asparagine, glutamine, serine, aspartic acid, glutamic acid, threonine, glycine, proline, tyrosine, valine, methionine, leucine/isoleucine, phenylalanine, ornithine dihydrochloride, tryptophan, lysine, 4-hydroxyproline and γ -amino butyric acid.

Of the 20 specified amino acids in the three types of mushrooms with the highest content is glutamine (from 11.91 mg kg⁻¹ in *Craterellus cornucopioides* to 21.54 mg kg⁻¹ in *Boletus pinophilus*), followed by arginine (from 4.06 mg kg⁻¹ in *Cantharellus cibarius* to 4.45 mg kg⁻¹ in *Boletus pinophilus*), ornithine (from 1.30 mg kg⁻¹ in *Cantharellus cibarius* to 3.25 mg kg⁻¹ in *Craterellus cornucopioides*) and serine (from 0.81 mg kg⁻¹ in *Cantharellus cibarius* to 2.89 mg kg⁻¹ in *Boletus pinophilus*).

The total free amino acid (TAA) contents in the analyzed samples ranged from 26.46 mg kg⁻¹ in *Cantharellus cibarius* to 44.18 mg kg⁻¹ in *Boletus pinophilus* (Table 2).

Table 2. Amino acid content in mushroom species per dry weight (DW), (mg kg⁻¹ DW).

Amino acid	Abbreviation	<i>Boletus pinophilus</i>	<i>Cantharellus cibarius</i>	<i>Craterellus cornucopioides</i>
Histidine*	His*	0.69 ± 0.14 ^{ghijk}	0.13 ± 0.04 ^f	0.73 ± 0.12 ^{efg}
Arginine	Arg	4.45 ± 0.35 ^b	4.06 ± 0.33 ^b	4.10 ± 0.34 ^b
Asparagine	Asn	1.38 ± 0.12 ^{efg}	0.26 ± 0.08 ^{ef}	0.76 ± 0.28 ^{efg}
Glutamine	Gln	21.54 ± 1.34 ^a	15.90 ± 1.28 ^a	11.94 ± 1.46 ^a
Serine	Ser	2.89 ± 0.24 ^c	0.81 ± 0.16 ^{de}	1.15 ± 0.21 ^{de}
Aspartic acid	Asp	1.08 ± 0.09 ^{fghij}	0.58 ± 0.16 ^{ef}	0.73 ± 0.16 ^{efg}
Glutamic acid	Glu	1.14 ± 0.26 ^{fghi}	1.88 ± 0.25 ^c	2.77 ± 0.29 ^c
Threonine*	Thr*	1.00 ± 0.35 ^{fghij}	0.18 ± 0.06 ^f	0.41 ± 0.08 ^{fg}
Glycine	Gly	1.18 ± 0.12 ^{fgh}	0.38 ± 0.08 ^{ef}	0.26 ± 0.09 ^{fg}
Proline	Pro	0.79 ± 0.13 ^{fghijk}	0.17 ± 0.04 ^f	0.35 ± 0.08 ^{fg}
Tyrosine	Tyr	0.45 ± 0.12 ^{ijk}	0.06 ± 0.02 ^f	0.74 ± 0.06 ^{efg}
Valine*	Val	0.48 ± 0.17 ^{hijk}	0.12 ± 0.02 ^f	0.10 ± 0.04 ^g
Methionine*	Met*	0.17 ± 0.04 ^k	n.d	n.d.
Leucine/Isoleucine*	Leu/Ile*	0.43 ± 0.14 ^{ijk}	0.10 ± 0.01 ^f	0.12 ± 0.04 ^g
Phenylalanine*	Phe*	0.41 ± 0.12 ^{jk}	0.06 ± 0.01 ^f	0.21 ± 0.07 ^g
Ornithine	Orn	2.33 ± 0.26 ^{cd}	1.30 ± 0.17 ^{cd}	3.25 ± 0.21 ^c
Tryptophan*	Trp*	0.37 ± 0.11 ^{jk}	n.d	0.99 ± 0.12 ^{def}
Lysine*	Lys	1.42 ± 0.29 ^{ef}	0.40 ± 0.05 ^{ef}	1.64 ± 0.12 ^d
4-Hydroxyproline	4-HYP	n.d	n.d	n.d.
γ -Amino butyric acid	GABA	1.97 ± 0.32 ^{de}	0.08 ± 0.01 ^f	0.18 ± 0.06 ^g
Total Amino acids		44.18	26.46	30.40
Essential amino acids		4.98	0.99	4.18
Ratios (EAA /TAA)		0.11	0.04	0.14

Each value is expressed as mean ± SD (n = 3). Means with different letters within a column are significantly different ($p < 0.05$). TAA, total amino acid; EAA*, essential amino acids, were calculated as the total content of Val, Leu/ Ile, His, Lys, Thr, Met, Phe and Trp.

n.d – not detected

The average total free amino acid concentration of the 3 species was 33.68 mg kg⁻¹. As far as we know, this is the first work in Bulgaria revealing the presence of 20 essential and nonessential free

amino acids in the referred wild edible mushroom species, which is very important considering their nutritional value, typical mushroom taste, and biological properties. Ribeiro *et al.* [19] reported that the total free amino acid contents in 11 wild

edible mushrooms from northeastern Portugal ranged from 153.09 mg 100 g⁻¹ in *F. hepatica* to 2267.32 mg 100 g⁻¹ in *B. edulis*, whereas, data from the literature showed ca. 897 mg 100 g⁻¹ of total free amino acids in *B. edulis* [20]. Kivrak *et al.* [21] determined free amino acid contents in *Calvatia gigantean* as ca. 199.6 mg 100 g⁻¹. It could be noted that up to 16.843 mg 100 g⁻¹ of total free amino acids were determined in five cultivated edible mushrooms, and the average content was 12.079 mg 100 g⁻¹ [16]. León-Guzmán *et al.* [22] reported that the total free amino acid range of four wild edible mushrooms from Querétaro, México was ca. 2317–4741 mg 100 g⁻¹. Concerning the species described above, the differences between the results in this study and those in published reports are assumed to be caused by the diversity of extraction, derivatization, or quantification methods used in the different studies. Nevertheless, these studies suggested that the free amino acid contents in mushrooms were considerably divergent between species, as demonstrated in our work. In addition, the different geographical origin, growth conditions, and harvesting times of the analyzed species cannot be excluded [9, 18, 23-28]. The ratios of the essential amino acids to nonessential amino acids were 0.11, 0.04 and 0.14 in *Boletus pinophilus*, *Cantharellus cibarius* and *Craterellus*

cornucopioides, respectively. This result meets well the reference values of 0.6 recommended by FAO/WHO [29].

Principal component analysis (PCA), also known as Karhunen-Loève (KL) transformation [30], is a mathematical procedure that transforms a number of (possibly) correlated variables into a (smaller) number of uncorrelated variables called principal components. The first principal component accounts for as much of the variability in the data as possible, and each succeeding component accounts for as much of the remaining variability as possible. Here, PCA was used to demonstrate similarities and differences in the accumulation of 20 amino acids in 3 species of wild edible mushrooms. From Table 3 we may notice that the accumulative variance contribution rate of the first two principal components (from nine principal components) was 90.57% [31], which reflected most of the information regarding the free amino acid compositional variability in the three wild edible mushrooms. The first principal component (PC1) explained 62.92% of the variation. The second principal component (PC2) contributed 27.65% of the total variation and positively loaded on Trp, Orn and Tyr, showing -0.432, -0.415 and -0.408 of the loading values, respectively.

Table 3. Factor loadings after normalized rotation.

Species	PC1	PC2	PC3	PC4	PC5	PC6	PC7	PC8	PC9
His	-0.185	-0.307	0.191	-0.262	0.263	-0.288	0.451	0.394	0.109
Arg	-0.193	0.002	-0.536	-0.658	0.228	0.170	-0.354	0.041	0.024
Asn	-0.280	-0.098	0.007	-0.008	-0.226	0.418	0.150	0.233	-0.123
Gln	-0.230	0.245	-0.185	0.026	-0.355	0.046	0.081	0.001	-0.621
Ser	-0.281	0.051	0.189	-0.112	-0.015	-0.099	-0.016	-0.148	0.085
Asp	-0.275	-0.038	-0.168	-0.203	-0.419	-0.441	0.119	-0.246	0.239
Glu	0.167	-0.330	-0.250	-0.125	-0.385	-0.066	0.260	-0.004	0.057
Thr	-0.246	0.017	0.502	-0.193	-0.315	0.390	-0.288	0.053	0.311
Gly	-0.263	0.163	0.158	-0.113	-0.104	-0.092	0.037	0.162	-0.071
Pro	-0.284	-0.017	-0.034	-0.010	0.424	0.067	0.289	-0.274	-0.205
Tyr	-0.097	-0.408	0.016	0.122	0.033	-0.010	-0.331	0.162	-0.180
Val	-0.262	0.080	-0.265	0.314	-0.053	-0.064	0.099	-0.016	0.286
Met	-0.263	0.126	0.290	-0.093	0.183	-0.173	-0.006	-0.035	-0.266
Leu/Ile	-0.266	0.061	-0.220	0.358	0.087	-0.253	-0.307	0.492	0.131
Phe	-0.271	-0.096	-0.173	0.241	0.029	0.453	0.313	0.092	0.160
Orn	-0.084	-0.415	0.064	0.075	-0.162	-0.159	-0.134	-0.044	-0.355
Trp	-0.034	-0.432	0.026	0.008	0.069	0.230	-0.009	-0.266	0.059
Lys	-0.165	-0.353	-0.012	0.164	0.056	-0.106	-0.233	-0.184	-0.017
GABA	-0.280	0.084	-0.010	0.193	0.088	-0.032	-0.095	-0.467	0.134
Eigenvalues	11.96	5.25	0.92	0.64	0.16	0.04	0.02	0.005	0.00
Variance	62.92%	27.65%	4.85%	3.38%	0.85%	0.20%	0.12	0.03%	0.00
Cumulative	62.92%	90.57%	95.42%	98.80%	99.65%	99.85%	99.97%	100.00%	100.00%

The percentages of variance explained by remainder seventh PCs were 4.85%, 3.38%, 0.85%, 0.20%, 0.12%, 0.03 and 0.06e-31%, respectively. The components with the greatest load were Arg (-0.658) in PC4 and Gln (-0.621) in PC9, respectively.

CONCLUSIONS

The edible mushrooms were found to be a good source of essential amino acids. It is also interesting to note that the majority of the wild mushrooms are consistently more nutritious than their cultivated relatives.

In general, wild edible mushrooms of Bulgaria could be a good source of essential nutrients to supplement the diet of the local people. Therefore, collected edible mushroom species are recommended in diets because of their low content of fat and energy and also can be consumed without any health risk.

REFERENCES

1. M. Friedman, *J. Agric. Food Chem.*, **63**, 7108 (2015).
2. S. Grosshauser, P. Schieberle, *J. Agric. Food Chem.*, **61**, 3804 (2013).
3. L. Wang, Z. Q. Ma, F. Du, H. X. Wang, T. B. Ng, *J. Agric. Food Chem.*, **62**, 7822 (2014).
4. L. Dospatliev, M. Ivanova, *C. R. Acad. Bulg. Sci.*, **70**, 795 (2017).
5. H. Manninen, M. Rotola-Pukkila, H. Aisala, A. Hopia, T. Laaksonen, *Food Chem.*, **247**, 23 (2018).
6. P. Kalač, *Food Chem.*, **113**, 9 (2009).
7. L. Dospatliev, *C. R. Acad. Bulg. Sci.*, **71**, 1458 (2018).
8. N. Rotzoll, A. Dunkel, T. Hofmann, *J. Agric. Food Chem.*, **54**, 2705 (2006).
9. L. Sun, Q. Liu, C. Bao, J. Fan, *Molecules*, **22**(3), 350 (2017).
10. L. Dospatliev, M. Ivanova, K. Gavazov, *Bulg. Chem. Commun.*, **50**(B), 32 (2018).
11. Y. T. Liu, J. Sun, Z. Y. Luo, S. Q. Rao, Y. J. Su, R. R. Xu, Y. J. Yang, *Food Chem. Toxicol.*, **50**, 1238 (2012).
12. S. L. Lin, T. Lai, L. Chen, H. Kwok, C. B. Lau, P. C. K. Cheung, *J. Agric. Food Chem.*, **62**, 9488 (2014).
13. M. Özyurek, M. Bener, K. Guclu, R. Apak, *Food Chem.*, **157**, 323 (2014).
14. L. Dospatliev, M. Ivanova, *Bulg. Chem. Commun.*, **49**(4), 787 (2017).
15. A. Mocan, Â. Fernandes, L. Barros, G. Crişan, M. Smiljković, M. Soković, I.C. F. R. Ferreira, *Food Funct.*, **9**, 160 (2018).
16. M. Y. Kim, L. M. Chung, S. J. Lee, J. K. Ahn, E. H. Kim, M. J. Kim, S. L. Kim, H. I. Moon, H. M. Ro, E. Y. Kang, S. H. Seo, H. K. Song, *Food Chem.*, **113**, 386 (2009).
17. J. Zhang, T. Li, Y. L. Yang, H. G. Liu, Y. Z. Wang, *Biol. Trace Elem. Res.*, **164**, 261 (2015).
18. T. Bakır, M. Boufars, M. Karadeniz, S. Ünal, *Afr. J. Tradit. Complement Altern. Med.*, **15**, 80 (2018).
19. B. Ribeiro, P. B. Andrade, B. M. Silva, P. Baptista, R. M. Seabra, P. Valentão, *J. Agric. Food Chem.*, **56**, 10973 (2008).
20. S. Y. Tsai, H. L. Tsai, J. L. Mau, *Food Chem.*, **107**, 977 (2008).
21. İ. Kivrak, S. Kivrak, M. Harmandar, *Food Chem.*, **158**, 88 (2014).
22. N. M. Sudheep, K. R. Sridhar, *Mycology*, **5**(2), 64 (2014).
23. L. A. Mendez, C. Castro, R. B. Casso, C. Leal, *J. Food Compost. Anal.*, **18**, 447 (2005).
24. K. Lee, I. Yun, K. Kim, S. Lim, H. Hamb, W. Eumc, J. Joo, *J. Food Compost. Anal.*, **24**, 175 (2011).
25. E. K. Seow, B. Ibrahim, S. A. Muhammad, L. H. Lee, L.H. Cheng, *LWT-Food Sci. Technol.*, **65**, 428 (2016).
26. N. Petkova, L. Ivanova, G. Filova, I. Ivanov, P. Denev, *Journal of Applied Pharmaceutical Science*, **7** (10), 055 (2017).
27. N. Petkova, I. Ivanov, R. Vrancheva, P. Denev, At. Pavlov, *Natural Product Communications*, **12**(2), 171 (2017).
28. G. M. Josiane, Y. M. Estelle, A. N. Francis, S. S. Kamdem, *Current Research in Agricultural Sciences*, **5**, 15 (2018).
29. WHO, World Health Organization Evaluation of Certain Foods Additives and Contaminants (Twenty-Six Report of the Joint FAO/WHO Expert Committee on Food Additives); WHO Library Cataloguing-in-Publication Data; WHO: Geneva, Switzerland, 1982.
30. P. Honeine, C. Richard, *IEEE Signal Process Mag.*, **28**(2), 77 (2011).
31. I. Gergen, M. Harmanescu, *Chem. Cent. J.*, **6**, 156 (2012).

Suppressive effect of salicylaldehyde benzoylhydrazone derivatives on ferrous iron-induced oxidative molecular damage – evaluation of the structure-protection activity relationship *via* Raman spectral analysis

V. A. Hadjimitova^{1*}, N. G. Hristova-Avakumova¹, B. I. Nikolova-Mladenova², E. Valcheva³

¹Department of Medical Physics and Biophysics, Faculty of Medicine, Medical University of Sofia, Bulgaria

²Department of Chemistry, Faculty of Pharmacy, Medical University of Sofia, Bulgaria

³Faculty of Physics, Sofia University “St. Kliment Ohridski”, Sofia, Bulgaria

Received October 29, 2018; Revised December 18, 2018

In the present research are included the iron chelator salicylaldehyde benzoylhydrazone (SBH) and two methoxy bearing derivatives - (3-methoxysalicylaldehyde benzoylhydrazone 3mSBH and 4-methoxysalicylaldehyde benzoylhydrazone 4mSBH). The goal was to correlate the experimental data concerning the vibrational characteristics (Raman spectra) of the tested hydrazone with its antioxidant potency in ferrous iron-induced oxidative damage model systems and others. The suppressive effect of the compounds on Fe-induced oxidative damage using as oxidisable substrates lecithin, egg yolk homogenate and deoxyribose was investigated and their potency to protect the deoxyribose molecules from UV-induced damage were tested. All the compounds demonstrated protection effect in the system of Fe-induced molecular damage. The extent of the witnessed effect is depending on the used oxidisable substrate and the position of the structural modification in the lead compound. All hydrazones have demonstrated better effectiveness in the more biologically plausible egg yolk lipoprotein containing model system compared to the lecithin containing one. The hydrazones proved that they can significantly decrease not only the iron-induced damage of deoxyribose but also reduce the “% molecular damage” of this oxidisable substrate upon experimental conditions of UV-irradiation. The calculated coefficient of correlation denoted R^2 ranges from 0.877 (lecithin system) to 0.98 (Fe-induced oxidative damage of deoxyribose) when seeking for relationship with the displacement of the peak around 1160 cm^{-1} , where are expected $\nu(\Phi\text{-OH})$ and $\delta(\text{O-H})$ vibrations. Only the C-50 values from the iron free deoxyribose model system had R^2 higher than 0.5 (0.997) with a shift to higher frequencies of the band around 1290 cm^{-1} , which is corresponding to the vibrations of the C-O in the phenol nucleus.

Keywords: Fe-induced oxidative damage, hydrazones, antioxidant activity, SAR, Raman spectrum

INTRODUCTION

Rational drug design is a continuous process which comprises several multidisciplinary approaches. Each year the medical chemists synthesize hundreds of series of biologically active molecules possessing desired pharmacological effects. The process of ranking the candidate compounds and disclosing the optimal structural parameters proving optimized biological effects, increased selectivity, and lessened toxicity requires significant capital and technical resources [1, 2].

The evaluation of the structure – activity relationship (SAR) is a primary tool optimizing the early points of the process of drug development and discovery. One used approach is to investigate the vibrational characteristics of the compounds which are molecular specific and determined by the compounds chemical structure. The obtained information by studying the infrared and the Raman spectra help optimizing the structure [3].

One of the possible ways of researching the relationship between structure and effects is studying separately the vibrational spectra and the

behaviour in biologically relevant systems [3]. Then the possible correlation between the changes in the vibrational energy of the molecules and their biological activities can be investigated.

The performed experiments with different groups of organic compounds including hydrazones denote that different biologically significant properties are associated with different structural modifications and the extent of the observed effect is determined by the type and the position of the substituent in the molecules of the newly synthesized compounds [4, 5].

Hydrazones are a group of organic compounds known with their exceptionally wide pharmaceutical activities. In the literature data have been reported numerous experiments proving their antimicrobial, analgesic, anti-inflammatory, antioxidant and anticancer activity [5]. As a result of the increased scientific interest the parallel synthesis of a series (structural derivatives of lead biologically active hydrazones) expanded significantly the diversity of the compounds available for study as new drugs [6, 7].

A key point in the overall process of

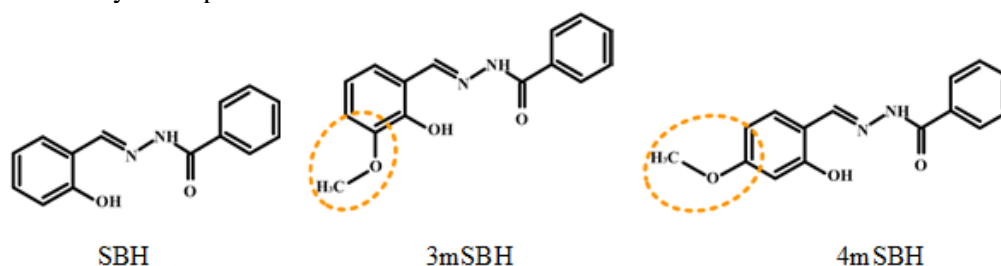
* To whom all correspondence should be sent.
E-mail: verah@mail.bg

V.A. Hadjimitova et al.: *Suppressive effect of salicylaldehyde benzoylhydrazone derivatives on ferrous iron-induced ...* investigation of the capability of new designed compounds to become clinically effective drugs is the pre-clinical estimation of their possible influence on free radical processes in the human body using *in vitro* and *in vivo* biologically relevant model systems. The collected experimental data are used to evaluate the possible therapeutic value of new designed compounds in the treatment of pathological conditions with increased generation of free radicals and change of the viable for the living organisms antioxidant balance like cancer, inflammatory and neurodegenerative disease.

The goal of the present investigation was to correlate the experimental data concerning the vibrational characteristics (Raman spectra) of methoxy derivatives of the iron chelator salicylaldehyde benzoylhydrazone (SBH) with their suppressive effect on ferrous iron-induced oxidative damage of biologically important molecules and their properties to scavenge free radicals. There are multiple pathophysiological conditions that are associated with disturbance of iron homeostasis and tissue iron accumulation – cancer, cardiovascular and neurodegenerative disease [8, 9]. The multiple side effects and described adverse reactions of the available at the moment pharmaceutical agents used to perform long-term treatment and prevention of iron-mediated toxicity of patients with these

conditions have implicated the need of development of new improved oral remedies.

In the research are included the initial compound, the iron chelator SBH and two methoxy bearing compounds (3-methoxysalicylaldehyde benzoylhydrazone 3mSBH and 4-methoxysalicylaldehyde benzoylhydrazone 4mSBH) – Scheme 1. All compounds were synthesized and structurally characterized by a research group from the Faculty of Pharmacy of the Medical University of Sofia. Anticancer drug screen was performed using human tumor cell lines in order to provide their cytotoxic effects and their ability to act as chelating agents coordinating different metal ions are estimated in order to determine compounds' capability for reduction of their toxic effects [10-12]. In the present investigation we aimed to evaluate the suppressive effect of these three arylhydrazones on ferrous iron-induced oxidative molecular damage using as oxidisable substrates lecithin, egg yolk homogenate and deoxyribose. Their capability to protect the deoxyribose molecules from UV-induced oxidative damage was tested. Furthermore, readings of the Raman spectra of the three compounds in solid phase were taken and evaluation of the structure-protection activity relationship was performed.



Scheme 1. Chemical structure of the investigated hydrazones.

EXPERIMENTAL

Raman spectroscopy

Raman spectroscopy is an efficient, fast and non-destructive technique. The method is based on the measurement of the oscillations of the atoms in the studied molecules and provides information about the molecular vibrational energy levels which are related to the molecular structure, its conformational characteristics, and intermolecular interactions. Due to this fact it has proven itself as a useful screening method for structural characterization of new-designed compounds.

The Raman spectra of the investigated hydrazones were recorded using micro-Raman spectrophotometer Lab RAM HR 800. The probe excitation was achieved at room temperature using

the 632 nm line of an argon ion laser. The spectra were collected with Raman microscope equipment with 50× objective resolution 1 cm⁻¹.

Antioxidant potency

Iron-induced lipid peroxidation (LP) – the determination of the level of Fe-induced LP was performed using systems containing egg yolk homogenate or lecithin [13, 14]. Hydrazones with different concentration were added to 1 ml of homogenate (diluted v/v 1:100). The reaction was initiated with 50 μL of FeCl₂ with final concentration of 1 mmol/L. Samples were incubated for 30 min at 37°C. Then to each sample was added 0.5 ml of 2.8% trichloroacetic acid solution and 0.5 ml of 1% thiobarbituric acid solution (TBA). After 20 min incubation at 100°C

V.A. Hadjimitova *et al.*: *Suppressive effect of salicylaldehyde benzoylhydrazone derivatives on ferrous iron-induced ...*
the samples were centrifuged and the absorbance of the supernatant was measured at 532 nm. The obtained results are presented as percentage of the control sample.

Iron-induced deoxyribose oxidative damage – the assay was carried out using one mL samples of phosphate saline buffer (PBS) – 50 mM K_2HPO_4/KH_2PO_4 , pH 7.4, containing 0.3 mM of 2-deoxy-D-ribose, 0.5 mmol/L of H_2O_2 , 50 μ mol/L of ascorbate, 50 μ mol/L of Fe(III) and 52 μ mol/L of EDTA [15]. The extent of deoxyribose oxidative degradation by the produced hydroxyl radicals was measured using TBA test. After the addition of the tested hydrazones at the investigated concentration the experimental procedure follows the same protocol used for determination of the TBARS products in the lipid containing model systems. The obtained results are presented as percentage of the control samples.

UV-induced deoxyribose damage – the deoxyribose assay was performed as described by Halliwell *et al.*, with small modifications [15]. The tested hydrazone derivatives and 0.6 mmol/L of 2-deoxy-D-ribose were added in phosphate buffer. In the control sample, hydrazones were omitted. After 30 min of balanced UV irradiation (UV 220 – 400), 0.6 ml of 1% TCA and 0.6 ml of 0.6% of thiobarbituric acid were added to 1 ml of the irradiated sample solution. Again the experimental procedure follows the same protocol used for determination of the TBARS products in the lipid containing model systems.

RESULTS AND DISCUSSION

Nowadays, from a scientific perspective, the *in vitro* model systems comprising evaluation of protection effect against different mechanisms of molecular damage of biologically important molecules enjoy increasing popularity as first-line experiments in the novel drugs discovery process. Due to this fact the first step of our investigation comprises evaluation of the effect of the tested hydrazones against oxidative damage in model systems containing lecithin, egg yolk homogenate and deoxyribose molecules. The used model systems have proven their applicability in determining the protection effect of aroyl hydrazones in our previous investigations. [16].

In both lipid-containing model systems the initial compound and its methoxy derivatives have demonstrated a protection effect. This is evident from the diminishment of both - the absorbance and the subsequently calculated by its values “degree of molecular damage” for the hydrazone containing samples compared to the control probes where hydrazones were omitted and maximal molecular

damage is being observed. The extent of the witnessed protection from Fe-induced oxidative damage is depending from the used oxidisable substrate – all compounds have demonstrated better effectiveness in diminishment of the generation of TBA-RS products in the egg yolk lipoprotein containing a model system.

In the lecithin-containing samples the basic compound SBH has decreased the “degree of molecular damage” to 71% compared to the control samples. The compounds possessing modification associated with incorporation of methoxy group at 3- and 4- position in the aldehyde part of the molecule also possess capability to diminish the generation of TBA-RS products but the “degree of molecular damage” is the same (4mSBH) or slightly elevated (3mSBH) compared with this of SBH.

In the egg yolk homogenate the SBH chelator has diminished the “degree of molecular damage” with approximately 60% compared to the control samples – the diminishment is approximately 30% more compared to the lecithin model system. The additional modifications, i.e. incorporation of methoxy groups in the aldehyde part of the molecule at third and fourth position, ameliorates the denoted by the initial compound protection effect and the “degree of molecular damage” is lessened to one-third compared to the controls.

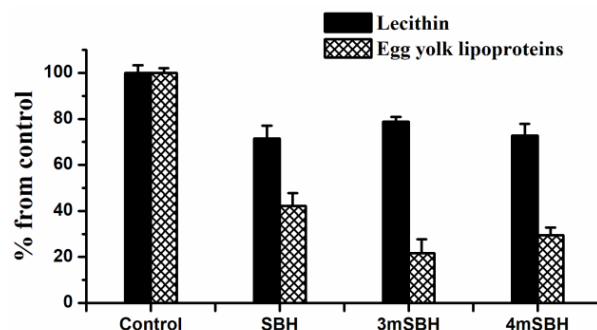


Figure 1. Degree of molecular damage in percentage during iron-induced peroxidation in lipid containing model systems in presence of the initial compound SBH and its 3- and 4-methoxy derivatives at a concentration of 120 μ mol/L.

The experiments on the evaluation of the capability of the tested hydrazones to decrease the deoxyribose molecular damage have also proven protection of the oxidisable substrate. The tests were performed in alternative model systems – in the first one we have used Fe (II) to induce oxidative damage and in the second - UV irradiation. In both systems we observed a statistically significant decrease of the degree of molecular damage at the lowest tested concentration in all samples containing hydrazones.

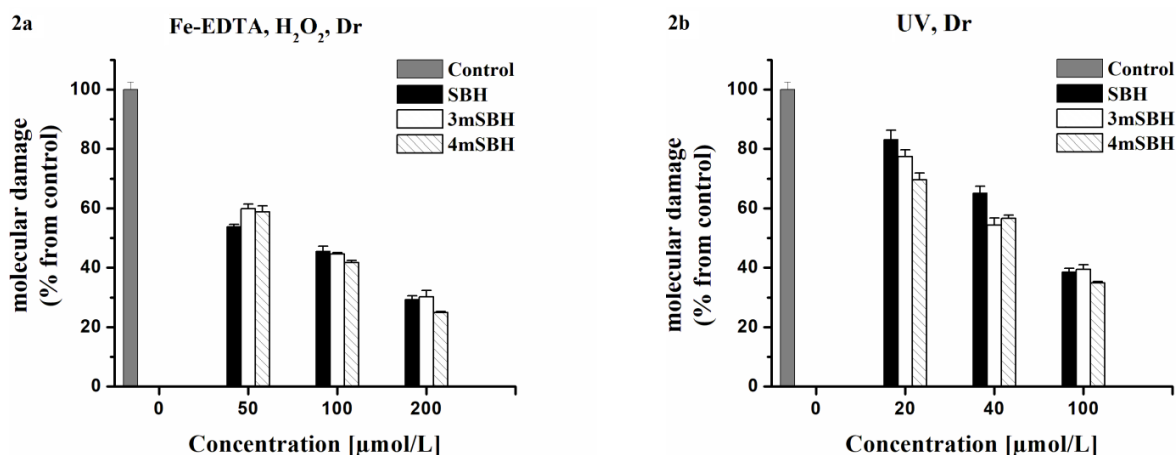


Figure 2. Effect of the chelator SBH and its 3- and 4-methoxy derivatives in spectrophotometric model systems with different mechanism of initiation of deoxyribose oxidative damage, respectively – 2a. Ferrous iron-induced oxidative molecular damage and 2b UV – induced deoxyribose damage.

Table 1. Comparison between the concentrations of hydrazones leading to 50% decrease of the deoxyribose molecular damage in the model system of iron-induced deoxyribose oxidative damage and UV initiated deoxyribose oxidative damage

Compound	C-50 [μmol/L] UV, Dr	C-50 [μmol/L] Fe-EDTA, H ₂ O ₂ , Dr
SBH	67.06 ± 0.06	66.88 ± 2.26
3mSBH	58.37 ± 2.36	78.81 ± 0.02
4mSBH	51.23 ± 0.22	71.38 ± 0.02

The observed effect of decrease of deoxyribose molecular damage is concentration-dependent – increasing the hydrazone concentration decreases the sample absorbance and respectively the molecular damage. In order to compare the influence of the structural modifications in the aldehyde part of the molecule on the properties evaluated in each system and to perform comparative evaluation of the influence of each hydrazone on the deoxyribose molecule oxidative damage in both systems we have calculated the C-50 values - hydrazone concentration inducing 50% inhibition of the % molecular damage using the data presented in Figure 2. The presented in Table 1 C-50 values denote that there is no statistically significant difference in the concentration which is needed to decrease with 50% the deoxyribose molecular damage for SBH. The structural modifications associated with incorporation of methoxy group have ameliorated the protection

effect in the system where we have used UV induced deoxyribose damage (lower C-50 values compared to SBH) and slightly decreased the initial compound protection effect in the system of Fe-induced oxidative damage (elevated C-50 values compared to SBH). In both tested model systems the 4-methoxy bearing compound demonstrated better ability to protect the deoxyribose molecules compared to the 3-methoxy derivative.

The Raman spectra of the substances, taken from samples in a solid phase at room temperature, are shown in Figure 3. The most intense bands were observed about 1600 cm⁻¹, the less intense ones are about 1300 cm⁻¹ and 1160 cm⁻¹. Typical for all spectra is the narrow band about 1000 cm⁻¹. The latter can be interpreted as ν deformation of the carbon atoms bands in the ring plane [17]. These oscillations are active in the Raman spectrum only if there are substitutions in the benzene nucleus. The position of the peak is not affected by the type of substitution, nor by the position of the group.

According to the literature, the vibrations affecting the hydroxyl group and its bonds with the core are located around 1300 cm⁻¹ [18], varying between different sources – 1025 cm⁻¹ [19], 1170 cm⁻¹ [20], ν(C-O) – 1290 cm⁻¹ [21]. The vibrations associated with bending deformations are in the range 1100-1400 cm⁻¹ [20]; Phenol-O stretching is about 1200 cm⁻¹ [22].

We found that addition of a methoxy group results in a shift of the peak around 1160 cm⁻¹ (SBH), where oscillations ν(Φ-OH) and δ(O-H) are expected and the one at 1290 cm⁻¹, where oscillation ν(C-O) is expected.

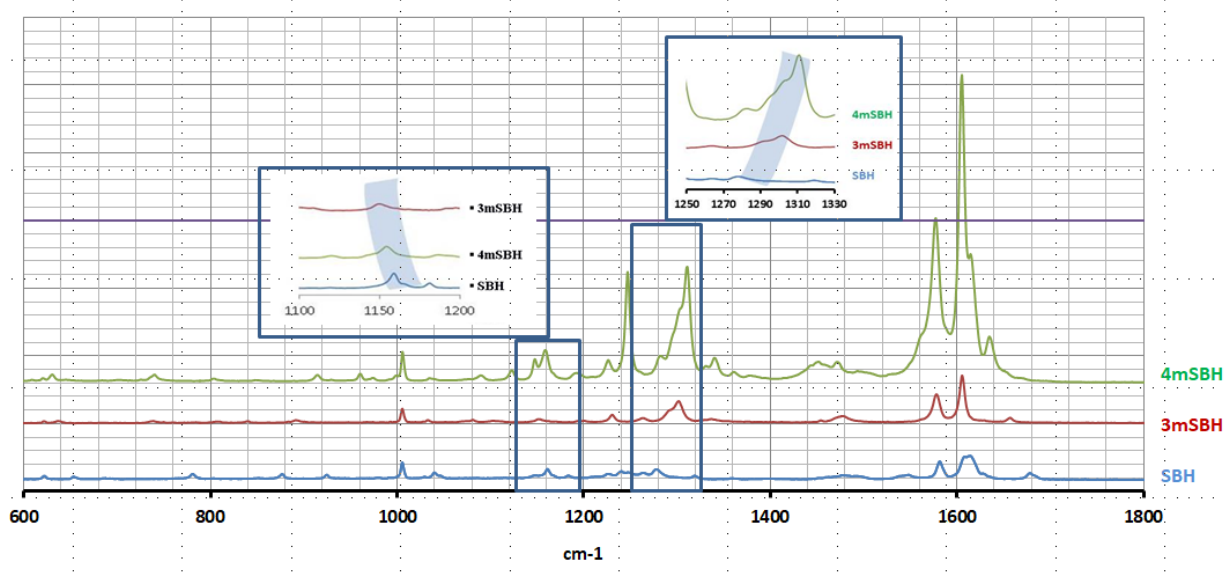


Figure 3. Raman spectra of the solid-state investigated hydrazones – excitation at 632 nm. The labeled bands illustrate the shift of the peaks in the frequency regions 1100-1200 and 1250-1350 cm^{-1} .

The Raman spectra of the tested substances were searched for frequency areas which could correlate with AOA. Since the AOA of substances with cyclic structure is determined by the presence and amount of hydroxyl groups, our attention was focused in the area where vibrations related to the OH group occur.

We evaluated the degree of correlation between the denoted antioxidant potential in the studied spectrophotometric model system (3 with iron induced oxidative damage and one lacking iron – the system with UV irradiation) and the Raman spectra of the compounds in the area of the mentioned vibrations. For this purpose we used the “molecular damage” for the lipid containing systems and C-50 values for the deoxyribose containing ones. The obtained data denoted linear correlation between the observed antioxidant potency in the systems and the shift of the peaks located around 1290 cm^{-1} and 1160 cm^{-1} when changing position with a constant step of cm^{-1} .

The calculated coefficient of correlation denoted R^2 is ranging from 0.877 (lecithin system) to 0.98 (Fe-induced oxidative damage of deoxyribose) when seeking for relationship with the displacement of the peak around 1160 cm^{-1} , where stretching $\nu(\Phi\text{-OH})$ and bending $\delta(\text{O-H})$ vibrations are expected. Only the C-50 values from the iron-free deoxyribose model system had R^2 higher than 0.5 (0.997) with the shift to higher frequencies of the band around 1290 cm^{-1} , which is corresponding to the vibrations of the C-O in the phenol nucleus. No correlation was observed between the observed protection effect in this system and the shift of the peak around 1160 cm^{-1} toward lower frequencies.

CONCLUSIONS

In conclusion we can assume that the compounds demonstrated a protective effect in the system and have the capability to diminish molecular damage of biologically important molecules. The extent of the witnessed effect is depending on the used oxidisable substrate, the used methods for initiation of the oxidative damage and the position of the structural modification in the lead compound. The analysis of the Raman spectra of the investigated compounds revealed that the incorporation of a methoxy group leads to a displacement of the peak at 1160 cm^{-1} , which, according to literature data, is assigned to $\nu(\Phi\text{-OH})$ and $\delta(\text{O-H})$ vibrations. A linear dependence was established between the position of the spectrum bands and the magnitude of the observed antioxidant potency of the compounds.

Acknowledgement: Financial support by the Medical University of Sofia (Counsel of Medical Science, Contract number № Д-133 / 02.05.2017) is gratefully acknowledged.

REFERENCES

1. R. Guha, *Methods in Molecular Biology*, **993**, 81 (2013).
2. K. Nepali, S. Sharma, M. Sharma, P.M. Bedi, K.L. Dhar, *Eur. J. Med. Chem.*, **77**, 422 (2014).
3. D. Pivonka, I. Noda, *Applications of Vibrational Spectroscopy in Pharmaceutical Research and Development*, John Wiley & Sons Ltd, 2007, p. 4082.
4. B. Suman, G. Uppal, A. Kajal, S. Kamboj, V. Sharma, *International Journal of Pharmaceutical Sciences Review and Research*, **18**, 65 (2013).

- V.A. Hadjimitova et al.: *Suppressive effect of salicylaldehyde benzoylhydrazone derivatives on ferrous iron-induced ...*
5. G. Verma, A. Marella, M. Shaquiquzzaman, M. Akhtar, M. Ali, M. Alam, *Journal of Pharmacy & Bioallied Sciences*, **6(2)**, 69 (2014).
 6. N. Anastassova, A. Ts. Mavrova, D. Yancheva, M. Kondeva-Burdina, V. Tzankova, S. Stoyanov, B. Shivachev, R. Nikolova, *Arab. J. Chem.*, **11(3)**, 353 (2018).
 7. N. Belkheiri, B. Bouguerne, F. Bedos-Belval, H. Duran, C. Bernis, R. Salvayre, A. Nègre-Salvayre, M. Baltas, *Eur J Med Chem.*, **45(7)** 3019 (2010).
 8. P. Bernhardt, P. Chin, P. Sharpe, D. Richardson, *Dalton Transaction*, **30**, 3232, (2007).
 9. R. Gozzelino, P. Arosio, *International Journal of Molecular Sciences*, **17(1)**, 130 (2016).
 10. B. Nikolova-Mladenova, N. Halachev, R. Iankova, G. Momekov, D. Ivanov, *Arzneim.-Forsch.*, **61(12)**, 714 (2011).
 11. B. I. Nikolova-Mladenova, L. P. Peikova, M. B. Georgieva, Al. B. Zlatkov, *Bulgarian Chemical Communications*, **49(D)**, 153 (2017).
 12. B. I. Nikolova-Mladenova, S. E. Angelova, *Bulgarian Chemical Communications*, **49(L)**, 237 (2017).
 13. R. Bird, H. Draper, *Methods Enzymology*, **105**, 299 (1984).
 14. N. Hristova-Avakumova, B. Nikolova-Mladenova, K. Yoncheva, V. Hadjimitova, *Journal of Physics: Conference Series*, **780**, (2016)
 15. B. Halliwell, J. M. Gutteridge, O. I. Aruoma, *Anal. Biochem.*, **165**, 215 (1987).
 16. N. Hristova-Avakumova, K. Yoncheva, B. Nikolova-Mladenova, T. Traykov, G. Momekov, V. Hadjimitova, *Redox Report*, **22(6)**, 408 (2017).
 17. D. Mayo, A. Foil, R. Miller, W. Hannah, *Course Notes on the Interpretation of Infrared and Raman Spectra*, 2004.
 18. C. Colonna, J. Doucet, A. Cossé-Barbi *Transition Metal Chemistry*, **20(4)**, 338 (1995).
 19. X. Lu, J. Wang, M. Hamzah, M. Al-Qadiri, C. Ross et al., *Food Chemistry*, **129(2)**, 637 (2011).
 20. R. Calheiros, N. Machado, S. Fiuza, A. Gaspar, J. Garrido et al., *Journal of Raman Spectroscopy*, **39(1)**, 95 (2008).
 21. A. Ertani, D. Pizzeghello, O. Francioso, A. Tinti, S. Nardi, *Molecules*, **21(2)**, 205 (2016).
 22. J. Coates, *Interpretation of Infrared Spectra*, in: *A Practical Approach in Encyclopedia of Analytical Chemistry*, R.A. Meyers (ed.), John Wiley & Sons Ltd, Chichester, 2000, p. 10815.

Neo-clerodane diterpenoids from *Scutellaria velenovskyi* Rech. fil.

P. I. Bozov, P. N. Penchev*

University of Plovdiv "Paisii Hilendarski", 24 Tzar Asen Str., 4000 Plovdiv

Received October 31, 2018; Revised January 4, 2019

A new neo-clerodane diterpenoid, (11S,13R,16S,19S)-3 β ,6 α -diacetoxy-19-*trans*-tigloyloxy-2 α ,19;4 α ,18;11,16;15,16-tetraepoxyneoclerodane (scutevelin A), was isolated from the acetone extract of the aerial parts of *Scutellaria velenovskyi* Rech. Fil., in addition to the previously known 14,15-dihydrojodrellin T. The structure of the new compound was established by ¹D and ²D NMR and other spectroscopic techniques and by comparison of its spectral data to those of the closely relative 14,15-dihydrojodrellin T.

Keywords: *Scutellaria velenovskyi*, Labiatae, neo-clerodane diterpenoids

INTRODUCTION

Neo-clerodane diterpenoids exhibit interesting biological properties – especially their action as insect antifeedant and antifungal agents [1-3]. *Scutellaria* (Labiatae) species was assessed to contain a great diversity of such compounds with different substructures. In Bulgaria, the investigation of this genus started in 1991 with the study of *Scutellaria alpina* [4]. In continuation of our ongoing efforts in searching for biologically active clerodanes we studied *Scutellaria velenovskyi*. Herein, we report the isolation and structural identification of two neo-clerodane diterpenoids, a new compound scutevelin A (1) and the already known 14,15-dihydrojodrellin T (2).

EXPERIMENTAL

Plant material

The plant material of *Scutellaria velenovskyi* Rech. fil. was collected in June 2016 in the region of Mezek near Svilengrad, Bulgaria and voucher specimens (N. 11927) were deposited in the Herbarium of the Agriculture University of Plovdiv, Bulgaria.

Extraction and isolation of the compounds

Dried and finely powdered aerial parts of *Scutellaria velenovskyi* (160 g) were extracted with acetone (2 \times 2 L) at room temperature for 1 week. After filtration, the solvent was evaporated to dryness under reduced pressure yielding a gum (8.2 g), which was dissolved in 50 % aq. acetone (v/v, 100 mL). The solution was cooled to 4 $^{\circ}$ C for 24 h and filtered. The filtrate was extracted with CHCl₃ (4 \times 50 mL). The organic extract was dried with Na₂SO₄ and evaporated under vacuum (giving 1.4 g of a bitter residue). This residue was chromatographed over a Si gel column (Merck N.

7734, deactivated with 10 % H₂O, w/w, 30 g) with a light petroleum / ethyl acetate solvent gradient (from 10:0 to 3:7) as eluent. Eluate fractions (100 mL each) containing scutevelin A (compound 1) based on TLC results were collected (8 flasks) and evaporated to obtain 24 mg of crude scutevelin A. After recrystallization from acetone 17 mg of pure substance was obtained. Analogously, 11 mg of compound 2 were obtained from 5 flasks.

Scutevelin A (1)

Colorless prisms from acetone, m.p. 190-192 $^{\circ}$ C. TLC: R_f 0.71 (EtOAc). IR bands, cm⁻¹ (KBr): 2963, 2922, 2851, 1740, 1715, 1653, 1636, 1378, 1261, 1093, 1025, 907, 879, 801, 733, 669, 618, 599. ¹H and ¹³C NMR: see Table 1. EIMS (70 eV, direct inlet) m/z (rel. int. in %): 489 [M – OAc]⁺ (33), 449 [M – OTig]⁺ (3), 389 [M – OAc, – OTig]⁺ (4), 316 [M – OAc, – OTig, – CH]⁺ (17), 224 (3), 171 (6). HREIMS m/z 571,2542 [M+Na]⁺ (calcd for C₂₉H₄₀O₁₀Na: 571,2519).

RESULTS AND DISCUSSION

Two compounds with very close R_f values on TLC were obtained after chromatography of the acetone extract of the aerial parts of *Scutellaria velenovskyi*. The IR spectra of the compounds are very close. Both indicate presence of acetyl groups characterized by a band at 1740 cm⁻¹ and tigloyl ester identified with the strong absorption for carbonyl function at 1715 cm⁻¹ in combination with the intensive band for conjugated double bond at 1653 cm⁻¹. Both substances have molecular formula C₂₉H₄₀O₁₀ which corresponds to the observed in the HREIMS spectra [M+Na]⁺ peaks at m/z 571.2542 for compound 1 and 571.2515 for 2, respectively. In accordance with the observations in the IR spectra, the mass spectra display fragment ions at m/z 489, 449 and 389 corresponding to the loss of an acetoxy, tigloyloxy unit or both functions,

* To whom all correspondence should be sent.
E-mail: plamen@uni-plovdiv.net

respectively. The noticeable difference is that in the spectrum of **1** the strongest fragment ion is at m/z 449, while in **2** that is at m/z 389. The presence of the mentioned above substitutes in the molecules of **1** and **2** is supported by the observed in the ^1H and ^{13}C NMR spectra typical signals corresponding to a tigloyl and an acetyl ester. The downfield signal at δ_{H} 7.07/6.81 (1H, qq, $J = 7.1, 1.1/7.3, 1.8$ Hz, H-3'), signals for methyl groups at 1.80/1.82 (3H, br d, $J = 7.6$ Hz, H_{3-4'}), 1.88/1.81 (3H, br s, H_{3-5'}) and carbon signals at δ_{C} 166.0/166.4 (C=O), 128.50/128.14 (C-2'), 139.02/137.77 (C-3') indicate the presence of a tiglate moiety (see Table 1). Signals for two acetate groups appeared at δ_{H} 2.05 / δ_{C} 169.42 and δ_{H} 1.78 / δ_{C} 169.95 for compound **1** and at δ_{H} 2.14 / δ_{C} 169.78 and δ_{H} 1.96 / δ_{C} 169.61 for **2**. In addition, signals for three geminal protons with ester groups are present at δ_{H} 4.64 (1H, dd, $J = 11.1, 4.6$ Hz), 5.38 (1H, t, $J = 2.2$ Hz) and 6.77 (1H, s) in the ^1H spectrum of **1** and at δ_{H} 4.64 (1H, dd, $J = 11.1, 4.6$ Hz), 5.38 (1H, t, $J = 2.2$ Hz) and 6.77 (1H, s) in the spectrum of **2**. Characteristic signals for two 4 α ,18-epoxy-neo-clerodane skeletons were easily distinguished (Tables 1 and 2) at δ_{H} 0.79 s / 0.80 s (Me-20), 0.787 d / 0.791 d (Me-17).

^1H and ^{13}C NMR spectral data of 14,15-dihydrojodrellin T coincide in all respects with those of an authentic sample and with those reported in the literature [5, 6]. The 600 MHz ^1H NMR spectrum of **1** indicates all structural features common to **2** with the expected differences for the signals corresponding to the ring A and to the C-4/C-18 oxirane fragment. For instance, the signals from the two doublets, corresponding to the C-18 two hydrogens observed in **2** at δ_{H} 2.45, (1H, d, $J = 4.6$ Hz, H-18A) and 3.05 (1H, d, $J = 4.7$ Hz, H-18B), are replaced in **1** with δ_{H} 2.88 (1H, d,

$J = 4.3$ Hz, H-18A) and 2.91 (1H, d, $J = 4.3$ Hz, H-18B). Such conciseness of the signals for 18A and 18B protons is a characteristic feature for compounds having electronegative substitute at third position. Another deviation of the signals in the ^1H NMR spectra of **1** and **2** is the shifted with 0.35 ppm downfield doublet of triplets characteristic of the C-2/C-19 etheral linkage (δ_{H} 4.07/4.42, H-2 dt). The signals from the hexahydrofurofuran substructure and the B ring were all well defined. The measured ^1H -broadband-decoupled ^{13}C NMR spectra of both compounds show 29 signals and the DEPT displayed 23 resonances for six methyls, six methylenes, ten methines (one of them olefinic) and seven quaternary carbons (one olefinic and three carbonyls). So we suggested that compound **1** was a positional isomer of **2** with β -ester group at carbon C-3 instead of C-1. This assumption is confirmed by comparison of their ^{13}C NMR spectra with that of scuteveprin, a compound with no substitutes in ring A, as it was described by us [7,8]. In the ^{13}C NMR spectrum of **1** the signal for the carbon atoms C-4 is downfield shifted with 2.89 ppm, compared with that of scuteveprin, while that for C-18 is high-field shifted with 5.65 ppm. In the ^{13}C NMR spectrum of **2** the value of these signals are not changed but the chemical shifts of carbon C-10 is downfield shifted by 7.42 ppm. The acceptance that C-3 is an oxygenated methine carbon atom is in agreement with the observed correlations: (1) in the HSQC spectrum the triplet at 5.38 ppm has a cross-peak with δ_{C} 71.69; (2) in the HMBC spectrum δ_{H} 5.38 has a cross-peak with δ_{C} 63.5 (C-4) and (3) in the ^1H - ^1H COSY spectrum that signal has cross-peaks with signals of H-1 α , H-2 β and H-18B.

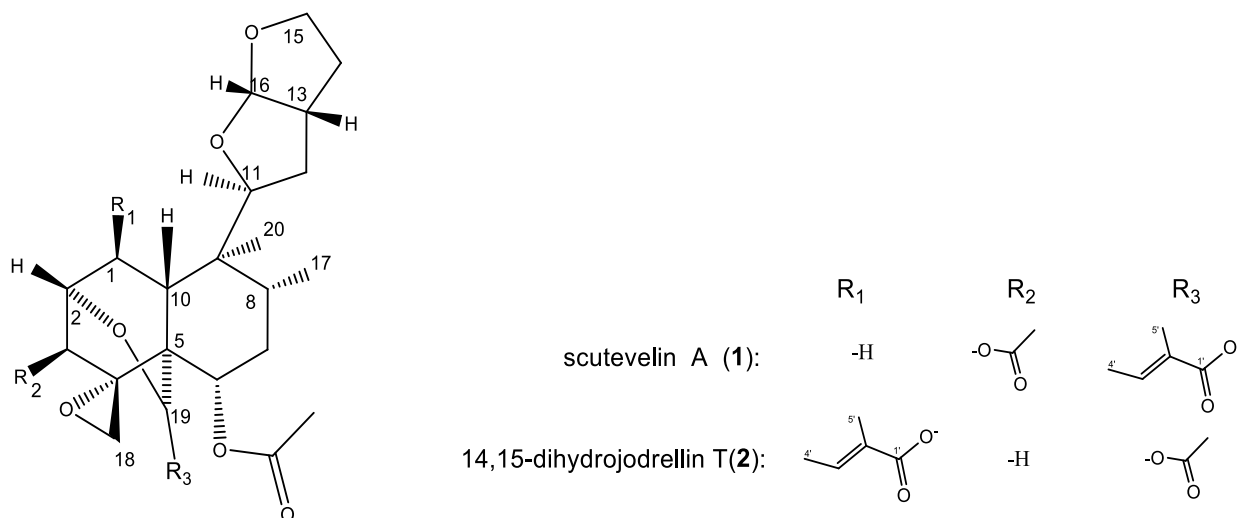


Figure 1. Structures of the *neo-clerodanes*.

Finally, the attachment of the tigloyloxy and the two acetoxy groups to the neo-clerodane skeleton in **1** needed to be rigorously established. The carbonyl resonance at δ_C 169.95 and downfield doublet of doublets at δ_H 4.64 ($J=11.1, 4.6$), assigned for an oxygenated methine proton, are very common structural features for clerodane diterpenoids with acetate at C-6 α position [5-7] as 14,15-dihydrojodrelin T (see Table 2). This conclusion was also supported by the HMBC correlations from H-6 to C-4 (δ_C 63.49), C-5 (δ_C

42.51), C-7 (δ_C 33.40), C-19 (δ_C 90.70), C=O (δ_C 169.95) and 1H - 1H COSY correlations of H-6 with H-7 α and H-7 β . The tiglate group was assigned to be attached to C-19 based on the HMBC correlation of H-19/C-1'. The NOESY correlations of H-11 with H-3, H₃-17, H₃-20 and of H-19 with H₃-20 indicated that these protons were cofacial and α -oriented. Respectively, the NOESY correlations of H-6 with H-8 and H-10 reveal its β -position.

Table 1. 1H and ^{13}C NMR spectral data^a and 1H - 1H COSY and HMBC correlations for scutevelin A (**1**).

Position	$\delta^{13}C, nH$	δ^1H	m, J (in Hz)	1H - 1H COSY	HMBC
1	23.1, CH ₂	2.23 (α) 1.79 (β) ^d	dt ^f , 14.9; - ov m	1 β , 2 β , 3 α ^b , 10 β 1 α , 10 β	2 ^{ew} , 10 ^{ew}
2	67.7, CH	4.07 (β)	ov m	1 α , 3 α ,	3 ^b , 4, 19 ^b
3	71.7, CH	5.38 (α)	t ^e , 2.2	1 α ^b , 2 β , 18B	4 ^b
4	63.5, C				
5	42.5, C				
6	67.9, CH	4.64	dd, 11.1; 4.6	7 α , 7 β	4 ^b , 5 ^b , 7, 19 ^b , 1' ^b
7	33.4 ^g , CH ₂	1.65 (α) ^d 1.39 (β) ^d	ov m m	6 6, 17 ^b	
8	35.0, CH	1.66 ^d	ov m	17	
9	41.4, C				
10	40.8, CH	2.05 (β) ^d	ov m	1 α , 1 β	
11	85.8, CH	4.05	ov m	12 α , 12 β	10, 7 (12) ^b , 20 ^b
12	33.5 ^g , CH ₂	1.66 (α) ^d 1.97 (β) ^d	ov m m	11, 12 β	
13	41.8, CH	2.86 (β)	m	11, 12 α , 13 β 12 β , 14 β , 16 β	15 ^{ew}
14	32.6, CH ₂	1.69 (α) ^d 2.15 (β) ^d	ov m m	13 β , 14 β , 15 14 α , 15	13 ^b , 15 ^b
15	68.3, CH ₂	3.87	m	14 α , 14 β	13 ^b , 16
16	108.2, CH	5.64 (β)	d, 5.0	13	11, 14 ^b , 13, 15
17	16.7, CH ₃	0.89	d, 5.8	7 β ^b , 8	
18	44.6, CH ₂	2.91 (B ^c) 2.88 (A)	d, 4.3 d, 4.3	18A 18B	4, 5 ^{ew} , 3 ^{ew} , 4, 5 ^{ew}
19	90.7, CH	6.77	s	-	1', 2, 4, 5 ^b
20	14.0, CH ₃	1.14	s		
1' (C=O)	166.0, C				
2'	128.5, C				
3'	139.0, CH	7.07	qq, 7.1; 1.1	4', 5' ^b	1' ^{ew} , 4' ^{ew} , 5' ^{ew}
4'	14.7, CH ₃	1.80	br d, 7.6	3'	2', 3', 1' ^b
5'	11.9, CH ₃	1.88	br s	4' ^b	2', 3', 1'
3 ¹ (C=O)	169.4, C				
3 ² (Me)	20.8 ^f , CH ₃	2.05	ov s		C=O
6 ¹ (C=O)	170.0, C				
6 ² (Me)	20.9 ^f , CH ₃	1.78	s		C=O

^a CDCl₃, 1H 600.13 MHz, δ_{ref} 7.26; ^{13}C 150.9 MHz, δ_{ref} 77.0 ppm; ov = overlapped; br = broad ^b weak; ^{ew} extremely weak; ^c endo hydrogen; ^d data from HSQC; ^e apparent multiplicity; ^{f,g} signals with the same letters may be interchangeable.

Table 2. ¹H and ¹³C NMR spectral data for 14,15-dihydrojodrellin T (2).

Position	$\delta^{13}\text{C}$, nH	$\delta^1\text{H}$	m, J (in Hz)
1	66.8, CH	5.51	m
2	69.6, CH	4.42	dt, 5.0; 2.6
3	31.1, CH ₂	2.47	br d, 15.3
4	59.7, C	1.86	dd, 15.0;3.0
5	43.0, C		
6	67.7, CH	4.65	dd, 12.0; 4.8
7	32.6, CH ₂	1.64-1.72 (α)	ov m
		1.38-1.43 (β)	m
8	35.3, CH	1.56-1.60	ov m
9	40.7, C		
10	48.2, CH	2.03	d, 2.6
11	86.0, CH	4.06	dd, 11.3; 5.4
12	32.9, CH ₂	1.64-1.72 (α)	ov m
		1.96 (β)	ov m
13	41.7, CH	2.63-2.68	m
14	33.2, CH ₂	1.64-1.72 (α)	m
		2.06-2.12 (β)	ov m
15	68.3, CH ₂	3.77-3.80	m
16	108.1, CH	5.35	d, 5.0
17	16.1, CH ₃	0.89	d, 6.6
18	50.3, CH ₂	3.05 (B ^c)	d, 4.7
		2.45 (A)	d, 4.6
19	90.4, CH	6.68	s
20	15.8, CH ₃	1.24	s
1' (C=O)	166.4, C		
2'	128.1, C		
3'	137.8, CH	6.81	qq, 7.3;1.8
4'	14.6, CH ₃	1.82	ov br d
5'	12.0, CH ₃	1.81	ov br s
3 ¹ (C=O)	169.8, C		
3 ² (Me)	21.8, CH ₃	2.14	s
6 ¹ (C=O)	169.6, C		
6 ² (Me)	21.2, CH ₃	1.96	s

^a CDCl₃, ¹H 600.13 MHz, δ_{ref} 7.26; ¹³C 150.9 MHz, δ_{ref} 77.0 ppm; ov = overlapped; br = broad ^b weak; ^{ew} extremely weak; ^c endo hydrogen; ^d data from HSQC; ^e apparent multiplicity; ^{f,g} signals with the same letters may be interchangeable.

CONCLUSION

The structure of a newly isolated *neo*-clerodane diterpenoid scutevelin A was unambiguously assigned by its spectral data that are very close to those of the known 14,15-dihydrojodrellin T.

REFERENCES

1. M. Bruno, F. Piozzi, S. Rosselli, *Nat. Prod. Rep.*, **19**, 357 (2002).
2. J.C. Anderson, W.M. Blaney, M.D. Cole, L.L. Fellows, S.V. Ley, R.N. Sheppard, M.S. J Simmonds, *Tetrahedron Lett.*, **30**, 4737 (1989).
3. M.D. Cole, P.D. Bridge, J.E. Dellar, L.E. Fellows, M. Clare Cornish, J.C. Anderson, *Phytochem.*, **30**, 1125 (1991).
4. P.I. Bozov, P.Y. Malakov, G.Y. Papanov, M.C. de la Torre, B. Rodríguez, A. Perales, *Phytochem.*, **34**, 453 (1993).
5. M.D. Cole, J.C. Anderson, W.M. Blaney, L.E. Fellows, S.V. Ley, R.N. Sheppard, M.S.J. Simmonds, *Phytochem.*, **29**, 1793 (1990).
6. B. Rodríguez, M.C. de la Torre, M. Bruno, F. Piozzi, G. Savona, M.S.J. Simmonds, W.M. Blaney, A. Perales, *Phytochem.*, **33**, 309 (1993).
7. P.I. Bozov, P.N. Penchev, *J. Coll. Nat. Prod. Commun.*, **9**, 347 (2014).
8. P.N. Penchev, J. Coll, K. Nicolova, I.N. Iliev, P.I. Bozov, *Phytochem. Lett.*, **15**, 103 (2016).

Surface coatings based on glycerol phase and waste polyethylene terephthalate

N. S. Todorov

University of Burgas “Prof. Dr. Assen Zlatarov”, 1 Prof. Yakimov Blvd., 8010 Burgas, Bulgaria

Received October 30, 2018; Revised December 12, 2018

The aim of this paper is to investigate the possibility for using two waste products - glycerol phase derived from biodiesel production and waste poly(ethylene terephthalate) (PET) from non-alcoholic beverage bottles for preparation of surface coatings. Four medium oil alkyds were prepared - two from organic substances, contained in glycerol phase, different amounts of PET and phthalic anhydride, the other two were for reference and were synthesized from glycerol, sunflower oil, ethylene glycol and phthalic anhydride. Structure of all alkyds was confirmed by FTIR and ¹H NMR spectroscopies.

From all alkyds surface coatings on glass plates were obtained. Their physical properties (drying degree, hardness, adhesion) and chemical resistance were investigated. The analysis showed that the alkyd resins based on the organic substances in glycerol phase, PET and phthalic anhydride are superior to reference alkyds in terms of drying degree and hardness.

Keywords: coatings, biopolymers, glycerol phase, alkyd resins.

INTRODUCTION

Surface coating is a solid or liquid material in combination with pigments and solvents, that is spread over a surface to form a thin film. This film can protect the surface from the elements or has a decorative function, or both. Therefore, surface coatings are widely used in most industries.

Alkyd surface coatings are the most consumed coatings used worldwide, despite the increasing use of other film formers. Alkyd resins are a special family of polyesters synthesized by condensation reaction of oils or fatty acids, dibasic acids or acid anhydrides and polyols with hydroxyl functionality greater than two. The traditional oils such as linseed oil, sunflower oil, soybean oil and safflower oil are used for their synthesis [1-3].

Sunflower oil has an iodine value of 110-140 g I₂/100 g and is accentuated to semi-drying oils. The advantages of semi-drying oils are that after curing their surface is smooth, stays clear, which makes them good for coloring.

Sunflower oil is the second most used feedstock for biodiesel production after rapeseed oil in Europe [4]. Biodiesel production generates glycerol phase (GPh) as a main byproduct. The excess GPh may become an environmental problem since it cannot be disposed to the environment [5]. Its utilization is difficult due to its complex and variable composition. It contains glycerol, water, methanol, soaps, fatty acid methyl esters (FAMES) biodiesel, free fatty acids (FFAs), mono-, di- and triglycerides. There have been many investigations considering the utilization of the glycerol from the glycerol phase [6, 7].

Information in literature about the use of other organic substances besides glycerol in the glycerol phase is scarce. Their quantity is ~30% [8] and utilization is of ecological and economic significance. Among the possibilities, much attention is drawn to the polymer chemistry and technology [9].

Besides utilization of the glycerol phase, for the present work it was also important to utilize waste poly(ethylene terephthalate) (PET). The increasing worldwide usage of PET, along with economic and ecological pressures, have caused the waste polymer recycling technologies to be in the scope of interest for many scientists [10].

Waste PET from non-alcoholic beverage bottles can be used in preparation of surface coatings [11-14].

Considering this background, the following goals of the current study were formulated - to use all organic substances in the glycerol phase and waste PET for synthesis of alkyds, and to expand the knowledge on composition and properties of the obtained alkyd resins.

EXPERIMENTAL

Materials

Glycerol phase (GPh-1S) was obtained from Biogaz Inzhenering SD, Burgas, Bulgaria. Sunflower oil (SFO) was purchased on the market. Waste PET from non-alcoholic beverage bottles, chopped into flakes with size 0.8 – 1.2 mm, was used. Glycerol (Gly), ethylene glycol (EG), potassium hydroxide (KOH), phthalic anhydride (PhA), methanol, potassium hydroxide, xylene,

Pb acetate and Co naphthenate were purchased from Aldrich and used without further purification.

Analytical methods

Basic characteristics of GPh-1S, crude glycerol (CGly-1S) and sunflower oil fatty acid (SOFA) were determined. Glycerol content and methanol content were determined by high performance liquid chromatography (HPLC-1200), pH - by pH meter (Metrohm, 827 pH Lab). According to standardized methods of analysis were determined water content [15], ash content [16], organic non glycerol (MONG) content [17], Gardner color [18], FFAs content [19], iodine value [20], acid value (AV) [21] and density [22].

Synthesis of alkyds Alk-1S12 and Alk-1S20

Calculated amount of CGly-1S, toluene as azeotropic solvent and a portion of SOFA-1S (to which 0.2% KOH was added) were charged into a round bottomed flask, equipped with mechanical stirrer, thermometer, inert gas inlet and Dean-Stark separator. Temperature at the beginning was 85°C until the water from CGly-1S was completely evaporated. The temperature was then raised to 200°C. The process of esterification was monitored by acid value determination every 15 min and conversion of SOFA-1S was calculated by the equation:

$$\text{Conversion, \%} = \frac{A_0 - A_t}{A_0} \cdot 100 \quad \text{Eq. 1}$$

where: A_0 is the initial acidity of the mixture; A_t acidity at any time t .

The process of esterification is considered to be accomplished, when conversion is ~100%.

The temperature was then raised to 220°C and a preliminarily calculated amount of PET flakes heated to 220°C was added to the reaction system. A heterogeneous mixture of solid PET flakes and liquid product of the esterification was formed. Interaction continued until full homogenization of the mixture. The temperature was then lowered to 170°C and calculated amounts of phthalic anhydride and toluene were added. When viscosity of the system started increasing, the temperature was gradually raised to 240°C and stirring was intensified.

The reaction was monitored by acid value determination every 30 min. The polyesterification reaction was carried out until 10 mg KOH/g was obtained.

Preparation of films from alkyd resins and testing

All alkyds after esterification process with phthalic anhydride were cooled to 70°C and a calculated amount of xylene was added to obtain 60% solutions (alkyd resins). Then only for alkyd

resins AR-1S12 and AR-1S20 hot filtration was carried out for separation of potassium phosphate, which is the last contaminant in alkyd resins resulting from the use of CGly-1S and SOFA-1S. To accelerate drying of all alkyd resins, 1% of Pb and 0.1% of Co were added. Using a 50 µm applicator, the prepared solutions were applied on glass plates. Films were air-dried at 25°C for 24 h and then were heated to 110°C for 2 h.

The physical properties and chemical resistance of the films were investigated according to standardized methods [23-26]. Drying degree was determined by Erichsen 415 apparatus. Hardness was determined by Elcometer 501 Pencil hardness tester. Adhesion strength was measured by Elcometer 107 Cross Hatch Cutter tester.

Instrumental methods of analysis

FTIR spectra were recorded with Bruker Tensor 27 within the interval 4000 to 400 cm^{-1} with resolution of 2 cm^{-1} . Samples were prepared as thin film fixed between two discs of KBr to avoid the presence of air.

^1H NMR spectra were recorded on a Bruker Avance II+ 600 (600.13 for ^1H NMR and 150.92 MHz for ^{13}C NMR) spectrometer with TMS as internal standard for chemical shifts (δ , ppm).

RESULTS AND DISCUSSION

Treatment of glycerol phase GPh-1S

The composition of GPh-1S was determined (Table 1). The content of non-glycerol organic matter (MONG) was 28.8% by weight of the glycerol phase and 66% by weight of the glycerol.

Table 1. Composition of GPh - 1S

Glycerol phase GPh - 1S	
Content, wt. %	Value
Glycerol	47.4
Methanol	7.8
Water	13.8
MONG	28.8
Ash	2.2

All organic substances (glycerol and MONG) can be successfully used after employing two easy chemical processes. The first one is saponification. It is carried out with alcoholic solution of KOH until pH reached 11. FAMES and the glycerides are converted to soaps.

The second process is acidification with phosphoric acid. This process transforms soaps into free fatty acids while KOH reacts to give potassium phosphate.

Table 2. Basic characteristics of the CGly-1S and SOFA-1S

CGly-1S		SOFA-1S	
Glycerol content, wt.%	82.3	FFAs content, wt.%	98.2
Density at 20°C, g/cm ³	1.23	Density at 20°C, g/cm ³	0.918
Water content, wt.%	12.9	Saponification value (mg KOH/g)	190
MONG content, wt.%	2.5	Iodine number, gI ₂ /100g oil	126.6
Ash content, wt.%	2.3	Average molecular weight (g/mol)	280
Gardner color	6	Gardner color	8

As a result, a solid phase of salts (potassium phosphate) in the liquid phase was formed. Potassium phosphate is the main contaminant in the reaction mixture. It was separated from the fluid after settling for about 1 h. Without special purification it can be used as fertilizer and as buffer solution.

The obtained liquid phase contained glycerol and SOFA-1S. They are mutually insoluble and quite different by density. If stored overnight, they form layers. The light one SOFA-1S contains mainly free fatty acids (FFAs) and the heavy layer contains mainly glycerol. Subsequently the lower layer was neutralized with 12.5 M KOH until the pH was 7. As a result, the crude glycerol CGly-1S was obtained. Some basic characteristics of SOFA-1S and CGly-1S, obtained from glycerol phase were determined (Table 2).

The obtained SOFA-1S contains 98.2 wt.% higher fatty acids. The other 1.8 % is glycerol. The color of fatty acids (Gardner color = 6) is darker than the typical for fatty acids color of sunflower oil (Gardner color = 4), which may be due to the production process. Complete removal of MONG, water and potassium phosphate from CGly-1S was not achieved.

Theoretical calculation of alkyds compositions

Four medium oil alkyds were formulated for the purpose of this work. CGly-1S, SOFA-1S, different amounts of PET waste and phthalic anhydride were used for synthesis of Alk-1S12 and Alk-1S20. Glycerol, sunflower oil, ethylene glycol and phthalic anhydride were the raw materials for Alk-RS12 and Alk-RS20.

To avoid gelation, all alkyds were formulated according to Patton's gel point calculation. Alkyds were formulated to have oil length of 50% (Table 3).

Values of the Patton's gel point constant K were from K = 1.07 to K = 1.08 which means that no gelation will occur at 100% reaction accomplishment.

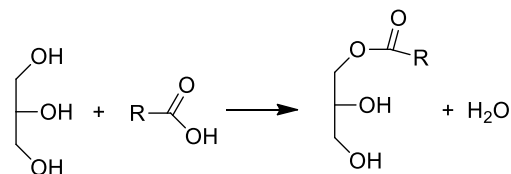
Preparation of alkyds Alk-1S12 and Alk-1S20

Alkyds Alk-1S12 and Alk-1S20 were synthesized by a three - stage process.

Table 3. Composition of alkyd resins

	Alk-1S12	Alk-1S20	Alk-RS12	Alk-RS20
SFO	-	-	52.3	52.3
SOFA	50.0	50.0	50.0	50.0
PhA	28.0	23.0	37.8	37.8
PET	12.0	20.0	-	-
EG	-	-	3.9	6.5
Gly	-	-	21.3	18.7
CGly:	25.8	22.0	-	-
Gly	21.2	18.1	-	-
MONG	0.4	0.4	-	-

During the first stage, monoglycerides from SOFA-1S and CGly-1S were obtained. The main reaction is the interaction of the SOFA-1S carboxyl groups with the primary OH groups of glycerol (Scheme 1):

**Scheme 1.** Esterification of glycerol with fatty acids

Along with the main reaction, side reactions may occur. It is known [11] that diglycerides are always formed simultaneously with monoglycerides. Side reactions may also occur because of impurities in the reaction system. In MONG composition there are FAMES. Under the reaction conditions, glycerolysis of FAMES may occur and monoglycerides can be obtained.

The esterification process was estimated by the changes in the acid value. Then conversion was calculated according to formula 1. The process of esterification was considered to be accomplished when conversion was ~100 % (Fig. 1).

Conversion of the carboxyl groups into the esters was confirmed by FTIR spectroscopy. For fatty acids, stretch vibrations of the C=O bonds appear at 1714 cm⁻¹, while in glycerides the same displace at 1737 cm⁻¹. At the end of the first stage in the reaction system there are monoglycerides, diglycerides, free glycerol and potassium phosphate.

During the second stage a process of solvolysis (simultaneous depolymerization and dissolution) of PET was carried out. The solvolysis reagents are both glycerides and glycerol. The depolymerization of the waste PET is represented by the chemical reactions of Scheme 2. It is considered that the process is completed after full homogenization of the reaction system.

For the purposes of the analysis, samples were taken. They were purified by twice washing with water, which is a solvent for both glycerol and potassium phosphate. They are wax-like substances with a yellowish-brown color. The chemical bonds in the samples were investigated by FTIR spectroscopy.

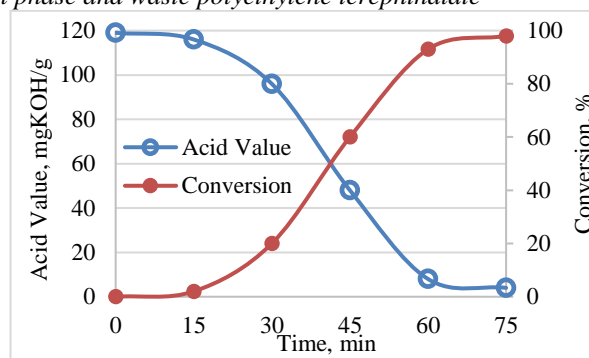
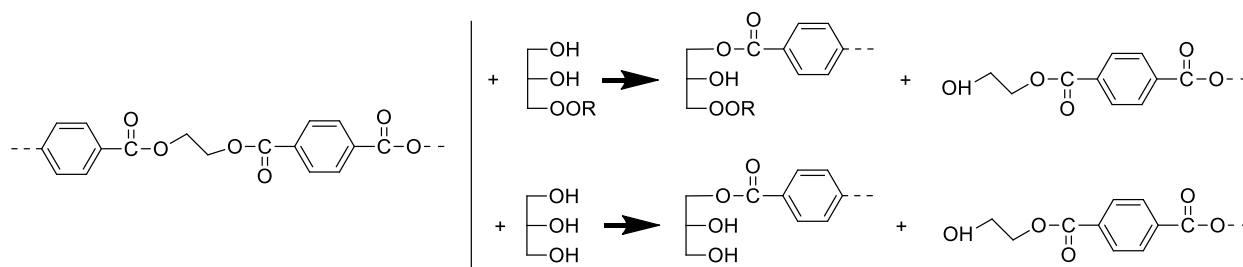
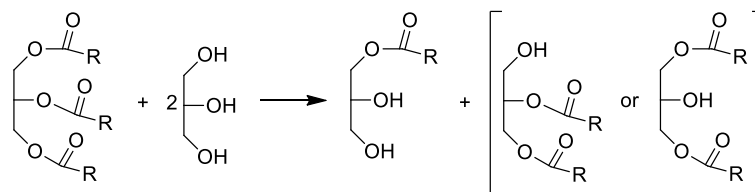


Fig. 1. Change of acid value and conversion during reaction time.



Scheme 2. Solvolysis of PET with monoglycerides and glycerol



Scheme 3. Preparation of glycerides from sunflower oil and glycerol

The simultaneous presence of long hydrocarbon bonds ($2926 - \nu_{as}CH_2$; $2854 - \nu_sCH_2$; $2956 - \nu_{as}CH_3$ and $2878 \text{ cm}^{-1} - \nu_s CH_3$), *p*-substituted benzene rings (1578 and 1506 cm^{-1}), esters ($1724 \text{ cm}^{-1} - \nu_{C=O}$) and hydroxyl groups ($3600-3100 \text{ cm}^{-1} - \nu_{OH}$), proves the process of depolymerization of PET and obtaining of polyester polyols.

At the end of the second stage in the reaction system there are polyester polyols, mono- and diglycerides, glycerol and potassium phosphate.

The third stage was esterification with phthalic anhydride. Reactions were followed with AV. Samples were taken every 30 min to determine the AV.

In the prepared alkyds potassium phosphate was still present as a contaminant. For the purposes of the analysis, samples were taken. They were purified by twice washing with water, which is a solvent for potassium phosphate. The samples were named Alk-1S12 and Alk-1S20.

Preparation of alkyds Alk-RS12 and Alk-RS20

Reference alkyds were synthesized by a two-stage alcoholysis-esterification method. The first stage was alcoholysis of unrefined sunflower oil and glycerol (Scheme 3).

Monitoring of reaction was made by methanol test every 15 min.

The second step was esterification with phthalic anhydride. In order to provide a structure identical to that of Alk-1S12 and Alk-1S20, ethylene glycol was added. The quantity was calculated to correspond to the amount of added PET (Table 3). The condensation process was followed by the acid value. For the purposes of the analysis, samples were taken. They are viscous liquid substances with light brown color.

Study of alkyds structure

Chemical bonds in alkyds were established by FTIR spectroscopy (Fig. 2.).

It is visible that in all spectra the doublet at 1601 and 1581 cm^{-1} , which corresponds to *o*-substituted Ar-rings, appeared. Some absorption bands were

registered only in the spectra for Alk-1S12, and Alk-1S20. They were: 1412 cm^{-1} - δCH_2 ; 1136 $\delta(\text{C}-\text{O}-\text{C})$ in esters, 875 and 728 for $\gamma =(\text{C}-\text{H})$ in p-substituted Ar-rings. These bands correspond to the bonds in the ethylene terephthalate units.

Results from FTIR spectroscopy were confirmed by the ^1H NMR analysis. In the ^1H NMR spectra of Alk-1S20 and Alk-RS20 the following signals appeared: δ 0.89 ppm for protons

in the CH_3 ; δ 5.35 – 5.37 ppm for vinyl protons in $\text{CH} = \text{CH}$; δ 7.5-7.9 ppm for aromatic protons of the o-phthalate esters; δ 3.6-4.0 ppm corresponding to methylene and methine protons in the CH_2OH and CHOH groups; multiplets at δ 4.3-4.4 and δ 4.1-4.2 ppm for methylene protons in $\text{CH}_2\text{CO}-\text{Ar}$ and $\text{CH}_2\text{CO}-\text{R}$ groups, δ 5.27 ppm for methine protons in $\text{CH}-\text{O}-\text{CO}$ groups.

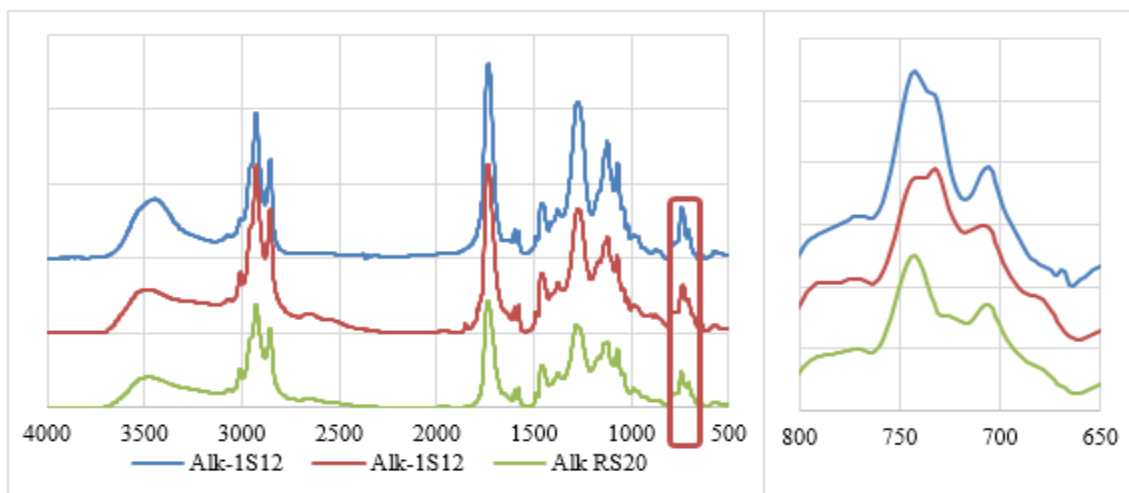


Fig. 2. FTIR spectra of Alk-1S12, Alk-1S20 and Alk-RS20

In Alk-1S20 spectrum, a signal at δ 8.13 ppm for protons in p-substituted benzene rings appeared. Gathered data confirmed the alkyd structure and the presence of ethylene terephthalate moieties in the alkyd structure.

Preparation and study of alkyd resins

From the obtained four medium-oil alkyds, 60% solutions in xylene were prepared. The last contaminant in Alk-1S12 and Alk-1S20 was potassium phosphate. It was removed by filtration.

For accelerated drying of the alkyd resins obtained, 1% of Pb and 0.1% of Co were added. Films were air-dried at 25°C for 24 h and then heated to 110°C for 2 h. Drying degree, hardness and adhesion were evaluated (Table 4).

It is visible that alkyd resins, obtained from Alk-1S12 and Alk-1S20 had better drying degree and higher hardness than reference resins.

Chemical resistance of the films was studied (Table 5).

Results from Table 5 showed that distilled water and sodium chloride solution had no effect on alkyd resins. Acids, however, made films opaque. The strongest effect had the alkali solution. It can be explained with the fact that the alkyds are polyesters which are easily hydrolyzed with hydroxides.

Table 4. Drying degree, hardness and adhesion of the films from alkyd resins

Alkyd resin	Drying degree	Hardness	Adhesion
Alk-1S12	5	1H	46
Alk-1S20	5	1H	46
Alk-RS12	4	HB	46
Alk-RS20	4	HB	46

Table 5. Chemical resistance of the films from alkyd resins

Alkyd resin	Solution			
	Distilled water	NaCl (5%)	H ₂ SO ₄ (0.1 M)	KOH (0.1M)
Alk-1S12	a	a	b	c
Alk-1S20	a	a	b	c
Alk-RS12	a	a	b	c
Alk-RS20	a	a	b	c

a - no change; b - opaque film; c - partially dissolved film

CONCLUSIONS

All organic substances in the glycerol phase can be used for preparation of alkyds. This utilisation can help stabilizing biodiesel industry. Waste PET was also successfully incorporated into the alkyd

composition, reducing the cost of surface coatings - part of the glycerol phthalate was replaced by polyester waste. It was found that the physical properties of alkyd resins are superior to those of reference alkyd resins. Glycerol phase and depolymerization products of waste PET are suitable for manufacturing of alkyd resins, ensuring sustainable development of two expanding industries.

REFERENCES

1. D. İ. Çağlar, E. Baştürk, B. Oktay, M. V. Kahraman, *Prog. Org. Coat.*, **77**(1), 81 (2014).
2. P. P. Chiplunkar, A. P. Pratap, *Prog. Org. Coat.*, **93**, 61 (2016).
3. X. Zheng, L. Yang, K. Wang, *Adv. Mater. Res.*, **239-242**, 1721 (2011).
4. <https://articles.extension.org/pages/29605/sunflowers-for-biofuel-production>.
5. E. N. Hidawati, A. M. M. Sakinah, *International Journal of Chemical and Environmental Engineering*, **2**(5), 309 (2011).
6. H. W. Tan, A. R. A. Aziz, M. K. Aroua, *Renew. Sustain. Energy Rev.*, **27**, 118 (2013).
7. A. B. Leoneti, V. A. Leoneti, S.V.W.B. Oliveira, *Renew. Energy*, **45**,138 (2012).
8. <https://www.enviengroup.eu/images/specifikacije-kvality/g-faza/Quality-specification-of-glycerol-phase-Biodizel-Vukovar.pdf>.
9. A. Hejna, P. Kosmela, K. Formela, Ł. Piszczyk, J. T. Haponiuk, *Renew. Sustain. Energy Rev.*, **66**, 449 (2016).
10. M. A. Mohsin, T. Abdulrehman, Y. Haik, *Int. J. Chem. Eng.*, **2017**, 1 (2017).
11. A. K. Khan, S. Chandra, *Paint India*, **45**,33 (1995).
12. G. Guclu, M. Orbay, *Prog. Org. Coat.*, **65**, 362 (2009).
13. N. S. Todorov, M. F. Radenkov, D. D. Todorova, *Journal of Chemical Technology and Metallurgy*, **50**, (3), 240 (2015).
14. S. Y. Tawfik, M. W. Sabaa, R. T. Botros, *Pigment & Resin Technology*, **46** (5), 408 (2017).
15. ISO 12937:2000. Petroleum products - Determination of water - Coulometric Karl Fischer titration method (2000).
16. ISO 3987:2000. Petroleum products - Determination of sulfated ash in lubricating oil and additives (2010).
17. ISO 2464:1973. Crude glycerol for industrial use - Calculation of matter (Organic) Non Glycerol (MONG) (1973). Revised 2007.
18. ASTM D1544 – 04. Standard Test Method for Color of Transparent Liquids (Gardner Color Scale) (2018).
19. AOCS Official Method Ca5a-40. Free Fatty Acids in Crude and Refined Fats and Oils (2017).
20. ISO 3961:2013. Animal and vegetable fats and oils - Determination of iodine value (2013). Revised 2018.
21. ISO 660:2009. Animal and vegetable fats and oils - Determination of acid value and acidity (2009). Confirmed 2014.
22. ISO 6883:2017. Animal and vegetable fats and oils - Determination of conventional mass per volume (2017).
23. ISO 9117-5:2012. Paints and varnishes - Drying tests - Part 5: Modified Bandow-Wolff test (2012).
24. ASTM D3363-05. Standard Test Method for Film Hardness by Pencil Test (2005). Confirmed 2011.
25. ASTM D3359–17. Standard Test Methods for Rating Adhesion by Tape Test (2017).
26. ASTM D 1647-00. Test Methods for Resistance of Dried Films of Varnishes to Water and Alkali (2000).

Determination of carbonyl compounds in tobacco smoke and factors influencing their composition

M. H. Docheva*, D. M. Kirkova, Y. G. Kochev, A. B. Stoilova

Tobacco and Tobacco Products Institute, Markovo 4108, Plovdiv, Bulgaria

Received October 31, 2018; Revised December 18, 2018

Over 500 carbonyl compounds were identified in tobacco smoke, but ten of them were classified as probably and possibly carcinogenic to humans. The aim of this study was to determine the content of carbonyl compounds in tobacco smoke of different varieties of Bulgarian tobaccos and industrial cigarettes brands and to establish the influence of the type of tobacco and the cigarette filter on their composition. Basic carbonyl compounds such as acetaldehyde, formaldehyde, acetone, propionaldehyde and acrolein were quantified by HPLC. The highest carbonyl content in tobacco smoke was found in Virginia tobacco varieties (average 1003 ± 129 $\mu\text{g}/\text{cig}$), followed by Oriental tobacco varieties (average 868 ± 112 $\mu\text{g}/\text{cig}$) and Burley tobacco varieties (850 ± 47 $\mu\text{g}/\text{cig}$). The greatest variation in the total amount of carbonyls and individual components - formaldehyde, acetaldehyde and acetone was reported in tobacco smoke from Oriental tobacco varieties. The activation of menthol capsule in the filter, the charcoal filter and recessed and charcoal filter system increased the carbonyl content in cigarette brands compared to the acetate filter. Cigarettes with filter ventilation had lower carbonyl content in tobacco smoke compared to those with unventilated filters. Positive correlations between total carbonyl content and tar, nicotine, CO and individual carbonyls in cigarette brands were found.

Keywords: carbonyl compounds, tobacco, cigarette brands, cigarette filter, filter ventilation

INTRODUCTION

Tobacco smoke is a dynamic aerosol system including particulate phase and gas phase and consists of more than 5000 chemical components [1]. The particulate phase contains of well-known constituents such as nicotine, tar, tobacco-specific N-nitrosamines (TSNA), polycyclic aromatic hydrocarbons (PAH), etc. The gas phase contains highly reactive oxygen species (ROS) and various carbonyl compounds that play a significant role in cigarette smoke toxicology (IARC) [2-4].

Due to the complex composition of cigarette smoke, WHO study group on tobacco product regulation (TobReg) proposed beginning regulation with a limited set of high-priority toxic emissions, except tar, nicotine and CO (TNCO) [5, 6]. One of the chemical classes identified by TobReg as a priority, due to their impact on human health, are the volatile aldehydes [6, 7].

More than 500 carbonyl compounds have been identified and some of them have been classified as probably and possibly carcinogenic to humans by the International Agency for Research of Cancer, including formaldehyde, acetaldehyde, acrolein [3, 4].

Several analytical methods (HPLC/UV-VIS; HPLC/DAD, UHPLC/MS, GC/MS) and derivatization agents (2, 4-dinitrophenylhydrazine, 1-methyl-2-pyrazoline, cysteamine-thiazolidine,

pentafluorophenyl hydrazine), used to investigate the carbonyl content in tobacco smoke, were reported in the literature [4, 6, 8]. Coresta special analytes sub group recommended derivatization with 2,4-dinitro-phenylhydrazine (DNPH) because it was the most suitable agent and thus was chosen as the basis of the Coresta recommended method [9].

The aim of this study was to investigate the content of carbonyl compounds in tobacco smoke and to establish the influence of tobacco type and cigarette filter on their composition.

EXPERIMENTAL

Reagents and equipment

Formaldehyde (CAS number 50-00-0), acetaldehyde (CAS number 75-07-0), acetone (CAS number 67-64-1), propionaldehyde (CAS number 123-38-6), acrolein (CAS number 102-07-8), 2,4-dinitrophenylhydrazine (CAS number 119-26-6), nicotine (CAS number 54-11-5); methanol (CH_3OH), acetonitrile (CH_3CN) and perchloric acid (HClO_4) were purchased from Merck, Germany.

- Single-channel smoking machine Borgwaldt, Germany;

- 8-channel linear cigarette smoking machine Filtrona 302, England;

- Gas chromatograph equipped with flame ionization detector and thermal conductivity detector GC-FID/TCD, Agilent 7890A; - HPLC

* To whom all correspondence should be sent.
E-mail: margarita_1980@abv.bg

M.H. Docheva et al.: Determination of carbonyl compounds in tobacco smoke and factors influencing ... with UV/VIS detector, Perkin Elmer, USA.

Material

Dry leaves of Oriental tobaccos (Krumovgrad 988 – Kr988, Krumovgrad 90 – Kr90, Muymuynovo seme – Ms, Djebel basma 1 – Db1, Basma 13- B13, Basma 79 – B79, Linia 30 –L30, Srednogorska yaka - Sy, Plovdiv 380 – P1380, Kozarsko 339 – Kz339), Virginia tobaccos (Virginia 385 – V385, Koker 254 – K254 and Linia 543- L254) and Burley tobaccos (Burley – Parvomay - BPar, Burley – Haskovo – BH, Burley – Plovdiv - BPI) were used as a material. The cultivars were from the collection of the Tobacco and Tobacco Products Institute, Plovdiv, Bulgaria. Laboratory cigarettes from all tobacco varieties were made.

Three industrial cigarette brands A, B and C with different composition and ventilation of filters were used for analysis. The description of the samples is presented in Table 1.

Table 1. Description of the analyzed cigarette brands

Cigarette	Cigarette filter	Filter ventilation
A1Ø	Acetate filter	No
A1V	Acetate filter	35 %
A2	Acetate filter with activated menthol capsule	No
A2V	Acetate filter with activated menthol capsule	35 %
B1Ø	Acetate filter	No
B2	Acetate and charcoal filter (two sectors filter)	No
B2V	Acetate and charcoal filter (two sectors filter)	30 %
C1Ø	Acetate filter	No
C1V	Acetate filter	40 %
C2	Acetate, recessed and charcoal filter system (three sectors filters)	No
C2V	Acetate, recessed and charcoal filter system (three sectors filters)	40 %
Ø -controls		

Methods

Determination of carbonyl compounds in tobacco smoke by HPLC-UV/VIS - Coresta recommended method №74, 2018 with some modifications [9]. Two cigarettes were smoked on a single-channel smoking machine according to ISO 3308-2012, that was fitted with impinger, containing 40 ml of acidified solution of 2,4-dinitrophenylhydrazine with concentration of 3.396 mg/ml. The carbonyls in tobacco smoke were trapped by passing each puff through an impinge. The solution was left in the dark for at least 5 hours

until the reaction was complete and the carbonyl hydrazone formed.

The high performance liquid chromatography (HPLC) equipment used was Perkin Elmer equipped with binary pump and UV/VIS detector. The chromatographic analysis was performed on an analytical column “Kromasil” C₁₈, 5 µm, 150 mm. The mobile phase composition was: A = CH₃OH:H₂O (60:40); B = CH₃OH:H₂O (80:20). Gradient elution profile was 100% A, 0 min; 30 min to 0 % A, λ=360 nm. All the analyses were conducted in triplicate.

Determination of tar, nicotine and carbon monoxide (TNCO) in tobacco smoke according to ISO 4387-2000, ISO 10315-2013 and ISO 8454-2007. The automatic process of smoking cigarettes was performed on the smoking machine according to ISO 3308-2012 [10]. The cigarettes were smoked under ISO smoking conditions (puff volume – 35 ± 0.3 ml, puffs frequency – once per minute, puff duration - 2.0±0.2 s) and the total particulate matter (TPM) as specified in ISO 4387-2000 was collected [11]. Gas chromatograph with flame ionization detector for determination of nicotine and NDIR analyzer for determination of CO in tobacco smoke was used [12, 13].

RESULTS AND DISCUSSION

Carbonyl content of different tobaccos and cigarette brands

Influence of type of tobacco. The content of carbonyl compound in the gas phase of tobacco smoke of Bulgarian tobaccos of three variety groups – Oriental, Virginia and Burley was investigated. Table 2 shows both the individual components of carbonyl compounds in tobacco smoke - formaldehyde, acetaldehyde, acetone, propionaldehyde and acrolein and the total carbonyl content (TCC).

Acetaldehyde and acetone with a maximum content of 655±98 µg/cig (K254) and 344±52 µg/cig (BPar) respectively were found to be predominant in the carbonyl content for all tobaccos, followed by acrolein - 86±17 µg/cig (Sy), formaldehyde - 80±20 µg/cig (Sy) and propionaldehyde - 48±10 µg/cig (Sy). The highest content of acetaldehyde, propionaldehyde and acrolein was reported in Virginia tobacco smoke, acetone - in Burley tobacco smoke, and formaldehyde in Oriental tobacco smoke. The largest variation of formaldehyde from 4±1 µg/cig (BPar) to 80±20 µg/cig (Sy) was found.

The total carbonyl content ranges from 723±144 µg/cig (Kr988) to 1137±227 µg/cig (K254). The largest amount of carbonyl compounds, as average

content, was reported in tobacco smoke of Virginia tobacco varieties, while the smallest - in Burley tobacco varieties. The largest variation in total carbonyl content of Oriental variety emissions -

from 723±144 µg/cig (K988) to 1064±212 µg/cig (Sy), was due to the diversity of ecotypes and varieties.

Table 2. Content of carbonyl compounds in tobacco smoke of Bulgarian tobaccos, µg/cig±SD

Tobaccos		Form-aldehyde	Acet-aldehyde	Acetone	Propion-aldehyde	Acrolein	TCC
Oriental tobaccos	Kr988	16±4	410±61	222±33	32±6	43±9	723±144
	Kr90	16±4	558±84	316±47	42±8	55±11	987±197
	Ms	12±3	451±68	290±43	34±7	55±11	841±168
	Db1	44±11	410±61	260±39	31±6	59±12	804±160
	B13	20±5	397±59	283±42	31±6	53±11	784±156
	B79	28±7	479±72	280±42	36±7	64±13	887±177
	L30	16±4	530±79	281±42	40±8	66±13	933±186
	Sy	80±20	560±84	290±43	48±10	86±17	1064±212
	Pl380	13±3	379±57	254±38	32±6	48±10	726±145
Virginia tobaccos	Kz339	46±11	487±73	282±42	39±8	72±14	926±185
	V385	14±3	600±90	275±41	39±8	63±13	991±198
	K254	28±7	655±98	331±50	44±9	79±16	1137±227
Burley tobaccos	L543	15±4	522±78	241±36	44±9	58±12	880±176
	BPar	4±1	373±56	344±52	29±6	46±9	796±159
	BH	7±2	524±79	258±39	37±7	55±11	881±176
	BPl	7±2	453±68	330±49	28±6	55±11	873±174

Table 3. Content of carbonyl compounds in tobacco smoke of different cigarette brands, µg/cig±SD

Cigarette	Form-aldehyde	Acetaldehyde	Acetone	Propion-aldehyde	Acrolein	TCC
A1Ø	40±10	481±72	237±35	33±7	61±12	852±170
A1V	17±4	323±48	184±28	24±5	43±9	591±118
A2	55±14	524±79	253±38	34±7	77±15	943±188
A2V	23±6	286±43	156±23	20±4	39±8	523±104
B1Ø	18±4	458±69	234±35	36±7	56±11	802±160
B2	26±6	484±73	245±37	33±7	62±12	851±170
B2V	11±3	335±50	177±26	24±5	41±8	588±117
C1Ø	18±4	510±76	274±41	34±7	60±12	896±179
C1V	8±2	186±28	125±19	14±3	20±4	353±70
C2	24±6	541±81	261±39	37±7	70±14	933±186
C2V	9±2	298±45	163±24	24±5	36±7	530±106

Carbonyl compounds in tobacco smoke are usually generated by pyrolysis of the saccharides (sugars and cellulose) or emitted directly from unburnt tobacco [14]. The result obtained for the carbonyl content was comparable to the sugar content of the tobaccos leaves [15, 16]. Virginia tobacco was characterized with the highest content of sugars while Burley tobacco – with the lowest [1].

The content of carbonyl compounds in tobacco smoke of different cigarette brands is shown in Table 3. The qualitative composition of the carbonyl compounds in cigarette brands was the same like tobaccos – with the highest content was acetaldehyde, following acetone, acrolein, propionaldehyde and formaldehyde. The total carbonyl content varied from 353±70 µg/cig (C1V) to 943±188 µg/cig (A2), which was lower than that

of tobaccos and due to the influence of different cigarette filters.

Influence of type of cigarette filters

The most widely used are acetate filters. In recent years, however, there has been a wide variety of cigarette filters - acetate filters containing activated charcoal or menthol capsule, recess filters and other. Sometimes the filters are combined and consist of two or three sectors. Filters can reduce "tar" and nicotine smoke yields up to 50%, with a higher removal rate for other classes of compounds (e.g. phenols), but are ineffective in filtering toxins such as carbon monoxide [17]. An investigation on the effect of filters on carbonyl compounds is insufficient.

In our study, we investigated filters with acetate filter, acetate filter with menthol capsule and combined filters (Table 1). Cigarette with different

filter composition (activated menthol capsule, two and three sectors) increased the carbonyl content in tobacco smoke $943 \pm 188 \mu\text{g}/\text{cig}$ (A2), $851 \pm 170 \mu\text{g}/\text{cig}$ (B2) and $933 \pm 186 \mu\text{g}/\text{cig}$ (C2), compared to the controls $852 \pm 170 \mu\text{g}/\text{cig}$ (A1Ø), $802 \pm 160 \mu\text{g}/\text{cig}$ (B1Ø) and $896 \pm 179 \mu\text{g}/\text{cig}$ (C1Ø) (Table 3).

The highest content of formaldehyde ($55 \pm 14 \mu\text{g}/\text{cig}$) and acrolein ($77 \pm 15 \mu\text{g}/\text{cig}$) was reported upon the activation of the menthol capsule in filter - cigarette brand A2 and of the acetaldehyde ($541 \pm 81 \mu\text{g}/\text{cig}$), acetone ($261 \pm 39 \mu\text{g}/\text{cig}$) and propionaldehyde ($37 \pm 7 \mu\text{g}/\text{cig}$) in the C2 cigarettes (three-sector filter).

Various results were described for the content of carbonyl compounds in tobacco smoke. This is due to the different methods and derivatization agents that used authors. Pang and Lewis [4] found that acetaldehyde was predominant, varying from $72.6 \mu\text{g}/\text{cig}$ to $187 \mu\text{g}/\text{cig}$; the content of formaldehyde, acetone and propionaldehyde was above $20 \mu\text{g}/\text{cig}$, while acrolein varied from 10 to $20 \mu\text{g}/\text{cig}$. The studies were performed by GC/MS and pentafluorophenyl hydrazin derivatization [4].

Fujioka [8] quantified carbonyl compounds in 14 cigarette brands by derivatization, solid phase extraction and gas chromatography methods with a nitrogen phosphorus detector. The content of formaldehyde varied from $87 \pm 3 \mu\text{g}/\text{cig}$ to $243 \pm 11 \mu\text{g}/\text{cig}$, acetaldehyde – from $1518 \pm 63 \mu\text{g}/\text{cig}$ to $2101 \pm 28 \mu\text{g}/\text{cig}$; propionaldehyde from $87 \pm 3 \mu\text{g}/\text{cig}$ to $176 \pm \mu\text{g}/\text{cig}$ and acrolein from $285 \pm 22 \mu\text{g}/\text{cig}$ to $468 \pm 17 \mu\text{g}/\text{cig}$ [8].

Influence of filter ventilation

Cigarettes without ventilation and with ventilation of 35% - 40% were analyzed (Table 1). Cigarettes with unventilated acetate filters A1Ø, C1Ø and unventilated filters with different composition A2, B2, C2 had the higher carbonyl content (average $895 \pm 43 \mu\text{g}/\text{cig}$) compared to the ventilated filters A1V, C1V and A2V, B2V, C2V (average $517 \pm 96 \mu\text{g}/\text{cig}$). The results confirmed our previous studies founding that filter ventilation had the most significant impact on reduction of carbonyls in tobacco smoke [18]. The data obtained are consistent with the studies of Pauwels (2018). It was found that trapping the filters vents, thereby eliminating the tip filter ventilation to 0 % lead to an increase in aldehyde yields in cigarette smoke [6].

The influence of filter ventilation on the reduction of carbonyls was so strong that it compensates the greatest expansion for cigarettes with activated menthol capsule in the filter, which was observed in our research. The results are shown in Table 3: Activation of menthol capsules in cigarette filters increased the content of carbonyl compounds in non-ventilated filters A2 ($943 \pm 188 \mu\text{g}/\text{cig}$) compared to the control A1Ø ($852 \pm 170 \mu\text{g}/\text{cig}$), while cigarette with ventilation filters A2V ($523 \pm 104 \mu\text{g}/\text{cig}$) contained lower carbonyls than A1V ($591 \pm 118 \mu\text{g}/\text{cig}$).

Content of TNCO of different tobaccos and cigarette brands

The content of tar, nicotine and CO of different tobaccos and cigarette brands is presented on fig. 1.

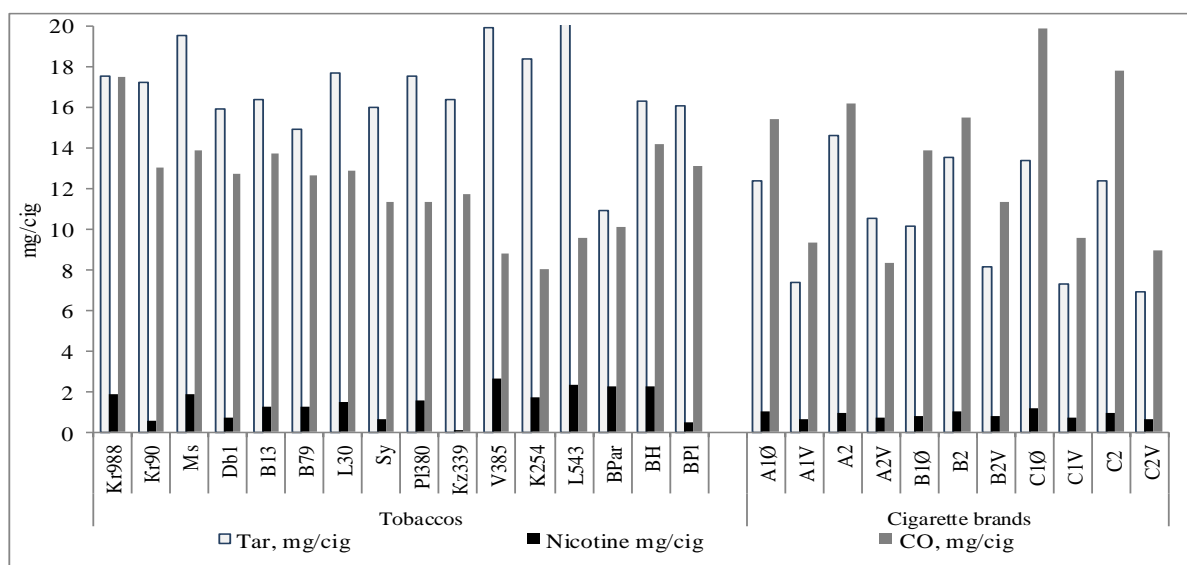


Fig. 1. Content of TNCO of different tobaccos and cigarette brands

Tobaccos were characterized with higher content of tar (average 17.01±2.38mg/cig) and nicotine (average 1.43±0.75 mg/cig) compared to cigarette brands – average 10.59±2.83 mg/cig, 0.83±0.17 mg/cig, respectively, while CO was approximately the same – average 12.15±2.34 mg/cig for tobaccos and 12.96±3.99 mg/cig for cigarette brands. Cigarette brands contain blends of different types of tobaccos and additives. Three main types of tobacco are commonly used in these blends; Virginia, Burley and Oriental in different ratios and over 500 additives, resulting in reduction in tar and nicotine content [19].

The results show the highest average tar for Virginia tobaccos (20.0±1.65 mg/cig), followed by Oriental tobaccos (16.9±1.27 mg/cig) and Burley tobaccos (14.4±3.06 mg/cig). The average nicotine content of smoke in tobaccos decreases as follows: Virginia (2.19±0.45 mg/cig), Burley (1.67±1.01 mg/cig), Oriental (1.12±0.59 mg/cig), while CO decreased in the order: Oriental tobaccos (13.06±1.80 mg/cig), Burley tobaccos (12.5±2.12 mg/cig) and Virginia tobaccos (8.77±0.8 mg/cig).

Trapping the cigarette filter led to increased tar yields between 39 % and 84 %, nicotine yield between 26 % and 72 % and CO yield between 37 % and 108 % (Fig. 1). The results are in accordance with Pauwels *et al.* [6].

Activation of the menthol capsule in the filter and the two-sector filter increase the TNCO content

of tobacco smoke compared to controls, while the three-section filter decreases them (Fig. 1).

Correlation between carbonyl content and TNCO

Additionally, the ratio between total carbonyl content (TCC) and individual carbonyls and TCC and TNCO in tobaccos and cigarette brands was investigated.

A better correlation between TCC and individual carbonyl components of cigarette brands was found compared to tobaccos. There was a strong correlation between TCC and acetaldehyde ($R^2=0.9957$), acetone ($R^2=0.9710$), propionaldehyde ($R^2=0.9232$) and acrolein ($R^2=0.9312$) in tobacco smoke of cigarette brands (Table 4). No correlation was observed between TCC and formaldehyde both in tobaccos and in cigarette brands. The content of formaldehyde in tobaccos and cigarette brands varied widely – from 4±1 µg/cig to 80±20 µg/cig in tobaccos and from 8±2 µg/cig to 55±14 µg/cig in cigarette brands (Table 3) and therefore it was difficult to find correlations.

The correlation between TCC and CO ($R^2=0.8225$), TCC and tar ($R^2=0.7671$) and TCC and nicotine content ($R^2=0.6584$) only in different cigarette brands was established (Table 5). Positive correlations between total carbonyl content, tar yield and CO yield was found by Pang and Lewis too [4]. Correlations between TCC and TNCO in tobaccos were not detected.

Table 4. Correlation between TCC and individual carbonyls

Samples		Formaldehyde	Acetaldehyde	Acetone	Propionaldehyde	Acrolein
Tobaccos	TCC	0.1792	0.8690	0.2007	0.6488	0.7216
Cigarette brands	TCC	0.3917	0.9957	0.9710	0.9232	0.9312

Table 5. Correlation between TCC and TNCO

Samples		Tar	Nicotine	CO
Tobaccos	TCC	0.0494	0.0209	0.3201
Cigarette brands	TCC	0.7671	0.6584	0.8225

CONCLUSIONS

The content of five main carbonyl components in tobacco smoke of tobaccos and cigarette brands such as formaldehyde, acetaldehyde, acetone, propionaldehyde and acrolein and factors influencing their composition were investigated. The qualitative composition of the carbonyl compounds in tobaccos and cigarette brands was the same. The highest content of acetaldehyde, followed by acetone, acrolein, propionaldehyde and formaldehyde was found in tobacco and cigarette brands. The highest carbonyl content in tobacco

smoke of Virginia tobacco varieties was established, followed by Oriental tobacco varieties and Burley tobacco varieties. The total carbonyl content in the investigated cigarette brands was lower than that of tobaccos. The activation of menthol capsule in the filter, the charcoal filter and recessed and charcoal filter system increased the carbonyl content in cigarette brands compared to the acetate filter. Cigarettes with filters ventilation had lower carbonyl content in tobacco smoke compared to those with unventilated filters. Positive correlations between total emission of carbonyls,

M.H. Docheva et al.: Determination of carbonyl compounds in tobacco smoke and factors influencing ...
tar, nicotine, CO and individual carbonyl content only in cigarette brands were found.

REFERENCES

1. J. Leffingwell, *Leffingwell Reports*, 1 (2), 1 (2001).
2. IARC working group on the evaluation of carcinogenic risks to humans, *IARC Monogr. Eval. Carcinog. Risks Hum.*, **83**, 1 (2004).
3. A. Rodgman, T. Perfetti, CRC Press, USA, 2013.
4. X. Pang, A. Lewis, *Science of Total Environmental* **409**, 5000 (2011).
5. Tobacco Products Directive (2014/40/EU), *Official Journal of the European Union*, EU, 2014.
6. C. Pauwels, W. Klerx, J. Pennings, A. Boots, F.J. van Schooten, A. Opperhuizen, R. Talhout, *Chem. Res. Toxicol.* **31**, 462 (2018).
7. World Health Organization. *Second report of a WHO study group*, 2008, p. 1.
8. K. Fujioka, T. Shibamoto, *Environ. Toxicol.* **21** (1), 47 (2006).
9. Coresta recommended method № 74. Determination of selected carbonyls in mainstream cigarette smoke by HPLC, 2018.
10. ISO 3308:2012. Routine analytical cigarette-smoking machine - Definitions and standard conditions.
11. ISO 4387:2000. Cigarettes - Determination of total and nicotine-free dry particulate matter using a routine analytical smoking machine.
12. ISO 10315:2013. Cigarettes - Determination of nicotine in smoke condensates - Gas-chromatographic method.
13. ISO 8454:2007. Cigarettes - Determination of carbon monoxide in the vapour phase of cigarette smoke - NDIR method.
14. R. Baker, *Food Chem. Toxicol.*, **42**, 53 (2004).
15. E. Roemer, K. Schorp, J. Piade, I. Seeman, E. Leyden, J. Haussmann, *Crit. Rev. Toxicol.* **42**, 244 (2012).
16. P. Cheah, PhD Thesis, Maastricht, 2016.
17. H. Bradford, *Tobacco Control*, 20 (1): 10-16 (2011).
18. A. Stoilova, M. Docheva *Jubilee International Scientific Conference "70 Years of Tobacco and Tobacco Products Institute"*, 06 – 08 November, Plovdiv, Bulgaria (2014).
19. N. Djulancic, V. Radojicic, M. Sbinovska, *Arh. Hig. Rada Toksikol.*, **64**, 107 (2013).

HPLC analysis of flavonoids from *Scutellaria altissima*

Y. Georgieva¹, M. Katsarova², K. Gercheva³, P. Bozov⁴, S. Dimitrova^{2*}

¹Department of Pharmacognosy and Pharmaceutical Chemistry, Faculty of Pharmacy, Medical University, 15A V. Aprilov Blvd, Plovdiv, Bulgaria

²Department of Bioorganic Chemistry, Faculty of Pharmacy, Medical University, 15A V. Aprilov Blvd, Plovdiv, Bulgaria

³Faculty of Medicine, Medical University, 15A V. Aprilov Blvd, Plovdiv, Bulgaria

⁴Department of Biochemistry and Microbiology, Faculty of Biology, Plovdiv University, 24 Tzar Assen str., Plovdiv, Bulgaria

Received November 8, 2018; Revised December 20, 2018

High-performance liquid chromatographic method with gradient elution and diode-array detection was developed to quantify flavonoids (scutellarin, baicalin, baicalein, wogonin, wogonoside, luteolin, chrysin) and verbascoside. The separation was performed on a Hitachi C18 AQ (250 mm × 4.6 mm, 5 μm) column with detection at 330 nm for verbascoside, scutellarin and 275 nm for baicalin, baicalein, wogonin, wogonoside, luteolin, chrysin. Validation procedures were conducted and the method was proven to be precise, accurate and sensitive. The limits of detection were from 0.067 to 0.229 μg/ml. The relative standard deviations ranged from 3.78 % to 7.78 %. Recoveries were between 96.5% and 103.2%. The method was applied to quantification of mentioned above substances in extracts of *Scutellaria altissima* from the area of Mezek. This is the first study in Bulgaria on the flavonoid composition of *Scutellaria altissima*

Keywords: HPLC-DAD, validation, flavonoids, verbascoside, *Scutellaria altissima*

INTRODUCTION

The plants of the genus *Scutellaria* belong to the Lamiaceae family and, thanks to the biologically active compounds contained therein, are used in the treatment of a number of diseases [1]. In 1910, the first flavonoid scutellarein was isolated from *Scutellaria altissima* [2]. To date, about 35 species of *Scutellaria* have been studied and more than 295 compounds have been identified, including flavonoids and diterpenes as major biologically active substances. One of the most famous species of this genus is *Scutellaria baicalensis*, also known as "Baical Scullcap", which is widely used in the traditional medicine of Russia and several East Asian countries [1, 3] and is listed in various Pharmacopoeias. According to European Pharmacopoeias. According to European Pharmacopoeia 8.0, the content of the baicalin in *Scutellariae Baicalensis* Radix should be not less than 9% (dried drug) [4].

There are eight species in Bulgaria, one of which is *Scutellaria altissima*, from which only terpene compounds have been isolated and identified and their cytotoxic and antifeedant activity has been proved [5]. So far, no studies of polyphenol compounds or of the biological activity of their aqueous and ethanol extracts have been carried out. This gives grounds for conducting a study in this direction which will enrich the information about the composition of the Bulgarian

Scutellaria altissima.

Chromatographic methods are some of the most commonly used methods for analyzing biologically active substances [6]. Gao *et al.* (2008) offer an HPLC method for the determination of the flavonoids baicalin, baicalein and wogonin in tinctures of two species of *Scutellaria* - aerial part of *Scutellaria lateriflora* and root of *Scutellaria baicalensis* [7]. A number of flavonoids, the most important of which are scutellarin, baicaline and chrysin, are identified in *Scutellaria galericulata* from 17 regions in eastern Poland by an HPLC method [8].

In the present work, a high-performance liquid chromatographic method with gradient elution and diode-array detection was developed and validated to quantify flavonoids (scutellarin, baicalin, baicalein, wogonin, wogonoside, luteolin, chrysin) and verbascoside. The method was applied to the quantification of the above mentioned substances in extracts of *Scutellaria altissima* from the area of Mezek, Bulgaria.

EXPERIMENTAL

Chemicals

Standards of flavonoids (scutellarin, baicalin, baicalein, wogonin, wogonoside, luteolin, chrysin), and verbascoside were purchased from Sigma-Aldrich (Germany). Methanol and acetonitrile (HPLC gradient grade) were purchased from

* To whom all correspondence should be sent.
E-mail: szd@abv.bg

Sigma-Aldrich (Germany). Water was obtained from a Milli-Q Gradient water purification system (Milipore, Barnstead).

Plant material

Aerial parts of *Scutellaria altissima* were collected during flowering in June 2017, from the area of Mezek, Bulgaria. Collected raw material was dried at 25°C. A voucher specimen (n.17494) was deposited in the Herbarium of the University of Agriculture, Plovdiv, Bulgaria.

Samples

Dried plant material was powdered and 0.2 g of each of it were extracted with 10 ml of distilled water, 70% ethanol, 96% ethanol and methanol, respectively. The extraction was performed at room temperature 25 °C for 24 hours. The obtained extracts were filtered through a microfilter (0.25 µm) and injected into the HPLC system. For each sample, the complete procedure was carried out in triplicate and the standard deviation was calculated.

HPLC analysis

The HPLC system was composed of a ProStar 230 solvent delivery module and photodiode array detector model 335 and Hitachi C18 AQ (250 mm × 4.6 mm, 5 µm) column. A solvent system including deionized water (A) adjusted to pH 3.0 with phosphoric acid and acetonitrile:methanol 40:60 (B) was used in the following gradient mode: 0-25 min 75A / 25B - 10A / 90B; 25-27 min - 10A / 90B; 27-30 min 10A / 90B - 75A / 25B. The flow rate was 0.9 ml/min and detection was at 330 nm for verbascoside, scutellarin and 275 nm for baicalin, baicalein, wogonin, wogonoside, luteolin, chrysin. The analysis was performed at the same temperature 25 °C. The compounds of interest in the extracts were identified through their retention times, as well as by comparing their absorption spectra with those of standard substances. They were quantified using a calibration curve. Star Chromatography Workstation Version 6.30 (build 5) software was used.

Validation of the HPLC method

Linearity. A linear range was established by using six mixed calibration solutions with concentrations from 2 to 25 µg/ml, each of which was injected three times into the HPLC system. Chromatographic data were then used to build the calibration curve of peak area to the concentration of each standard substance. The coefficients of determination were used as the measure of linearity.

Limit of detection (LOD) and limit of quantification (LOQ). LOD was defined as the lowest concentration of sample determined by the

analytical method to obtain the ratio of signal to noise (3:1). LOQ as the lowest concentration of compounds was determined by injecting a known concentration of the diluted standards until the signal-to-noise ratio reached the ratio of 10:1

Precision. The repeatability of the retention times was determined from all injections of the six mixed calibration solutions made for linearity and were expressed by relative standard deviation.

Accuracy. The accuracy was reported in two ways. The accuracy of the method was assessed by performing a recovery study. Three samples with known concentrations (low, medium and high, different from those analyzed for the calibration) of the investigated compounds were analysed [9]. Results of five replicates of the same sample were averaged and recovery (R^a) was calculated as follows:

$$R^a (\%) = 100 \times \text{found concentration} / \text{true concentration}$$

The evaluation of the matrix effect through the recovery (R^b) was studied too [9,10]. A known amount of standards was added to a certain amount (0.5 g) of plant material, and then extracted and analyzed using the method described above. Five replicates were performed for the test. R^b was determined using the formula:

$$R^b (\%) = 100 \times (C_f - C_u) / C_a$$

where C_f is the concentration detected in the spiked sample, C_u is the concentration detected in the sample before the spiking, and C_a is the true added concentration.

RESULTS AND DISCUSSION

According to the literature, reversed phase columns C18 are some of the most commonly used ones in the separation of polyphenol compounds [8, 11] in combination with mobile phases containing water and acetonitrile, water and methanol or water/acetonitrile/methanol and various values of the pH of the medium [7]. The authors' team has experience in the determination of polyphenol compounds in plant substances and combined extracts [12] and has developed this method on the basis of this experience.

In the present experiment, the Hitachi C18 AQ columns (250 mm × 4.6 mm, 5 µm) and Microsorb-MV C18 column (150×4.6 mm, 5 µm) were used to find the most suitable conditions for the best possible separation of flavonoids (scutellarin, baicalin, baicalein, wogonin, wogonoside, luteolin, chrysin) and the phases: water and acetonitrile and water/acetonitrile/methanol in different gradient modes were used as well. To obtain symmetrical peaks the ratio of acetonitrile to methanol in the organic phase was varied, as well as the pH of the

aqueous phase - 3.0; 3.5 and 3.8. Best results were obtained using a Hitachi C18 AQ column, mobile phase containing water at pH 3 (A) and organic phase 40 acetonitrile / 60 methanol (B). The glycosides scutellarin, baicalin and wogonoside are more polar compounds compared to the aglycones baicalein, wogonin, and chrysin, due to their shorter retention time under the specified process conditions. Verbascoside is retained for an even shorter time compared to them due to its specific structure of caffeoyl phenylethanoid glycoside. Figure 1 shows a chromatogram of a model mixture with a concentration of 10 µg/ml.

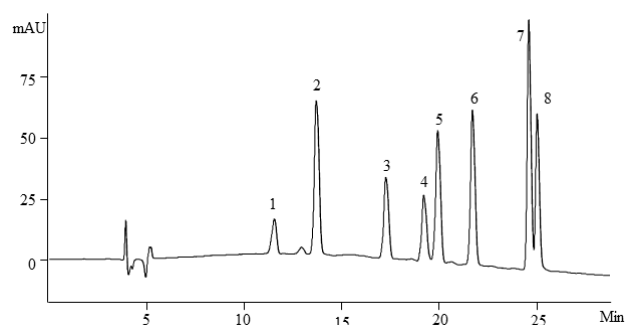


Figure 1. Chromatogram of a model mix (10 µg/ml) of verbascoside-1 and flavonoids (scutellarin-2, baicalin-3, luteolin-4, wogonoside-5, baicalein-6, wogonin-7, chrysin-8)

The validation procedure for the HPLC method includes the determination of the following

parameters: linearity, LOD, LOQ, accuracy and precision. Three series of standard solutions of the pure substances were analyzed under the specified conditions, and it was established that in the chosen concentration ranges (Table 1, column 3) there is a linear relationship between the concentration and the area of the chromatographic peak ($r^2 = 0.9924 \div 0.9985$). This means that the method can be used to quantify the test substances. Regression equations of their standard curve coefficients of determination (r^2) and LOD and LOQ are listed in Table 1.

Recovery experiments were performed to study the reliability and suitability of the method. Three samples with known concentrations of the eight investigated compounds and a spiked sample were analysed (n=5). Recoveries between 96.6% and 102.7% (R^a) were obtained through the first experiment. Good recoveries in the range were obtained by the fortification of the samples at a concentration of 12 µg/ml for verbascoside, scutellarin, baicalin, luteolin, wogonoside, baicalein, wogonin and chrysin through the second experiment. It was evident from the results that the percent recoveries for all the eight analytes of interest were in the range of 96.5%-103.2% (R^b) which is a confirmation for the accuracy of the method [13]. The data are reported in Table 2.

Table 1. Parameters of calibration curves, LOD and LOQ for HPLC method validation

Analyte	λ (nm)	Concentrations (µg/ml)						RT (min)	Regression equations	r^2	LOD (µg/ml)	LOQ (µg/ml)
		S ₁	S ₂	S ₃	S ₄	S ₅	S ₆					
Verbascoside	330	2	5	10	15	20	25	11.81	$y=2.9511e+005x$	0.9937	0.229	0.735
Scutellarin	330	2	5	10	15	20	25	13.98	$y=1.0303e+006x$	0.9924	0.088	0.281
Baicalin	275	2	5	10	15	20	25	17.52	$y=6.4478e+005x$	0.9938	0.102	0.368
Luteolin	275	2	5	10	15	20	25	19.41	$y=4.8185e+005x$	0.9984	0.133	0.409
Wogonoside	275	2	5	10	15	20	25	20.16	$y=9.7821e+005x$	0.9955	0.079	0.269
Baicalein	275	2	5	10	15	20	25	21.90	$y=1.0883e+006x$	0.9974	0.096	0.284
Wogonin	275	2	5	10	15	20	25	24.76	$y=1.4736e+006x$	0.9985	0.067	0.210
Chrysin	275	2	5	10	15	20	25	25.26	$y=1.0024e+006x$	0.9963	0.084	0.278

Table 2. Parameters related to precision and accuracy for HPLC method validation

Analyte	Parameters		Real concentration, (µg/ml)				Concentration found, (µg/ml)			Recovery ^a , (%±0.1)		Recovery ^b , (%±0.1)	
	RSD(%)		4	12	22	4.05	11.52	21.90	101.3	96.1	99.5	97.0	
Verbascoside	7.78		4	12	22	4.05	11.52	21.90	101.3	96.1	99.5	97.0	
Scutellarin	7.01		4	12	22	3.87	12.32	21.79	96.8	102.7	99.0	101.7	
Baicalin	6.76		4	12	22	4.11	11.76	21.97	99.9	98.0	100.1	98.3	
Luteolin	3.78		4	12	22	3.86	11.87	21.66	96.6	98.9	98.5	99.2	
Wogonoside	3.85		4	12	22	3.97	11.76	22.29	99.3	98.0	101.3	103.2	
Baicalein	7.39		4	12	22	4.09	11.82	22.34	102.4	98.5	101.5	102.3	
Wogonin	5.96		4	12	22	3.97	11.94	21.70	99.3	99.5	98.6	99.0	
Chrysin	6.13		4	12	22	3.94	11.99	22.06	98.6	99.9	100.2	96.5	

Analysis of extracts

The relative standard deviation ranged from 3.78 % to 7.78 %. This indicates that the proposed method is accurate and precise. By analyzing the results, presented in Tables 1 and 2, it can be concluded that the developed method is precise, accurate and sensitive enough for the simultaneous quantitative evaluation of eight investigated compounds in dry extracts, plant material or food supplements.

A number of authors have studied the flavonoid composition of various species of the genus *Scutellaria* and have demonstrated the presence of baicalin, baicalein, scutellarin and chrysin in wild growing *Scutellaria galericulata* [8], baicalin, baicalein and wogonin in tinctures derived from *Scutellaria lateriflora* and *Scutellaria baicalensis* [7] as well as baicalin and wogonoside in wild type root culture of *Scutellaria barbata* [11]. Grzegorzczak-Karolak *et al.* have also identified luteolin and verbascoside in *Scutellaria altissima* callus cultures [14, 15] in addition to the baicalin and wogonoside which are characteristic of the species. The developed method was applied to the quantification of flavonoids (scutellarin, baicalin, baicalein, wogonin, wogonoside, luteolin, chrysin) and verbascoside in *Scutellaria altissima* extracts. For this purpose, aqueous, methanolic and ethanol extracts of dry plant material were prepared. The results we obtained show that they contain the specific to the genus *Scutellaria* scutellarin, baicalin, baicalein, as well as wogonoside, wogonin, chrysin and verbascoside. Chromatograms of aqueous and methanolic extract are shown in Figs. 2 and 3, respectively.

Under the chosen operating conditions, 70% ethanol extracts the highest degree of baicalin, baicalein, scutellarin and wogonoside, 31250 ± 291 , 288 ± 11 , 4131 ± 29 and 2827 ± 102 $\mu\text{g/g}$, respectively. The amounts obtained are twice as

much compared to the extraction with methanol and six times more than the extraction with water (Table 3). On the other hand, methanol also extracts verbascoside, wogonin and chrysin, but in quantities less than the limit of quantification of the method. This is a prerequisite for conducting experiments to optimize extraction conditions to increase the yield.

In the available literature, data on the flavonoid composition of *Scutellaria altissima* are only found in shot cultures and the amounts of baicalin and wogonoside shown are commensurate with those obtained by us [14, 15].

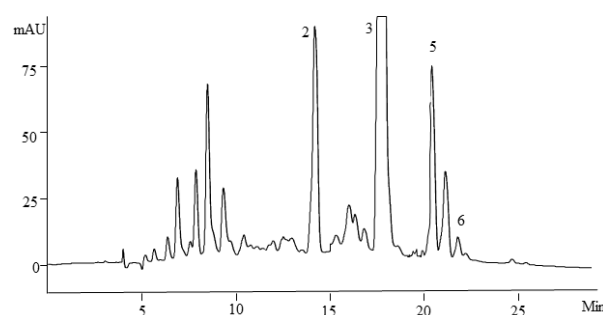


Figure 2. Chromatogram of *Scutellaria altissima* aqueous extract

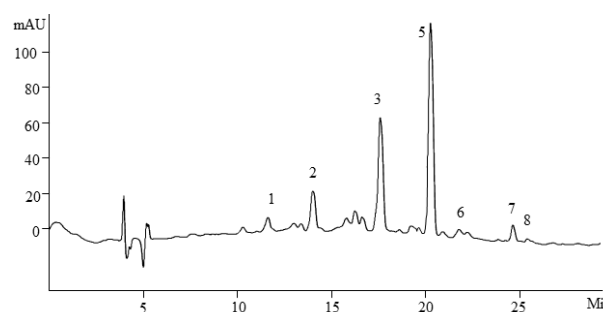


Figure 3. Chromatogram of *Scutellaria altissima* methanolic extract.

Table 3. Quantities of scutellarin, baicalin, baicalein, wogonin, wogonoside, luteolin, chrysin and verbascoside, determined in $\mu\text{g/g}$ dry plant material

Analyte, $\mu\text{g/g}$ Extraction solvent	Verbas coside	Scute llarin	Baicalin	Luteolin	Wogono side	Baica lein	Wogonin	Chrysin
H ₂ O	-	687±53	2469±127	-	497±26	144±9	-	-
70% EtOH	-	4131±29	31250±291	-	2827±102	288±11	-	-
96% EtOH	-	590±33	5992±203	-	1412±61	82±5	-	-
MeOH	traces	2165±98	17230±342	-	2210±95	85±5	traces	traces

All values are mean \pm SD (n=3)

CONCLUSIONS

An HPLC method for the determination of polyphenol compounds: the flavonoids - scutellarin, baicalin, baicalein, wogonin, wogonoside, luteolin,

chrysin and the caffeoyl phenylethanoid glycoside - verbascoside was developed. The proposed HPLC assay showed good separation of the compounds and proved to be efficient, precise and accurate, therefore, it could be used for the simultaneous

determination of biologically active compounds in plant material and dry extracts or phyto products. The method can also be used to prove the authenticity of plants of the genus *Scutellaria*. This is the first study in Bulgaria on the flavonoid composition of *Scutellaria altissima*, which implies the continuation of the experiments to determine the composition and the comparison of the quantities of the tested compounds in the other *Scutellaria* species, which occur on the territory of the country.

Acknowledgement: This work was supported by Research Project HO-01/2018, funded by Medical University of Plovdiv, Bulgaria.

REFERENCES

1. X. Shang, X. He, X. He, M. Li, R. Zhang, P. Fan, Q. Zhang, Z. Jia, *J. Ethnopharmacol.*, **128**, 279 (2010).
2. G. Zeng, Z. Chen, *Yao Xue Xue Bao*, **1**, 47 (in Chinese) (1957).
3. Q. Zhao, Y. Chen, C. Martin, *Sci. Bull.*, **61**, 1391 (2016).
4. European Pharmacopoeia - 8th edn. European Directorate for the Quality of Medicines & HealthCare (EDQM) Council of Europe, Strasbourg 2014.
5. P. Bozov, Y. Georgieva, *Nat. Prod. Commun.*, **12**, 327 (2017).
6. M. Siddiqui, Z. Alothman, N. Rahman, *Arab. J. Chem.*, doi:10.1016/j.arabjc.2013.04.016 (2013).
7. J. Gao, A. Sanchez-Medina, B. Pendry, M. Hughes, G. Webb, O. Corcoran, *J. Pharm. Pharm. Sci.*, **11**, 77 (2008).
8. O. Kosakowska, K. Bączek, J. Przybył, E. Pióro-Jabrucka, Z. Węglarz, *Herba Pol.*, **62**, 7 (2016).
9. J. Peris-Vicente, J. Esteve-Romero, S. Carda-Broch, in: Analytical Separation Science, J. L. Anderson, A. Berthod, V. Pino Estévez, A. M. Stalcup (eds.), Wiley-VCH Verlag, 2015, p. 21.
10. C.-H. Wang, Y.-X. Wang, H.-J. Liu, *Journal of Pharmaceutical Analysis*, **1**, 291 (2011).
11. A. Wilczańska-Barska, M. Krauze-Baranowska, M. Majdan, D. Głód, *BioTechnologia*, **92**, 369 (2011).
12. M. Katsarova, S. Dimitrova, L. Lukanov, F. Sadakov, *C. R. Acad. Bulg. Sci.*, **70**, 947 (2017).
13. Huber L. *LC/GC International*, **2**, 96 (1998).
14. I. Grzegorzczak-Karolak, Ł. Kuz'ma, H. Wysokin'ska, *Acta Physiol. Plant.*, **37**, 1736 (2015).
15. I. Grzegorzczak-Karolak, Ł. Kuz'ma, H. Wysokin'ska, *J. Med. Plants Res.*, **7**, 3003 (2013).

Multicomponent reactions for the synthesis of bis-heterocyclic pyrrole derivatives

Y. Stremiski¹, D. Kirkova^{1,2}, S. Statkova-Abeghe^{1*}, P. Angelov¹, I. Ivanov^{1,3}

¹University of Plovdiv "Paisii Hilendarski", Department of Organic Chemistry,
24 Tzar Asen Str., 4000 Plovdiv, Bulgaria,

²Tobacco and Tobacco Products Institute, 4108 Markovo, 4000 Plovdiv, Bulgaria

³University of Plovdiv "Paisii Hilendarski", Branch-Smolyan, 32 Dicho Petrov Str., 4700 Smolyan, Bulgaria

Received November 11, 2018; Revised January 4, 2019

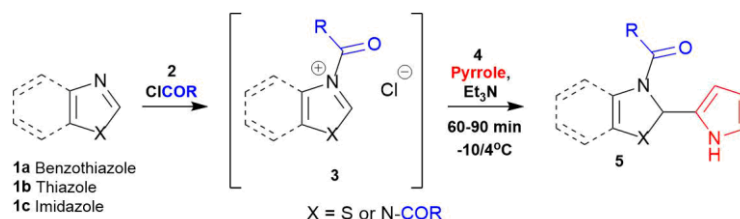
New pyrrole derivatives are synthesised in high yields (55–95%) by one-pot α -amidoalkylation reactions of various *N*-heterocycles (benzothiazole, thiazole and imidazole) and pyrrole. Further oxidation of the obtained derivatives leads to fully aromatic bis-heterocyclic products, bearing structural similarity to the natural product *Camalexin*.

Keywords: Camalexin, Pyrroles, One-pot amidoalkylation reactions

INTRODUCTION

The natural product *Camalexin* and its analogs have attracted a great deal of recent attention because of their interesting biological profile [1]. In a previous publication we reported a new and convenient synthesis of *Camalexin* and its benzo- and aza-analogs [2]. The underlying concept of this synthesis can be traced back to works of Bergman *et al.* [3] and is extendable to many other structurally related heterocyclic systems with

potential biological activity. In the recent literature there are some interesting examples of biologically active pyrroles containing a thiazole fragment in their structure with prospects for their use as potential antifungal and antituberculosis agents [4]. Taking this into consideration, herein we describe the application of our previously published multicomponent approach for the synthesis of new pyrrole derivatives (Scheme 1).



Scheme 1. One-pot synthesis of 2-substituted pyrroles **5**

EXPERIMENTAL

General information

All reagents and solvents were obtained from commercial suppliers (Merck) and were used without further purification. Melting points were determined on a Boetius PHMKO5 hot stage apparatus and are uncorrected. IR and MS spectra were measured on VERTEX 70 FT-IR spectrometer (Bruker Optics, Germany) and HRMS "Q-Exactive Orbitrap" (Thermo Fisher Scientific, Waltham, MA, USA) spectrometer, respectively. NMR spectra were measured on Bruker Avance AV600 and DRX250 spectrometers in CDCl₃ and DMSO as solvents. Chemical shifts (δ , ppm) are downfield from TMS. To average out the rotamers observed in compounds **5** most of the NMR spectra

were taken at 80°C in DMSO. TLC was done on precoated 0.2 mm Merck silica gel 60 plates. Neutral alumina was used for column chromatographic separation.

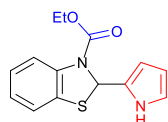
Synthesis of amidoalkylated pyrroles **5aa-5ae**, **5ba**, **5bb**, general procedure

The corresponding acyl chloride or alkyl chloroformate (1.2 equiv.) is slowly added with magnetic stirring to a solution of benzothiazole or thiazole (1 equiv.) in dry dichloromethane (4–8 mL/mmol) at the temperature indicated in Table 1. Immediately after that pyrrole is added (1 equiv.). Then, gradually, in the course of 30 min, triethylamine (1 equiv.), dissolved in dichloromethane (2 mL/mmol) is added. The reaction mixture is stirred for the time and at the temperature specified in Table 1. After completion

* To whom all correspondence should be sent.

E-mail: stab@uni-plovdiv.bg

of the reaction, the mixture is transferred to a separatory funnel with dichloromethane (20 – 30 mL/mmol) and is consecutively extracted with equal volumes of aqueous Na₂CO₃ (3%), water and brine. The combined organic layers are dried (Na₂SO₄) and the solvent is removed under reduced pressure. Analytically pure samples were obtained by column chromatography on neutral alumina, using mixtures of diethyl ether/petroleum ether as eluents.



Ethyl 2-(1H-pyrrol-2-yl)benzo[d]thiazole-3(2H)-carboxylate **5aa**

Chromatographed on neutral alumina with petroleum/diethyl ether (8:1); Yield: 55%; Oil.

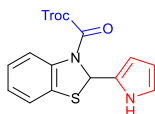
¹H-NMR (600 MHz, 20°C, CDCl₃, δ ppm, *J* Hz): 1.41 (t, *J* = 6, 3H, CO₂CH₂CH₃), 4.34 – 4.40 (m, 2H, CO₂CH₂CH₃), 6.12 (m, 1H), 6.33 (br s, 1H), 6.74 (m, 1H), 6.88 (s, 1H, *CH), 7.02 – 7.12 (m, 2H), 7.24 (m, 2H), 7.58 (br s, 1H, NH); ¹³C-NMR (150 MHz, 20°C, CDCl₃, δ ppm): 14.5, 60.6, 62.8, 107.9, 108.3, 117.8, 118.8, 122.3, 124.3, 125.5, 131.0, 132.1, 136.6, 152.5; IR (KBr, cm⁻¹): 3371, 2982, 1703, 1580, 1471, 1249, 747; HRMS *m/z* (ESI): calcd for C₁₄H₁₄N₂NaO₂S⁺ [M+Na]⁺ 297.0668, found 297.0660; calcd for C₁₄H₁₃N₂O₂S⁻ [M-H]⁻ 273.0703, found 273.0687.



Methyl 2-(1H-pyrrol-2-yl)benzo[d]thiazole-3(2H)-carboxylate **5ab**

Chromatographed on neutral alumina with petroleum/diethyl ether (8:1); Yield: 67%; mp = 111–113°C.

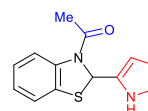
¹H-NMR (600 MHz, 20°C, CDCl₃, δ ppm, *J* Hz): 3.81 (s, 3H, CO₂CH₃), 6.02 (m, 1H), 6.22 (br s, 1H), 6.63 (m, 1H), 6.77 (s, 1H, *CH), 6.92 – 7.02 (m, 2H), 7.12 (m, 2H), 7.51 (br s, 1H, NH); ¹³C-NMR (150 MHz, 20°C, CDCl₃, δ ppm): 53.5, 60.6, 107.9, 108.2, 108.3, 117.8, 118.9, 122.3, 124.4, 125.5, 130.9, 139.2, 151.1; IR (KBr, cm⁻¹): 3372, 2957, 1686, 1580, 1515, 1472, 1241, 745; HRMS *m/z* (ESI): calcd for C₁₃H₁₂N₂NaO₂S⁺ [M+Na]⁺ 283.0512, found 283.0507; calcd for C₁₃H₁₁N₂O₂S⁻ [M-H]⁻ 259.0547, found 259.0549.



2,2,2-trichloroethyl 2-(2-(1H-pyrrol-2-yl)benzo[d]thiazol-3(2H)-yl)-2-oxoacetate **5ac**

Chromatographed on neutral alumina with petroleum/diethyl ether (2:1 increasing polarity to 1:1); Yield: 93%; mp = 116–118°C.

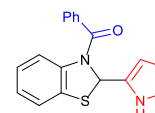
¹H-NMR (600 MHz, 80°C, DMSO-d₆, δ ppm, *J* Hz): 4.96 (d, 2*J* = 12, 1H, CO₂CH₂CCl₃), 5.06 (d, 2*J* = 12, 1H, CO₂CH₂CCl₃), 5.88 (m, 2H), 6.67 (m, 1H), 6.96 (s, 1H, *CH), 7.09 (t, *J* = 8.2, 1H), 7.17 (t, *J* = 8.2, 1H), 7.28 (d, *J* = 7.6, 1H), 7.78 (d, *J* = 8.2, 1H) 10.56 (br s, 1H, NH); ¹³C-NMR (150 MHz, 80°C, DMSO-d₆, δ ppm): 61.9, 75.5, 105.9, 107.8, 117.9, 119.2, 123.3, 125.4, 125.7, 127.0, 129.2, 131.2, 137.3, 151.1; IR (KBr, cm⁻¹): 3382, 2992, 1698, 1576, 1480, 1260, 746; HRMS *m/z* (ESI): calcd for C₁₄H₁₁C₁₃N₂NaO₂S⁺ [M+Na]⁺ 398.9499, found 398.9497.



1-(2-(1H-pyrrol-2-yl)benzo[d]thiazol-3(2H)-yl)ethan-1-one **5ad**

Chromatographed on neutral alumina with petroleum/diethyl ether (4:1 increasing polarity to 2:1); Yield: 58%; mp = 118–120°C.

¹H-NMR (600 MHz, 80°C, DMSO-d₆, δ ppm, *J* Hz): 2.23 (s, 3H, COCH₃), 5.83 (m, 1H), 5.89 (m, 1H), 6.69 (m, 1H), 6.99 (s, 1H, *CH), 7.05 (t, *J* = 7.6, 1H), 7.13 (t, *J* = 7.6, 1H), 7.25 (d, *J* = 7.6, 1H), 7.88 (d, *J* = 7.6, 1H) 10.60 (br s, 1H, NH); ¹³C-NMR (150 MHz, 80°C, DMSO-d₆, δ ppm): 23.7, 62.2, 106.0, 107.9, 119.0, 119.3, 123.2, 125.3, 125.4, 129.6, 131.6, 138.8, 169.1; IR (KBr, cm⁻¹): 3394, 2987, 1705, 1560, 1475, 1272, 749; HRMS *m/z* (ESI): calcd for C₁₃H₁₂N₂NaOS⁺ [M+Na]⁺ 267.0563, found 267.0563; calcd for C₁₃H₁₁N₂OS⁻ [M-H]⁻ 243.0598, found 243.0599.



(2-(1H-pyrrol-2-yl)benzo[d]thiazol-3(2H)-yl)(phenyl)methanone **5ae**

Chromatographed on neutral alumina with petroleum/diethyl ether (1:1); Yield: 57%; mp = 173–175°C.

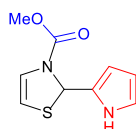
¹H-NMR (600 MHz, 80°C, DMSO-d₆, δ ppm, *J* Hz): 5.87 (m, 2H), 6.67 (m, 1H), 6.77 (s, 1H, *CH), 7.03 (t, *J* = 7.6, 1H), 7.07 (t, *J* = 7.6, 1H), 7.29 – 7.31 (m, 2H), 7.39 – 7.43 (m, 4H), 7.50 – 7.53 (m, 1H), 10.46 (br s, 1H, NH); ¹³C-NMR (150 MHz, 80°C, DMSO-d₆, δ ppm): 64.0, 106.3, 107.8, 119.1, 119.7, 123.7, 125.1, 125.8, 127.5, 128.9, 130.4, 131.2, 131.4, 135.9, 138.8, 169.0; IR (KBr, cm⁻¹): 3362, 2966, 1625, 1572, 1468, 1282, 753; HRMS *m/z* (ESI): calcd for C₁₈H₁₄N₂NaOS⁺ [M+Na]⁺ 329.0719, found 329.0713; calcd for C₁₈H₁₃N₂OS⁻ [M-H]⁻ 305.0754, found 305.0748.



Ethyl 2-(1H-pyrrol-2-yl)thiazole-3(2H)-carboxylate 5ba

Chromatographed on neutral alumina with petroleum/diethyl ether (8:1 increasing polarity to 4:1); Yield: 60%; mp = 85–87°C.

¹H-NMR (250 MHz, 80°C, DMSO-d₆, δ ppm, *J* Hz): 1.19 (t, *J* = 7.1, 3H, CO₂CH₂CH₃), 4.13 (q, *J* = 7.1, 2H, CO₂CH₂CH₃), 5.85 (d, *J* = 4.7, 1H), 5.93 – 5.96 (m, 1H), 5.99 – 6.02 (m, 1H), 6.53 (d, *J* = 4.7, 1H), 6.59 (s, 1H, *CH), 6.66 – 6.69 (m, 1H), 10.49 (br s, 1H, NH); ¹³C-NMR (62.5 MHz, 80°C, DMSO-d₆, δ ppm): 14.1, 59.6, 61.7, 103.3, 105.4, 107.3, 118.2, 120.9, 131.6, 152.2; IR (KBr, cm⁻¹): 3312, 3086, 2981, 1685, 1597, 1564, 1467, 1382, 1251, 733; HRMS *m/z* (ESI): calcd for C₁₀H₁₂N₂NaO₂S⁺ [M+Na]⁺ 247.0512, found 247.0516; calcd for C₁₀H₁₁N₂O₂S⁻ [M-H]⁻ 223.0547, found 223.0555.



Methyl 2-(1H-pyrrol-2-yl)thiazole-3(2H)-carboxylate 5bb

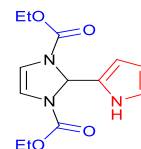
Chromatographed on neutral alumina with petroleum/diethyl ether (8:1 increasing polarity to 4:1); Yield: 63%; mp = 92–94°C.

¹H-NMR (250 MHz, 80°C, DMSO-d₆, δ ppm, *J* Hz): 3.69 (s, 3H, CO₂CH₃), 5.87 (d, *J* = 4.7, 1H), 5.93 – 5.96 (m, 1H), 5.99 – 6.02 (m, 1H), 6.53 (d, *J* = 4.7, 1H), 6.60 (s, 1H, *CH), 6.67 – 6.69 (m, 1H), 10.53 (br s, 1H, NH); ¹³C-NMR (62.5 MHz, 80°C, DMSO-d₆, δ ppm): 52.9, 59.6, 103.6, 105.4, 107.4, 118.3, 120.9, 131.5, 152.7; IR (KBr, cm⁻¹): 3332, 3093, 2957, 1691, 1597, 1561, 1449, 1366, 1250, 742; HRMS *m/z* (ESI): calcd for C₉H₁₀N₂NaO₂S⁺ [M+Na]⁺ 233.0355, found 233.0358; calcd for C₉H₉N₂O₂S⁻ [M-H]⁻ 209.0390, found 209.0396.

Synthesis of amidoalkylated pyrroles 5ca–5cd, general procedure

The corresponding acyl chloride or alkyl chloroformate (4.4 mmol) is slowly added to a cooled (0°C) and magnetically stirred solution of imidazole (2 mmol, 0.136 mg) and Et₃N (2 mmol, 0.28 mL) in dry 1,2-dichloroethane (10 mL). Immediately after that, pyrrole (2 mmol, 0.139 mL) is added. In the course of the next 30 minutes Et₃N (2 mmol) in 1,2-dichloroethane (4 mL) is gradually added. After completion of the reaction (Table 1), the mixture is transferred to a separatory funnel with dichloromethane (50 mL) and is successively extracted with equal volumes of aqueous HCl (1:4), Na₂CO₃ (3%), water and brine. The combined organic layers are dried (Na₂SO₄) and the solvent is removed under reduced pressure. The solid residue

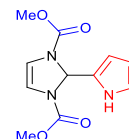
is then triturated and washed with small amount of hexane and petrol/diethyl ether (4:1) to remove any unreacted pyrrole. This sequence induces crystallization of the products. The material obtained in this way is usually sufficiently clean to be taken to the next stage without further purification. Analytically pure samples of **5cc** and **5cd** were obtained by column chromatography on neutral alumina, using mixtures of diethyl ether/petroleum ether as eluents.



Diethyl 2-(1H-pyrrol-2-yl)-1H-imidazole-1,3(2H)-dicarboxylate 5ca

Yield: 81%; mp = 104–106°C.

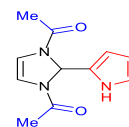
¹H-NMR (600 MHz, 80°C, DMSO-d₆, δ ppm, *J* Hz): 1.16 (t, *J* = 7.0, 6H, 2×CO₂CH₂CH₃), 4.06 – 4.11 (m, 4H, 2×CO₂CH₂CH₃), 5.95 – 5.97 (m, 1H), 6.02 – 6.03 (m, 1H), 6.35 (s, 2H), 6.61 (s, 1H, *CH), 6.65 (m, 1H), 10.60 (br s, 1H, NH); ¹³C-NMR (150 MHz, 80°C, DMSO-d₆, δ ppm): 14.7, 61.9, 69.4, 106.3, 107.8, 112.8, 118.4, 129.2, 150.8; IR (KBr, cm⁻¹): 3385, 3154, 2988, 1706, 1627, 1561, 1463, 1410, 1383, 1265; HRMS *m/z* (ESI): calcd for C₁₃H₁₇N₃NaO₄⁺ [M+Na]⁺ 302.1111, found 302.1101; calcd for C₁₃H₁₆N₃O₄⁻ [M-H]⁻ 278.1146, found 278.1147.



Dimethyl 2-(1H-pyrrol-2-yl)-1H-imidazole-1,3(2H)-dicarboxylate 5cb

Yield: 95%; mp = 123–125°C.

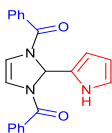
¹H-NMR (600 MHz, 80°C, DMSO-d₆, δ ppm, *J* Hz): 3.65 (s, 6H, 2×CO₂CH₃), 5.95 – 5.97 (m, 1H), 6.02 – 6.03 (m, 1H), 6.35 (s, 2H), 6.63 (s, 1H, *CH), 6.65 (m, 1H), 10.56 (br s, 1H, NH); ¹³C-NMR (150 MHz, 80°C, DMSO-d₆, δ ppm): 53.1, 69.4, 106.3, 107.9, 112.9, 118.5, 129.0, 151.2; IR (KBr, cm⁻¹): 3331, 3133, 2958, 1689, 1626, 1562, 1450, 1402, 1392, 1272; HRMS *m/z* (ESI): calcd for C₁₁H₁₃N₃NaO₄⁺ [M+Na]⁺ 274.0798, found 274.0797; calcd for C₁₁H₁₂N₃O₄⁻ [M-H]⁻ 250.0833, found 250.0829.



1,1'-(2-(1H-pyrrol-2-yl)-1H-imidazole-1,3(2H)-diyl)bis(ethan-1-one) 5cc

Chromatographed on neutral alumina with petroleum/diethyl ether (1:1 increasing polarity to diethyl ether); Yield: 66%; mp = 141–143°C.

¹H-NMR (600 MHz, 80°C, DMSO-d₆, δ ppm, J Hz): 2.07 (s, 6H, 2×COCH₃), 5.93 – 5.95 (m, 1H), 6.01 (br s, 1H), 6.33 (s, 2H), 6.63 (m, 1H), 6.94 (s, 1H, *CH), 10.34 (br s, 1H, NH); ¹³C-NMR (150 MHz, 80°C, DMSO-d₆, δ ppm): 24.2, 70.1, 106.8, 108.0, 112.8, 117.5, 128.8, 152.5; IR (KBr, cm⁻¹): 3406, 3119, 1646, 1612, 1551, 1442, 1399, 1260; HRMS *m/z* (ESI): calcd for C₁₁H₁₃N₃NaO₂⁺ [M+Na]⁺ 242.0900, found 242.0890; calcd for C₁₁H₁₂N₃O₂⁻ [M-H]⁻ 218.0935, found 218.0927.



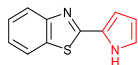
(2-(1H-pyrrol-2-yl)-1H-imidazole-1,3(2H)-diyl)bis(phenylmethanone) **5cd**

Chromatographed on neutral alumina with petroleum/diethyl ether (1:1); Yield: 65%; mp = 153–155°C.

¹H-NMR (600 MHz, 80°C, DMSO-d₆, δ ppm, J Hz): 5.96 (s, 1H), 6.06 (br s, 1H), 6.45 (s, 2H), 6.68 (s, 1H, *CH), 7.29 – 7.55 (m, 11H), 10.59 (br s, 1H, NH); ¹³C-NMR (150 MHz, 80°C, DMSO-d₆, δ ppm): 70.5, 106.9, 107.8, 115.2, 118.8, 127.0, 128.5, 129.0, 131.2, 134.9, 165.0; IR (KBr, cm⁻¹): 3372, 3137, 1653, 1615, 1577, 1447, 1392, 1281; HRMS *m/z* (ESI): calcd for C₂₁H₁₇N₃NaO₂⁺ [M+Na]⁺ 366.1213, found 366.1212; calcd for C₂₁H₁₆N₃O₂⁻ [M-H]⁻ 342.1248, found 342.1257.

Oxidation of amidoalkylated pyrroles 5aa, 5ab, 5ba, 5bb to 2-(1H-pyrrol-2-yl)benzo[d]thiazole 6a and 2-(1H-pyrrol-2-yl)thiazole 6b

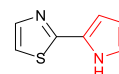
The corresponding compound **5** (0.5 mmol) is dissolved in CH₃CN (8 mL), then the oxidant (*o*-chloranil) (2 equiv. for the benzothiazole derivatives **5a** or 1 equiv. for thiazole derivatives **5b**) is added and the reaction mixture is magnetically stirred under the conditions specified in Table 2. After completion of the reaction the solvent is evaporated under reduced pressure and the mixture is then dry-loaded onto neutral alumina. Chromatography on a short alumina column with diethyl ether/petroleum as the eluent gave 2-(1H-pyrrol-2-yl)benzo[d]thiazole **6a** or 2-(1H-pyrrol-2-yl)thiazole **6b** in yields indicated in Table 2.



2-(1H-pyrrol-2-yl)benzo[d]thiazole **6a**

Chromatographed on neutral alumina with petroleum/diethyl ether (8:1 increasing polarity to 4:1); Yield: 91%, 86%; mp = 158–159°C; lit. 151–154°C [5^a], 155–156°C [5^b].

¹H-NMR (600 MHz, 80°C, DMSO-d₆, δ ppm, J Hz): 6.24 (m, 1H), 6.84 (m, 1H), 7.02 (m, 1H), 7.35 (t, *J* = 7.6, 1H), 7.47 (t, *J* = 7.6, 1H), 7.88 (d, *J* = 8, 1H), 7.99 (d, *J* = 8, 1H), 11.82 (br s, 1H, NH); ¹³C-NMR (150 MHz, 80°C, DMSO-d₆, δ ppm): 110.5, 112.7, 122.0, 122.3, 123.6, 124.9, 126.2, 126.7, 134.1, 154.1, 160.3; IR (KBr, cm⁻¹): 3125, 2854, 1572, 1559, 1113, 742; HRMS *m/z* (ESI): calcd for C₁₁H₇N₂S⁻ [M-H]⁻ 199.0335, found 199.0330.



2-(1H-pyrrol-2-yl)thiazole **6b**

Chromatographed on neutral alumina with petroleum/diethyl ether (4:1); Yield: 89%, 82%; mp = 74–76°C; lit. mp = 75°C [4^a].

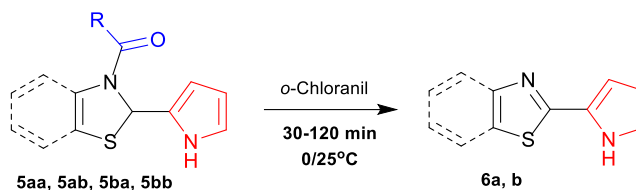
¹H-NMR (250 MHz, 80°C, DMSO-d₆, δ ppm, J Hz): 6.18 (t, *J* = 3.1, 1H), 6.64 – 6.66 (m, 1H), 6.90 – 6.91 (m, 1H), 7.47 (d, *J* = 3.4, 1H), 7.72 (d, *J* = 3.4, 1H), 11.46 (br s, 1H, NH); ¹³C-NMR (62.5 MHz, 80°C, DMSO-d₆, δ ppm): 109.3, 109.4, 116.8, 121.2, 126.2, 142.5, 165.3; IR (KBr, cm⁻¹): 3108, 2964, 1572, 1487, 1098, 738; HRMS *m/z* (ESI): calcd for C₇H₅N₂S⁻ [M-H]⁻ 149.0179, found 149.0170.

RESULTS AND DISCUSSION

Our primary aim was to develop an efficient multicomponent one-pot procedure for the synthesis pyrrole derivatives through the reaction of benzothiazole, thiazole or imidazole **1a-c**, acid chlorides **2** and pyrrole **4**. The aforementioned azoles react with acyl chlorides or alkyl chloroformates to give acyliminium reagents **3** which further react with pyrrole in the presence of triethylamine as HCl scavenger. In this way a range of 2-substituted pyrroles **5** were obtained in good yields (55–95%, Table 1). The reaction conditions were optimized by varying the solvent, temperature and time. Low temperature (-10 to +4 °C) was beneficial in all cases. At higher temperature there were competing reactions which led to complicated mixtures of products and lowered the yields of the targeted monosubstituted pyrrole derivatives. Although in principle the amidoalkylation of aromatic rings can take place in the absence of base, the presence of Et₃N was of crucial importance in all of the examples studied here, because both pyrrole and its amidoalkylated products **5** were adversely affected by the HCl released in the course of the reaction. Dichloromethane was found to be the optimal solvent for the reactions with thiazoles, while in the case of imidazole dichloroethane performed better.

Table 1. Reaction conditions and yields of amidoalkylated pyrroles **5**

N-heterocycle	Product	R	Conditions	Yield, %
Benzothiazole 1a	5aa	CH ₃ CH ₂ O	0 – 4°C, 1.5h	55
	5ab	CH ₃ O	0 – 4°C, 1.5h	67
	5ac	CCl ₃ CH ₂ O	0 – 4°C, 1.5h	93
	5ad	CH ₃	0 – 4°C, 1.5h	58
	5ae	C ₆ H ₅	0 – 4°C, 1.5h	57
Thiazole 1b	5ba	CH ₃ CH ₂ O	-10 – -5°C, 1h	60
	5bb	CH ₃ O	-10 – -5°C, 1h	63
Imidazole 1c	5ca	CH ₃ CH ₂ O	0 – 4°C, 1.5h	81
	5cb	CH ₃ O	0 – 4°C, 1.5h	95
	5cc	CH ₃	0 – 4°C, 1.5h	66
	5cd	C ₆ H ₅	0 – 4°C, 1.5h	65

**Scheme 2.** Oxidation of **5aa**, **5ab**, **5ba**, **5bb** to products **6a**, **6b****Table 2.** Reaction conditions and yields of **6a**, **6b**, obtained according to Scheme 2

Starting material	Product	<i>o</i> -Chloranil oxidation		
		T, °C	Time, h	Yield 6, %
5aa	6a	25	2	91
5ab	6a	25	2	86
5ba	6b	0 – 4	0.5	89
5bb	6b	0 – 4	0.5	82

After the optimization of the conditions for the coupling of the heterocyclic rings we proceeded with experiments to remove the alkoxycarbonyl groups and rearomatize the thiazole moiety in the obtained products **5a**, **5b**. This was successfully accomplished by oxidation with *o*-chloranil (Scheme 2, Table 2).

All products were purified by column chromatography and characterized by IR, ¹H-NMR, ¹³C-NMR and ESI-MS analysis.

CONCLUSIONS

An efficient one-pot method for the synthesis of bis-heterocyclic pyrrole derivatives has been developed. Thirteen new derivatives bearing structural similarity to the natural product *Camalexin* were successfully synthesized.

Acknowledgement: We gratefully acknowledge funding from the scientific research fund of the Bulgarian Ministry of Education and Science (Grant DN09/15-2016) and the University of Plovdiv (Grant SP17-HF018). The work was supported by the Bulgarian Ministry of Education and Sciences, Grant DKOF7RP02/20. The authors are thankful to Dr. M. Naydenov, University of

Plovdiv, Faculty of Biology, Department of Plant Physiology and Molecular Biology, too, for the technical support in the mass spectral characterization.

REFERENCES

- (a) M. S. C. Pedras, A. Abdoli, *Bioorganic Med. Chem.*, **26**, 4461, (2018); (b) M. S. C. Pedras, E. E. Yaya, E. Glawischnig, *Nat. Prod. Rep.*, **28**, 1381, (2011); (c) R. Mezenzev, T. Updegrove, P. Kutschy, M. Repovská, J. F. McDonald, *J. Nat. Med.*, **65**, 488, (2011); (d) V. Odero-Marrah, B. Smith, *US Patent 0 096 166 A1*, (2013); (e) M. Pilatova, L. Ivanova, P. Kutschy, L. Varinska, L. Saxunova, M. Repovska, M. Sarisky, R. Seliga, L. Mirossay, J. Mojzic, *Toxicol. Vit.*, **27**, 939, (2013); (f) M. Chripkova, F. Zigo, J. Mojzic, *Molecules*, **21**, 1, (2016).
- Y. Stremski, S. Statkova-Abeghe, P. Angelov, I. Ivanov, *J. Heterocycl. Chem.*, **55**, 1589, (2018).
- (a) J. Bergman, *Tetrahedron Lett.*, **46**, 4723, (1972); (b) J. Bergman, L. Renstrom, B. Sjoberg, *Tetrahedron*, **36**, 2505, (1980).
- (a) T. Nußbaumer, C. Krieger, R. Neidlein, *J. Org. Chem.*, 2449, (2000); (b) H. Kobayashi, T. Honda, Y. Matsui, M. Konishi, T. Matsufuji, K. Ueda, *EU Patent 2 239 253 A1*, (2009); (c) W. Guba, W. Haap, H. P. Marty, R. Narquizian, *US Patent 0 147 572 A1*, (2004); (d) G. Camaggi, L. Filippini, M. Gusmeroli, R. Riva, G. Zanardi, V. Garavaglia, L. Mirena, *EU Patent 0 554 956 A1*, (1993); (e) S. D. Joshi, U. A. More, S. R. Dixit, H. H. Korat, T. M. Aminabhavi, A. M. Badiger, *Med. Chem. Res.*, **23**, 1123, (2014).
- (a) A. Arora, J. D. Weaver, *Org. Lett.*, **18**, 3996, (2016); (b) Y. M. Poronik, V. P. Yakubovskiy, M. P. Shandura, Y. G. Vlasenko, A. N. Chernega, Y. P. Kovtun, *European J. Org. Chem.*, **14**, 2746, (2010).

Study of the effect of structure on the kinetics and mechanism of the redox reactions of Fe(III)/Fe(II) complexes

R. Khattak^{1,2*}, I. Imam Naqvi²

¹Department of Chemistry, Shaheed Benazir Bhutto Women University, Peshawar, Pakistan

²Department of Chemistry, University of Karachi, Karachi-75270, Pakistan

Received October 29, 2018; Revised January 16, 2019

This study reveals the kinetics and mechanism of the redox reactions between a few selected Fe(III) and Fe(II) complexes. Through comparison, the outcomes of the study highlight the effect of structural variation upon the electron-transfer mechanism. Structural variation exhibits effects on the properties of transition metal complexes, more specifically, reduction potential and reaction mechanism. A change in the reduction potential may lead to altering the electron-transfer mechanism and biochemical applications of the compounds. We oxidized acetylferrocene, 1-ferrocenylethanol, and ferrocyanide by ferricyphen in the aqueous-organic co-solvent mixture. All of the reactions were completed in three phases, and followed a complex kinetics such as an overall second order, and, the zeroth order in the second and the first phases, respectively with a subsequent competition phase until the reaction was completed. The concentration of nitric acid was varied and its effect on the rate constant(s) was probed in each phase of the reaction(s) to recognize the probable protonation of the reducing agent(s), and its participation in the electron-transfer mechanism(s). The reactions, although, followed the same kinetic orders, but the rate-controlling species were specific to each phase in each reaction.

Keywords: Redox reaction, Fe(III)/Fe(II) complexes, ferrocyanide, acetylferrocene, 1-ferrocenylethanol, ferricyphen

INTRODUCTION

The chemical structure of the coordination compounds plays a leading role in their electrochemical behaviour. The electron-transfer chemistry mostly revolves around the structure of these compounds, which are oxidized and reduced during a reaction [1]. An outer-sphere or an inner-sphere mechanism can lead the redox chemistry, consequently. Each of these mechanisms is structure-dependent, which further divides the applications of the coordination compounds in our everyday life such as industry, pharmacy, technology, etc. Our interest was to study the effect of structure on the kinetics of the electron-transfer mechanism of a total of three selected reducing agents and an oxidizing agent, where Fe(II) or Fe(III) was the central metal part, respectively. For such purpose, we chose those compounds, which were structurally correlated. They were derivatives, for example, two derivatives of ferrocene were chosen for this study, which show solubility in the aqueous medium to a certain extent. We considered this property in order to avoid the use of expensive organic solvents during the study and to keep this project environmentally friendly. Alcohols cannot be used to compose the reaction media during such redox processes considering the oxidation of alcohols by the Fe(III) complexes [2]. 1,4-dioxane was used for its miscibility in water, as well as

neriness towards oxidation. Acetylferrocene and 1-ferrocenylethanol were the target compounds to oxidize in this study. The reduction potential ($E_{1/2}$) of acetylferrocene was reported to be 0.740 V and of 1-ferrocenylethanol - 0.204 V [3,4]. The redox ability of these compounds has previously been studied electrochemically without exploring the thorough mechanisms of the electron-transfer [5-9]. However, the reaction of these compounds with other transition metal complexes has rarely been focused yet. The importance of the derivatives of ferrocene appears from their antineoplastic characteristics, and their probable use in chemotherapy [10,11]. We also chose the well-known compound ferrocyanide for this study and oxidized it by ferricyphen. The reduction potential ($E_{1/2}$) of the mixed ligand complex (ferricyphen) increased to 0.80 V over ferrocyanide (0.40 V) upon addition of 1,10-phenanthroline chelate [3, 12]. A few of its studies appeared, where this compound has been used as an oxidizing agent for different compounds of biological importance [3,4, 12-16]. However, the literature review shows the oxidation of ferrocyanide by various other compounds [17-20]. Our study will significantly include the data, and surface the effect of structural variation upon the kinetics and mechanism of the reduction of ferricyphen ($[\text{Fe}^{\text{III}}(\text{phen})_2(\text{CN})_2]^+$) by either acetylferrocene (FcCOMe), 1-ferrocenylethanol (FcCHOHMe), and/or,

* To whom all correspondence should be sent.
E-mail: rznkhattak@sbbwu.edu.pk

R. Khattak, I. Imam Naqvi: Study of the effect of structure on the kinetics and mechanism of the redox reactions of ... ferrocyanide ($[\text{Fe}^{\text{II}}(\text{CN})_6]^{4-}$) in aqueous-organic and aqueous media. We determined the effects of various experimental parameters such as the concentration of the reducing agents, the oxidizing agent, and the acid (nitric acid) on the rate constants of each reaction in each phase. In view of our results and literature, we found the reactive species that are involved in the rate-determining step(s), and that control the mechanism(s). We proposed a rate law for each of the electron-transfer processes with an outer-sphere mechanism. Through comparison, we surfaced the effect of the structure upon the kinetics and the electron-transfer mechanism of the compounds.

EXPERIMENTAL

We used Analar-grade materials. The oxidizing agent; $[\text{Fe}^{\text{III}}(\text{phen})_2(\text{CN})_2]\text{NO}_3 \cdot 2\text{H}_2\text{O}$ was synthesized and crystallized out by following all steps of the procedures mentioned earlier [3, 21]. The reagents such as potassium ferrocyanide, potassium nitrate, nitric acid and 1,4-dioxane were provided by Merck and used without any treatment. Acetylferrocene and 1-ferrocenylethanol were purchased from Sigma Aldrich and used without purification. The double-beam spectrophotometer (UV-Visible range/200 to 800 nm, Shimadzu UV-160A) helped to analyze the reactants and the products of the reaction(s).

The instrumental assembly was home-built in our laboratory to monitor the rapid reactions [3,4]. The increase in absorbance along time was recorded upon the reduction of $[\text{Fe}^{\text{III}}(\text{phen})_2(\text{CN})_2]^+$, and the formation of ferrocyphe; $[\text{Fe}^{\text{II}}(\text{phen})_2(\text{CN})_2]$ was monitored at 510 nm and

530 nm in aqueous and dioxane-aqueous (20% v/v) media, respectively. The pseudo-first order condition was maintained to probe the reactions. The oxidation reactions of acetylferrocene and 1-ferrocenylethanol were studied in 20% (v/v) dioxane-aqueous co-solvent mixture at 0.18 mM ionic strength (I) and at room temperature. However, the oxidation of ferrocyanide was probed in the aqueous medium at 60 mM ionic strength and room temperature. The concentration of the reducing agent such as acetylferrocene, 1-ferrocenylethanol, and ferrocyanide was always in excess over the oxidizing agent such as ferricyphen. The results acquired through kinetic studies showed that the reduction of $[\text{Fe}^{\text{III}}(\text{phen})_2(\text{CN})_2]^+$ was completed in three phases (Fig. 1) regardless of the reducing agent, i.e., an overall zeroth order (first phase), an overall second order (second phase), and a competition between the rate of reaction and insolubility of ferrocyphe (third phase).

Three to six experimental trials helped to deduce an average value of the slope to determine the rate constant with standard deviation. The integration method was preferred over others to determine the pseudo-first order rate constant ($k'_{\text{obs}}/\text{s}^{-1}$) because of the completion of reactions in the phases. The increase in absorbance was monitored with respect to time as the ferricyphen reduced. The plot of log natural of the absorbance at a certain time point "t" ($\ln [\text{Absorbance}]_t$) versus time yielded a straight line with an intercept such as the log natural of the absorbance at zero time ($\ln [\text{Absorbance}]_0$), i.e., before starting the reaction. The slope of the plot yielded a pseudo-first order rate constant.

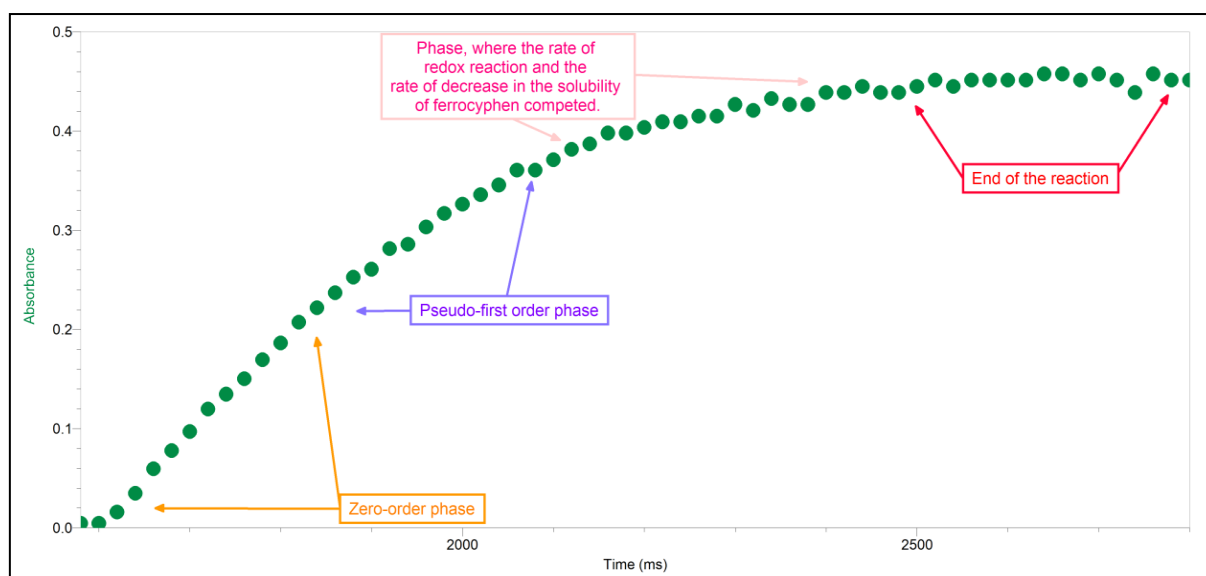


Fig. 1. A representative plot to show the kinetic pathway of the redox reaction between $[\text{Fe}^{\text{III}}(\text{phen})_2(\text{CN})_2]^+$ (0.08 mM) and FcCHOHMe (1.3 mM) at 0.18 mM ionic strength and 291 ± 0.5 K in 20% (v/v) dioxane-aqueous medium.

The zeroth order kinetic data were also acquired by the integration method. The plots of absorbance at time point “t” $[Absorbance]_t$ versus time passed through the origin and the slopes of the plots yielded the observed zeroth order kinetic data. We did not observe any intercept because we did not have any concentration of the product; ferrocypen, initially. The slope of the plot ($\epsilon \cdot b \cdot k_{obs}$; s^{-1}) was not converted into the observed zero-order rate constant (k_{obs} ; $M s^{-1}$). The symbols “ $\epsilon \cdot b$ ” have their conventional meanings to represent the molar absorptivity ($M cm^{-1}$) of ferrocypen and the path length of the cuvette (1 cm). The slope reduces to ‘ $\epsilon \cdot k_{obs}/s^{-1}$ ’ if we put ‘1’ for b, whereas “ ϵ ” carries a constant value and does not change our result of the rate constant (k_{obs}) except the addition of a constant number in all such data.

RESULTS AND DISCUSSION

Kinetic parameters

The effects of varying concentration of the reactants were studied to determine the order of reaction with respect to each reactant. All the other parameters were kept constant for these experiments. The ionic strength was maintained by potassium nitrate (KNO_3) considering the common ions; potassium and nitrate that come from the oxidizing agent and the reducing agent. However, dioxane was used to maintain a 20% (v/v) dioxane-aqueous co-solvent mixture. The experiments were performed at constant concentration (0.08 mM) of $[Fe^{III}(phen)_2(CN)_2]^+$ when the effect of varying concentration of the reducing agent(s) was studied. Meanwhile, 1.3 mM of $FcCOMe/FcCHOHMe/[Fe^{II}(CN)_6]^{4-}$ was maintained constant and the concentration of the oxidizing agent was varied in the experimental setup to study the effect of the concentration of the oxidizing agent on the rate constants. The rest of the experimental conditions were constant such as 0.18 mM (I), 20% (v/v) dioxane-aqueous medium, $304 \pm 0.5 K$ ($FcCOMe$), and $291 \pm 0.5 K$ ($FcCHOHMe$) for the reactions of $FcCOMe/FcCHOHMe$. However, the oxidation of $[Fe^{II}(CN)_6]^{4-}$ was studied at 60 mM (I) and $298 \pm 0.5 K$ in aqueous medium.

In the first phase of the reactions, we did not observe any effect of change in the concentration of $[Fe^{III}(phen)_2(CN)_2]^+$, $FcCOMe$, $FcCHOHMe$, and $[Fe^{II}(CN)_6]^{4-}$ over the value of the product of molar absorptivity of $[Fe^{II}(phen)_2(CN)_2]$ and observed zeroth order rate constant(s) ($\epsilon \cdot k_{obs}$). The results are shown in Fig. 2. The results confirmed an initial zeroth order with respect to $[Fe^{III}(phen)_2(CN)_2]^+$, $FcCOMe$, $FcCHOHMe$, and $[Fe^{II}(CN)_6]^{4-}$ in the first phase of the reaction. We also did not observe

any influence of the increasing concentration of $[Fe^{III}(phen)_2(CN)_2]^+$ upon the value of the observed pseudo-first order rate constant(s) (k'_{obs}) in the second phase of the reactions (Fig. 3). This supported the suitability of our maintained experimental conditions because under the pseudo-first order conditions the observed rate constant remains constant, however the rate of reaction changes with respect to the concentration of $[Fe^{III}(phen)_2(CN)_2]^+$ as follows.

$$Rate = k_{obs} + k'_{obs}[Fe^{III}(phen)_2(CN)_2]^+ \dots (1)$$

where, $FcCOMe/FcCHOHMe/[Fe^{II}(CN)_6]^{4-} \gg \gg [Fe^{III}(phen)_2(CN)_2]^+$

k_{obs} = observed zeroth order rate constant

$$k_{obs} = k_1[FcCOMe/FcCHOHMe/Fe^{II}(CN)_6]^{4-} = k_1 \dots (2)$$

$$k'_{obs} = \text{pseudo-first order rate constant} = k_2 [FcCOMe/FcCHOHMe/Fe^{II}(CN)_6]^{4-} \dots (3)$$

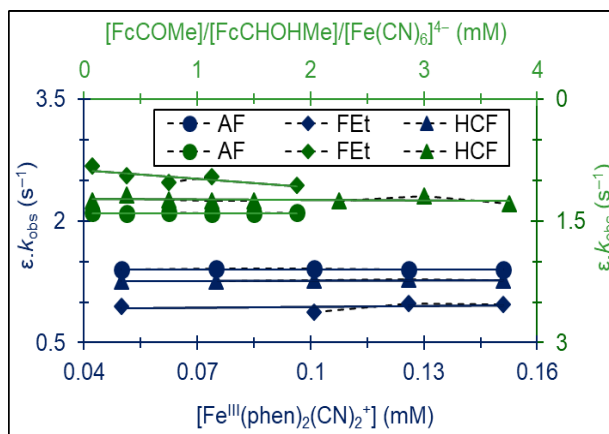


Fig. 2. Effect of variation in the concentration of oxidant and reductant on the observed zeroth order rate constant(s). The AF/FET/HCF corresponds to acetylferrocene/1-ferrocenylethanol/ferrocyanide.

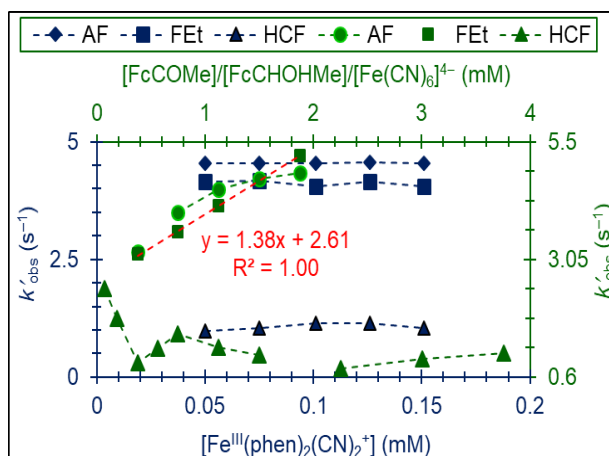


Fig. 3. Effect of variation in the concentration of oxidant and reductant on the observed pseudo-first order rate constant(s). The AF/FET/HCF corresponds to acetylferrocene/1-ferrocenylethanol/ferrocyanide.

Different results on the effect of increasing concentration of the reducing agents in the reaction mixture upon the observed pseudo-first order rate constants (k'_{obs}) were observed (Fig. 3). The effect was an increasing curvature in case of FcCOME (acetylferrocene), a linear dependence with respect to FcCHOHMe (1-ferrocenylethanol), and a sine-wave pattern of k'_{obs} when the concentration of ferrocyanide ($[\text{Fe}^{\text{II}}(\text{CN})_6]^{4-}$) was increased. The value of the rate constant (k'_{obs}) increased initially, then decreased and then at the higher concentration of $[\text{Fe}^{\text{II}}(\text{CN})_6]^{4-}$, it again increased. The results are shown in Fig. 3. All of the reactions followed the first order with respect to the oxidizing agent ($[\text{Fe}^{\text{III}}(\text{phen})_2(\text{CN})_2]^+$) in the second phase of the reactions according to the outcomes of the integration method. The increasing curvature with respect to the increasing concentration of acetylferrocene when plotted against k'_{obs} shows the formation of other species in the reaction mixture. A well-known characteristic of the carbonyl group is to get protonated. We assume the formation of the conjugate acid of acetylferrocene, and its oxidation subsequently during the reaction. The rate constant, k'_{obs} , showed a linear increase with increasing concentration of 1-ferrocenylethanol, and confirmed the first order reaction corresponding to 1-ferrocenylethanol. The sine-wave pattern of k'_{obs} upon increasing concentration of $[\text{Fe}^{\text{II}}(\text{CN})_6]^{4-}$ revealed that the oxidation of $[\text{Fe}^{\text{II}}(\text{CN})_6]^{4-}$ involved its other species as well. The protonation of $[\text{Fe}^{\text{II}}(\text{CN})_6]^{4-}$ may yield mono-, di-, tri-, and/or, tetra-protonated species. The protonation of ferrocyanide is condition-dependent such as the concentration of ferrocyanide in the reaction mixture, and/or, the composition of the medium for reaction to occur with the available concentration of the proton/ H^+ ions [3]. However, the protonation of ferricyphen does not take place under the experimental conditions employed for this study [3, 21]. In order to confirm our assumptions and to rectify the results, we studied the effect of acid (H^+) on the rate constants.

Effect of the concentration of acid (H^+) on the rate constants

The concentration of proton (H^+) was varied by increasing the concentration of nitric acid in the reaction mixture. We used nitric acid (HNO_3) regardless of its strong oxidizing properties because its concentrated solution was employed initially to oxidize the reduced form of the oxidizing agent during the synthesis of $[\text{Fe}^{\text{III}}(\text{phen})_2(\text{CN})_2]^+$ [3,4]. The oxidizing agent is stable in the nitric acid, consequently. The concentrations of the nitric acid used in this study were dilute, and unable to oxidize

the stable reducing agents such as FcCOME, FcCHOHMe, and $[\text{Fe}^{\text{II}}(\text{CN})_6]^{4-}$. The nitrate ion was, however, the common ion because the nitrate salt of the oxidizing agent was the reactant to prepare the solutions. We observed that $\varepsilon.k_{\text{obs}}$ did not accept any effect of increasing concentration of H^+ ions in the reaction(s) mixture, as was expected due to obeying the zeroth order rate law in the first phase (Fig. 4). The molar concentrations of $[\text{Fe}^{\text{III}}(\text{phen})_2(\text{CN})_2]^+$ and FcCOME/FcCHOHMe/ $[\text{Fe}^{\text{II}}(\text{CN})_6]^{4-}$ were maintained at a ratio of “1” (0.08 mM) and “10” (0.75 mM), respectively, to follow the reactions under the condition of pseudo-first order. The concentration of acid/proton (H^+) was always in excess over the concentration of FcCOME/FcCHOHMe/ $[\text{Fe}^{\text{II}}(\text{CN})_6]^{4-}$. The other parameters were kept constant such as 5.1 mM (I) and 306 ± 0.5 K (FcCOME) or 291 ± 0.5 K (FcCHOHMe) in 20% dioxane-aqueous (v/v) medium. For the $[\text{Fe}^{\text{II}}(\text{CN})_6]^{4-}$ system, the experimental conditions were settled at 0.12 M (I) and 302 ± 0.5 K in the aqueous medium. The observed pseudo-first order rate constant; k'_{obs} , decreased upon increasing the concentration of proton (acid/ H^+) in each of the reactions between $[\text{Fe}^{\text{III}}(\text{phen})_2(\text{CN})_2]^+$ and FcCHOHMe or $[\text{Fe}^{\text{II}}(\text{CN})_6]^{4-}$, and gradually became constant at the higher concentration of acid (proton/ H^+). In case of the reduction of FcCOME, the value of the rate constant, k'_{obs} , increased rather than showing a decrease, as was observed in the former two cases, and became constant at the higher concentration of acid (H^+) similar to that of the other two reactions. The results are shown in Fig. 5 (plot of k'_{obs} versus $[\text{H}^+]$). The effect of acid (H^+) rectifies our result with a clear conclusion of the formation of protonated FcCOME/FcCHOHMe/ $[\text{Fe}^{\text{II}}(\text{CN})_6]^{4-}$. These protonated reducing agents influenced the rate of reactions, and the rate constants consequently. The oxidizing agent did not protonate, because, during its synthesis, we did not observe any protonated product/yield. The product was the hydrated salt of $[\text{Fe}^{\text{III}}(\text{phen})_2(\text{CN})_2]^+$ in the form of $[\text{Fe}^{\text{III}}(\text{phen})_2(\text{CN})_2]\text{NO}_3 \cdot 2\text{H}_2\text{O}$. (FcC⁺OHMe/FcCO⁺HMe). The rate acceleration upon increasing the concentration of acid (H^+) in the reaction mixture leads to the conclusion that the protonated acetylferrocene (FcC⁺OHMe/FcCO⁺HMe) is basically the reactant involved in the rate-determining step of the redox reaction between $[\text{Fe}^{\text{III}}(\text{phen})_2(\text{CN})_2]^+$ and FcCOME. The reducing agent, 1-ferrocenylethanol (FcCHOHMe) has an oxygen atom in its structure also, with two lone pairs of electrons that attract the proton (H^+) from the medium and gets protonated to form FcCHO⁺H₂Me.

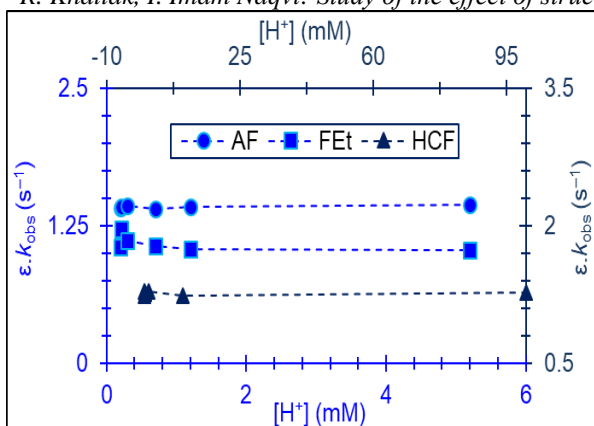


Fig. 4. Effect of variation in the concentration of acid (H^+) on the observed zeroth order rate constant(s). The AF/FEt/HCF corresponds to acetylferrocene/1-ferrocenylethanol/ferrocyanide.

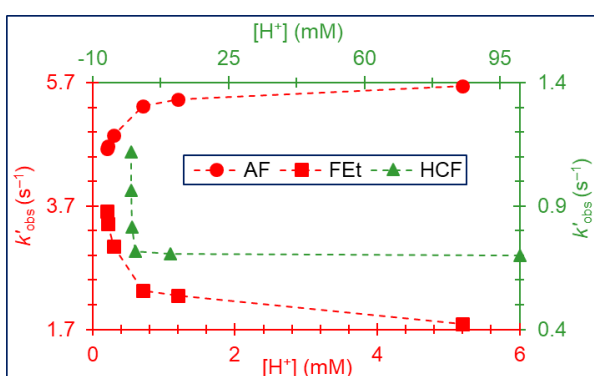
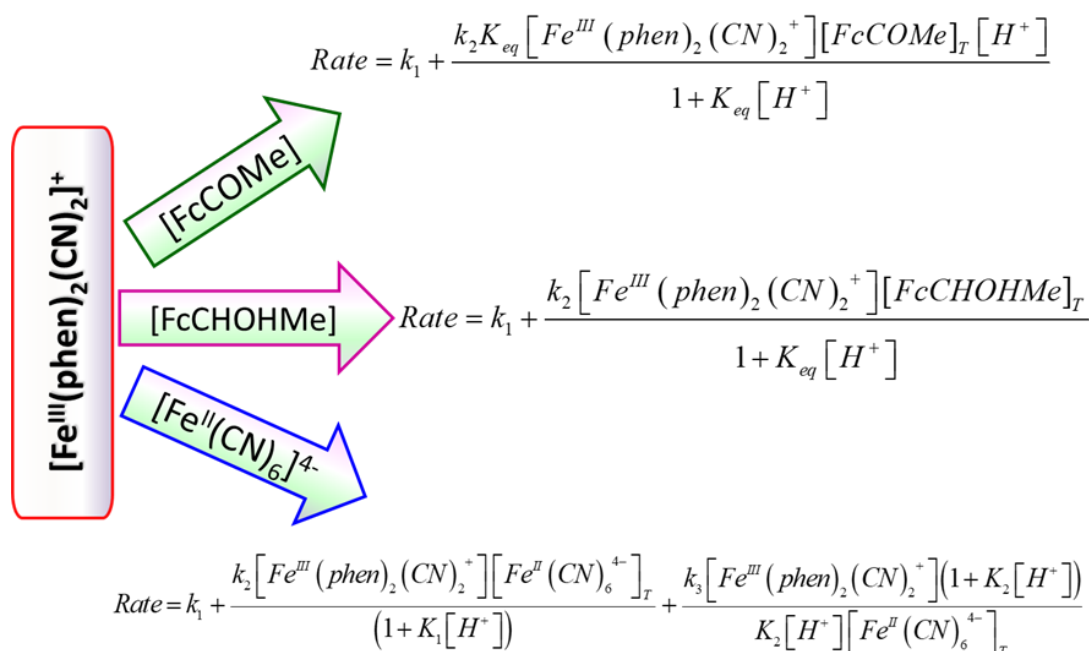


Fig. 5. Effect of variation in the concentration of acid (H^+) on the observed pseudo-first order rate constant. The AF/FEt/HCF corresponds to acetylferrocene/1-ferrocenylethanol/ferrocyanide.

The deceleration of the rate upon protonation of FcCHOHMe helped to conclude that the free compound (FcCHOHMe) donates an electron in the rate-determining step of the reaction. However, under the conditions we maintained for our reaction between $[Fe^{III}(phen)_2(CN)_2]^+$ and $[Fe^{II}(CN)_6]^{4-}$, the existence of $H_4[Fe^{II}(CN)_6]$ and $H_3[Fe^{II}(CN)_6]^-$ was not possible, but that of $H_2[Fe^{II}(CN)_6]^{2-}$ and $H[Fe^{II}(CN)_6]^{3-}$ was possible at the high concentrations of ferrocyanide and proton (H^+). The decrease in the rate constant (k'_{obs}) with increasing proton (H^+) concentration reflected the formation of protonated ferrocyanide either in the form of monobasic or dibasic acid such as $H[Fe^{II}(CN)_6]^{3-}$ and $H_2[Fe^{II}(CN)_6]^{2-}$ in the reaction mixture, which retarded the rate of reaction by decreasing the concentration of free ferrocyanide ion in the vicinity. This leads to the conclusion that free $[Fe^{II}(CN)_6]^{4-}$ gets oxidized in the rate-determining step. The rate constant (k'_{obs}) became constant at the higher concentration of proton/ H^+ because of the constant concentration of the limiting reactant, i.e., FcCOMe/FcCHOHMe/ $[Fe^{II}(CN)_6]^{4-}$.

The structural difference between the reducing agents containing Fe(II) as a central metal ion exhibited the explicit effect on the oxidation of these compounds by the same oxidizing agent containing Fe(III). Each of the redox reactions followed an outer-sphere mechanism and a complex kinetics with the different rate law as follows (Scheme 1).



Scheme 1. Proposed rate law(s) of the oxidation of Fe(II) complex(es) by $[Fe^{III}(phen)_2(CN)_2]^+$.

REFERENCES

1. S. Summer, I. I. Naqvi, R. Khattak, S. Gulzar, F. Reyaz, *J. Chem. Soc. Pak.*, **38**, 384 (2016).
2. R. Khattak, I. I. Naqvi, M. A. Farrukh, *J. Iran. Chem. Soc.*, **5**, 631 (2008).
3. R. Khattak, Comparative kinetic study for the electron transfer reactions of some iron complexes, University of Karachi, Karachi, 2011.
4. R. Khattak, I. I. Naqvi, S. Summer, M. Sayed, *Arab. J. Chem.* doi 10.1016/j.arabjc.2016.05.007, (2016).
5. L. Bechki, T. Lanez, *Asian J. Chem.*, **22**, 5523 (2010).
6. J. S. Casas, M. V. Castaño, M. C. Cifuentes, J. C. García-Monteagudo, A. Sánchez, J. Sordo, A. Touceda, *J. Organometal. Chem.*, **692**, 2234 (2007).
7. M. Li, F. Gayet, J. Rosselgong, D. M. Haddletto, *Polymer Preprints*, **52**, 375 (2011).
8. A. D. Ryabov, V. N. Goral, E. V. Ivanova, M. D. Reshetova, A. Hradsky, B. Bildstein, *J. Organomet. Chem.*, **589**, 85 (1999).
9. B. Wang, J.-i. Anzai, *Int. J. Electrochem. Sci.*, **10**, 3260 (2015).
10. R. F. Shago, J. C. Swarts, E. Kreft, C. E. J. V. Rensburg, *Anticancer Research*, **27**, 3431 (2007).
11. D. Osella, M. Ferrali, P. Zanello, F. Laschi, M. Fontani, C. Nervi, G. Cavigliolo, *Inorg. Chim. Acta*, **306**, 42 (2000).
12. E. Pelizzetti, E. Mentasti, E. Pramauro, *Inorg. Chem.*, **17**, 1181 (1978).
13. R. Blake, K. J. White, E. A. Shute, *J. Biol. Chem.*, **266**, 19203 (1991).
14. H. D. Takagi, N. Kagayama, M. Matsumoto, T. Tarumi, S. Funahashi, *J. Mol. Liq.*, **65-66**, 277 (1995).
15. M. Matsumoto, T. Tarumi, K.-i. Sugimoto, N. Kagayama, S. Funahashi, H. D. Takagi, *Inorg. Chim. Acta*, **255**, 81 (1997).
16. R. Khattak, M. Nazir, S. Summer, M. Sayed, A. Minhaz, I. I. Naqvi, *Chemical Papers*, (2017).
17. T. Rennert, A. Pohlmeier, T. Mansfeldt, *Environ. Sci. Technol.*, **39**, 821 (2005).
18. D. M. Kardel, H. B. Dunford, S. Alexandre, *Eur. J. Biochem.*, **194**, 259 (1990).
19. G. Rabai, I. R. Epstein, *Inorg. Chem.*, **28**, 732 (1989).
20. A. E. M. Abdel-Hady, *Transit. Met. Chem.*, **33**, 887 (2008).
21. A. A. Schilt, *J. Am. Chem. Soc.*, **82**, 3000 (1960).

The effect of bovine myoglobin on ultraviolet fluorescence of gadolinium-doped zinc oxide films

I.A. Hayrullina^{1*}, E. A. Boruleva², I.A. Nagovitsyn^{3,4}, T.F. Sheshko¹,

A.G. Cherednichenko¹, E.A. Sarycheva¹, G.K. Chudinova^{3,2}

¹RUDN University - Peoples' Friendship University of Russia, Moscow Miklukho-Maklaya str.6, Moscow, Russia

²National Research Nuclear University MEPhI (Moscow Engineering Physics Institute), Moscow, Russia

³General Physics Institute RAS, Moscow, Russia

⁴Semenov Institute of Chemical Physics RAS, Moscow, Russia

Received October 30, 2018; Revised January 16, 2019

ZnO thin films doped with 0.1 mass% of Gd have been firstly developed with the aim of using as sensitive surfaces for bioanalysis with fluorescent registration. Gd-doped films were prepared by sol-gel and spin coating techniques on monocrystalline silicon supports. Adding Gd³⁺ ions resulted in a red shift maximum ($\lambda_{em} = 380$ nm) band of ZnO fluorescence by 8-10 nm. Bovine myoglobin (MB) at neutral pH =7 (isoelectric point) was deposited from solutions with concentrations of MB in the interval from 10⁻⁶ to 10⁻¹² M on Gd-doped ZnO surfaces by spin coating techniques. This led to 5-8 % fluorescence quenching for 10⁻⁶ – 10⁻¹⁰ M MB concentrations and 20 % fluorescence enhancing for the 10⁻¹² M one.

Keywords: ZnO thin film, gadolinium, sol-gel method, ultraviolet fluorescence, myoglobin (MB)

INTRODUCTION

In the last few decades, considerable attention has been paid to studies of zinc oxide thin films and composite thin film materials containing ZnO due to their photoluminescence properties. There is great interest in the ultraviolet luminescence (UVL) of ZnO, which band lays in the region of about 360 nm [1-5]. It was established that the intensity of UVL of ZnO-containing materials substantially depends on the type and the amount of various substances included in the film composition of ZnO, in particular, oxides of rare-earth elements [6-12]. Therefore, these substances with a narrow intense luminescence band can be used as the basis for the development of biosensor elements highly sensitive to bioobjects with a ratio «signal/noise» significantly more than one. The research on the development of composite materials, in which the intensity of the UVL would be enhanced in comparison with zinc oxide films, was carried out. The doping of zinc oxide film by metals, their oxides, and nonmetals was used to this purpose [13-15].

What is more, rare-earth ions have received considerable attention in terms of doping the films, because they have unique electronic configuration, and moreover, it becomes possible to significantly modify the optical properties of films.

In the present work, zinc oxide films doped with Gd³⁺ ions were obtained for the first time; the

optical characteristics were studied by absorption and fluorescence spectroscopy. Optical properties of the films were tested on a model system containing different concentrations of bovine myoglobin solution.

EXPERIMENTAL

ZnO thin films doped by gadolinium (Gd) were synthesized using sol-gel method [16]. For the preparation of precursor sol, zinc nitrate Zn(NO₃)₂•6H₂O and gadolinium nitrate Gd(NO₃)₂•6H₂O were dissolved in ethanol (CH₃CH₂OH) at room temperature during an hour. Monoethanolamine (HOCH₂CH₂NH₂) was added as a stabilizer to the nitrate mixture. Glass substrates (15×15 mm) were thoroughly cleaned in ethanol, acetone and after that were boiled in a solution of distilled water, hydrogen peroxide (35 %) and NH₄OH (25%) in a volume ratio of 4:1:1 for 20 min. The prepared sol was deposited with a rotation speed of 3000 rpm in the centrifuge "Elekon" CLMN-P10-02 (Russia). Then, films were preheated to 130°C for 15 min to eliminate the organic residuals. Finally, the obtained films were annealed in air at 450°C for an hour in a muffle furnace.

Bovine myoglobin (Sigma-Aldrich) was used in concentrations of 10⁻⁸, 10⁻¹⁰ and 10⁻¹² M obtained from a base solution of 10⁻⁶ M (pH = 7.0) by sequential dilution. 20 μl of MB solution was applied on the surface of ZnO (Gd) films on a glass

* To whom all correspondence should be sent.
E-mail: spaldingtm@mail.ru

I.A. Hayrullina et al.: The effect of bovine myoglobin on ultraviolet fluorescence of gadolinium-doped zinc oxide films substrate by the spin coating method at a spin speed of 2000 rpm using a modified centrifuge "Elekon" CLMN-P10-02 (Russia). Fluorescence spectra of the samples were measured with a spectrofluorometer RF-5300pc (Shimadzu).

Fluorescence intensity was registered on 0.2 nm intervals, with slits of excitation and registration of 3 and 5 nm, respectively. Origin 8.1 software was used for data processing. Spectra processed by an "adjacent averaging" curve smoothing method (number of pixels for averaging was 20) were used for the calculation of maxima of fluorescent bands. The integral fluorescence was evaluated as an area beneath the curve of fluorescence intensity vs wavelength relationship in the 320-450 nm wavelength range. The use of integral intensity is convenient for unifying the results, including situations in which various devices with different optical characteristics were used.

RESULTS AND DISCUSSION

Figure 1 shows the fluorescence spectra at $\lambda_{ex} = 280$ nm for thin films of ZnO and ZnO doped with 0.1 mass% of Gd (280 nm myoglobin absorption maximum).

In the fluorescence spectra of ZnO films, there are two bands with maxima at 357 nm and 362 nm (Figure 1). Doping with Gd^{3+} leads to a decrease in the intensity of the shortwave band by 10% with a slight bathochromic shift (5 nm), as well as adduces to noticeable increase in the fluorescence intensity in the region of long wavelengths ($\lambda_{em} = 389$ nm) and the shift of the maximum fluorescence band with doping was 7 nm ($\lambda_{em} = 382$ nm).

Figure 2 A, B shows the fluorescence spectra at different concentrations of bovine myoglobin applied to the surface of zinc oxide and zinc oxide- Gd^{3+} films. There are differences in the interaction of bovine myoglobin with zinc oxide films and zinc oxide- Gd^{3+} films. In the case of (figure 2, A) zinc oxide films the maximal fluorescence intensity was observed at bovine myoglobin concentration of 10^{-6} M, while for the doped films at 10^{-10} M ($\lambda_{em} = 358$ nm). According to figure 2 the doping of films changes fluorescence intensity by 5% while without doping – by 10 nm.

Figure 3 A, B shows the change in the integral fluorescence (S) versus the concentration of bovine myoglobin on the surface of ZnO and ZnO films doped with 0.1 mass. % Gd, as an average of three parallel measurements. Obviously, doping with low concentrations of gadolinium qualitatively changes the fluorescent response of the system to different protein concentrations. Dependencies for ZnO

undoped samples are not linear while for ZnO doped with Gd thin films they have a linear relationship.

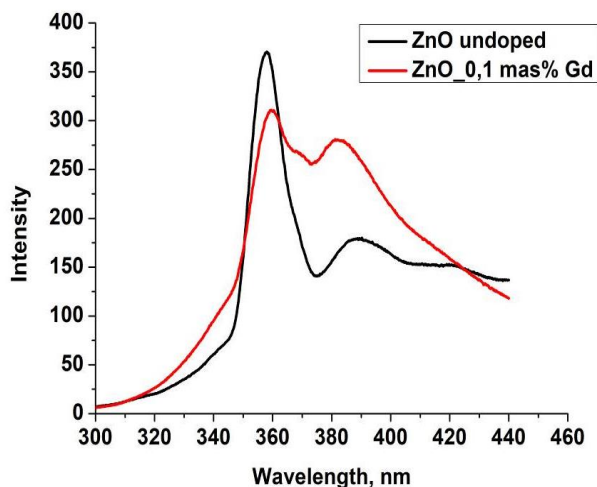


Figure 1. Fluorescence spectra of ZnO (black line) and ZnO- Gd^{3+} films (0.1 mass. % Gd) (red line)

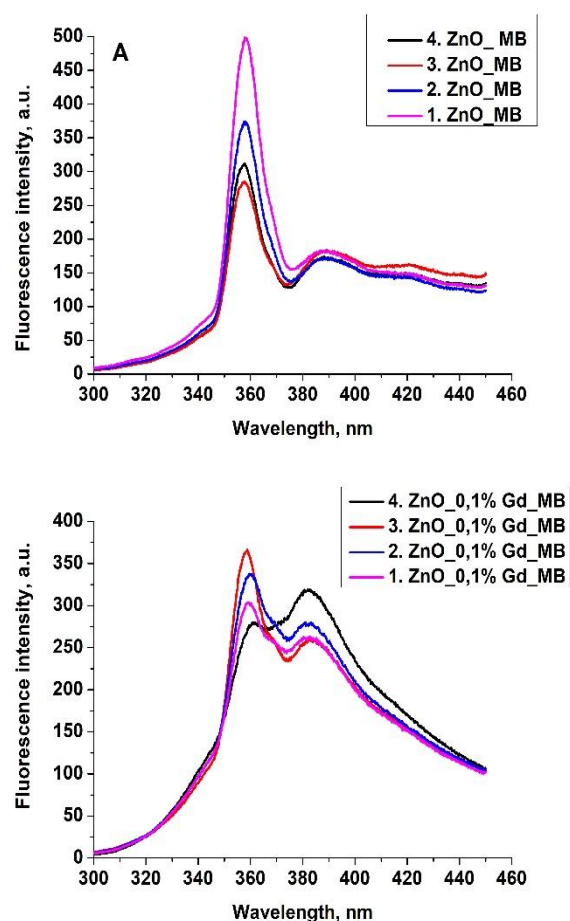


Figure 2. Fluorescence spectra of ZnO (A) and ZnO- Gd^{3+} (B) films (0.1 mass. % Gd) under the action of myoglobin. Myoglobin concentration in solution for depositing on films surfaces: **1** – 10^{-6} , **2** – 10^{-8} , **3** – 10^{-10} , **4** – 10^{-12} M.

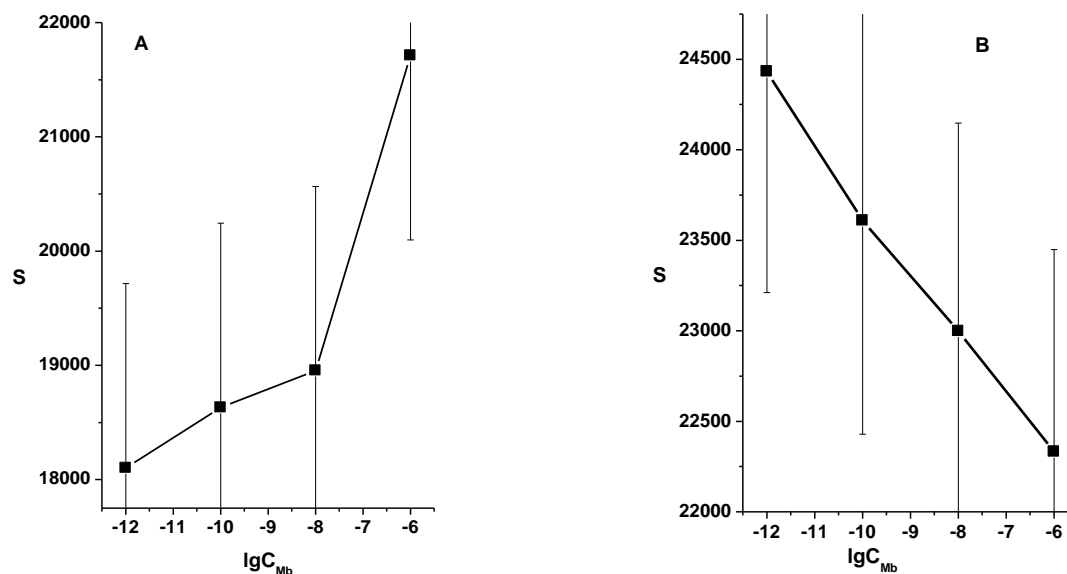


Figure 3. Dependence of the fluorescence intensity on the myoglobin concentration for ZnO (A) and ZnO-Gd³⁺ films (B).

Thus, on glass containing ZnO with dopant Gd³⁺, small concentrations of protein can be determined.

CONCLUSIONS

Thin films of a new composite material were prepared by the sol-gel method. Zinc oxide doped with gadolinium was obtained, and its photoluminescence properties were studied in the UV range. The experiments revealed that the presence of Gd dopant significantly affects the change in the intensity of the photoluminescence of ZnO ($\lambda_{em} = 340-400$ nm) during the adsorption of globular protein (bovine myoglobin), and the luminescence intensity depends on the small protein concentration adsorbed on the films surface. Based on the above discussion the ZnO thin films doped with Gd³⁺ can be used as sensitive systems for fluorescent determination of very small quantities of protein.

Acknowledgement: This publication was prepared with the support of the “RUDN University Program 5-100”. This work was supported by the competitiveness program of NRNU MEPHI.

REFERENCES

1. Y.-S. Kim, W.-P. Tai, S.-J. Shu, *Thin Solid Films*, **491**, 153 (2005).
2. R. Deng, B. Yao, Y.F. Li, Y. Xu, J.C. Li, B.H. Li, Z.Z. Zhang, L.G. Zhang, H.F. Zhao, D.Z. Shen, *Journal of Luminescence*, **134**, 240 (2013).
3. J. Jie, A. Morita, H. Shirai, *Journal of Applied Physics*, **108**, 033521 (2010).
4. L. Xu, X. Li, Y. Chen, F. Xu, *Applied Surface Science*, **257**, 4031 (2011).
5. I. A. Nagovitsyna, G. K. Chudinova, A. V. Lobanov, E. A. Boruleva, V. A. Moshnikov, S. S. Nalimova, I. E. Kononova, *Russian Journal of Physical Chemistry B*, **12**, 651 (2018).
6. F. Xian, X. Li, *Optics & Laser Technology*, **45**, 508 (2013).
7. R. Elleuch, R. Salhi, S.I. Al-Quraishi, J.-L. Deschanvres, R. Maâlej, *Physics Letters A*, **378**, 1733 (2014).
8. Y. Li, J.-ch. Liu, X.-x. Lian, T. Lü, F.-x. Zhao, *Transactions Nonferrous Metals Society of China*, **25**, 3657 (2015).
9. R. Sreeja Sreedharan, R. Reshmi Krishnan, R. Jolly Bose, V.S. Kavitha, S. Suresh, R. Vinodkumar, S.K. Sudheer, V.P. Mahadevan Pillai, *Journal of Luminescence*, **184**, 273 (2017).
10. X.Y. Yi, C.Y. Ma, F. Yuan, N. Wang, F.W. Qin, B.C. Hu, Q.Y. Zhang, *Thin Solid Films*, **636**, 339 (2017).
11. Y. Luo, K. Wang, Q. Qian, W. Zheng, H. Xue, B. Huang, L. Xiao, Q. Chen, *Materials Letters*, **149**, 70 (2015).
12. H. Çolak, E. Karaköse, *Journal of Rare Earths*, **36**, 1067 (2018).
13. F. Xian, X. Li, *Optics & Laser Technology*, **45**, 508 (2013).
14. Y. Geng, Zh.-Y. Xie, W. Yang, S.-S. Xu, Q.-Q. Sun, Sh.-J. Ding, H.-L. Lu, D. W. Zhang, *Surface & Coatings Technology*, **232**, 41 (2013).
15. X. Zhou, D. Jiang, F. Lin, X. Ma, W. Shi, *Physica B*, **403**, 115 (2008).
16. N. Kaur, S. Sharma, D. Youngkim, N. Singh, *Physica B*, **500**, 179 (2016).

Catalytic performance of LnFeO₃ complex oxides for dry reforming of methane to synthesis gas

V. V. Kost^{1*}, T. A. Kryuchkova¹, V. D. Zimina¹, T. F. Sheshko¹,

A. G. Cherednichenko¹, V. V. Kurilkin², M. G. Safronenko², L. V. Yafarova³

¹Peoples' Friendship University of Russia (RUDN University), Faculty of Science, Physical and Colloidal Chemistry Department, Miklukho-Maklaya str. 6, Moscow, 117198 Russia

²Peoples' Friendship University of Russia (RUDN University), Faculty of Science, Inorganic Chemistry Department, Miklukho-Maklaya str. 6, Moscow, 117198 Russia

³Saint-Petersburg State University, Institute of Chemistry, Universitetsky avenue 26, Petergof, St. Petersburg, 198504, Russia

Received October 30, 2018; Revised December 3, 2018

Nanostructured perovskite-type oxides LnFeO₃ (Ln = La, Nd, Gd, Yb, Ho, Lu) were prepared using a method of high-temperature solid state reactions. The effects of lanthanides substitution at the A-site on the catalytic performance of the complex oxides during the dry reforming of methane (DRM) were investigated. It was found that there is a correlation between the nature of the element in A-site of perovskite and its catalytic performances (CH₄ and CO₂ conversion, CO and H₂ formation rate). Moreover, the “gadolinium angle” was established in products formation rate, which was related to the features of changing the electronic configuration in lanthanide series.

Keywords: perovskite-type oxides, dry reforming of methane (DRM), syngas, lanthanides, gadolinium angle

INTRODUCTION

Currently, due to the growing demand for energy and transportation, excessive amounts of fossil fuels are being used, which leads to negative consequences for the environment. The presence of a large amount of greenhouse gases in the atmosphere is becoming one of the most important socio-environmental issues of the modern world, which requires immediate action [1]. There are several ways to solve this problem; one of them is dry reforming of methane (DRM) to synthesis gas. Methane and carbon dioxide (two main greenhouse gases) are used as reagents, and consequently DRM provides us with an opportunity of their effective disposal. It is also worth noting that the synthesis gas obtained by the DRM process has a CO: H₂ ratio close to 1, suitable for further production of valuable liquid fuels by the Fischer-Tropsch method [2-8].

As catalysts for dry reforming of methane, systems of various composition and structure are used. For example, supported catalysts containing transition metals (Ni, Co, Fe) show high activity during the DRM process, but quickly fail by carbon formation on the surface. In fact, the loss of activity *via* carbon deposition does not allow the dry reforming of methane be fully launched on industrial scale. Speaking of precious metal systems, their industrial application is limited

because of their high cost. Using the perovskite-type complex oxides as catalysts for DRM allows overcoming these drawbacks due to a well-defined structure, a more dispersed surface and an increased stability [2-8]. Nowadays perovskites have received considerable attention as a serious alternative for various catalytic systems. Their low cost, rather simple synthesis and also the wide range of changing the structure by replacing the elements are responsible for that [9-14]. The experiments [2-8] reveal that the substitution of various metals in the A-position leads to a significant improvement of activity and strongly influences the physicochemical properties of catalysts samples.

EXPERIMENTAL

Preparation

The synthesis of the perovskites LnFeO₃ (Ln = La, Nd, Gd, Yb, Ho, Lu) by the method of high-temperature solid state reactions [15] was carried out in an air atmosphere using gadolinium oxide and a transition metal oxide (purity of 99%) as follows:



Further the samples were annealed in a muffle furnace at a temperature of 1573 K for 17 hours.

Characterization

The obtained catalysts were evaluated by X-ray diffraction (XRD) using Cu-K α radiation in an

* To whom all correspondence should be sent.
E-mail: kost.veronika6@gmail.com

V.V. Kost et al.: Catalytic performance of LnFeO₃ complex oxides for dry reforming of methane to synthesis gas automated DRON-7 diffractometer (wavelength $\lambda=0.154$ nm) with 0.03° ($\Delta 2\theta$) steps and 3 s counting time in the Bragg angle range of 9° - 80°.

The surface morphology and particle size of the perovskites was investigated by a Zeiss Merlin scanning electron microscope (SEM) with an accelerating voltage of 10 kV, which operates in low vacuum mode and does not require sputtering for non-conducting samples, and with a Carl Zeiss Supra 40VP SEM with a voltage of 20 kV.

The state of iron atoms was determined by Mössbauer spectroscopy on a WISSEL spectrometer. The ⁵⁷Co isotope in the Rh-matrix with an activity of 10 mKu was used as a source of radioactive radiation; all measurements were carried out at room temperature in the absorption geometry. The α - Fe foil was used to calibrate the velocity scale and the zero position of the chemical shift.

Catalytic tests

The DRM reaction was performed under atmospheric pressure in the temperature range 773-1223 K (flow rates of the reaction mixture - 0.5-1.0 l/h). The catalyst (0.1 g) was loaded into a fixed-bed tubular quartz reactor (1 cm in diameter). The gas mixture was supplied for analysis on a gas chromatograph Crystal 2000M, equipped with thermal conductivity and flame ionization detectors connected in series, in the presence of argon as a carrier gas.

The catalytic properties were evaluated in terms of CH₄ and CO₂ conversions, H₂ and CO selectivity, H₂/CO ratio and carbon deposition, as follows:

$$X(\text{CH}_4) = \frac{(n\text{CH}_{4\text{int}} - n\text{CH}_{4\text{out}})}{n\text{CH}_{4\text{int}}} \times 100\% \quad (1)$$

$$X(\text{CO}_2) = \frac{(n\text{CO}_{2\text{int}} - n\text{CO}_{2\text{out}})}{n\text{CO}_{2\text{int}}} \times 100\% \quad (2)$$

$$S_{\text{H}_2} = \frac{n(\text{H}_2)_{\text{form}}}{2n(\text{CH}_4)_{\text{react}}} \times 100\% \quad (3)$$

$$S_{\text{CO}} = \frac{n(\text{CO})_{\text{form}}}{n(\text{CH}_4)_{\text{react}} + n(\text{CO}_2)_{\text{react}}} \times 100\% \quad (4)$$

$$\frac{\text{H}_2}{\text{CO}} = \frac{n(\text{H}_2)}{n(\text{CO})} \quad (5)$$

$$\text{Carbon balance (\%)} = \frac{n(\text{CH}_4)_{\text{out}} + n(\text{CO}_2)_{\text{out}} + n(\text{CO})_{\text{form}}}{n(\text{CH}_4)_{\text{int}} + n(\text{CO}_2)_{\text{int}}} \times 100\% \quad (6)$$

RESULTS AND DISCUSSION

Catalyst characterization

The distinct perovskite crystal structure related to single-phase LnFeO₃ with an orthorhombic lattice structure was established by X-ray diffraction analysis (Table 1).

The results of scanning electron microscopy revealed that the complex oxides are crystallites of irregular shape with an average particle size of 10 μm . The typical image of SEM observation is shown in Fig. 1 for GdFeO₃ as an example.

According to the data of Mössbauer spectroscopy, a single magnetically ordered state of iron is observed in the structure of the perovskite samples - Fe³⁺.

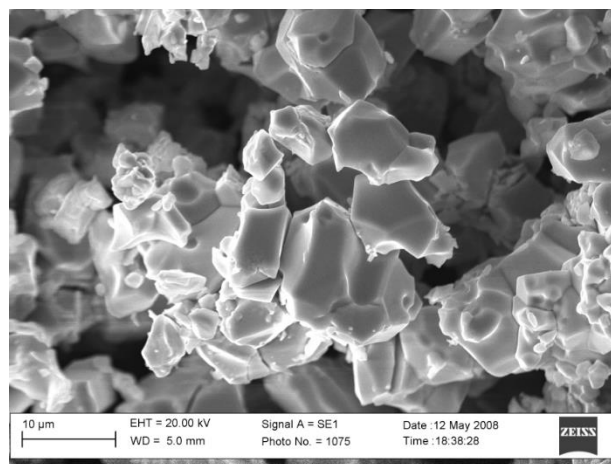


Figure 1. Micrograph of a complex oxide GdFeO₃

Table 1. Catalytic characteristics of the studied samples (at T = 1223K).

Sample	Elemental chemical composition		Phase	Iron state
	Ln, mass. %	Fe, mass. %		
LaFeO ₃	63.80%	36.20%	LaFeO ₃ perovskite	Fe ³⁺
NdFeO ₃	66.68%	33.32%	NdFeO ₃ perovskite	Fe ³⁺
GdFeO ₃	79.35%	20.65%	GdFeO ₃ perovskite	Fe ³⁺
HoFeO ₃	61.84%	38.16%	HoFeO ₃ perovskite	Fe ³⁺
YbFeO ₃	66.01%	33.99%	YbFeO ₃ perovskite	Fe ³⁺
LuFeO ₃	75.46%	24.54%	LuFeO ₃ perovskite	Fe ³⁺

The perovskite type oxides LnFeO₃ containing different A-site cations (Ln = La, Nd, Gd, Yb, Ho, Lu) were evaluated as catalysts for their performance in dry reforming of methane.

Methane and carbon dioxide conversion

Fig. 2 shows that the reactant conversions did not exceed 10% up to a temperature of 1023 K over LaFeO₃ during the process. A similar pattern was observed in the case of substitution of La by Nd and Gd. Still, further increasing in the reaction temperature led to an improvement in the performance of the catalysts. In high-temperature areas the reactant conversions went up in the following order: LaFeO₃ < NdFeO₃ < GdFeO₃. So, at T = 1223 K, methane and carbon dioxide conversion for LaFeO₃ were 20% and 33%, for NdFeO₃ - 21% and 36%, and for GdFeO₃ - 26% and 49%, respectively. According to the obtained values, the introduction of gadolinium in the A-site of the cationic sublattice of the composite oxide caused an increase in the reactant conversions by 5-10% compared with lanthanum ferrite.

Low conversion values were observed over HoFeO₃ and LuFeO₃ perovskite oxides under the DRM whereas the perovskite containing ytterbium as lanthanide in the structure shows superior activity in terms of the conversion of methane and carbon dioxide (34 and 55%, respectively). These results suggest that ytterbium tends to be involved

in side processes (the Boudoir reaction and decomposition of methane), [16] which is indirectly confirmed by the low values of carbon balance (Table 2).

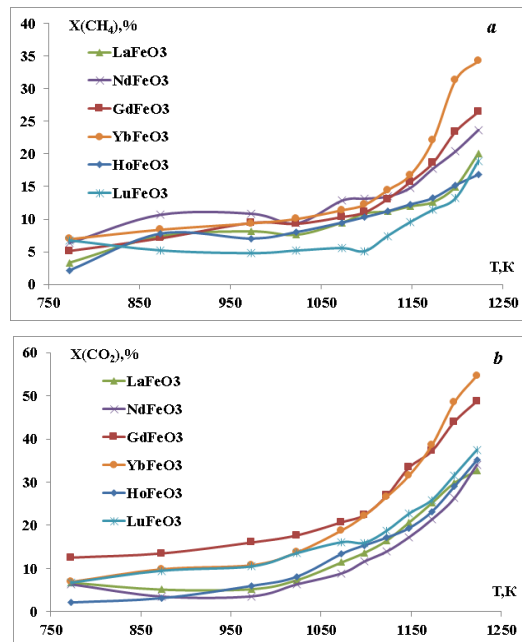


Figure 2. Temperature dependences of CH₄ (a), CO₂ (b) conversions over AFeO₃ (A = La, Nd, Gd, Yb, Ho, Lu)

Table 2. Catalytic characteristics of the studied samples (at T = 1223K)

Sample	X(CH ₄), %	X(CO ₂), %	r (CO), mole/(h*g)	r (H ₂), mole/(h*g)	S(CO), %	S(H ₂), %	H ₂ /CO	Carbon balance, %	Electronic configuration
LaFeO ₃	20	33	0.096	0.025	87	29	0.26	96	4f ⁰ 5d ¹ 6s ²
NdFeO ₃	21	36	0.106	0.038	74	36	0.36	92	4f ⁴ 6s ²
GdFeO ₃	26	49	0.130	0.046	76	38	0.36	91	4f ⁷ 5d ¹ 6s ²
HoFeO ₃	17	35	0.096	0.029	85	39	0.30	96	4f ¹¹ 6s ²
YbFeO ₃	34	55	0.088	0.030	58	25	0.34	81	4f ¹⁴ 6s ²
LuFeO ₃	19	38	0.094	0.031	79	39	0.33	94	4f ¹⁴ 5d ¹ 6s ²

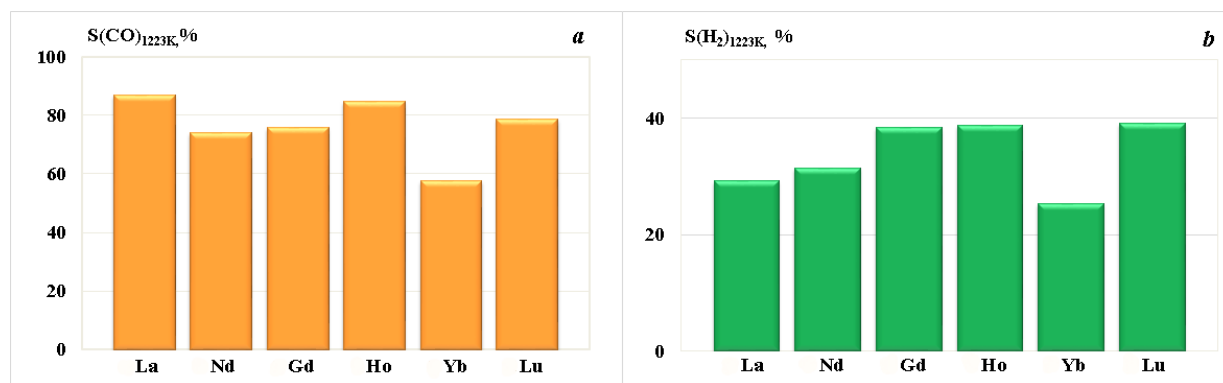


Figure 3. CO (a) and H₂ (b) selectivities for the perovskite oxides in the high-temperature area

Fig. 3 represents the temperature dependences of the carbon monoxide and hydrogen selectivities. It follows that an increase in temperature leads to the growth of CO and H₂ selectivities for all the studied samples. AFeO₃ (A = Gd, Ho, Lu) are worth noting since carrying out the reaction on these perovskites allows to obtain a higher value of hydrogen selectivity (40%). However, with respect to CO, such dependence was not observed: carbon monoxide S (CO) reached a maximum over LaFeO₃ perovskite compared with the other samples.

Fig. 4 presents the temperature dependence of the syngas ratio for all catalyst samples. The diagram clearly demonstrates the maximum value of 0.36 observed over GdFeO₃ and NdFeO₃ oxides.

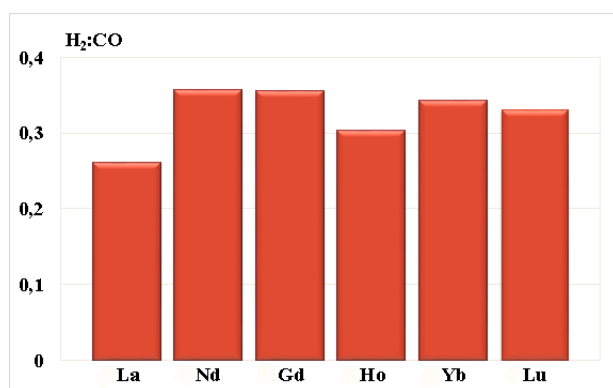


Figure 4. H₂:CO ratio for all catalyst samples in the high-temperature area

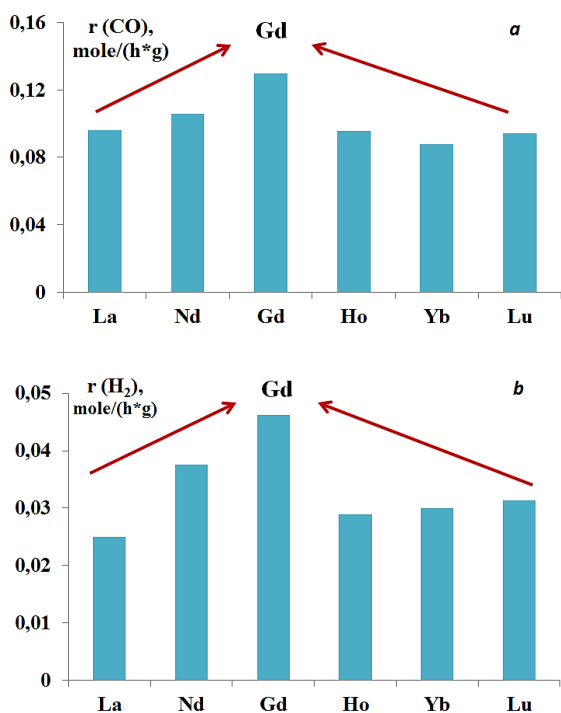


Figure 5. The formation rate of CO (a) and H₂ (b) depending on the nature of the element in the A-position

Analysis of the obtained experimental data revealed some dependence on the nature of the A-element for all studied catalysts: the rates of hydrogen and carbon monoxide formation reached a maximum on GdFeO₃ (Fig. 5) that is the so-called “gadolinium angle” [17, 18].

Most likely, the appearance of the “gadolinium angle” in the catalytic properties is associated with the peculiarities of the electronic configuration change in the lanthanide series. Starting with lanthanum and moving towards gadolinium the number of electrons at the 4f-level increases, while the 5d-level remains unoccupied. An additional electron occupies the 5d level in gadolinium structure, forming the 4f⁷5d¹6s² electron configuration. The next element in the lanthanide series (terbium) is characterized by transition of the 5d-electron to the 4f-level (4f⁹6s²) as well as cerium. Further, up to ytterbium, a monotonous increase in the number of electrons to 4f¹⁴ is observed [17]. Moreover, gadolinium has the largest ion radius among others in the Ln³⁺ series [18]. Thus, it can be assumed that the Me-CO₂ bond weakens on moving from La and Lu to Gd, which promotes the dissociative adsorption of carbon dioxide and increases the rate of CO formation.

CONCLUSIONS

In this study, the catalytic activity of complex perovskite-type oxides AFeO₃ (A = La, Nd, Gd, Ho, Yb, Lu) was investigated in dry reforming of methane. It was considered that methane conversion does not depend on the nature of the element in the A-position of the catalyst structure. Furthermore, a correlation between the nature of the element in the cation sublattice (A-position) and the catalytic characteristics of perovskite (CO₂ conversion and the rate of CO formation) was established. Our results also suggest the presence of a “gadolinium angle” in the rate values of products formation, which is connected with the peculiarities of electronic configuration changes in the lanthanide series.

Acknowledgements: This work was supported by Russian Foundation for Basic Research, research project No 17-03-00647. The publication has been prepared with the support of the «RUDN University Program 5-100. The studies for catalysts characterization at the Research Park of Saint Petersburg State University: Interdisciplinary Center for Nanotechnology, Centre of Thermal Analysis and Calorimetry and Center for X-ray Diffraction Methods. The phase composition analysis of the samples was carried out on the basis

V.V. Kost et al.: Catalytic performance of LnFeO₃ complex oxides for dry reforming of methane to synthesis gas of the Collective Center of Physico-chemical Research at the RUDN University; authors are grateful to the director of the center - Lobanov N.N.

REFERENCES

- O. Edenhofer, R. Pichs-Madruga, Y. Sokona, E. Farahani, S. Kadner, K. Seyboth, et al. Climate change 2014: mitigation of climate change – contribution of Working Group III to the fifth assessment report of the Intergovernmental Panel on Climate Change, Cambridge, Cambridge University Press, 2014, p. 603.
- K. Sutthiumporn, T. Maneerung, Y. Kathiraser, S. Kawi, CO₂ dry-reforming of methane over La_{0.8}Sr_{0.2}Ni_{0.8}M_{0.2}O₃ perovskite (M = Bi, Co, Cr, Cu, Fe): Roles of lattice oxygen on C–H activation and carbon suppression, Department of Chemical & Biomolecular Engineering, National University of Singapore, 4 Engineering Drive 4, Singapore 119260, Singapore
- X. Gao, Zh. Tan, K. Hidajat, S. Kawi, *Catalysis Today*, **281**, 250 (2017).
- J. Juan-Juan, M. C. Roman-Martinez, M. J. Illan-Gomes, *Applied Catalysis A: General*, **355**, 27 (2009).
- M. Radlik, M. Adamowska-Teyssier, A. Krzton, K. Kozieł, W. Krajewski, W. Turek, P. da Costa, *C. R. Chimie*, **18**, 1242 (2015).
- B. de Caprariis, P. De Filippis, V. Palma, A. Petruccio, A. Ricca, C. Ruocco, M. Scarsella, *Applied Catalysis A: General*, **517**, 47 (2016).
- A. Erdohelyi, K. Fodor, F. Solymosi Proc. IV Int. National Gas Conversion Symp. Kruger National Park, South Africa, 1995. Amsterdam, Elsevier, 1997, p. 525.
- J. H. Bitter, V. Seshan, J. A. Lercher, *J. Catal.*, **171**, 279 (1997).
- W. F. Libby, *Science*, **171**, 499 (1971).
- R. J. H. Voorhoeve, J. P. Remeika, P. E. Freeland, B. T. Matthias, *Science*, **177**, 353 (1972).
- R. J. H. Voorhoeve, J. P. Remeika, D. W. Johnson, *Science*, **180**, 62 (1973).
- P. K. Gallagher, D. W. Johnson Jr., F. Schrey, *Mater. Res. Bull.*, **9**, 1345 (1974).
- V. M. Gonzalez-Delacruz, F. Ternero, R. Pereniguez, A. Caballero, J.P. Holgado, *Appl. Catal. A: Gen.*, **384**, 1 (2010).
- T. Odedairo, J. Chen, Z. Zhu, *Catal. Commun.*, **31**, 25 (2013).
- J. Gregory, McCarthy, V. Paul, The Pennsylvania State University, Crystal chemistry of catalyst materials. I. Composition and unit cell parameters of «ReMnO₃» Phases prepared in air, p. 1277.
- K. Świrk, M. E. Gálvez, M. Motak, T. Grzybek, M. Rønning, Patrick Da Costa, *Journal of CO₂ Utilization*, **27**, 247 (2018).
- G. V. Ionova, V. G. Vokhmin, V. I. Spitsyn, Regularities of the change in the properties of lanthanides and actinides, Moscow, Nauka, 1990, p. 7.
- G. A. Bandurkin, B. F. Dzhurinsky, I. V. Tananaev, Crystal chemistry features of compounds containing rare-earth metals, Moscow, Nauka (Chemistry of Rare Elements), 1984, p.190, 203.

Effect of substituting Fe by Mn in GdFeO₃ perovskite catalyst for CO hydrogenation

A. A. Sharaeva^{1*}, T. F. Sheshko¹, T. A. Kryuchkova¹, L. V. Yafarova², I. A. Zvereva²

¹Peoples' Friendship University of Russia (RUDN University), Faculty of Science, Physical and Colloidal Chemistry Department, Miklukho-Maklaya str. 6, Moscow, 117198 Russia

²Saint-Petersburg State University, Petrodvorets, Universitetsky pr. 26, Saint-Petersburg, 198504 Russia

Received October 31, 2018; Revised December 3, 2018

Gd(Fe,Mn)O₃ nanoperoovskites were prepared by sol-gel method and were characterized using different techniques: XRD, SEM+EDX, BET, TG to study structure and morphology. Oxidation states of Fe and Mn were determined by XPS. The performance of GdFe_{1-x}Mn_xO₃ perovskite catalysts with different Mn substitution levels was evaluated in the CO hydrogenation for light olefins production. The complex of physico-chemical methods showed that all investigated samples confirmed the presence of a single phase with perovskite-type structure. Experimental data suggested that catalysts can operate over a wide temperature range without any loss of activity and are practically unaffected by surface carbonation; their phase composition and morphology of the surface change insignificantly in catalytic processes at high temperature (~ 673 K). It was determined that the introduction of manganese into perovskite structure led to a change in the quantitative composition: the amount of butylene was much higher than that of ethylene on the samples containing manganese in the B-site. Activation of catalytic centers and their further stabilization taking place under the action of the reaction medium was established for all the systems studied.

Keywords: carbon monoxide hydrogenation, perovskite catalysts, light olefins, Fischer-Tropsch synthesis

INTRODUCTION

Fischer-Tropsch synthesis (carbon monoxide hydrogenation) converts syngas (mixture of carbon monoxide and hydrogen) into hydrocarbons and oxygenates. The syngas for CO hydrogenation can be produced from fossils and renewable resources (natural gas, coal, carbon residues, and biomass), making this reaction suitable for manufacturing alternative sustainable liquid fuels.

Different types of catalysts with a wide range of metal atoms have been studied, such as higher alcohol synthesis catalysts (based on Cu, Zn, Cr, Al) [1-3], modified Fischer-Tropsch synthesis catalysts (based on Fe, Co, Mn) [4-7] and molybdenum-based catalysts [8]. Zhao *et al.* [9] reported about technologies like MTO (methanol to olefins) and SDTO (synthesis gas through dimethyl ether to olefins) that are already used in industry on zeolite catalysts. However, high operating costs and rapid deactivation of the catalyst, as well as low selectivity to C₂=- C₄= hydrocarbons are the main disadvantages of these technologies in industrial applications.

Recently, perovskite oxides with an ABO₃ type structure (where A and B represent different metallic elements) have been studied for light olefins production [10].

Partial substitution at the A- or/and B-sites of the perovskite (ABO₃) leads to changes in the perovskite structure, the oxygen mobility and the

redox properties of the perovskite, which affects the catalytic activity. Partial substitution at the B-site was found to be an effective method for improvement of product selectivity in carbon monoxide hydrogenation. In our previous work [11], we have reported about catalytic properties of GdFe_{1-x}Mn_xO₃ (x = 0, 0.01, 0.05, 0.2, 0.5, 0.8 and 1) nanoperoovskites prepared by ceramic and sol-gel method. The highest stability, catalytic activity, and unsaturated hydrocarbons (ethylene and propylene) selectivity in the carbon oxides hydrogenation were achieved over GdFeO₃, GdFe_{0.95}Mn_{0.05}O₃, 5 % wt Mn/GdFeO₃ samples.

The main objective of this study is to investigate the effect of manganese substitution on the catalytic activity of GdFeO₃ perovskite in syngas conversion, and to find correlation between the composition of complex oxides and their catalytic activity.

EXPERIMENTAL

Catalyst preparation

A series of GdFe_{1-x}Mn_xO₃ (x=0, 0.5, 0.8 and 1) perovskite-type oxides were synthesized *via* sol-gel method in which citric acid (C₆H₈O₇·H₂O) was used as the complexing agent. Gd(NO₃)₃·5H₂O, Fe(NO₃)₃·9H₂O and Mn(NO₃)₂·4H₂O were mixed and dissolved in deionized water. The solution was heated and vigorously stirred until the temperature reached 363-373K, citric acid was added to the

* To whom all correspondence should be sent.
E-mail: alminasharaeva@gmail.com

A.A. Sharaeva et al.: Effect of substituting Fe by Mn in GdFeO₃ perovskite catalyst for CO hydrogenation solution at that moment. Ammonia solution was used to maintain pH = 6. Thereafter, it was slowly heated up to ~393K until self-ignition of the gel obtained and formation of black powder occurred. The resulting powder was calcined *via* increasing the temperature from ambient one to 723K and the maximum temperature remained constant for 2 h in order to obtain perovskite phases with the same order of crystallinity.

Catalyst characterization

X-ray diffraction data were determined at room temperature on ARL X'TRA and Rigaku "MiniFlex II" devices using CuK α radiation. The surface morphology and microstructure of the samples was investigated by scanning electron microscopy (SEM) by Zeiss EVO@40 microscope and a Carl Zeiss Supra 40VP electron microscope. Specific surface area measurements were carried out by using Brunauer-Emmett-Teller (BET) method based on N₂ adsorption at 77 K on Nova 4200e instrument (Quantachrome). X-ray photoelectron spectroscopy (XPS) of the samples was performed using a Thermo Fisher Scientific Escalab 250Xi with Al K α ($\lambda = 0.1541$ nm) radiation which was used for material excitation.

Catalytic activity measurements

The catalyst performance in CO hydrogenation was evaluated in a fixed-bed quartz U-shaped tubular reactor, containing ~0.1 g of sample. The samples were diluted using quartz particles with a mesh size of 0.25-0.5 mm. The reactor was imbedded in an insulated electric furnace, equipped with a temperature programmable controller. The experiments were carried out in the temperature range from 523 to 708K under atmospheric pressure with a feed composition of CO:H₂= 1:2 and a total flow of 1.5 L/h, with a continuous feed of the reactants. The reactor was placed vertically in the center of a tubular furnace and its temperature was measured/controlled by a K-type thermocouple, placed in the center of the catalyst bed without direct contact with the catalyst.

The temperature was increased from 523 to 708K and remained steady for the desired reaction time. All catalytic reactions were conducted at this temperature. Each experiment took about 7 h. In all experiments the perovskite catalyst was used without previous reduction. The streams were analyzed with a gas chromatograph (Crystal 5000.2, Russia) equipped with thermal conductivity and flame ionization detectors, stainless steel column packed with Porapack Q for detecting reaction products. The rate of formation the reaction products R or space time yields (STY) (mol/h*g_{cat}) was measured after the system reached

an equilibrium state, estimated from the constant chromatographic peaks and normalized per unit mass of catalyst.

The rate of formation of the reaction products R (mol/h*g_{cat}) and the product selectivity (S_i) were calculated according to the following equations:

CO conversion (X_{CO}, % by moles)

$$X_{CO}(\%) = \frac{\text{Moles CO}_{in} - \text{Moles CO}_{out}}{\text{Moles CO}_{in}} \times 100\% \quad (1)$$

The rate of formation of the reaction products R (mol/h*g_{cat}) was calculated as:

$$R_i = \frac{K_x S_i w}{V_{loop} m_{cat}} \quad (2)$$

where, K_x – correction factor for the i-reaction product; S_i – chromatographic peak area, mV/min; R_i – the rate of formation of the i-reaction product per 1 g of catalyst, mol/h*g_{cat}; w – reaction space velocity, 1 – 1.5 L/h; V_{loop} – chromatography sample loop volume, 0.001 L; m_{cat} – the mass of the catalyst metal phase, g.

C_n selectivity (% by C-atoms):

$$S_i = \frac{R_i}{\sum R_i} \times 100\% \quad (3)$$

where, R_i – the rate of formation of the i-reaction product per 1 g of catalyst, mol/h*g_{cat}; $\sum R_i$ – the sum of the rates of formation of the i-reaction products per 1 g of catalyst, mol/h*g_{cat}.

RESULTS AND DISCUSSION

Catalyst characterization

In the literature the complex oxide GdFeO₃ [12] is described as an oxide with a distorted perovskite structure. The results in Fig 1 show the X-ray phase analysis of samples of GdFeO₃, GdMnO₃ and GdMn_{0.5}Fe_{0.5}O₃. All diffractograms are typical for compounds with a well-pronounced perovskite crystal structure. Peaks refer to single-phase GdFeO₃, GdMnO₃ and GdMn_{0.5}Fe_{0.5}O₃ (PDF cards 01-072-9906, 01-070-9199) these connections have an orthorhombic structure. The diffractogram of the synthesized GdMn_{0.5}Fe_{0.5}O₃ is similar with that described in the reported research [13]

Representatives of scanning electron microscopy images of GdFeO₃, GdMnO₃ and GdMn_{0.5}Fe_{0.5}O₃ samples are shown in Fig. 2. SEM images of GdMnO₃ and GdMn_{0.5}Fe_{0.5}O₃ samples show a porous structure with uniformly distributed size grains ~ 200 nm before the catalytic process. The morphology of GdFeO₃ particles is somewhat different from that of particles with paramagnetic Fe and Mn ions: polycrystals are more elongated with an average diameter of 30–60 nm and a length of about 200 nm.

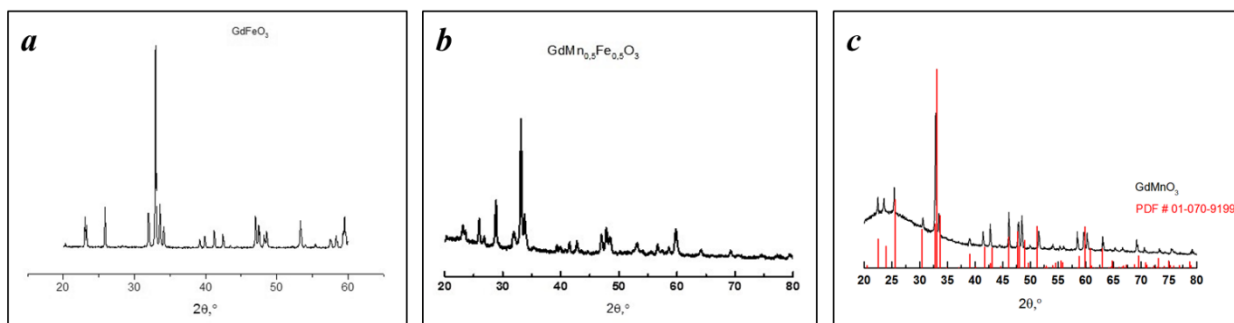


Figure 1. XDR patterns of complex oxides: (a) GdFeO₃; (b) GdMnO₃; (c) GdMn_{0.5}Fe_{0.5}O₃

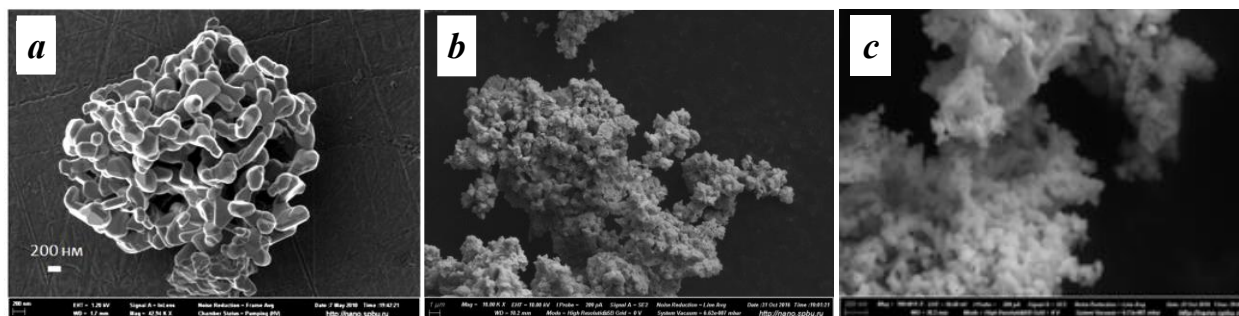


Figure 2. SEM images of GdFe_{1-x}Mn_xO₃ complex oxide: (a) x=0, (b) x=0.5, (c) x=1

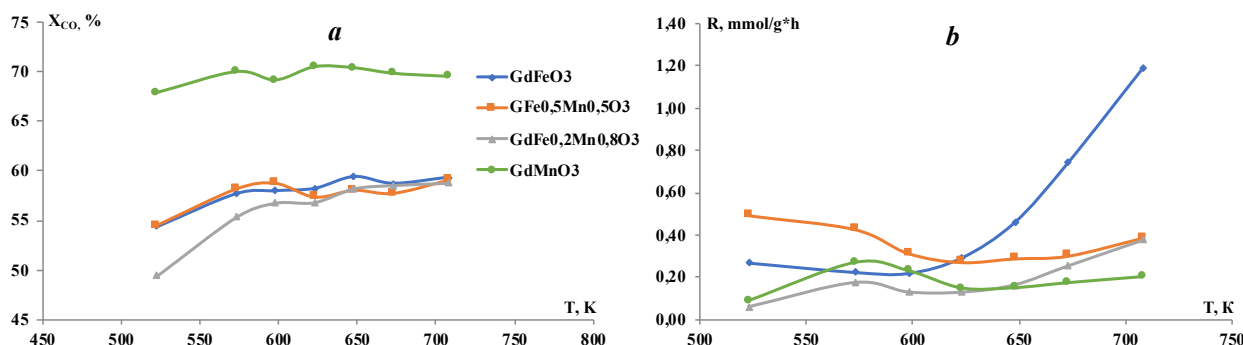


Figure 3. Temperature dependence of (a) the CO conversion and (b) the rate of formation of CO₂ (at a ratio of CO:H₂ = 1:2)

Mössbauer spectra of the solid solutions synthesized *via* sol-gel technology showed the iron atoms in the GdFeO₃ samples to be in state Fe³⁺ in two fields with different symmetry.

The XPS spectra of GdFe_{1-x}Mn_xO₃ and GdMnO₃ samples have the satellite peak at 641.8 eV present in the spectra, which corresponds to the state of Mn³⁺. [14] The Fe2p spectrum showed that iron is in the Fe³⁺[15] state. Gd³⁺ in all compounds before and after catalysis did not change the degree of oxidation.

Catalytic data

Carbon monoxide hydrogenation was carried out within the temperature range of 523-708 K, with a ratio of CO: H₂ = 1: 2. The conversion of CO on all samples is given in Fig. 3a: it was 50–70% and varied slightly with increasing temperature, and on GdMnO₃ it turned out to be a little higher. The formation of CO₂ in the catalytic temperature range

was observed (Fig. 3b), the CO₂ amount on all studied GdFe_{1-x}Mn_xO₃ perovskites, in the temperature range 596-708 remained approximately the same.

Since the course of the curves describing the temperature dependences of CO conversion and CO₂ content in the reaction mixture on the studied catalysts did not differ significantly, it can be assumed that only carbon particles are involved in the formation of reaction products resulting from dissociative adsorption in the noncatalytic temperature range. The CO₂ formation becomes possible when the adsorbed CO_{ads} molecule interacts either with perovskite surface oxygen (O_S) or with oxygen released during dissociative adsorption of CO [16]: CO_{ads} + O_S → CO₂

Since catalytic synthesis proceeds through the interaction of chemisorbed reagents, it is logical to expect a correlation of the catalytic activity and

A.A. Sharaeva et al.: Effect of substituting Fe by Mn in GdFeO₃ perovskite catalyst for CO hydrogenation transition metals selectivity with both absolute heat values of CO and H₂ adsorption on the surface of metals, and with their difference, in the first approximation. According to [17], the difference in the energy of adsorption of CO and H₂ on the surface decreases in the series of Mn, Fe, Co, and these energies themselves are not too large, and therefore the energy barrier to the reaction of adsorbed CO and H₂ will be small. Furthermore, the energy of the bond Me - CO increases in the same series of Mn, Fe, Co. These results [17] correlate well with the obtained CO conversions values.

The reaction products were C₁-C₆ hydrocarbons over all catalytic systems. Among them there are the main ones: methane, ethylene, propylene, butylene. The product formation started at 523K, and further increased with the temperature, but at T > 623 K the rate of C₃-C₆ hydrocarbons formation went down. For example, Fig. 4 shows the

temperature dependences of the hydrocarbons formation rates during the reaction conducted on GdMnO₃. The results from Table 1 clearly demonstrate that increasing the amount of manganese in the B-site of the perovskite structure leads to decline of the products formation rate in the following order: GdFeO₃ > GdFe_{0.5}Mn_{0.5}O₃ > GdFe_{0.2}Mn_{0.8}O₃ > GdMnO₃.

Varying the composition of the catalysts caused changes in the reaction products ratio that can be seen in Table 2. So, in the case of using GdFeO₃ as a catalyst, the amount of methane and light olefins in the reaction mixture at T = 673 K was 71% and 26%, respectively and over complex oxides with partial or full substitution of iron by manganese, the methane content decreased to 30%, and olefins increased to 35%, as well as the hydrocarbons C₅-C₆ ratio.

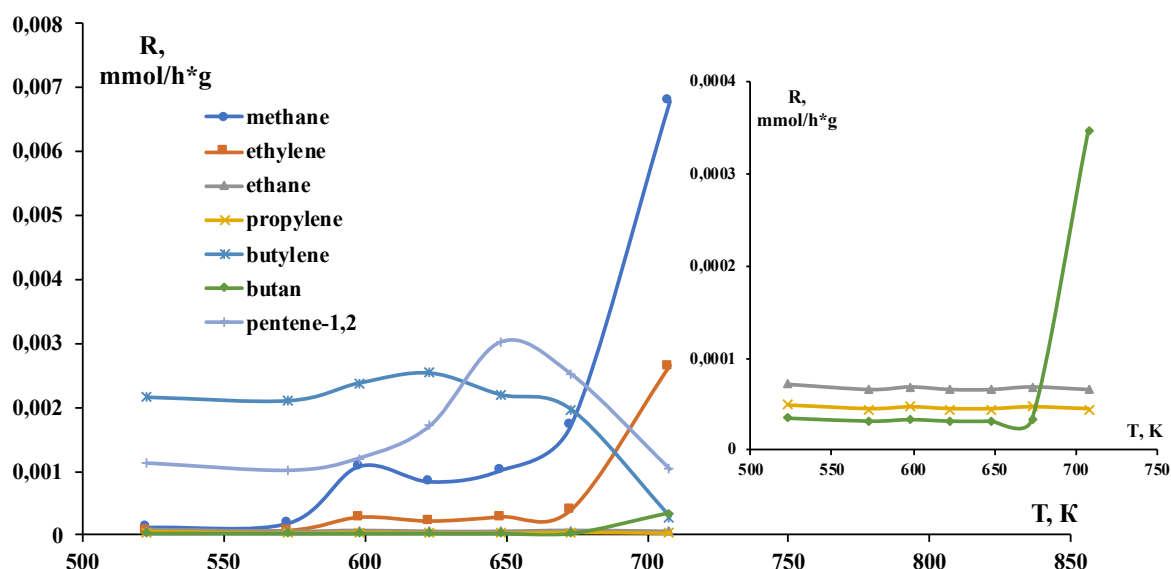


Figure 4. The temperature dependences of the hydrocarbons formation rates over GdMnO₃ (at ratio of CO:H₂=1:2)

Table 1. The rates of formation C₁, C₂, C₄, CO₂ (at T = 708 K)

Sample	R(CH ₄), mmol/h*g _{cat}	R(C ₂ H ₄), mmol/h*g _{cat}	R(C ₄ H ₈), mmol/h*g _{cat}	R(CO ₂), mmol/h*g _{cat}
GdFeO ₃	2536.0	727.0	0.3	1190.0
GdFe _{0.5} Mn _{0.5} O ₃	99.3	22.9	1.0	387.0
GdFe _{0.2} Mn _{0.8} O ₃	17.0	6.2	0.7	375.0
GdMnO ₃	66.8	2.6	0.3	201.0

Table 2. Products composition of carbon monoxide hydrogenation process (at T = 673 K)

Sample	S(CH ₄), %	S(C ₂ H ₄), %	S(C ₃ H ₆), %	S(C ₄ H ₈), %	S(C ₅ -C ₆), %
GdFeO ₃	71.07	18.37	7.29	0.08	3.19
GdFe _{0.5} Mn _{0.5} O ₃	61.26	17.00	7.97	7.37	6.39
GdFe _{0.2} Mn _{0.8} O ₃	27.53	6.31	2.99	28.10	35.06
GdMnO ₃	25.01	5.65	0.68	28.61	40.05

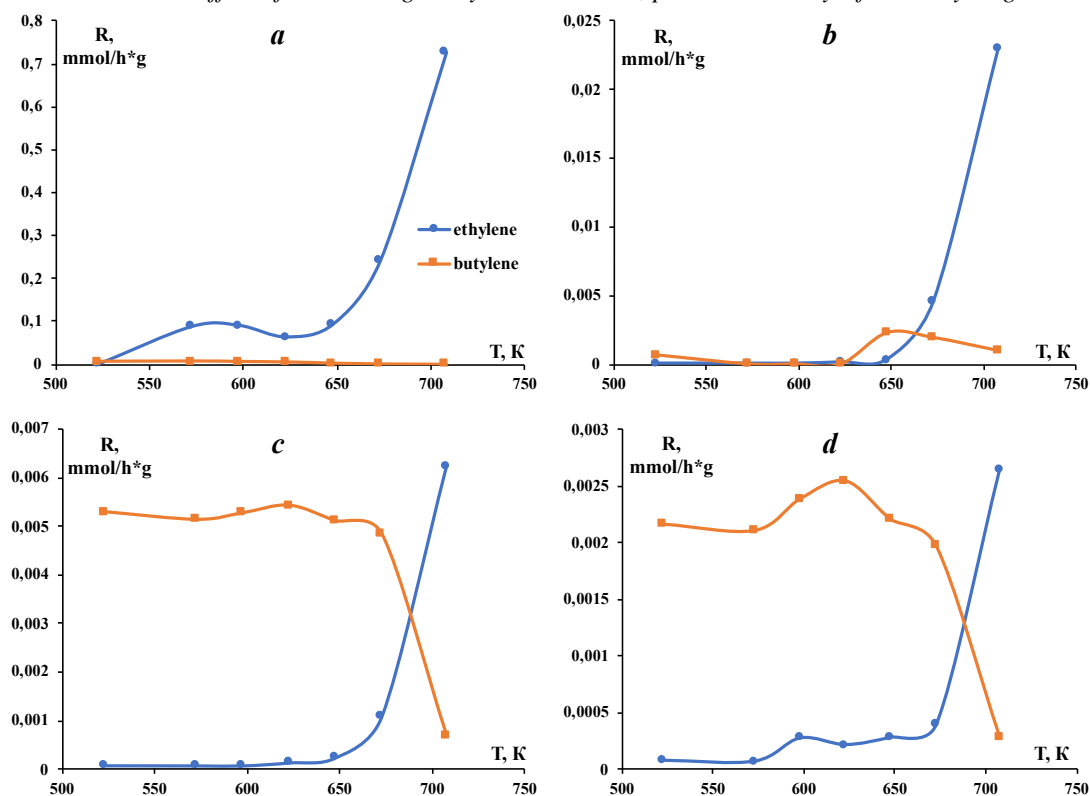


Figure 5. The temperature dependences of ethylene and butylene production rates over GdFe_{1-x}Mn_xO₃ perovskite catalysts: (a) x=0, (b) x=0.5, (c) x=0.8, (d) x=1

Table 3. Experimental values of activation energy and pre-exponential factor

Catalyst	E _a (CH ₄), kJ/mol	Ln K ₀ (CH ₄)	E _a (C ₂ H ₄), kJ/mol	Ln K ₀ (C ₂ H ₄)
GdFeO ₃	70	5.70	65	3.49
GdFe _{0.5} Mn _{0.5} O ₃	135	15.81	131	13.21
GdFe _{0.2} Mn _{0.8} O ₃	87	4.76	102	6.79
GdMnO ₃	67	-1.05	98	3.46

It should be noted that carrying out the reaction over GdFeO₃, ethylene prevailed in products among olefins and butylene was practically absent while on samples with manganese in the anionic sublattice of perovskite at low temperatures butylene prevailed (Fig. 5). An increase in temperature resulted in lower rates of butylene formation and sharp increase in ethylene production rates.

For assessing the activation energy and the number of active centers on the surface test data were processed in linear references of the Arrhenius equation.

The results in Table 3 show that an increase in the manganese fraction in the samples, with the exception of GdFe_{0.5}Mn_{0.5}O₃, led to a decrease in the pre-exponential factor logarithms, in this case, the activating energies did not change significantly. It was suggested that the decrease in the number of active centers affected the decrease in the rates of formation of products. The higher values of

activation energies for the sample with the stoichiometric content of iron and manganese were observed with a sufficiently large number of active centers. The reason why fall in speeds may be due to the “competition” between active centers can be assumed.

In [18] it was found that the introduction of manganese oxide into the supported iron-containing catalyst leads to a significant increase in the selectivity to olefins in the co-hydrogenation of carbon oxides. It was suggested that the iron-generated CH_x radicals are transported through the gas phase (“jumper effect”) onto the surface of manganese oxide, on which sorbed hydrogen is practically absent, where they are subsequently recombined into olefins. The differences in the catalytic activity of the samples are due to the different diffusion rates of weakly bound atomic hydrogen (H_i) over the surface of the catalysts (spillover effect). The results obtained by us are in good agreement with this assumption: at low

temperatures, on samples containing manganese, the CH_x-radicals interact with each other, leading to the formation of mainly butylene. An increase in the temperature of the process leads to an increase in the mobility of both CH_x particles and atomic hydrogen, which leads to an increase in the amount of ethylene produced. The calculation of the total selectivities for olefins showed that the introduction of manganese in the B-position of the perovskite lattice leads to an increase in the selectivity of the process with respect to light olefins C₂-C₄ (Fig. 6). So, if on ferrite selectivity was 25% -30%, then for samples where manganese prevailed, it reached 80%.

All the tested catalysts showed a high stability. It was established that the phase composition of all ferrites remains unchanged after catalytic reactions. Partial decomposition of catalysts and significant changes in the samples morphology did not occur. Catalytic characteristics were preserved during the repeated experiments and were not changed after 50 hours of the experiment. The mass change of the catalyst after completion of all tests did not exceed 1% for all investigated systems. It may indicate a slight carbonization surface of the tested ferrites and their potential use in further studies.

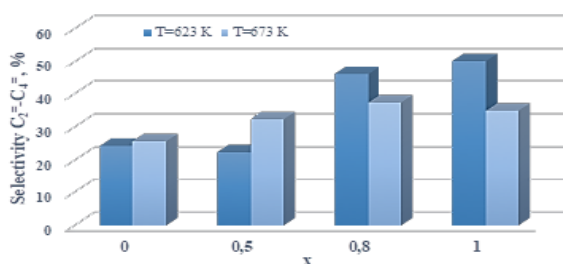


Figure 6. Correlation between CO selectivity and composition of the catalysts.

CONCLUSIONS

GdFe_{1-x}Mn_xO₃ perovskite catalysts were successfully synthesized by sol-gel method. The effect of different additions the Mn on the catalytic performance and the quantitative ratio of the products of hydrogenation was investigated. The x(Mn) = 1 perovskite displays a content of methane and light olefins of 71% and 26%, respectively, at T = 673 K. While on complex oxides with partial or full substitution of Fe by Mn (x(Mn) = 0.5, 0.8, 1) the amount of methane decreased to 40%, and olefins increased to 35%, while increasing the proportion of hydrocarbons C₅-C₆. It was found that GdMnO₃ catalyst has shown better selectivity for light olefins (ethylene and butylene) production while the highest catalytic activity in the carbon oxides hydrogenation was obtained over GdFeO₃.

Acknowledgements: This work was supported by the Russian Foundation for Basic Research, research project No 17-03-00647. The publication has been prepared with the support of the «RUDN University Program 5-100. Scientific researches were performed at the Center of X-ray Diffraction Methods and Nanotechnology, Center for Studies in Surface Science, Center for Thermogravimetric and Calorimetric Research of Research park of St. Petersburg State University.

REFERENCES

1. S. M. Choi, Y. J. Kang, S. W. Kim, *Applied Catalysis A, General*, **549**, 188 (2018).
2. T.-W. Kim, F. Kleitz, J. Won Jun, H.-J. Chae, Ch.-U. Kim, *Journal of Industrial and Engineering Chemistry* **51**, 196 (2017).
3. E. Heracleous, E. T. Liakakou, A. A. Lappas, A. A. Lemonidou, *Applied Catalysis A: General*, **455**, 145 (2013).
4. E. van Steen, M. Claeys, K.P. Möller, D. Nabaho, *Applied Catalysis A, General*, **549**, 51 (2018).
5. J.-L. Zhang, X. Wang, L.-P. Ma, X.-F. Yu, Q.-X. Ma, S.-B. Fan, T.-S. Zhao, *J. Fuel Chem. Technol.*, **45**, 1489 (2017).
6. J.-L. Zhang, L.-H. Ma, S.-B. Fan, T.-Sh. Zhao, Y.-H. Sun, *Fuel*, **109** 116 (2013).
7. M. Arsalanfar, A. A. Mirzaei, H. R. Bozorgzadeh, A. Samimi, R. Ghobadi, *Journal of Industrial and Engineering Chemistry*, **20**, 1313 (2014).
8. T. Li, M. Virginie, A. Y. Khodakov, *Applied Catalysts A, General*, **542**, 154 (2017).
9. M. Zhao, Y. Cui, J. Sun, Q. Zhang, *Catalysis Today*, **316**, 142 (2018).
10. N. Escalona, S. Fuentealba, G. Pecchi, *Applied Catalysis A: General*, **381**, 253 (2010).
11. T. Sheshko, T. Kryuchkova, Yu. Serov, A. Shulga, I. Chislova, L. Yafarova, I. Zvereva, NANOCON 2017, Brno, Czech Republic, EU 187-192.
12. B.S. Mathur, H. Shen, N. Lecerf, A. Kjekshus, H. Fjellvaag, G. F. Goya, *Adv. Mater. (Weinheim, Ger.)* **14** 19, 1405 (2002); Inst. Anorg. Chem., Univ. des Saarlandes, D-66123 Saarbruecken, Germany; Eng.
13. M. Romero, R. Faccio, J. Martinez, H. Pardo, B. Montenegro, C. Campos Pla Cid, A. A. Pasa, A. W. Mombru, *Journal of Solid State Chemistry*, **221**, 325 (2015).
14. J. F. Moulder, W. F. Stickle, P. E. Sobol, K. D. Bomben, Handbook of X-ray photoelectron spectroscopy: a reference book of standard spectra for identification and interpretation of XPS data, Surf. Interface Anal., 1992, p. 261.
15. H. Liu, G. Wei, Z. Xu, P. Liu, Y. Li, *Appl. Surf. Sci.*, **389**, 438 (2016).
16. A. L. Lapidus, A. Yu. Krylova, *Russian Journal of General Chemistry*, **44**, 43 (2000).
17. P. C. Keith, *Oil Gas J.*, **45**, 102 (1946).
18. T. F. Sheshko, Yu. M. Serov, *Russ. J. Phys. Chem. A*, **86**, 283 (2012).

Electrooxidation and bioelectrooxidation of L- and D-ascorbic acids

K. V. Kamarska¹, N. D. Dimcheva^{2*}

¹Technical University- Sofia, Branch Plovdiv, Department of Mathematics, Physics and Chemistry
25 Tsanko Dyustabanov St., Plovdiv 4000, Bulgaria

²University of Plovdiv "P. Hilendarski", Department of Physical Chemistry 24 Tsar Asen St., Plovdiv 4000, Bulgaria

Received November 1, 2018; Revised January 16, 2019

Electrooxidation and bioelectrooxidation of L- and D-iso ascorbic acids over gold nanoparticles-modified glassy carbon electrode was examined at pH 5.6 (optimal for enzyme activity). The glassy carbon electrode was modified through electrodeposition of gold nanoparticles under potentiodynamic conditions. The enzyme ascorbate oxidase was then chemisorbed onto their surface after electrochemical pre-treatment in 0.5 M H₂SO₄. Electrochemical oxidation of the enzyme substrates L- and D-isoascorbic acid was investigated by cyclic voltammetry under both aerobic and anaerobic conditions and by constant potential amperometry at the same pH. The experimental results showed that there is no difference in the electrooxidation rates of both enantiomers when electrooxidised on bare gold nanoparticles-modified glassy carbon electrode; whilst the enzyme electrode showed ca. 30% higher electrocatalytic activity to D-isoascorbic acid as deduced from cyclic voltammograms and ca. 12% higher sensitivity towards D-isoascorbic acid than to L-ascorbic acid as estimated by constant potential amperometry.

Keywords: biosensor, L- and D-ascorbic acid, ascorbate oxidase, gold nanoparticles-modified glassy carbon electrode

INTRODUCTION

Ascorbate oxidase (AOx) belongs to the group of blue multicopper oxidases, and catalyses the oxidation of L-ascorbic acid to dehydroascorbic acid in the presence of molecular oxygen with its concomitant reduction to water. The enzyme has two active sites consisting of three spectroscopically distinct copper centres which comprise one type 1 (T1), one type 2 (T2), and two type 3 (T3) copper ions [1].

As many oxidoreductases, the enzyme has been utilized in a wide variety of first generation biosensors for ascorbic acid, employing enzyme immobilization on various matrices: collagen membrane[2]; nylon net [3]; glassy carbon [4]; carbon nanotubes [5]; screen-printed carbon electrode [6]. In all these studies the measurable biosensor response was either the current from ascorbate oxidation or the detection of oxygen consumption.

Similarly to other multicopper oxidases, ascorbate oxidase has been reported to be electrochemically active [7-12] under both aerated and de-aerated conditions [11]. However, the observed electrochemical activity was associated only with the enzyme capability to catalyse the electrochemical oxygen reduction.

On this background, there are two literature precedents communicating not only the electrochemical activity of the immobilized AOx, but also its capability to act as a catalyst of the electrochemical oxidation of L-ascorbate [13, 14].

In both studies the enzyme was immobilized through chemisorption on electrochemically deposited gold structures onto carbonaceous electrodes.

In this paper, the electrooxidation and bioelectrooxidation of L- and D-ascorbic acid over Au modified glassy carbon electrode with and without chemisorbed AOx were compared in order to get a deeper insight into the mechanism of bioelectrocatalytic oxidation process.

EXPERIMENTAL

The materials used were ascorbate oxidase (AOx) (E.C. 1.10.3.3) from *Cucurbita sp.* (Sigma - Aldrich); L-ascorbic acid and D-isoascorbic (erythorbic) acid (Acros, Belgium); K₂HPO₄ and KH₂PO₄ (Sigma - Aldrich); HAuCl₄.H₂O (Acros), all of analytical grade and used without further pre-treatment.

The working surface of the cleaned and polished glassy carbon electrodes was modified through electrodeposition under potentiodynamic conditions at a scan rate of 0.100 V s⁻¹ from electrolyte containing 0.4 mM HAuCl₄ dissolved in 0.1M HCl.

Before the enzyme immobilization the gold-modified electrode was cleaned electrochemically in 0.5 M H₂SO₄ by cyclic voltammetry (CV) over the potential range from 0 to 1.7 V (vs. Ag/AgCl, 3 M KCl) for at least 10 cycles. The chemisorption of AOx was carried out under static conditions by immersing the modified electrodes in solutions containing 5 mg mL⁻¹ of AOx dissolved in 0.1 M potassium phosphate buffer, pH =5.6, for 24 hours.

* To whom all correspondence should be sent.

E-mail: ninadd@uni-plovdiv.bg

All electrochemical experiments were performed in a conventional three-electrode cell with a working volume of 25 mL. The working modified glassy carbon (with or without enzyme), the Ag/AgCl reference electrode and a platinum wire (auxiliary electrode), were connected to a computer-controlled electrochemical workstation PalmSens (Palm Instruments BV, The Nederland). Cyclic voltammograms (CVs) were registered at a scan rate of 5 mV s^{-1} . When necessary, the solutions were purged with either Ar gas or air. All the potentials are reported vs. Ag/AgCl (3 M KCl) reference electrode.

The amperometric detection of ascorbic acid was performed by successive addition of aliquots of 0.1 M solution of L- and D-ascorbic acid with the simultaneous registration of the current at a constant potential of 200 mV (vs. Ag/AgCl). The solution was stirred at 350 rpm during the measurements with a magnetic stirrer.

Buffer solutions (0.1 M) were made of potassium phosphates (K_2HPO_4 and KH_2PO_4) dissolved in double distilled water, pH = 5.6, adjusted with a pH meter pH 211 (Hanna Instruments, USA).

RESULTS AND DISCUSSION

The enzyme electrode produced on the basis of the gold-modified glassy carbon electrode through chemisorption of AOx was screened for electrochemical activity by cyclic voltammetry at a scan rate of 5 mV s^{-1} performed under both aerobic and anaerobic conditions (Fig. 1) at the optimal for the enzyme functioning pH = 5.6. On the CVs recorded under deaerated conditions (dashed line) an anodic peak at $245 \pm 5 \text{ mV}$ and a cathodic hump spanning over 100 mV to 50 mV were observed. In presence of oxygen a pronounced catalytic wave (solid line) appears on the CV, which lacks under deoxygenated conditions. Based on these observations one can account this wave for the catalytic oxygen reduction associated with the redox transformation of the (T2/T3) copper cluster of the immobilized AOx. The current of the anodic peak at $245 \pm 5 \text{ mV}$ remains unchanged by the presence and absence of oxygen and therefore it could be assigned to the redox transformation of the T1 copper site. The appearances of the anodic peak and cathodic catalytic wave present an indication that the enzyme is not denatured during the immobilization, since it is both electrochemically and enzymatically active.

The addition of either L-ascorbate (red) or D-isoascorbate (blue), results in well-defined oxidative peaks (Fig. 2) with identical peak potentials that slightly exceed the potential of the

T1 site redox transformation. Surprisingly, ca. 30% higher oxidative current was noted upon addition of D-isoascorbic acid as compared to the oxidative peak current for L-ascorbic acid with the same concentration. This finding implies preference of the immobilized AOx for the D-iso enantiomer over the L- one.

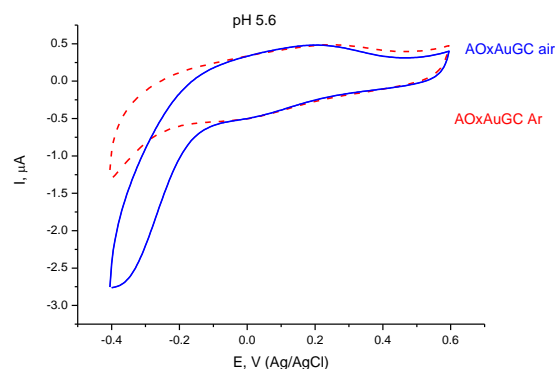


Fig. 1. CVs of the enzyme electrode in 0.1 M potassium phosphate buffer pH=5.6 under deoxygenated with Ar buffer (dashed line) and under aerobic conditions (solid line); $v = 5 \text{ mV s}^{-1}$; reference electrode Ag/AgCl, 3M KCl.

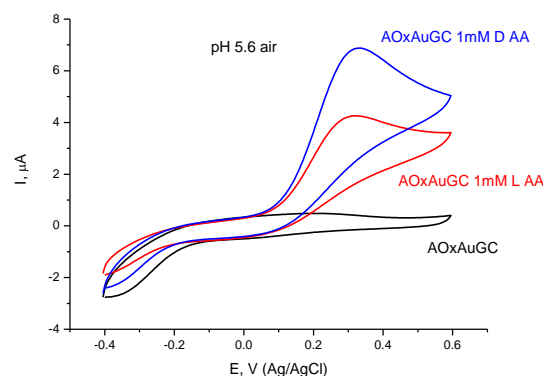


Fig. 2. CV of the enzyme electrode in 0.1 M potassium phosphate buffer pH 5.6 - background (black); in the presence of 1 mM D-isoascorbic acid (blue) and 1 mM L-ascorbic acid (red); $v = 5 \text{ mV s}^{-1}$; reference electrode Ag/AgCl, 3M KCl.

Comparative studies on the oxidation of L-ascorbic or D-isoascorbic acid on a gold – modified GC electrode without enzyme showed (Fig. 3) that the peak currents are identical, i.e. there are no differences in the rates of the electrochemical oxidation of both enantiomers. The potentials of the oxidative peaks for the two enantiomers were found virtually the same ($\pm 5\%$), however negatively shifted with ca. 80 mV as compared to the peak potential for the oxidation of these compounds on the enzyme electrode (Fig. 4). Bearing in mind that the potential of the T1 copper site of the

immobilized AOx falls in the middle between the oxidative potentials of the L-, D-enantiomers onto enzyme-less electrode and on the enzyme electrode, we can only hypothesize that the phenomenon observed in Fig. 2. (different oxidative currents generated on the enzyme electrode in the presence of L- and D-enantiomers) results not from the oxidation of the substrates themselves, but is rather due to the oxidation of the T1 site of the immobilized enzyme. Therefore, the T1 copper site gains one electron (and gets reduced) every time it reacts with a substrate molecule (biocatalytic substrate oxidation), then the reduced T1 site sends one electron to the electrode surface (electrochemical process) and becomes oxidized. In this case both processes – the biocatalytic and the electrochemical one are conjugated: a phenomenon which is denoted as bioelectrocatalysis, because the immobilized enzyme acts as an electrocatalyst. The manifested differences in the peak maxima for the two enzyme substrates (Fig. 2), suggest different rates of the biocatalytic interaction, which precedes the electron transfer process. Provided that the biocatalytic stage is much slower than the charge transfer stage, this may eventually result into a

positive shift of the oxidative peak potential in the presence of the enzyme substrate as compared to the redox transformation of the active site in its absence, as it was observed in the present study.

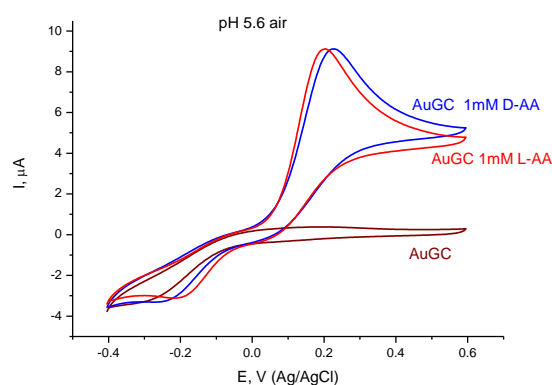


Fig. 3. CV of the modified glassy carbon in 0.1 M potassium phosphate buffer pH= 5.6 (black); in the presence of 1 mM D- isoascorbic acid (blue) and 1 mM L- ascorbic acid (red); $v = 5 \text{ mV s}^{-1}$; reference electrode Ag/AgCl, 3M KCl.

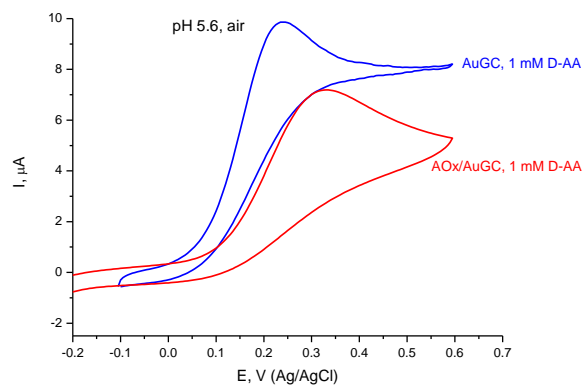
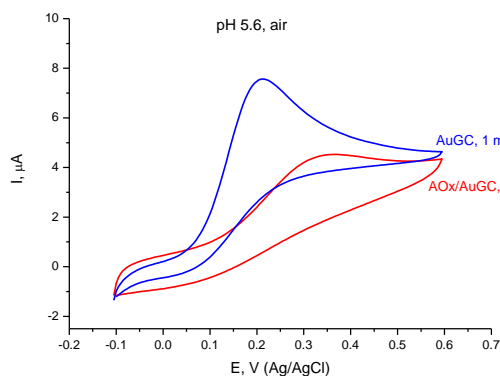


Fig. 4. CVs of the modified glassy carbon electrode without (blue) and with immobilized AOx (red) in 0.1 M potassium phosphate buffer pH = 5.6; in the presence of 1 mM L- ascorbic acid (on the left) and 1 mM D- isoascorbic acid (on the right); $v = 5 \text{ mV s}^{-1}$; reference electrode Ag/AgCl, 3M KCl.

The enzyme electrode was further tested under the same conditions as in previous studies as an amperometric biosensor prototype for quantification of L- or D-enantiomer at an applied potential of 0.2 V where the noise level was the lowest (Fig. 5).

The results show that the oxidative current increased stepwise upon introducing in the buffer aliquots of the 0.1 M L- and D-ascorbic acid. Values of the slope (biosensor sensitivity calculated

from the regression analysis of the experimental points, were respectively $1380.0 \pm 16.7 \mu\text{A mM}^{-1}$ for substrate L-ascorbic acid and $1547.5 \pm 26.1 \mu\text{A mM}^{-1}$ for substrate D-isoascorbic acid.

These values of the biosensor sensitivity indicate that the immobilized enzyme possesses high affinity towards both substrates, but under the given experimental conditions it exhibits certain "preferences" for D-isoascorbic acid.

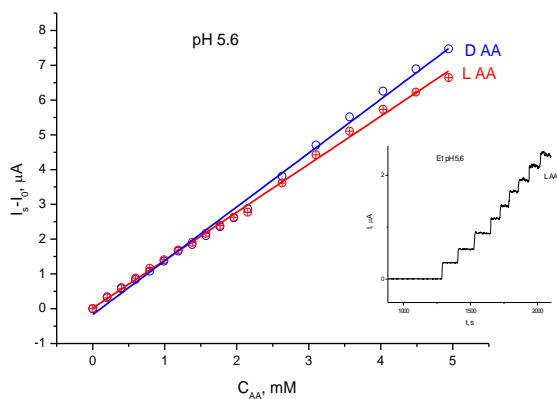


Fig. 5. Background-corrected steady-state response of the enzyme electrode as a function of ascorbic acid concentration at an operating potential of 200 mV (vs. Ag/AgCl, 3M KCl); stirring rate: 350 rpm; supporting electrolyte: 0.1 M potassium phosphate buffer, pH= 5.6; Inset: part of the authentic record of the current change upon addition of L-ascorbic or D- is-ascorbic acid aliquots.

CONCLUSIONS

The results presented in this study showed that: there is no difference in the oxidation rates of both enantiomers of ascorbic acid when electrooxidized on enzyme-less gold nanoparticles modified glassy carbon electrode; however the immobilized enzyme acts as bioelectrocatalyst for electrochemical oxidation of L- and D-enantiomers of ascorbic acid, and is capable of discriminating between them.

Acknowledgement: Authors acknowledge the financial support from the Fund for Scientific Research of the University of Plovdiv (grant $\Phi\Pi\Pi 7 X\Phi 013$).

REFERENCES

1. A. Messerschmidt, R. Huber, *Eur. Biochem.*, **187**, 341 (1990).
2. K. Matsumoto, K. Yamada, Y. Osajima, *Anal. Chem.*, **53**, 1974 (1981).
3. I. Tomita, A. Manzoli, F. Fertonani, H. Yamanaka, *Eclética Química*, **30**, 37 (2005).
4. G. Greenway, P. Ongomo, *Analyst*, **115**, 1297 (1990).
5. M. Liu, Y. Wen, D. Li, H. He, J. Xu, C. Liu, R. Yue, B. Lu, G. Liu, *J. Appl. Polym. Sci.*, **122**, 1142 (2011).
6. G. Csiffáry, P. Fütő, N. Adányi, A. Kiss, *Food Technol. Biotechnol.*, **54**, 31 (2016).
7. T. Sakurai, *Chem. Letters*, **25**, 481 (1996).
8. R. Santucci, T. Ferri, L. Morpurgo, I. Savini, L. Avigliano, *Biochem. J.*, **332**, 611 (1998).
9. S. Shleev, J. Tkac, A. Christenson, T. Ruzgas, A. Yaropolov, J. Whittaker, L. Gorton, *Biosens. Bioelectron.*, **20**, 2517 (2005).
10. K. Murata, N. Nakamura, H. Ohno, *Electroanalysis*, **19**, 530 (2007).
11. D. M. Ivniński, C. Khripin, H. R. Luckarift, G. R. Johnson, P. Atanassov, *Electrochim. Acta*, **55**, 7385 (2010).
12. B. Patil, S. Fujikawa, T. Okajima, T. Ohsaka, *Int. J. Electrochem. Sci.*, **7**, 5012 (2012).
13. T. Dodevska, E. Horozova, N. Dimcheva, *Mat.Sci. and Eng.*, **178**, 1497 (2013).
14. N. Dimcheva, T. Dodevska, E. Horozova, *J. Electrochem. Soc.*, **160**, H414 (2013).

Balloon-borne measurements in the upper troposphere and lower stratosphere above Bulgaria (N41-43° E24-26°)

A. Terziyski^{1,2*}, S. Tenev¹, V. Jeliakov³, N. Kochev¹, G. Dimitrov¹,
N. Jeliakova³, L. Iliev³, Ch. Angelov⁴, I. Kalapov⁴, T. Arsov⁴

¹Department of Analytical Chemistry and Computer Chemistry, University of Plovdiv, 24 Tsar Assen St., Plovdiv 4000, Bulgaria

²Institute of Information and Communication Technologies, Bulgarian Academy of Sciences, Acad. G. Bonchev St., Block 25A, 1113 Sofia, Bulgaria

³IDEAconsult Ltd., 4 Angel Kanchev St., Sofia 1000, Bulgaria

⁴Institute for Nuclear Research and Nuclear Energy, Laboratory BEO Moussala, Bulgarian Academy of Sciences, 72 Tsarigradsko chaussee Blvd., 1784 Sofia, Bulgaria

Received November 6, 2018; Revised December 12, 2018

We present balloon-borne measurements obtained from several missions in 2017 and 2018, within longitude of 24-26°E and latitude of 41-43°N. Our equipment ascended up to 35 km above sea level and measured with a time resolution of one second the relative humidity, temperature, pressure, and gamma radiation. We used in-house built, self-designed electronics, equipped with additional sensors for measuring the magnetic field, geographic coordinates, and altitude, which allowed us to estimate the wind speed vectors at different altitudes and the landing speed with and without a parachute. In this article we present our results, which are in good agreement with those obtained by other researchers. We have also estimated the tropopause temperature annual oscillations and the Regener–Pfotzer maximum.

INTRODUCTION

Weather balloons are a common tool for studying the lower parts of the atmosphere up to 50 km, including the Earth's troposphere and stratosphere. The balloons are made of synthetic rubber or latex and filled with lighter than air gas. Such gases can be hydrogen or methane, but because of their high flammability the widely-used gas nowadays for filling balloons is helium. The volume of carrier gas may vary from one cubic meter up to several millions cubic meters [1], depending on the weight of the payload, specificity of the mission, equipment on board, etc. Weather balloons may ascend and descend freely without human control—like the very first balloon recorded in history in 1892 by Gustave Hermite [2]—but in recent years weather balloons with controlled ascent and descent have also been launched [3]. The missions carried by balloons are very diverse, varying from e.g. surface observation in the past century [4] to daily collecting of weather data above the Earth on many sites and even delivering internet connectivity to rural and remote communities [5]. The lightweight daily weather balloons flight is around 1-2 hours, but monitoring balloons—like NASA's Antarctic mission—last several days, and a 100-day flight has been reported by Google's project Loon for internet beaming [5, 6].

EXPERIMENTAL

Campaign description

A group of experienced scientists coming from different areas, together with university and high school students, decided to combine their skills in order to study the lower to mid stratosphere *via* high altitude balloons and self-designed electronics on board. In total, four balloons were launched in 2017 and 2018: #1 on 8 September 2017, #2 on 6 November 2017, #3 on 31 March 2018 and #4 on 27 April 2018. The flights took place between 41 and 43°N latitude and 24 and 26°E longitude. During the four missions we improved our sensor selection, payload shape, weight and isolation properties, electronics, and communication protocols, and obtained experience for further, more specific studies.

Instrumentation

In this chapter, we explain in detail our experimental setup and design.

Balloon selection

We managed to optimize our payload weight at around 800 grams, which allowed us to choose weather balloon type 800 [7]. The maximum height of its burst is around 30 000 meters as given by manufacturer's specifications; however, we ascended up to 35 167 meters during mission #2 with a payload weight of 802 grams.

* To whom all correspondence should be sent.
E-mail: atanas@uni-plovdiv.net

Payload design

The payload is a polystyrene sphere that consists of multiple lightweight circles with varying diameter, as shown in figure 1.

The circles are glued together one by one and form two hemispheres (fig. 2) that are sealed after placing the board computer, external sensors, battery, camera, etc.

Board computer

In the course of the project we have designed and developed our own on-board computer, based on a PIC microcontroller, Microchip PIC18LF46K22 [8], which reads the sensors data as explained in the next chapter and records it in a

Microchip EEPROM memory 24FC1025 [9] once per second (see figure 3).

The FM LoRa transceiver module, RF-LORA-868-SO [10], sends in a 20-second cycle the GPS coordinates of the balloon and several sensor readings to multiple receivers on the ground. The complete electronics set is powered by 3.3 V DC from a power-supply module and a battery 3.6 V, 19 Ah UHR-ER34615 [11]. The latter is able to operate at temperatures down to -55°C, which has been of critical importance given the expected temperature profile of the balloon flight.



Figure 1. The payload polystyrene components



Figure 2. The two payload hemispheres

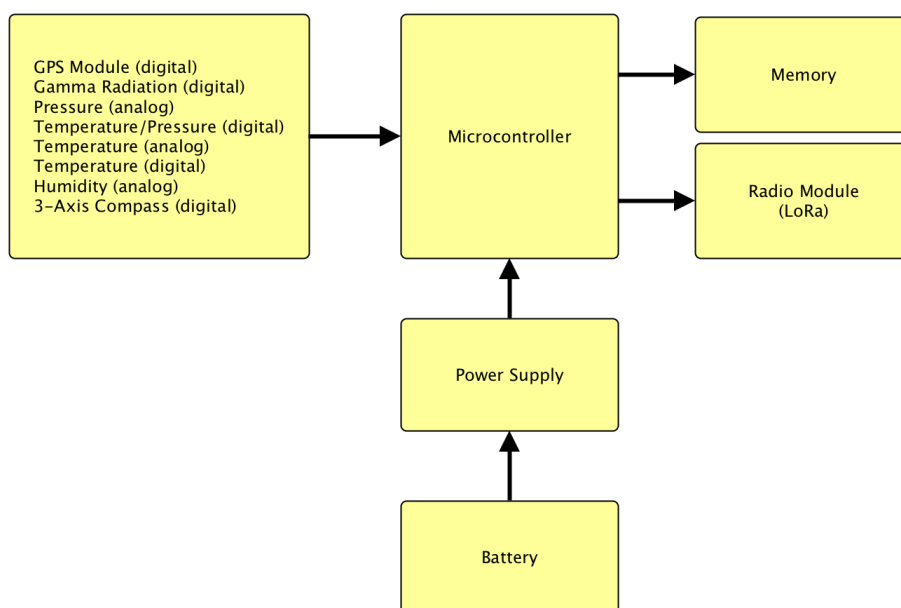


Figure 3. Block diagram of the electronics module

Sensors

The measured values were recorded by multiple sensors, placed on both the internal board and externally, on the edge of the payload sphere. The following table summarizes the sensors chosen for our missions.

The set of sensors was chosen as a result of extensive research and considerations about operating range and atmospheric conditions, sensitivity, power consumption, weight, etc. Some

values were measured by combining both digital and analogue sensors.

Communications and data protocols

The measured data from the sensors and the GPS location of the balloon were reliably transmitted from the on-board computer to several ground receivers *via* a radio connection in the 868 MHz range. We developed our own data protocol to meet the set requirements, e.g., having as efficient as possible one-way communication at the lowest possible bandwidth of 295 bps.

Table 1. Complete set of sensors used in our experiments

Variable	Internal (on board)	External
Temperature	MCP9800 (digital) [12] LMT84 (analog) [13]	MCP9800 (digital) [12] HTU21 (digital) [14]
Pressure	NPP-301-100 (analog) [15]	-
Relative humidity	-	HTU21 (digital) [14] HIH-5031 (analog) [16]
Digital compass	HMC5883 [17]	-
Gamma radiation	RD2014 [18]	-
GPS	L80-M39 [19]	-

RESULTS AND DISCUSSION

In this chapter, we present the observations we made, as measured during the four balloon missions. For simplicity, some of the data are purposely omitted. All raw data are available at <https://meter.ac/balloons>.

Temperature

Figure 4 represents the temperature change immediately after the balloon launch, including ascent, burst at 32 250 m, the free descent without a parachute, landing at around 12:30, and thermalizing until the balloon was found two hours later. The lowest measured temperature during the ascent was recorded around 11:00 at an altitude of 12 km, where the tropopause is located. However, the lowest flight temperature was recorded during the descent, which is explained by the more intensive cooling of the external sensors (blue lines). The red line is recorded by the internal MCP9800 [12] sensor which measures the temperature inside the polystyrene sphere. After the crash landing this sensor apparently has recorded some erroneous data.

Relative humidity

It is well known that most of the atmospheric water vapor, or moisture, is contained in the troposphere [20, 21]. We measured the relative humidity by both digital [14] and analogue [16] sensors. The following graph (fig. 5) represents the relative humidity in percent as the balloon ascended on 31 March 2018. The two sensors report equal values up to 7 000 meters of altitude; then some

discrepancies appear due to the extremely low ambient pressure and temperature.

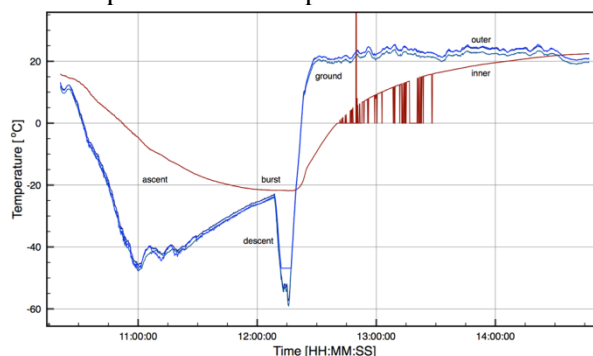


Figure 4. Temperatures measured during the third balloon mission.

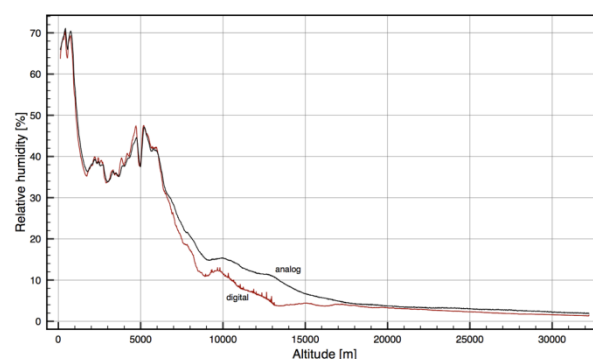


Figure 5. The relative humidity measured as a function of the altitude.

Regener–Pfotzer maximum in the stratosphere

In 1930s, the German scientist Erich Regener and his student Georg Pfotzer measured [22, 23] the ionization maximum occurring in the stratosphere (15-25 km of altitude), nowadays known as the Regener–Pfotzer maximum [24].

In figure 6, the raw measurements for the four balloons are represented by dots, while the same color lines show the moving averaged signal, respectively. It can be seen that our measurements [18] reach the Regener–Pfotzer maximum between 15 km and 20 km above sea level and latitude of 41–43°N. The reference plots, performed by Phillips *et al.* [25] are in good agreement with our measurements.

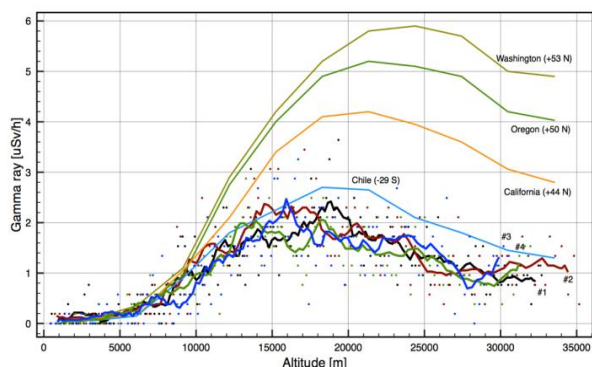


Figure 6. Regener–Pfotzer maximum – a comparison of our measurements with those of other groups.

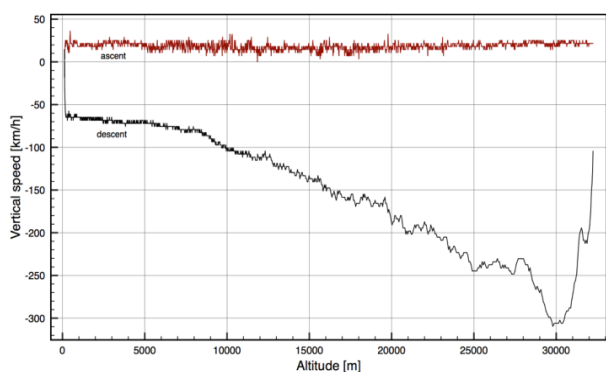


Figure 7. Vertical component of the balloon speed during mission #3.

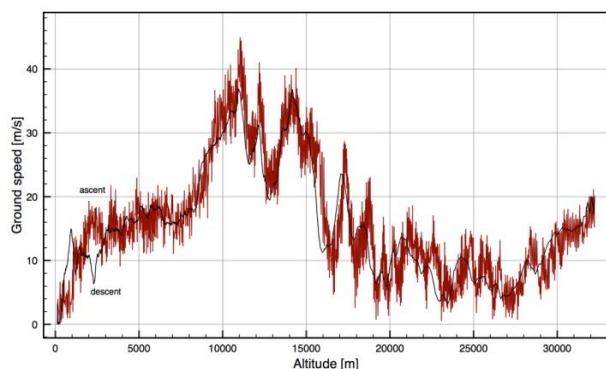


Figure 8. Horizontal component of the balloon speed during mission #3.

Altitude variations of wind speed and direction

The on-board computer was equipped with a GPS sensor [19] which not only allowed us to track the balloon trajectory during its flight, but also made it possible to estimate both its vertical and horizontal speed. Figure 7 shows that the balloon ascent speed was constant around 18 km/h from the launch until the burst (the red plot). The black line represents the free-fall (i.e. no parachute) speed, which shortly after the burst exceeded 300 km/h at an altitude of around 30 km. The ambient pressure at this altitude was measured to be around 10 mbar—100 times lower than the sea level pressure, with the associated lower air resistance force acting on the balloon as it began its fall.

The next figure visualizes the “ground” (horizontal) speed, i.e. how the balloon projection is moving on Earth’s surface during mission #3. It was recorded both during ascent (red) and descent (black). The strongest wind was measured around altitude of 11 km, exceeding 40 m/s (144 km/s).

Mission summary

Four balloon missions were performed during autumn 2017 and spring 2018 on the territory of Bulgaria. Figure 9 presents the corresponding balloon traces. The launch point of each mission is the westernmost point of the map trace.

Further, more detailed information, including planned future missions, can be found on <https://meter.ac/balloons>.

Acknowledgements: *This work is supported by FP17-HF-013 funded by the University of Plovdiv and by the National Science Fund of Republic of Bulgaria through project DN 04/1, 13.12.2016: “Study of the combined effect of the natural radioactivity background, the UV radiation, the climate changes and the cosmic rays on the model groups of plant and animal organisms in mountain ecosystems”.*

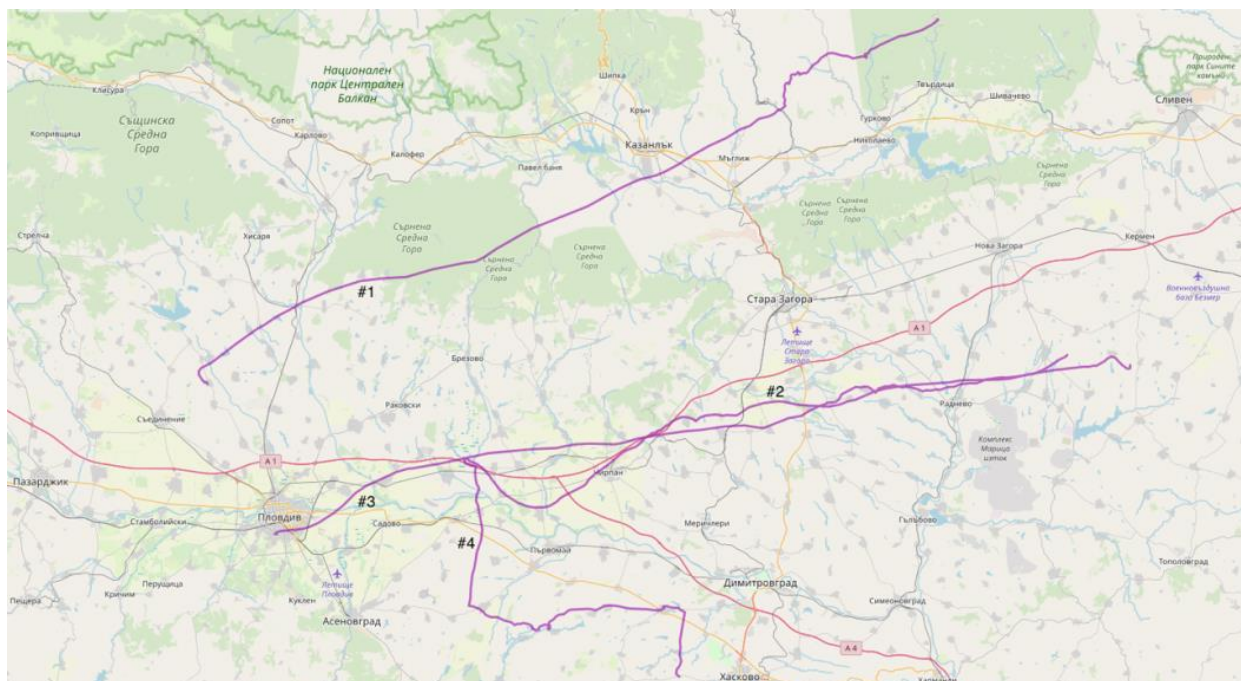


Figure 9. The map of Bulgaria and our four missions

REFERENCES

1. NASA Scientific Balloons, <https://www.nasa.gov/scientificballoons>.
2. G. Hermite, *Compt. Rend. Bulg. Acad. Sci.*, **115**, 862 (1892).
3. A. Kräuchi, R. Philipona, G. Romanens, D. F. Hurst, E. G. Hall, A. F. Jordan, *Atmos. Meas. Tech.*, **9**, 929 (2016).
4. S. Kidd, Astronomical ballooning: the Stratoscope program, *New Scientist*, **23** (409), 702 (1964).
5. F. Lardinois, TechCrunch, <https://techcrunch.com/2013/06/14/google-x-announces-project-loon-balloon-powered-internet-for-rural-remote-and-underserved-areas/> (2013).
6. Project Loon, <https://www.google.com/intl/es419/loon/>
7. Strato Flights <https://www.stratoflights.com>.
8. Microchip PIC18LF46K22, <https://www.microchip.com/wwwproducts/en/PIC18F46K22>.
9. Microchip 24FC1025, <https://www.microchip.com/wwwproducts/en/24FC1025>.
10. RF Solutions RF-LORA-868-SO, <https://www.rfsolutions.co.uk/radio-modules-c10/frequency-c57/fm-lora-transceiver-module-pre-set-to-868mhz-p468>.
11. ULTRALIFE 3.6V 19.0Ah LiSOC12 Non-rechargeable D-Size Bobbin Cell UHR-ER34615, <https://www.ultralifecorporation.com/ECommerce/product/er34615/thionyl-cl-d-size-bobbin-cell>.
12. Microchip MCP9800, <https://www.microchip.com/wwwproducts/en/en020949>.
13. Texas Instruments LMT84, <http://www.ti.com/lit/ds/symlink/lmt84.pdf>.
14. TE Connectivity HTU21, <https://www.te.com/us-en/product-CAT-HSC0004.html>.
15. Amphenol Advanced Sensors NPP-301-100, <https://www.amphenol-sensors.com/en/novasensor/pressure-sensors/3159-novasensor-npp-301-series-surface-mount-pressure-sensors>.
16. Honeywell International Inc. HIH-5031, <https://sensing.honeywell.com/HIH-5031-001-humidity-sensors>.
17. Honeywell International Inc. HMC5883, <http://www.farnell.com/datasheets/1683374.pdf>.
18. Teviso Sensor Technologies Ltd. RD2014, <https://www.teviso.com/products.htm>.
19. RS Components Ltd. L80-M39, <https://uk.rs-online.com/web/p/gps-chips-gps-modules/9084088/>.
20. A. Ruzmaikin, H. H. Aumann, E. M. Manning, *J. Atm. Sci.*, (2014).
21. S. Manabe, R. T. Wetherald, *J. Atm. Sci.*, (1967).
22. E. Regener, G. Pfozter, *Nature*, **134**, 325 (1935).
23. E. Regener, G. Pfozter, *Nature*, **136**, 718 (1935).
24. P. Carlson, A. A. Watson, *Hist. Geo Space Sci.*, **5**, 175 (2014).
25. T. Phillips, S. Johnson, A. Koske-Phillips, M. White, A. Yarborough, A. Lamb, A. Herbst, F. Molina, J. Gilpin, O. Grah, G. Perez, C. Reid, J. Harvey, J. Schultz, *Space Weather*, **14**, 697 (2016).

Catalytic activation of PMS by Co_3O_4 modified $g\text{-C}_3\text{N}_4$ for oxidative degradation of the azo dye Acid Orange 7 in aqueous solutions

V. V. Ivanova-Kolcheva, M. K. Stoyanova*

Department of Physical Chemistry, University of Plovdiv, 24 Tzar Assen Str, Plovdiv, 4000, Bulgaria

Received November 14, 2018; Revised January 16, 2019

Co_3O_4 modified $g\text{-C}_3\text{N}_4$ catalysts were prepared by a facile one-pot thermal polycondensation method using pure and HNO_3 protonated melamine as graphitic carbon nitride precursors. The materials were thoroughly characterized by a variety of techniques including XRD, TEM, BET, ICP-OES, and FT-IR-spectroscopy and their catalytic activity for degradation of the model azo dye Acid Orange 7 (AO7) in aqueous solutions based on the activation of peroxymonosulfate (PMS) without light irradiation was evaluated. The prepared composite catalysts demonstrated to be much more efficient in activating PMS for AO7 degradation than pure Co_3O_4 . The $\text{Co-g-C}_3\text{N}_4$ (pm) hybrid exhibited better catalytic activity ($k=0.1391 \text{ min}^{-1}$) than the catalyst prepared by sintering melamine without protonation ($k=0.0646 \text{ min}^{-1}$). The enhanced catalytic performance of the $\text{Co-g-C}_3\text{N}_4$ (pm) could be attributed to the larger specific surface area, supplying more surface active sites and to the higher condensation degree of the $g\text{-C}_3\text{N}_4$. The degradation of AO7 was found to follow the first order kinetics. The effect of catalyst dosage, PMS concentration and pH on the rate of AO7 degradation was investigated. The radical species generated from the catalytic decomposition of PMS were identified by quenching studies.

Keywords: graphitic carbon nitride, Co_3O_4 , peroxymonosulfate, catalytic degradation, Acid Orange 7

INTRODUCTION

The uncontrolled disposal of refractory organic contaminants in aquatic systems is an essential environmental issue, as pollutants could not only be accumulated in the various components of the environment but by migration, they can fall into the food chains and can induce severe public health problems. A considerable source of water pollution is the discharge of dye effluents by various industries (e.g. textile, pulp and paper, leather, food, dyestuff manufacturing, etc.). It is estimated that approximately 15% of the textile dyes produced are lost in the industrial effluents during manufacturing or processing operations [1]. In the recent years, advanced oxidation processes based on peroxymonosulfate (PMS) activation for generating sulfate radicals (SRs) is extensively investigated as an effective and eco-friendly technology for degrading organic pollutants in water [2,3]. Compared to the conventional Fenton process, SRs generating processes have a number of advantages because sulfate radicals have similar or even higher oxidation potential than hydroxyl radicals, are effective over a wide range of pH (pH 2–9), have a significantly longer lifetime (30–40 μs vs 20 ns), and exhibit a much higher selectivity in the presence of complex environmental matrices [4, 5].

The most commonly used PMS activators are

transition metals-based catalysts (Co, Mn, Cu, Fe) used both in homogeneous and heterogeneous systems [6, 7]. Homogeneous catalytic activation of PMS by transition metal ions is proven to be the most efficient route for quick production of SRs at room temperature, with cobalt ions being identified as the most efficient PMS activator [1]. However, this process causes secondary pollutions and requires recovering the homogeneous catalyst from the treated water that is not often technically or economically feasible. Therefore, the heterogeneous catalysts are preferred for PMS activation. Various transition metal oxides and their combinations have been used to activate PMS, such as Co_3O_4 , Mn_3O_2 , CuFe_2O_4 , Fe_3O_4 , CuO , CoFe_2O_4 , etc. [6, 7]. Due to the highest efficiency of cobalt-containing catalysts for generating SRs by PMS decomposition, the Co_3O_4 /PMS system has been thoroughly investigated for organic pollutants degradation [8]. Despite the excellent performance of Co_3O_4 nanoparticles in PMS activation, they easily agglomerate, resulting in a decrease in catalytic effectiveness [9]. In order to improve the catalytic activity and stability of Co_3O_4 , it was immobilized on different supports such as MgO , TiO_2 , SiO_2 , activated carbon, graphene, zeolite, etc. [10, 11]. Recently, the photocatalytic activation of PMS using environmentally friendly nonmetal carbon-based catalysts as activated carbon, graphene oxide, and carbon nanotubes is of

* To whom all correspondence should be sent.

E-mail: marianas@uni-plovdiv.bg

increasing interest. It was found that nitrogen doping on carbon catalysts boosted their catalytic activity for PMS decomposition [12, 13]. Although graphitic-carbon nitride (g- C_3N_4) is a nitrogen-rich material, its sole use for PMS activation was ineffective even under visible light irradiation [14]. Modifying g- C_3N_4 with iron oxide and cobalt oxide leads to enhanced photocatalytic activity toward organics degradation [15, 16]. So far there are no published data on the activation of PMS by g- C_3N_4 modified with transition metal oxides at ambient conditions.

The aim of the present study is to evaluate the PMS activation performance of Co_3O_4 modified g- C_3N_4 prepared from protonated melamine for oxidative degradation of AO7 dye in aqueous solution without light irradiation.

EXPERIMENTAL

Pristine g- C_3N_4 (represented as g- C_3N_4 (pm)) was prepared by thermal condensation of protonated melamine according to the procedure, described in [17]. In brief, 12 g of melamine was dissolved into 100 cm^3 of methanol (MeOH) at 60 °C and stirred for 10 min. Then, a certain amount of 0.2 M HNO_3 was added dropwise into the above solution. The obtained white precipitate was separated out, washed several times with MeOH, dried at 60 °C for 10 h, and finally calcined at 550 °C for 2 h in static air. Co-g- C_3N_4 (pm) composite was prepared by a one-pot synthetic approach. A certain amount of $\text{Co}(\text{NO}_3)_2 \cdot 6\text{H}_2\text{O}$ to reach 5 wt.% Co in the final catalyst was dissolved in 50 cm^3 of MeOH and added to the desired amount of protonated melamine under continuous stirring. The suspension was stirred at 50 °C until MeOH was evaporated, then the obtained solid was dried at 60 °C for 10 h and calcined at 550 °C for 2 h. For comparison, pristine and Co_3O_4 modified g- C_3N_4 were prepared following the procedure mentioned above using melamine without protonation with HNO_3 .

The amount of cobalt in the prepared catalysts was measured by ICP-OES analysis (iCAP 6300 Thermo Scientific). XRD patterns of the samples were obtained on a TUR-MA 62 powder diffractometer, using $\text{Co-K}\alpha$ radiation ($\lambda = 1.789 \text{ \AA}$) at 40 kV and 20 mA. The morphology of the samples was characterized by a JEOL JEM 2100 high resolution transmission electron microscope (TEM) using an accelerating voltage of 200 kV. The BET specific surface area was determined using a Micromeritics apparatus (Tristar 3000 porosimeter). Infrared spectra were recorded with a Fourier transform infrared spectrometer (Vertex 70, Bruker Optics).

The degradation of AO7 was carried out at room temperature ($20 \pm 2^\circ\text{C}$) in 400 cm^3 batch reactor with constant stirring at 400 rpm. In a typical run, a fixed amount of PMS (in the form of Oxone, $2\text{KHSO}_5 \cdot \text{KHSO}_4 \cdot \text{K}_2\text{SO}_4$) was added to 200 cm^3 of 50 mg dm^{-3} AO7 aqueous solution to achieve the predefined PMS/AO7 molar ratio and was stirred until dissolved. Degradation reaction was initiated by the addition of a specified amount of catalyst. Aliquots of 4.0 cm^3 were taken at given time intervals, quenched immediately by adding 1 cm^3 of methanol, and centrifuged at 4000 rpm for 1 min to remove the catalyst. The AO7 concentration in the filtrate was determined by UV-Vis spectroscopy (Cintra 101, GBS) at 486 nm. All experiments were conducted in triplicate.

RESULTS AND DISCUSSION

The cobalt weight percentage in the final composite catalysts as determined by ICP-OES was found to be close to preparation settings, corresponding to 5 wt% .

Fig. 1 displays the XRD patterns of the pristine g- C_3N_4 (pm) and Co-doped g- C_3N_4 (pm) catalysts. The pure g- C_3N_4 (pm) shows two distinct diffraction peaks at $2\theta = 15.2^\circ$ and 32.2° (higher intensity), which confirms its graphitic-like layer structure. The strongest peak indexed for (002) diffraction planes in g- C_3N_4 (pm) reveals graphitic stacking of C_3N_4 layers. A relatively weak peak at 15.2° can be attributed to an in-planar ordering of tri-s-triazine units, which was indexed as (100). The Co-g- C_3N_4 (pm) catalyst shows similar XRD patterns with no shifting in the two characteristic g- C_3N_4 (pm) peaks. However, the intensity of (002) peak decreases and also broadens in case of the doped sample, which indicates that Co_3O_4 species restrain the growth of crystal structure of g- C_3N_4 . Diffraction peaks of Co_3O_4 species are not observed in the patterns of Co-g- C_3N_4 (pm) catalyst, which could be attributed to the low Co content (5 wt%) as well as to the very small grain size effects, thus not detected by this technique.

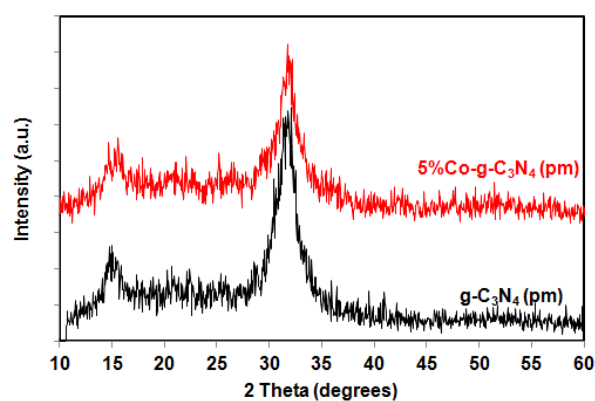


Figure 1. XRD patterns of pristine and Co_3O_4 modified $g\text{-C}_3\text{N}_4$ (pm)

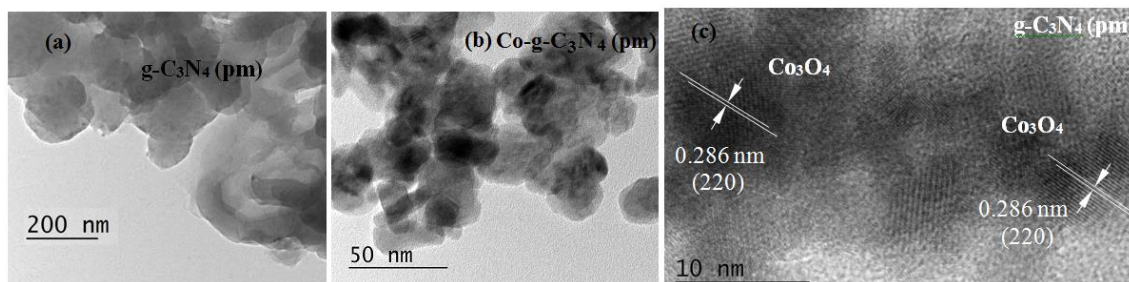


Figure 2. TEM images of (a) $g\text{-C}_3\text{N}_4$ (pm) and (b, c) $\text{Co-g-C}_3\text{N}_4$ (pm)

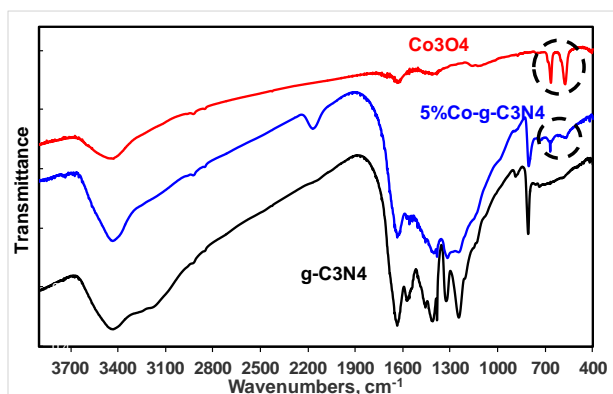


Figure 3. FTIR spectra of synthesized catalysts

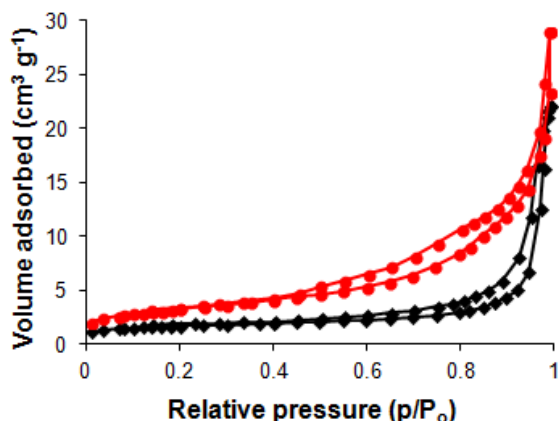


Figure 4. N_2 adsorption/desorption isotherms of $g\text{-C}_3\text{N}_4$ (pm) and $\text{Co-g-C}_3\text{N}_4$ (pm)

The bright field TEM images of $g\text{-C}_3\text{N}_4$ (pm) and $\text{Co-g-C}_3\text{N}_4$ (pm) are presented in Fig. 2. Pristine $g\text{-C}_3\text{N}_4$ (pm) sample shows a typical layer structure with planar aggregates of $g\text{-C}_3\text{N}_4$ sheets as observed in Fig. 2a. For $\text{Co-g-C}_3\text{N}_4$ (pm) catalyst, Co_3O_4 species (dark spots in Fig. 2b) with close to the spherical shape and sizes ranging from 10 to 25 nm are distributed throughout the sheets of $g\text{-C}_3\text{N}_4$ particles. Although not detectable by the XRD technique, Fig. 2c confirms the presence of catalytically active Co_3O_4 phase in the $\text{Co-g-C}_3\text{N}_4$ (pm) hybrid. The HRTEM image shows well-defined lattice fringes with d-spacing value of

0.286 nm, which can be assigned to (220) plane of Co_3O_4 cubic spinel phase.

The graphitic structures of the as-prepared samples were further demonstrated by FTIR spectra. Fig. 3 compares FTIR spectra of pristine $g\text{-C}_3\text{N}_4$ (pm), pure Co_3O_4 and $\text{Co-g-C}_3\text{N}_4$ (pm) taken in transmittance mode between 400 and 4000 cm^{-1} . It can be clearly observed that the features of the condensed C–N heterocycles are present in the spectra of both pure and Co_3O_4 doped graphitic carbon nitride. For these samples, the sharp peak located at about 809 cm^{-1} can be assigned to the out-of-plane bending vibration mode of tri-s-triazine rings, whereas the other bands in the $1250\text{-}1650\text{ cm}^{-1}$ region correspond to the typical stretching vibrations of aromatic C–N heterocycles. Furthermore, no peaks shift was observed in $\text{Co-g-C}_3\text{N}_4$ (pm), signifying that the molecular structure of $g\text{-C}_3\text{N}_4$ is not changed upon Co doping. The FTIR spectrum of $\text{Co-g-C}_3\text{N}_4$ (pm) displays two additional absorption bands at 571 and 667 cm^{-1} , arising from the stretching vibrations of Co–O bonds, which confirms the formation of spinel Co_3O_4 [18]. Two bands represent the vibrations of octahedrally and tetrahedrally coordinated Co^{3+} and Co^{2+} with oxygen in spinel lattice.

The N_2 adsorption and desorption isotherms were measured to characterize the specific surface area of $g\text{-C}_3\text{N}_4$ (pm) and $\text{Co-g-C}_3\text{N}_4$ (pm) (Fig. 4). The isotherms of both samples feature typical type-IV properties, which suggest the presence of porous (mesoporous and macroporous) structures. The hysteresis loop in the low pressure range ($0.5 < P/P_0 < 0.9$) is associated with the intra-aggregated pores. The calculated BET specific surface areas of pure and Co_3O_4 modified $g\text{-C}_3\text{N}_4$ (pm) was 5.8 and $11.7\text{ m}^2/\text{g}$, respectively. Almost 2-fold enhanced specific area of the $\text{Co-g-C}_3\text{N}_4$ (pm) after doping with cobalt could be attributed to the dispersion of fine Co_3O_4 nanoparticles in the C_3N_4 sheets thus preventing aggregation, which is also evident from the XRD result. A higher surface area of $\text{Co-g-C}_3\text{N}_4$ (pm) would favor the diffusion of reactants and provides

more active sites, leading to improved catalytic performance. For comparison, the surface area of the samples prepared from non-protonated melamine was 3.0 and 5.7 m^2/g , respectively.

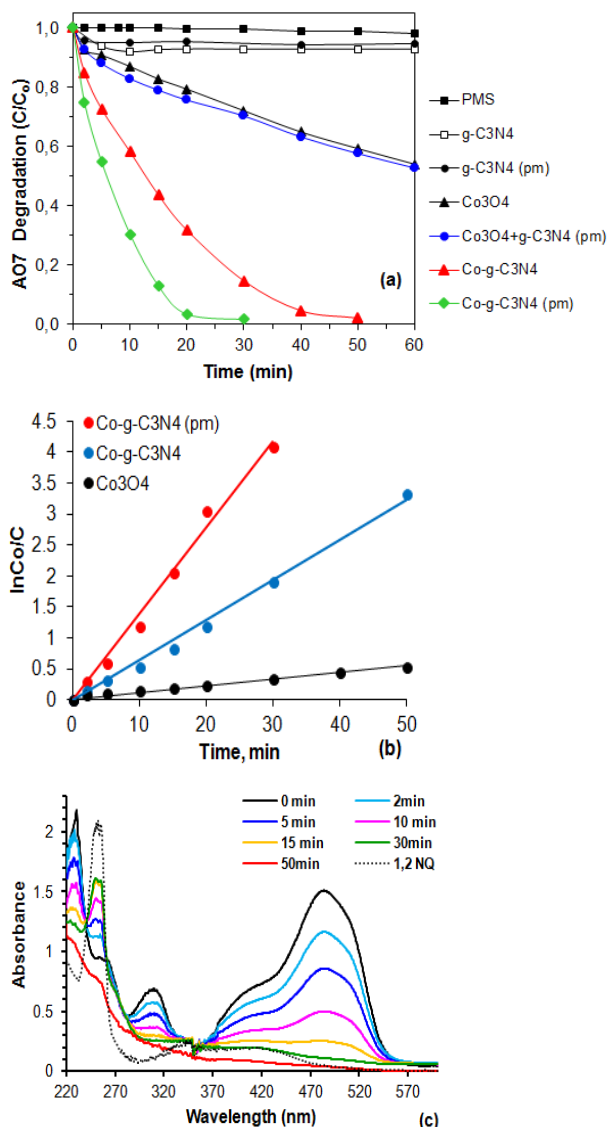


Figure 5. (a) Degradation profile of AO7 degradation in different systems, (b) degradation kinetics of AO7 by PMS activated by different catalysts, and (c) UV-vis spectral changes during AO7 degradation with Co-g- C_3N_4 (pm)/PMS system. Reaction conditions: 50 mg dm^{-3} AO7; 0.5 g dm^{-3} catalyst loading; PMS/AO7= 10/1; pH=3.0

The removal of AO7 based on chemical oxidation with PMS and catalytic degradation with different catalysts in the presence of PMS was evaluated, and the results are presented in Fig. 5a. The degradation of AO7 occurred very slowly in the presence of PMS alone without a catalyst. Less than 1 % AO7 removal was achieved after 1 h of reaction, implying that the chemical oxidation of dye occurs through a non-radical mechanism. Only 7% of the dye was removed after 60 min with

pristine g- C_3N_4 and g- C_3N_4 (pm) coupled with PMS, pointing out that pure graphitic nitride possess negligible PMS activation ability at ambient conditions. A significant improvement of the catalytic performance of g- C_3N_4 was observed after modifying with Co_3O_4 , indicating that PMS can be activated by the composite catalysts with the production of active radical species. The highest degradation rate was achieved in the Co-g- C_3N_4 (pm)/PMS system with complete dye removal after 30 min. When a composite obtained from non-protonated melamine was used as a catalyst, only 85% of AO7 was degraded for the same duration, but the dye could also be fully decolorized within 50 min. Evidently, synthesizing g- C_3N_4 by heating HNO_3 protonated melamine influences the PMS decomposition activity of the composite catalysts. The faster AO7 degradation kinetics assisted by Co-g- C_3N_4 (pm) catalyst may be related to its larger surface area, which can afford more active sites for catalysis than that of Co-g- C_3N_4 . Further investigations on the effect of the protonation on the improved catalytic activity over the Co-g- C_3N_4 (pm) sample are underway. These results clearly indicated that the Co_3O_4 modified g- C_3N_4 is an active catalyst for remediation of dyes wastewater in the presence of PMS without light irradiation. Bare Co_3O_4 exhibited a much lower catalytic activity than Co-g- C_3N_4 hybrids with only about 41% AO7 removal efficiency after 50 min under similar conditions. Therefore, the enhanced catalytic performance of the composite catalysts could be attributed to the synergistic effect between the g- C_3N_4 and Co_3O_4 oxide. Decomposition of PMS to reactive radicals is based on the electron transfer from the catalyst to PMS. Besides basic surface functionalities, which are important for PMS activation, the delocalized d-electrons from the tri-s-triazine units of g- C_3N_4 can also contribute to electron transfer, so that PMS can decompose to radicals [12]. The crucial role of the close contact between the Co_3O_4 particles and the g- C_3N_4 was further confirmed by experiments using a physical mixture of Co_3O_4 and g- C_3N_4 (pm) as a catalyst for PMS activation. The results showed that the catalytic efficiency of the mechanical mixture is much lower than that of Co-g- C_3N_4 (pm) and close to that, exhibited by pristine Co_3O_4 .

As shown in Fig. 5b, the AO7 degradation follows a pseudo-first-order kinetics. The rate constants are estimated to be 0.1391 min^{-1} ($R^2= 0.991$) and 0.0646 min^{-1} ($R^2= 0.994$) in the Co-g- C_3N_4 (pm)/PMS and Co-g- C_3N_4 /PMS systems, respectively. By contrast, corresponding to Co_3O_4 /PMS system rate constant is 0.0109 min^{-1} ($R^2= 0.987$), which is about 12.4 and 5.9 times

lower than that exhibited by the composite catalysts, respectively. This strongly confirms the improved catalytic behavior of Co_3O_4 for activating PMS after dispersion on the $g\text{-C}_3\text{N}_4$ surface.

Representative UV-vis spectral changes observed during the $\text{Co-g-C}_3\text{N}_4(\text{pm})$ -mediated AO7 degradation are presented in Fig. 5c. As seen, the addition of catalyst and PMS into the dye solution caused a continuous decrease of the characteristic absorption bands in the visible region with time and finally disappeared after 20 min, indicating the destruction of the chromophore-containing azo-linkage. In parallel, the absorbance in the UV region is also reduced, due to the destruction of the conjugated π -system. Furthermore, concurrently with the decay in the visible region, a new band at 254 nm appeared at the very beginning of the reaction and then descended gradually in the late reaction stage. 1,2-naphthoquinone (1,2 NQ) was identified to contribute to the peak by comparing spectra of the reaction mixture and a standard solution containing 1,2 NQ.

Further kinetic studies were carried out using the most active $\text{Co-g-C}_3\text{N}_4(\text{pm})$ catalyst to explore the effects of main operating parameters, namely catalyst dosage, PMS concentration, and initial solution pH on the AO7 degradation rate.

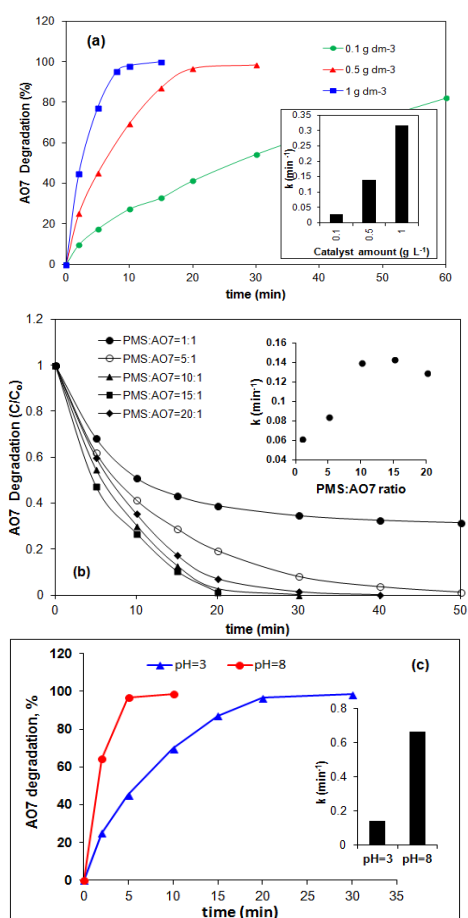


Figure 6. Effect of (a) catalyst dosage: PMS:AO7=1:1, pH=3; (b) PMS concentration: [catalyst]=0.5 g dm⁻³, pH=3; (c) initial solution pH: [catalyst]=0.5 g dm⁻³, PMS:AO7=1:1 on the AO7 catalytic oxidation over $\text{Co-g-C}_3\text{N}_4(\text{pm})$.

As clearly shown in Fig. 6a, the increase in the catalyst amount from 0.1 g dm⁻³ to 1 g dm⁻³ resulted in an 11-fold increase in the degradation rate and accordingly, AO7 removal in 15 min was enhanced from about 33% to 100%. The observed trend can be attributed to the increased numbers of active sites for PMS activation and, hence, more radicals generated per unit time. These results also confirm the crucial role of the catalyst for the effective activation of oxidant, as well as indicate that the surface reaction is the rate limiting step.

The catalytic degradation of AO7 was also affected by the PMS dosage, as illustrated in Fig. 6b. As observed, both the AO7 degradation efficiency and the rate constant significantly increased first with increasing PMS:AO7 ratio from 1:1 to 10:1 and then only slightly changed at higher PMS dosages. At a molar ratio of 1:1 complete removal of AO7 was not achieved due to the lack of sufficient oxidant amount, whereas the ten-fold increase in PMS dosage led to more than 99% extent of dye decolorization for 30 min. As the concentration of PMS increases, more active radicals are produced and, hence, faster AO7 degradation occurs. However, the degradation rate becomes slower when the PMS:AO7 ratio is higher than 15:1, probably due to the self-quenching of sulfate radicals by PMS [19].

As shown in Fig. 6c, AO7 degradation in $\text{Co-g-C}_3\text{N}_4(\text{pm})/\text{PMS}$ system is strongly affected by the initial pH of the solution. With increasing pH from 3 to 8 (adjusted with 1M NaOH), the rate constant increased from 0.1347 ($R^2 = 0.997$) to 0.6632 min⁻¹ ($R^2 = 0.984$). Accordingly, at pH 8 almost 99% of AO7 is removed for only 5 min while 30 min are needed to achieve the same degradation efficiency in acidic medium. The observed pH dependence of the degradation rate is unexpected given the influence of pH on the surface charge of the catalyst and the fractions of different PMS species. As the isoelectric point of $g\text{-C}_3\text{N}_4$ obtained from melamine is reported to be about 5.0, below this value the surface of $g\text{-C}_3\text{N}_4$ was positively charged [20]. On the other hand, PMS exists in the form of HSO_5^- at acid-neutral conditions, while SO_5^{2-} are the dominant PMS species when pH was above 9.2 [21]. When pH is increased, the interaction between PMS and catalyst surface tends to decrease due to the electrostatic repulsion among them, thus less PMS could be activated and AO7 degradation rate could decrease.

However, a homogeneous activation of PMS by NaOH may take place in basic conditions. A mechanism of base-activation of PMS is proposed, according to which H_2O_2 is formed upon NaOH-catalyzed hydrolysis of PMS and subsequently, was decomposed to superoxide anion radicals [22]. Besides, PMS can decompose into sulfate and hydroxyl radicals in the presence of H_2O_2 [23]. Therefore, the observed higher AO7 degradation at pH 8 could be attributed to the simultaneous homogeneous activation of PMS by NaOH and its decomposition to radicals on the catalyst surface. At acidic pH, due to the formation of H-bond between H^+ and the O–O group of HSO_5^- , the PMS ions acquire a pseudo-positive charge, resulting in surface repulsion effect [24]. Moreover, under acidic condition the SRs could be scavenged by H^+ , resulting in production of less reactive HSO_4^- [25]. Therefore, a lower degradation rate was observed at a lower pH.

Previous investigations have pointed out that sulfate radical ($\text{SO}_4^{\cdot-}$) and hydroxyl radical ($\cdot\text{OH}$) can be the main reactive species generated by heterogeneous catalytic activation of PMS in the presence of Co-containing catalyst [21]. To confirm that AO7 degradation was a radical-involved process and to ascertain the dominant radical species generated in the Co-g- C_3N_4 (pm)/PMS system, quenching tests were conducted with the addition of ethanol and *tert*-butyl alcohol (TBA) as radical scavengers. Ethanol is considered as a universal scavenger for $\text{SO}_4^{\cdot-}$ and $\cdot\text{OH}$, because it readily react with both radicals at high and comparable rate. For TBA, the scavenging rate constant is approximately 1000 times greater for $\cdot\text{OH}$ than that for $\text{SO}_4^{\cdot-}$, therefore it is considered as a particular scavenger for $\cdot\text{OH}$ [8, 21]. As shown in Fig. 7, the degradation efficiency of AO7 with the addition of TBA was slightly less than that without any scavenger, indicating that $\cdot\text{OH}$ radicals had a negligible contribution to the degradation of dye in Co-g- C_3N_4 (pm)/PMS system. However, when using the same amount of ethanol as a scavenger, a more significant inhibiting effect was observed and AO7 degradation decreased to 56% only, suggesting that sulfate radicals were the main reactive species in the Co-g- C_3N_4 (pm)/PMS system.

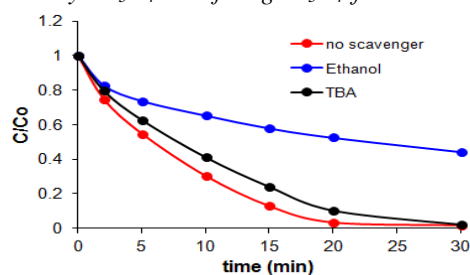


Figure 7. Inhibiting effect of scavengers (ethanol (TBA):PMS=1000:1 molar ratio) on AO7 degradation with Co-g- C_3N_4 (pm)/PMS system. Reaction conditions: as indicated in Fig. 5.

CONCLUSIONS

Co_3O_4 nanoparticles-modified g- C_3N_4 composites were prepared using a one-pot synthesis methodology and characterized by several techniques. The as-prepared materials were used as catalysts for PMS activation without light irradiation to produce sulfate radicals for degrading azo dye AO7. The Co-g- C_3N_4 (pm) composite prepared from protonated melamine showed the best performance in catalytic activation of PMS and was also proved more efficient than the bare Co_3O_4 . The removal efficiency of AO7 with an initial concentration of $50 \text{ mg}\cdot\text{dm}^{-3}$ was greatly increased from 28% to 100% within 30 min with about 13 fold increase in the first order rate constant. Increasing catalyst dosage and pH was favorable to AO7 degradation, while high PMS concentration caused a slight decrease in the efficiency of the Co-g- C_3N_4 (pm)/PMS system. Radical pathway was proposed to contribute to AO7 degradation as sulfate radicals, being the dominating species, were generated by the catalyst/PMS interaction.

Acknowledgement: Authors gratefully acknowledge financial support from by the University of Plovdiv Research Fund (Project NI HF-2017).

REFERENCES

1. S. Yang, P. Wang, X. Yang, L. Shan, W. Zhang, X. Shao, R. Niu, *J. Hazard. Mater.*, **179**, 552 (2010).
2. L.W. Matzek, K.E. Carter, *Chemosphere*, **151**, 178 (2016).
3. W.-D. Oh, Z. Dong, G. Ronn, T.-T. Lim, *J. Hazard. Mater.*, **325**, 71 (2017).
4. A. Ghauch, A.M. Tuqan, *Chem. Eng. J.*, **183** 162 (2012).
5. M.M. Ahmed, S. Barbati, P. Doumenq, S. Chiron, *Chem. Eng. J.*, **197**, 440 (2012).
6. Y. Feng, J. Liu, D. Wu, Z. Zhou, Y. Deng, T. Zhang, K. Shih, *Chem. Eng. J.*, **280**, 514 (2015).
7. P. Hu, M. Long, *Appl. Catal. B*, **181**, 103 (2016).
8. G. Anipsitakis, D. Dionysiou, *Environ. Sci. Technol.*, **37**, 4790 (2003).

9. J. Deng, S. Feng, K. Zhang, J. Li, H. Wang, T. Zhang, X. Ma, *Chem. Eng. J.*, **308**, 505 (2017).
10. C. Wang, P. Shi, X. Cai, Q. Xu, X. Zhou, X. Zhou, D. Yang, J. Fan, Y. Min, H. Ge, W. Yao, *J. Phys. Chem. C*, **120**, 336 (2016).
11. H. Yang, K. Lv, J. Zhu, Q. Li, D. Tang, W. Ho, M. Li, S.A.C. Carabineiro, *Appl. Surf. Sci.*, **401**, 333 (2017).
12. C. Wang, J. Kang, H. Sun, H.M. Ang, M.O. Tadé, S. Wang, *Carbon*, **102**, 279 (2016).
13. H. Liu, P. Sun, M. Feng, H. Liu, S. Yang, L. Wang, Z. Wang, *Appl. Catal. B*, **187**, 1 (2016).
14. Y. Zheng, Y. Jiao, Y. Zhu, Q. Cai, A. Vasileff, L. H. Li, Y. Han, Y. Chen, S-Z. Qiao, *J. Am. Chem. Soc.*, **139**, 3336 (2017).
15. F. Ghanbari; M. Moradi, *Chem. Eng. J.*, **310**, 41 (2017).
16. J. Li, J. F. P. Ye, D. Wu, M. Wang, X. Li, A. Xu, *J. Photoch. Photobio. A*, **342**, 85 (2017).
17. S. Hu, X. Chen, Q. Li, F. Li, Z. Fan, H. Wang, Y. Wang, B. Zheng, G. Wu, *Appl. Catal. B-Environ.*, **201**, 58 (2017).
18. Z.S. Wu, W.C. Ren, L. Wen, L. Gao, J. Zhao, Z. Chen, G. Zhou, F. Li, H.-M. Cheng, *ACS Nano*, **4**, 3187 (2010).
19. M. Antoniou, A. de la Cruz, D. Dionysiou, *Appl. Catal., B*, **96**, 290 (2010).
20. B. Zhu, P. Xia, W. Ho, J. Yu, *Appl. Surf. Sci.*, **344**, 188 (2015).
21. J. Deng, C. Ya, Y. Ge, Y. Cheng, Y. Chen, M. Xu, H. Wang, *RSC Adv.*, **8**, 2338 (2018).
22. R. Xiao, Z. Luo, Z. Weis, S. Luo, R. Spinney, *Curr. Opin. Chem. Eng.*, **19**, 51 (2018).
23. J. Zhao, Y. Zhang, X. Quan, S. Chen, *Sep. Purif. Technol.*, **71**, 302 (2010).
24. Y. Guan, J. Ma, X. Li, J. Fang, L. Chen, *Environ. Sci. Technol.*, **45**, 9308 (2011).
25. Y.-H. Huang, Y.-F. Huang, C.-I. Huang, C.-Y. Chen, *J. Hazard. Mater.*, **170**, 1110 (2009).

Automatic generation of molecular zwitterionic forms with Ambit-Zwitterion

N. T. Kochev^{1*}, V. H. Paskaleva¹, N. Jeliaskova²

¹University of Plovdiv "Paisii Hilendarski", Department of Analytical Chemistry and Computer Chemistry,
24 Tzar Asen Str., 4000 Plovdiv, Bulgaria

²Ideaconsult Ltd, 4 A. Kanchev str., Sofia 1000, Bulgaria

Received November 12, 2018; Revised December 10, 2018

We present a new open source tool for automatic generation of all zwitterionic forms of a given organic compound. Ambit-Zwitterion is an extension of Ambit-Tautomer software, part of the open source software platform Ambit and developed on top of a Chemistry Development Kit. All acidic centers in the target molecule (e.g. carboxylic groups, sulfonic groups, phosphoryl groups, etc.), as well as all basic centers (e.g., amino groups) are preliminarily identified. Ambit-Zwitterion implements a combinatorial algorithm for exhaustive generation of all zwitterions by making all combinations of k anions out of n acidic centers ($C_{k,n}$) and respectively all combinations of k cations out of m basic centers ($C_{k,m}$). Each combination from $C_{k,n}$ anionic set is combined with each combination from the $C_{k,m}$ cationic set to generate all zwitterionic forms containing k zwitterionic pairs. All zwitterions are obtained by iterating $k=1,2,\dots,\min(n,m)$. Zwitterion generation algorithm is customized by a set of configuration options. Ambit-Zwitterion module is available for download as a Java library or as a command line application (<https://doi.org/10.5281/zenodo.1481752>). Software example usage and test results with Drug Bank structure set are presented.

Keywords: zwitterion, software, open-source, combinatorial, Ambit

INTRODUCTION

Zwitterions are neutral molecules that have separate positive and negative charge groups [1] in their structure. A lot of important biochemical and pharmaceutical compounds exist in zwitterionic forms. In physiological conditions, amino acids exist mainly as their zwitterions (see figure 1). Many zwitterionic structures have been used as drugs or prodrugs e.g. antibiotics, anti-HIV agents, diabetic drugs, etc. [2]. Zwitterion-derived materials have different organizational behaviors and they can be used as building blocks for nanostructured ionic materials [3]. The positive and negative charges of the zwitterions create specific ionic environment around proteins used as drugs and thus they can stabilize it with no affection of its bindings to the target [4]. They show potential as biocompatible coating for nanomaterials used in various drug formulations [5] and for passivating the surface of gold nanoparticles intended for *in vivo* applications [6]. Zwitterionic buffer additives are found to be useful in capillary zone electrophoresis for preventing the adsorption of proteins on the capillary wall and to improve the separation of proteins [7]. In molecular electronics, they can be used as molecular switches. Al-Kaysi *et al.* [8] reported the synthesis of a fluorescent molecular switch which is based on the interconversion between the fluorescent zwitterionic form and the non-fluorescent anionic

state of a spiro-cyclic Meisenheimer complex of 1,3,5-trinitrobenzene.

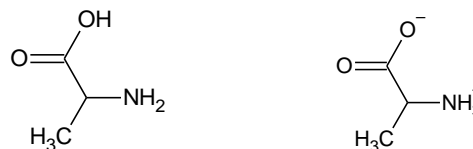


Figure 1. Alanine zwitterion

Computer-assisted drug design methodologies apply computer simulation to predict molecular properties as a function of the structure and are used to find the isomer responsible for bioactivity [2]. Adequate chemical structure representations are mandatory for the efficient utilization of cheminformatics methodologies [9]. Molecular zwitterionic forms directly influence the topological structures and in this manner influence molecular descriptors and QSAR/QSPR models. Computer programs could be very helpful for the exploration of zwitterionic properties and predicting their activities. There are software tools for protonation and deprotonation of specific atomic types [10]. So far in the literature there are no reported open source software systems for exhaustive generation of zwitterions. The latter are especially needed for cheminformatics handling of molecular structures with more zwitterionic centers. In this paper we present our newest development - Ambit-Zwitterion, a software tool for exhaustive generation of all zwitterionic forms of a target

* To whom all correspondence should be sent.
E-mail: nick@uni-plovdiv.net

chemical compound. We discuss its basic characteristics, usage examples and test results.

EXPERIMENTAL

Software characteristics

Ambit-Zwitterion is implemented in object-oriented programming language Java. It is an open source, OS independent software module distributed under LGPL license [11]. *Ambit-Zwitterion* is an extension of *Ambit-Tautomer* [12] (previously developed by us software tool) part of the cheminformatics platform *Ambit* [13] where it is integrated as a separate module (*ambit2-tautomers.zwitterion*). *Ambit* integration allows usage of plenty of cheminformatics functionalities from other *Ambit* modules [13] developed by our group, as well as utilities from external open-source resources. The source code of the java library extension (*ambit2.tautomers.zwitterion*) is available at <http://ambit.sourceforge.net/>. The source code of *Ambit-Zwitterion* command line application is available at <http://ideaconsult.github.com/apps-ambit> (folder *tautomers-example*) and an executable *.jar file can be downloaded from <https://doi.org/10.5281/zenodo.1481752>.

Software architecture

Ambit-Zwitterion implementation includes four basic components:

(1) *Data input/output utilities.* *Ambit-Zwitterion* supports basic formats for structure presentation: SMILES [14] and InChI [15] linear notations, CML chemical format, MOL/SDF file formats, CSV and TXT file formats. The software configuration can be done from command-line interface options. The variety of supported file formats allows easy integration of our tool with other software applications.

(2) *Structural information management.* Chemical structure representation in *Ambit-Zwitterion* is based on Java class *AtomContainer* which is part of the cheminformatics library Chemistry Development Kit (CDK) [16]. *AtomContainer* implements the molecular connection table which is the foundation for all zwitterionic transformations (see figure 2).

(3) *Chemical groups management.* There are several dedicated java classes for handling the molecular groups corresponding to acidic and basic centers. For each group (acidic or basic) there are utilities for group detection and state changing e.g. NEUTRAL to ION and vice versa (see Carboxylic Group example in figure 2).

(4) *Zwitterion generation.* This is the most crucial software component. The exhaustive generation of all zwitterionic forms is based on the combinatorial algorithm described in the following section.

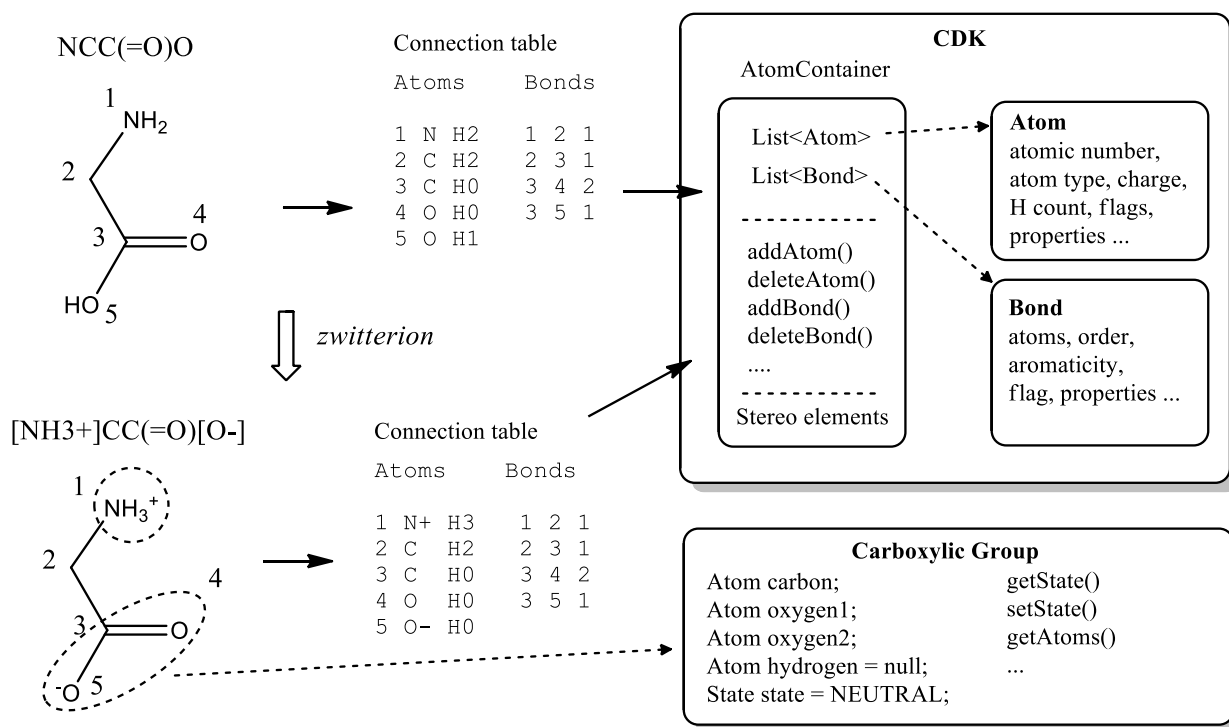


Figure 2. Chemical object management in *Ambit-Zwitterion*

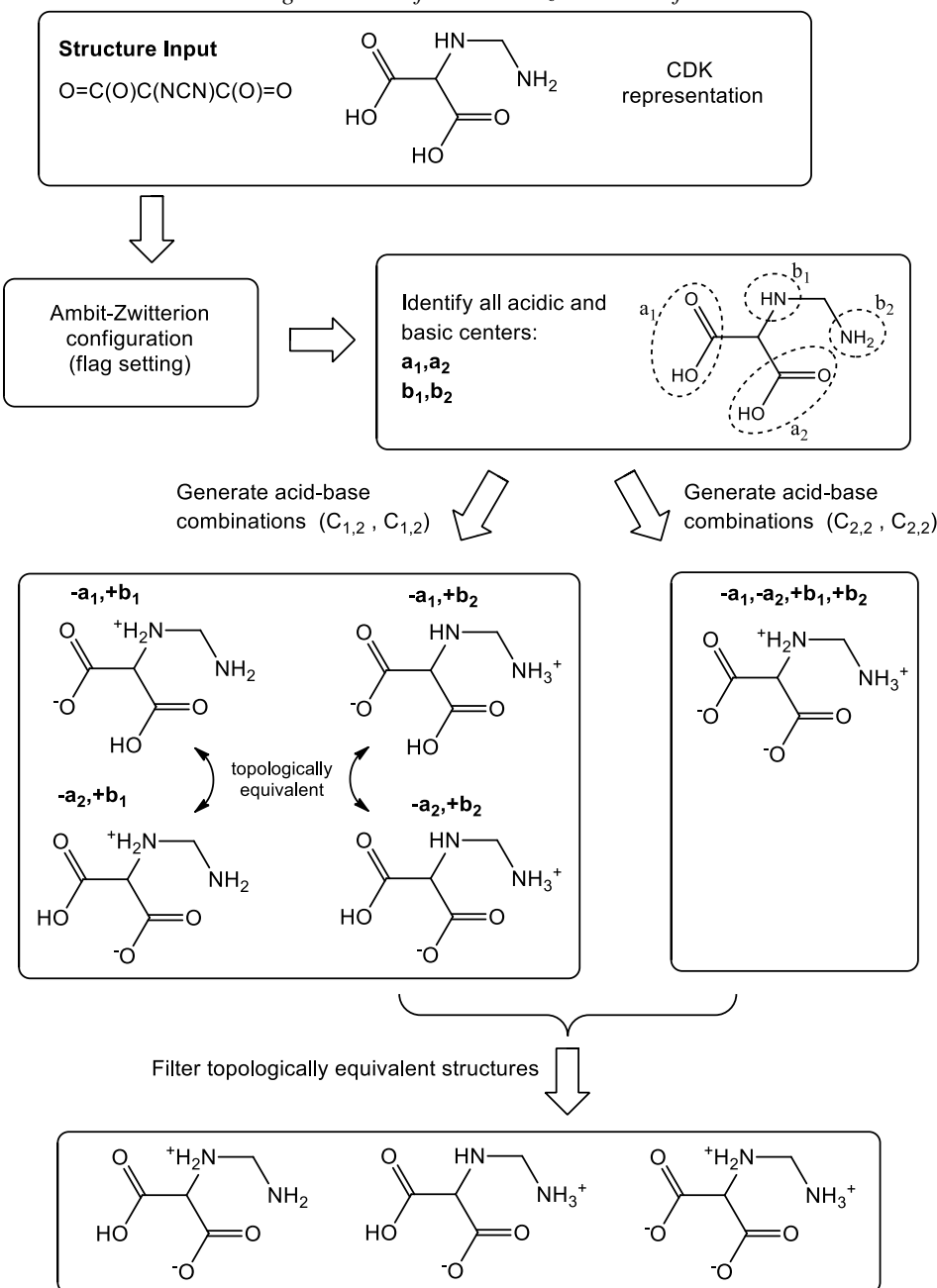


Figure 3. Flow chart of the Ambit-Zwitterion basic generation sequence

Zwitterion generation algorithm

The basic workflow of Ambit-Zwitterion is summarized in figure 3. The molecule input is taken from one of the popular molecular formats (SMILES, MOL etc.) and converted into the internal CDK representation. All acidic and basic centers are recognized (current version of Ambit-Zwitterion supports: carboxylic groups, sulfonic groups, sulfinic groups and phosphoryl groups).

After group detection, the initial sets of acidic centers $\{a_1, a_2, \dots, a_n\}$ and basic centers $\{b_1, b_2, \dots, b_m\}$ are obtained. The maximal number of simultaneous zwitterionic pairs, max_{zp} , in the target molecule is $min\{n, m\}$. All theoretically possible zwitterionic forms are obtained as a unification of all subsets of

zwitterions containing k zwitterionic pairs simultaneously. The total number of generated zwitterions is:

$$Z = \sum_{k=1}^{max_{zp}} Z_k, \quad (1)$$

where Z_k is the number of zwitterions containing exactly k acid-base pairs. Ambit-Zwitterion implements a combinatorial algorithm for exhaustive generation by making all combinations of k anions out of n acidic centers ($C_{k,n}$) and respectively all combinations of k cations out of m basic centers ($C_{k,m}$). Each combination from $C_{k,n}$ anionic set is combined with each combination from $C_{k,m}$ cationic set to generate all zwitterionic

forms containing k zwitterionic pairs. Thus the value of Z_k is obtained as:

$$Z_k = \binom{n}{k} \binom{m}{k} \quad (2)$$

Figure 4 illustrates the combinatorial case: $n=2$ and $m=3$ for the molecule of glutathione. Initially sets $\{a_1, a_2\}$ and $\{b_1, b_2, b_3\}$ are all in neutral state which corresponds to original molecule of glutathione with no zwitterions. The value of max_{zp} is $min(2,3) = 2$.

For $k=1$, six combinations are obtained:

$\{-a_1, +b_1\}$ $\{-a_1, +b_2\}$ $\{-a_1, +b_3\}$
 $\{-a_2, +b_1\}$ $\{-a_2, +b_2\}$ $\{-a_2, +b_3\}$.

For $k=2$, three combinations are obtained:

$\{-a_1, -a_2, +b_1, +b_2\}$
 $\{-a_1, -a_2, +b_1, +b_3\}$
 $\{-a_1, -a_2, +b_2, +b_3\}$

Totally, nine zwitterions are generated for the molecule of glutathione (figure 4).

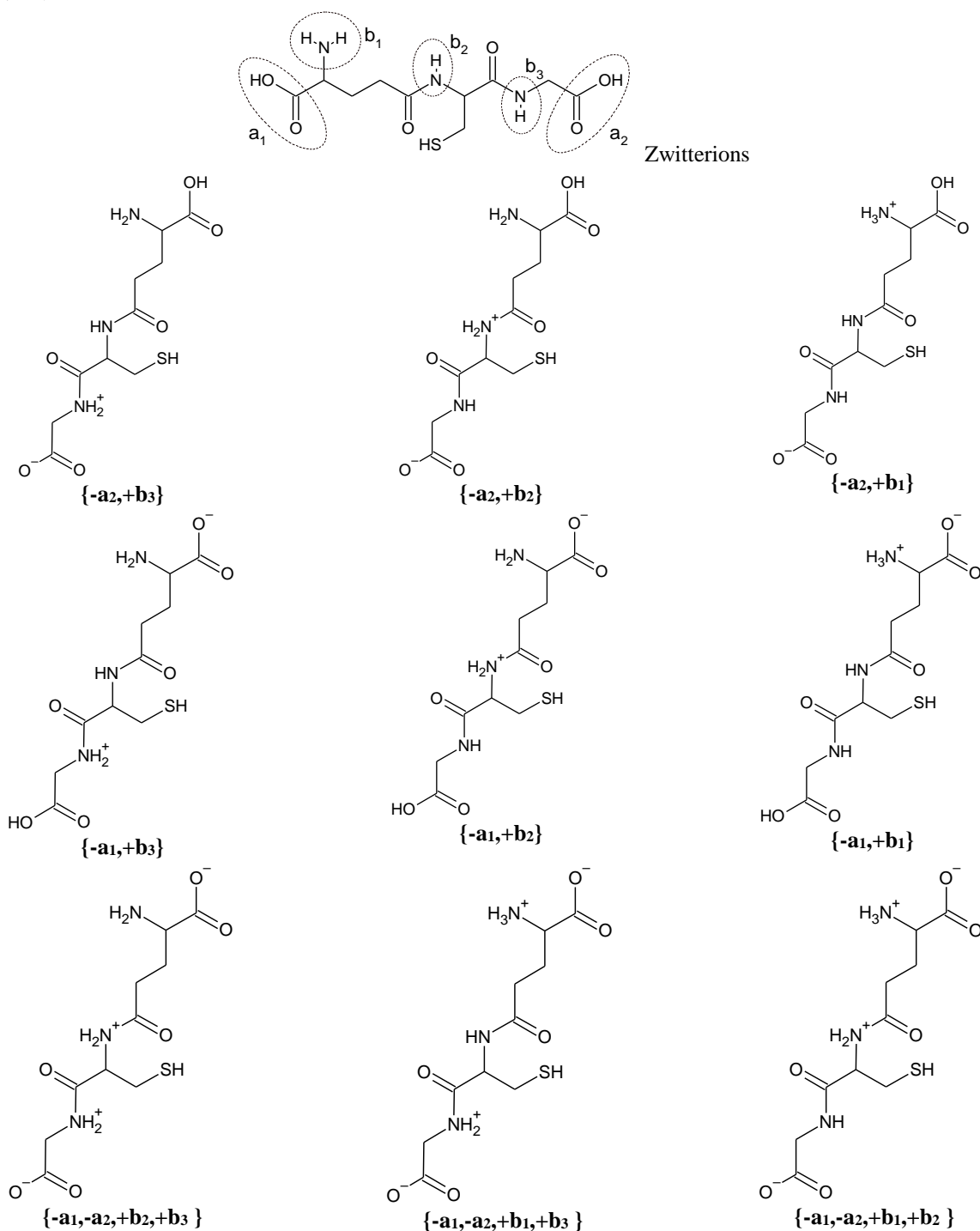


Figure 4. Zwitterion combinations for the molecule of glutathione ((2S)-2-amino-4-[(1R)-1-[(carboxymethyl)carbamoyl]-2-sulfanylethyl]carbamoyl]butanoic acid)

As can be seen for the example input molecule from figure 3, topologically equivalent groups generate topologically equivalent zwitterions. For this purpose we have implemented a filtration option in *Ambit-Zwitterion* where structure duplications are removed by means of InChI keys [15] calculated with fixed H atoms option (the default InChI algorithm does not distinguish the zwitterionic forms).

Ambit-Zwitterion software version 1.0 is available as a command-line interface application with following options:

```
Zwitterion CLI
-c,--count                Output count
                           statistics only
-f,--filter                Filter duplicated
                           zwitterions (InChI
                           based)
-h,--help                  Zwitterion CLI
-i,--input <input>        Input molecule file
                           (*.smi, *.sdf, *.csv)
-m,--max_zwitterions <max> Maximal number of
                           registered
                           zwitterions
-o,--output <output>       Output file name
                           (*.csv)
-p,--max_pairs <max>      Maximal number of
                           zwitterion pairs
-s,--smiles <smiles>      Input molecule smiles
-v,--verbose                Verbose console
                           output
```

Example of *Ambit-Zwitterion* application for a molecule directly inputted as a SMILES notation from the command line is given as follows:

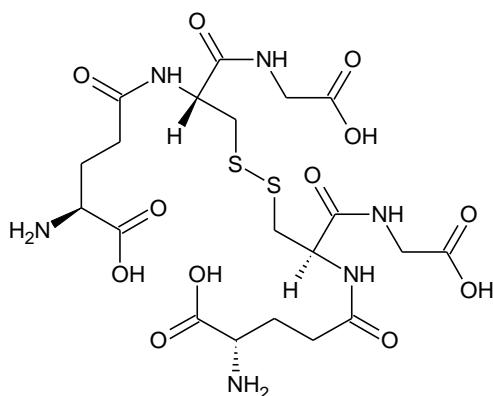


Figure 5. Molecular structure of oxigluthathione and the theoretical number of its zwitterions and corresponding zwitterionic pairs

```
java -jar ambit-zwitterion.jar -s O=C(O)C(NCN)C(O)=O
-f
```

Input molecule: O=C(O)C(NCN)C(O)=O

Zwitterions:

```
C(N)[NH2+]C(C(=O)O)C(=O)[O-]
C([NH3+])NC(C(=O)O)C(=O)[O-]
C([NH3+])[NH2+]C(C(=O)[O-])C(=O)[O-]
```

Ambit-Zwitterion can be also applied in a batch mode for a set of molecules specified by means of *-i* option. Executable jar files and more examples are available at:

<https://doi.org/10.5281/zenodo.1481752>.

RESULTS AND DISCUSSION

The molecular structure of oxigluthathione as well as zwitterion generation statistics obtained with and without filtration of topologically equivalent zwitterion structures are given in Figure 5. The total number of generated zwitterionic forms is 109. Figure 5 shows the number of structures containing one (Z1), two (Z2), three (Z3) and four (Z4) zwitterionic pairs of the type {acidic anion – basic cation}. As it can be seen, 12 zwitterionic structures are generated that contain one zwitterionic pair while most of the predicted theoretically possible zwitterions are obtained using combinations of two or three zwitterionic pairs.

Another test result for the structure of arginine is given in figure 6. All arginine tautomers were generated using *Ambit-Tautomer* [12] software tool applying Incremental approach with tautomeric rules covering 1-3 and 1-5 proton shift.

Number of theoretical zwitterions:

Filter (no-filter)

109 (209)

Zwitterionic pairs	Number of zwitterions generated
Z1	12 (24)
Z2	48 (90)
Z3	40 (80)
Z4	9 (15)

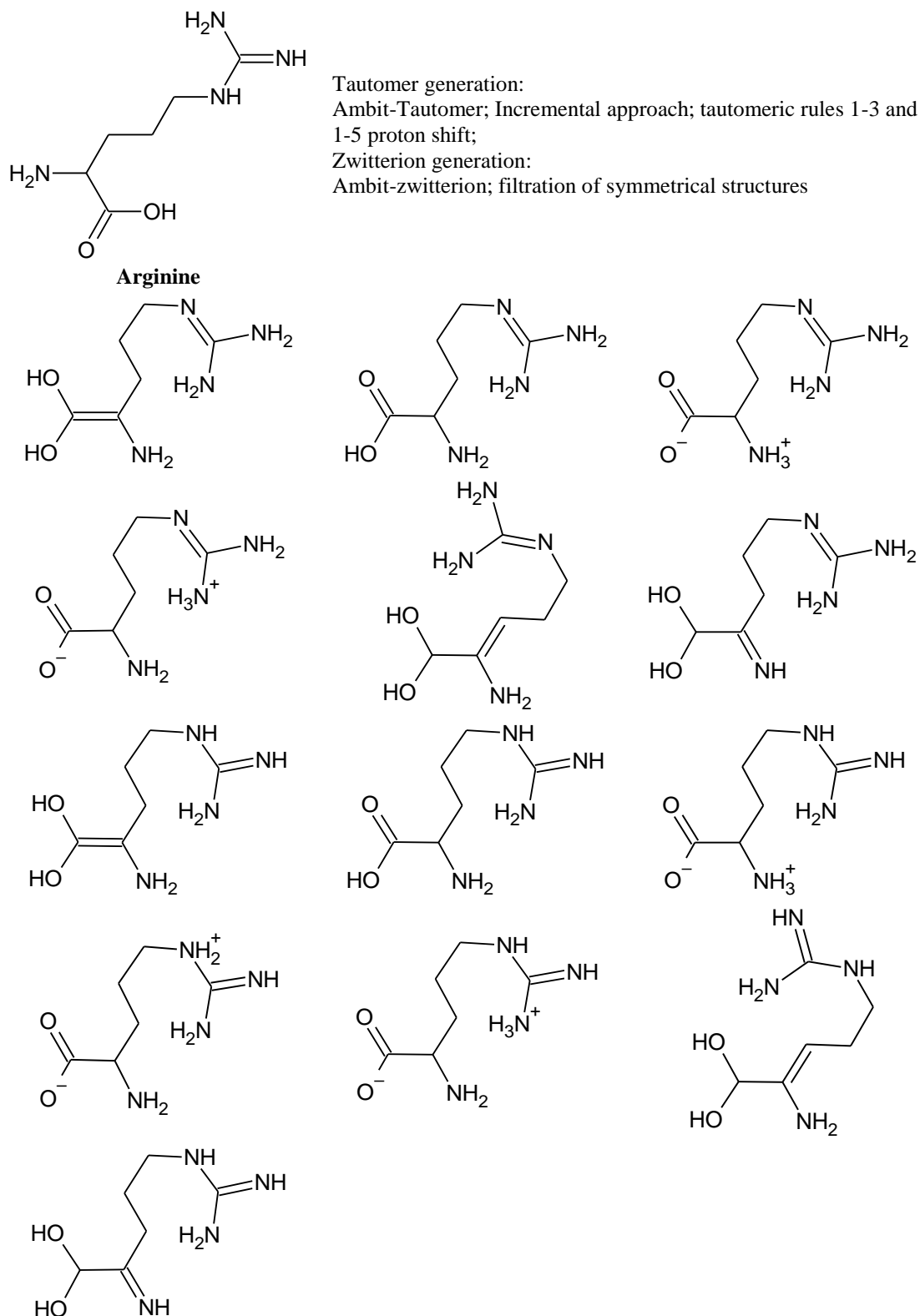


Figure 6. Arginine molecule, generated tautomeric and zwitterionic forms

We have performed automatic tests generating all zwitterionic forms for a dataset of 6406 molecular structures (Drug Bank v.5.0.6 without salt containing substances). Computational time comparison was made for the zwitterion counting procedure with and without filtration of the

topologically equivalent structures, as well as for the procedure of full generation of all theoretical zwitterions. The tests were made on a PC computer with RAM 8GB, Processor Intel® Core™ i5-8250U CPU @ 1.60GHz 1.80GHz, working on Windows 10, 64-bit operation system. The

measured times, presented in table 1, also include the time for file reading and writing operations and SMIELS generation procedures.

Table 1. Zwitterion generation computational times for Drug Bank dataset

	Count (h:min:sec)	Full (h:min:sec)
Filter	0:04:40	0:09:45
No-filter	0:00:12	0:05:10

As it can be seen from table 1, all zwitterions (about 90 000 zwitterions for the entire Drug Bank set) were generated and counted for 12 sec. The actual storage on the output files took about 5 minutes that is mainly due to the SMILES generation (file operations time could be neglected). Accordingly, the needed time for filtration is about 4 minutes and 30 seconds and it is due to the computation of InChI keys used for topologically equivalent structures filtration.

Also, we have performed structural analysis of the obtained Drug Bank zwitterions summarized in figures 7, 8 and 9 (the shown statistics are with filtration of symmetrical molecules). Only 1451 molecular structures gave at least one zwitterion. Most of these molecules (36%) gave exactly one zwitterionic form and 27% showed theoretical possibility for two zwitterionic forms. Figure 7 shows the percentages of structures giving a number of zwitterions in the range 1-34 (i.e. statistical bins greater than or equal to 1%).

Figure 8 visualizes the percentages of structures that gave a number of zwitterions less than 1% (i.e. the histogram of rare zwitterionic counts).

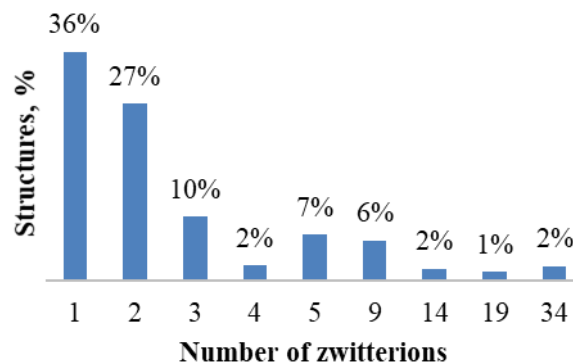


Figure 7. Distribution of the relative number (>1%) of structures generating from 1 to 34 zwitterionic forms

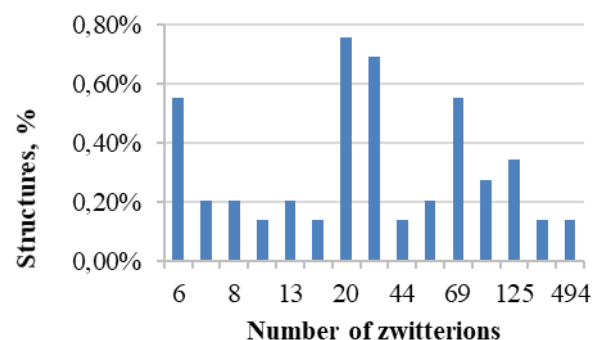


Figure 8. Distribution of the relative number (<1%) of structures generating a higher number of zwitterions (from 6 to 494+)

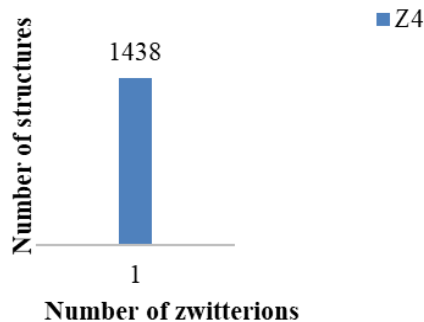
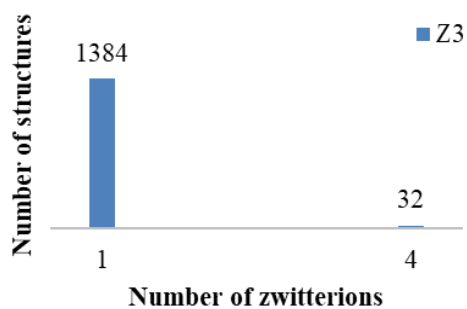
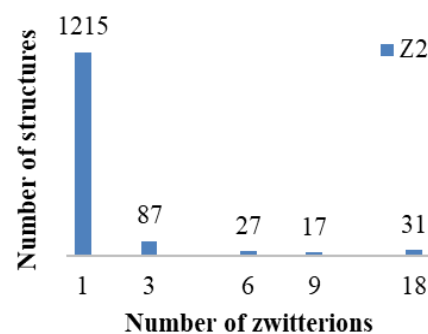
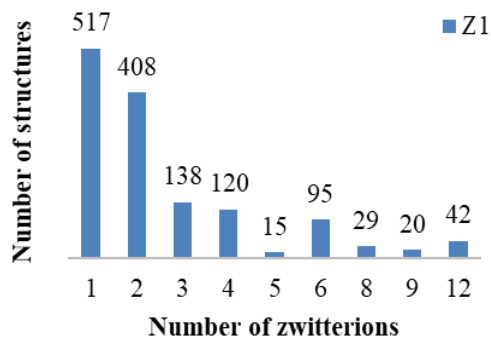


Figure 9. Distribution of generated zwitterions containing one (Z1), two (Z2), three (Z3) and four (Z4) zwitterionic pairs

Figure 9 shows the structure frequency distribution according to the number of zwitterionic pairs. Detailed test results are available at Zenodo repository at the following address: <https://doi.org/10.5281/zenodo.1481752>.

CONCLUSIONS

A new software tool (Ambit-Zwitterion) for exhaustive generation of all theoretically possible zwitterionic forms is developed. Software performance is demonstrated with various use cases and large-scale tests performed with Drag Bank molecules. Ambit-Zwitterion source code is available at <http://ambit.sourceforge.net/> and the software can be easily integrated as part of bigger scientific workflows. Executable jar file with the latest version, additional examples and full test results are available at:

<https://doi.org/10.5281/zenodo.1481752>.

Acknowledgement: We thank Plovdiv University Scientific Fund (project MUI7-HF-027) for supporting this scientific work.

REFERENCES

1. <https://goldbook.iupac.org/html/Z/Z06752.html>, last accessed on 27.09.2018.
2. Z. Yang, Q. Li, G. Yang, *Future Med. Chem.*, **8**, 2245 (2016).
3. T. Ichikawa, *Polymer Journal*, **49**, 413 (2017).
4. A. Keefe, Sh. Jiang, *Nature Chemistry*, **4**, 59 (2012).
5. N. Hadjesfandiari, A. Parambath, Stealth coatings for nanoparticles: Polyethylene glycol alternatives, *Eng. Biomater. Drug Deliv. Syst.*, 345 (2018).
6. L. Knittel, P. Schuck, C. Ackerson, A. Sousa, *RSC Adv.*, **6**, 46350 (2016).
7. X. Fang, T. Zhu, V. Sun, *J. High Resolut. Chromatogr.*, **17**, 749 (1994).
8. R. Al-Kaysi, G. Guirado, E. Valente, *European J. Org. Chem.*, 2004 (16), 3408 (2004).
9. T. Engel, J. Gasteiger, Chemoinformatics: basic concepts and methods, Wiley-VCH Verlag GmbH, 2018.
10. N. O'Boyle, M. Banck, C. James, C. Morley, T. Vandermeersch, G. Hutchison, *J. Cheminform.*, **3**, 33 (2011).
11. LGPL: <https://www.gnu.org/licenses/lgpl-3.0.en.html>, last accessed on 27.09.2018
12. N. Kochev, V. Paskaleva, N. Jeliaskova, *Mol. Inform.*, **32**, 481 (2013).
13. N. Jeliaskova, V. Jeliaskov, *J. Cheminform.*, **3**, 18 (2011).
14. D. Weininger, *J. Chem. Inf. Comput. Sci.*, **28**, 31 (1988).
15. InChI: <https://iupac.org/who-we-are/divisions/division-details/inchi/>, last accessed on 27.09.2018.
16. E. Willighagen, J. Mayfield, J. Alvarsson, A. Berg, L. Carlsson, N. Jeliaskova, S. Kuhn, T. Pluskal, M. Rojas-Chertó, O. Spjuth, G. Torrance, Ch. Evelo, R. Guha, Ch. Steinbeck, *J. Cheminform.*, **9**, 33 (2017).

Characterization and application of spent brewer's yeast for silver nanoparticles synthesis

N. S. Yantcheva¹, D. B. Karashanova², B. C. Georgieva², I. N. Vasileva¹, A. S. Stoyanova³,
P. N. Denev⁴, R. H. Dinkova⁵, M. H. Ognyanov⁴, A. M. Slavov^{1*}

¹Department of Organic Chemistry and Inorganic Chemistry, University of Food Technologies,
26 Maritza Blvd., 4002 Plovdiv, Bulgaria,

²Institute of Optical Materials and Technologies "Acad. J. Malinowski", Bulgarian Academy of Sciences,
Acad. Georgi Bonchev Str., bl. 109, Sofia 1113, Bulgaria;

³Department Technology of Tobacco, Sugar, Vegetable and Essential Oils, University of Food Technologies,
26 Maritza Blvd., Plovdiv 4002, Bulgaria

⁴Institute of Organic Chemistry with Centre of Phytochemistry, Bulgarian Academy of Sciences,
Laboratory of Biologically Active Substances, 139 Ruski Blvd., 4000 Plovdiv, Bulgaria

⁵Department Food Preservation and Refrigeration Technology, University of Food Technologies,
26 Maritza Blvd., Plovdiv 4002, Bulgaria

Received October 17, 2018; Revised December 20, 2018

The brewer's yeast is an abundant and valuable by-product of the beer industry. In the last years numerous studies have focused on different possibilities for its valorization. The aim of the present study was to characterize spent brewer's yeast and to investigate its application as a reducing agent with combination of extracts of *Rosa damascena* wastes for synthesis of silver nanoparticles (AgNPs). The non-pasteurized and pasteurized brewer's yeast was found to contain small amounts of phenolic compounds: 8.40 and 1.53 $\mu\text{molGAE}/100\text{ mL}$, respectively, but they were rich in carbohydrates (40.20 \pm 1.5%), proteins (41.33 \pm 0.11%) and dietary fibers (23.94 \pm 1.5%). The water extract of *Rosa damascena* waste was able to reduce the Ag⁺ quickly and AgNPs with sphere-like shape were formed. This is typical for the AgNPs obtained by reduction with extracts rich in polyphenols. The pasteurized and non-pasteurized brewer's yeasts induced the AgNPs synthesis (proved by visual observation and by UV-Vis measurements) relatively slowly and the average particle size was smaller than that of the particles synthesized by water extract of *Rosa damascena* waste. The combinations of pasteurized and non-pasteurized brewer's yeast with water extract of *Rosa damascena* waste were able to produce AgNPs relatively quickly. The transmission electron microscope images confirmed the observed synthesis of AgNPs.

Keywords: brewer's yeast, *Rosa damascena*, silver nanoparticles, "green" synthesis, waste valorization, polyphenols.

INTRODUCTION

Valorization of biodegradable food wastes became an important issue in the last years. The spent brewer's yeast is a valuable biomass and represents 1.7-2.3 g/L beer. The major species used for bottom fermenting lager beers are *Saccharomyces pastorianus* or *Saccharomyces carlsbergensis* strains. The brewer's yeast was found to be rich in glucans and manoproteins with potential biological activity [1]. Due to the higher amounts of proteins and dietary fibers brewer's yeast is suitable for functional foods formulations [2], and was also investigated as additive for fermentation and production of bread [3]. With its various applications in the food, agricultural and industrial sector the brewer's biomass was proven as a valuable renewable material [4, 5].

In the last two decades nanomaterials and nanoparticles (NPs) with their unique properties (high surface to volume ratio, enhanced surface

reactivity or increased ion release, etc.) became a base for obtaining of new improved biosensors, catalyzers, antimicrobial agents, etc. [6]. An alternative and novel approach for obtaining of NPs is the so-called "green" synthesis based on the reduction of metal cations with natural reducing agents, such as: plant extracts, fungi, microorganisms, waste materials, etc. The advantage of this method consists in the single stage environmentally procedure with renewable and usually abundant, cheap materials. Various raw materials and wastes were investigated but experiments with combined wastes and microorganisms are scarce. Beside, this approach allows more complete utilization and valorization of the wastes. This observation gave ground to the purpose of the present study: to investigate and characterize spent brewer's yeast, to utilize it along with fresh brewer's yeast and with combination of *Rosa damascena* waste for synthesis of silver nanoparticles.

* To whom all correspondence should be sent.
E-mail: antons@uni-plovdiv.net

Table 1. Combinations of 0.01M AgNO₃, water, *Rosa damascena* extract and brewer's yeasts for different samples investigated.

Sample	<i>Rosa damascena</i> extract, mL	Water, mL	Pasteurized brewer's yeast, mL	Non-pasteurized brewer's yeast, mL	0.01M AgNO ₃ , mL
0B	0.1	0.1	-	-	0.3
1B	-	0.1	0.1	-	0.3
2B	-	0.1	-	0.1	0.3
3B	0.1	0.1	0.1	-	0.3
4B	0.1	0.1	-	0.1	0.3

EXPERIMENTAL

Waste materials

The *Rosa damascena* wastes were obtained from Mirkovo distillery (Mirkovo, region of Sofia, Bulgaria, 2017 harvest). The wastes were inspected for impurities, dried at 50°C, and kept at -18°C until further treatment. The brewer's yeasts (both pasteurized and non-pasteurized) were obtained from ABM Production (Plovdiv, Bulgaria). Prior to synthesis the pasteurized brewer's yeast was dissolved overnight in distilled water at 1% w/v and then filtered. The non-pasteurized brewer's yeast was diluted with distilled water (1:13) to 1% dry matter.

Extraction of *Rosa Damascena* waste with distilled water

150 g dry residues were treated with 1000 mL of water for 1 h at 60°C then left for 24 h at room temperature at constant stirring. The mass was filtered and the insoluble residue was extracted with additional 500 mL of water at the same conditions.

The "green" synthesis of AgNPs was performed by mixing the necessary amounts of 0.01M AgNO₃ (Merck, Germany), water, *Rosa damascena* extract and brewer's yeasts according to Table 1.

Analytical methods

The total polyphenol content of ethanolic extracts was determined as described by Singleton and Rossi [7]. The antioxidant activity by DPPH and FRAP assays was determined as described by Slavov *et al.* [8]. The protein content in the brewer's yeast was determined by the Kjeldahl method with automated nitrogen analyzer UDK152 (Velp Scientifica, Italia) using a correction factor N×6.25 for calculation of total protein. Crude lipid content was determined according to AOAC 922.06 method. The total dietary fibers (TDF) were determined by the enzymatic-gravimetric method, using the total dietary fiber assay kit Bioquant 1.12979.0001 (Merck, Germany) according to manufacturer's instructions. The total ash content was determined by igniting 5 g of sample in a muffle furnace at 605°C until constant weight. The total carbohydrate quantity of wastes was

calculated by difference after determination of protein, crude lipid, lignin, total polyphenols, and ash quantities. The moisture content was determined with Kern MLB 50-3 moisture analyzer (Kern & Sohn GmbH, Germany). The individual amino acids were determined after derivatization [9] using the HPLC system ELITE LaChrome (Hitachi) equipped with diode array detector Elite LaChrome L-2455. The separation was performed on AccQ-TagTM (3.9×150 mm) column. The contents of calcium, magnesium, iron, copper and manganese were determined according to AOAC 2014.004.

UV-Vis measurements of the AgNPs synthesis were carried out on a Helios Omega spectrophotometer (Thermo Scientific, Madison, WI, USA) equipped with VISIONlite software and operated at a resolution of 1 nm. The scanning was performed in the 350-700 nm range at a scan speed of 1600 nm min⁻¹. The samples of the AgNPs were prepared for TEM analysis by placing a drop of the suspension on a standard copper grid, covered by amorphous carbon layer and allowing the water to evaporate at room temperature. Bright field TEM and Selected Area Electron Diffraction (SAED) images were acquired with the high-resolution transmission electron microscope JEOL JEM 2100 (JEOL, Japan) at an accelerating voltage of 200 kV. Statistical analysis of AgNPs particles size distribution was carried out with Image J software. The identification of the phase composition of the samples was achieved using PDF-2 Database of the International Center for Diffraction Data (ICDD).

Statistical analysis

All analyses were performed in triplicate and the results were presented as mean values. Statistical differences were detected by analysis of variance (ANOVA, Tukey's test) and a value of p<0.05 indicated statistical significance.

RESULTS AND DISCUSSION

The brewer's yeasts were investigated for their total polyphenol content and antioxidant activity. Having in mind that the polyphenols are among the major substances responsible for green synthesis of metal NPs, this information is related to the

N.S. Yantcheva *et al.*: Characterization and application of spent brewer's yeast for silver nanoparticles synthesis capability for biogenic synthesis. The results from the analysis are shown in Table 2.

The results suggested that both brewer's yeasts are poor in polyphenolic substances and this also reflects on the observed antioxidant activities. The water extract of *Rosa damascena* waste was rich in polyphenolic compounds: 133.70 ± 0.11 μmol GAE/100 g waste and it confirmed the observation made by Slavov *et al.* [8] that the higher the concentration of polyphenols, the higher is the antioxidant activity: the DPPH method showed 8550 ± 0.98 μmol TE/100 g waste and FRAP – 905.83 ± 0.99 μmol TE/100 g waste.

Furthermore we investigated the overall composition of the brewer's yeasts and the results are presented in Table 3.

Both brewer's yeasts were rich in carbohydrates and proteins while the crude lipids were relatively low: less than 1 %. On contrary, Blagović *et al.* [10] found around 4% in the *Saccharomyces uvarum* yeast obtained as a by-product of industrial beer production. Calcium was the predominating metal and the amounts of dietary fibers were between 21-24 %.

Table 2. Polyphenols and antioxidant activity of brewer's yeasts

Brewer's yeast	Total phenolics, μmol GAE/100 g	FRAP, μmol TE/100 g	DPPH, μmol TE/100 g
Pasteurized	1.53 ± 0.09^a	2.45 ± 0.11^a	2.05 ± 0.13^a
Non-pasteurized	8.40 ± 0.12^b	13.40 ± 0.45^b	12.00 ± 0.21^b

^{a, b} – different letters in a row indicate statistically different values ($p < 0.05$; ANOVA, Tukey's test).

Table 3. Proximate composition of the brewer's yeasts

Substances	Brewer's yeast	
	Pasteurized	Non-pasteurized
Total carbohydrates, % DM	40.20 ± 1.5^a	38.61 ± 1.39^a
Moisture, %	2.00 ± 0.7	-
Crude lipids	0.08 ± 0.03^a	0.09 ± 0.02^a
Ash content, %	0.07 ± 0.01^a	0.09 ± 0.01^a
Sodium chloride, %	0.41 ± 0.09^a	0.04 ± 0.01^b
Protein content, %	41.33 ± 0.11^a	43.38 ± 0.24^b
Sugars, %	18.47 ± 0.10^a	11.32 ± 0.21^b
Total dietary fibers, %	23.94 ± 1.53^a	21.18 ± 1.21^a
Calcium, mg/kg	5960 ± 0.22^a	6742 ± 0.32^b
Magnesium, mg/kg	1377 ± 0.12^a	1221 ± 0.42^b
Iron, mg/kg	1.44 ± 0.05^a	0.86 ± 0.03^b
Copper, mg/kg	4.40 ± 0.07^a	2.13 ± 0.06^b
Manganese, mg/kg	5.20 ± 0.13^a	3.38 ± 0.24^b

^{a, b} – different letters signify statistical significance.

Table 4. Individual amino acids in the brewer's yeasts

Amino acid, g/100 g product	Brewer's yeast	
	Pasteurized	Non-pasteurized
Valine	1.22 ± 0.06^a	1.58 ± 0.07^a
Isoleucine	0.97 ± 0.11^a	1.15 ± 0.13^a
Leucine	0.33 ± 0.09^a	0.45 ± 0.08^a
Lysine	3.86 ± 0.17^a	4.97 ± 0.13^b
Methionine	0.55 ± 0.13^a	0.62 ± 0.11^a
Cysteine	0.48 ± 0.16^a	0.59 ± 0.17^a
Threonine	1.94 ± 0.09^a	2.14 ± 0.11^a
Tyrosine	2.04 ± 0.09^a	2.21 ± 0.09^a
Phenylalanine	2.02 ± 0.08^a	2.47 ± 0.09^b
Alanine	5.38 ± 0.07^a	5.86 ± 0.06^b
Arginine	2.50 ± 0.06^a	2.43 ± 0.05^a
Aspartic acid	2.04 ± 0.12^a	2.15 ± 0.14^a
Glycine	0.98 ± 0.12^a	1.53 ± 0.12^b
Proline	2.46 ± 0.10^a	2.66 ± 0.18^a
Serine	6.65 ± 0.08^a	6.96 ± 0.10^a
Hydroxyproline	2.46 ± 0.16^a	2.13 ± 0.06^a
Hystidine	5.08 ± 0.12^a	5.19 ± 0.14^a

^{a, b} – different letters signify statistical significance.

In the subsequent analysis the individual amino acids building the proteins in the brewer's yeasts were determined by HPLC and the results are presented in Table 4. The results from the analysis demonstrated that both yeasts have similar amounts of amino acids with slightly higher content for the non-pasteurized brewer's yeast. Between the indispensable amino acids, lysine and tyrosine appeared in the highest quantities.

Furthermore, brewer's yeasts alone and in combination with water extract of *Rosa damascena* waste were investigated for ability to synthesize AgNPs. The results of the visual observation and UV-Vis studies are presented in Figs. 1 and 2, respectively.

The synthesis of AgNPs by water extract of *Rosa damascena* was fast – a darkening of the solution was observed between the 3rd and 4th minute (the UV-Vis studies confirmed this

observation as the absorption increased – Fig. 2). For samples 3B and 4B with combinations of water extract of *Rosa damascena* and non-pasteurized and pasteurized brewer's yeasts formation of AgNPs after the 5th minute was also observed (both visually and by UV-Vis). For sample 1B (pasteurized brewer's yeast) no synthesis of AgNPs was observed; sample 2B was able to produce nanoparticles around 1 hour after the beginning of the reaction. This observations with the results in Table 2 for polyphenol content revealed that the polyphenolic compounds were among the main reducing agents. Nevertheless, the fact that non-pasteurized brewer's yeast was able to produce AgNPs showed that sugars, polysaccharides and proteins also played a role in the process of synthesis, although the synthesis has taken place relatively slower.

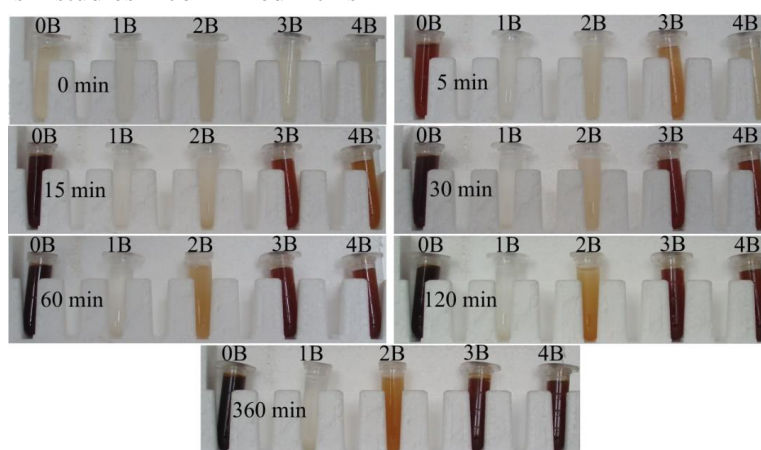


Figure 1. Visual observation of AgNPs synthesis. The sample numbers are according to Table 1.

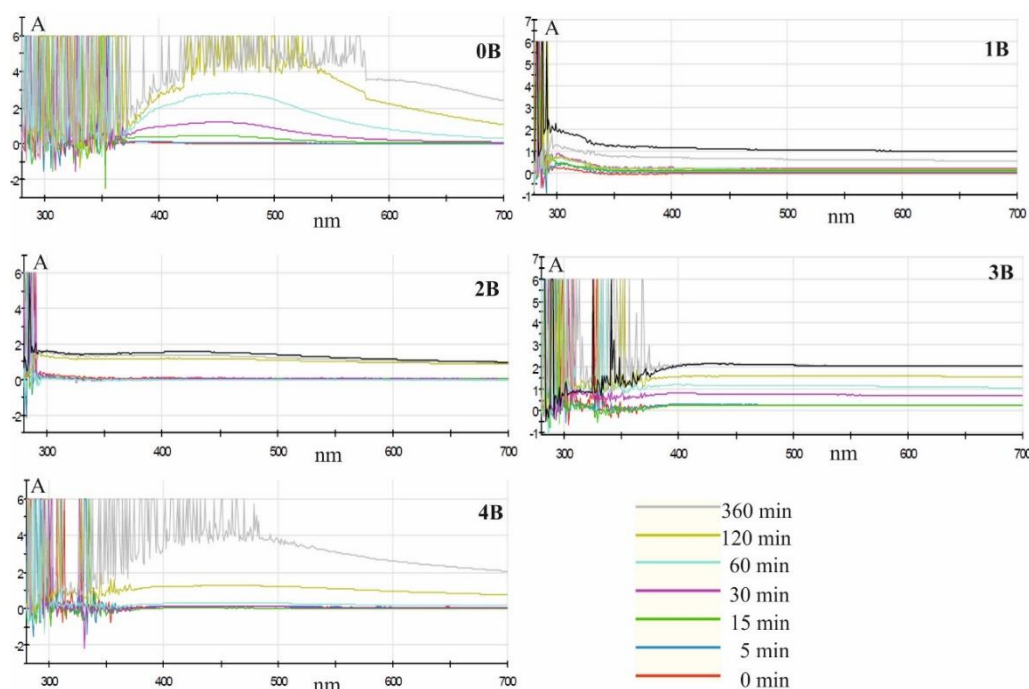


Figure 2. UV-Vis studies of the formation of AgNPs with time. The sample numbers are according to Table 1.

The TEM analysis confirmed the formation of nanoparticles with spherical shapes. Selective Area Electron Diffraction (SAED) results proved the AgNPs synthesis (Phase identified: Ag cubic, $a=4.077$, PDF 87-0720) – Fig. 3.

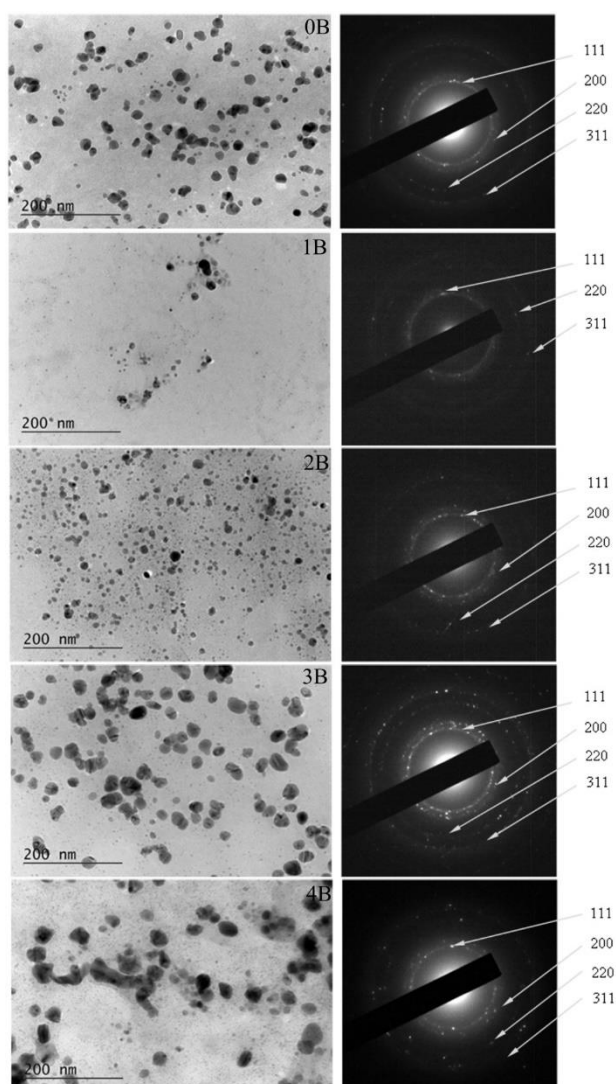


Figure 3. TEM analysis of AgNPs. The sample numbers are according to Table 1.

CONCLUSIONS

The present study focused on the characterization of brewer's yeast and its potential application (alone or in combination with water extract of *Rosa damascena* waste biomass) for "green" synthesis of AgNPs. The brewer's yeast was found to be rich in carbohydrates (polysaccharides and sugars), proteins and dietary

fibers while having lower amounts of lipids which make them an excellent source for obtaining of functional foods. The water extract of *Rosa damascena*, rich in polyphenolic substances, was able to synthesize AgNPs quickly while both brewer's yeasts, owing to lower amounts of polyphenols, led to obtaining of silver nanoparticles with a significant delay in time. This slower process however, contributes to the aggregation of AgNPs and to a certain extent it could be beneficial for the final size and distribution pattern of the nanoparticles.

Acknowledgement: We acknowledge the financial support from the National Science Fund of Bulgaria; project DN 17/22 from 12.12.2017: Valorization and application of essential oil industry wastes for "green" synthesis of metal nanoparticles.

REFERENCES

1. M. Pinto, E. Coelho, A. Nunes, T. Brandão, M.A. Coimbra, *Carboh. Polym.*, **116**, 215 (2015).
2. B. Podropa, F. Świdorski, A. Sadowska, R. Rakowska, G. Wasiak-Zys, *Czech J. Food Sci.*, **34(6)**, 554 (2016).
3. M. Heitmann, E. Zannini, E.K. Arendt, *J. Cereal Sci.*, **63**, 49 (2015).
4. G. Pancrazio, S.C. Cunha, P.G. de Pinho, M. Loureiro, S. Meireles, I.M.P.L.V.O. Ferreira, O. Pinho, *Meat Sci.*, **121**, 382 (2016).
5. R. Pérez-Torrado, E. Gamero, R. Gómez-Pastor, E. Garre, A. Aranda, E. Matallana, *Trends Food Sci. Technol.*, **46**, 167 (2015).
6. R.J.B. Peters, H. Bouwmeester, S. Gottardo, V. Amenta, M. Arena, P. Brandhoff, H.J.P. Marvin, A. Mech, F.B. Moniz, L.Q. Pesudo, H. Rauscher, R. Schoonjans, A.K. Undas, M.V. Vettori, S. Weigel, K. Aschberger, *Trends Food Sci. Technol.*, **54**, 155 (2016).
7. V.L. Singleton, J.A.J. Rossi, *Am. J. Enol. Vitic.*, **16**, 144 (1965).
8. A. Slavov, P. Denev, I. Panchev, V. Shikov, N. Nenov, N. Yantcheva, I. Vasileva, *Ind. Crops Prod.*, **100**, 85 (2017).
9. A.P. Aronal, N. Huda, R. Ahmad, *Int. J. Poultry Sci.*, **11(3)**, 229 (2012).
10. B. Blagović, J. Rupčić, M. Mesarić, K. Georgiú, V. Marić, *Food Technol. Biotechnol.*, **39(3)**, 175 (2001).

Utilization of essential oil industry chamomile wastes as a source of polyphenols

N. S. Yantcheva¹, I. N. Vasileva¹, P. N. Denev², H. N. Fidan³, R. S. Denkova⁴, A. M. Slavov^{1*}

¹Department of Organic Chemistry and Inorganic Chemistry, University of Food Technologies,
26 Maritza Blvd., 4002 Plovdiv, Bulgaria,

²Institute of Organic Chemistry with Centre of Phytochemistry, Bulgarian Academy of Sciences,
Laboratory of Biologically Active Substances, 139 Ruski Blvd., 4000 Plovdiv, Bulgaria

³Department of Catering and Tourism, University of Food Technologies, 26 Maritza Blvd., Plovdiv 4002, Bulgaria

⁴Department of Biochemistry and Molecular Biology, Technological Faculty, University of Food Technologies,
26 Maritza Blvd., Plovdiv 4002, Bulgaria

Received October 17, 2018; Revised December 20, 2018

The annual global production of chamomile (*Matricaria Chamomila*) essential oil was roughly estimated between 80 and 100 tonnes. Due to the low content of essential oil in the chamomile (around 0.30-0.45 % on dry basis) large quantities of wastes are generated every year by the essential oil industry. The aim of the present work was to investigate the possibility for valorization of chamomile waste. Three wastes were investigated – after extraction of chamomile with 1,1,1,2-tetrafluoroethane (F), after hydrodistillation (HD) and after steam distillation (S). It was found that extraction of the raw materials by fluorocarbons preserves to a large extent the polyphenols – F wastes had 2697.81±84.90 mg/L total polyphenols compared to 1500.30±36.22 mg/L and 366.24±26.37 mg/L for S and HD wastes, respectively. Similar trend was observed for antioxidant activity results: F wastes showed 31235.42±238.21 µmol TE/L (by ORAC method) and 12235.23±267.68 µmol GAE/L (by HORAC method) while S showed 2 times (by ORAC method) and 3 times (by HORAC method) lower values. The individual phenolic acids and flavonoids were determined by HPLC and the main compounds found were *p*-coumaric acid, chlorogenic acid, catechin, quercetin, and naringin. The polar metabolites and aroma compounds in the ethanolic extracts were investigated by GC-MS. The results suggested that the chamomile waste could be a valuable and cheap source for obtaining of by-products with pronounced antioxidant activity.

Keywords: *Matricaria Chamomila* (chamomile), waste valorization, antioxidant activity, polyphenols.

INTRODUCTION

Valorization of biodegradable agricultural and food wastes became a priority in the last years. Novel promising and uninvestigated waste materials are residues from the essential oils industry. Such underexplored waste is obtained from *Matricaria Chamomila* (chamomile) which is the fifth top-selling herb / essential oil plant with wide application in cosmetics, foods, aromatherapy, and as pharmaceutical additive [1]. Among the main biologically active substances giving the chamomile its beneficial effects are terpenoids (α -bisabolol and its oxides, chamazulene, farnesene, etc.), lactones, glycosides ((*Z*)- and (*E*)-2- β -D-glucopyranosyloxy-4-methoxy cinnamic acids), phenolic compounds – apigenin, quercetin, luteolin, etc. [2].

The annual global production of chamomile essential oil was roughly estimated between 80 and 100 tonnes [3]. Industrially the main approach for obtaining of chamomile essential oils is by steam distillation. The hydrodistillation process is an alternative method which involves covering the

plant tissues with water during the distillation and hence some part of the polyphenols could be extracted. In the last years supercritical CO₂ extraction also became an alternative approach having the advantage to operate at lower temperatures but the initial investments are much higher compared, for example, to steam distillation facilities [4, 5]. Treatment of essential oil crops with fluorocarbons resembles to a large extent CO₂ extraction although the pressure applied is lower. The solvent has the ability to penetrate in the cells and disrupts the plant cell walls, which facilitates further extraction of biologically active substances from the waste material.

Due to the low content of essential oil in the chamomile plants – around 0.30-0.45 % on dry basis [6] large quantities of wastes are generated every year. Approaches and methods for valorization of chamomile residues in the scientific literature are relatively scarce [7, 8]. Recently it was demonstrated that the waste obtained after steam distillation of chamomile could be a source of water-soluble pectic polysaccharides [9].

* To whom all correspondence should be sent.

E-mail: antons@uni-plovdiv.net

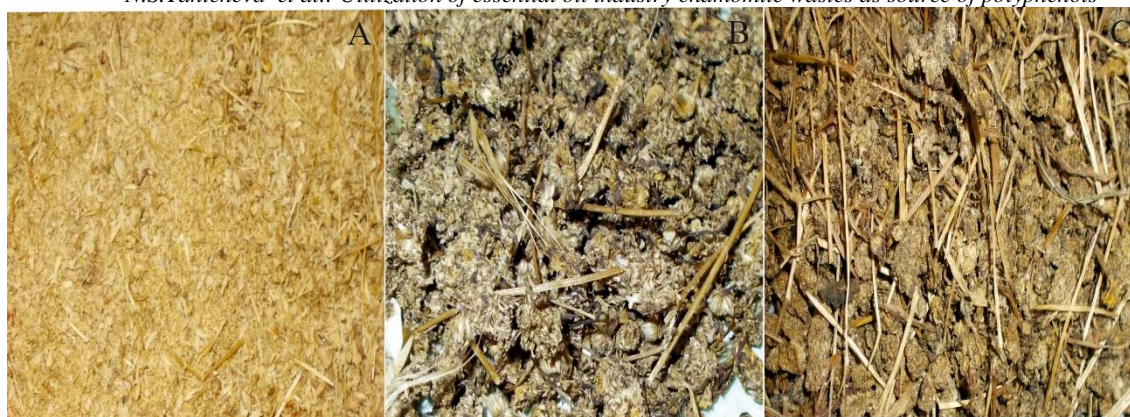


Figure 1. Chamomile wastes investigated: A. after extraction with 1,1,1,2-tetrafluoroethane (F); B. after hydrodistillation (HD); C. after steam distillation (S)

Nevertheless, information about polyphenol content, antioxidant activity and aroma substances in the chamomile waste could not be found in the literature, to the best of our knowledge.

This observation gave ground to the purpose of this study: to investigate chamomile wastes as a source of polyphenol-rich extracts, as a novel approach for valorization of chamomile waste biomass. Three residues were examined: generated by industrial steam distillation (S), by hydrodistillation (HD) and by extraction with 1,1,1,2-tetrafluoroethane (F) of chamomile flowers (Fig. 1).

EXPERIMENTAL

Waste materials

The chamomile wastes (*Matricaria chamomilla*) – after steam distillation and hydrodistillation (water distillation), were obtained from Strelcha distillery, (Strelcha, region of Plovdiv, Bulgaria, 2016 harvest). The chamomile wastes obtained after extraction with 1,1,1,2-tetrafluoroethane [10] of the fresh *Matricaria chamomilla* flowers were provided from Zelenikovo distillery (region of Plovdiv, Bulgaria, 2016 harvest). The wastes were inspected for impurities, dried at 50°C under vacuum, and kept at -18°C.

Extraction with 70% ethanol

Prior to extraction the dry wastes were ground and sieved (0.5 mm). 100 g of dry chamomile residues were treated with 500 mL of 70% ethanol for 1 h at 60°C, then left for 24 h at room temperature at constant stirring. The mass was filtered and the insoluble residue was extracted with additional 500 mL of 70 % ethanol at the same conditions.

Analytical methods

The total polyphenol content of ethanolic extracts was determined as described by Singleton and Rossi [11]. The antioxidant activity by Oxygen Radical Absorbance Capacity (ORAC) and Hydroxyl Radical Averting Capacity (HORAC) assays was measured according to Číž *et al.* [12]. The results of ORAC analysis were expressed as $\mu\text{mol Trolox}^{\text{®}}$ equivalents per liter extract ($\mu\text{mol TE/L}$) and the results of HORAC: as $\mu\text{mol gallic acid equivalents per liter extract}$ ($\mu\text{mol GAE/L}$).

The content of individual phenolic and flavonoid components was analyzed on an Agilent 1220 HPLC system (Agilent Technology, USA), equipped with binary pump and UV-Vis detector. Detection was performed at a wavelength of $\lambda=280$ nm. Separation was carried out on an Agilent TC-C18 column (5 μm , 4.6 mm \times 250 mm) at 25°C. Mobile phases consisted of 0.5 % acetic acid (A) and 100% acetonitrile (B) at a flow rate of 0.8 mL/min. The gradient conditions started with 14% B, between 6 min and 30 min linearly increased to 25% B, then to 50% B for 40 min. The standard compounds (gallic acid, 3,4-dihydroxy benzoic acid, chlorogenic acid, caffeic acid, p-coumaric acid, ferulic acid, ellagic acid, catechin, epicatechin, rutin, naringin, myricetin, quercetin, naringenin and kaempferol) were from Sigma-Aldrich (Steinheim, Germany).

The individual volatile (aroma) and non-volatile polar compounds in the ethanolic extracts were determined as described by Yantcheva *et al.* [13].

Statistical analysis

All analyses were triplicated and the results were presented as mean values. Statistical differences were detected by analysis of variance (ANOVA, Tukey's test) and a value of $p < 0.05$ indicated statistical significance.

RESULTS AND DISCUSSION

The three waste materials: 1) obtained after extraction of chamomile with 1,1,1,2-tetrafluoroethane (F); 2) obtained after hydrodistillation of chamomile (HD) and 3) obtained after steam distillation of chamomile (S), were subjected to extraction with 70% ethanol and ethanol extracts and alcohol insoluble residues (AIR) were obtained. In a previous study [14] the influence of the ethanol concentration on the extractability of polyphenols and polysaccharides from waste rose petals was investigated and it was found that the 70% ethanol extraction gave the best results. For this reason, in the present study extraction with 70% ethanol solution was chosen. Besides, this procedure allows the AIRs to be further used as a source of pectic polysaccharides with minimum losses during ethanol pretreatment [14]. The extracts obtained were subjected to preliminary analysis for their total phenolic substances and antioxidant activity. The results from the analysis are shown in Table 1.

The results from the preliminary experiments suggested that steam distillation led to significant reduction of polyphenols due to their partial extraction compared with 1,1,1,2-tetrafluoroethane (freon) extraction. The hydrodistillation includes

utilization of more water during the process and hence the extraction of polyphenols from the material was much more pronounced. Extraction with halocarbons (freons) preserves to a large extent the polyphenolic substances: their amount is almost two and seven times higher than S and HD wastes, respectively. The higher is the concentration of polyphenols, the higher is the antioxidant activity measured by ORAC and HORAC methods, and the highest results were observed for the F waste: 31235.42±238.21 TE/L (by ORAC method) and 12235.23±267.68 GAE/L (by HORAC method). It seems also that the extraction with 1,1,1,2-tetrafluoroethane led to better disintegration of the cell walls of the plant materials, which is beneficial for the further extractions of biologically active substances. In this regard extraction of the plant materials by halocarbons resembles the extraction with supercritical CO₂ although the state of the extractant used is above its critical point.

Furthermore, we investigated the content of phenolic acids and major flavonoids of the 70 % ethanolic extracts and the results are presented in Table 2.

Table 1. Polyphenols and antioxidant activity of 70 % ethanol extracts of wastes

Waste	Total phenolics, mg/L	ORAC, μmol TE/L	HORAC, μmol GAE/L
F	2697.81±84.90 ^a	31235.42±238.21 ^a	12235.23±267.68 ^a
S	1500.30±36.22 ^b	14985.66±196.85 ^b	4562.32±201.56 ^b
HD	366.24±26.37 ^c	3982.25±168.82 ^c	1142.39±157.84 ^c

^{a, b, c} – different letters signify statistical significance.

Table 2. Phenolic acids and flavonoids in 70% ethanolic extracts

Phenolic acids, mg/100 mL	F	S	HD
Chlorogenic acid	21.62±0.42 ^a	17.60±1.39 ^b	2.79±0.65 ^c
Neochlorogenic acid	8.37±0.36 ^a	-	1.48±0.12 ^c
Vanillic acid	1.55±0.11 ^a	1.23±0.10 ^a	-
Caffeic acid	1.58±0.14 ^a	0.59±0.09 ^b	-
p-Coumaric acid	21.42±1.65 ^a	6.47±1.02 ^b	4.85±0.89 ^b
Ellagic acid	2.76±0.45 ^a	1.42±0.12 ^b	1.28±0.08 ^b
Cinnamic acid	2.88±0.68 ^a	1.17±0.54 ^b	0.70±0.08 ^b
Gallic acid	0.88±0.03 ^a	1.28±0.05 ^b	0.37±0.04 ^c
TOTAL, mg/100 mL	61.06±1.85 ^a	29.76±1.45 ^b	11.47±1.11 ^c
Flavonoids, mg/100 mL	F	S	HD
Quercetin	24.26±1.25 ^a	27.25±1.85 ^a	13.47±1.42 ^b
Quercetin-3-β-glucoside	29.22±1.37 ^a	17.07±1.14 ^b	5.83±1.08 ^c
Myricetin	16.47±0.98 ^a	5.66±0.87 ^b	8.83±0.99 ^c
Kaempferol	1.24±0.08 ^a	1.82±0.10 ^b	1.23±0.05 ^a
Naringin	28.56±1.06 ^a	8.64±0.95 ^b	9.86±0.96 ^b
Naringenin	3.29±0.58 ^a	3.44±0.65 ^a	3.47±0.44 ^a
Catechin	21.78±1.14 ^a	46.82±1.62 ^b	11.13±1.17 ^c
Epicatechin	-	-	17.74±1.26
TOTAL, mg/100 mL	124.82±1.52 ^a	110.70±1.96 ^b	71.56±1.75 ^c

^{a, b, c} – different letters signify statistical significance.

The highest contents of total phenolic acids were observed for the F waste: 61.06±1.85 mg/100 mL extract and the main representative was *p*-coumaric acid. *p*-Coumaric acid was also present in significant amounts in the S and HD wastes but the total amounts of phenolic acids were considerably lower: 29.76±1.45 and 11.47±1.11 mg/100 mL for S and HD, respectively, compared to F. Chlorogenic acid, a compound with pronounced antioxidant activity [15] was the most abundant one in the S waste. Other phenolic acids contributing to the higher antioxidant activity of the ethanolic extract from chamomile treated with halocarbons were neochlorogenic and chlorogenic acids. Comparing the total amount of flavonoids the same

trend could be confirmed: the highest amounts were found in the F waste (124.82±1.52 mg/100 mL) while S and HD had 110.70±1.96 and 71.56±1.75 mg/100 mL, respectively. The most abundant flavonoids were quercetin-3-β-glucoside and quercetin, naringin, and catechin. These results suggested that the halocarbon extraction of plant material extracted mainly the essential oils and some non-polar metabolites but significant part of the phenolic compounds was preserved in the waste and it could be a promising source of polyphenols.

In the next analysis the non-volatile polar compounds present in the extracts were determined by GC-MS and the results are presented in Table 3.

Table 3. Polar non-volatile substances in ethanolic extracts. RI - relative index (Kovats retention index); % of TIC - total ion current.

Compound	RI	F	S	HD
		% of TIC		
L-Valine	1228	0.98±0.05 ^a	0.77±0.04 ^b	0.33±0.05 ^c
Glycerol	1266	4.13±0.21 ^a	4.31±0.31 ^a	4.52±0.28 ^a
L-Leucine	1272	0.20±0.01 ^a	0.35±0.05 ^b	0.05±0.01 ^c
L-Isoleucine	1299	0.69±0.07 ^a	0.56±0.02 ^b	0.09±0.01 ^c
L-Proline	1307	3.28±0.54 ^a	6.65±0.41 ^b	0.15±0.10 ^c
Succinic acid	1310	0.26±0.04 ^a	0.38±0.03 ^b	1.47±0.09 ^c
Fumaric acid	1355	0.40±0.02 ^a	0.47±0.03 ^a	0.87±0.05 ^b
Serine	1362	0.84±0.05 ^a	1.20±0.08 ^b	0.04±0.01 ^c
L-Threonine	1390	0.49±0.04 ^a	0.39±0.03 ^b	0.05±0.01 ^c
L-Homoserine	1446	0.14±0.02 ^a	0.11±0.01 ^a	0.05±0.01 ^c
Malic acid	1488	2.23±0.11 ^a	1.74±0.14 ^b	2.26±0.19 ^a
Salicylic acid	1516	0.16±0.01 ^a	0.05±0.01 ^b	0.09±0.01 ^c
L-Aspartic acid	1531	0.26±0.05 ^a	2.15±0.09 ^b	0.47±0.06 ^c
L-Threonic acid	1528	0.32±0.04 ^a	0.76±0.06 ^b	0.14±0.02 ^c
L-Phenylalanine	1646	0.55±0.09 ^a	0.63±0.08 ^a	0.19±0.04 ^b
L-Asparagine	1682	0.22±0.04 ^a	0.44±0.03 ^b	0.87±0.05 ^c
L-Lysine	1737	0.45±0.01 ^a	0.42±0.02 ^a	0.41±0.02 ^a
Vanillic acid	1758	0.18±0.01 ^a	0.28±0.01 ^b	0.15±0.01 ^a
Protocatechuic acid	1813	0.19±0.02 ^a	0.16±0.02 ^a	0.41±0.03 ^b
Quinic acid	1843	0.34±0.02 ^a	0.22±0.02 ^b	1.59±0.06 ^c
Syringic acid	1888	0.20±0.01 ^a	0.13±0.01 ^b	0.43±0.03 ^c
Gluconic acid	1991	1.40±0.21 ^a	1.68±0.12 ^a	1.58±0.15 ^a
Palmitic acid	2039	2.22±0.24 ^a	6.49±0.32 ^b	7.10±0.28 ^b
Glucaric acid	2013	0.68±0.09 ^a	1.65±0.08 ^b	1.55±0.10 ^b
Myo-Inositol	2090	0.68±0.07 ^a	0.42±0.04 ^b	0.39±0.04 ^b
Stearic acid	2132	0.20±0.01 ^a	0.12±0.01 ^b	0.89±0.02 ^c
Caffeic acid	2140	0.83±0.03 ^a	0.54±0.04 ^b	0.51±0.02 ^b
Linoleic acid	2209	1.60±0.24 ^a	6.53±0.32 ^b	8.14±0.38 ^c
α-Linolenic acid	2217	1.10±0.10 ^a	5.13±0.19 ^b	6.82±0.25 ^c
Stigmasterol	3315	1.27±0.09 ^a	0.95±0.08 ^a	1.89±0.12 ^b
β-Sitosterol	3355	1.17±0.14 ^a	1.35±0.09 ^a	1.66±0.12 ^b

^{a, b, c} – different letters signify statistical significance.

Table 4. Aroma (volatile) substances in ethanolic extracts. RI - relative index (Kovats retention index); % of TIC - total ion current

Compound	RI	F	S	HD
		% of TIC		
β -Cubebene	1391	0.19±0.01 ^a	1.89±0.08 ^b	1.11±0.12 ^c
(Z)- β -Farnesene	1442	0.11±0.01 ^a	2.38±0.12 ^b	1.97±0.20 ^b
Decanoic acid	1449	2.22±0.11 ^a	1.40±0.14 ^b	4.68±0.32 ^c
(-)-Spathulenol	1578	0.14±0.02 ^a	1.24±0.15 ^b	1.15±0.14 ^b
Lauric acid	1622	2.09±0.13 ^a	1.27±0.15 ^b	1.53±0.18 ^b
α -Cadinol	1641	2.06±0.12 ^a	1.94±0.21 ^a	2.56±0.18 ^b
α -Bisabolol oxide B	1648	0.10±0.01 ^a	7.95±0.32 ^b	10.05±0.29 ^c
7-Methoxycoumarin	1737	0.08±0.01 ^a	10.23±0.62 ^b	3.57±0.52 ^c
α -Bisabolol oxide A	1792	0.10±0.01 ^a	8.11±0.41 ^b	10.29±0.55 ^c
7-Hydroxycoumarin	1813	0.09±0.01 ^a	0.65±0.05 ^b	2.45±0.15 ^c
Myristic acid	1839	10.72±0.27 ^a	7.94±0.36 ^b	5.08±0.44 ^c
(2E)-2-(2,4-Hexadiynylidene)-1,6-dioxaspiro[4.4]non-3-ene	1892	0.82±0.12 ^a	8.03±0.21 ^b	11.11±0.33 ^c
Phytol	2164	1.29±0.15 ^a	2.23±0.20 ^b	4.50±0.26 ^c

^{a, b, c} – different letters signify statistical significance.

The results from the analysis suggested that even after extraction / distillation a high amount of linoleic and linolenic acids (which also includes amounts of calendic acid – a conjugated linoleic acid) [16] remain in the S and HD wastes.

Due to the nature of the halocarbon extraction process the less polar compounds were predominantly extracted and for this reason the amounts of linoleic and linolenic acids in the F residue were 4 to 6 times lower compared to S and HD residues. The extract from F waste was rich in malic, quinic, caffeic and syringic acid. The industrial essential oil processes (distillation or extraction) always left part of the aroma (volatile) and polar non-volatile substances in the residual materials [13, 14]. This is due to the nature of the raw materials, to the chemical bonding of the compounds in the plant matrix or to technological reasons. Although present in low amounts, a great number of these substances possess beneficial effects: antimicrobial, antioxidant, anti-inflammatory, etc. [1, 2]. For this reason, in the next experiments aroma (volatile) metabolites kept in the chamomile wastes were determined (Table 4).

The information derived from these analyses allowed comparing the extractability of different classes of biologically active substances, and advantages and disadvantages of the different techniques for essential oil production – steam distillation, hydrodistillation and extraction with halocarbons (freons). Considering the less polar terpenes (aroma compounds) it could be concluded that the freon extraction extract to a higher extent

the non-polar substances. For this reason, β -cubebene, (Z)- β -farnesene, (-)-spathulenol, α -bisabolol oxide A and B were present in much higher concentrations in S and HD residues. From this point of view, having in mind the anti-irritant, anti-inflammatory, and anti-microbial properties of these substances, the S and HD wastes could be also used as sources of natural healing and bio-preservative substances [2, 17].

CONCLUSIONS

The present study focused on the investigation of the potential application of chamomile wastes as a source of biologically active substances – dietary polyphenols, volatile (aroma) and non-volatile polar metabolites. The 70% ethanolic extracts obtained from three wastes: generated by industrial steam distillation (S), hydrodistillation (HD) and extraction with 1,1,1,2-tetrafluoroethane (F), showed pronounced antioxidant effects and also were rich in phenolic acids and flavonoids. To a larger extent the extraction with non-polar solvents (halocarbons) led to significant preservation in the wastes of valuable biologically active substances (phenolic acids, flavonoids, etc.). Steam distillation and even more hydrodistillation, due to the formation of water phase in the distillation still, led to extraction and loss of some of the more polar substances but preserved to a higher degree the non-polar terpene compounds. The investigated approach of treatment of the wastes with 70% ethanol and obtaining of valuable by-products also have the advantage of possible combining with further extraction of the plant residues in order to

obtain polysaccharides and thus will lead to a better valorization of the wastes.

REFERENCES

1. O. Singh, Z. Khanam, N. Misra, M.K. Srivastava, *Pharmacogn. Rev.*, **5(9)**, 82 (2011).
2. J.K. Srivastava, E. Shankar, S. Gupta, *Mol. Med. Rep.*, **3**, 895 (2010).
3. A. Lubbe, R. Verpoorte, *Ind. Crop. Prod.*, **34**, 785 (2011).
4. R. da Silva, T.A. Rocha-Santos, A.C. Duarte, *Trends Anal. Chem.*, **76**, 40 (2016).
5. M. Herrero, A. Cifuentes, E. Ibañez, *Food Chem.*, **98**, 136 (2006).
6. L.M. Falzari, R.C. Menary, Project № UT-28A–publication № 02/156 (2003).
7. A. Kalra, S. Kumar, N. Katiyar, J.R. Bahl, R.P. Bansal, H.S. Chauhan, A. Prasad, R. Pandey, O.P. Dhawan, A. Krishna, R. Srivastava, *US Patent 6488733 B2* (2002).
8. R. Pandey, A. Kalra, *Curr. Sci.*, **98(6)**, 833 (2010).
9. A. Slavov, I. Panchev, D. Kovacheva, I. Vasileva, *Food Hydrocoll.*, **61**, 469 (2016).
10. N. Nenov, *Scientific Works of University of Food Technologies*, **53**, 195 (2005).
11. V.L. Singleton, J.A.J. Rossi, *Am. J. Enol. Vitic.*, **16**, 144 (1965).
12. M. Číž, H. Čížová, P. Denev, M. Kratchanova, A. Slavov, A. Lojek, *Food Control*, **21**, 518 (2010).
13. N. Yantcheva, I. Vasileva, P. Denev, P. Lutova, S. Mitov, Z. Iordanova, M. Galabova, I. Panchev, A. Slavov, *Bull. Chem. Comm.*, **49(G)**, 21 (2017).
14. A. Slavov, P. Denev, I. Panchev, V. Shikov, N. Nenov, N. Yantcheva, I. Vasileva, *Ind. Crops Prod.*, **100**, 85 (2017).
15. Y. Sato, S. Itagaki, T. Kurokawa, J. Ogura, M. Kobayashi, T. Hirano, M. Sugawara, K. Iseki, *Int. J. Pharmaceut.*, **403**, 136 (2011).
16. H.T.H. Cromack, J.M. Smith, *Ind. Crops Prod.*, **7**, 223 (1998).
17. G.P.P. Kamatou, A.M. Viljoen, *J. Am. Oil Chem. Soc.*, **87**, 1 (2010). [AS1]

Isolation and purification of lipase produced from *Rhizopus arrhizus* in solid state fermentation by fractional precipitation

A. P. Hambarliiska¹, V. T. Dobрева², H. N. Strinska¹, B. Y. Zhekova¹, G. T. Dobrev^{1,*}

¹Department of Biochemistry and Molecular Biology, University of Food Technologies,
26 Maritza Blvd., 4002 Plovdiv, Bulgaria

²Department of Engineering Ecology, University of Food Technologies,
26 Maritza Blvd., 4002 Plovdiv, Bulgaria

Received October 17, 2018; Revised December 14, 2018

A study on the selection of precipitating agent and determination of the optimal conditions for precipitation of lipase, produced from *Rhizopus arrhizus* in solid-state fermentation, was conducted with the aim of enzyme isolation and purification. The highest purification degree of 3.8-fold was achieved, when the enzyme was precipitated with 65% isopropanol and the activity yield was above 80%. The precipitation of lipase with acetone also allowed enzyme isolation and purification. With 50% acetone, 3.6-fold purification and 70% activity yield were achieved. Isolation and purification of the enzyme by salting-out with $(\text{NH}_4)_2\text{SO}_4$ was an inappropriate technique due to the low yield and the absence of purification. With the use of polyethylene glycol 4000 (PEG 4000) as a precipitating agent, low yields of lipase activity of less than 20% were obtained, but about 2-fold degree of purification was achieved, indicating a high selectivity of PEG 4000 to lipase precipitation. As a result of the various techniques used for lipase isolation and purification by fractional precipitation and the performed zymographic analysis of the resulting enzyme preparations, the presence of two multiple forms of lipase with a molecular weight of 28 000 Da and 55 000 Da was found.

Keywords: Lipase, Solid state fermentation, *Rhizopus arrhizus*, Purification

INTRODUCTION

Lipases (EC 3.1.1.3) catalyze the hydrolysis reaction of emulsified triglycerides to glycerol and composition of free fatty acids. The hydrolase activity of lipases determines their wide industrial application in the detergents. Lipases are also used in the dairy industry to develop a specific flavor in the products due to the oxidation of the free fatty acids obtained. Under certain conditions, lipases also catalyze the esterification, transesterification and aminolysis reactions in organic solvent media, which allows them to be used as a tool for developing “green” technologies in organic synthesis.

The possibilities for lipases applications make them one of the most important classes of industrially produced enzymes, accounting for about 5% of the world's enzyme market [1].

The study of new microbial strains producing lipases and the study of the specific characteristics of purified microbial lipase enzymes is an important scientific task with the possibility of practical application.

Lipases obtained from different sources are usually subjected to certain pre-purification steps before they are further purified. Typically, this is a one-step procedure involving precipitation by

saturation with an $(\text{NH}_4)_2\text{SO}_4$ solution. The yield and the degree of purification depend on the concentration of $(\text{NH}_4)_2\text{SO}_4$ used [2].

Borkar *et al.* [3] obtained a relatively low yield of lipase (13.18%) but a significant degree of purification (20.84-fold) at 30% $(\text{NH}_4)_2\text{SO}_4$. Ji *et al.* [4] precipitated lipase from *Pseudomonas* with 20% $(\text{NH}_4)_2\text{SO}_4$ and achieved 1.8-fold purification and 58.7% enzyme yield. Pabai *et al.* [5] reported that the maximum increase in lipase activity in the precipitate occurred at 20-40% saturation with $(\text{NH}_4)_2\text{SO}_4$, with a 18.9-fold increase in purification and a yield of 52.93%.

Another method for selective precipitation of proteins is the use of water-soluble organic solvents with a low dielectric constant such as ethanol, acetone and isopropanol. As the principles causing precipitation are different, it is not necessarily an alternative to $(\text{NH}_4)_2\text{SO}_4$, but can be used as an additional step. Addition of a solvent such as ethanol or acetone to an aqueous extract containing proteins has a variety of effects which, combined, lead to protein precipitation. The principal effect is the reduction in water activity. The solvating power of water for a charged, hydrophilic enzyme molecule is decreased as the concentration of organic solvent increases [6].

Ameri *et al.* [7] achieved a 7.21-fold purification degree and an activity yield of 40.12% in the

* To whom all correspondence should be sent.

E-mail: g_dobrev2002@yahoo.fr

precipitation of lipase from *Bacillus atrophaeus* FSHM2 by 80% saturation of the culture liquid with chilled ethanol. Isolation of lipase by ethanol precipitation was also applied by Rua *et al.* [8], achieving a 1.8-fold purification degree and lipase activity yield of 84%.

Cao *et al.* [9] isolated lipase by specific precipitation from the culture medium at 60% acetone concentration. The precipitation was carried out at 0°C for 4 h. A 2.9-fold purification of the enzyme and a 68.7% activity yield were achieved. Razak *et al.* [10] used saturation of the culture liquid of two *Rhizopus* strains with 80% acetone to isolate lipase. As a result of the procedure, the authors obtained 3-fold purification and 62-76% yield of the precipitated lipases.

In the investigated literature no results for the use of isopropanol for specific lipase precipitation have been found.

Salts and organic solvents are not the only precipitation agents that can cause aggregation of proteins without denaturation. Polson *et al.* [11] investigated the ability of a variety of high-molecular-weight, neutral, water-soluble polymers to precipitate plasma proteins. The authors obtained best results with polyethylene glycol (PEG) with a molecular weight of 4000-20000. Although several types of PEG were effective in precipitation, the high viscosity of most solutions made their use as protein precipitants impractical [6]. PEG is not as easy to remove from a protein fraction as either salt or organic solvent. Nevertheless, a residual low level of PEG is not detrimental to many procedures – salting-out, ion exchange, affinity chromatography, or gel filtration can be carried out without having to remove the PEG first [6].

Görgün and Akpınar [12] applied 30% PEG 6000 precipitation to isolate and purify lipase from carp liver, yielding an enzyme activity of 60% and a minimum purification degree of 1.01-fold.

The aim of the present work is selection of precipitation agent and optimization of the conditions for isolation and purification of lipase by selective precipitation by salting-out with $(\text{NH}_4)_2\text{SO}_4$, ethanol, acetone, isopropanol and PEG.

EXPERIMENTAL

Microorganism

The studied *Rhizopus arrhizus* strain used in this study was provided by Biovet® Peshtera. It was grown in the following medium, g/l: malt extract 10.00; yeast extract 4.00; glucose 4.00; agar-agar 20.00. pH was adjusted to 7.0. The strain was cultivated at 28°C for 14 days and stored at 4°C.

Lipase biosynthesis

Solid state fermentation (SSF) was carried out in 500-ml Erlenmeyer flasks. The flasks contained nutrient medium of 10 g wheat bran and salt solution (g/l): $\text{NH}_4\text{H}_2\text{PO}_4$ 6.5, $(\text{NH}_4)_2\text{C}_2\text{O}_4$ 0.90, MgSO_4 0.95, KCl 0.95. pH of the salt solution was adjusted to 7.0, and the final moisture content was adjusted to 66% with the salt solution before autoclaving. The solid substrate was supplemented with 1% (w/w) of glucose and 5% (w/w) of tryptone. After sterilization at 121°C for 30 min, the flasks were inoculated with 5 ml inoculum with 10^7 spores/ml and incubated at 30°C for 168 h.

Following SSF, extraction of lipase from the fermented solids was performed with 50 ml of eluent containing 1% commercial surfactant Disponil NP3070 for 30 min with constant agitation. The solids were removed by filtration, the filtrates were centrifuged and the resulting extract solution, containing lipase was tested for enzyme precipitation.

Fractional precipitation with $(\text{NH}_4)_2\text{SO}_4$

To the extract solution containing lipase, known volume of $(\text{NH}_4)_2\text{SO}_4$ was added, in such quantity that 20-70% degree of saturation to be reached. The samples were incubated at 4°C for 1 h for precipitate stabilization, and were centrifuged at 4000 rpm for 30 min. The precipitates were diluted with distilled water to a defined volume and lipase activity and protein content were determined.

Fractional precipitation with organic solvents

Organic solvents (acetone, ethanol or isopropanol) were added to the extract solution containing lipase, in such quantity that defined concentration (20-80%) to be achieved. The precipitates were stabilized at 4°C for 1 h, centrifuged at 4000 rpm for 30 min, and tested for lipase activity and protein content.

Fractional precipitation with PEG 4000

PEG 4000 was added to the lipase extract solution in a final concentration of 5-60%, the samples were kept at 4°C for 1 h, centrifuged at 4000 rpm for 30 min, and the precipitates were analyzed for lipase activity and protein concentration.

Sodium dodecyl sulfate-polyacrylamide gel electrophoresis (SDS-PAGE)

SDS-PAGE was performed in 15% polyacrylamide gel in the presence of SDS on Cleaver Scientific Ltd. OmniPAGE electrophoresis system CVS10DSYS by the method of Laemmli [13].

Lipase zymogram

The enzymes with lipase/esterase activity were detected by zymographic analysis. After non-denaturing PAGE, the gel was treated with 0.02% (w/v) α -naphthyl acetate and 0.05% (w/v) Fast Blue RR salt in 0.05 M Tris-HCl buffer with pH 7.2, revealing bands with lipase activity [14].

Determination of lipase activity

For lipase activity determination the method proposed by Babu *et al.* [15] and Saifuddin *et al.* [16] was adapted. Substrate solution was prepared by dissolving 30 mg of p -nitrophenyl palmitate in 10 ml of isopropanol, mixed with 90 ml of 0.05 M Tris-HCl buffer with pH 7.2, 0.4 g of Triton X-100 and 0.1 g of gum arabic. 2.4 ml of the substrate solution were incubated at 35°C for 10 min and 0.1 ml of suitably dissolved enzyme was added. The enzyme reaction was performed at 35°C for 30 min and the enzyme was inactivated by addition of 1.0 ml of 0.5 M solution of EDTA with pH 8.0. The absorbance at 405 nm was measured against a reference sample with an inactivated enzyme. One unit (U) of lipase activity was defined as the amount of enzyme releasing 1.0 μ mol of p -nitrophenol for 1 min at 35°C and pH 7.2.

Protein assay

Protein content was determined by the method of Bradford [17].

RESULTS AND DISCUSSION

Fractional precipitation with various concentrations of $(\text{NH}_4)_2\text{SO}_4$ is the most commonly used technique for pre-purification and isolation of enzymes and proteins. The results for salting-out with $(\text{NH}_4)_2\text{SO}_4$ for isolation of lipase produced in SSF by *Rhizopus arrhizus* are presented in Fig. 1.

It should be noted that at all tested concentrations of $(\text{NH}_4)_2\text{SO}_4$, the yields of lipase activity were relatively low - below 40%, which determined the low degree of enzyme purification - below 1.0. At 40% concentration of the salt, about 80% of the protein in the extract solution was precipitated, but the yield of lipase activity was about 30%, which determined a low degree of purification. Low yields of lipase activity were probably due to enzyme inactivation at higher salt concentrations or the enzyme had not been precipitated. It was clear from this study that this classical isolation and purification step was not applicable to the lipase studied.

The fractional precipitation of lipase by ethanol is shown in Fig. 2. At ethanol concentrations above 70%, significantly higher yields of lipase activity were obtained. At 80% ethanol concentration, the yield of lipase activity was about 65%, and the

yield of protein was about 46.5%, which defined a purification degree of 1.44-fold.

Isolation and purification of the examined lipase with different concentrations of acetone are shown in Fig. 3.

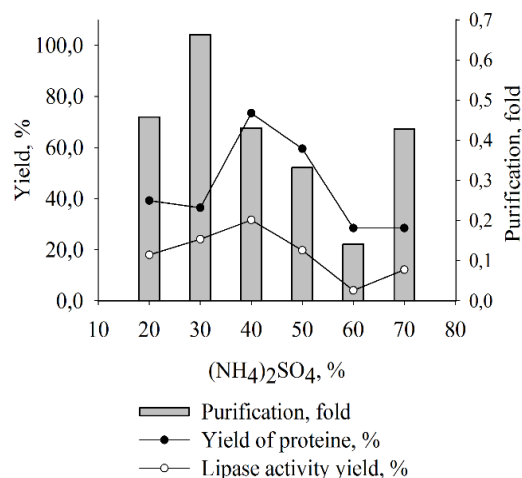


Fig. 1. Precipitation of lipase with $(\text{NH}_4)_2\text{SO}_4$

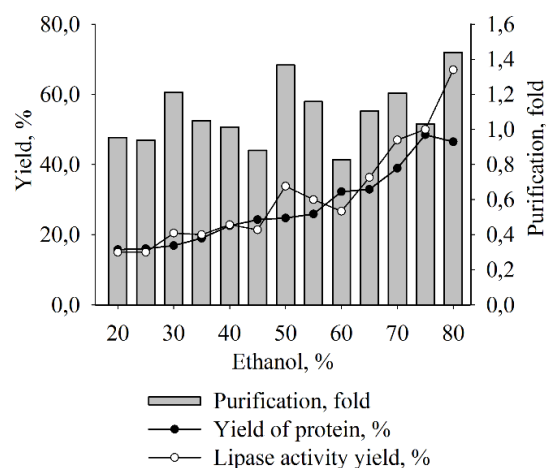


Fig. 2. Precipitation of lipase with ethanol

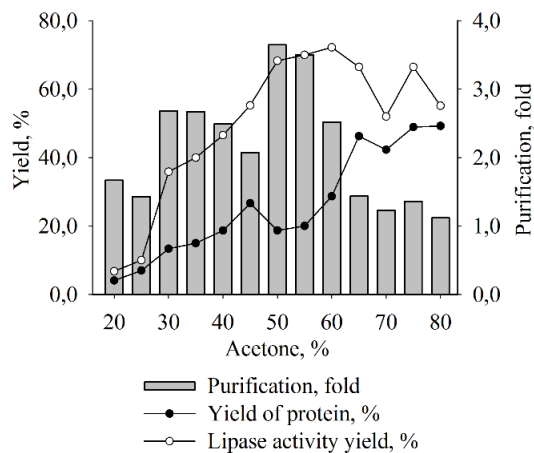


Fig. 3. Precipitation of lipase with acetone

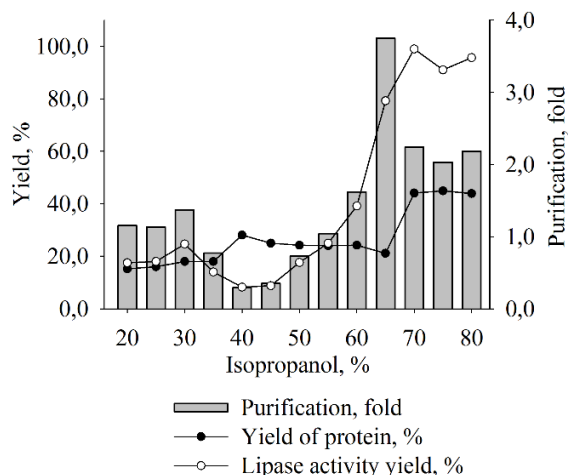


Fig. 4. Precipitation of lipase with isopropanol

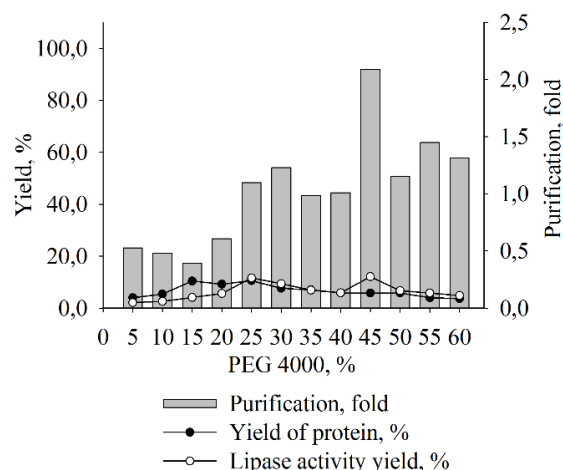


Fig. 5. Precipitation of lipase with PEG 4000

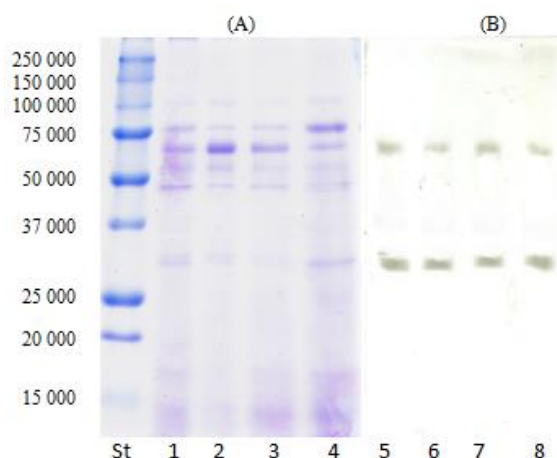


Fig. 6. (A) SDS-PAGE of lipase in denaturing conditions: 1-precipitation with 65% isopropanol, 2-precipitation with 50% acetone, 3-precipitation with 80% ethanol, 4-crude enzyme; (B) Zymogram of lipase in non-denaturing conditions: 5-crude enzyme, 6-precipitation with 65% isopropanol, 7-precipitation with 50% acetone, 8-precipitation with 80% ethanol.

The highest purification degree of about 3.5-fold was achieved at 50-55% acetone and the yield of lipase activity was about 70%. Similar results were obtained by Cao *et al.* [9] and Razak *et al.* [10], they achieved a degree of enzyme purification of about 3-fold and a yield of lipase activity of about 70%, at acetone concentration of 60% and 80%, respectively. Singh and Banerjee [18] obtained yield of 42% and 6.85-fold purification after precipitation with acetone in a ratio supernatant:acetone = 1:2.

Very good results on the isolation and purification of lipase produced in SSF of *Rhizopus arrhizus* were obtained by using isopropanol to selectively precipitate the enzyme (Fig. 4). At concentrations of isopropanol 65-80%, yields of lipase activity were above 80%. The maximum purification degree was 3.8-fold, achieved at 65% isopropanol. The high degree of purification was determined by the lack of concomitant proteins – the maximum yield of protein was only 40%.

An alternative method for fractional protein precipitation is the use of high-molecular-weight, neutral, water-soluble polymers [11]. The influence of PEG 4000 concentration on lipase precipitation is presented in Fig. 5.

After precipitation of lipase with PEG 4000, low yields of enzyme activity, below 20% were found. The maximum degree of purification was about 2.1-fold.

The process of lipase purification was monitored by SDS-PAGE and zymographic analysis (Fig. 6).

The analysis with SDS-PAGE (Fig. 6A) showed that as a result of the precipitation (line 1-3) a portion of the proteins with low molecular weight of about 15 000 Da and some proteins with high molecular weight of about 100 000 Da were removed in comparison to the crude enzyme (line 4). Zymographic analysis indicated that *Rhizopus arrhizus* produced in SSF 2 multiple forms of lipase with a molecular weight of 28 000 Da and 55 000 Da (Fig. 6B).

CONCLUSIONS

As a result of the research on the selection of a suitable precipitation agent and optimization of the conditions for isolation and purification of lipase, it was found that the highest degree of lipase purification (3.8-fold) was achieved by precipitation of the enzyme with 65% isopropanol with the yield of enzyme activity being above 80%. No data were found so far on the use of isopropanol as a precipitation agent in the isolation and purification of lipase. The precipitation of lipase tested with acetone also allowed isolation and purification of the enzyme. At 50% acetone, 3.6-

fold purification and about 70% activity yield were achieved. Salting-out with $(\text{NH}_4)_2\text{SO}_4$ was an inappropriate technique tested for isolation and purification of lipase. Despite the high yield of precipitated protein, about 80%, the lipase activity of the precipitates was low, below 40%. The use of PEG 4000 as a precipitation agent was characterized by very low yields of lipase activity of less than 20%, but about 2-fold purification was achieved, indicating a high selectivity of PEG 4000 to lipase precipitation. As a result of the procedures of isolation and purification of lipase, produced by *Rhizopus arrhizus* in SSF, the presence of two multiple forms of lipase with molecular weights of 28 000 Da and 55 000 Da was found.

Acknowledgement: The research was financially supported by the Bulgarian National Science Fund (BNSF), Project 17/25-2017.

REFERENCES

1. H. Jooyandeh, K. Amarjeet, K.S. Minhas, *J. Food Sci. Technol.*, **46**(3), 181 (2009).
2. G. Müller, S. Petry, *Lipases and Phospholipases in Drug Development*, WILEY-VCH Verlag GmbH & Co. KGaA, Weinheim, 2004.
3. P. Borkar, R. Bodade, S. Rao, C. Khobragade, *Braz. J. Microbiol.*, **40**, 358 (2009).
4. Q. Ji, S. Xiao, B. He, X. Liu, *J. Mol. Catal. B: Enzym.*, **66**, 264 (2010).
5. F. Pabai, S. Kermasha, A. Morin, *Appl. Microbiol. Biotechnol.*, **43**, 42 (1995).
6. R. Scopes, *Protein Purification. Principles and Practice*, Second Edition, Springer Science+Business Media, LLC, 1987.
7. A. Ameri, M. Shakibaie, S. Amirpour-Rostami, A. Ameri, M. Adeli-Sardou, P. Khazaeli, H. Rahmani, H. Forootanfar, *Biotech.*, **14**(4), 154 (2015).
8. M. Rua, T. Diaz-Maurino, V. Fernandez, C. Otero, A. Ballesteros, *Biochim. et Biophys. Acta*, **1156**, 181 (1993).
9. Y. Cao, Y. Zhuang, C. Yao, B. Wu, B. He, *Biochem. Eng. J.*, **64**, 55 (2012).
10. C. Razak, A. Salleh, R. Musani, M. Samad, M. Basri, *J. Mol. Catal. B: Enzym.*, **3**, 153 (1997).
11. A. Polson, G. M. Potgieter, J. F. Largier, G. E. Mears, F. J. Joubert, *Biochimica et Biophysica Acta*, **82**, 463 (1964).
12. S. Görgün, A. Akpınar, *Turk. J. Fish. Aquat. Sci.*, **12**, 207 (2012).
13. U. Laemmli, *Nature*, **227**, 680 (1970).
14. J. Silva, M. Godoy, M. Gutarra, D. Freire, *Plos One*, **9**(8), 1 (2014).
15. I. Babu, G. Rao, *Res. J. Microbiol.*, **2**(1), 88 (2007).
16. N. Saifuddin, A. Raziah, *E-J. Chem.*, **5**(4), 864 (2008).
17. M. Bradford, *Analyt. Biochem.*, **72**, 248 (1976).
18. S. Singh, U. C. Banerjee, *Process. Biochem.*, **42**, 1063 (2007).

Luminescent properties of cerium (IV) -doped zinc oxide films

A. Shulga^{1*}, E. A. Boruleva², T. F. Sheshko¹, I. A. Nagovitsyn^{3,4},

A. G. Cherednichenko¹, G. K. Chudinova^{3,2}

¹ Peoples' Friendship University of Russia (RUDN University), Miklukho-Maklaya str. 6, Moscow 117198, Russia

²National Research Nuclear University "MEPhI", Kashirskoye ch., 31, Moscow 115409, Russia

³A.M. Prokhorov Institute of General Physics, RAS, Vavilov str. 38, Moscow 119991, Russia

⁴Semenov Institute of Chemical Physics, RAS, Kosygina str. 4, Moscow 119991, Russia

Received October 28, 2018; Revised December 5, 2018

Zinc oxide films doped by Ce⁴⁺ (0.1 – 1 molar %) were for the first time obtained by sol-gel technique and their spectral luminescent properties on monocrystalline silicon supports were studied with the aim to develop sensitive surfaces for biosensor devices. It was found that adding Ce⁴⁺ enhances the ultraviolet luminescence (UVL) of ZnO films by a factor of 7 (0.7 % mass Ce⁴⁺). Films structures were controlled by SEM. Changes in UVL ($\lambda_{\text{ex}} = 280 \text{ nm}$, $\lambda_{\text{em}} = 356 \text{ nm}$) of ZnO and ZnO-Ce⁴⁺ films were investigated under the action of bovine myoglobin ($10^{-8} - 10^{-12} \text{ M}$, deposited on the film surface by a spin-coating method).

Keywords: sol-gel method, zinc oxide, cerium, optical biosensors, new materials, photoluminescence

INTRODUCTION

In recent years the need for sensitive, high-speed and also economic thin-film materials for various branches of science and equipment grows. In this regard most prospective are thin films of cerium dioxide which are successfully used in the developing fields of lighting industry and electronic equipments. Cerium dioxide and materials on its basis possess a wide range of applications in the industry, including production of biomedications, fuel elements [1], three-route catalysts [2], sensors [3], and production of fire-resistant materials. It is interesting to researchers of CeO₂ as an inorganic antioxidant which effectively protects live systems from oxidizing stress [4].

Cerium dioxide is a wide-gap semiconductor material with a band gap of $\sim 3.2 \text{ eV}$ (which is comparable to the band gap of zinc oxide — 3.4 eV). CeO₂ is optically transparent in the visible region of the spectrum. Its absorption band is located in the UV region of the spectrum at wavelengths of about 320 nm [5].

Cerium has good luminescent properties and application prospects for chemical sensors, as a dopant in matrices of other materials [6–9]. As an impurity, Ce attracts attention due to its special optical and catalytic properties, resulting from the presence of shielded 4f levels, and the redox pair Ce³⁺/Ce⁴⁺ [10]. Cerium oxides are characterized by high catalytic activity. The reason for this is the instability of oxygen stoichiometry, which causes a fairly free Ce³⁺ \rightarrow Ce⁴⁺ transition and a reverse transition [10]. Thus, cerium oxide is always mixed

and contains CeO₂ and Ce₂O₃ in various ratios. Also due to this feature, cerium oxide has a high ionic conductivity of oxygen, and therefore it is of interest as a material for solid-state oxide fuel cells in an impurity form.

Among the numerous functional oxide nanomaterials, ZnO oxide doped with CeO₂, which is of particular interest due to a set of specific properties, was chosen as the object of study in this work: high chemical and thermal stability, and numerous practical applications, including the use of highly efficient catalysts, sorbents, sensors, solid electrolytes.

On the basis of all the above, the purpose of this work was to create a new composite material based on zinc oxide doped with different amounts of cerium oxide and to study the optical properties of the samples: change in the fluorescence of the material obtained. Influence of myoglobin (MB) in various concentrations on ZnO and ZnO-Ce⁴⁺ UVL was studied.

EXPERIMENTAL

The preparation of materials based on zinc oxide is currently carried out using various techniques having both advantages and disadvantages. In the present work the sol-gel method was used, one of the most effective methods for the formation of films whose surface is structured at the nano level (nanosize). The change in their spectral characteristics was studied with varying concentrations of dopant-cerium ion – 0.1-1 stoichiometric percentage (mass %). These films are the basis of an optical biosensor device with

* To whom all correspondence should be sent.
E-mail: aleksandra-box@mail.ru

fluorescent detection, designed to investigate biomacromolecules in low concentrations by fluorescence spectroscopy method.

Sample preparation was carried out in the following order:

$Zn^{2+}/Ce^{4+} + C_2H_5OH \rightarrow (\approx 60\text{ }^\circ C \rightarrow \text{stirring}) \rightarrow ZnO/CeO_4 \text{ (sol)} \rightarrow \text{(monoethanolamine)} \rightarrow ZnO/CeO_4 \text{ (sol/gel)} \rightarrow \text{depositing the seed layer of the sol onto a substrate} \rightarrow \text{drying in an oven at } 140\text{ }^\circ C \text{ to obtain oxide films.}$

Synthesis of undoped and Ce-doped ZnO was carried out using analytical grade zinc acetate $[(CH_3COO)_2Zn]$, cerium acetate $[Ce(CH_3COO)_3]$ and monoethanolamine (C_2H_2NO) in as-received condition. In the synthesis process, a required amount of zinc acetate was completely dissolved in deionized water and a required amount of aqueous C_2H_2NO solution was added dropwise to the aqueous zinc acetate. The solution was stirred and maintained at room temperature for 40 min, and then kept at $60\text{ }^\circ C$ for 2 h until complete dissolution of the white precipitate. For maturing the solution was kept at ambient temperature $(22 \pm 2)\text{ }^\circ C$ for 2-7 days. After applying the seed layer sol with thickness of 70 nm on a silicon substrate placed in a muffle furnace for drying at a temperature of $150\text{ }^\circ C$ for 10 min, then annealed at a temperature of $500\text{ }^\circ C$ for 2 h. The processes of deposition, drying and annealing were repeated until the desired coating thickness. For the synthesis of $Zn_{1-x}CeO_x$ (from 0.01 to 0.33) NPs, a calculated amount of cerium acetate was mixed with zinc acetate solution. The required amount of aqueous C_2H_2NO solution was added dropwise to the homogenous mixture to get a white precipitate. Further, a similar procedure was adopted for the preparation of undoped ZnO.

Bovine myoglobin (Sigma-Aldrich Co) (Mb) solutions were prepared in distilled water. 20 μl of Mb solution was applied on the surface of ZnO- Ce^{4+} films on a monocrystalline silicon substrate by a spin-coating method (2000 rpm) on a centrifuge "Elekton" CLMN-P10-02 (Russia). Fluorescence spectra of the samples were measured with a spectrofluorometer RF-5300pc (Shimadzu).

RESULTS AND DISCUSSION

ZnO films with a fluorescence intensity of 40 relative units were obtained. Doping with cerium leads to an increase in luminescence by a factor of 7 with a maximum gain in films containing 0.7 % cerium. Films containing 0.7 wt. % cerium were further used to study changes in UV light by the action of bovine myoglobin. The adsorption of Mb was found to reduce the intensity of UV light (Figure 1). The dependence of the intensity of UV

light ($\lambda_{em} = 280\text{ nm}$) on the concentration of Mb is nonlinear, the intensity decreases several times as compared with undoped zinc oxide.

The excitation wavelength of 280 nm corresponds to tryptophan in the myoglobin globule with emission in the region of 340-360 nm, while we observe small "shoulders" in the region of 350-360 nm. In addition to tryptophan, the protein contains a porphyrin prosthetic group, which, however, was not detected at concentrations below 10^{-6} mg/ml ($\lambda_{ex} = 420\text{ nm}$).

The band at 356 nm belongs to ZnO, which is evident from Figure 1 showing the spectrum of ZnO without myoglobin. The shape of the spectrum does not change when myoglobin is applied. Hence, MB influence on ZnO UVL is negligible. The longwave fluorescence of ZnO and $ZnO-Ce^{4+}$ is determined by the defects of the ZnO crystal lattice, so the fluorescence at 630 nm (Figure 2) is due to interstitial oxygen atoms in the ZnO lattice [11] Changes in the concentration of myoglobin have little effect on the long-wave fluorescence of the films.

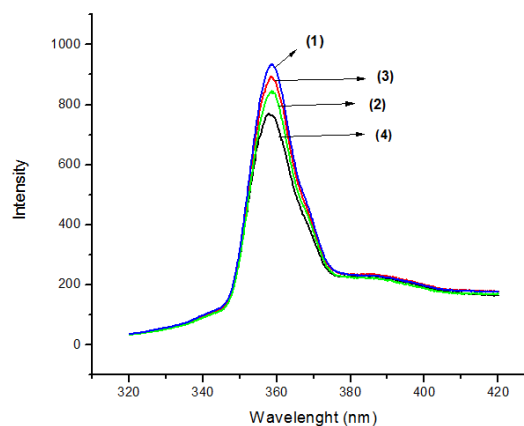


Figure 1. Fluorescence spectra at $\lambda_{ex} = 280\text{ nm}$ of $ZnO-Ce^{4+}$ film without Mb (1) and $ZnO-Ce^{4+}$ film with Mb 10^{-8} M (2), 10^{-10} M (3), 10^{-12} M (4).

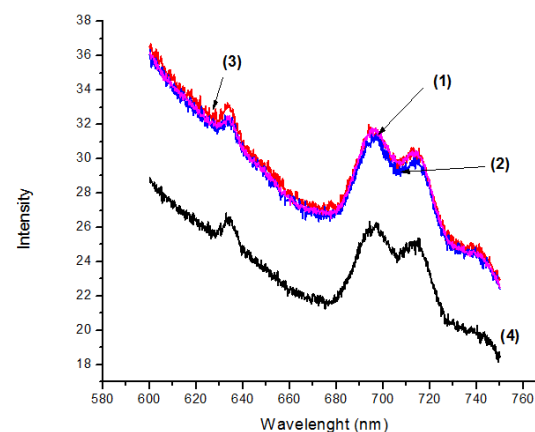


Figure 2. Fluorescence spectra at $\lambda_{ex} = 420\text{ nm}$ of $ZnO-Ce^{4+}$ film without Mb (1) and $ZnO-Ce^{4+}$ film with Mb 10^{-8} M (2), 10^{-10} M (3), 10^{-12} M (4).

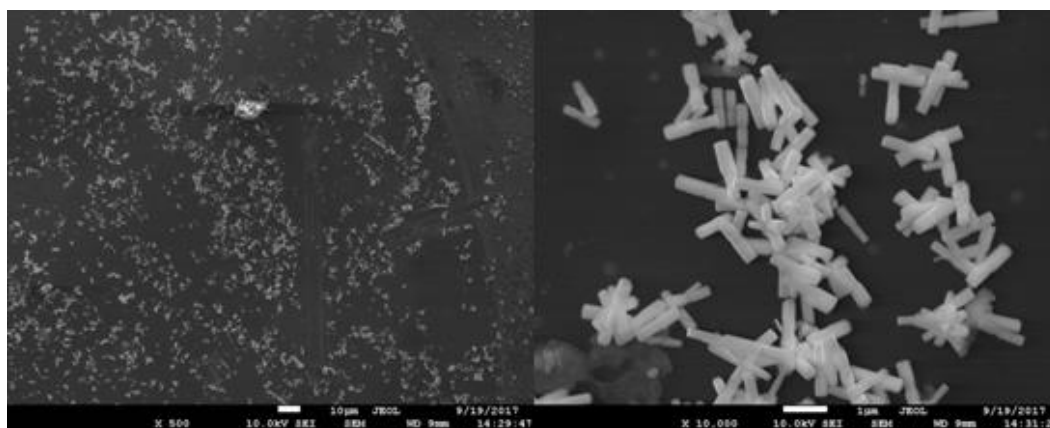


Figure 3. SEM images of ZnO.

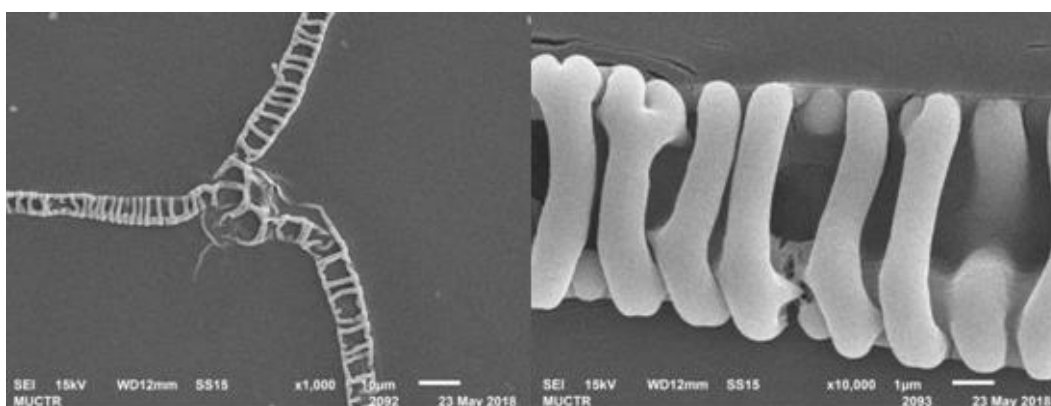


Figure 4. SEM images of ZnO modified by 0.7 weight percent of Ce.

The results indicate a good perspective of cerium-doped zinc oxide structures as a fluorescent optical sensor for detecting biomacromolecules in the near ultraviolet region, apparently in the visible light region, quenching of the fluorescent response appears, which can also be used in specific cases. the scanning electron microscope image of ZnO and ZnO-Ce⁴⁺ shows a significant change in the surface relief (figures 3 and 4). in the first case, the structures are cylinders with a size of about 10 μm. in figure 4, the structures are “bones” with a size of 8 μm, the average width of such threads is 20-30 μm, and the length can reach several tens of μm. thus in doped materials the size and shape of the structures of zno cylinders changes and their ordered aggregation occurs.

CONCLUSIONS

Studies of films of zinc oxide doped with cerium using a sol-gel method were carried out. Ce⁴⁺-doping of ZnO films leads to UVL enhancing by a factor of 7. Bovine myoglobin adsorption on ZnO-Ce⁴⁺ films surfaces causes UVL quenching by 0.7 % at concentrations of 10⁻⁸, 10⁻¹⁰ and 10⁻¹² M, correspondingly. Noticeable changes in the intensity of UV light of the material obtained by us show its promise as a recording element of a

biosensor device with fluorescence detection for the qualitative and quantitative determination of protein with high sensitivity.

Acknowledgement: This publication was prepared with the support of the “RUDN University Program 5-100”.

REFERENCES

1. B.T. Killbourn, Cerium: a guide to its role in chemical technology, NY, Molycorp, 1992.
2. S. Mihaiu, L. Marta, M. Zaharescu, *J. Eur. Ceram. Soc.*, **27**, 551 (2007).
3. A. A. Antonova, O. V. Zhilina, et al., *Colloid Magazine*, **63**, 728 (2001).
4. V. K. Ivanov, A. B. Shcherbakov, A. V. Usatenko, *Advances in Chemistry*, **78**, 924 (2009).
5. S. Debnath, M. R. Islam, M. S. R. Khan, *Bull. Mater. Sci.*, **30**, 315 (2007).
6. Xi-Hong Lu et al, *J. Mater. Chem*, **20**, 7118 (2010)
7. W. Tiebao, C. Chunxiang, W. Xiaodong, Li Guobin, *Journal of Nanomaterials*, (2010), doi:10.1155/2010/768251.
8. M. Faisal et al, *J. Mater. Sci. Technol.*, **27**, 594 (2011).
9. C. Xu, X. Qu, *NPG Asia Materials*, **6**, 16 (2014).
10. M. Škoda et al., WDS'07 Proceedings of Contributed Papers, Part III, 2007, p. 128.
11. X. Liu, X. H. Wu, H. Cao, *J. Appl. Phys.*, **95**, 3141 (2004).

Biosynthesized silver nanoparticles: electrochemical application

Y. L. Lazarova¹, T. M. Dodevska^{1*}, A. M. Slavov¹, D. B. Karashanova², B. C. Georgieva²

¹Department of Organic Chemistry and Inorganic Chemistry,
University of Food Technologies, 26 Maritza Blvd., Plovdiv 4002, Bulgaria
²Institute of Optical Materials and Technologies, Bulgarian Academy of Sciences,
109 Academic Georgi Bonchev Str., Sofia 1113, Bulgaria

Received October 30, 2018; Revised December 13, 2018

In this research, a fast, simple, “green” method for synthesis of silver nanoparticles (AgNPs) using flower water extracts of *Achillea millefolium* and *Lavandula angustifolia* wastes as reducing agents was demonstrated. The morphology and phase composition of the biosynthesized AgNPs were determined by Transmission Electron Microscopy (TEM) and Selected Area Electron Diffraction (SAED). AgNPs were deposited onto a spectroscopic graphite surface, applying two different procedures, and stabilized using chitosan to build modified electrodes-catalysts for reduction of hydrogen peroxide (H₂O₂). The electrochemical performance of the modified electrodes was studied by means of cyclic voltammetry and chronoamperometry at pH 7.0 and their applicability for amperometric detection of H₂O₂ was demonstrated. The modified electrodes exhibited a rapid, sensitive and reproducible response for quantitative determination of H₂O₂ at applied potentials of –0.2 V and –0.3 V (vs. Ag/AgCl, 3M KCl). It was established that the electrocatalytic activity of the electrodes modified with biosynthesized AgNPs significantly depends on the nature of the used plant extract. In the target reaction (electroreduction of H₂O₂) the electrode based on AgNPs, synthesized using *Achillea millefolium* waste, possesses significantly higher catalytic activity in comparison with the modified electrode based on AgNPs, synthesized using *Lavandula angustifolia* waste.

Keywords: biosynthesis, silver nanoparticles, waste valorization, hydrogen peroxide, amperometric sensor

INTRODUCTION

Silver nanoparticles are known to have broad-spectrum and robust antimicrobial properties and have been extensively applied in medicine. In the field of electrocatalysis, due to their unique physical and chemical properties, AgNPs play an important role in improving the electrochemical detection of various analytes. A number of research groups confirmed the remarkable catalytic activity of AgNPs for H₂O₂ reduction and successfully employed AgNPs-modified electrodes as a sensing interface to construct enzyme-free H₂O₂ electrochemical sensors. Modification of the electrode surface with AgNPs has been performed to enhance the rate of electron transfer and decrease the required large overpotential – the major barrier for electrochemical determination of H₂O₂ at ordinary solid electrodes. Hydrogen peroxide is an analyte of great interest in medicine because it acts as a precursor in the formation of highly reactive and potentially harmful hydroxyl radicals and is one of the most important markers for oxidative stress. An excessive accumulation of H₂O₂ in the body causes various diseases such as cardiovascular disorders, Alzheimer’s, DNA fragmentation, tissue damage and cancer. Hydrogen peroxide is also an industrially relevant analyte – it is used as an

oxidizing and bleaching agent in the pharmaceutical, textile and paper industries; as a sterilizing agent in the dairy industry – addition of H₂O₂ to milk decelerates the growth of bacteria and retains the fermentation.

Different methods have been used for the synthesis of AgNPs – chemical reduction of Ag⁺ in a solution [1, 2], microwave-assisted reduction [3], electrochemical methods [4 - 6], UV irradiation [7, 8], radio frequency magnetron sputtering [9] and latterly “green” synthesis [10]. The use of renewable materials, environmentally benign reducing agents and nontoxic solvents are the key points of “green” chemistry and the focus of researchers over the past decade. Recently AgNPs have been successfully eco-friendly synthesized using microorganisms (bacteria or fungi) and some plant products (*Aloe vera* plant extract, lemongrass leaves extract, green tea, neem leaf, neem kernel extract, etc.). Despite substantial progress in obtaining and applying AgNPs, the development of new methods for synthesis of AgNPs is still imperative.

To the best of our knowledge, there are no reports on the use of extracts of *Achillea millefolium* and *Lavandula angustifolia*, wastes from essential oil industry, for the synthesis of AgNPs. In this connection, the aims of the present

* To whom all correspondence should be sent.
E-mail: dodevska@mail.bg

work were: 1/ to explore the capability of flower water extracts of *Achillea millefolium* and *Lavandula angustifolia* wastes in precipitating AgNPs from an aqueous solution of silver nitrate, and 2/ to investigate the morphology of the so-obtained biosynthesized AgNPs, as well as their ability for amperometric quantitative detection of H₂O₂. For the electrochemical studies as a bare electrode was used graphite – inexpensive, readily available material with a wide working potential range. The graphite electrode was modified with biosynthesized AgNPs, applying two different procedures. The electroactive layer was stabilized by applying thin film of chitosan onto the modified electrode surface. Chitosan is a preferable material in designing sensors and biosensors – it is a natural linear amine-rich polysaccharide, non-toxic biocompatible polymer, distinguished by its ability to form flexible, transparent membranes with sufficient mechanical strength, high adhesive consistency and protein-binding capacity. The electrochemical behaviour of the developed four different types of graphite electrodes modified with biosynthesized AgNPs was studied and their applicability for highly sensitive quantitative amperometric detection of H₂O₂ was demonstrated. The obtained electroanalytical data were compared to the state of the art, i.e. to published electroanalytical parameters for other electrodes modified with AgNPs.

EXPERIMENTAL

Materials

The working electrode was a disc from spectroscopic graphite with visible surface area *ca.* 25 mm² (RWO, Ringsdorf, Germany). Na₂HPO₄ and NaH₂PO₄ (Sigma-Aldrich), AgNO₃, NaNO₃ and CH₃COOH (Merck), uric acid, ascorbic acid, citric acid, D-glucose and H₂O₂ (Fluka), chitosan (Acros) were of analytical grade and used as received. Phosphate buffer solution, 0.1 M, was prepared with monobasic and dibasic sodium phosphates dissolved in double distilled water with pH 7.0, adjusted with a pH-meter model MS 2006 (Microsyst, Bulgaria). Double distilled water was used to prepare aqueous solutions.

The *Achillea millefolium* wastes were obtained from Mirkovo distillery (Mirkovo, region of Sofia, Bulgaria, 2017 harvest). The *Lavandula angustifolia* wastes were obtained from Zelenikovo distillery (Zelenikovo, region of Plovdiv, Bulgaria, 2017 harvest). Both wastes were generated after steam distillation of the fresh biomass. The wastes were inspected, dried at 50 °C, and kept frozen until further treatment.

Extraction of wastes with distilled water was performed as follows: 150 g of dry residue were treated with 1000 mL of water for 1 h at 60 °C and left for 24 h at room temperature at constant stirring. The mass was filtered and the insoluble residue was extracted with additional 500 mL of water at the same conditions.

Apparatus and measurements

The samples of the AgNPs for TEM analysis were prepared by placing a drop of the suspension on a standard copper grid, covered by amorphous carbon layer and allowing the solvent to evaporate at room temperature. Images were acquired by high resolution transmission electron microscope JEOL JEM 2100 (JEOL, Japan) at accelerating voltage 200 kV. Statistical analysis of AgNPs size distribution was carried out with Image J software. The identification of the phase composition of the samples was achieved using PDF-2 Database of the International Center for Diffraction Data (ICDD).

All the electrochemical measurements were performed using potentiostat EmStat3 (PalmSens BV, The Netherlands) interfaced with a computer and controlled by 'PSTrace 2.5.2' software. A conventional thermostated three-electrode cell including a working electrode, an Ag/AgCl (3 M KCl) as a reference electrode, and a platinum wire as a counter electrode was used. All the electrochemical measurements were carried out in 0.1 M phosphate buffer solution (PBS) at temperature of 25 °C. Before the measurement the background electrolyte was purged with pure argon for 15-20 min to remove dissolved oxygen.

The modified electrodes were investigated using cyclic voltammetry (CV) and amperometry at a constant potential. Amperometric (*i-t*) curves were registered at a constant applied potential under hydrodynamic condition. The H₂O₂ stock solution was freshly prepared before each measurement. The experimental data analysis was performed using software package 'OriginPro 8.0'.

Biosynthesis of AgNPs

Two mL of aqueous extract (*Achillea millefolium* or *Lavandula angustifolia*) was added to 6 mL of 10⁻² M AgNO₃ solution and the final volume was adjusted to 10 mL with double distilled water. The addition of the extract to the aqueous AgNO₃ solution turned the initial yellowish color to brown indicating the formation of AgNPs.

Preparation of the modified electrodes

Prior to the modification, the bare graphite electrode (Gr) was carefully polished to mirror-like finish with emery paper with decreasing particle size, rinsed, sonicated in double distilled water for

5 min and allowed to dry at room temperature. The working surface of the cleaned and polished electrode was modified using two different approaches: 1/ through dropwise addition of 40 μL of the colloidal AgNPs solution, after applying the electroactive substance, the electrode surface was dried at room temperature; 2/ under static conditions by immersing the graphite electrode in the colloidal AgNPs solution; the duration of the adsorption process was 2 hours at temperature 25 $^{\circ}\text{C}$. In order to stabilize the electroactive layer, a thin polymer film was applied by dropping onto the electrode surface of 5 μL of 0.5 % chitosan (in a solvent 0.1 M CH_3COOH) and drying it in air. The resulting modified electrodes, developed using *Achillea millefolium* extract as a reducing agent, will be denoted as electrode type AgNPs(AM)-CS/Gr1 and type AgNPs(AM)-CS/Gr2. The electrodes, developed using *Lavandula angustifolia* extract, will be denoted as electrode type AgNPs(LA)-CS/Gr1 and type AgNPs(LA)-CS/Gr2, respectively.

RESULTS AND DISCUSSION

Transmission electron microscopy (TEM) studies

The morphologies of AgNPs synthesized with water extracts of *Achillea millefolium* and *Lavandula angustifolia* are presented in Fig. 1 a) and b), respectively. The representative SAED pattern for AgNPs is included in the same figure (Fig. 1 c). As seen, the nanoparticles grew very tiny with spherical shape. The size distribution of *Achillea millefolium* and *Lavandula angustifolia* AgNPs and their mean sizes, 2.8 nm for AM and 3.1 nm for LA, are presented in the histograms (d) and (e). The indexing of SAED pattern reveals that Ag cubic (PDF 870720) is the only phase in the composition of both samples AM and LA. Summarized data for interplanar distances and Miller indices are presented in Table 1.

Table 1. Indexing of SAED pattern

d [\AA]	hkl	Phase	PDF
2.3540	111	Ag cubic	870720
1.4415	220	Ag cubic	870720
1.1671	222	Ag cubic	870720

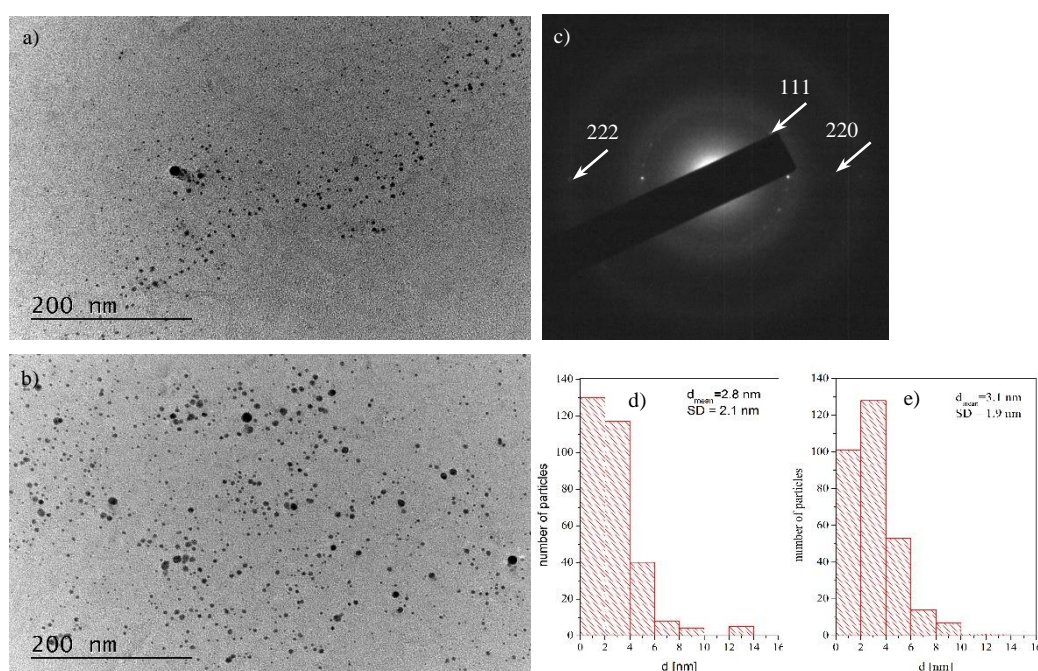


Fig. 1. TEM micrographs of AgNPs synthesized with extract of *Achillea millefolium* (a) and *Lavandula angustifolia* (b) wastes, representative SAED patterns (c) and size distribution of the corresponding particles (d) and (e).

Electrochemical studies

The presence of Ag on the surface of graphite electrodes was evidenced by cyclic voltammetry. Fig. 2 presents the cyclic voltammogram of the modified electrode type AgNPs(AM)-CS/Gr1 in deaerated 0.1 M PBS (pH 7.0) recorded in the potential range from -0.2 to 0.8 V. A pair of well-

defined redox peaks was observed at 0.44 and 0.17 V, respectively, which was ascribed to the redox of silver.

In order to obtain prior information about the catalytic activity of the modified electrodes towards the electroreduction of hydrogen peroxide and to evaluate the effect of the applied potential on the current response of the electrodes, an amperometric

signal was recorded in the presence of H_2O_2 at a constant potential.

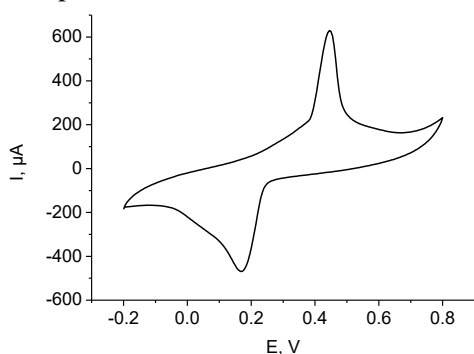


Fig. 2. Cyclic voltammogram of the modified electrode AgNPs(AM)-CS/Gr1 in 0.1 M PBS (pH 7.0); scan rate of 25 mV s^{-1} .

Fig. 3 shows the background-corrected steady-state response of the electrodes in presence of 2.3 mM H_2O_2 at applied potentials of -0.3 , -0.2 , -0.1 and 0.0 V , respectively. From the data presented it is evident that the catalytic activity of both electrodes increases as the polarization potential shifts negatively (for type AgNPs(AM)-CS/Gr1 the dependence was linear with a correlation coefficient of 0.994). A comparison of the current values for the two catalysts shows that electrode type AgNPs(AM)-CS/Gr1 is distinguished by a significantly higher catalytic activity than type AgNPs(AM)-CS/Gr2.

The reproducibility of the current response of the modified electrode is essential for its successful application as a sensing element. In this connection, the current signal for electrode AgNPs(AM)-CS/Gr1 (which possesses a higher response) to 2.3 mM H_2O_2 at applied potentials of -0.3 V and -0.2 V was examined. For 5 successive independent measurements at -0.3 V in presence of 2.3 mM H_2O_2 the electrode response was $271.6 \pm 18.6 \mu\text{A}$ and the relative standard deviation (R.S.D.) was calculated to be 6.8 %. Analogous studies carried out at a potential of -0.2 V show electrode response of $233.4 \pm 14.8 \mu\text{A}$ and R.S.D. of 6.3 %. The results prove that the modified electrode possesses satisfactory reproducibility of the current signal.

In the next step, the graphite electrodes modified with biosynthesized AgNPs were tested for amperometric quantitative detection of H_2O_2 . The concentration dependence of the amperometric response of the electrodes was investigated by means of constant potential amperometry. Calibration plots for AgNPs(AM)-CS/Gr1 (Fig. 4), clearly show that the sensitivity (determined as the slope of the linear section of the calibration graph) increases and the portion of the strict linear concentration dependence of the signal is extended as the working potential shifts to the cathodic

direction. The electrode sensitivity at potential of -0.3 V was found to be 1.2 times higher than the sensitivity registered at -0.2 V .

Fig. 5 shows the typical steady-state current response of the modified electrode type AgNPs(AM)-CS/Gr2 to successive additions of 0.5 mM H_2O_2 into stirred 0.1 M PBS (pH 7.0) at a constant potential of -0.3 V . Upon addition of H_2O_2 the modified electrode shows increasing reduction currents (staircase current response), corresponding to the electrochemical conversion of the analyte. The inset in Fig. 5 presents the calibration curve for H_2O_2 (14 points), built on the basis of the chronoamperometric data. The response of AgNPs(AM)-CS/Gr2 was linear up to 5.7 mM H_2O_2 ($R^2 = 0.997$).

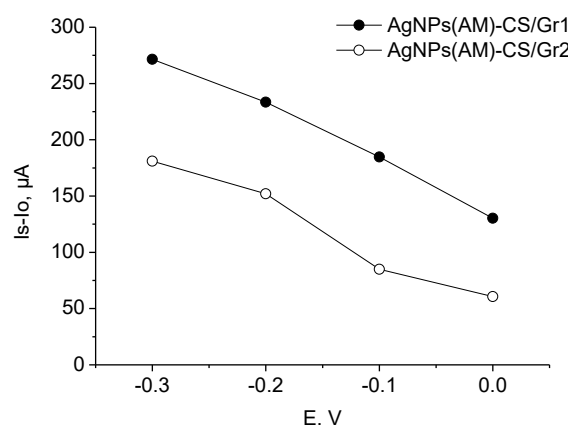


Fig. 3. Background corrected steady-state response of the modified electrodes type AgNPs(AM)-CS/Gr1 (solid circles) and type AgNPs(AM)-CS/Gr2 (open circles) in presence of 2.3 mM H_2O_2 ; supporting electrolyte 0.1 M PBS (pH 7.0).

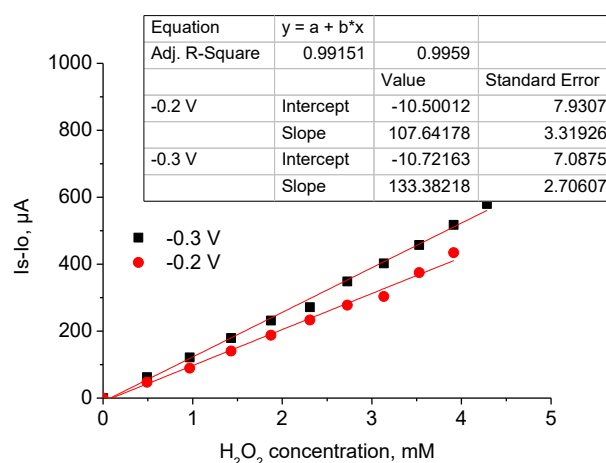


Fig. 4. Background-corrected steady-state response of the modified electrode AgNPs(AM)-CS/Gr1 as a function of H_2O_2 concentration; supporting electrolyte 0.1 M PBS (pH 7.0).

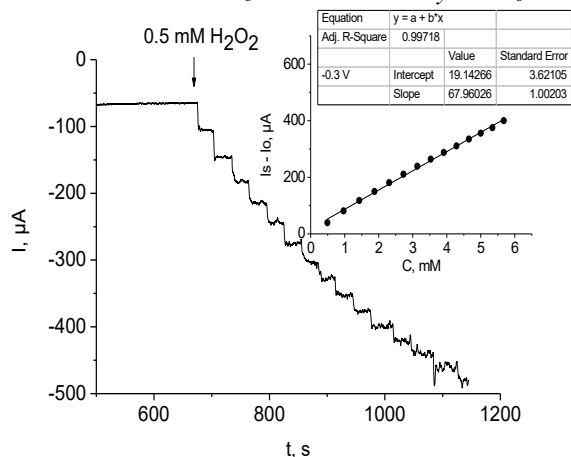


Fig. 5. Amperometric response of modified electrode AgNPs(AM)-CS/Gr2 to successive addition of 0.5 mM H_2O_2 into stirred 0.1 M PBS (pH 7.0) at an applied potential of -0.3 V; Inset: corresponding calibration plot.

Table 2 presents an overview on the main operational parameters of the electrodes modified with biosynthesized AgNPs. Concerning the analytical characteristics of the all four type modified electrodes, the graphite modified with AgNPs, biosynthesized using extract of *Lavandula angustifolia* wastes, exhibited lower activity as compared to the graphite modified with AgNPs, synthesized with extract of *Achillea millefolium* wastes.

The electrocatalytic activity of the developed electrodes also significantly depends on the modification procedure – the sensitivity of the electrode type AgNPs(AM)-CS/Gr1 was found to be about 2 times higher than this one of AgNPs(AM)-CS/Gr2 estimated under the same conditions.

Table 2. Operational parameters of graphite electrodes modified with biosynthesized AgNPs; background electrolyte 0.1 M PBS (pH 7.0).

Type of modified electrode	E, V	Sensitivity, $\mu\text{A mM}^{-1}\text{cm}^{-2}$	R^2	Linearity, mM
AgNPs(AM)-CS/Gr1	-0.3	533.5	0.996	4.3
	-0.2	430.6	0.992	4.0
AgNPs(AM)-CS/Gr2	-0.3	271.8	0.997	5.7
	-0.2	252.0	0.999	2.7
AgNPs(LA)-CS/Gr1	-0.3	374.7	0.999	3.5
	-0.2	304.5	0.999	3.5
AgNPs(LA)-CS/Gr2	-0.3	248.3	0.996	3.5
	-0.2	127.4	0.993	5.0

Table 3. Comparison of the operational characteristics of amperometric sensors based on AgNPs for H_2O_2 quantitative detection, with the achieved in the present work.

Sensing platform/Support electrode*	E, V	Sensitivity, $\mu\text{A mM}^{-1}\text{cm}^{-2}$	Linearity, M	Ref.
AgNWs/SPCE	-0.4^a	138.4	1.42×10^{-2}	5
AgNPs/GC	-0.85^b	–	6.5×10^{-3}	11
GR-AgNCs/GC	-0.5^a	183.5	1.0×10^{-2}	6
Ag-NFM/GC	-0.58^a	157	1.65×10^{-2}	9
Ag-HNTs-MnO ₂ /GC	-0.3^b	11.9	4.71×10^{-3}	12
GO-AgNPs/GC	-0.3^a	0.1218 ^c	1.1×10^{-2}	13
AgNPs-PANI-HNTs/GC	-0.2^b	74.8	4.7×10^{-3}	1
AgNPs-porous silicon/CPE	-0.45^a	34.07 ^c	5.0×10^{-3}	14
AgNPs(AM)-CS/Gr	-0.3^a	533.5	4.3×10^{-3}	Present work
AgNPs(LA)-CS/Gr	-0.3^a	374.7	3.5×10^{-3}	Present work

^a referred to an Ag/AgCl (3 M KCl) electrode; ^b referred to a saturated calomel electrode (SCE); ^c the unit is: $\mu\text{A mM}^{-1}$; *AgNWs – silver nanowires, SPCE – screen printed carbon electrode, GC – glassy carbon, GR – graphene, AgNCs – silver nanocrystals, NFM – nanofibrous membrane, HNTs – halloysite nanotubes, GO – graphene oxide, PANI – polyaniline, CPE – carbon paste electrode, CS – chitosan, Gr – graphite.

The experimental data indicate that the range of the strict linear dependence of the electrode signal for AgNPs(AM)-CS/Gr1 is almost the same for both applied potentials. At a potential of -0.3 V electrode type AgNPs(AM)-CS/Gr2 possesses twice as long linear portion of the calibration plot as compared to this one at potential of -0.2 V.

The performance of the here presented electrocatalysts, based on biosynthesized AgNPs, was compared with other carbonaceous electrodes modified with AgNPs. In Table 3 we have summarized various amperometric H_2O_2 sensors, with respect to the applied potential, the sensitivity and the linearity of the signal. All data presented have been published in the last 6 years. It can be seen that the proposed modified electrodes show an excellent sensitivity, several times higher than that obtained by using other carbon-based electrodes modified with AgNPs.

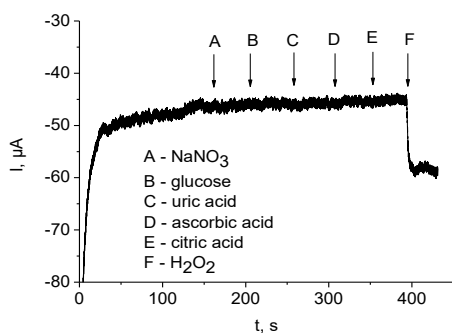


Fig. 6. Amperometric $i-t$ curve of modified electrode AgNPs(LA)-CS/Gr1 for the determination of 0.15 mM H_2O_2 (F) in the presence of 3.0 mM of different interfering species, added one by one with an interval of 50 s to 0.1 M PBS (pH 7.0) at an applied potential of -0.2 V.

It is well known that some co-existing electroactive species in real samples will affect the sensor response, which could have compromised the measured value of the analyte. In order to study the selectivity of the electrodes modified with biosynthesized AgNPs, we have monitored the response of type AgNPs(LA)-CS/Gr1 in the presence of common interfering species such as NaNO_3 , glucose, uric acid, ascorbic acid and citric acid. Amperometric response of AgNPs(LA)-CS/Gr1 towards the additions of these substances (3.0 mM), followed by H_2O_2 addition (0.15 mM), was examined at a constant potential of -0.2 V. The authentic record of the response of modified electrode (Fig. 6) clearly shows that the tested species had no effect on the H_2O_2 detection – no response was observed for modified electrode in the presence of the above mentioned substances and the current response for H_2O_2 , registered after adding

the substances, corresponds to the one determined in the calibration study (I (μA) = $76.13C$ (mM) + 2.331 , $R^2 = 0.999$). These results demonstrate that the modified electrode has good selectivity for H_2O_2 and reveal the application potential of biosynthesized AgNPs for sensing of H_2O_2 in real samples.

CONCLUSIONS

Flower water extracts of *Achillea millefolium* and *Lavandula angustifolia* wastes were used as reducing agents for efficient synthesis of AgNPs, which is a novel simple approach, inexpensive and eco-friendly in nature. The graphite electrodes modified with as-obtained biosynthesized AgNPs were successfully used for reduction of H_2O_2 and their applicability for amperometric quantitative determination of H_2O_2 in micromolar concentrations was demonstrated. The modified electrodes showed a remarkable activity at applied potentials of -0.3 V and -0.2 V (vs. Ag/AgCl, 3 M KCl), stable amperometric response, high sensitivity in a wide linear range for H_2O_2 detection and provided a new platform for the development of electrochemical sensors.

Acknowledgement: We acknowledge the financial support from the National Science Fund of Bulgaria; project DN 17/22 from 12.12.2017: Valorization and application of essential oil industry wastes for “green” synthesis of metal nanoparticles.

REFERENCES

- Z. Yang, Z. Zheng, J. Zheng, *RCS Adv.*, **6**, 58329 (2016).
- P. Miao, B. Wang, J. Yin, X. Chen, Y. Tang, *Electrochem. Commun.*, **53**, 37 (2015).
- S. Liu, J. Tian, L. Wang, X. Sun, *J. Nanopart. Res.*, **13**, 4539 (2011).
- Q. Wang, J. Zheng, *Microchim. Acta*, **169**, 361 (2010).
- W. Hsiao, H. Chen, T. Cheng, T. Huang, Y. Chen, C. Lee, H. Chi, *J. Chin. Chem. Soc.*, **59**, 500 (2012).
- L. Zhong, S. Gan, X. Fu, F. Li, D. Han, L. Guo, L. Niu, *Electrochim. Acta*, **89**, 222 (2013).
- Y. Miao, S. He, Y. Zhong, Z. Yang, W. Tjiu, T. Liu, *Electrochim. Acta*, **99**, 117 (2013).
- C. Lin, Y. Lai, A. Balamurugana, R. Vittal, C. Lin, K. Ho, *Talanta*, **82**, 340 (2010).
- D. Li, L. Luo, Z. Pang, X. Chen, Y. Cai, Q. Wei, *RSC Adv.*, **4**, 3857 (2014).
- V. Shukla, R. Yadav, P. Yadav, A. Pandey, *J. Hazard. Mater.*, **213-214**, 161 (2012).
- J. Raoof, R. Ojani, E. Hasheminejad, S. Nadimi, *Appl. Surf. Sci.*, **258**, 2788 (2012).
- S. Zhang, Q. Sheng, J. Zheng, *RSC Adv.*, **5**, 26878 (2015).
- A. Noor, M. Shahid, P. Rameshkumar, N. Huang, *Microchim. Acta*, **183**, 911 (2016).
- A. Ensafi, F. Rezaei, B. Rezaei, *Sens. Actuat. B*, **231**, 239 (2016).

Innovative treatment of livestock manure by a single – compartment microbial fuel cell with air-breathing cathode

G. P. Peeva^{1*}, B. N. Midyurova², V. A. Nenov¹

¹ Department of Water Treatment Technologies, Faculty of Technical Sciences, Burgas “Asen Zlatarov” University, 1 Y. Yakimov str. 8010 Burgas, Bulgaria

² Department of Ecology and Environment Protection, Faculty of Natural Sciences, Burgas “Asen Zlatarov” University, 1 Y. Yakimov str. 8010 Burgas, Bulgaria

Received October 30, 20118; Revised December 20, 2018

Livestock manure (LM) is characterized with high level of organic matter, suspended solids, phosphorus and nitrogen. The application of LM as a fertilizer in agriculture is often restricted by pathogen organisms contained in this waste, as the waste fluids are often used as fertilizers after their stabilization. In this sense, developments of methods for LM stabilization by alternative approaches are of great interest. One way for such stabilization of LM is the application of bio-electrochemical systems (BES). Microbial fuel cell (MFC) as a typical BES can be used for conversion of the organic matter into electricity by electrogens activity.

The study is focused on monitoring of a MFC behavior. LM was used as a fuel, whilst oxygen from the air acted as an oxidizer. The process was monitored via the potential generated. The open circuit potential (OCP) was measured against different resistance- loads (closed circuit, CCP). It was found that at an applied resistance of 1000 Ω the output voltage was 0.547 V. After a few days of microorganism acclimation, the generated voltage was found to be 0.5 V. Over a period of 264 h, the organic matter content (assessed through the chemical oxygen demand, COD) decreased substantially from the initial value of 15.92 g O₂/L down to 0.03 g O₂/L per hour.

Keywords: livestock manure, wastewater treatment, microbial fuel cell

INTRODUCTION

During the past few years, microbial fuel cells have been of great interest since they can find application for simultaneous waste water purification and electricity generation. The basic role in these systems is played by the biofilm which is formed on the anode surface and, on one hand, microorganisms oxidize organic substances to end products (CO₂, H⁺, electrons), while on the other hand, biofilm participates in the transfer of generated electrons to the anode surface [1]. Classic microbial fuel cell consists of anode and cathode space divided by a separator (proton-exchange membrane, cation-exchange membrane); however, due to the weaker internal resistance and better system behavior, systems have recently been without separation, and the cathode is directly exposed to the air [2, 3]. Air-breathing cathode consists of the following layers: electrode, oxygen reduction reaction (ORR) catalyst layer, and air-diffusion layer [4].

The optimization of cathodes and anodes through different catalysts, the number of layers and new structures, aims at increase of the initial resistance and the productivity of MFC, increase of the activity of the anode biofilm, reduction of the internal

resistance, and improvement of the efficiency of the processes [5, 6].

A classis method is permanently searched for characterization and understanding of the complex biochemical processes in the biochemical stimulators. Cyclic voltammetry (CV) is such a method which helps to conduct an optimal kinetic analysis of the cathode as an independent section, and of the anode biofilm [7, 8].

Cyclic voltammetry provides useful thermodynamic information as well as quality information on the nature of electronic transfer, bioelectrocatalytically active factors, and on other processes. The analysis of kinetic parameters through CV can give us important information, assessment of the mechanisms, and of the complex microbe-electrode interactions. Such experiments are conducted by Harnisch and Freguia who review cyclic voltammetric measurements with different basic techniques of Geobacter biofilms [9, 10].

Manure is one of the biggest pollutants which is directly dumped into the soil or waters as eutrophication. Waste waters from animal breeding contain significant quantities of organic substances, nutrients (nitrogen, phosphorus), heavy metals, pathogenic microorganisms [11, 12]. There are different methods of treating these deposits, as their application as fertilizer [13], after their initial

* To whom all correspondence should be sent.

E-mail: peeva.gergana@abv.bg

stabilization through composting, is a conventional method. This process aims to reduce the organic contents of the obtained compost, the ratio C/N, pH, the temperature, the inorganic nitrogen, the contents of carbon [14, 15] is changed. Anaerobic digestion is a method applied for stabilization of deposits under the influence of microbiologic activity when organic matter turns into methane, carbon dioxide, hydrogen sulfide, ammonia, other organic substances, etc. Anaerobic digestion is the basic process of treating the so-called anaerobic lagoons [16]. There are also methods of treatment like wet extraction, phosphorus recovery by struvite precipitation, nitrification-denitrification, deammonification [17].

Despite for generating electricity, bio-electrochemical systems can be also used for treating waste waters. There is a statement of a microbial fuel cell of tubular type, charged with deposits from a big breeding farm, which has a generated power density of 1.143 W m^{-3} [18], while another analysis has applied air-breathing cathode for improving the process, and the reached power density is 4.725 W m^{-3} [19]. The maximum values of power density is up to 20.2 W m^{-3} when applying waste waters from dairy factories and up to around 15.1 W m^{-3} from waste waters originating from dairy farms [20,21]. Along with electricity generation, the values of organic pollution, nitrogen and phosphorus are reduced. Zhang *et al* [22] have reached to an effect of removing nitrogen from the anolite in the bio-electrochemical system with

83.4% and of phosphorus – with 52.4 % as well as to 95 % reduction of the organic matter for a period of 144 hours. Another analysis has reached values of removing nitrogen and phosphorus with 96 % and 64 %, respectively [23].

EXPERIMENTAL

Laboratory single-chamber microbial fuel cell (MFC)

The structured system is a plastic cylindrical corpus (with a capacity of 130 cm^3), without separation between the two electrodes, the anode is from a carbon brush (with a surface of 200 cm^2), while the cathode is of air type, with a surface of 3.77 cm^2 (VITO-Belgium), directly exposed to air contact. The cathode consists of the following layers: activated carbon and polytetrafluoroethylene in ratio 40:60.

The two electrodes are connected in an electric circuit with external resistance $R=1000 \ \Omega$. Waste waters of a buffalo farm are used as a fuel of organic matter and microbiological culture in the cell. Initially, the deposit which is taken after anaerobic digestion is centrifuged under laboratory conditions (centrifuge JANETZKI, for 15 minutes, 3000 rpm). The obtained centrate is used for the experiments. The principal scheme of the process is presented in Fig. 1, and the real laboratory single-chamber microbial fuel cell is presented in Fig. 2. Table 1 shows the initial contents of this centrate:

Table 1. Characteristics of livestock manure

Sample	Analysis	PO ₄ -P, g/L	PO ₄ , g/L	NH ₄ -N, g/L	NH ₄ , g/L	COD, gO ₂ /L	TSS, g/L
Centrate of buffalo manure		0.94	2.88	1.21	1.56	15.92	17.8

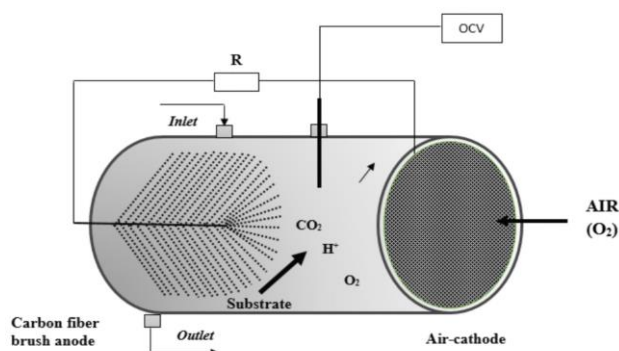


Figure 1. Schematic representation of the single-compartment microbial fuel cell with air-breathing cathode.



Figure 2. Laboratory prototype of the MFC.

The experiment lasts 15 days, as the concentrations of nitrogen (g/L), phosphorus (g/L), COD (chemical oxygen demand) (g/L) in the anolite is measured every 3 days. Spectrophotometric cuvette test is used for this purpose (HACH LANGE 3900 spectrophotometer).

The potential between an anode and a cathode is measured with a multimeter (MASTECH MY-66). Cyclic voltammetry (potentiostat/galvanostat Metrohm Autolab) is used for the electrochemical characteristics of the process.

Electrochemical cell for testing electrode materials:

The test cell used for conducting electrochemical tests consists of a glass reactor with electrolyte background (250mM water solution of NaCl). 3 stationary electrodes are put in it (working, comparative and referential) so that to create conditions analogical to the MFC structure. The first electrode is VITO Belgium 40:60 (air-breathing cathode), the second electrode consists of a carbon canvas the carbon brush is made of (anode). The silver-silver chloride electrode: Ag/AgCl/KCl (saturated aqueous solution) with 0.222 V potential (vs. SHE) is used as a reference. Cyclic voltammograms are recorded with AUTOLAB PGSTAT101 device with step 0.00244 and scanning rate of 0.1Vs⁻¹ at room temperature (25 ± 2°C). In order to receive more complete information on the stability of electrodes two more methods with linear change of the potential with time are applied – the so-called Linear polarization – LP and the so-called Linear sweep voltammetry – LSV.

RESULTS AND DISCUSSION

The laboratory microbial fuel cell was tested over a 15 days period, as up to the 11th day a reduction of the indicators monitored in the residual fluid, namely – nitrogen, phosphorus, COD was observed. Fig. 3 presents the results regarding these pollutants and their change over time. The chart shows that after the acclimation of the microbiological culture in the system, reduction of the content of nitrogen, phosphorus and organic matter (like COD) is observed. It was found that for a period of 264 hours the initial organic substances content (estimated as COD of 30 mgO₂/L) decreased with up to 54.8 %, whilst the starting levels of phosphate and ammonia ions were reduced with 37.5 % and 74.2 % (4.1 and 4.3 mg/L) respectively.

The change of the concentration of the COD, the ammonia and phosphate ions with time can be presented with the respective polynomial equations, as the coefficients (R²) show that there is a very high correlation:

$$COD = 0,0403.t^2 - 1,2325.t + 16,335, \quad R^2 = 0.97$$

$$NH_4^+ = 0,0051.t^2 - 0,1546.t + 1,518, \quad R^2 = 0.95$$

$$PO_4^{3-} = 0,0059.t^2 - 0,1703.t + 2,8096, \quad R^2 = 0.95$$

where: COD – organic content in wastewater presented as COD (COD, gO₂/L); NH₄⁺ - ammonia ions concentration, g/L; PO₄³⁻ – phosphate ions concentration, g/L; R² – correlation coefficient.

The process is also followed in accordance with the change of the potential between an anode and a cathode on a daily basis, and the results are presented in Fig. 4. An initial value of the voltage of 0.547 V is reported, as the following 7 days the potential was reduced to a value of around 0.4-0.45 V. The reason for this is the period of adaptation of microorganisms during the first few days. On the 7th day the potential is again observed to increase up to 0.54 V. By the end of the 15-day experiment, the potential is relatively stable, with values of around 0.55 V. The maximum power density was calculated to be 2.33 W/m². This value is comparable with the reported power densities of bio-electrochemical systems fueled with the deposits of animal breeding [12, 13].

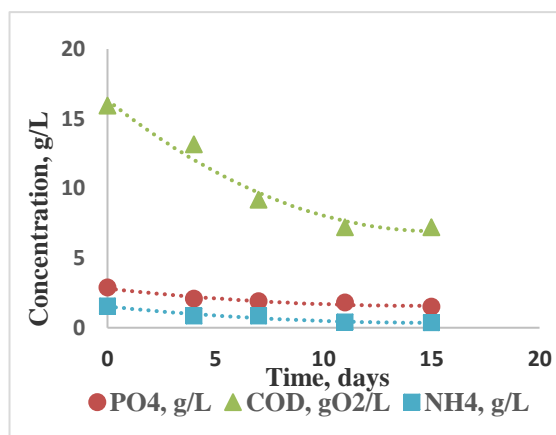


Figure 3. Changes in the concentrations of phosphates, ammonia ions and COD with time

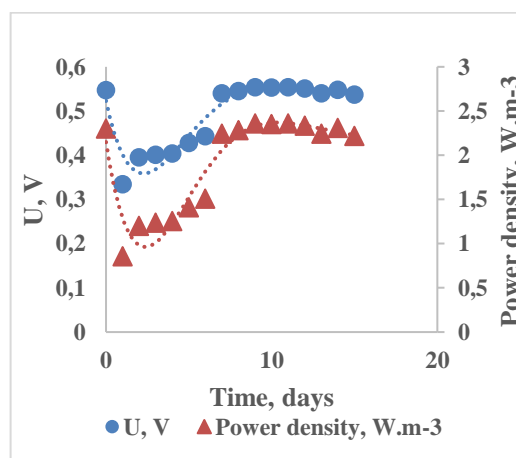


Figure 4. Variations of the cell voltage and power density over time

The electrochemical analyses were carried out on an apparatus: “AUTOLAB POTENTIOSTAT-

GALVANOSTAT”, product of METROHM AUTOLAB B.V. The voltammogram of air-breathing cathode VITO represents a typical cyclic polarization curve, the forward scan of which corresponds the increased potential. The increased potential is accompanied by reduced surface concentration and mass transfer to reaching the maximal current which is then reduced due to the effect of exhaustion (resulting from slower diffusion). As a result, the current reaches its maximum and starts falling. After passing the maximum current, the scan of the potential reverses, (Fig. 5).

This result is was most probably due to some catalytic effect of the carbon black and the activation of cathodic reactions. The reported peak shifts in the voltammogram [24] is related to the improved reduction of oxygen resulting from the presence of the catalyts.

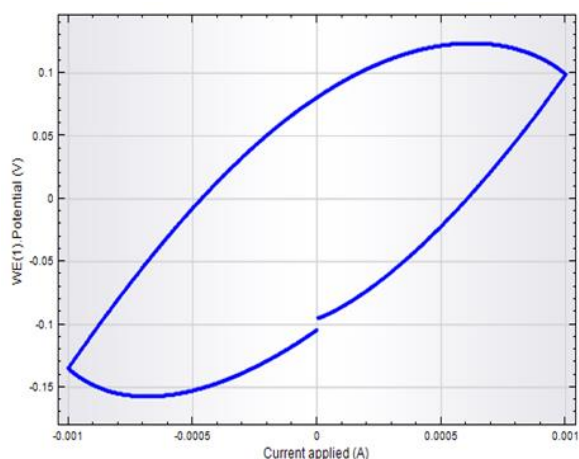


Figure 5. Dependence of the potential of the VITO electrode on the applied current over the range from -1 mA to +1 mA.

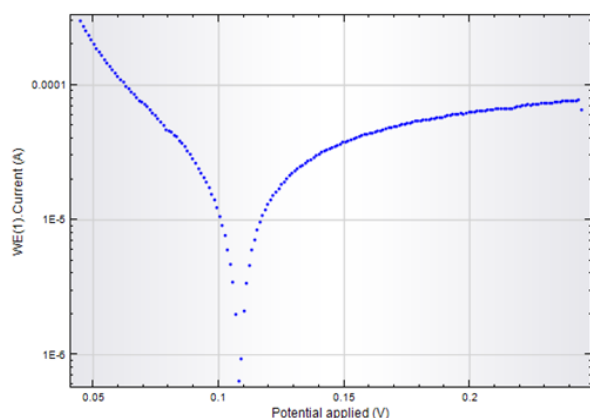


Figure 6. The Linear polarization curve (dependence of the current on the potential applied) for the air-breathing cathode VITO.

The dependence of the current on the applied potential of the air-breathing cathode VITO and

the obtained curve of linear polarization is depicted in Fig. 6 This curve suggests that at ca. 0.11 V oxygen reduction takes place on the cathode – a clear reduction maximum is present.

CONCLUSIONS

Bio-electrochemical systems are an alternative of the conventional, expensive methods of purifying waste waters, as, together with the reduction of the pollutants, there is a generation of electricity. The constructed single-chamber fuel cell shows the abilities of these systems to reduce organic pollution and the phosphate and ammonium contents in waste waters from animal breeding by simultaneously generating a potential of around 0.5 V with the help of microbiological conenoses with the residual fluid. The system is stable within the test period of 15 days. Future studies shall be necessary in order to improve the work and to prove the resistance of the constructed microbial cell.

Acknowledgment: The authors thank the National Science Fund of Bulgaria (BNSF) for the financial support of these investigations. Grant DN 17/14 and Grant DM 17/5.

REFERENCES

1. M. Rahimnejada, A. Adhami, S. Darvari, A. Zirepour, S. Oh, *Alexandria Engineering Journal*, **54**, 745 (2015)
2. H. Liu, B.E. Logan, *Environ. Sci. Technol.*, **38**, 4040 (2004)
3. H. Liu, S. Cheng, B.E. Logan, *Environ. Sci. Technol.*, **40**, 2426 (2006)
4. Z. Wang, G. Mahadevan Y. Wu, F. Zhao, *Journal of Power Sources*, **356**, 245 (2017)
5. Liao Q., J. Zhang, J. Li, D. Ye, X. Zhu, B. Zhang. 2015. Increased performance of a tubular microbial fuel cell with a rotating carbon-brush anode. *Biosens Bioelectron.*, 63:558-561.
6. Liu J., J. Liu, W. He, Y. Qu, N. Ren Y., Feng. *J. Power Sour.*, **265**: 391 (2014)
7. M. Rosenbaum, F. Aulenta, M. Villano, L. T. Angenent, *Bioresour. Technol.*, **102**, 324 (2011)
8. D. R. Lovley, D. E. Holmes, K. P. Nevin, *Advances in Microbial Physiology*, Vol. 49, R. K. Poole. London, Academic Press Ltd-Elsevier Science Ltd., 2004, p. 219.
9. F. Harnisch, S. A. Patil, K. H. Ly, U. Schröder, P. Hildebrandt, *Angew. Chem.* 2011, 123, 2680 –2683; *Angew. Chem. Int. Ed.* 2011, 50, 2625 –2627
10. R. Nakamura, K. Ishii, K. Hashimoto, *Angew. Chem.* 2009, 121, 1634 – 1636; *Angew. Chem. Int. Ed.* 2009, 48, 1606 –1608.
11. Hsu J, Lo S., *Environ. Pollut.*, **104**, 189 (1999)
12. A. F. Nicholson, S. J. Groves, B. J. Chambers. *Bioresour. Technol.*, **96**, 135143 (2005)

13. M. A. Bustamante, C. Paredes, F. C. Marhuenda-Egea, A. Pérez-Espinosa, M. P. Bernal, R. Moral, *Chemosphere*, **72**, 551 (2008)
14. K. Wang, C. He, S. J. You, W. Liu, W. Wang, R. J. Zhang et al., *J. Hazard. Mater.*, **300**, 745 (2015)
15. M. P Bernal, C. Paredes, M. A Sanchez-Monedero, J. Cegarra, *Bioresour. Technol.*, **63**, 91 (1998)
16. USDA-NRCS, Agricultural Waste management System Component Design, in Part 651, Agricultural Waste Management Field Handbook. 2009.
17. A. A. Szogi, Vanotti, M.B. & Ro, K.S. Curr Pollution Rep (2015) 1: 47. <https://doi.org/10.1007/s40726-015-0005-1>
18. K. Scott, C. Murano, *J. Chem. Technol. Biotechnol.*, **82**, 809 (2007),
19. P.D. Kiely, R. Cusick, D.F. Call, P.A. Selembo, J.M. Regan, B.E. Logan, *Bioresour. Technol.*, **102**, 388 (2011)
20. M.M. Mardanpour, M. Nasr Esfahany, T. Behzad, R. Sedaqatvand, *Biosens. Bioelectron.*, **38**, 264 (2012)
21. G. Zhang, Q. Zhao, Y. Jiao, K. Wang, D.J. Lee, N. Ren, *Biosens. Bioelectron.*, **31**, 537 (2012)
22. F. Zhang, J. Li, Zh. He, *Bioresource Technology*, **166**, 630 (2014)
23. X. Chen, D. Sun, X. Zhang, P. Liang, X. Huang, Novel self-driven microbial nutrient recovery cell with simultaneous wastewater purification, 2015, Sci. Rep., 5.
24. S. Khilari, S. Pandit., M. M. Ghangrekar., D. Das, D. Pradhan., *RSC Adv.*, **3**, 7902 (2013).

Carbonaceous materials modified with iridium oxide as an electrochemical sensing platform

T. M. Dodevska*, I. G. Shterev, Y. L. Lazarova

*Department of Organic Chemistry and Inorganic Chemistry,
University of Food Technologies, 26 Maritza Blvd., Plovdiv 4002, Bulgaria*

Received October 31, 2018; Revised December 20, 2018

The electrochemical sensor devices provide the opportunity for sensitive, selective, interference-free, fast, cost-effective and susceptible to automation analysis, and are a promising alternative of the traditional analytical techniques. In this work the modification of carbonaceous carriers (glassy carbon, spectroscopic graphite and pyrolytic graphite) with iridium oxide applying two-step electrodeposition procedure is described. Developed electrodes showed attractive performance for electroanalytical applications, proving to be suitable for the sensitive and selective electrochemical detection of ascorbic acid, sulfite and hydrogen peroxide – analytes of interest in food quality and safety. The electrochemical behavior of the modified electrodes was explored by means of cyclic voltamperometry (CV), differential pulse voltamperometry (DPV) and constant potential amperometry. The effect of carrier type on the electrocatalytic activity of the modified electrodes in reduction of hydrogen peroxide was also evaluated. The results obtained from the quantitative detection measurements offer potential application of the modified with iridium oxide electrodes in electrochemical sensor devices for quick and accurate monitoring of these analytes.

Keywords: *electrochemical sensor, iridium oxide, ascorbic acid, sulfite, hydrogen peroxide*

INTRODUCTION

The strong antioxidant activity of ascorbic acid (AA), also known as vitamin C, and its ability to protect oxidizable constituents, including phenolic and flavor compounds, is the main factor AA to be frequently used in food industry to prevent unwanted changes in color or flavor. Additives, based on AA, are widely used in production of foods and drinks such as beer, jam, sweets, fruit juices, fish products and meats. AA is used as well as in cosmetics as a skin conditioning agent and in pharmaceutical industry as a diet supplement in various forms. Normal AA intake is about 70 – 90 mg for adults [1]. Sulfite (SO_3^{2-}) has an antioxidant and inhibitory characteristics in enzymatic activity and it is utilized as a preservative for various food, meat products and wine to prevent oxidation and bacterial growth [2]. Hydrogen peroxide (H_2O_2) is an industrially relevant analyte – it is widely used as an oxidizing, disinfecting and bleaching agent in the pharmaceutical, textile, cosmetic and paper industries; as a sterilizing agent in food processing and packing. In medicine, H_2O_2 is one of the most important markers for oxidative stress.

Due to the crucial role of the above-mentioned substances in food quality and in industrial applications, recently there is a considerable research interest to develop electrochemical sensors for quantitative detection in various samples including foods and biological fluids [3-18]. In this

connection, novel modified carbonaceous electrodes have been fabricated applying cyclic voltammetry (CV) to form iridium oxide layers at the electrode surface as the fastest and simplest electrodeposition technique, that not requires expensive equipment or special experimental conditions. The developed electrodes showed good performances and potential application in electroanalysis for quantitative detection of ascorbic acid, sulfite and H_2O_2 with sensitivity and selectivity comparable to or better than existing nonenzymatic sensors.

EXPERIMENTAL

Materials

Na_2IrCl_6 , HCl, H_2SO_4 , 30 % H_2O_2 , NaOH, NaOOCCH_3 , NaCl, Na_2CO_3 , Na_2SO_3 , KBr, KI, MgCl_2 were purchased from Fluka; $\text{Na}_2\text{HPO}_4 \cdot 12\text{H}_2\text{O}$, $\text{NaH}_2\text{PO}_4 \cdot 2\text{H}_2\text{O}$, sodium citrate ($\text{Na}_3\text{C}_6\text{H}_5\text{O}_7$), ascorbic acid ($\text{C}_6\text{H}_8\text{O}_6$) and D-glucose ($\text{C}_6\text{H}_{12}\text{O}_6$) were purchased from Sigma-Aldrich. All chemicals used were of analytical grade and double distilled water was used to prepare aqueous solutions. Buffer solution, 0.1 M, was made of monobasic and dibasic sodium phosphates dissolved in double distilled water with pH 7.0 adjusted with NaOH. Three different types of carbonaceous materials were used as working electrodes: glassy carbon (GC) with visible surface area 7.07 mm^2 (Metrohm), spectroscopic graphite (Gr) with area ca. 25 mm^2 and pyrolytic graphite (PGr) with area ca. 26.4 mm^2 (RWO, Ringsdorff, Germany).

* To whom all correspondence should be sent.
E-mail: dodevska@mail.bg

Apparatus and measurements

All the electrochemical measurements were performed using potentiostat EmStat2 (PalmSens BV, The Netherlands) interfaced with a computer and controlled by 'PSTrace 2.5.2' software. A conventional thermostated three-electrode cell including a working electrode, an Ag/AgCl (3 M KCl) as a reference electrode, and a platinum wire as a counter electrode was used. Before the measurement the background electrolyte was purged with pure argon for 15-20 min to remove dissolved oxygen. The modified electrode was investigated using cyclic voltammetry (CV), differential pulse voltammetry (DPV) and amperometry at a constant potential. The DPV parameters were chosen as follows: scan rate 9 mV s^{-1} , pulse amplitude 50 mV, pulse interval 70 ms. Amperometric (*i-t*) curves were monitored at a constant applied potential under hydrodynamic condition. The experimental data analysis was performed using software package 'OriginPro 8.0'. The value of the electrode sensitivity was calculated from the slope of the corresponding regression line and normalized to the electrode geometric surface area.

Electrodeposition of iridium oxide

The electrodeposition of IrO_x onto the electrode surface (polished and sonicated in double distilled water) was carry out in two-step procedure as follows: deposition of iridium from 2.0 % Na₂IrCl₆ in 0.1 M HCl solution using CV from -0.3 to 0.3 V applying 100 cycles at scan rate of 100 mV s^{-1} and subsequent oxidation of iridium applying 100 cycles from -0.3 to 1.4 V in electrolyte 0.5 M H₂SO₄. The modified electrodes will be denoted in the text as: IrO_x/GC, IrO_x/Gr and IrO_x/PGr, respectively.

RESULTS AND DISCUSSION

Electrocatalytic oxidation of ascorbic acid

To study the application of the modified electrode IrO_x/GC in electrochemical sensing of AA and sulfite, electrooxidation and quantitative detection of each of the substances in neutral medium was evaluated using two electrochemical techniques – DPV and constant potential

amperometry, according to the sensitivity, linear range and detection limit.

DPV technique was first employed to study the electrochemical oxidation of AA on IrO_x/GC and bare GC electrode in PBS, pH 7.0 (Fig. 1A). The electrooxidation of AA was shown in the form of peak shaped differential pulse voltammogram with maximum current intensity at 0.25 V on bare GC and at 0.025 V on IrO_x/GC, respectively. The oxidation peak potential of AA at the modified electrode is significantly shifted (by $\sim 0.225 \text{ V}$) in the negative direction compared with the bare GC, and 2.5-fold increase in the peak current at the modified IrO_x/GC was observed. This result clearly shows that the modified electrode possesses a better sensitivity and selectivity in comparison to the bare GC. The oxidation potential value (0.025 V) is significantly lower than the AA oxidation potential reported in previous research articles [3-7], indicating that the presented modified electrode IrO_x/GC is distinguished by a higher efficiency in the selective detection of AA compared to other electrocatalysts. Measurements ($n = 7$) done with the presented modified electrode in presence of 1.0 mM AA showed current signal of $9.315 \pm 0.125 \text{ } \mu\text{A}$ featuring extremely high reproducibility (relative standard deviation R.S.D. equal to 1.34 %). A clear increase in DPV peak current was observed upon increasing the concentration of AA and the peak current was found to increase linearly (correlation coefficient of 0.999) as a function of the concentration up to 1.9 mM (Fig. 1B); the electrode sensitivity was calculated $135 \text{ } \mu\text{A mM}^{-1} \text{ cm}^{-2}$. Fig. 1B (Inset) presents the authentic current-time response of IrO_x/GC recorded after successive additions of AA into stirred PBS (pH 7.0) at a constant potential of 0.025 V. The proposed electrode shows sensitivity of $96.2 \text{ } \mu\text{A mM}^{-1} \text{ cm}^{-2}$ in the range from 0.01 to 3.0 mM AA ($I_p (\mu\text{A}) = 6.8042 C (\text{mM}) + 0.9428$, $R^2 = 0.994$). From the comparative review presented in Table 1, it can be seen that the analytical parameters of the proposed IrO_x/GC electrode are superior in working potential, sensitivity and linear concentration range, as compared to the previously reported modified electrodes for AA detection.

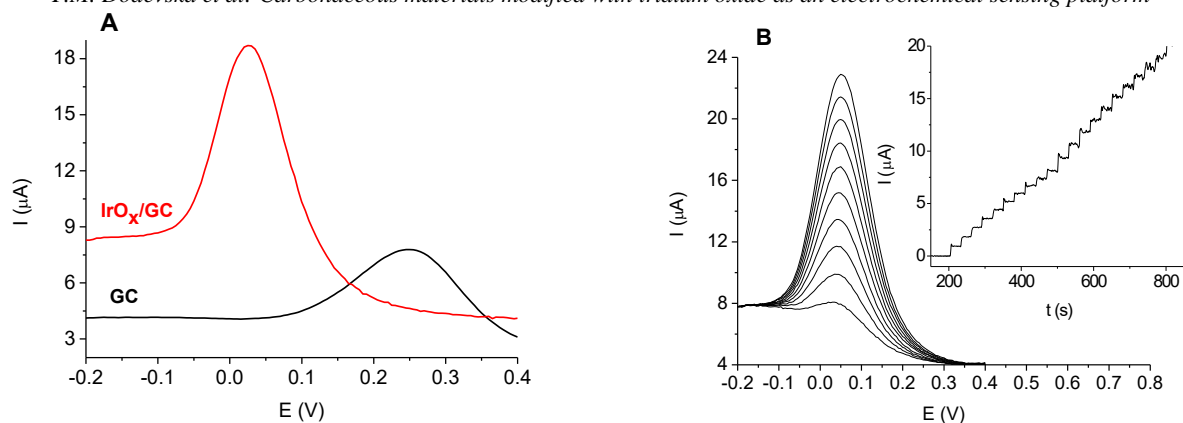


Fig. 1. A) DPV response of bare GC and modified IrO_x/GC for 1.0 mM ascorbic acid in PBS (pH 7.0); B) DPVs of modified electrode IrO_x/GC in the presence of various concentrations of AA (in mM) as follows: 0.2, 0.4, 0.6, 0.78, 0.97, 1.15, 1.34, 1.52, 1.7, 1.88. Inset: Amperometric response of IrO_x/GC for successive additions of AA (10 injections of 0.1 mM and 11 injections of 0.2 mM) at an applied potential of 0.025 V.

Table 1. Comparison of the operational characteristics of electrochemical sensors for quantitative detection of AA, sulfite and H₂O₂, with the achieved in the present work.

Sensing platform/Support electrode*	E, V	Sensitivity, $\mu\text{A mM}^{-1} \text{cm}^{-2}$	Linearity, M	Ref.
<i>Sensors for ascorbic acid</i>				
AuNPs/GO/GC	0.15 ^a	101.86	$1.1 \times 10^{-7} - 6 \times 10^{-4}$	3
Q-chitosan/C	0.1 ^a	76	$1 \times 10^{-5} - 5 \times 10^{-3}$	4
Au/EPA/CPE	0.3 ^a	21.7 ^c	$5 \times 10^{-5} - 7.5 \times 10^{-4}$	5
GDSP/CPE	0.4 ^b	21.879 ^c	$1.5 \times 10^{-4} - 8 \times 10^{-3}$	6
EMGON/CPE	0.38 ^b	78.63 ^c	up to 1×10^{-3}	7
IrO _x /GC	0.025 ^a	96.2	$1 \times 10^{-5} - 3 \times 10^{-3}$	This work
<i>Sensors for sulfite</i>				
BFCNTs/CPE	0.4 ^a	0.05 ^d	$1 \times 10^{-7} - 4 \times 10^{-4}$	8
FeHCF/GC	0.85 ^b	2.18 ^c	up to 4×10^{-3}	9
GC	0.75 ^a	5.37 ^e	$1 \times 10^{-5} - 1 \times 10^{-3}$	10
CS-Fc/MWCNTs/GC	0.35 ^b	13.08 ^c	$5 \times 10^{-6} - 1.5 \times 10^{-3}$	11
PrHCF/GC	0.65 ^a	36	up to 8×10^{-3}	12
IrO _x /GC	0.5 ^a	81	$5 \times 10^{-5} - 9.1 \times 10^{-3}$	This work
<i>Sensors for H₂O₂</i>				
AgNPs-PANI-HNTs/GC	-0.2 ^b	74.8	$5 \times 10^{-7} - 4.7 \times 10^{-3}$	13
Ag-HNTs-MnO ₂ /GC	-0.3 ^b	11.9	$2 \times 10^{-6} - 4.71 \times 10^{-3}$	14
RuNPs/CRGR/GC	-0.6 ^a	1.1 ^d	$1 \times 10^{-5} - 1.7 \times 10^{-4}$	15
PtIr/MWCNTs/GC	0.25 ^b	58.8	$2.5 \times 10^{-6} - 7.25 \times 10^{-5}$	16
Au@Ag@C/GC	-0.55 ^a	76.02	$5 \times 10^{-6} - 7.5 \times 10^{-5}$	17
PdNPs/PEDOT/GC	-0.2 ^b	215.3	$2.5 \times 10^{-6} - 1 \times 10^{-3}$	18
IrO _x /Gr	-0.2 ^a	240	$5 \times 10^{-6} - 1.09 \times 10^{-2}$	This work

^a referred to an Ag/AgCl (3 M KCl) electrode; ^b referred to a saturated calomel electrode (SCE); ^c the unit is: $\mu\text{A mM}^{-1}$; ^d the unit is: $\mu\text{A } \mu\text{M}^{-1}$; ^e the unit is: mA mM^{-1} ; * NPs – nanoparticles, GC – glassy carbon, Gr – graphite, CPE – carbon paste electrode, GO – graphene oxide, Q-chitosan – hydroquinone modified chitosan, Au/EPA – gold/aniline-pentamer-based electroactive polyamide, GDSP – gold decorated SiO₂@polyaniline (PANI) core-shell microspheres, EMGON – electroactive mesoporous gold-organosilica nanocomposite, BF – benzoylferrocene, CNTs – carbon nanotubes, CS – chitosan, Fc – ferrocene, HCF – hexacyanoferrate, MWCNTs – multiwall carbon nanotubes, PANI – polyaniline, HNTs – halloysite nanotubes, CRGR – chemically reduced graphene, PEDOT – poly(3,4-ethylenedioxythiophene).

The selectivity of the modified electrode IrO_x/GC for AA detection was also studied by amperometric measurements at potential of 0.025 V in the presence of eight different electroactive species. Fig. 2 shows the authentic response of electrode IrO_x/GC for the

interval additions of 0.3 mM AA and a 10-fold concentration (3.0 mM) of the above mentioned interfering substances. A well defined amperometric response was observed for AA. Obvious additional signals were not observed for the modified electrode

after injection of interfering substances and the electrode response for AA after adding interfering substances was not changed. The results reveal the application potential of IrO_x/GC for precise sensing of AA in real samples.

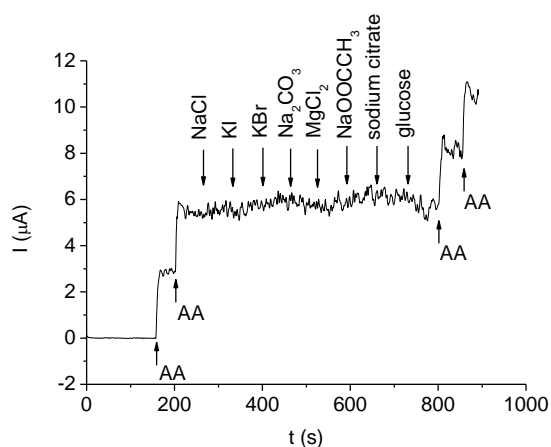


Fig. 2. Amperometric curve of IrO_x/GC for the determination of 0.3 mM ascorbic acid (AA) in the

presence of 3.0 mM of different interfering species, added one by one with an interval of 60 s to 0.1 M PBS (pH 7.0) at an applied potential of 0.025 V.

Electrocatalytic oxidation of sulfite

Fig. 3A shows DPVs recorded for the modified electrode IrO_x/GC and the bare GC electrode in presence of 1.0 mM sulfite in PBS, pH 7.0. The peak potential was determined to be 0.5 V and 0.78 V at the IrO_x/GC and GC electrodes, respectively. This result indicated that the IrO_x-deposit also had an electrocatalytic activity for the sulfite oxidation. The DPV response of IrO_x/GC upon subsequent addition of sulfite ranging from 0.1 to 1.5 mM is presented in Fig. 3B. The electrocatalytic current for the oxidation of sulfite increased with increasing sulfite concentration. The oxidation peak currents were proportional to the sulfite concentration, following linear regression equation $I_p (\mu A) = 4.7774 C (mM) + 0.0027$. The plot showed good linearity with a 0.995 correlation coefficient (Fig. 3B, Inset).

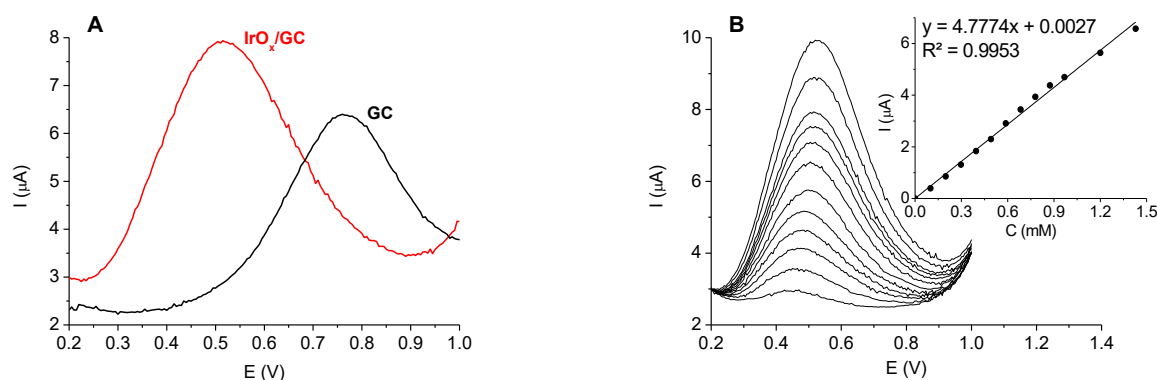


Fig. 3. A) DPV response of bare GC electrode and modified electrode IrO_x/GC for 1.0 mM sulfite in PBS (pH 7.0); B) DPVs of IrO_x/GC in the presence of various concentrations of sulfite; *Inset*: the corresponding calibration plot.

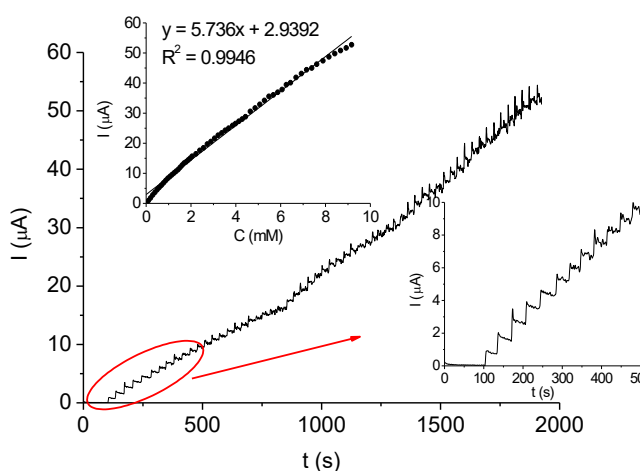


Fig. 4. Amperometric response of modified electrode IrO_x/GC to successive additions of Na₂SO₃ stock solution into stirring 0.1 M PBS (pH 7.0) at an applied potential of 0.5 V; *Inset*: calibration plot and enlarged initial section of the same graph.

Constant potential amperometry also was applied to determine the capability of IrO_x/GC for quantitative determination of sulfite. Fig. 4 displays the authentic record of the amperometric response of IrO_x/GC to successive additions (in 30 s intervals) of Na₂SO₃ stock solution into magnetically stirred PBS (pH 7.0) at a working potential of 0.5 V. Upon injection of sulfite the modified electrode shows increasing staircase current response, corresponding to the electrochemical oxidation of the analyte, which evidences that IrO_x/GC efficiently promoted the electrooxidation of sulfite. The response time of the sensor system was 10 s. The background subtracted steady-state response of the electrode was proportional to the sulfite concentration up to 9.1 mM (correlation coefficient of 0.995) with a sensitivity of 81 $\mu A \text{ mM}^{-1} \text{ cm}^{-2}$, calculated on the basis of 58 points. The IrO_x/GC sensor showed a

comparatively lower working potential and better sensitivity toward sulfite detection [8-12] (Table 1).

It is well known that the long-term stability is one of the main factors that determine the possibility of using the modified electrode as a sensing element. The developed electrode IrO_x/GC was stored at room temperature and measured every 4 days. After 20 days storage the current response to 1 mM sulfite (measured by constant potential amperometry at 0.5 V) retained 94 % of the initial value, demonstrating the good stability of the electrodeposited catalytically active phase.

Electrocatalytic reduction of hydrogen peroxide

The catalytic activity of the proposed IrO_x in the electroreduction of H₂O₂ was also evaluated. In order to assess the impact of type of carbonaceous carrier on the activity of the electrocatalysts, spectroscopic graphite and pyrolytic graphite electrodes have been modified applying the same procedure for electrodeposition of IrO_x. It is well known that the applied potential strongly affects the amperometric response of the electrochemical sensors. Therefore, we have investigated the impact of the applied potential on the amperometric response on the three types of carbonaceous electrodes modified with IrO_x (IrO_x/GC, IrO_x/Gr, IrO_x/PGr) towards reduction of H₂O₂. Chronoamperometric measurements of different concentrations of H₂O₂ at the modified electrodes were done by setting the working potential at -0.1, -0.2 and -0.3 V, respectively. The results indicate that for all types of modified electrodes the reductive current increased stepwise upon introducing in the buffer aliquots of the H₂O₂ stock solution. Table 2 summarizes the operational parameters in terms of sensitivity and linearity of the modified electrodes. The data clearly show that the modified graphite IrO_x/Gr possesses optimal operational characteristics. At an applied potential of -0.2 V the analytical detection of H₂O₂ with IrO_x/Gr is distinguished by the highest sensitivity (240 μA mM⁻¹ cm⁻²) in extended linear range (up to 10.9 mM). The merits of the presented modified electrode IrO_x/Gr can be evaluated by the comparative review presented in Table 1. As can be seen, the IrO_x/Gr exhibits better analytical performance than other published electrochemical sensors for H₂O₂ detection [13-18]. The low working potential of H₂O₂ detection suggests successful application of IrO_x-modified carbonaceous electrodes for quantitative analysis in real samples.

From the data presented it is evident that the electrode type IrO_x/PGr exhibits much lower current response than the other two modified electrodes. It is well known that the activity of heterogeneous catalysts strongly depends on the content and the

dispersity of the catalytically active phase. The observed low activity of IrO_x/PGr is probably due to the lower amount of catalytically active phase deposited onto the pyrolytic graphite surface. We are convinced that the sensitivity of the proposed electrodes could be improved by optimizing the scan rate and the number of cycles applied for modification of the carbonaceous carrier. In this regard, the aim of our future research is to determine how the parameters of electrodeposition process affect shape and size of the structures formed onto electrode surface and to establish correlation with catalytic activity of the modified electrodes in the target reaction.

Table 2. Operational parameters of carbonaceous electrodes modified with IrO_x for amperometric sensing of H₂O₂; background electrolyte 0.1 M PBS (pH 7.0).

Modified electrode	E, V	Sensitivity, μA mM ⁻¹ cm ⁻²	R ²	Linearity, mM
IrO _x /GC	-0.3	135	0.999	7.2
	-0.2	117	0.988	6.3
	-0.1	61	0.996	7.2
IrO _x /Gr	-0.3	215	0.983	9.1
	-0.2	240	0.985	10.9
	-0.1	180	0.994	8.0
IrO _x /PGr	-0.3	35	0.997	9.5
	-0.2	41	0.999	10.9
	-0.1	37	0.983	10.9

CONCLUSIONS

In the present study, we have fabricated iridium oxide-based electrochemical sensor platform for sensitive detection of AA, sulfite and H₂O₂ through a fast and simple electrochemical strategy for surface modification. The developed sensor platform exhibited a remarkable direct electrocatalytic activity towards the oxidation of AA and sulfite as well as reduction of H₂O₂ in the absence of any other electron transfer mediators or enzyme immobilization at the electrode surface. The results obtained from the quantitative detection measurements offer potential application of the carbonaceous electrodes modified with iridium oxide in electrochemical sensor devices for quick and sensitive monitoring of these analytes for environment security and food safety. In addition, the modified electrodes may have potential applications in biosensing.

REFERENCES

1. H. Jirimali, R. Nagarale, D. Saravanakumar, J. Lee, W. Shin, *Carbohydr. Pol.*, **92**, 641 (2013).
2. S. Irwin, P. Fisher, E. Graham, A. Malek, A. Robidoux, *PLoS ONE*, **12(10)**: e0186629 (2017).
3. J. Song, L. Xu, R. Xing, Q. Li, C. Zhou, D. Liu, H. Song, *Sci. Rep.*, **4**, 7515 (2014).

4. H. Jirimali, R. Nagarale, D. Saravanakumar, J. Lee, W. Shin, *Carbohydr. Pol.*, **92**, 641 (2013).
5. M. Tsai, S. Lu, Y. Lai, G. Lai, G. Dizon, T. Yang, Y. Lin, Y. Chou, *eXPRESS Pol. Lett.*, **12**, 71 (2018).
6. C. Weng, Y. Chen, C. Chien, S. Hsu, Y. Jhuo, J. Yeh, C. Dai, *Electrochim. Acta*, **95**, 162 (2013).
7. C. Weng, P. Hsu, S. Hsu, C. Chang, W. Hung, P. Wu, J. Yeh, *J. Mater. Chem. B*, **1**, 4983 (2013).
8. H. Moghaddam, M. Malakootian, H. Beitollah, P. Biparva, *Int. J. Electrochem. Sci.*, **9**, 327 (2014).
9. T. Garcia, E. Casero, E. Lorenzo, F. Pariente, *Sens. Actuat. B*, **106**, 803 (2005).
10. R. Arce, C. Baez, J. Muena, M. Aguirre, J. Romero, *J. Chil. Chem. Soc.*, **61**, 3206 (2016).
11. H. Zhou, W. Yang, C. Sun, *Talanta*, **77**, 366 (2008).
12. B. Devadas, M. Sivakumar, S. Chen, S. Cheemalapati, *Electrochim. Acta*, **176**, 350 (2015).
13. Z. Yang, Z. Zheng, J. Zheng, *RCS Adv.*, **6**, 58329 (2016).
14. S. Zhang, Q. Sheng, J. Zheng, *RSC Adv.*, **5**, 26878 (2015).
15. A. Abdelwahab, M. Talha, M. Abdelmotaleb, *Appl. Chem.*, **92**, 38653 (2016).
16. K. Chen, K. Pillai, J. Rick, C. Pan, S. Wang, C. Liu, B. Hwang, *Biosens. Bioelectron.*, **33**, 120 (2012).
17. Y. Li, Y. Zhang, Y. Zhong, S. Li, *Appl. Surf. Sci.*, **347**, 428 (2015).
18. F. Jiang, R. Yue, Y. Du, J. Xu, P. Yang, *Biosens. Bioelectron.*, **44**, 127 (2013).

Coefficient of diffusion of tannins in extracts from physalis leaves (*Physalis peruviana* L.)

S. T. Tasheva¹, T. A. Ivanova^{1*}, V. T. Popova¹, I. Z. Iliev¹, S. S. Stankov¹,
H. N. Fidan¹, N. N. Mazova¹, A. S. Stoyanova¹

¹ University of Food Technologies, 26 Maritsa blvd, 4002 Plovdiv, Bulgaria

Received October 4, 2018; Revised January 4, 2019

Physalis peruviana L. (Cape gooseberry, Inca berry, goldenberry, physalis) is the most commercially important among the species of the genus *Physalis* (family Solanaceae). *P. peruviana* fresh or processed fruits are highly valued for their palatability and the high concentration of bioactive compounds. The other vegetative parts of the plants (calyx, leaves, stems) are relatively less studied and are currently unutilized. The aim of this study was to determine the coefficient of diffusion of tannins in extracts obtained from the leaves of two physalis genotypes grown in Bulgaria (provided by the Agricultural University, Plovdiv and by Versol bio-farm, Lik village). The dynamics of tannin accumulation in the extracts obtained by a scheme including four solvent concentrations (30, 50, 70 and 95 % ethanol) and three temperature regimes (20, 40 and 60°C) has been presented. Our data reveal that, regardless of the origin of the leaves, the quantity of extracted tannins decreases with process duration, as well as that the maximum amount of tannins is achieved at 60°C. Subsequently, the respective values of the coefficient of diffusion of tannins, known as a characteristic index of the extraction of plant materials, have been determined. The highest values of the coefficient were 0.28×10^{-9} m²/s and 0.31×10^{-9} m²/s (at 60°C), respectively for the two genotypes. To the best of our knowledge, these are the first reported results about the extraction of tannins from physalis leaves, and in particular – about the coefficient of diffusion. The outcomes of the study provide grounds for further investigation on the physalis varieties grown in Bulgaria, with the purpose of revealing more aspects of their composition, bioactivity, benefits and potential for use.

Keywords: *Physalis peruviana* L., coefficient of diffusion, tannins, extracts.

INTRODUCTION

Physalis peruviana L. (also called Cape gooseberry, Inca berry, goldenberry, Peruvian groundcherry, physalis, along with a number of domestic names) belongs to the genus *Physalis* of the Solanaceae family. Originally cultivated as a minor crop in the Andean zone, the production of physalis has expanded to the tropical and subtropical countries, the United States, Australia, New Zealand, and Europe [1, 2].

Although physalis has been evaluated as a promising crop under the environmental conditions of Bulgaria more than 15 years ago [3], currently its production is rather an exception, and the species remains comparatively unknown to the farmers. Still, there are a few Bulgarian farms (mainly organic), which produce physalis fruit based on introduced Colombian (or Peruvian) varieties, and supply selected markets and restaurants. Nevertheless, a local Bulgarian variety of physalis named “Plovdiv” has been selected (in the Department of Horticulture of the Agricultural University in Plovdiv), officially recognized in 2006 by the Executive Agency for Variety Testing, Field Inspection and Seed Control, and registered in the Official Variety List of Bulgaria [4]. In a series of

publications, the research team of Prof. N. Panayotov determined the optimal agro-ecological conditions and technologies for the production of high-quality physalis fruit in Bulgaria, as well as the options of extending the post-harvest storage and market supply with locally-produced fruits [5-11].

The oval, golden-to-orange colored, calyx-protected fruits of *P. peruviana* are highly valued for their palatability (combining an excellent taste, flavor and texture) and attractiveness, but mostly for their nutritional and health benefits. The fruit is rich in fructose, pectin, vitamins A, B, C and K, phytoosterols, tocopherols, polyunsaturated fatty acids, minerals, and many other macro- and micronutrients [1, 12-15]. The broad spectrum of medicinal properties of physalis fruit include antioxidant, antimycobacterial, immunomodulatory, anti-apoptotic, hypoglycemic, hepatoprotective, and many other activities [1, 15-19].

The other vegetative parts of the plant (calyx, leaves, stems, roots), however, are relatively less studied. Currently, they remain unutilized, although there is evidence of the presence of biologically active and other substances of potential interest [12], and they can be considered as a promising raw material for obtaining various extraction products. Ertürk et al. [20] identified a variety of phenolic and

* To whom all correspondence should be sent.
E-mail: tantoniewa@mail.bg

volatile compounds in ethanol extracts prepared from different parts (fruit, seeds, leaves, roots, body) of *P. peruviana* collected from Trabzon province, Turkey. The total phenolic and flavonoid contents in the leaf extracts were 1.368 mg GA/g and 0.635 mg QE/g, respectively, and they demonstrated antimicrobial and antioxidant activity. Wu et. al. [21, 22] determined the total flavonoid and phenol contents in ethanolic, aqueous and supercritical carbon dioxide extracts from physalis leaves, as well as various aspects of their biological activity (antioxidant, anticancer, anti-inflammatory, etc.). In a study on non-structural carbohydrate partitioning between plant organs, Fischer et al. [23] showed that physalis leaves accumulated considerable quantities of glucose, fructose, sucrose, and starch.

The dynamics of the process of extraction of biologically active substances from physalis leaves, however, has not been studied. From a theoretical point of view, the driving force of extraction, until the moment of the transfer of the soluble substances onto the solid-phase surface (i.e. within the plant particles), is the molecular diffusion, which is carried out in a static medium and abides by Fick's first law of diffusion [24]. The transfer of substances in the extracting liquid (effectiveness of the extraction) is a resultant from this driving force, which encompasses the concentration gradient within the solid particle and on its surface, and the diffusion resistance. The diffusion resistance depends mainly on the structure and composition of cell walls and protoplasm, the nature of the solvent and the temperature. A generalized expression of the diffusive properties of the plant material in the solid-liquid extraction is the coefficient of internal molecular diffusion (D_{int}) [25, 26], which is individual for each solid body. It reflects the cumulative effect of various factors on the mass transfer of soluble substances from the solid matrix to the liquid medium, such as the structure and the physical properties of the plant material and the solvent, as well as the abundance of extractible molecules, the temperature and duration of the process, etc. The coefficient increases with temperature and varies with time, since plant tissues undergo physicochemical transformations during the extraction, which alter their permeability. The coefficient of molecular diffusion is currently determined only experimentally, due to the heterogeneity and complexity of solid bodies [27]. Data about the coefficients of diffusion of various aromatic and edible plants are summarized by Georgiev and Stoyanova [28].

To the best of our knowledge, there is no data available about the content of tannins, or about the diffusion coefficients of tannins in extracts from

physalis leaves. Therefore, the aim of this study was to determine the coefficient of diffusion of tannins in ethanolic extracts obtained from the leaves of two physalis genotypes grown in Bulgaria.

EXPERIMENTAL

Plant material

Leaves of two genotypes of cultivated physalis (*Physalis peruviana* L.) were investigated. The first genotype represented the only Bulgarian variety named "Plovdiv" (PA), and was kindly provided by Prof. N. Panayotov from the Department of Horticulture at the Agricultural University, Plovdiv, Central South Bulgaria. The second genotype was organically-grown introduced variety, kindly provided by Mr. M. Peshovsky from Versol bio-farm, located in Lik village, municipality of Mezdra, North-West Bulgaria (PB).

Physalis leaves were hand-picked, air-dried at room temperature, and then stored in tightly closed plastic bags at a temperature of 5-8 °C until processing.

Methods

The raw material was characterized in terms of: moisture content – by drying it up to constant weight, at 105°C, and content of tannins – by titration of hot water extract with potassium permanganate solution using indigo carmine as indicator [29].

Determination of the diffusion coefficients

Extraction of dried physalis leaves was carried out in a batch static mode by maceration in the solvent under the following conditions: solvent – 30, 50, 70 and 95 % ethanol; size of leaf particles – 0.002×0.00125 m; ratio of raw material to solvent (hydromodule) = 1:10; temperature – 20, 40 and 60 °C; duration of extraction – 1 h. The solvent was fully replaced and analyzed for extracted tannins after each 10 min interval. The criterion for effectiveness of the process was the quantity of extracted tannins.

The coefficients of internal molecular diffusion (D_{int}) of tannins were determined for each 10-minute interval of extraction by the following equation [30]:

$$D_{int} = \frac{l^2 \cdot 2.3 \lg(E_1 - E_2)}{\pi^2 (\tau_1 - \tau_2)} \quad (1)$$

where: l - size of the material, cm; $(\tau_1 - \tau_2)$ – duration of extraction, s; E_1, E_2 – initial and final concentration of tannins in the solid phase, %.

All experiments were carried out in threefold repetition and mean values are presented on the figures below (created with MicroCal™ Origin software).

RESULTS AND DISCUSSION

The moisture content of the analyzed physalis leaves from the two genotypes (PA and PB) was 8.32 % and 8.79 %, respectively. The total concentration of tannins in the leaves was estimated to 9.62 % and 10.58 %, respectively, for the leaves from PA and PB.

In order to compute the diffusion coefficients, the content of extracted tannins for each 10-minute interval was determined, and the values were subsequently used to calculate the initial and the final concentration of tannins in the solid phase for the respective time period. The analysis of these experimental data supported the strong dependency of tannin yield on temperature and duration of the extraction. The quantity of extracted tannins for 10 min decreased with time (i.e. there was a steady trend of decrease in each series of six consecutive 10-minute extractions), irrespective of temperature, solvent concentration or genotype. Regardless of the origin of the leaves, maximum amount of tannins was extracted at 60°C, which could be attributed to

the positive influence of temperature on the extractive potential of the solvent. On the other hand, the solvent influenced the quantity of extracted tannins, too, and there were significant (at $p < 0.05$) differences in the extraction efficacy between the respective concentrations of ethanol (30 and 50% vs. 70 and 95%). The profiles of tannin transfer dynamics (i.e. tannin concentration change for the entire 1-hour period of extraction) were similar for the two genotypes in the case of 30 and 50% (and partially – of 70 %) ethanol, but differed significantly for the 95% solvent. It reflects the impact of solvent nature (decelerated solubility of tannins in concentrated ethanol, the occurrence of oxidative transformations in water), as well as the influence of the altered structure of the solid matrix, the different diffusion resistance in and around the particle, and other complex mechanisms on tannin extraction, changing with time and temperature.

On the basis of these experimental data the diffusion coefficients of tannins (D_{int}) were calculated, and their variations are presented on figures 1 – 4.

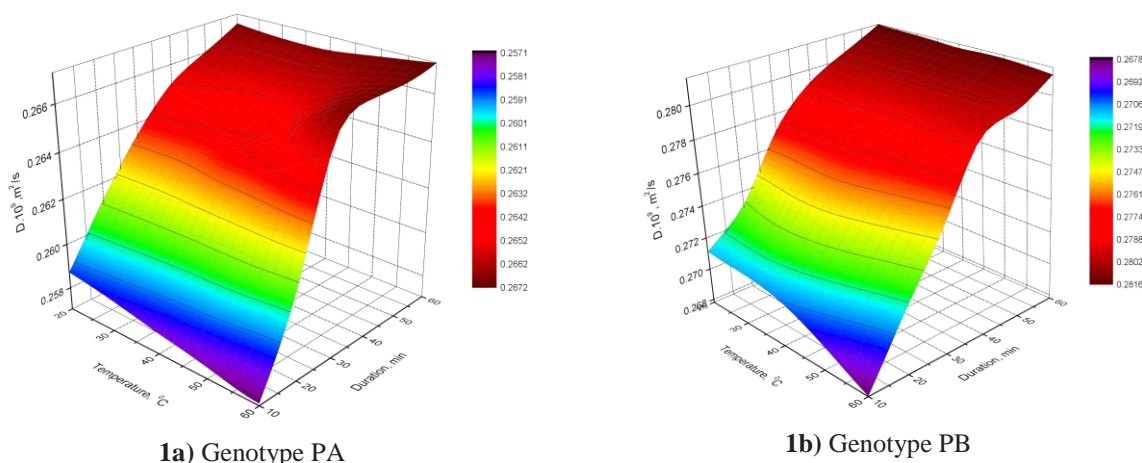


Fig. 1. Diffusion coefficients of tannins in extracts from physalis leaves with 30 % ethanol.

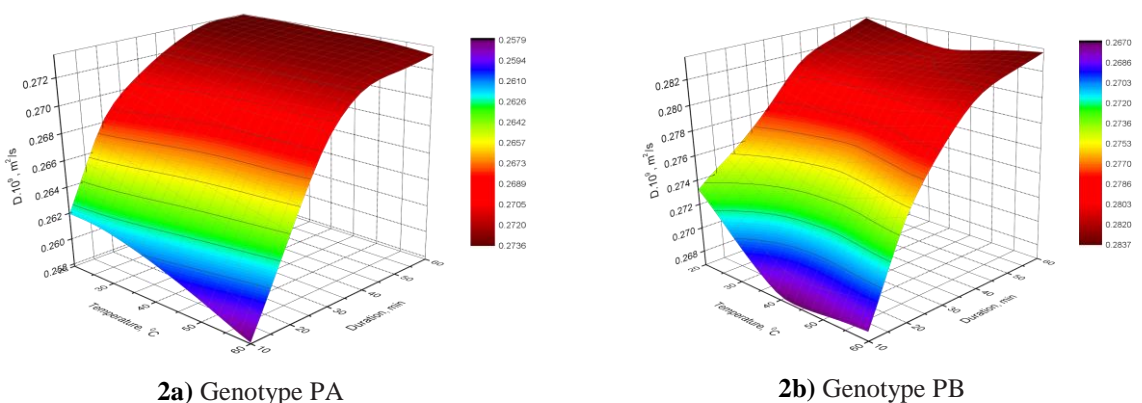


Fig. 2. Diffusion coefficients of tannins in extracts from physalis leaves with 50 % ethanol.

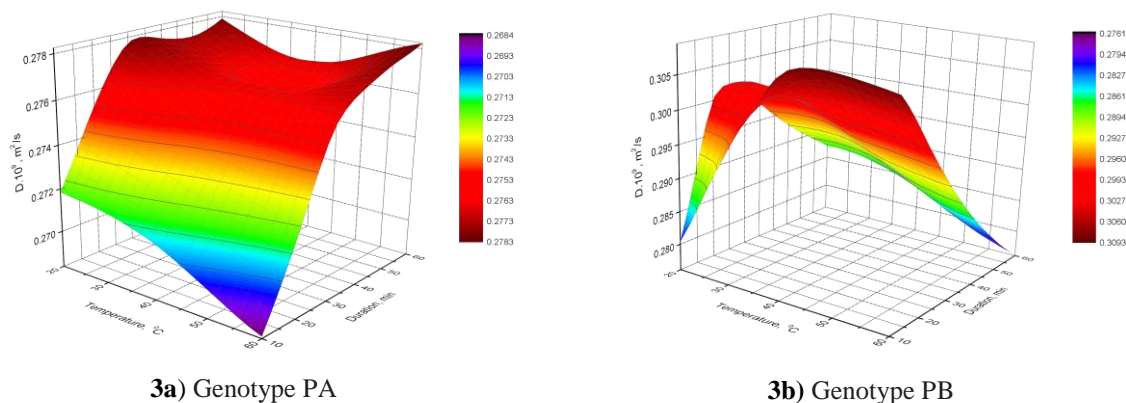


Fig. 3. Diffusion coefficients of tannins in extracts from physalis leaves with 70 % ethanol.

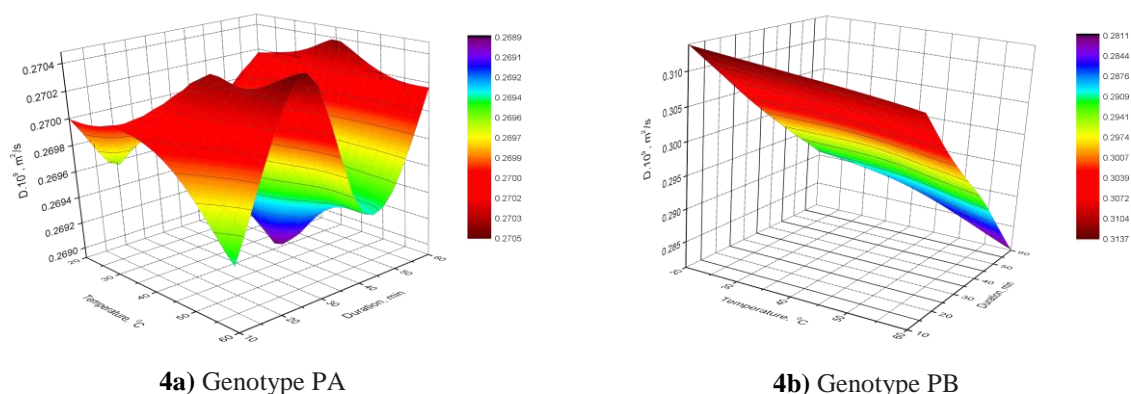


Fig. 4. Diffusion coefficients of tannins in extracts from physalis leaves with 95 % ethanol.

Reasonably, with the increase in the temperature, the values of the diffusion coefficient also increased (with maximums established at 60°C), for the two leaf genotypes.

The highest values of the coefficient of internal molecular diffusion at 60°C for the leaves from PA genotype were as follows: with 30% ethanol – $0.267 \times 10^{-9} \text{ m}^2/\text{s}$, with 50% ethanol – $0.273 \times 10^{-9} \text{ m}^2/\text{s}$, with 70% ethanol – $0.278 \times 10^{-9} \text{ m}^2/\text{s}$, and with 95% ethanol – $0.271 \times 10^{-9} \text{ m}^2/\text{s}$.

The highest values of D_{int} for the leaves from PB genotype (at 60°C) were as follows: with 30% ethanol – $0.281 \times 10^{-9} \text{ m}^2/\text{s}$, with 50% ethanol – $0.283 \times 10^{-9} \text{ m}^2/\text{s}$, with 70% ethanol – $0.308 \times 10^{-9} \text{ m}^2/\text{s}$, and with 95% ethanol – $0.310 \times 10^{-9} \text{ m}^2/\text{s}$.

The differences in the values of the coefficients on a solvent-concentration base were minimal, for the two genotypes studied. Still, as the graphics reveal, slightly higher values of the coefficient were obtained in the case of extraction with 50 and 70% ethanol, which supports the suggestion that these concentrations favor the diffusion of tannins.

Although the respective values of D_{int} were slightly higher for the leaves from PB genotype, the numerical differences between the genotypes were insignificant. The outline of the graphical dependencies of the diffusion coefficient was practically equal for genotypes PA and PB in the case of extraction with 30 and 50% ethanol. The coefficient of diffusion took higher values in the final time intervals, which could be explained by the higher concentration of the extracted molecules, due to the overcome diffusion resistance in the end of the process. An exception was the decreasing trend of D_{int} variation during the extraction of genotype PB with 95% ethanol (and to some extent - with 70%). It could be attributed to the maximal amounts of substances extracted in the initial periods of the process, and their reduced availability by its end.

Our study on physalis leaves showed lower values ($0.28 \times 10^{-9} - 0.31 \times 10^{-9} \text{ m}^2/\text{s}$) of the diffusion coefficients of tannins, compared to data about ethanol extracts from other plants, for example – from laurel leaves ($2.05 \times 10^{-9} \text{ m}^2/\text{s}$) [31], from sage leaves ($16.61 \times 10^{-9} \text{ m}^2/\text{s}$) [32], from hawthorn leaves ($9.82 \times 10^{-9} - 548 \times 10^{-9} \text{ cm}^2/\text{s}$) [33], from paulownia leaves ($68.9 \times 10^{-12} \text{ cm}^2/\text{s}$) [34]. These results are

connected to the nature of the raw material (cell structure, porosity, size, etc.), the available bioactive substances and the specific conditions of the extraction process – solvent and temperature.

CONCLUSIONS

To the best of our knowledge, this study presents for the first time results about the extraction of tannins from physalis (*P. peruviana* L.) leaves, and in particular – about the coefficient of diffusion of tannins, known as a characteristic index of the extraction of plant materials. The highest values of the diffusion coefficients for the two studied physalis genotypes were obtained at 60°C – 0.28×10^{-9} m²/s and 0.31×10^{-9} m²/s, respectively for PA and PB genotypes. The outcomes of the study provide grounds for further investigation on the physalis varieties grown in Bulgaria, with the purpose of revealing more aspects of their composition, bioactivity, benefits and potential for use.

Acknowledgements: We acknowledge the financial support from the Science Fund of the University of Food Technologies, project 04/18-N. We are most thankful to Prof. N. Panayotov from the Agricultural University, Plovdiv and to Mr. M. Peshovsky from Versol Bio-farm, Lik village for providing the physalis leaves.

REFERENCES

1. L. Puente, C. Pinto-Munoz, E. Castro, M. Cortes, *Food Res Int.*, **44**, 1733 (2011).
2. J.G. Alvarez-Herrera, H.E. Balaguera-López, G. Fischer, *Acta horticulturae*, **928**, 163 (2012).
3. N. Panayotov, S. Tsorlianis, *Acta Hort.*, **579**, 373 (2002).
4. N. Panayotov, *Agrarian Sciences*, **1**, 9 (2009) (in Bulgarian).
5. N. Panayotov, *Agriculture and Food*, **4**, 115 (2016).
6. N. Panayotov, A. Popova, *Turkish J. Agric. Nat. Sci.*, **SI 1**, 1134 (2014).
7. N. Panayotov, A. Popova, *Turkish J. Agric. Nat. Sci.*, **SI 1**, 1141 (2014).
8. N. Panayotov, A. Popova, *Agro-knowledge J.*, **17**, 267 (2016).
9. N. Panayotov, A. Popova, *Acta Horticulturae et Regiotecturae*, **SI 1**, 18 (2016).
10. N. Panayotov, M. Dimitrova, L. Krasteva, D. Dimova, D. Svetleva, *Agro-knowledge J.*, **13**, 547 (2012).
11. N. Panayotov, D. Dimova, A. Popova, V. Ivanova, D. Svetleva, *Optimization of ornamental and garden plant, technologies and environment*, **7**, 157 (2016).
12. Y.-J. Zhang, G.-F. Deng, X.-R. Xu, S. Wu, S. Li, H.-B. Li, *Int. J. Food Nutr. Saf.*, **3**, 15 (2013).
13. M. Yilmaztekin, *Sci. World J.*, **2014**, 8 pages (2014).
14. M. Sathyadevi, S. Subramanian, *Asian J. Pharm. Clin. Res.*, **8**, 152 (2015).
15. M. Ramadan, A. El-Ghorab, K. Ghanem, *J. Arab Soc. Med. Res.*, **26**, 56 (2017).
16. M. Dkhil, S. Al-Quraishy, M. Diab, M. Othman, A. Aref, A. Abdel Moneim, *Food Chem. Toxicol.*, **74**, 98 (2014).
17. A. Puspaningtyas, *Int. Curr. Pharm. J.*, **3**, 265 (2014).
18. A. Eken, B. Ünlü-Endirlik, A. Baldemir, S. Ilgün, B. Soykut, O. Erdem, G. Akay, *J. Clin. Anal. Med.*, **7**, 291 (2016).
19. D. Dag, M. Kilercioglu, M. Oztop, *LWT – Food Sci. Technol.*, **83**, 86 (2017).
20. O. Ertürk, M. Colayvaz, Z. Can, Ü. Karaman, K. Korkmaz, *Indian J. Pharm. Educ. Res.*, **51**, 213 (2017).
21. S. Wu, J. Tsai, S. Chang, D. Lin, S. Wang, S. Huang, L. Ng, *J. Ethnopharmacol.*, **108**, 407 (2006).
22. S. Wu, S. Chang, D. Lin, S. Wang, F. Hou, L. Ng, *Food Chem. Toxicol.*, **47**, 1132 (2009).
23. G. Fischer, C. Ulrichs, G. Ebert, *Agronomía Colombiana*, **33**, 155 (2015).
24. A. Kasatkin. Basic processes and apparatuses in chemical technology, Nauka I izkustvo, Sofia, 1960 (in Bulgarian).
25. V. Kafarov. Basics of mass transfer, Visshaya shkola, Moskva, 1962 (in Russian).
26. G. Akselrud, V. Lisyanski. Extraction in the system “solid – liquid”, Khimia, Leningrad, 1974 (in Russian).
27. A. Stoyanova, E. Georgiev. Technology of essential oils, Acad. publ. house UFT, Plovdiv, 2007 (in Bulgarian).
28. E. Georgiev, A. Stoyanova. A guide for the specialist in aromatic industry, BNAEOPC, Plovdiv, 2006 (in Bulgarian).
29. Russian Pharmacopoeia, 11th Edition, Moscow, 1990.
30. V. Beloborodov, V. Dementii, B. Voronenko, *Sci. Works VNIIJ*, **28**, 102 (1971) (in Russian)
31. G. Stefanova, S. Tasheva, S. Damianova, A. Stoyanova, *Sci Works UFT*, **64**, 70 (2017).
32. S. Mollova, PhD Thesis, UFT, Plovdiv (2017) (in Bulgarian).
33. M. Ergezen, PhD Thesis, UFT, Plovdiv (2014) (in Bulgarian).
34. S. Tasheva, DSc Thesis, UFT, Plovdiv (2014) (in Bulgarian).

Chemical composition of the dill essential oils (*Anethum graveolens* L.) from Bulgaria

M. D. Dimov^{1*}, K. Z. Dobрева¹, A. S. Stoyanova²

¹Trakia University, Faculty of Technics and Technologies, 38 Graf Ignatiev Str., 8600 Yambol, Bulgaria,

²University of Food Technologies, Technological Faculty, 26 Maritza Blvd., 4003 Plovdiv, Bulgaria

Received October 4, 2018; Revised January 4, 2019

The oil of dill (*Anethum graveolens* L.) from Bulgaria harvested during various growth stages of the plant (flower, herb and fruits) was investigated by GC and GC/MS. The yields of flower, herb and fruit oils were 0.36 % v/w, 0.90 % v/w and 3.61 % v/w, respectively. The main compounds (over 3 %) in flower oil were: myristicin (23.24 %), carvacrol (22.04 %), carvone (18.93 %), limonene (11.20 %), 3,9-oxy-*p*-menth-1-ene (7.59 %), α -phellandrene (6.50 %), and dihydrocarvone (4.63 %). The major constituents (over 3 %) in herb oil were: α -phellandrene (21.83 %), carvacrol (20.85 %), limonene (18.96 %), 3,9-oxy-*p*-menth-1-ene (12.31 %), carvone (8.40 %), myristicin (7.11 %) and *p*-cymene (3.34 %). The main components (over 3 %) in fruit oil were: carvone (33.57 %), myristicin (24.21 %), limonene (15.02 %), dihydrocarvone (13.13 %) and carvacrol (4.92 %).

Keywords: *Anethum graveolens* L., essential oils, chemical composition

INTRODUCTION

Dill (*Anethum graveolens* L.) is an annual aromatic plant of the Apiaceae family. The plant is native to Europe and commercially produced in a number of European, American, and Asian countries [1, 2].

Dill seed oil is prepared by distillation from the crushed ripe fruits. Its main constituents are limonene (over 40 %) and (+)-carvone (over 60 %) [1–13].

Dill weed oil is obtained by distillation from dill weed (herb) before the fruit become mature. The typical flavor of the oil is due to α -phellandrene (10 – 20 %), limonene (30 – 40 %); (+)-carvone (30 – 40 %) and dill ether (over 10%) [1, 2, 6, 12–18].

Dill oils are used as flavoring in different foods [1, 2, 12, 19, 20].

The most important medicinal effects of dill oils are due to its antimicrobial [7, 11–13] and antioxidant [12, 13] activities, and pharmacological [12, 18] properties. Some of these activities are related to the major compound of the oils (+)-carvone.

The aim of present investigated is to examine the oil and its chemical composition of different parts (flowers, herb, and fruits) of dill grown in Bulgaria.

EXPERIMENTAL

Plant material

The plant parts of dill (*Anethum graveolens* L.) were harvested in the vicinity of the town of Yambol, Bulgaria of 2017.

The plant parts were air-dried immediately after harvesting in a shady site for 10 days, packed in paper bags and kept in a dark, dry and cool place.

The moisture content of the fresh raw materials was determined by drying to constant weight, at 105 °C [21].

Essential oil isolation

The air-herbs were cut in pieces (1 cm long) and the air-fruits were ground in laboratory mill to a size of 0.7 – 1.0 cm. The oil content in the plant parts was determined for 3 h in laboratory glass apparatus according to the British Pharmacopoeia, modified by Balinova and Diakov [22]. The oil obtained was dried over anhydrous sodium sulfate and stored in tightly closed dark vials at 4°C until analysis.

Chemical composition of the essential oil

Gas chromatography (GC) analysis was performed using an Agilent 7890A gas chromatograph, an HP-5 ms (30 m×250 μ m ×0.25 μ m) column, a temperature of 35 °C/3 min, 5 °C/min to 250 °C for 3 min, 49 min in total; helium gas as carrier at 1mL/min constant speed; split ratio 30:1.

GC/MS analysis was carried out on an Agilent 5975C mass spectrometer, with helium gas as a carrier, the column and temperature being the same as the GC analysis.

The identification of chemical compounds was made by comparison to their relative retention time and library data. The components identified were arranged according to the retention time and their quantity was given in percentage.

* To whom all correspondence should be sent.

E-mail: midimow@abv.bg

All experiments were carried out in threefold repetition and the mean values with the respective error have been presented in the tables and figures below.

RESULTS AND DISCUSSION

The moisture of the flowers was 70.27 %, of herb was 79.71 %, and of fruits was 10.64 %.

The essential oil yield has been shown in Table 1. All essential oils were light yellow liquids and had a specific odor.

The data in the Table 1 shown that the oil yield during vegetative stage was different with those reported in literature, for example for flower oil (0.08 – 0.32 %) [9, 10], for herb oil (0.3 – 1.0 %) [6, 10, 16 – 18], and for fruit oil (1.75 – 4.0 %) [6, 8 – 10]. The differences in the oil quantities with those reported in literature were probably due to the climatic conditions in the respective place where the plant grows and the part of the plant processed.

The changes in the oil quality have been shown in Table 1.

The essential oil from the different plant organs contained the same compounds, but the quantitative differences between all main compounds were quite large.

As seen 14 components representing 98.11 % of the total content were identified in the flower oil. Nine of them were in concentrations over 1 % and the rest 5 constituents were in concentrations under 1 %. As seen the major constituents (over 3 %) of the

oil are as follows: myristicin (23.24 %), carvacrol (22.04 %), carvone (18.93 %), limonene (11.20 %), 3,9-oxy-*p*-menth-1-ene (7.59 %), α -phellandrene (6.50 %) and dihydrocarvone (4.63 %).

Seven compounds representing 92.88 % of the total content identified in the herb oil. As seen the major constituents (over 3 %) of the oil are as follows: α -phellandrene (21.83 %), carvacrol (20.85 %), limonene (18.96 %), 3,9-oxy-*p*-menth-1-ene (12.31 %), carvone (8.40 %), myristicin (7.11 %) and *p*-cymene (3.34 %).

As seen nine components representing 92.01 % of the total content were identified in the fruit oil. Five of them were in concentrations over 1 % and the rest four constituents were in concentrations under 1 %. As seen the major constituents (over 3 %) of the oil are as follows: carvone (33.57 %), myristicin (24.21 %), limonene (15.02 %), dihydrocarvone (13.13 %) and carvacrol (4.92 %).

The data shown that the highest percentage for myristicin and carvacrol is in the flowering stage, limonene and α -phellandrene in the vegetative stage, and carvone and myristicin in the fruiting stage. We also find that carvone percentage has reverse behavior, where carvone and myristicin percentage increase with the vegetative stage.

The difference in chemical composition of our investigations and the reported data may be due to environmental conditions under which the plant has grown as well as the variation in conditions of analysis.

Table 1. Percent composition of dill essential oils.

№	Components	RI*	Content, %		
			Flower oil	Herb oil	Fruit oil
1	α -Pinene	939	0.19±0.00	nd**	nd
2	β -Pinene	979	0.14±0.00	nd	nd
3	α -Phellandrene	998	6.50±0.02	21.83±0.08	0.19±0.00
4	<i>p</i> -Cymene	1024	2.05±0.00	3.34±0.01	0.40±0.00
5	Limonene	1030	11.20±0.04	18.96±0.06	15.02±0.05
6	Terpinolene	1088	0.15±0.00	nd	nd
7	3,9-oxy-1-menth-1-ene	1073	7.59±0.03	12.31±0.05	0.32±0.00
8	Dihydrocarvone	1179	4.63±0.01	nd	13.13±0.05
9	Carvone	1205	18.93±0.06	8.40±0.03	33.57±0.11
10	Thymol	1266	1.15±0.00	nd	0.25±0.00
11	Carvacrol	1277	22.04±0.08	20.85±0.07	4.92±0.02
12	β -Caryophyllene	1419	0.17±0.00	nd	nd
13	β -Bisabolene	1496	0.13±0.00	nd	nd
14	Myristicin	1502	23.24±0.09	7.19±0.03	24.21±0.09
Yield of essential oils, % (v/w)			0.36±0.00	0.90±0.02	3.61±0.01

* The retention index was calculated for all volatile constituents using a homologous series of *n*-alkanes C₈ – C₁₆, ** nd - not determined.

The classification of the identified compounds, based on functional groups, is summarized in Figure 1.

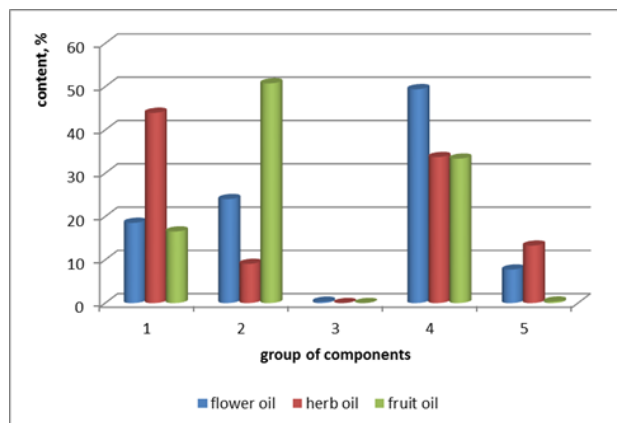


Fig. 1. Group of components in dill oils, %:
1 – monoterpene hydrocarbons; 2 – oxygenated monoterpenes; 3 – sesquiterpene hydrocarbons; 4 – phenyl propanoids; 5 – others (benzofurans)

Phenyl propanoids (49.41 %) are the dominant group in the flower oil, followed by oxygenated monoterpenes (24.01 %), monoterpene hydrocarbons (18.53 %), others (7.74 %) and sesquiterpene hydrocarbons (0.31 %).

Monoterpene hydrocarbons (43.95 %) are the dominant group in herb oil, followed by phenyl propanoids (33.73 %), others (13.27 %) and oxygenated monoterpenes (9.05 %).

Oxygenated monoterpenes (50.76 %) are the dominant group in the fruit oil, followed by phenyl propanoids (33.37 %), monoterpene hydrocarbons (16.53 %) and others (0.34 %).

CONCLUSIONS

Significant qualitative and quantitative differences in chemical composition of dill oils were detected. The main components in the flower oil are the phenyl propanoids myristicin (23.24 %) and carvacrol (22.04 %), oxygenated monoterpene carvone (18.93 %) and monoterpene hydrocarbon limonene (11.20 %), in the herb oil dominated the phenyl propanoid carvacrol (20.85 %) and monoterpene hydrocarbons α -phellandrene (21.83 %) and limonene (18.96 %), while in the fruit oil dominated oxygenated monoterpene carvone (33.57 %) and phenyl propanoid myristicin (24.21 %).

REFERENCES

1. K. Bauer, D. Garbe, H. Surburg, Common fragrance and flavour materials. Preparation, properties and uses. IV Compl. Revised Edition. Wiley-VCH Verlag GmbH, Weinheim. Germany. 2001.
2. E. Georgiev, A. Stoyanova, A guide for the specialist in aromatic industry, Plovdiv. 2006.
3. R. K. Baslas, R. Gupta, K. K. Baslas, *Flavour Ind.*, **2**, 241 (1971).
4. M. B. Embong, D. Hadziyev, S. Molnar, *Can. Inst. Food Sci. Technol.*, **10**, 208 (1977).
5. J. J. C. Scheffer, A. Koedam, A. Baerheim-Svendsen, *Medd. Nor. Farm. Selsk.*, **39**, 161 (1977).
6. D. Charles, J. Simon, M. Widrlechner, *J. Essent. Oil Res.*, **7**, 11 (1995).
7. L. Jirovetz L., G. Buchbauer, A. Stoyanova, E. Georgiev, S. Damianova, *Food Chemistry*, **51**, 3854 (2003).
8. A. Yili, H. Yimamu, V. V. Maksimov, H. A. Aisa, O. N. Veshkurova, S. Salikhov, *Chemistry of Natural Compounds*, **42**, 491 (2006).
9. V. Radulescu, M. L. Popescu, D.-C. Ilies, *Farmacia*, **58**, 594 (2010).
10. H. A. H. Said Al Ahl, A. M. Z. Sarhan, A. D. M. Abou Dahab, El-S. N. Abou Zeid, M. S. Ali, N. Y. Naguib, *Int. Journal Plant Sci Ecol.*, **1**, 93 (2015).
11. H. A. H. Said Ahl, A. M. Sarhan, A.D. M. Abou Dahab, El-S. N. Abou-Zeid, M. S. Ali, N. Y. Naguib, M. A. El-Bendary, *Int. Journal Plant Sci Ecol.*, **1**, 98 (2015).
12. K. K. Chahal, Monika, A. Kumar, U. Bhardwaj, R. Kaur, *Journal of Pharmacognosy and Phytochemistry*, **6**, 295 (2017).
13. M. Dimov, K. Dobreva, S. Damyanova, A. Stoyanova, Annual of Assen Zlatarov University, Burgas, Bulgaria, **46**, 37 (2017).
14. P. Schreier, F. Drawert, I. Heindze, *Lebensm.-Wiss. Technol.*, **14**, 150 (1981).
15. R. Huopalahti, R. R. Linko, *J. Agric. Food Chem.*, **31**, 331 (1983).
16. J. A. Pino, E. Roncal, *J. Essent. Oil Res.*, **7**, 219 (1995).
17. M. Baeva, T. Sapundzhieva, P. Merdzhanov, A. Pavlova, I. Alexieva, A. Stoyanova, *Journal of Food and Packaging Science Technique and Technologies*, **2**, 129 (2013).
18. M. Kazemi, *Nat. Prod. Res.*, **29**, 551 (2015).
19. I. Kostova, D. Dimitrov, M. Ivanova, R. Vlaseva, S. Damianova, N. Ivanova, A. Stoyanova, O. Gubenia, *Ukrainian Food Journal*, **3**, 516 (2014).
20. I. Kostova, S. Damyanova, N. Ivanova, A. Stoyanova, *Proceeding of University of Ruse*, **56**, 113 (2017).
21. Russian Pharmacopoeia. Moscow. 1990.
22. A. Balinova, G. Diakov, *Plant Science*, **2**, 79 (1974) (in Bulgarian).

Physicochemical characteristic of chia seed oil from Peru

G. Uzunova¹, M. Perifanova-Nemska¹, Zh. Petkova², St. Minkova³, Kr. Nikolova^{3*}

¹University of Food Technology, Technological Faculty, 26 Blvd. Maritza, Plovdiv 4000, Bulgaria,

²University of Plovdiv "Paisii Hilendarski", Faculty of Chemistry, Dept. of Chemical Technology, 24 Tzar Asen Str., Plovdiv 4000, Bulgaria

³Medical University, Faculty of Pharmacy, Dept. of Physics and Biophysics, 84 Blvd. Tzar Osvoboditel, Varna 9000, Bulgaria

Received October 17, 2018; Revised January 4, 2019

Main chemical components of chia seeds (imported from Peru) and physicochemical characteristics of their oil were examined. The oil content of the seeds was 30.37% and protein content was 37.96%. The oil was obtained by pressing the chia seeds in Bulgarian factory. The main important physicochemical characteristics of chia seed oil have also been determined. The relative density of the oil at 20 °C was 0.9288, refractive index at 20 °C – 1.4810, acid value – 1.68 mgKOH/g, peroxide value – 1.95 meq active oxygen/kg and oxidative stability – 2.4 h.

Unsaturated fatty acids (85.7%) predominated in the fatty acid profile. The amount of linolenic and linoleic fatty acids was 94% of unsaturated fatty acids in the oil. The content of saturated fatty acids was 14.3%. The quantity of unsaponifiable matters was 0.83%. Total sterols in the oil were 0.28% and the content of tocopherols – 140 mg/kg.

Keywords: Chia seed oil, *Salvia hispanica* L., physicochemical characteristic, oxidative stability

INTRODUCTION

The chia seeds (*Salvia hispanica* L.) are used for a long time as a food additive in America by Indians and by people from Mexico. This plant is grown in the regions with tropic and subtropical climate. The different climate, the area of growth and agrochemical factors influence the physicochemical properties of the seeds.

At the current stage the chia is cultivated in Mexico, Peru, Argentina etc. [1, 2, 3]. The seeds, which are similar to these from *Salvia*, are small and hard. The plant was mainly used for decoration in the past. Chia seeds have been an object of various investigations and it has been shown that they are a source of important food ingredients. The seeds are rich in glyceride oil (25-38%), proteins (15-25%), carbohydrates (26-41%) and fibers (18-30%), and also contain minerals (4-5%) and vitamins [1, 2, 3].

Chia seed oil is rich in polyunsaturated fatty acids (PUFAs), particularly omega-3 (n-3) and omega-6 (n-6) which are beneficial to human health. The major fatty acids in the oil from chia are as follow: n-6 and n-3 (60.4-63.04%), which can contribute to a good cleaning of the blood vessels from LDL cholesterol and this way improve the circulation of the blood [4].

Except linolenic acid, chia seed oil also contains biologically active substances – sterols, tocopherols, phospholipids. There are some results about basic physicochemical characteristic of different chia oils from different countries. For example, extracted chia

seed oils from Guatemala, Argentina and Mexico have relative density of 0.9241-0.9248 and the refraction index is 1.4763 – 1.4768. Saponification value ranges from 193 to 222 mg KOH/g. The acid value of the pressed and extracted oil is 0.91 and 1.64 – 2.053 mg KOH/g, respectively. The iodine value of the oils from different regions (Argentina, Mexico, Guatemala) is 193-210 gI₂/100g, which is connected with the amount of saturated fatty acids in the oils [1, 2, 3]. Peroxide value of oil from Mexico and Guatemala is – 17.5 and 1.64 meq active oxygen/kg, respectively [1, 2, 5]. Unsaponifiable matters in the pressed oil are 0.68 – 0.85%, in the extracted oil – 0.839-1.27% and it is related to region where the seed is grown [1, 2, 3, 5]. The oxidative stability for pressed and extracted oil (2.3-2.8 h) is lower than that of other vegetable oils [1, 2].

According to some previous studies in the fatty acid composition predominate unsaturated fatty acids – linolenic (63-69%), followed by linoleic acid (16-26%). From the saturated fatty acids palmitic (5.5-6.6%) and stearic (2.7-4.4%) acids are in the highest amount [1, 2, 3, 6, 7].

Total tocopherols in the chia oils from Argentina and Mexico is 446 and 200 mg/kg, respectively and γ - tocopherols (94.4%) predominate in the tocopherol fraction. Sterol content in the oil is 4132 mg/kg and β -sitosterol is in the highest amount (49.8%) [6, 7].

The aim of the present work is to be investigated the main chemical components of chia seeds

* To whom all correspondence should be sent.
E-mail: kr.nikolova@abv.bg

(imported from Peru) and physicochemical characteristics of their oil and to be compared the obtained results to these of chia seed oils from other countries.

EXPERIMENTAL

Samples

Analyzed chia seeds, used in Bulgaria, are imported from Peru. The oil content, moisture and protein were determined. Oil was extracted from ground seeds with hexane for 4 h by Soxhlet equipment. The extract was dried in vacuum drier at 60 °C after evaporation of solvent and the oil content in the seeds was determined [8]. Protein determination is performed by using the method of Kjeldahl [9]. The moisture was determined by standard procedure by AOAC [10].

The examined sample of chia seed oil is obtained by cold pressing method in a small factory in Bulgaria.

Methods

Analysis of fatty acids. The fatty acid composition of oils is determined by gas chromatography (GC) after transmethylation of the respective sample following the procedures by ISO [11]. GC was performed on a HP 5890 gas chromatograph equipped with a 75 m × 0.18 mm capillary column Supelco FP - 2560 and a flame ionization detector. The column temperature was programmed from 140°C (5 min), at 4 °C/min to 240 °C (3 min); injector and detector temperatures were kept at 250°C. Identification of fatty acids is performed by comparison of retention times with those of a standard mixture of fatty acids subjected to GC under identical experimental conditions [12].

Analysis of tocopherols. Tocopherols were determined directly in the oil by high performance liquid chromatography on a "Merck-Hitachi" instrument equipped with 250 mm × 4 mm Nucleosil Si 50-5 column and fluorescent detector "Merck-Hitachi" F 1000. The operating conditions were as follows: mobile phase of n-hexane:dioxan 96:4 (v/v), flow rate 1.0 ml/min, excitation 295 nm, emission 330 nm [13]. 20 µl 1% solution of oil in hexane was injected. Tocopherols are identified by comparing the retention times with those of authentic individual tocopherols.

Table 2. Physicochemical properties of chia oils from different countries

Parameters	Chia oil			
	Peru	Mexico, [5]	Argentina, [1,6]	Guatemala, [1, 2]
Peroxide value, meq active oxygen/kg	1.95	17.5	No data-	No data
Acid value, mgKOH/g	1.68	2.053	2.05	1.64
Free fatty acids, % (oleic acid)	0.85	1.02	1.02	0.82
Iodine value, g I ₂ /100g	208.3	193.45	210.5	No data
Saponification value, mgKOH/g	197.9	222.66	193.09	193.01
Relative density 20 °C	0.9288	0.9241	No data	No data
Refractive index, 20 °C	1.481	1.4761	1.4768	1.4763
Oxidative stability, h	2.4	No data	No data	No data

Analysis of sterols. Unsaponifiables are determined after saponification of the glyceride oil and extraction with hexane [14]. Quantification of sterols was carried out spectrophotometrically (at 597 nm), after isolation of sterols from other unsaponifiable matter by thin layer chromatography on Silica gel 60 G in the mobile phase diethyl ether: hexane (1:1 v/v) [15].

Sterol composition is determined on HP 5890 gas chromatograph equipped with 30 m × 0.25 mm DB 5 capillary column and flame ionization detector. Temperature gradient is from 90 °C (held for 2 min) to 290 °C at 15 °C /min then to 310 °C at 4 °C /min and held at this temperature for 10 min; the injector temperature is 300 °C and the detector temperature is 320 °C. Identification was performed by comparison of the retention times with those of a standard mixture of sterols [16].

Physicochemical characteristics. The physicochemical properties (iodine value, acid value, peroxide value, saponification value, refractive index and relative density) of cold pressed chia seed oil were analysed following the standard procedures by ISO [17, 18, 19, 20, 21, 22]. Oxidative stability is measured at 100 °C by Rancimat 679 equipment (Metron Switzerland) [23].

All experiments were carried out in triplicates.

RESULTS AND DISCUSSION

The oil content, moisture and protein content of chia seeds have been determined. The results are given in table 1.

The oil content is 30.37%, it is similar to the data from authors from different countries [1, 2, 3]. Seeds are with moisture 8.66%, protein content - 37.96%. The content of protein is higher than the data from other countries [1, 2, 3].

There are not differences in more of physicochemical properties of investigated chia oil from Peru and oils from other countries.

Table 1. Main chemical components of chia seeds

Components	%
Oil	30.37
Moisture	8.66
Protein	37.96

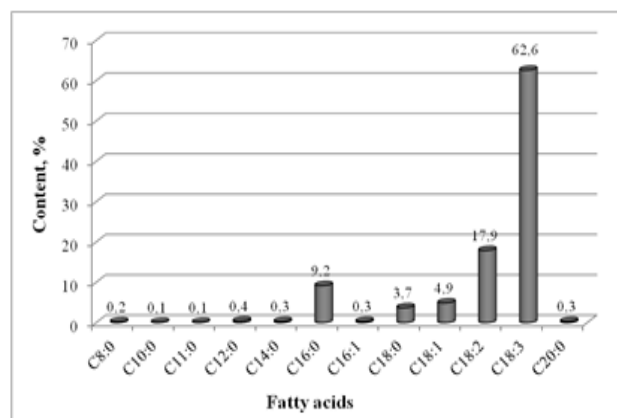


Figure 1. Fatty acid composition of chia oil from Peru C_{8:0} – Caprylic; C_{10:0} – Capric; C_{11:0} – Undecanoic; C_{12:0} – Lauric; C_{14:0} – Myristic; C_{16:0} – Palmitic; C_{16:1} – Palmitoleic; C_{18:0} – Stearic; C_{18:1} – Oleic; C_{18:2} – Linoleic; C_{18:3} – Linolenic; C_{20:0} – Arachinic

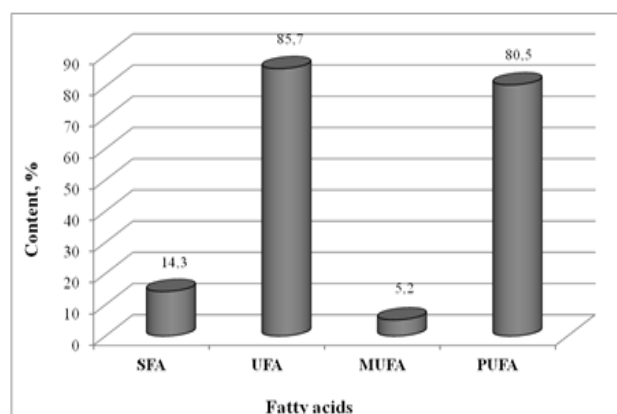


Figure 2. Content of saturated (SFA), unsaturated (UFA), monounsaturated (MUFA) and polyunsaturated fatty acids (PUFA)

Table 3. Biologically active components

Components	Content
Sterols, %	
- in the oil	0.28
- in unsaponifiable matter	34.3
Sterol composition, %	
Campesterol	10.6
Stigmasterol	2.5
β -Sitosterol	85.5
Δ^5 -Avenasterol	1.4
Tocopherols, mg/kg	
- in the oil	140
Tocopherol composition, %	
α – tocopherol	4.8
γ – tocopherol	95.2

The peroxide and the acid values of oil from Peru are lower than other oils [1, 5, 6]. The iodine value

is higher, because there is higher quantity of unsaturated fatty acids in the examined oil.

The fatty acid /FA/ composition is presented on figure 1.

The main fatty acids in the triacylglycerol fraction are linolenic and linoleic – 62.6% and 17.9%. Palmitic acid predominates in the fraction of saturated fatty acids representing 9.2% of the total fatty acid content. Unsaturated fatty acids predominate and their amount is 85.7%. The linolenic and linoleic fatty acids are 94% of unsaturated fatty acids in the oil.

The content of saturated (SFA), unsaturated (UFA), monounsaturated (MUFA) and polyunsaturated fatty acids (PUFA) of chia seed oil is presented in Figure 2.

Saturated fatty acids are 14.3% of all fatty acids in the oil. The content of polyunsaturated fatty acids (80.5%) is considerably higher than monounsaturated fatty acids (5.2%).

The quantity of unsaponifiable matter is 0.83%. The total tocopherol and sterol content in the oil are lower than the results for oil from other countries 140 mg/kg to 400 mg/kg [8] for tocopherols and 0.28% to 0.41% for sterols. γ - Tocopherol (95.2%) predominates in the tocopherol fraction, which is in agreement with results from previous studies of chia oil from different regions (Table 3).

Sterols are present in the unsaponifiable matters and their amount is 34.3%. Their total content in the oil was found to be 0.28%. β -Sitosterol (85.5%) predominates in the sterol fraction, which is higher than those in chia seed oil from different region (49.8%) [7]. Apart from β -sitosterol are also observed campesterol (10.6%), stigmasterol (2.5%) and Δ^5 -avenasterol (1.4%).

CONCLUSIONS

The examined chia seeds, imported from Peru, are a good source of oil and protein. The oil possesses a good quality and has higher quantity of unsaturated fatty acids, especially linolenic acid. The oxidative stability of the oil is 2.4 h. Total tocopherol and sterol content is lower than the result from previous studies, but the amount of β -sitosterol is two times higher than that of chia seed oils from other countries.

REFERENCES

1. V.Y. Ixtaina, M.L. Martínez, Sportono, V. Mateo, C.M. Maestri, D.M. Diehl, B.W.K. Nolasco, M.C. Tomás, *Journal of Food Composition and Analysis*, **24**, 166-174 (2011).
2. V. Ixtaina, S. Nolasco, Mabel C. Tomás, *JOCS*, **89**, 1077-1090, (2012).

3. Y.V. Ixtaina, S.M. Nolasco, and M.C. Tomas, *Industrial Crops and Products*, **28**, 286-293 (2008).
4. E. Villanueva, E., G. Rodríguez, E. Aguirre, E. Castro, V. *Scientia Agropecuaria*, **8**, 19-27, (2017).
5. M. Segura-Campos, N. Ciau-Solis, G. Rosado-Rubio, Luis Chel-Guerrero, D. Betancur-Ancona, *Agricultural Sciences*, **5**, 220-226 (2014).
6. R. Ayerza, *JAACS*, **72**, 1079-1081 (1995).
7. O. Ciftci, R. Przybylski, M. Rudzinska, *Eur.J. Lipid science and technology*, **114**, 794-800 (2012).
8. ISO 659:2014. Oilseeds. Determination of oil content (Reference method)
9. Approved Methods of the American Association of Cereal Chemists, vol. 2, compiled by the Approved Methods Committee, AACC Ins., St. Paul, MN, 1976, Modified Kjeldahl-Boric acid method p.46-12
10. AOAC - Association of Official Analytical Chemist (2016). Official methods of analysis, 20th edn. Washington, DC
11. ISO 12966-2:2011. Animal and vegetable fats and oils. Gas chromatography of fatty acid methyl esters. Part 2: Preparation of methyl esters of fatty acids
12. ISO 12966-1:2014. Animal and vegetable fats and oils. Gas chromatography of fatty acid methyl esters. Part 1: Guidelines on modern gas chromatography of fatty acid methyl esters.
13. ISO 9936:2016. Animal and vegetable fats and oils. Determination of tocopherol and tocotrienol contents by high-performance liquid chromatography.
14. ISO 18609:2000. Animal and vegetable fats and oils. Determination of unsaponifiable matter. Method using hexane extraction. 2000. p.8.
15. S. Ivanov, P. Bitcheva, B. Konova, *Revue Francaise des Corps Gras*, **19**, 1 77 (1972).
16. ISO 12228-1:2014. Part 1: Animal and vegetable fats and oils. Determination of individual and total sterols contents. Gas chromatographic method.
17. AOCS (American Oil Chemists Society), 5th ed. Official Methods and Recommended Practices of the American Oil Chemists Society, "Calculated iodine value", AOCS Press, Champaign, IL, p. Cd 1c-8, 1999.
18. ISO 660:2009. Animal and vegetable fats and oils. Determination of acid value and acidity, p. 5.
19. ISO 3960:2007. Animal and vegetable fats and oils. Determination of Peroxide value, p. 9.
20. ISO/FDIS 3657:2001. Animal and vegetable fat and oils. Determination of Saponification value.
21. EN ISO 6320:2000. Animal and vegetable fats and oils. Determination of Refractive index, p. 6
22. ISO 6883:2017. Animal and vegetable fats and oils. Determination of conventional mass per volume ("litre weight in air").
23. ISO 6886:2006. Animal and vegetable fats and oils. Determination of oxidative stability (Accelerated oxidation test), p. 13.

Fatty acids, phospholipids, health risk index and daily intake of metals in edible wild mushroom (*Tricholoma equestre*) from the Batak mountain, Bulgaria

L. Dospatliev^{1*}, M. Ivanova², P. Papazov³

¹Department of Pharmacology, Animal Physiology and Physiological Chemistry, Trakia University, 6000 Stara Zagora, Bulgaria

²Department of Informatics and Mathematics, Trakia University, 6000 Stara Zagora, Bulgaria

³Department of Organic Chemistry and Inorganic Chemistry, University of Food Technology, 4000 Plovdiv, Bulgaria

Received October 23, 2018; Revised January 4, 2019

Samples were collected from the Batak Mountain, Bulgaria. The aim of this study was to perform analysis of the content of Pb, Cd, Ni, Cr, Mn, Co, Cu and Zn, fatty acid and phospholipids, in wild edible mushroom *Tricholoma equestre*. The average content of studied elements: Pb, Cd, Ni, Cr, Mn, Co, Cu and Zn in *Tricholoma equestre* samples was: 1.16 mg kg⁻¹, 1.09 mg kg⁻¹, 0.74 mg kg⁻¹, 0.08 mg kg⁻¹, 0.85 mg kg⁻¹, 0.15 mg kg⁻¹, 1.16 mg kg⁻¹ and 8.63 mg kg⁻¹. The content of Saturated fatty acids (SFA) consisted of 50.5 %. Unsaturated fatty acids (UFA) in the oil from mushroom (49.5 %) and the content of monounsaturated fatty acids (MUFA) consisted of 43.9 %. On the other hand, the amount of monounsaturated fatty acids (PUFA) was lower (5.6 %).

In the phospholipid fraction from mushrooms, there predominated phosphatidylcholine (PC) (37.90 %) as a major component, followed by diphosphatidylglycerol DPG (16.50 %). The quantities of monophosphatidylglycerol (MPG) and lysophosphatidylcholine (LPC) in the phospholipid fraction were from 1.50 % to 3.20%.

Keywords: Health risk index, Fatty acid, Phospholipids, Mushroom (*Tricholoma equestre*), Bulgaria

INTRODUCTION

Mushrooms have been viewed as gourmet food over the globe since vestige for their unique taste and inconspicuous flavor. As of late, it has been found that many mushroom species are miniature pharmaceutical factories producing thousands of novel constituents with exceptionally helpful biologic properties. They have a long history of utilization in Oriental prescription, however their incredible impacts in advancement of good health and imperativeness are being upheld by contemporary reviews. Recently, mushrooms have developed as great wellspring of nutraceuticals, antioxidants, anticancer, prebiotic, immune modulating, anti-inflammatory, cardiovascular, anti-microbial and anti-diabetic [1-9].

The known essential micronutrient minerals are iron, zinc, selenium, manganese, cobalt and copper. These microminerals play an important role in the catalytic processes within the enzyme system that includes a wide range of enzyme activities associated with metabolic, endocrine and immune system [10-19].

The aims of this study were to determine Pb, Cd, Ni, Cr, Mn, Co, Cu and Zn, phospholipids and fatty acid in edible wild mushroom (*Tricholoma equestre*) growing in the Batak Mountain, Bulgaria and thus to

assess the health risk index arisen from the long-term consumption of them.

EXPERIMENTAL

Analytical procedure

Quantitative determination of the concentration of the studied trace elements (Pb, Cd, Ni, Cr, Mn, Co, Cu and Zn) was carried out in the mineralized samples by Perkin Elmer AAnalyst 800 atomic absorption spectrometer with deuterium background corrector.

Mushroom Samples

Mushroom samples were collected in 2014 and 2018 from the Batak Mountain by the authors themselves.

The Batak Mountain is located in western Rhodopes. Its western border is defined by the Chepinska river, the southern border – by Dospatska river and Dospat dam, the eastern border – by Vacha river and the northern border – by the Thracian Plane (GPS41°46'02.6"N 24°08'48.4"E). The regions is industry-free and is characterised with forests, land and low buildings.

Reagents and Moisture content

Reagents are qualified "AR" (pa Merck & Fluka). The fresh weight of each mushroom sample was taken using chemical balance. These samples were then oven dried separately at 105 °C for 24 h. The

* To whom all correspondence should be sent.
E-mail: lkd@abv.bg

loss in weight obtained after drying was regarded as the moisture content.

Digestion procedures

Multiwave 3000 closed vessel microwave system (maximum power was 1400 W, and the maximum pressure in Teflon vessels - 40 bar) was used in this study mushroom samples (0.25 g) were digested with 6 ml of HNO₃ (65 %) and 1 mL of H₂O₂ (30 %) in microwave digestion system for 23 min and diluted to 25 ml with deionized water. A blank digest was carried out in the same way. All sample solutions were clear. Digestion conditions for the microwave system are given in Table 1.

Table 1. Microwave acid digestion programme

Step	Ramp time, (min)	Hold time, (min)	Cooling period, (min)	Pressure (MPa)	Temperature (°C)
1	10	10	5	0.758	110
2	10	10	5	1.023	150
3	20	10	5	0.758	190

Accuracy and precision

In order to validate the method for accuracy and precision the certified reference materials (CRM) - Virginia Tobacco Leaves (CTA-VTL-2) was analysed for the corresponding elements. The results are shown in Table 3. For evaluation of the correctness of the results, three generally accepted criteria are used as follows:

$$D = X - X_{CRM}, \tag{1}$$

where X is the measured value and X_{CRM} is the certified value. When D is within the borders of ± 2σ, where σ is the standard deviation from the certified value, the result is considered to be good; when it is -3σ ≤ D ≤ 3σ - satisfactory, and beyond these limits the result is unsatisfactory.

$$D\% = D / X_{CRM} \cdot 100 - \text{percentage difference.} \tag{2}$$

When the values of D % are in the limits ± 200σ / X_{CRM}, the result is considered to be good; when the value is in the limits ± 200σ / X_{CRM} and ± 300σ / X_{CRM} - satisfactory; and when it is out of the limits ±300σ / X_{CRM}, the result is unsatisfactory.

Table 2. R_fD₀ value, mg kg⁻¹ bw day

Elements	Pb	Cd	Ni	Cr	Mn	Co	Cu	Zn
R _f D ₀	0.004	0.001	0.02	0.003	0.14	0.043	0.04	0.30

$$Z = X - X_{CRM} / \sigma. \tag{3}$$

When Z ≤ 2, the result is considered to be good; when 2 ≤ Z ≤ 3 - satisfactory; when Z > 3 - unsatisfactory.

For evaluation of the accuracy of the digestion and measuring procedures, we have used R criterion showing the extent of extraction of the element in percent from the certified value. When the measured value X is within the borders of X_{CRM} ± U_{CRM}, where U_{CRM} is the indefiniteness of the certified value, we accept an extent of extraction to be 100 %. In all the remaining cases, the extent of extraction is equal to X / X_{CRM} · 100. As can be seen from the tables, the results obtained for all certified materials yield a recovery of 100 % for both elements.

Daily intake of metals

The daily intake of metals (DIM) was determined by the following equation

$$DIM = \frac{C_{\text{metal}} \times C_{\text{factor}} \times D_{\text{food intake}}}{BW},$$

where C_{metal}, C_{factor}, D_{food intake} and BW represent the heavy metal concentrations in the mushroom given for dry weight (mg kg⁻¹), conversion factor, daily intake of mushrooms and average body weight (kg), respectively [20, 21].

Health risk index

The health risk index (HRI) for the locals through the consumption of contaminated mushrooms was assessed based on the food chain and the reference oral dose (R_fD₀) for each metal (Table 2) [22].

The health risk index (HRI) for the local population through the consumption of mushrooms was assessed using the following formula [21-23]

$$HRI = \frac{DIM}{R_f D_0}.$$

HRI of < 1 means the exposed population is assumed to be safe [22-24].

The total HRI (THRI) formula prescribed in Saha et al. [25] is a summation of the individual HRI value, as shown below

$$THRI = HRI_{Pb} + HRI_{Cd} + HRI_{Ni} + HRI_{Cr} + HRI_{Mn} + HRI_{Co} + HRI_{Cu} + HRI_{Zn}.$$

Fatty acids

The fatty acid composition was determined by gas chromatography (GC) after transmethylation of the sample with 2 % H₂SO₄ in CH₃OH at 50 °C [26]. GC was performed on a HP 5890 series II gas chromatograph equipped with a 75 m × 0.18 mm × 25 µm capillary column Supelco and a flame ionization detector. The column temperature was programmed from 140 °C (5 min), at 4 °C min⁻¹ to 240 °C (3 min); injector and detector temperatures were kept at 250 °C. Hydrogen was the carrier gas at a flow rate 0.8 mL min⁻¹. Identification of fatty acids was performed by comparison of retention times with those of a standard mixture of fatty acids subjected to GC under identical experimental conditions [27].

Phospholipids

Air-dried mushrooms (10 g) were subjected to Folch [28] extraction. Polar lipids were isolated from the total lipids by column chromatography according to Christie [29]. The phospholipid classes were isolated by a variety of two-dimensional thin-layer chromatography (TLC). In the first direction the plate was developed with chloroform:methanol:ammonia, 65:25:5 (by volume) and in the second – with chloroform:acetone:methanol:acetic acid:water, 50:20:10:10:5 (by volume). The identification was performed by comparing the

respective R_f values with those of authentic commercial standards subjected to Silica gel TLC under identical experimental conditions. The quantification was carried out spectrophotometrically at 700 nm after scrapping the respective phospholipid spot and mineralization of the substance with a mixture of perchloric acid and sulphuric acid, 1:1 (by volume) [30].

Statistical

Statistical Package for Social Science (SPSS) program for Windows was used for statistical data processing.

RESULTS AND DISCUSSION

In order to validate the method for accuracy and precision the certified reference material (CRM) - Virginia Tobacco Leaves (CTA-VTL-2) was analysed for the corresponding elements. The results are shown in Table 3.

In this study, Pb, Cd, Ni, Cr, Mn, Co, Cu and Zn concentrations in dry matter basis of wild edible mushrooms were analyzed (Table 4).

The daily intake of heavy metals was estimated according to the average mushroom consumption. The estimated DIM through the food chain is given in Table 5, for both adults and children.

Table 3. Effectiveness of microwave mineralization in the determination of Fe, Ni, Cr, Cu, Co, Zn, Mn, Pb and Cd in Virginia Tobacco-CTA-VTA-2 certified reference material (mg/kg dry matter) (n = 15)

Elements	Certified value	Observed value Microwave digestion	Recovery (%)
Pb	22.1 ± 1.2	23.0 ± 0.8	104
Cd	1.52 ± 0.17	1.50 ± 0.05	98.7
Ni	1.98 ± 0.21	1.92 ± 0.17	98.1
Cr	1.87 ± 0.16	1.83 ± 0.14	93.6
Mn	79.7 ± 2.6	77.5 ± 2.1	97.2
Co	0.429 ± 1.4	0.420 ± 0.02	98.0
Cu	18.2 ± 0.8	18.1 ± 0.7	99.4
Zn	43.3 ± 2.1	44.1 ± 1.6	101.8

Table 4. Concentration of trace elements in mushroom samples (*Tricholoma equestre*) collected from Batak Mountain, Bulgaria (mg kg⁻¹ dry matter) (n = 15)

Elements	Pb	Cd	Ni	Cr	Mn	Co	Cu	Zn
Mean	1.16	1.09	0.74	0.08	0.85	0.15	1.16	8.63
SD	0.14	0.20	0.12	0.01	0.13	0.05	0.14	0.19

Table 5. DIM for individual heavy metals caused by the consumption of mushrooms *Tricholoma equestre* grown in Batak Mountain, Bulgaria.

Average body weight (kg)	12	23	43	61	70
Age-groups	1 - 3	3 - 10	10 - 14	14 - 18	adult
DIM _{Pb}	0.000618	0.000322	0.000172	0.000122	0.000213
DIM _{Cd}	0.000580	0.000303	0.000162	0.000114	0.000200
DIM _{Ni}	0.000394	0.000206	0.000110	0.000078	0.000136
DIM _{Cr}	0.000043	0.000022	0.000012	0.000008	0.000015
DIM _{Mn}	0.000453	0.000236	0.000126	0.000089	0.000156
DIM _{Co}	0.000080	0.000042	0.000022	0.000016	0.000028
DIM _{Cu}	0.000618	0.000322	0.000172	0.000122	0.000213
DIM _{Zn}	0.004595	0.002398	0.001282	0.000904	0.001587

Table 6. Health risk index values for mushrooms *Tricholoma equestre* grown in the Batak Mountain

Average body weight (kg)	12	23	43	61	70
Age-groups	1 - 3	3 - 10	10 - 14	14 - 18	adult
HRI _{Pb}	0.154425	0.080570	0.043095	0.030379	0.053319
HRI _{Cd}	0.580425	0.302830	0.161979	0.114182	0.200404
HRI _{Ni}	0.019703	0.010280	0.005498	0.003876	0.006803
HRI _{Cr}	0.014200	0.007409	0.003963	0.002793	0.004903
HRI _{Mn}	0.003233	0.001687	0.000902	0.000636	0.001116
HRI _{Co}	0.001858	0.000969	0.000518	0.000365	0.000641
HRI _{Cu}	0.015443	0.008057	0.004310	0.003038	0.005332
HRI _{Zn}	0.015318	0.007992	0.004275	0.003013	0.005289
THRI	0.804604	0.419793	0.224541	0.158283	0.277807

Health risk index

In order to assess the contribution of some heavy metals to the HRI of mushroom consumption, we calculated the hazard quotients. We evaluated the health risk of mushroom consumption concerning different age-groups relying on the HRI (Table 6).

According to the above results, all calculated HRI values of heavy metals were within the safe limits for children and adults ($HRI < 1$). Furthermore, the THRI values, which varied from 0.158283 to 0.804604 for children and 0.277807 for adult, were also in the safe limit ($THRI < 1$). Therefore, we can conclude that people might have no potential significant health risk through only consuming mushrooms from the studied area.

The values HRI_{Cd} (72.14 %) and HRI_{Pb} (19.19 %) have the highest percentage content from THRI, followed by HRI_{Ni} (2.45 %), HRI_{Cu} (1.92 %), HRI_{Zn} (1.90 %), HRI_{Cr} (1.76 %), HRI_{Mn} (0.40 %) and HRI_{Co} (0.23 %).

The element Cd (72.14 %) have the highest percentage content from THRI for the mushroom type *Tricholoma equestre*, the concentration of which is 1.09 mg kg⁻¹ dry weight at 90 % moisture. This concentration in relation to Directive No 1881 [31] is below the permissible weight of 0.2 mg kg⁻¹ wet weight (from 10 kg of wet mushrooms 1 kg of dried mushrooms is obtained).

Fatty acid composition

The content of Saturated fatty acids (SFA) consisted of 50.5 %. Unsaturated fatty acids (UFA) in the oil from mushroom (49.5 %) and the content of monounsaturated fatty acids (MUFA) consisted of 43.9 %. On the other hand, the amount of monounsaturated fatty acids (PUFA) was lower (5.6 %).

The data of fatty acid composition are shown in Fig. 1. In general, the major fatty acid found in the studied species was oleic acid (42 %), followed by palmitic acid (39.8 %), stearic acid (7.9 %) and linoleic acid (3.4 %). Besides the four main fatty

acids already described, eleven more were identified and quantified. The results obtained in this study are consistent with the previously reported results in the literature [11,32].

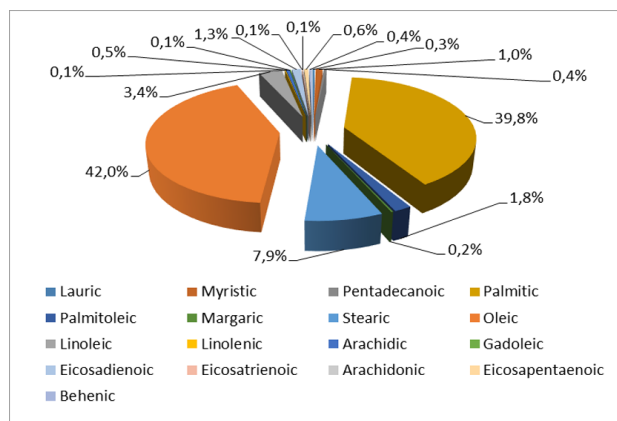


Fig. 1. The data of fatty acid composition

Phospholipid composition

The composition of the phospholipid fraction of the mushrooms oils is presented in Fig. 2. In the phospholipid fraction of the mushrooms oils from different varieties, there were identified all major classes of phospholipids. On the grounds of the obtained data, it can be seen that in the phospholipid fraction from mushrooms, there predominated phosphatidylcholine (37.90 %) as a major component, followed by diphosphatidylglycerol (16.50 %). The quantities of monophosphatidylglycerol and lysophosphatidylcholine in the phospholipid fraction were from 1.50 % to 3.20%.

The results obtained in this study are consistent with the previously reported results in the literature [31,34].

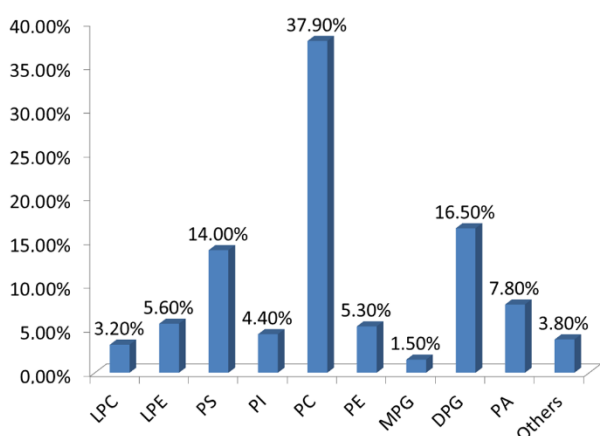


Fig. 2. Individual composition of phospholipid fraction of mushrooms

Legend: LPC – Lysophosphatidylcholine; LPE – Lysophosphatidylethanolamine; PS – Phosphatidylserine; PI – Phosphatidylinositol; PC – Phosphatidylcholine; PE – Phosphatidylethanolamine;

MPG – Monophosphatidylglycerol; DPG – Diphosphatidylglycerol; PA – Phosphatidic acids; Others

CONCLUSIONS

Mushrooms consumption data collected are used for several purposes: to monitor nutrient and food intakes in the population as well as to carry out mushrooms-based risk-benefit assessments and policy making within the European Union. It is therefore important that the data collected meet the requirements set out both on a national level as well as by the European Food Safety Agency [35] and are as accurate as possible.

REFERENCES

- G. Kanagasabapathy, S. N. A. Malek, U. R. Kuppasamy, S. Vikineswary, *J. Agric. Food Chem.*, **59**, 2618 (2011).
- M. A. Ebrahimzadeh, Y. Safdari, M. Khalili, *Int. J. Med. Mushrooms*, **17**, 557 (2015).
- E. Jablonska-Ryrs, A. Sławirska, D. Szwajgier, *Food Sci. Biotechnol.*, **25**, 439 (2016).
- M. Kosanić, B. Ranković, A. Rančić, T. Stanojković, *JFDA*, **24**, 477 (2016).
- L. Figueiredo, W. C. B. Régis, *Nutrire*, **42**, 1 (2017).
- M. Gąsecka, P. Rzymiski, M. Mleczeek, M. Siwulski, S. Budzyńska, Z. Magdziak, P. Niedzielski, K. Sobieralski, *J. Environ. Sci. Heal B*, **52**, 171 (2017).
- S. Kathiravan, S. Krishnakumari, *Int. J. Recent Sci. Res.*, **8**, 21362 (2017).
- S. P. Wasser, *Int. J. Med. Mushrooms*, **19**, 279 (2017).
- L. Dospatliev, M. Ivanova, *Cr. Acad. Bulg. Sci.*, **70**, 795 (2017).
- I. Ivanov, N. Petkova, I. Tumbarski, I. Dincheva, I. Badjakov, P. Denev, A. Pavlov, *Zeitschrift für Naturforschung C*, **73(1-2)**, 41 (2018).
- C. L. Keen, J. Y. Uriu-Adams, J. L. Ensuma, M. E. Gershwin, in: *Handbook of nutrition and immunity*, M. E. Gershwin, P. Nestel, C. L. Keen (eds), Humana Press: Totowa, NJ, 2004, p. 117.
- M. Kuka, I. Cakste, R. Galoburda, in: *Food for Consumer Well-Being (Proc. 9th Baltic Conference on Food Science and Technology, Foodbalt, Jelgava, Latvia, 2014)* E. Straumite (ed.), Jelgava, Latvia, 2014, p. 248.
- J. Falandysz, M. Drewnowska, *J. Environ. Sci. Heal B*, **50**, 374 (2015).
- M. Khalili, M. A. Ebrahimzadeh, M. Kosaryan, A. Abbasi, M. Azadbakht, *RSC Advances*, **5**, 4804 (2015).
- S. Sumaira, M. Ghulam, M. Hira, M. W. Connie, J. Yasir, S. Muhammad, *JFNR*, **4**, 703 (2016).
- L. Dospatliev, M. Ivanova, *Bulg. Chem. Commun.*, **49**, 5 (2017).
- X. Wang, H. Liu, J. Zhang, T. Li, Y. Wang, *J. Environ. Sci. Heal B*, **52**, 178 (2017).
- A. M. Massadeh, A. T. Al-Massaedh, *Environ. Sci. Pollut. Res.*, **25**, 1914 (2018).

19. I. Ivanov, I. Dincheva, I. Badjakov, N. Petkova, P. Denev, A. Pavlov, *International Food Research Journal*, **25**(1), 1 (2018).
20. Q. M. Ru, Q. Feng, J. Z. He, *Food Chem. Toxicol.*, **53**, 256 (2013).
21. J. Guo, T. Yue, X. Li, Y. Yuan, *Environ. Sci. Pollut. Res. Int.*, **23**, 14560 (2016).
22. USEPA, Risk Based Concentration Table. United States Environmental Protection Agency, Philadelphia, Washington, 2016.
23. M. Harmanescu, L. M. Alda, D. M. Bordean, I. Gogoasa, I. Gergen, *Chem. Cent. J.*, **5**, 64 (2011).
24. Q. Liang, Z. J. Xue, F. Wang, Z. M. Sun, Z. X. Yang, S. Q. Liu, *Environ. Monit. Assess.*, **187**, 754 (2015).
25. N. Saha, M. Zaman, *Environ. Monit. Assess.*, **18595**, 3867 (2013).
26. ISO 12966-2. Animal and vegetable fat and oils. Gas chromatography of fatty acid methyl esters – Part 2: Preparation of methyl esters of fatty acids, 2017.
27. ISO 12966-1. Animal and vegetable fats and oils. Gas chromatography of fatty acid methyl esters – Part 1: Guidelines on modern gas chromatography of fatty acid methyl esters, 2014.
28. J. Folch, M. Lees, G. Sloane-Stanley, *J. Biol. Chem.*, **226**, 497 (1957).
29. W. Christie, *Lipid Analysis*, The Oily Press: Bridgwater, U.K., 2003.
30. ISO 10540-1. Animal and vegetable fats and oils. Determination of phosphorus content. Part 1, 2014.
31. Commission, EC. Commission Regulation (EC) No 1881/2006 of 19 December 2006 Setting Maximum Levels for Certain Contaminants in Foodstuff, 2006.
32. L. Barros, T. Cruz, P. Baptista, L. M. Estevinho, I. C. F. R. Ferreira, *Food Chem. Toxicol.*, **46**, 2742 (2008).
33. D. D. De Silva, S. Rapior, E. Sudarman, M. Stadler, J. Xu, S.A. Alias, K. D. Hyde, *Fungal Divers.*, **62**, 1 (2013).
34. M. Kolundžić, T. Stanojković, J. Radović, A. Tačić, M. Dodevska, M. Milenković, F. Sisto, C. Masia, G. Farronato, V. Nikolić, T. Kundaković, *J. Med. Food*, **20**, 790 (2017).
35. European Food Safety Authority (2009) General principles for the collection of national food consumption data in the view of a pan-European dietary survey. *EFSA J* 7, 1435, 2009.

Residual levels and tissue distribution of polychlorinated biphenyls (PCBs) in fish from the Danube River, Bulgaria

S. K. Georgieva^{1*}, M. Stancheva¹, Zl. Peteva¹

¹Department of Chemistry, Medical University - Varna, 55 Marin Drinov str., Varna,

Received October 30, 2018; Revised January 4, 2019

Polychlorinated biphenyls (PCBs) are widespread synthetic chemicals, which tend to accumulate in aquatic organisms, due to their lipophilic properties. Fish species accumulate persistent chemicals particularly in the fatty tissues and therefore they are widely used to assess pollution of the aquatic ecosystems. The PCBs occurrence was evaluated in tissues of six fish species: common carp (*Cyprinus carpio*), catfish (*Silurus glanis*), common nase (*Chondrostoma nasus*), beluga (*Vimba vimba*), bream (*Abramis brama*) and pike-perch (*Sander lucioperca*). Sampling was carried out in spring and autumn 2015 in the Danube River, near Silistra, Bulgaria.

The aim of the study was to examine PCB concentrations in muscle and liver of fish from the Danube River in order to evaluate toxicological levels of PCB in different tissues. Six indicator and six dioxin-like PCBs were determined by capillary gas chromatography system with mass spectrometry detection.

In muscle tissues analyzed the sum of Indicator PCBs ranged from 2.51 to 10.67 ng/g wet weight in pike-perch and catfish, respectively, and did not exceed the European maximum level. The dominant congeners in all samples analyzed were PCB138 and PCB153. When concentration was calculated on a wet weight basis, tissue distribution of PCBs showed higher levels in muscle than in liver of carp and catfish. On the contrary, in common nase higher concentration of PCBs in liver than in muscle tissue were measured. On a lipid normalized basis, sum PCBs in the liver of all fish studied was higher compared to levels in muscle tissue.

The levels of dioxin-like PCBs measured varied from 0.52 to 3.76 ng/g ww. The results were used for calculation of Toxic equivalent quotient (TEQ) in order to assess the human health risk via consumption of fish. TEQs of dl-PCBs were calculated in the range 0.016 - 0.186 pg TEQ/g ww and did not exceed the EC limit of 3 pg TEQ/g ww.

Keywords: PCBs; fish; Danube River; Bulgaria

INTRODUCTION

The Danube River was listed as one of the world's top 10 rivers at risk in report of World Wildlife Fund (WWF), 2007 [1]. One of the most significant factors affecting the water quality of the Danube River basin is the hazardous substances pollution [2]. Historically, the Danube has been home to 103 fish species, including seven fish species found nowhere else in the world, 88 freshwater mollusks and over 18 amphibian species [3].

Polychlorinated biphenyls (PCBs) are toxic contaminants of concern because they tend to disrupt the endocrine system, cause neurobehavioral deficits and possibly induce cancer [4]. Fish and other seafood can be used as indicator species for the evaluation of the environment pollution, because they accumulate organochlorinated compounds from water, including PCBs.

The persistent organochlorine substances have high solubility in fatty tissues, which may lead to higher concentrations in some fatty foods (dairy products, fish, meat). Mostly human exposure is through ingestion of contaminated food. Organochlorine compounds, including PCBs,

accumulate in fatty tissue with typical half-lives of about 7 years by humans [5]. Several studies have investigated organochlorine pollution of fish species and the dietary exposure of general population to toxic organic chemicals, such as polychlorinated biphenyls, through fish consumption [6, 7, 8].

The most commonly PCBs found in food of animal origin are PCB 28, 52, 101, 138, 153 and 180 (2,4,4'-Trichlorobiphenyl, 2,2',5,5'-Tetrachlorobiphenyl, 2,2',4,5,5'-Pentachlorobiphenyl, 2,2',3,4,4',5'-Hexachlorobiphenyl, 2,2',4,4',5,5'-Hexachlorobiphenyl, 2,2',3,4,4',5,5'-Heptachlorobiphenyl, respectively) which account for approximately half of total non dioxin-like PCB congeners. These six congeners are called indicator PCBs (I-PCBs) [9]. The mono-ortho and non-ortho PCBs have toxicological properties similar to those of the highly toxic compound 2,3,7,8-tetrachlorodibenzo-p-dioxin (2,3,7,8-TCDD) and are defined as "dioxin-like" (dl-PCBs). Each congener of dl-PCBs exhibits a different level of toxicity. The concept of "toxic equivalency factors" (TEFs) has been developed to facilitate evaluating of human health risk and

* To whom all correspondence should be sent.
E-mail: stanislavavn@mail.bg

regulatory control [10]. TEF represents the individual toxic potency of each dl-PCB compound compared to 2,3,7,8-TCDD, which is considered as the reference congener. The total WHO toxic-equivalency quotient (WHO-TEQ) concentration of a food product (including fish) can be calculated as a sum of the concentration of each dl-PCB congener multiplied by its TEF [10]. Commission Regulation (EU) No 1259/2011 has set maximum levels for I-PCBs and dl-PCBs in various food groups, including fish and fish liver [11].

The aim of the present study was to examine PCB concentrations in muscle and liver of freshwater fish from the Danube River in order to evaluate toxicological levels of PCB in different tissues.

EXPERIMENTAL

Sampling

Silistra is a harbour in northeastern Bulgaria. The city lies on the southern coast of the lower Danube river and is also the part of the Romanian border. Fish species were sampled in the area of Silistra, Bulgaria from the Danube River: common carp (*Cyprinus carpio*), catfish (*Silurus glanis*), pike-perch (*Sander lucioperca*), common nase (*Chondrostoma nasus*), beluga (*Vimba vimba*) and bream (*Abramis brama*). Samples were caught by local professional fishermen in Spring 2015 and in Autumn 2015. All fish samples were transported into the laboratory in foam boxes filled with ice, where they were measured (cm), and weighted (g), before separating the muscles and livers. In the laboratory from each fish species a pooled sample of muscle tissue and livers of individuals was compiled by filleting and dissecting. The fish tissue from several individuals was homogenized by a blender (about 300 grams muscle tissue and about 70 grams liver tissue).

Analytical method

The extraction and clean-up of the samples, and quantitative determinations of PCBs in fish were conducted according to the method previously described by Stancheva *et al.* [12]. Fish muscles and livers (ten grams) were extracted with a mixture of dichloromethane: hexane in Soxhlet Extractor. Total lipid content was determined gravimetrically on an aliquot of each lipid extract of fish analyzed for PCBs. The extracts were concentrated by a rotary evaporator, cleaned up on a multilayer column - neutral silica and acidified silica (Merck KGaA, Darmstadt, Germany) and were eluted with hexane. The eluates were concentrated to near dryness and reconstituted in 0.5 ml in hexane. One microliter of purified extract was injected into GC/MS.

Gas chromatographic analyses of PCBs were carried out by GC FOCUS (Thermo Electron Corporation, Austin, Texas, USA) using POLARIS Q Ion Trap mass spectrometer. The gas chromatography oven was programmed as follows: 90 °C for 1 min, then programmed 30 °C/min to 180 °C, 2° C/min to 270 °C, 30 °C/min to 290 °C with a final hold for 3.0 min. The PCB chromatographic separation was achieved by splitless injections of 1 µl on a TR-5MS capillary column (Bellefonte, PA, USA) with a length of 30 m, 0.25 mm ID and a film thickness of 0.25 µm. Helium was applied as carrier gas - a flow rate of 1 ml/min.

For instrument calibration, recovery determination and quantification of compounds were used pure reference standard solutions (PCB Mix 20 - Dr. Ehrenstorfer Laboratory, Augsburg, Germany). Measured compounds: six Indicator PCBs (I-PCBs IUPAC No. 28, 52, 101, 138, 153 and 180) and six dioxin-like PCBs (non-ortho PCBs 77, 126, 169 and mono-ortho PCBs 105, 118, 156). Each sample was analyzed three times and was taken an average of the results obtained.

Quality control

Quality Control procedures were implemented for each 5 samples, including procedural blanks, analysis of replicate samples, use of recovery surrogates, analysis of certified reference material BB350 (PCBs in Fish oil – Institute for Reference Materials and Measurements, European Commission). Recovery of PCBs from certified reference material varied in the range 85 -109% for individual congeners. Blanks did not contain traces of contaminants. The detection limits for individual PCBs ranged between 0.2 and 0.5 ng/g ww.

Fish weight and lengths were measured individually throughout the experiment. Fulton's condition factor (CF), used as an index of fish overall fitness, was calculated for each fish using [13]:

$$CF = (W/L^3) \times 100$$

whereby W is fish weight in grams and L is individual fish length in cm.

Statistical analysis

The statistical analysis of the data was based on the comparison of average values by a t-test. A significance was set at level of $p < 0.05$. When the p value was lower than 0.05, it was considered statistically significant. Concentrations below LODs were considered as zero for all statistical analyses. All statistical tests were performed using SPSS 16 software.

RESULTS AND DISCUSSION

Biometry data, condition factor (CF) and total lipid content of fish species are presented in Table 1. Muscle tissue presented higher lipid content (0.6-14.1%) than liver - lipid content in the range 1.8–6.9% (Table 1). The value of CF is influenced by age of fish, sex, season, feeding preferences and amount of fat reserve. The condition factor provides

information on the variation of fish physiological status and can be influenced by environmental contaminants [13].

Indicator PCB concentrations

Residue concentrations of individual PCBs congeners in each fish species are provided in Table 2 and Table 3.

Table 1 Biometry data, Condition factor (CF) and lipid content (%), in muscle and liver according to fish species

Fish	n	Weight, g	Length, cm	CF	Lipids (%)	
					muscle	liver
<i>Cyprinus carpio</i>	3	1717±65	49±12	1.5	9.8±0.4	1.8±0.2
<i>Silurus glanis</i>	3	1378±72	48±11	1.3	6.2±0.4	2.2±0.2
<i>Chondrostoma nasus</i>	3	1788±84	52±13	1.3	9.4±0.3	6.9±0.4
<i>Vimba vimba</i>	6	660±35	38±6	1.2	14.1±0.5	-
<i>Abramis brama</i>	5	660±26	37±7	1.3	6.3±0.3	-
<i>Sander lucioperca</i>	5	663±43	40±11	1.0	0.6±0.1	-

Table 2. Concentration levels of Indicator PCBs (ng/g wet weight) determined in fish species from Danube River

I-PCB	common carp	catfish	common nase	beluga	bream	pike-perch
PCB 28+31	0.72± 0.06	1.08± 0.08	0.73± 0.06	1.38± 0.11	1.62± 0.13	0.46± 0.03
PCB 52	1.07± 0.09	1.35± 0.11	1.09± 0.07	1.30± 0.10	1.36± 0.10	0.39± 0.03
PCB 101	0.79± 0.08	0.91± 0.08	0.72± 0.06	nd	nd	nd
PCB 153	2.40± 0.19	3.32± 0.22	3.18± 0.24	2.12± 0.18	1.97± 0.16	0.96± 0.08
PCB 138	2.08± 0.18	2.94± 0.21	2.16± 0.19	1.73± 0.15	1.42± 0.12	0.70± 0.06
PCB 180	1.03± 0.08	1.07± 0.08	0.80± 0.08	nd	nd	nd
Sum I-PCBs, ng/g ww	8.09	10.67	8.68	6.53	6.37	2.51

nd – not detected

The highest concentration on wet weight bases were observed in catfish (10.67 ng/g ww like Sum of Indicator PCBs) and the lowest in pike-perch (2.51 ng/g ww). The high levels of PCBs in catfish may be due to its feeding preference and nature of the habitat. European catfish (*Silurus glanis*) is the largest freshwater fish of Europe and is historically known to take a wide range of food items. European catfish is bottom feeder and is known to feed on many anadromous species, worms, insects, crustaceans, fish, frogs, mice, rats and some aquatic birds [14]. The European Legislation has recommended a maximum level of 75 ng/g wet weight (as the sum of the six I-PCBs) in muscle meat of fish [11]. Our results for I-PCBs in all species analyzed did not exceed the permissible limit.

The levels of I-PCBs in common carp and common nase were found 8.06 and 8.69 ng/g ww, respectively. These species are bottom feeders, do not migrate extensively, have long life spans and reproduce rapidly [15]. Bottom-feeding fish ingest and accumulate PCBs from sediment. For these

reasons, carp and nase are a good species to assess bioaccumulation of organic pollutants.

Jankovič S. *et al.* [16] reported results for PCBs level in ten freshwater fish species from Danube River, Serbia: I-PCBs content in fish in 2006 was in the range 14.4–107.2 ng/g ww, with median value of 42.9 ng/g. Our results for sum of indicator PCBs in catfish were about four times lower than reported by Jankovič, S. *et al.* [16].

Our previous study found low levels of I-PCBs in freshwater fish gibel carp (*Carassius gibelio*), roach (*Rutilus rutilus*) and perch (*Perca fluviatilis*) from Varna Lake, Burgas Lake and Mandra Lake, Bulgaria (1.60, 1.06 and 1.06 ng/g ww for Sum of I-PCBs) [17]. These findings showed the concentrations of PCBs in wild fish from the Danube River were higher than the levels in fish species from some lakes in Bulgaria.

Hexachlorinated PCB 153 accounted for the greatest proportion of I-PCBs (mean 32.6%), followed in order by PCB 138 (25.7%) and pentachlorinated PCB105 (15.3%). The percent distribution of I-PCB was in accordance with reports

for cod from Baltic Sea [18], shark from Mediterranean [19] and in tissue of wild carp from eastern Lake Erie [15].

The congener profile in fish tissue depends on metabolization degree. The half-life of congeners varies from months to several years. The high chlorinated congeners (xexa- and hepta-chlorobiphenyls) metabolically degrade slowly and can accumulate higher levels in fish tissue [5, 20]. Thus, the profile of congeners detected may differ from the profile of the initially released PCBs in the environment [5].

Dioxin-like PCB concentrations

All the samples analyzed, with the exception of bream, were positive to the presence of dioxine-like PCBs, as shown in Table 3. The levels of dl-PCBs measured varied from 0.52 (pike-perch) to 3.76 ng/g ww (catfish).

The statistical test indicated that the levels of PCBs found in catfish were significantly higher than those detected in pike-perch ($p < 0.05$, $t = 0.001$). Concentrations of the most toxic non-ortho congeners (PCBs 77, 126, 156 and 169) were found below LOD for most of the samples.

Table 3. Concentration levels of dl- PCBs (ng/g wet weight) determined in fish species from Danube River

dl-PCB	common carp	catfish	common nase	beluga	bream	pike-perch
PCB 77	nd	1.04	1.04	nd	nd	nd
PCB 105	0.91± 0.07	1.29± 0.10	0.97± 0.08	1.27± 0.09	nd	0.52± 0.05
PCB 118	1.47± 0.11	1.43± 0.12	1.19± 0.10	nd	nd	nd
PCB 126	nd	nd	nd	nd	nd	nd
PCB 156	nd	nd	nd	nd	nd	nd
PCB 169	nd	nd	nd	nd	nd	nd
Sum dl-PCBs, ng/g ww	2.38	3.76	3.20	1.27	nd	0.52

nd – not detected

Table 4 Concentrations of dl-PCBs expressed in pg WHO-TEQ/g ww and total TEQ values estimated for fish studied

dl-PCBs UPAC №	TEF, WHO 2005	common carp	catfish	common nase	beluga	bream	pike-perch
PCB 77	0.0001	nd	0.104	0.104	nd	nd	nd
PCB 105	0.00003	0.027	0.039	0.029	0.038	nd	0.016
PCB 118	0.00003	0.044	0.043	0.036	nd	nd	nd
PCB 126	0.1	nd	nd	nd	nd	nd	nd
PCB 156	0.00003	nd	nd	nd	nd	nd	nd
PCB 169	0.03	nd	nd	nd	nd	nd	nd
Total TEQ, pg WHO-TEQ/g ww		0.071	0.186	0.169	0.038	nd	0.016

nd – not detected

Tissue distribution of PCBs

The distribution of Indicator PCBs was investigated in the muscles and liver of the three fish species (common carp, catfish and common nase) collected from the Danube River. Distribution of I-PCBs and dl-PCBs in different fish tissues was

The results were used for calculation of Toxic Equivalence (TEQ) in order to assess the human health risk via consumption of fish – Table 4. TEQ values were calculated by multiplying the congener concentrations measured in each sample with its TEF, expressed in pg WHO-TEQ/g ww [10].

Fish and seafood has been shown to be the main contributors to total toxic equivalent (TEQ) intake from PCBs for humans [6]. The TEQ values of dioxin-like PCBs in the fish studied are presented in Table 4. The means of total TEQ ranged from 0.016 to 0.186 pgTEQ-WHO/g wet weight (for pike-perch and catfish, respectively). The highest TEQ value observed in catfish may be due to its high capacity to accumulate dioxin-like PCB congeners. This results were comparable to TEQ values for fish from the Black Sea in our recent study, Stancheva *et al.* [21]. The European Commission has set a limit of 3.0 pg TEQ/g wet weight in muscle of fish for the sum of dioxin-like PCBs [11]. Our results for TEQ values of the six dl-PCBs for all fish studied did not exceed this limit.

summarized in Fig. 1. The PCB concentrations reported for muscle and liver are expressed on the basis of lipid content because of the lipophilic properties of PCBs. Muscle tissues contain higher amount of lipids (6.9 - 9.8% lipid) than liver samples (1.8 – 6.9% lipid).

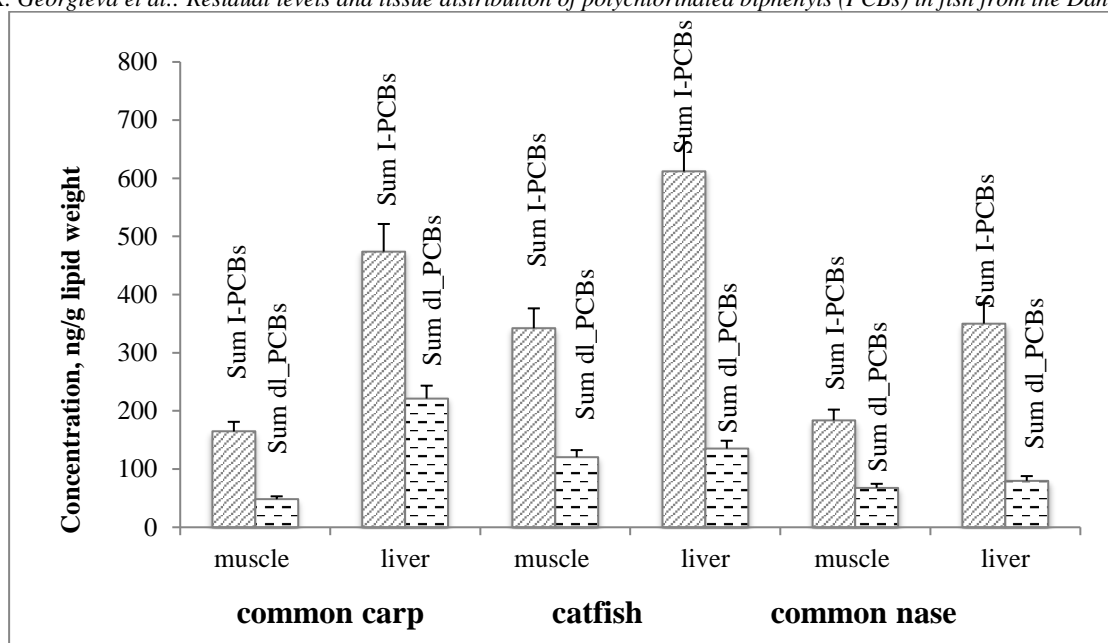


Figure 1 Sum of I-PCBs and Sum of dl-PCBs, ng/g lipids in muscle and liver of fish

The highest levels of I-PCBs were found in catfish: 342 ng/g lw in the muscle and 612 ng/g lw in the liver (Figure 1). Hexachlorine substituents (PCB 153 and 138) made the greatest contribution to the accumulation of PCBs in both tissues. The PCBs levels in all fish species studied revealed that liver tissue contains higher concentrations than muscles samples. Our results were in accordance with several previous studies investigated the presence of PCBs in various fish tissues. Solé *et al.* [22] reported higher concentrations of PCBs in tissues with greater lipid content (liver, gills and muscles) in fish from the Mediterranean. Higher concentrations of PCBs in liver than in muscle of fish from Huston River were observed by Monosson *et al.* [23]. Sapozhnikova *et al.* [24] report higher concentrations of PCBs in liver than in muscles in fish from the Salton Sea.

Stefanelli *et al.* [25] investigated the presence of PCBs in tissues of swordfish (*Xiphias gladius*) from Mediterranean Sea and Azores islands. They reported sum of 34 chlorobiphenyl congeners from 80.7 ng/g w.w. (in muscle) to 246.2 ng/g w.w. (in liver). In present study the concentration of PCBs in muscle tissue and liver of fish from the Danube River were observed to be much lower.

CONCLUSIONS

WHO recommended consumption of fish due to the high protein, unsaturated fatty acids, vitamins and minerals content. On the other hand, a frequent contaminated fish consumption may pose a potential risk for humans. The current investigation on toxicological levels of Indicator PCBs and dioxine-like PCBs in fish from the Danube River showed that

the concentrations remained well below the existing European limits. We can conclude that the consumption of fish do not pose any significant risk to human health. However, it would be necessary the investigation of the PCBs in freshwater fish to continue, as they represent one of the major contributors to the pollution of Danube River waters.

Acknowledgment: This study was supported by the EEA Grants and Ministry of Environment and water, Bulgaria, project contract № Д-33-49/30.06.2015.

REFERENCES

1. C. M. Wong, C. E. Williams, J. Pittock, U. Collier, and P. Schelle. *WWF International*. <https://www.wwf.org.uk/updates/worlds-top-10-rivers-risk> (2007).
2. C. Gasparotti, *Euro Economica*, (33)1, 91-106 (2014).
3. WWF (2004). <http://www.wwf.eu/?67440/Danube-floods-Natural-retention-areas-needed>
4. J. Salama, T.R. Chakraborty, L. Ng, A. C. Gore, *Environ Health Perspect.*, **111**, 1278-1282 (2003).
5. O. Faroon & P. Ruiz, *Toxicology and industrial health*, **32**(11), 1825 (2016).
6. J.L. Domingo, A. Bocio, *Environ. Int.*, **33**, 397 (2007).
7. I. Sioen, J. Van Camp, F. Verdonk, W. Vebeke, F. Vanhonacker, J. Willems, *Chemosphere*, **71**, 1056–(2008).
8. S. Mezzetta, M. Cirilini, P. Ceron, A. Tecleanu, A. Caligiani, G. Palla, G.E. Sansebastiano, *Chemosphere*, **82**, 1293 (2011).
9. N. Arnich, A. Tard, J. Leblanc, B. Le Bizec, J. Narbonne, et al. *Regulatory Toxicology and Pharmacology*, **54**(3), 287 (2009).
10. M. Van den Berg, L. S. Birnbaum, M. Denison, M. De Vito, W. Farland, M. Feeley, et al. *Toxicological Sciences*, **93**(2), 223 (2006).

S.K. Georgieva et al.: Residual levels and tissue distribution of polychlorinated biphenyls (PCBs) in fish from the Danube river...

11. EC. Commission Regulation (EU) No 1259/2011. *Off J of EU*, **L320**, 18, (2011).
12. M. Stancheva, S. Georgieva, L. Makedonski, *Qual Assur and Safety of Foods and Crops*, **5**(3), 243, (2013).
13. J. Baptista, P. Pato, A. C. Duarte, M. A. Pardal, *Chemosphere*, **93**, 1632 (2013).
14. J. Syväranta, J. Cucherousset, D. Kopp, A. Crivelli, R. Céréghino, F. Santoul. *Aquat. Biol.*, **8**, 137 (2010).
15. A. Pérez-Fuentetaja, S. Lupton, M. Clapsadl, F. Samara, L. Gatto, R. Biniakewitz, D.S. Aga, *Chemosphere*, **81**, 541 (2010).
16. S. Jankoviç, M. Curcic, T. Radicevic, S. Stefanovic, M. Lenhardt, K. Durgo, B. Antonijevic, *Environ. Monit. Assess.*, **181**, 153 (2010).
17. S. K. Georgieva, Zl. V. Peteva, *Bulgarian Chemical Communications*, **49** G, 205 (2017).
18. H. Dabrowska, E. Bernard, I. Barska, K. Radtke, *Ecotoxicology and Environmental Safety*, **72**, 1975 (2009).
19. M. M. Storelli, G. Barone, A. Storelli, G. O. Marcotrigiano, *Chemosphere*, **82**, 37 (2011).
20. J.-P. Wu, X.-J. Luo, Y. Zang, Y. Luo, S.-J. Chen, B.-X. Mai, Z.-Y. Yang, *Environ. Int.*, **34**, 1109 (2008).
21. M. Stancheva, S. Georgieva, L. Makedonski, *Food Control*, **72**, part B, 205 (2017).
22. M. Solé, C. Porte, J. Albaigés, *Deep Sea Res. Part 1 Oceanogr. Res. Pap.*, **48**, 495 (2001).
23. E. Monosson, J. T. F. Ashley, A. E. McElroy, D. Woltering, A. A. Elskus, *Chemosphere*, **52**, 777 (2003).
24. Y. Sapozhnikova, O. Bawardi, D. Schlenk, *Chemosphere*, **55**, 797 (2004).
25. P. Stefanelli, A. Ausili, A.D. Muccio, C. Fossi, S.D. Muccio, D. Rossi, A. Colasanti, *Mar. Pollut. Bull.*, **49**, 938 (2004).

Evaluation of paralytic shellfish poisoning toxin profile of mussels from Bulgarian North Black Sea coast by HPLC-FID with post and pre-column derivatization

Z. V. Peteva^{1*}, G. N. Kalinova², B. Krock³, M. D. Stancheva⁴, St. K. Georgieva⁵

¹Medical University - Varna, Department of Chemistry, Tsar Osvoboditel, 84, 9000 Varna, Bulgaria,

²National Diagnostic and Research Veterinary Medicine Institute, National reference Laboratory for Marine Biotoxins, Bulgaria, Pencho Slaveikov Blvd., 15, 1606 Sofia,

³Alfred Wegener Institut, Helmholtz Zentrum für Polar- und Meeresforschung, Chemische Ökologie, am Handelshafen 12, 27570 Bremerhaven, Germany

⁴Medical University - Varna, Department of Chemistry, Tsar Osvoboditel, 84, 9000 Varna, Bulgaria,

⁵Medical University - Varna, Department of Chemistry, Tsar Osvoboditel, 84, 9000 Varna, Bulgaria,

Received October 27, 2016; Revised December 2, 2016

Marine toxins are produced by certain toxic phytoplankton species. Harmful toxins may accumulate in the shellfish tissue, potentially impacting human health. Paralytic shellfish poisoning (PSP) is a syndrome caused by ingestion of shellfish contaminated with paralytic shellfish toxins (PST) that comprise saxitoxin and its variants (neosaxitoxin, gonyautoxins and their decarbamoyl and *N*-sulfofocarbamoyl analogs).

The aim of this study was to evaluate the presence of paralytic shellfish toxins (PSTs) in plankton samples and in mussels intended for human consumption.

Mussels collected in the main areas of production and recreational harvesting off the north coast of Bulgaria have been investigated for PSP toxins. Individual toxins were determined using two methods both involving fluorescence detection: ion pair-liquid chromatography with post-column derivatization (method 1) and high-performance liquid chromatographic procedure employing pre-column oxidation of the toxins (method 2). The results according method 1 demonstrated the presence of gonyautoxin 2 in 53% of the mussel samples and no toxins were detected in the plankton samples. The toxicity level - 1.6 µg STX.2HCl .kg⁻¹ was far beneath the EU legislative limit of 800 µg STX.2HCl .kg⁻¹ concluding in negligible risk for human health.

Due to higher limits of detection no toxins were detected via method 2. Even though, considering method 2 is recognized by European Commission as official for regulatory purposes and the relative high value of the legislative threshold, thus obtained toxin levels are enough representative to conclude if mussels are safe for consumption or not. On the other hand, the more sensitive method 1 provides important data on extremely low toxin levels which would be useful for chronic exposure estimation and for completing the knowledge about occurrence of PSTs in certain locations.

Keywords: paralytic shellfish toxins, gonyautoxin 2, Bulgaria, mussels, plankton, LC-FLD

INTRODUCTION

Seafood products such as shellfish are a rich source of proteins and mineral components [1, 2]. Mussels and rapana are an important source of income for the fishing community in Bulgaria [3]. However, shellfish such as mussels may contain compounds harmful to human health such as marine biotoxins.

Among them are paralytic shellfish poisoning (PSP) toxins (PSTs) that comprise saxitoxin (STX) and its variants. A dose of approximately 1 mg of saxitoxin from a single serving of contaminated shellfish is fatal to humans. PSTs are neurotoxins that specifically bind to voltage gated sodium channels and thereby block the excitation current in nerve and muscle cells, finally resulting in paralysis and other disorders in consumers of contaminated

shellfish [4]. Intoxication with PSTs produces several symptoms that include tinkling, sensation or numbness around the lips, numbness of extremities, gastrointestinal problems, difficulty in breathing, and, in fatal cases, death [5]. The human PSP fatality cases vary worldwide and depend essentially on local health - care practitioner awareness of the intoxication and its treatment and the local medical system's capacity on assisting respiratory support needing victims. For example, in a series of intoxications in Europe and North America, no deaths occurred among more than 200 cases. In similar outbreaks in Southeast Asia and Latin America, where clinicians may be unexperienced with PSP, the case fatality proportion ranged between 2-14% [4]. Worldwide, PSP affects some 2000 people annually, with a 15% mortality rate [6].

* To whom all correspondence should be sent.
E-mail: zlatina.peteva@mu-varna.bg

PSP toxins are produced by some cosmopolitan marine eukaryotic dinoflagellates belonging to the genera *Alexandrium* [7], *Gymnodinium* [8] and *Pyrodinium* [9]. *Alexandrium* spp., however, are the most abundant and widespread producers of PSTs [6]. Eight of the 30 known species within the genus are documented to synthesize PSTs [10]. Additionally, PST production within *Alexandrium* appears paraphyletic, and there are seemingly toxic and non-toxic strains of the same species [11]. The toxins are passed through the marine food web via

vector organisms, e.g. shellfish as mussels, which accumulate the toxins by feeding on PST producing dinoflagellates without apparent harm to themselves [12].

PSP toxins are tetrahydro purine derivatives (Figure 1). Classification of these toxins includes carbamoyl (STX, neosaxitoxin (NEO) and gonyautoxins (GTX1-4), *N*-sulfocarbamoyl (B1 and B2, C1-4), decarbamoyl (dcSTX, dcNEO, dcGTX1-4) derivatives and hydroxylated PSTs (M1-4).

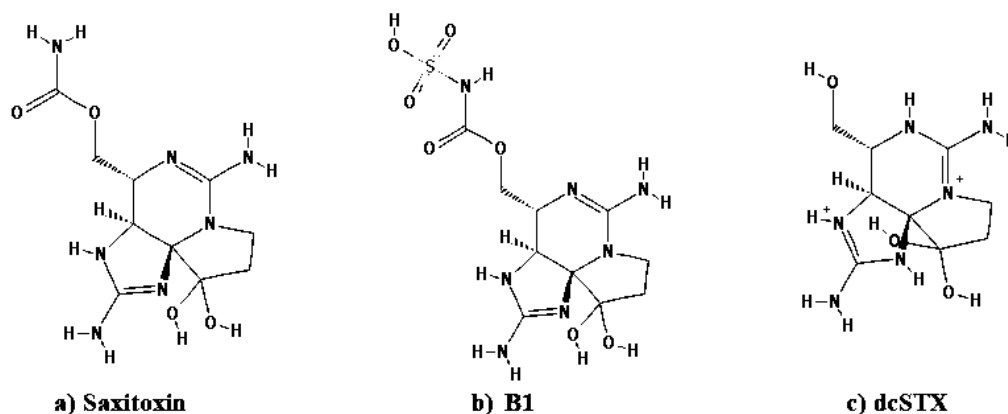


Figure 1. Chemical structures of selected representatives from the three main groups of PSTs

Within the saxitoxin group around 30 different analogues have been detected [13] but recently many more are discovered [14]. Not every analogue exhibits the same toxicity and nowadays for the most prominent analogues, toxic equivalent factors (TEF) have been established [15].

In order to be able to determine PSP toxins as non-fluorescent tetrahydro purine compounds by highly sensitive fluorescence detection (FD), PSTs have to be oxidized to fluorescent imino purine derivatives. The Official AOAC detection method is HPLC-FD with precolumn derivatization [16], the so called Lawrence method, which is widely used [17]. It is based on of prechromatographic oxidation followed by chromatographic separation of the oxidation products. However, the implementation of this method is relatively complex due to the different ionic charge states of PSTs. STX e.g. is highly polar due to the presence of two guanidino groups [18], where as C-toxins do not possess a net charge. To confirm the presence of PSTs in a sample, a detailed sample preparation procedure including solid phase extraction (SPE) separation into three distinct fractions is required. Thereafter the fractions are treated with different oxidizing agents [19].

An alternative HPLC method for the determination of PSTs consists in chromatographic separation of underivatized PSTs followed by continuous post column derivatization and FD, the so called post-column oxidation or PCOX method.

[20]. This method is very sensitive and highly specific. It can provide excellent quantitative results for known analogues and its results come in agreement with other recognized methods [20].

The aim of this study was to provide scientific information regarding the occurrence of PSTs and to assess common PSP profiles of mussel and plankton samples harvested along the north coast of Bulgaria in 2017. Total PST content was investigated by using both, the Lawrence and PCOX methods in order to assess their applicability and discuss their suitability for different applications and purposes.

EXPERIMENTAL

Sample material

Eighteen phytoplankton and 17 mussel samples were taken from 5 sites (Varna, Albena, Balchik, Kavarna and Shabla) along the north Bulgarian coast in two sampling campaigns – spring 2017 and summer – autumn 2017. Cultivated mussels were sampled from mussel farms and wild mussels from recreational harvesting sites. Locations of plankton sampling were selected in accordance of the presence of mussel aquaculture sites and wild mussel beds.

For plankton sampling a 20 µm mesh size plankton net was used. The net was hauled in different sites and depths (1 m to 5 m) depending on mussel breeding locations. In total 18 plankton samples were collected.

Wild mussels (7 samples) were harvested manually by recreational harvesters and by our co-workers. Farmed mussels (10 samples) were provided from mussel farmers directly from cultivation ropes.

Sample preparation:

The digestive glands of at least 1.5 kg specimen (~ 37.3 g) were dissected and homogenized with dispersing instrument (POLYMIX®PT 1200E, KINEMATIKA AG, Germany) for 5-10 min at maximum speed.

Extraction of Plankton:

The sample concentrate from the plankton net was collected on 20 µm mesh size sieve and washed in 50 mL centrifuge tube. The suspension was centrifuged (4000 × g, 10 min at 10 °C), the supernatant was removed and 1 mL 0.03 M acetic acid was added to the plankton pellet. For the extraction of PSTs from the plankton cells, the resulted suspension was sonicated (40 Hz, 15 min) and centrifuged again. The supernatant was filtered through syringe filters (0.45 µm pore size, ø 25 mm, Minisart, Sartorius, Germany). Filtrates were transferred into chromatographic vials and kept at -20 °C until further analysis.

Extraction of digestive glands:

- for PCOX analysis:

An average 2.14 g of hepatopancreas homogenate was extracted in duplicate with 4 mL 0.2 M acetic acid with dispersing instrument for 2 min at maximum speed and centrifuged for 10-15 min at 4000 × g. The resulting supernatants were transferred to 50 mL centrifuge tubes and centrifuged again. An aliquot (1 mL) was filtered through syringe filters. Filtrates were kept in chromatographic vials at -20 °C until further analysis.

- for Lawrence method [16]:

Hepatopancreas homogenate (~ 5g) was extracted in duplicate with 3 mL 1% acetic acid. First extraction was performed at boiling water for 5 min. Subsequently a centrifugation at 4000 × g for 10 min was performed. Supernatants were combined and made up to volume of 10 mL.

Clean-up of 1 mL extract was performed with SPE C18 cartridge (SUPELCO, 500mg/3 ml) and the extract was adjusted to pH 6.5 with 1M NaOH.

Pre-column derivatization

The sample extracts were oxidized with periodate oxidant - 100 µL of sample extract were added to 100 µL of matrix modifier (PSP-free oysters were extracted and cleaned-up by the same procedure as samples) in a 1.5 mL vial. 500 µL of periodate

oxidant (prepared daily by mixing 5 mL each of 0.03 M periodic acid, 0.3 M ammonium formate, and 0.3 M Na₂HPO₄, and adjusted to pH to 8.2 with 0.2 M NaOH using pH meter) were added to the vial and mixed. The solution reacted at room temperature for 1 min. Glacial acetic acid (5 µL) was added to interrupt the reaction.

HPLC- FD analysis

PCOX method (Method 1)

All mussel and plankton extracts were analyzed for PSTs by reverse-phase ion-pair liquid chromatography on a LC1100 series liquid chromatograph (Agilent Technologies, Waldbronn, Germany) coupled to a PCX 2500 post-column derivatization system (Pickering Laboratories, Mountain View, CA, USA) and dual monochromator fluorescence detector (G1321A) following minor modifications of previously published methods [20]. Chromatographic conditions were as follows: Eluent A - 6 mM octanesulfonic acid, 6 mM heptanesulfonic acid and 40 mM ammonium phosphate; Eluent B - 13 mM octanesulfonic acid and 50 mM phosphoric acid by isocratic elution program. The flow rate was 1 mL/min and injection volume - 20 µL. The separation of analytes was performed on a 250 mm × 4.6 mm i.d., 5 µm, Luna C18 reversed-phase column (Phenomenex, Aschaffenburg, Germany) equipped with a Phenomenex SecuriGuard pre-column.

Post column derivatization

To the column eluate 10 mM periodic acid in 555 mM ammonium hydroxide was added continuously at a flow of 0.4 mL/min before the reaction coil (50 °C). After the reaction coil acidification of the eluate with 0.75 M nitric acid was performed. The toxins were detected by a dual monochromator fluorescence detector (λ_{ex} 333 nm; λ_{em} 395 nm).

Lawrence method (Method 2)

The analyses were performed on a liquid chromatograph UltiMate 3000 Thermo Fisher Scientific Dionex, equipped with quaternary pump, vacuum degasser, autosampler, injector, fluorescent detector Dionex RF 2000, chromatographic column Kinetex: C18, 150 mm × 4.6 mm, 5µm; flow rate of the mobile phase 1mL/min (Eluent A: 0.1 M ammonium formate, pH 6 with 1 M acetic acid; Eluent B: 0.1 M ammonium formate in 5% acetonitrile, pH 6 with 1 M acetic acid). Elution was achieved by a gradient program (0-5% mobile phase B/5 min, 5-70% B/4 min and 100% A for the last 6 min), injection volume was 50 µL.

The identification of PSTs for both methods was accomplished by comparison of retention time and fluorescence response at specified wavelengths to certified reference materials (CRMs) (C1/2, GTX1/4, dcGTX2/3, GTX2/3, GTX5, NEO, dc-STX, STX).

To prevent false positives caused by interference of auto-fluorescent compounds, using both methods, PSP extracts were analyzed with and without derivatization.

The limits of detection (LODs) of the nine toxins for both methods were calculated (Table 1).

Table 1. LODs of investigated PSTs via HPLC-FD with post- and pre-column derivatization (NH- net haul)

PSP toxins	HPLC FD with post column derivatization		HPLC FD with pre-column derivatization
	ng/NH/m plankton	LOD ($\mu\text{g STX.2HCl eq/kg}$) mussels	mussels
C1/C2	1.4	0.2	3
GTX 1	17.5	9.4	
GTX 4			60
	13.5	7.2	
dc GTX 2	0.6	0.9	
dc GTX 3	0.6	0.9	13
GTX 2	0.7	0.4	
GTX3	0.8	0.7	15
B1	3.7	0.5	3
NEO	6.9	12.1	36
dcSTX	1.0	2.2	11
STX	0.6	1.1	15

Calculations

Based on the relative potency of each STX-analogue, by means of their effect in sodium channels and in the mouse bioassay (MBA), the European Food Safety Authority (EFSA) published the toxicity equivalency factors (TEF) [15].

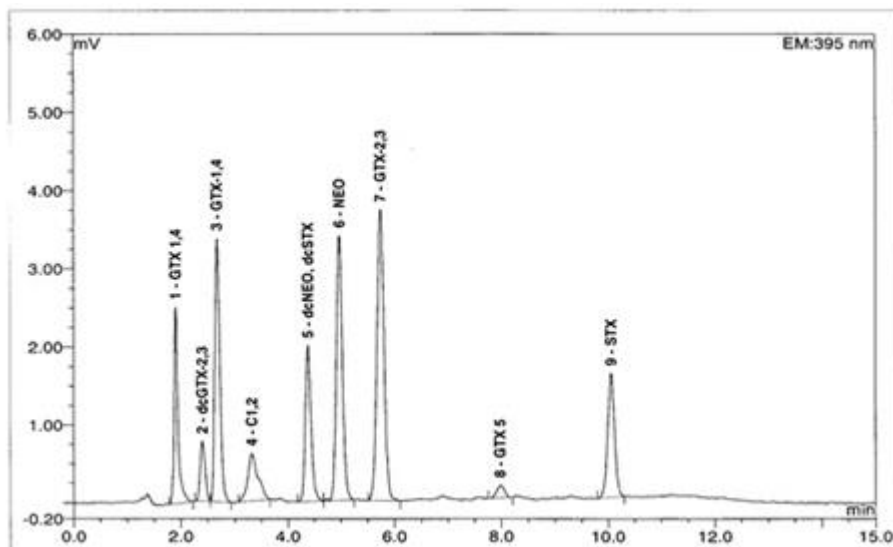
As the Lawrence pre-column HPLC-FD method [16] cannot distinguish between PST stereoisomers (GTX1 and GTX4; C1 and C2, dc-GTX2 and dc-GTX3, GTX2 and GTX3) by choosing the highest toxicity factor of the two co-eluted compounds. Total PSP toxicity was calculated by summing the toxicity contribution of each quantified toxin expressed in terms of $\mu\text{g STX .2HCl eq. kg}^{-1}$.

In the present study, mussel and plankton samples were subjected to HPLC-FD analysis in order to detect the presence of the following PSP toxin types: dc-GTX2/3, C1/2, dc-STX, GTX2/3; B1, STX, NEO, GTX1/4 and dc-NEO.

Initially we applied the official AOAC (Lawrence) method for PSTs determination in shellfish samples. No PSTs were detected in any of the investigated samples with the precolumn derivatization method (Figure 2). The calculated LODs (Table 1) were much lower than the legislative threshold ($800 \mu\text{g STX.2HCl eq.kg}^{-1}$) which concluded that obviously there was no risk for PSP if investigated samples were consumed.

However, investigations on plankton species of the Institute of Oceanology of Bulgaria documented the presence of *Alexandrium spp.* in the studied area [21]. This lead us to conclude that there was a principal possibility for PSTs to be detected in plankton and mussels. Therefore, we performed PSTs analysis firstly of plankton samples but no PSTs were detected in any of the analyzed samples. This result came in agreement with our previous study on plankton samples from the same region where no PSTs were detected as well [22]. However, since plankton toxin data represents the situation at the time of sampling and is not valid for longer periods, we considered to reanalyze PSTs in mussels with a more sensitive PCOX method, as mussels accumulate and retain toxins for a longer period of time. The data obtained would be more informative and allow statements for longer periods.

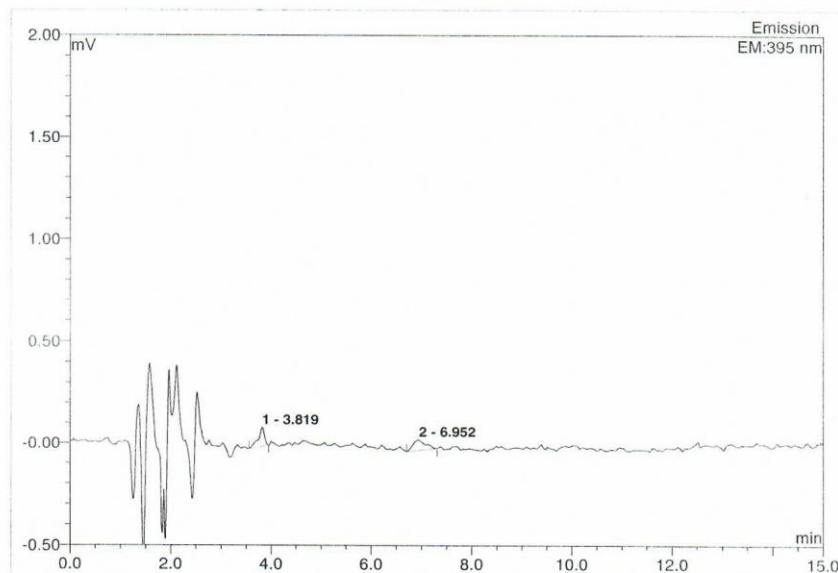
Surprisingly, low levels of PSTs were detected by this method. Figure 3 shows the chromatogram of the sample with the highest toxicity (MU48P), analyzed by HPLC-FD with pre-column derivatization method.



Operator:User Timebase:hplc Sequence:PSP_Varna_08062018

Page 1-1
11/5/2018 11:24 AM

MU 48 P			
Sample Name:	samp15-MU48 P ox	Injection Volume:	50.0
Vial Number:	RB5	Channel:	Emission
Sample Type:	unknown	Wavelength:	n.a.
Control Program:	PSP_Kinetex_flow_1	Bandwidth:	n.a.
Quantif. Method:	MIX-6_PERIODAT_guard Kinetex_flow 1	Dilution Factor:	1.0000
Recording Time:	6/8/2018 12:39	Sample Weight:	
Run Time (min):	15.00	Sample Amount:	



No.	Ret.Time min	Peak Name	Height mV	Area mV*min	Rel.Area %	Amount	Type
Total:			0.000	0.000	0.00	0.000	

Fig. 2. Chromatograms of a PSP CRMs after periodate oxidation (top) and extract of cultured mussel sample MU48P (bottom) obtained via HPLC-FD with pre-column derivatization

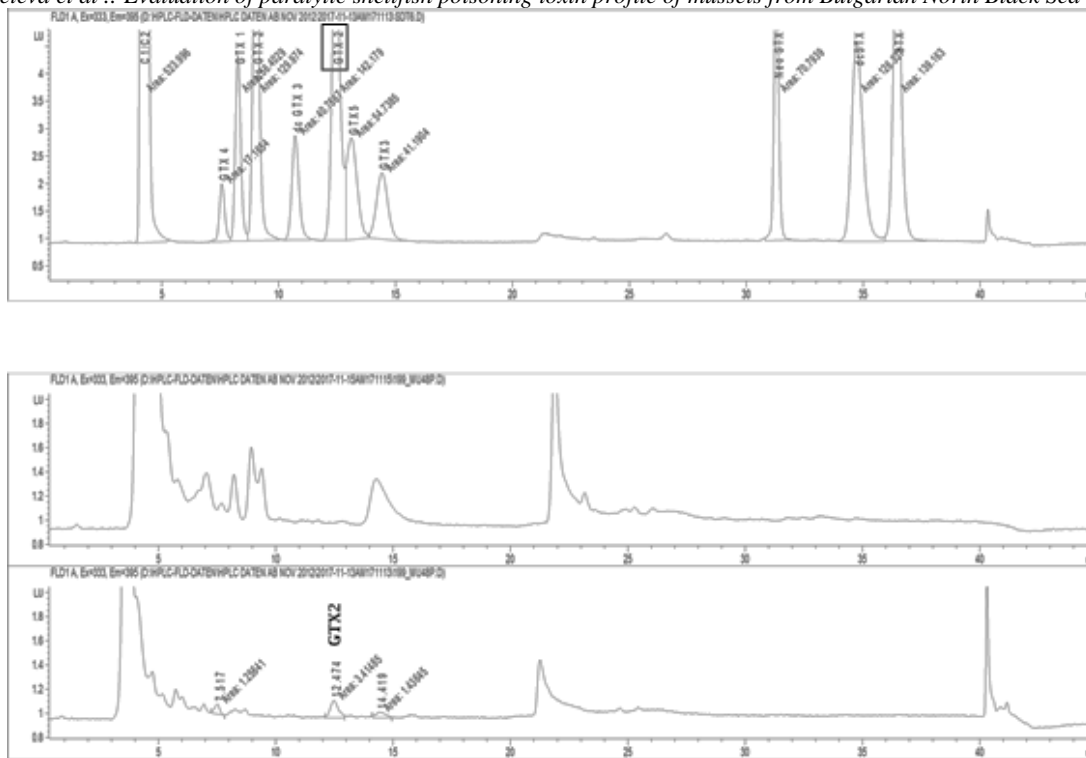


Fig. 3. HPLC-FD with post column derivatization PCOX chromatograms of a PSP standard mix containing B1, C1/2, GTX1-4, dcGTX2/3, NEO, dcSTX and STX(top) and extract of cultured mussel sample MU48P without derivatization (middle) and with derivatization (bottom).

Table 2. PSTs levels in positive samples as determined via HPLC-FD with post-column derivatization

Sample N	PSTs, $\mu\text{g STX.2HCl. kg}^{-1}$ C1/2, GTX1/4, dc GTX2/3, GTX3, GTX5, NEO, dcSTX, STX	GTX 2	Total toxicity, $\mu\text{g STX.2HCl. kg}^{-1}$
MU37P farmed	nd	0.8	0.8
MU45P wild	nd	0.5	0.5
MU48P farmed	nd	1.6	1.6
MU72P farmed	nd	1.0	1.0
MU75P wild	nd	0.5	0.5
MU86P wild	nd	0.5	0.5
MU88P farmed	nd	0.7	0.7
MU87P farmed	nd	0.7	0.7
MU85P wild	nd	0.6	0.6

Table 2 summarizes the PSP toxicity of positive mussel samples, as determined by the PCOX method. As evident, only GTX2 was detected in 9 out of 17 samples investigated. Within the positive samples 5 were of cultivated mussels. This result is in contrast to our previous investigation performed at the location Kavarna, where no PSTs had been

detected [22]. The highest detected level (MU48P, cultivated mussel sample) - $1.6 \mu\text{g STX.2HCl. kg}^{-1}$ was significantly lower than the EU legislative limit of $800 \mu\text{g STX.2HCl. kg}^{-1}$. These low values confirmed the results of the measurements according to the official method and the conclusion that there was no PSP risk for mussel consumers in 2017.

As samples were collected regularly throughout the investigated period a seasonal change in PSTs contamination throughout the year 2017 (Figure 4) became evident.

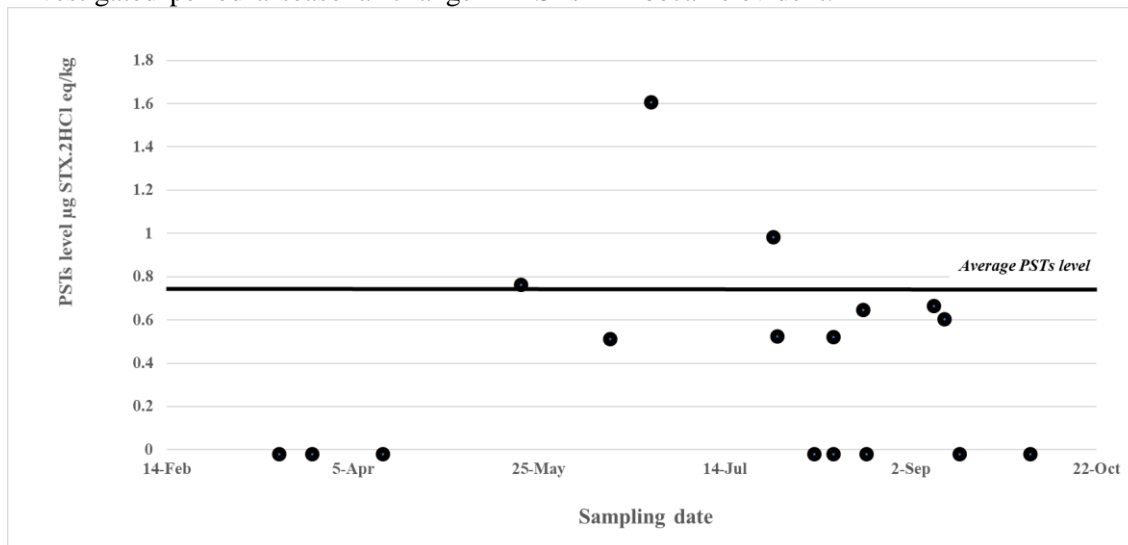


Figure 4. Seasonal changes in PSTs levels

With respect of the overall low contamination a peak in the PST level (1.6 µg STX.2HCl /kg) was observed in early summer. This increased concentration is more than two times higher than the mean PST level, which was around 0.78 µg STX.2HCl /kg. Obvious is the presence of PSTs overall harvesting seasons with exception of early spring and late autumn. However, it is still unclear whether 2017 was a typical situation or changes in environmental conditions could lead to higher *Alexandrium* densities and PSTs levels in mussels.

In similar study conducted in the same location and during the same period of time in 2015-2016 among 55 samples analyzed both STX and GTX_{2,3} were detected in only one sample with total toxicity of 55.1 µg STX.2HCl /kg [23], much higher than here determined.

The two methods used have their advantages and in certain cases result of both of them should be considered. HPLC-FD with pre-column derivatization is the official method recognized by the EU legislation. Thereby detected levels are low enough to consider if mussels are suitable for consumption or not. On the other hand, the method HPLC-FD with post-column derivatization is quick and lower levels of PSTs could be detected. This is important e.g. when exposure to chronic low levels of PSTs is investigated. Even more, it is still unclear whether *Alexandrium* is really responsible for PSTs in the mussels, and whether it can come in the future to higher PST loads. Therefore, research is needed to identify sources of PSTs on the Bulgarian coast, as well as whether *Alexandrium* (as a potential source of PSP) could form harmful blooms in the Black Sea.

CONCLUSIONS

This study highlights the low contamination with PSTs in mussels off the north coast of Bulgaria in 2017. Via HPLC-FD with post column derivatization were detected GTX₂ levels that were lower than the LOD of the other method used – HPLC-FD with precolumn derivatization. Thus, combination of both methods will contribute in increasing awareness about PSP and by estimation of PSTs exposure.

Acknowledgement: This work was supported by Science Fund of Medical University Varna, Project Incoming number 16012/2016 and partially funded by the Helmholtz-Gemeinschaft Deutscher Forschungszentren through the research program “Polar regions And Coasts in the changing Earth System” (PACES II) of the Alfred Wegener Institut-Helmholtz Zentrum für Polar- und Meeresforschung.

REFERENCES

1. A. Fuentes, I. Fernández-Segovia, I. Escriche, J. Serra, *Food Chem.*, **112**(2) (2009).
2. O. Ozden, S. Ulusoy, N. Erkan, *J für Verbraucherschutz und Lebensmittelsicherheit*, **5**, (3-4),407 (2010).
3. Ministry of Agriculture and Food, *Annual Report on the situation and development of agriculture*, Sofia (2016).
4. C.Y. Kao, *Algal Toxins in Seafood and Drinking Water*, Academic, San Diego, 1993.
5. N. Lagos and D. Andrinolo, in: *Seafood and freshwater toxins*, Marcel Dekker, New York, 2000, p. 203.
6. G. Hallegraeff, in: *Manual of Harmful Marine Microalgae*, G. Hallegraeff, D. Anderson and A. Cembella, (Eds) International Oceanographic

- Z.V. Peteva et al.: Evaluation of paralytic shellfish poisoning toxin profile of mussels from Bulgarian North Black Sea coast ... Commission (IOC) Manual and Guides UNESCO, Paris, 1995, p. 1.
7. A. Chapelle, M. Le Gac and C. Labry, *Harmful Algae News*, **51**, 2015.
 8. P. Costa, A. Robertson and M. Quilliam, *Marine Drugs*, **13** (4), 2046 (2015).
 9. M. Rañada, R. Tabbada, A. Mendoza, *Regional studies in Marine Sciences*, **3**, 176 (2016).
 10. A. Cembella, in: Physiological Ecology of Harmful Algal Blooms, A. Cembella and G. Hallegraeff, (Eds.), Springer, Berlin, 1998, p. 381.
 11. R. Orr, A. Stüken, T. Rundberget, W. Eikrem and K. Jakobsen, *Harmful Algae*, **10**, 676 (2011).
 12. L. Gainey, J. Shumway, S. Shumway, *J. Shellfish Res*, **7**, 623 (1988).
 13. C. Dell'Aversano, J. Walter, I. Burton, D. Stirling, E. Fattorusso and M. Quilliam, *J. Nat. Prod*, **71**, 518 (2008).
 14. L.M. Durán-Riveroll, B. Krock, A. Cembella, J. Peralta-Cruz, J.J. Bustillos-Guzman, C.H. Band-Schmidt. *Natural Products Chemistry & Research*, **5**, 275 (2017).
 15. J. Alexander, D. Benford, A. Cockburn, J.-P. Cradevi, E. Dogliotti A. Domenico et al., *EFSA J.*, **1019**, 1 (2009).
 16. AOAC. Method 2005.06: Paralytic Shellfish Poisoning Toxins in Shellfish. Prechromatographic Oxidation and Liquid Chromatography with Fluorescence Detection (First Action 2005," *AOAC INTERNATIONAL*, 83 (2006).
 17. A. Turner, M. Dhanji-Rapkova, C. Baker and M. Algoet, *Journal of AOAC International*, **97** (2), 492 (2014).
 18. R. Berlinck, M. Kossuga, *Nat. Prod. Rep.*, **22**, 516 (2005)
 19. M. S. Harwood and M. Boundy, in: Comprehensive Analytical Chemistry Recent Advances in the Analysis of Marine Toxins, J. Diogène, M. Campàs, Elsevier, Amsterdam, 2017.
 20. B. Krock, C. G. Seguel and A. D. Cembella, *Harmful Algae*, **6**(5), 734 (2007).
 21. BAS-IO, Protocols phytoplankton, 2017. http://www.bgodc.io-bas.bg/monitoring_program.html
 22. Z. Peteva, S. Georgieva, B. Krock and M. Stancheva, in: CBU International Conference Proceeding 2018: Innovations in Science and Education, [In press] (2018).
 23. G. Krumova-Valcheva, G. Kalinova, *Acta Microbiologica Bulgarica*, **33**(1), 30 (2017)

Estimation of THQ and potential health risk for metals by consumption of some black sea marine fishes and mussels in Bulgaria

K. Peycheva*, V. Panayotova, A. Merdzhanova, R. Stancheva

Medical University Varna, Department of Chemistry, 84 Tzar Osvoboditel Blv, Bulgaria

Received October 31, 2018; Revised January 4, 2019

Seafood is an essential component of the world population's diet being an important source of proteins, vitamins and unsaturated essential fatty acids. Despite this, seafood products are a commodity of potential health concern as they can be contaminated with a wide range of environmentally chemicals among which are heavy metals.

Human exposure to As, Cd, Hg, Cu, Cr, Mn, Fe, Ni, Zn and Pb through consumption of three marine fish species (European anchovy, garfish and leaping mullet) and mussels was estimated by evaluation of target hazard quotient (THQ), target risk (TR), and hazard (HI) indexes.

The heavy metals analysis show that Zn and Fe are with maximum values in comparison to the other elements. The results from this study show that the THQ for the toxic and essential elements understudied are less than 1; signified that a daily exposure at this level is unlikely to cause any adverse effects during a person lifetime. Additionally, HI of each trace element were also lower than 1 suggesting that these pollutants perhaps pose no hazard to local residents. The TR values were between 10^{-6} and 10^{-4} mean that there is no important cancer risks associated with the consumption of the marine fish species subject to this study.

Keywords: heavy metals, marine fishes, mussels THQ, HI, Black Sea

INTRODUCTION

Contamination of many ecosystems, including aquatic one, arise from both antropogenic sources of pollution and natural weathing. Among the serious chemical pollutants are heavy metals which are toxic, persistent and not easily degradable. The major source of human exposure to heavy metals is via food web. Humans require, for the proper function of most body processes, adequate levels of some essential elements such as magnesium, manganese, selenium, chromium (III), copper, cobalt, iron, and zinc. However, humans may be exposed to harmful non-essential elements such as arsenic, lead, mercury, cadmium, and nickel mainly through consumption of fresh and processed foods such as marine fishes and molluscs.

Fish is widely consumed in many parts of the world by humans because it has high protein content, low saturated fat and also contains omega fatty acids known to support good health [1]. Fish and other aquatic life forms such as mussels are constantly exposed to chemicals in polluted and contaminated waters [2]. Fish and marine mussels have been found to be good indicators of heavy metal contamination in aquatic systems because they occupy different trophic levels [3]. Cantillo found good agreement among the data sets of metal concentrations in mussels, validating the use of mussels in metal monitoring [4].

The heavy metal pollution may cause acute and chronic effect to human [5]. Several methods have been proposed for estimation of the potential risks to

human health of heavy metals in fishes [6]. The risks may be divided into carcinogenic and non-carcinogenic effects [7]. Risk assessment is one of fastest method which is need to evaluate the impact of the hazards on human health and also need to determine the level of treatment which are tend to solve the environmental problem that occur in daily life [7]. Today the methods, which are used the most, are based on calculation on Target Hazard Quotients (THQ), Hazard Index (HI) and Target Risks (TR).

The aim of this study was 1.) to determine the concentration of As, Cd, Hg, Cu, Cr, Mn, Fe, Ni, Zn and Pb in three marine fish species (European anchovy, garfish and leaping mullet) and mussels caught from Bulgarian Black Sea coast; 2.) to evaluate the human exposure to As, Cd, Hg, Cu, Cr, Mn, Fe, Ni, Zn and Pb through consumption of these three marine fish species and mussels by estimating the hazard quotient (THQ), target risk (TR), and hazard (HI) indexes; 3.) to compare the data obtained for the marine species with those of black sea mussel samples.

EXPERIMENTAL

Sampling, sample preparation and storage

The fishes used in this study were European anchovy (*E. encrasicolus*), garfish (*Belone belone*), leaping mullet (*Chelon saliens*). Samples of fish and wild Black Sea mussels (*M. galloprovincialis*) were randomly acquired in local fishermen market from cities across the coastal waters of Bulgarian Black Sea. These sampling sites of Bulgarian Black Sea

* To whom all correspondence should be sent.
E-mail: peycheva@hotmail.com

coast are Varna, Varna Lake, Pomorie, and Kavarna. All the fish species were sampled from spring and fall of the year 2016.

In order to obtain a representative sample at the each location more than 2 kg of mussels and 2 kg of fishes of similar length were collected, placed in plastic bags collected and transported to the laboratory. Total length and weight of the fish sample brought to laboratory after collection were measured to the nearest millimeter and gram before dissection. Only fillets of edible part of each individual were collected and included in the respective composite samples. Approximately 1 g sample of muscle from each fish were dissected, washed with distilled water, weighted, packed in polyethylene bags and stored at -18°C until chemical analysis. The molluscs were cleaned, rinsed and dissected fresh. The soft tissue of the samples was rinsed with Milli-Q water to remove any remaining sand and/or other particles, freeze-dried and homogenized using a mill. About 25–30 mussels from each sampling site were selected, pulverized and analyzed for the trace elements.

Chemical analysis

Wet digestions were performed in triplicate by weighing approximately 1.0 g of the fish and mussel tissues with a mixture of 10 ml HNO₃ (65% Merck, Suprapur) in a microwave digestion system MARS 6 (CEM Corporation, USA) delivering a maximum power and temperature of 800 W and 200 °C, respectively, and internal temperature control, was used to assist the acid digestion process. The digested fish and mussel samples were diluted to 25 ml with Milli-Q water and stored in polyethylene bottles. A blank digest was performed in the same way. The concentrations of As, Cd, Cr, Cu, Fe, Mn, Ni, Pb, Zn in the samples were determined using ICP-OES Spectrometer (Optima 8000, Perkin Elmer, USA) with plasma gas flow – 10 L/min, auxiliary gas flow -0.7 L/min, nebulizer gas flow - 0.2 L/min and axial plasma view. The analyses of total Hg was performed using continuous flow hydride generation inductively coupled plasma - optical emission spectrometry (CF-HG-ICP-OES, Optima 8000, Perkin Elmer, USA) with reducing agent 0.2% NaBH₄ prepared in 0.05% (w/v) NaOH. The accuracy of the applied analytical procedure for the determination of trace metals in mussels was tested using SRM 2976 (Mussel homogenate, NIST) certified reference material. The recovery ranges were between 95.3 and 102.6%. A DORM-2 (NRCC, Ottawa) certified dogfish tissue was used as the calibration verification standard. Recoveries between 90.5 and 108% were accepted to validate the calibration.

Statistical analysis

The whole data were subjected to a statistical analysis. Student's- test was employed to estimate the significance of values.

RESULTS AND DISCUSSION

Heavy metal concentration in marine products

The concentration levels of studied heavy metals (As, Cd, Cr, Cu, Hg, Ni, Zn, Pb, Mn, Fe) detected in the analyzed samples from different stations of Bulgarian Black Sea coast are illustrated in Table 1. Among the different metals analyzed lead, cadmium, chromium and nickel are classified as chemical hazards [8].

Seafood could be a major source of total arsenic exposure for man, since it contains mg/kg [9]. Arsenic exists in many forms. Arsenobetaine and arsenocholine are more efficiently accumulated from seawater by the fish and mussel than other chemical forms such as arsenite and arsenate and other organometallic complexes [10]. The lowest mean total arsenic concentration is found in mussel samples (0.094 mg/kg) and the highest mean in leaping mullet (0.218 mg/kg w.w). In the literature the data corresponding to As show values of 0.98±0.07 µg/g in muscle tissues of *Lophius budegassa* from Iskenderun Bay (Turkey) [11] between 0.38 mg/kg w.w in shad (*Alosa pontica*) and 1.1 mg/ kg w.w. in gray mullet (*M. cephalus*) for samples from Bulgarian Black Sea [12] and between 1.67 and 16.37 mg/kg fresh weight in edible part of the *M. galloprovincialis* taken from offshore along the Northern Adriatic coast in Rijeka Bay (Croatia) during different season [13]. The concentration of As in this study was generally low in all the species compared with the data in the literature and world food standards (Table 1).

European Union countries strictly monitor the concentration of Cd in marine environment since this element is very toxic, easily transported in the air. The maximum permissible value for fish (0.05 mg/kg w.w) and mussels (1.0 mg/kg w.w) do not exceed the values obtained in this study (Table 1). Levels of Cd reported in the literature vary between 0.012 mg/ kg w. w for muscle tissues of gray mullet and 0.015 mg/kg w.w for atlantic bonito caught from the waters of Black Sea [12], between 0.25- 1.16 µg/g w.w. in the soft tissue of green-lipped mussel *P. viridis* collected from coastal waters off Peninsular Malaysia [14] and between 0.10 mg/g d.w and 0.48 mg/g d.w. in *Alosa caspia*, *Engraulis encrasicolus*, *Trachurus trachurus*, *Sarda sarda* and *Clupea sprattus* of the middle Black Sea (Turkey) [15].

Table 1: Mean concentrations (mg/kg w.w) and standart deviation of heavy metals for each species (N is the number of analyzed fish and mussel species)

	European anchovy (<i>E. encrasicolus</i>) N=12	Leaping mullet (<i>C. saliens</i>) N=3	Garfish (<i>Belone belone</i>) N=6	Guidelines (in mg/kg w.w)			Wild Black Sea mussels (<i>M. galloprovincialis</i>) N=20	Guidelines (in mg/kg w.w)	
				BFC (2004)	EC (2006)	FAO (2003)		BFC (2004)	EC (2006)
As	0.134±0.020	0.218±0.103	0.128± 0.029	5.0	---	---	0.094±0.014	2.0	
Cd	0.013±0.0005	0.014±0.001	0.048±0.002	0.05	0.05	0.05	0.018±0.002	---	1.0
Cr	0.023±0.005	0.024±0.003	0.048±0.004	0.3	---	---	0.013±0.001	---	---
Cu	0.210±0.020	0.169±0.021	0.218±0.022	10	---	---	0.088±0.001	30	---
Fe	5.078±0.800	1.556±0.264	1.496±0.166	---	---	---	1.949±0.085	---	---
Hg	n.d*	0.123±0.011	0.096±0.005	0.50	0.50	---	0.023±0.006	---	0.50
Mn	0.328±0.056	0.166±0.0127	0.256±0.026	---	---	---	0.241±0.002	---	---
Ni	0.025±0.003	0.022±0.0418	0.029±0.026	0.5	---	---	0.034±0.016	---	---
Pb	0.082±0.0015	0.088±0.0110	0.160±0.036	0.30	0.20	---	0.017±0.061	---	1.50
Zn	3.044±0.144	1.282±0.0340	5.365±0.590	50	---	---	2.111±0.019	200	---

*n.d-under limit of detection

**BFC-Bulgarian Food Codex, EC-European Commission, FAO- Food and Agriculture Organization

Of particular concern is Cr which is considered as a heavy metal and pollutant, but at the same time as a microelement, whose biologically usable form plays an essential role in glucose metabolism [11]. Chromium together with arsenic and nickel are considered as hazardous elements by the USFDA [16] even though not covered by EC regulations for fish and other aquatic products. Chromium was detected in all the samples-mussel has less concentration of Cr than fish samples (0.013 mg/kg w.w for *M.galloprovincialis* and between 0.023 and 0.048 mg/kg for *E.encrasicolus*, *C. saliens* and *B.belone*). Usero et al. [17] found that Cr concentration in common sole vary between 0.015 and 0.031 mg/kg from salt marshes on the southern Atlantic coast of Spain; between 2.0 and 4.2 mg/kg d.w. in the sampled mussels from five sites on the Montenegrin coastal area (southeastern Adriatic Sea) [18]; and between 0.03 and 0.07 mg/kg f.w. in five most consumed marine fishes from Bulgarian Black Sea Coast [19]. Since there is no MPL for Cr in food set by various organizations it can be concluded that the level of Cr in analyzed samples is in accordance with the literature data.

Maximum concentration of Cu was detected in the sample of *B.Belone* (0.218 mg/mg w.w) and the minimum in wild black Sea mussel (0.088 mg/ kg w.w). In the literature the concentration of this essential element vary between 4.9 mg/kg and 17.2 mg/kg in Mediterranean blue mussels from five sites on the Montenegrin coastal area (southeastern Adriatic Sea) [18]; up to 17.2 mg/kg in *Mugil cephalus* from Bulgarian section of Black Sea (Sinemoretz) [20] and between 1.3 and 4.54 mg / kg d.w for the muscle of *Dicentrarchus labrax* from The Bay of Güllük in Southeastern Aegean Sea (Turkey) [21]. The maximum copper level permitted for marine fishes is 10 mg/kg (30 mg/kg for mussel) according to Bulgarian Food Authority [22]. Our values were lower than the values from the literature and the ones stated by the Bulgarian Food Authorities.

The minimum and maximum iron levels observed were 1.496 mg/kg w.w in *B. Belone* and 5.078 mg/kg w.w in *E. encrasicolus*. Iron contents in the literature have been reported in the range of 0.82– 27.35 µg/g d. w in fish species from Iskenderun Bay, Northern East Mediterranean Sea, Turkey [23], 9.52– 32.40 µg/g d.w. in fish samples of the middle Black Sea (Turkey) [24], 7.46– 40.1 µg/g in seafoods from Aegean, Marmara and Mediterranean seas in Turkey [25]. There is no information about maximum iron levels in fish samples in Bulgarian standards [22] but the values from this study are within the data in the literature.

Mercury (Hg) is one of the most hazardous pollutants in the environment. It can exist in various forms like marine products are rich to methylmercury. The purpose of this study was focused on total mercury determination. The maximum level was found in mussel samples (0.023 mg/kg w.w) and minimum level-for garfish (0.0960 mg/kg w.w). For *E. encrasicolus* the concentrations was under limit of detection. In a study of ten different fish species from the Black Sea, Turkey it was found that the total Hg level vary between 25 mg/kg in *S. sarda* and 84 mg/kg in *M. merlangus* [15], between 0.99 and 14.79 mg/ kg d.w. whole soft tissue of mussels collected at 14 locations along the eastern Adriatic coast [26] and between 0.04 and 0.08 mg/kg w. w in the muscle tissues of the anchovy, mackerel, red mullet and picarel from the Adriatic Sea, Croatia [27]. However, mean metal levels in the analyzed marine samples were below the maximum permissible value indicated by the European Community [28] and the Bulgarian legislation (0.5 mg /kg w.w) [22].

There is no MPL for Mn set by EU [28] or Bulgarian food legislation [22] but in the literature it was found that the concentration of this element vary between 76 µg/g and 9.10 µg/g for ten different fish species from the Black Sea, Turkey [15] between 1.06 and 3.76 mg/g d.w. in *A. caspia*, *E. encrasicolus*, *T. trachurus*, *S. sarda* and *C. sprattus* from Black Sea [24]. The results from current study are less than that values for both fish and mussel samples.

Nickel and lead are two chemical elements considered as priority pollutants according to Water Frame Directive [28]. Fishes and other molluskans accumulate these elements from the surrounding environment. According to Bulgarian Food Codex the level of Ni and Pb in fish and mussels should not be over 0.5 mg/kg w.w and 0.30 mg/kg w.w, respectively. As it can be seen from Table 1 the results from this study are within these limits. Moreover, Pb concentration was in the range of 0.03 mg/kg w.w and 0.09 mg/kg w.w for three fish samples from from salt marshes on the southern Atlantic coast of Spain while Ni concentration – between 0.08 mg/kg w.w and 0.33 mg/kg w.w [17]. In our previous study of seven most consumed Bulgarian fish species collected from north-east coast of Black Sea, the concentrations of Pb ranged between 0.03 mg/kg w.w and 0.08 mg/kg w.w while Ni – between 0.008 mg/kg w.w and 0.028 mg/kg w.w [12]. For bivalve species from Sea of Marmara in Turkey, the concentration of Ni was significantly higher in *D. frunculus* than in *C. gallina* in the winter (1.556 mg/kg), summer (3.633 mg/kg), and autumn

K. Peycheva et al.: Estimation of THQ and potential health risk for metals by consumption of some black sea marine fishes ...
 (1.503 mg/kg) and the maximum contents of Pb were 1.342 mg/kg for *C. gallina* [29].

Among the ten metals under study, zinc showed the highest level of accumulation. A similar situation was observed in studies [30]. The concentration of zinc varied from 1.282 (for *L. Mullet*) to 5.365 mg/kg w.w (for garfish). The wild Black sea mussel sample show concentration of 2.111 mg/kg w. The maximum Zn level permitted for fishes is 50 mg/kg and 200 mg/kg for mussels according to Bulgarian Food Codex [31]. Tuzen [15] found zinc concentration to be between 38.8 µg/g in *E. encrasicolus* and 93.4 µg/g in *P. saltor* for samples from Black Sea, between 9.296-25.901 mg/kg for *D. trunculus* from Turkey [32]. The concentration of Zn from current study is within the limits set by various organizations and the data in the literature.

Assessment of health risk

THQs were used to estimate the risks associated with marine fish and mollusk consumption. THQs, calculated by the ratio of exposed heavy metal concentrations to the reference dose concentrations, are used to explain for long-term non-carcinogenic exposure probabilities [33]. A THQ value >1 means that the metal is likely to have adverse health effects. HI from THQs can be expressed as the sum of the hazard quotients [33]. Target cancer risk (TR) was used to indicate carcinogenic risks and it is calculated only for As, Ni and Pb since Cu, Hg, Zn, Mn, Fe, Cd, Cr do not cause any carcinogenic effects. Calculation of THQ, HI and TR is done as follows:

The THQs, HI and TR through consumption of *E. Encrasicolus*, *B.belone*, *C.saliens* and *M. galloprovincialis* from the Black Sea coast separately for males and females are illustrated in Figure 1.

Table 2: Model for estimating various health risks associated with consumption of marine products

TARGET HAZARD QUINTET	HAZARD INDEX	TARGET RISK
$THQ = \frac{(M_C \cdot I_R \cdot 10^{-3} \cdot EF \cdot ED)}{(RfD \cdot BW_a \cdot ATn)}$	$HI = THQ_{As} + THQ_{Cd} + THQ_{Cr} + THQ_{Cu} + THQ_{Fe} + THQ_{Ni} + THQ_{Zn} + THQ_{Pb} + THQ_{Mn} + THQ_{Hg}$	$TR = \frac{(M_C \cdot I_R \cdot 10^{-3} \cdot CPSo \cdot EF \cdot ED)}{(BW_a \cdot ATc)}$
<p>M_C is the metal concentration in muscle tissues of fish (µg/g) I_R is the mean ingestion rate of fish EF is the exposure frequency or number of exposure events per year of exposure, ED is the exposure duration, total for adults RfD is the reference dose (Cu = 0.04, As = 3×10^{-4}, Zn = 0.3, Ni= 0.02, Cr = 3×10^{-3}, Fe = 9×10^{-3}, Cd = 13×10^{-3}, Pb = 4×10^{-3}, Mn = 0.14 4 µg/g day), BW_a is the body weight, adult ATn is the averaging time, noncarcinogens; calculated by multiplying exposure frequency in exposure duration over lifetime (day/year). $CPSo$ is the carcinogenic potency slope, oral (As = 1.5 and for Ni= 1.7 mg/kg bw-day); ATc is the averaging time, carcinogens (day/years) and was calculated by multiplying exposure frequency in exposure duration over lifetime</p>		

Detected THQ values were below the limit value of 1, which indicates that the heavy metals may not possibly have adverse health effects on a human being by daily average consumption of those three fish species and mussels. In addition to this, HI has been observed that these values were up to 0.25 (for both males and females), meaning the values were below the threshold value of 1. Comparing the TR values with guideline values (10^{-6} - 10^{-4}), indicates that marine fishes and mussels from Bulgarian Black Sea coast are safe for human consumption.

CONCLUSIONS

The present study provides new information on the distribution of trace elements in three fish and one wild mussel species from the Black Sea in

Bulgaria. Based on the samples analyzed, the edible parts of fish and mussel samples do not carry heavy mineral loads, and the mineral concentrations are below the legal values for fish and fishery products established by various organizations.

Cancerogenic HI did not exceed one and it is assumed that no chronic risks were likely to occur at the site. Calculated average value of carcinogenic risk (TR) of the fishes and mussel under analysis was performed for As, Pb and Ni and indicates that analyzed fish are safe for human consumption. There is no significant difference in the analytical levels, HI and TR for the analyzed heavy metals between marine fishes and mussel samples.

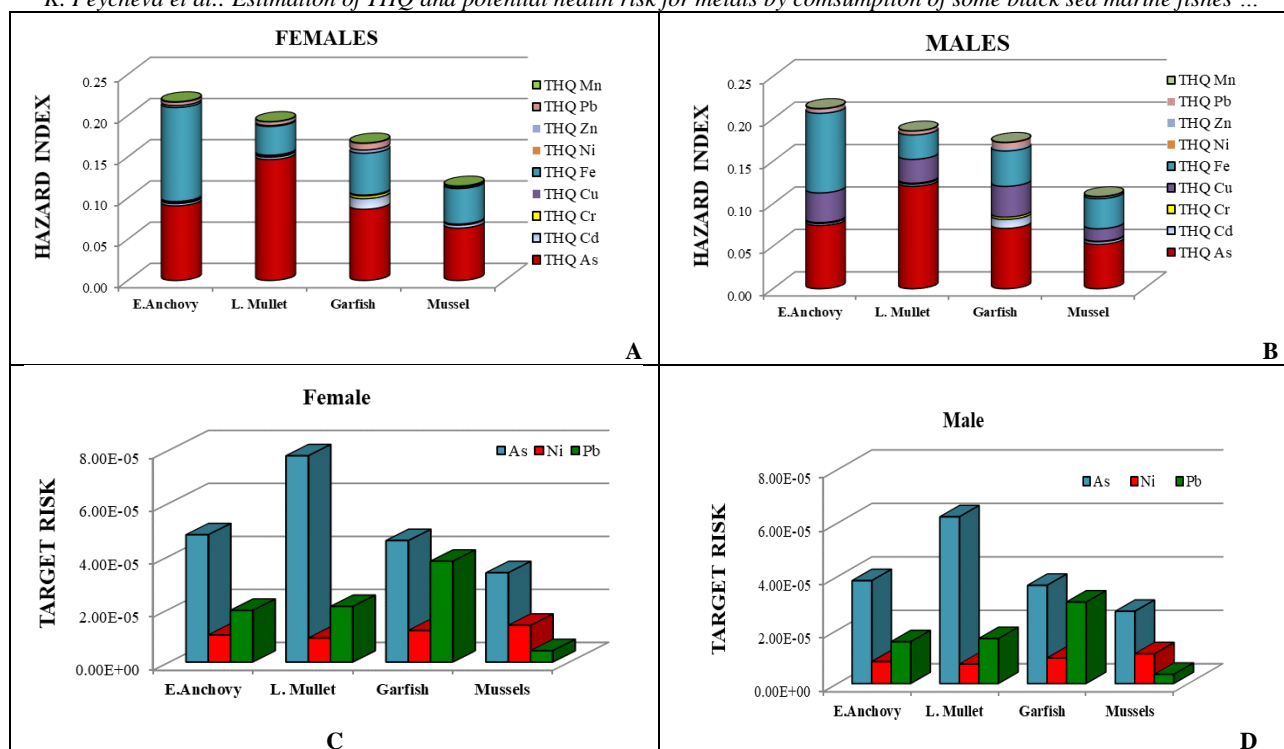


Figure 1: Risk values of each metal contaminant of the marine product for females and males: a.) Hazard Index (females); b) Hazard Index (males); c.) Target risk (females); d.) Target risk (males)

REFERENCES

- US EPA (United States Environmental Protection Agency) EPA-823-F-04-009, 2pp, available at: <http://www.epa.gov/waterscience/fish/MethylmercuryBrochure.pdf>. (2004)
- A. Ikem, N.O. Egiebor, *J. Food Comp. Analysis*, **18**, 771 (2005)
- J. Burger, K. F. Gaines, C. Shane Boring, W. L. Stephens, J. Snodgrass, C. Dixon, M. McMahon, S. Shukla, T. Shukla, M. Gochfeld, *Environ. Research*, **89**, 85 (2002)
- A. Y. Cantillo, *Marine Pollution Bull.*, **26**, 712 (1998)
- A. F. Fidan, H. Cigerci, M. Konuk, I. Kucukkurt, R. Aslan and Y. Dundar, *Environ. Monit. Assess.*, **147**, 35 (2008).
- A. S. Amirah, W. I. W. Afiza, M. H. Faizal, Nurliyana, S. Laili, *J. Environ. Pollution Human Health*, **1**, 1 (2013)
- Y. Yujun, Y. Zhifeng, Z. Shanghong, *J. Environ. Pollution*, **159**, 2575 (2011)
- FAO, FAO Fishery Circular No. 464, pp. 5–100 (1983)
- I. Karadjova, P. Petrov, I. Serafimovski, T. Stafilov, D. Tsalev, *Spectrochim. Acta Part B: Atomic Spectroscopy*, **62**, 258 (2007)
- J. Gaisler, K. A. Francesconi, J. S. Edmonds, K. J. Ingolic, *Appl Organomet. Chem*, **9**, 341 (1995)
- A. B. Yilmaz, M. K. Sangun, D. Yağlıoğlu, C. Turan, *Food Chemistry*, **123**, 410 (2010)
- L. Makedonski, K. Peycheva, M. Stancheva, *Food Control*, **72**, 313 (2017)
- S. Klarić, D. Pavičić-Hamer, Č. Lucu, *Helgoland Marine Research*, **58**, 216 (2004)
- C. K. Yap, A. Ismail, S. G. Tan, *Marine Pollution Bull.*, **46**, 1035 (2003)
- M. Tüzen, *Food Chem. Toxicology*, **47**, 1785 (2009)
- USFDA, Food and drug administration. DHHS/PHS/FDA/CFSAN/Office of Seafood, Washington, DC. (1993).
- J. Usero, C. Izquierdo, J. Morillo, I. Gracia, *Environ. Int.*, **29**, 949 (2003)
- D. Joksimovic, I. Tomic, A. R. Stankovic, M. Jovic, S. Stankovic, *Food Chemistry*, **127**, 632 (2011)
- M. Stancheva, L. Makedonski, K. Peycheva, *Bul. Chem. Commun.*, **46**, 195 (2014)
- G. Buchvarov, D. Kirin, N. Kuzmanov, *J. Environ. Protection Ecol.*, **4**, 365 (2003)
- Ö. Dalman, A. Demirak, A. Balcı, *Food Chem.*, **95**, 157 (2006)
- Anonymous, Darjaven Vestnik, 08 October 2004, 88 (2004)
- A. Turkmen, M. Turkmen, Y. Tepe, I. Akyurt, *Food Chem.*, **91**, 167 (2005)
- M. Tuzen, *Food Chem.*, **80**, 119 (2003)
- M. Turkmen, A. Turkmen, Y. Tepe, A. Ates, K. Gokkus, *Food Chem.*, **108**, 794 (2008)
- Z. Kljaković-Gašpić, S. Herceg-Romanić, D. Kožul, J. Veža, *Marine Pollution Bulletin*, **60**, 1879 (2010)
- N. Bilandžić, M. Dokić, M. Sedak, *Food Chem.*, **124**, 1005 (2011)
- Directive 2000/60/EC of the European Parliament
- B. P. Cid, C. Boia, L. Pombo and E. Rebelo, *Analyt. Lett.*, **33**, 3333 (2001)
- Reglament (EO) № 1881/2006, 19.12.2006
- O. Ozden, *Int. J. Food Sci. Technol.*, **45**, 578 (2010)
- USEPA (2011). Available at: <http://www.epa.gov/regshwmd/risk/human/Index.htm> last update: 6.12.2011

Quality-related changes of biologically active lipids in bluefish muscle tissue after cooking

D. A. Dobрева*, A. Merdzhanova, V. Panayotova

Medical University of Varna, Faculty of Pharmacy, Varna, Bulgaria

Received November 5, 2018; Revised January 4, 2019

The aim of the present study was to evaluate the effect of different cooking methods (steaming, grilling, conventional baking and microwaving) on total lipids, fatty acid composition, fat soluble vitamins (A, D₃ and E), and cholesterol contents of bluefish tissue (*Pomatomus saltatrix*) from the Black Sea coast.

There were no significant differences in the amounts of total lipids between raw, steamed, grilled and oven baked samples. In contrast, there was a significant increase in the total lipid content of microwaved bluefish, probably due to the significant decrease in moisture content. Fatty acids (FA) groups were affected by all thermal treatment, but their distributions kept similar pattern: SFA>MUFA>PUFA. All three fat soluble vitamins showed significantly higher values during culinary treatment, with the exception of vitamin E after grilling. However, all cooking methods were found to be appropriate culinary treatment, which preserves well nutritional lipid quality of bluefish meat.

Keywords: fat soluble vitamins, fatty acids, thermally treatment, *Pomatomus saltatrix*

INTRODUCTION

Marine fish are a very good source of several biologically active compounds as fat soluble vitamins, unsaturated fatty acids and cholesterol. The vitamins control a variety of processes in human organism. On the other side, fish lipids were known as rich of active substances with cardio protective role. The most active constituents are identified to be n3 polyunsaturated fatty acids (n3 PUFAs), eicosapentaenoic acid (EPA) and docosahexaenoic acid (DHA) [1].

Bluefish (*Pomatomus saltatrix*) is a marine, pelagic fish, which is found in most seas and oceans around the world. It is known for its delicious taste and high nutrition quality. Many studies observed the information about PUFAs content and fat soluble vitamins' in raw fish edible tissue, which have limited application on human health. Traditionally culinary treatment of this species involves grilling and baking. Temperature processing of fish fillets is applied to inactivate pathogenic microorganisms and enhances its taste, but this treatment influences the fat soluble vitamins and essential fatty acids contents. It is known that many of the biologically active substances (vitamins etc.) degrade in presence of oxygen and under the influence of high temperatures. Therefore, many studies focused their research to calculating the changes in content of these components in fish tissues, after thermally treatment [2 - 6]. The most commonly used methods of culinary processing of edible fish tissue are steaming, grilling, oven baking, microwave oven treatment. It has been found, however the changes in

nutrient content depend on one side from the variety of heat treatment, but the other side - from fish type [7].

There is limited information in the scientific literature about changes in lipid composition of the Black Sea bluefish edible tissue occurring after cooking process.

EXPERIMENTAL

Sample preparation

Fifteen Black Sea bluefish specimens were purchased from the local Varna fresh fish marketplace. In the laboratory fish was filleted with the skin and the fillets were randomly divided into five groups: first (n = 6) - analyzed in raw state; a second (n = 6) was analyzed after steaming (in a steamer for 10 min, 90°C), the third (n = 6) – after grilling (on a grill for 15 min, 220°C), the fourth (n = 6) – after baking (on an oven for 25 min, 200 °C) and the fifth (n = 6) – after microwaving (on a microwave oven for 15-20 min, ~800 W). After processing, the samples were weighed in order to obtain the weight loses compared with raw state.

Moisture analysis

The moisture content of raw and cooked samples was determined by the AOAC method and calculated as weight loss [8]. The results were calculated as percentage losing weight after drying the samples.

Vitamin's and cholesterol analysis

Fat soluble vitamins (A, D₃ and E) and cholesterol were determined simultaneously using

* To whom all correspondence should be sent.
E-mail: didobрева@gmail.com

HPLC system (Thermo Scientific Spectra SYSTEM) equipped with Synergi 4 μ Hydro-RP 80A pore 250 \times 4,6 mm reversed-phase column. The sample preparation was performed using the method of Dobreva et al. [9]. The received data were calculated and expressed as μg per 100 g wet weight ($\mu\text{g}\cdot 100\text{g}^{-1}\text{ww}$).

Total lipid and fatty acid analysis

The extraction of total lipids from analyzed edible fish tissue was done according to Bligh & Dyer method [10]. Total lipid (TL) content was determined for each group of sample (n=6) and the results were presented as g per 100g wet weight ($\text{g}\cdot 100\text{g}^{-1}\text{ww}$).

Fatty acid methyl esters were prepared by base catalyzed transmethylation and directly analyzed by gas chromatography system, model FOCUS Gas Chromatograph A3000, equipped with Polaris Q MS detector (Thermo Scientific, USA). The chromatography system was equipped with capillary column TR-5 MS, 30m length, 0.25mm i.d. The observed data were calculated and expressed as the percentage of total fatty acids.

Statistical analysis

The received chromatography data were statistically analyzed using Graph Pad Prism 6 software. The nonparametric test - one-way ANOVA statistical analysis, was used for calculation of differences between raw and cooked by different techniques samples (significant at $p<0.05$). The recalculated results were presented as mean and standard deviations.

RESULTS AND DISCUSSION

Moisture content

The moisture content of all bluefish samples (cooked and raw) was determined and compared. The highest percentage showed the raw sample (56.5%). During all the processes of cooking a significant decrease with raw tissue was observed. The established amounts for thermally processed

fillets were – 62.10 % in steamed, 59.40% in grilled, 60.0% in oven cooked and 49.19% in microwaved samples. These results are in agreement with our previous research for Shad fillets [11]. The other authors presented similar research and conclusions for cooked trout edible tissue [3].

Fat soluble vitamins' and cholesterol contents

The effect of different types of heat treatment on fat soluble vitamins (A, D₃ and E) and cholesterol contents was examined in bluefish edible tissue. Traditional thermal techniques such as steam processing, grilling, oven cooking and microwaving were selected for the preparation of fish fillets. The received results are presented in Table 1. The presented data shows that the varied types of thermal treatment of fish tissue influenced in different ways the content of the three fat soluble vitamins and cholesterol. Only in the case of vitamin D₃ content, we observed decreases after all methods of heat treatment.

A statistically significant reduction in the levels of vitamin D₃ of the treated samples compared to the untreated was found in grilling - 32% ($p<0.01$) and microwaving - 47% ($p<0.001$) (Table 1). For the other thermal treatments, the differences are statistically insignificant ($p>0.05$). The amount of these analyte in processed fish fillets remains almost unchanged after two different cooking methods – steaming (12% decrease) and oven cooking (10% decrease) ($p>0.05$). The temperature influenced the vitamin D₃ levels on a very small extent compared to the other two vitamins.

On the other hand, vitamin A amount decreased significantly after process of steaming and oven cooking ($p<0.001$) with 25.3% and 22.6%, respectively (Table 1). But after other two types of thermal processing he remains almost unchanged. The grilling and microwaving processes did not affect the vitamin A levels in the fish tissue - 146.2 $\mu\text{g}\cdot 100\text{g}^{-1}\text{ww}$ in the raw state, compared to 154.4 $\mu\text{g}\cdot 100\text{g}^{-1}\text{ww}$ and 155.3 $\mu\text{g}\cdot 100\text{g}^{-1}\text{ww}$, respectively ($p>0.05$).

Table 1 Fat soluble vitamin's and cholesterol contents in raw and cooked fish fillets

Analyte	Black Sea Bluefish				
	raw	steamed	grilled	oven cooked	microwaved
Vitamin A, $\mu\text{g}\cdot 100\text{g}^{-1}\text{ww}$	146.2 \pm 3.7	109.0 \pm 12.1 ^a	154.4 \pm 16.7	113.2 \pm 14.2 ^a	155.3 \pm 17.4
Vitamin D ₃ , $\mu\text{g}\cdot 100\text{g}^{-1}\text{ww}$	40.9 \pm 2.3	35.8 \pm 7.4	27.7 \pm 3.4 ^a	36.8 \pm 4.3	22.4 \pm 2.8 ^a
Vitamin E, $\text{mg}\cdot 100\text{g}^{-1}\text{ww}$	4.4 \pm 0.3	4.8 \pm 0.5	5.3 \pm 0.5 ^b	2.1 \pm 0.2 ^a	5.6 \pm 0.6 ^b
Cholesterol, $\text{mg}\cdot 100\text{g}^{-1}\text{ww}$	41.40 \pm 3.1	55.74 \pm 6.4 ^b	45.09 \pm 6.2	62.43 \pm 5.4 ^a	80.28 \pm 9.1 ^a

^a $p<0.001$ raw vs cooked; ^b $p<0.05$ raw vs cooked

The influences of selected types of heat treatment on bluefish edible tissue were also monitored for vitamin E levels (Table 1). The most significant decrease in the amount of vitamin E (by 50%) was after cooking the raw fish tissue in oven. Like vitamin D, and vitamin E showed increases in its amount after two of the heat treatment methods – on grilling and microwaving with almost 20 %. The reasons are probably the same - the changes are related with those in moisture content of the sample, which improve on the hydrolysis rate of the treated tissue. On the other side, the process of steaming does not change statistically the levels of this vitamin ($p > 0.05$).

The data for cholesterol content shows different behaviors. Its amount increased after four type of thermal processing on fish tissue. This correlated with changes in moisture and total lipids contents of the analyzed samples.

In the scientific literature it is observed a discrepancy in the effect of different types of thermal processing on the fat soluble vitamin contents in edible tissue of fish [2, 4, 5, 7, 12]. A study of the influence of variety cooking methods (grilling, microwaving, oven baking and frying) on changes in vitamin A and vitamin E levels in African catfish tissue was reported by Ersoy and Özeren [5]. They found significant differences in the content of both analytes after all thermal treatments. The slightest decrease in vitamin A was observed after the process of microwaving (10%), and the strongest - after baking in oven (36%). The same authors also found significant changes in the vitamin E content. The data showed that the quantity of vitamin E was the most influenced in the case of oven baking - vitamin E levels are increased several times (4.5 times). In the other two processing methods, the changes are also high - grilling and microwaving shows increases of 73% and 53%. When compared to our results, we can say that the changes they made relative to raw tissue are much higher than those observed in our study (Table 1).

The scientific group of Erkan found out losses of vitamin A (75%) and vitamin E (55%) levels in steamed tissue of horse mackerel, which is in agreement with our results [6]. On the other side Mattila et al. reported decreased amount below 10% for vitamin D₃ in herring tissue after oven baking process, which is also close to our results [2].

Total lipids and fatty acid composition

The TL contents in raw and processed edible tissue of bluefish are presented and compared in Table 2. The observed data showed different influence of the cooking techniques on TLs in analyzed samples. Only one is the significant

increase of analyte - for microwaved fish fillets, compared to the raw.

The other authors comment that the changes in TL amounts after thermal processing (steaming and roasting) strongly depend on the fish species, the temperature, the size of the sample and the heatable surface area. The data are in accordance with those by other authors. Gladyshev et al. and Gülgün et al. observed losses of lipids under the influence of heat treatment on edible tissue of rainbow trout and king salmon [13, 14].

As a result of the research, on raw and processed bluefish fillets were observed changes also and in the FA composition of the samples. In Table 2 we presented the results for the major FA groups and their ratios as a percentage of total FAs. They were calculated and compared after the four processes of cooking methods on bluefish fillets. The considered scientific groups presented this effect of heat treatment on FA composition of various fish species. They reached very different conclusions [2, 4, 13, 14].

The SFA was the most abundant (38.86 %) FA group in raw samples, followed by MUFA (33.30 %) and PUFA (27.84 %). This distribution was also confirmed in the processed fish fillets - in the four different methods of preparation (Table 2). These results are in agreement with those of other authors [12]. However, the data obtained, shows different changes in the groups, depending on the applied processing method. The SFA group shows no significant changes after all cooking technics. But the other groups – MUFA and PUFA showed different behaviors. The MUFA significantly decreased ($p < 0.05$) in the steamed fillets. As the PUFA increased ($p < 0.05$) after process of oven cooking, compared with raw bluefish tissue. In two of the thermal treatments, all three FA groups were significantly changed – oven cooking and microwaving (Table 2).

The other authors established significant decreases in the levels of PUFA and MUFA groups. Larsen et al. was found for steaming salmon decreasing of MUFA and PUFA levels [15]. These differences of the FA groups, after various thermal treatments, were attributed in most cases to the tissue specificity of the fish species.

The sum of n3 PUFAs slightly decreased after steam cooking the bluefish fillets. The n6 PUFAs showed different behavior – they increased after the same process. But the changes in two cases were not significant ($p > 0.05$).

The sum of n3 FA content was found to be higher than n6 FAs in all - raw and cooked fish fillets.

Table 2 Total lipid contents and fatty acid groups in raw and cooked fish fillets

Analyte	Black Sea Bluefish				
	raw	steamed	grilled	oven cooked	microwaved
Total lipid, g.100g ⁻¹ ww	4.05	4.046	4.33	4.22	6.06 ^a
Σ SFA	38.86	42.00	36.88	36.62	36.50
Σ MUFA	33.30	30.55	32.21	32.03	34.30
Σ PUFA	27.84	27.45	30.91	31.35	29.20
Σ n3	21.44	20.55	24.80	26.33	23.09
Σ n6	6.90	7.35	6.61	6.50	6.61
n-6/n-3	0.32	0.36	0.27	0.26	0.29
PUFA/SFA	0.63	0.65	0.84	0.86	0.80

^a p<0.001 raw vs cooked

The nutritional value of fats often characterized with ratios of PUFA/SFA and n6/n3. The most Health organizations have nutritional recommendations connected with fatty acid content of foods [16, 17]. They considered the PUFA/SFA ratio in human diets should be above 0.45 and the n6/n3 ratio should not exceed 4.0.

In the present research were observed changes in the two discussed ratios. The thermally processed samples showed significantly higher (p<0.05) PUFA/SFA and n6/n3 ratios, compared with raw. And in two cases they were over the minimum of recommended values.

CONCLUSIONS

The impact of the four different cooking methods on fat soluble vitamins, cholesterol and fatty acids composition of bluefish fillets were investigated.

Cholesterol content increased after steaming, conventional baking and especially microwaving.

All three fat soluble vitamins showed significantly higher values during culinary treatment, with the exception of vitamin E after grilling. Vitamin A and E presented highest increase after microwaving and grilling, while vitamin D₃ – after steaming.

Most abundant FAs in the polyunsaturated FA group were eicosapentaenoic acid (C20:5 n-3, EPA) and docosahexaenoic acid (C22:6 n-6, DHA), which accounted more than 50% of total PUFA. The raw bluefish edible tissue shows the FAs pattern in the order: SFA>MUFA>PUFA, which was validated after the steaming, grilling, oven baking and microwaving processes.

Among the methods used, microwave cooking showed most significant effect on the analysed fish tissue, which resulted in 50% weight and 30% moisture loss, thus affecting the content of lipid components.

The nutrition of lipids of the Black Sea Bluefish tissue was characterized with high levels of fat

soluble vitamins, n3 and n6 FAs and good cholesterol content. And the conclusion is that the positive beneficial effect of fish lipids based on n3/n6 and PUFA/SFA ratios, and fat soluble vitamins' content are preserved after that treatment.

REFERENCES

1. C. Cahu, P. Salen, M. de Lorgeril, *Nutrition, Metabolism Cardiovasc. Diseases*, **14**, 34 (2004)
2. P. Mattila, R. Ronkainen, K. Lehtikainen, V. Piironen, *J. Food Comp. Analysis*, **12**, 153, (1999)
3. Z. E. Sikorski, E. K. Olakowska, *Boca Raton: CRC Press*, (2002)
4. S. Kumara, B. Aalbersberg, *J. Food Comp. Analysis*, **19**, 311, (2006)
5. B. Ersoy, A. Ozeren, *Food Chem.*, **115**, 419, (2009)
6. N. Erkan, A. Selcuk, O. Ozden, *Food Anal. Methods*, **3**: 269, (2010)
7. A. Escriva, M.J. Esteve, R. Farre, A. Frigola, *J. Chromatography A*, **947**, 313, (2002)
8. Moisture in Meat, Official Method of analysis 950.46 of AOAC international, AOAC (1991)
9. D.A. Dobрева, V.Z. Panayotova, R.S. Stancheva, M. Stancheva, *Bul. Chem. Commun.*, **49**, 112 (2017)
10. E. Bligh, W.J. Dyer, *Canad. J. Biochem. Physiol.*, **37**, 913, (1959)
11. D. A. Dobрева, A. Merdzhanova, M. Stancheva, *Scientific Works Univ. Food Technol.*, **LXII**: 310, (2015)
12. A. Polat, Y. Özogul, E. Kuley, F. Özogul, G. Özyurt, A. Simsek, *J. Food Biochem.*, 1745-4514, (2011)
13. M.I. Gladyshev, N.N. Sushchik, G.A. Gubanenko, O.N. Makhutova, G.S. Kalachova, E.A. Rechkina and K.K. Malyshevskaya, *Czech J. Food Sci.*, **32**, 226, (2014)
14. F. Gülgün, Ü. Şengör, D. Ü. Alakavuk, Ş. Yasemin Tosun, *J. Aquatic Food Product Technol.*, **22**, 160, (2013)
15. D. Larsen, S. Young Quek, L. Eyres, *Food Chem.*, **119**: 785, (2010)
16. UK: HMSO, Department of Health, Nutritional aspects of cardiovascular disease: Health and social subjects. London. (1994)
17. D. Mozaffarian, E. Rimm, *J. American Medical Assoc.*, **296**, 1885 (2006)

Seasonal variation in fat-soluble vitamins, cholesterol and fatty acid profile of lipid classes of *Rapana venosa*

V. Z. Panayotova*, A. V. Merdzhanova, D. A. Dobрева, R. S. Stancheva, K. Peycheva

Medical University of Varna, Faculty of Pharmacy, Department of Chemistry,
84 Tzar Osvoboditel St., 9002 Varna, Bulgaria,

Received November 5, 2018; Revised January 4, 2019

Nowadays, invasive species *Rapana venosa* is commercially important and widely harvested in the Black Sea. The aim of this study was to evaluate the seasonal changes in lipid bioactive compounds as fat-soluble vitamins (A, E and D₃), cholesterol, carotenoids (astaxanthin, beta-carotene), lipid classes and their fatty acid profiles. Among fat soluble vitamins, the amounts of vitamin D₃ supplied 100% of recommended daily intake for adults according to Bulgarian food standards. Vitamin E increased in summer period (up to 2825 µg.100⁻¹g ww), whereas vitamin A showed opposite trend. Both carotenoid pigments: beta-carotene and astaxanthin insignificantly decreased in summer season. Strong seasonal influence on the lipid classes and their fatty acid (FA) profile was determined. Despite of the seasons, polar lipids (PL) prevailed in total lipids (TL). In both seasons, FA groups showed similar distribution: PUFA> SFA>MUFA, regardless of lipid class. The most abundant FAs in the polyunsaturated FA group were eicosapentaenoic acid (C20:5 n-3, EPA), docosahexaenoic acid (C22:6 n-3, DHA) and docosapentaenoic acid (C22:5 n-3, DPA), which accounted more than 65% of total PUFA. The high content of vitamin D₃, long chain omega-3 FAs, different FA ratios, low values of cholesterol and nutrition quality indices (atherogenic and thrombogenic indices) confirm the very good functional properties of rapana lipids. In conclusion, the studied rapana harvested from Bulgarian Black Sea coast presents preferable lipid quality in terms of human health protection. Further investigation is required to determine the biological potential of rapana lipids during the year.

Keywords: *Rapana venosa*, lipid classes, fat-soluble vitamins, carotenoids, seasonal changes

INTRODUCTION

Health benefits associated with seafood consumption have been intensively studied over the past three decades. Mollusks are rich sources of polyunsaturated fatty acids (PUFA), phospholipids, sterols, carotenoids, vitamins (vitamin D₃ and B₁₂) and various micronutrients and essential amino acids. The veined rapa whelk *Rapana venosa* (Valenciennes, 1846) is a large predatory marine gastropod, an invasive species in the Black Sea with nutritional and economic importance in Bulgaria. The main food sources of rapana are *Mytilus galloprovincialis* and *Chamelea gallina*. This species is in high demand on the Asian market, which has lead to increase catch and exportation to Japan, South Korea, China, USA and even Germany. *Rapana venosa* is known to be very resilient and tolerant to temperature, salinity and pollution fluctuations [1]. Chemical composition of mollusks is strongly influenced by season and reproductive cycle [2, 3]. There is scarce literature on the seasonal changes of fat-soluble vitamins, cholesterol and fatty acid profile of *Rapana venosa* from the Black Sea.

EXPERIMENTAL

Sampling

Live samples of *Rapana venosa* were purchased from a local enterprise for fish and seafood

processing near Varna, Bulgaria in April and August, 2017. Animals were transported to the laboratory in ice boxes. They were brushed, washed and processed immediately. Body length was measured and edible soft tissue was taken for further analyses. Specimens were chosen in same length to avoid misinterpretation of the results due to different life stages.

Lipid extraction, separation and purification

Total lipids were extracted by the method of Bligh and Dyer (1959) [4]. An aliquot of the lipid extract (10 mg/ml in chloroform) was used for separation of lipid classes. Neutral lipids (NL) and polar lipids (PL) were fractionated by column chromatography using a glass column (10 mm dia × 20 cm) packed with slurry of activated silicic acid (70 to 230 mesh; Merck, Darmstadt, Germany) in chloroform. The fraction containing NL was eluted with chloroform, while PL – with methanol. The amounts of total lipids and lipid classes were determined gravimetrically. The purity of each fraction was tested by thin-layer chromatography, using Silica gel F254 plates (thickness = 0.25 mm; Merck, Darmstadt, Germany).

* To whom all correspondence should be sent.
E-mail: veselina.ivanova@hotmail.com

Fatty acid derivatization and analysis

Lipid fractions were derivatized by acid-catalyzed transesterification with 2% H₂SO₄ in anhydrous methanol and n-hexane [5]. Fatty acid compositions of TL, NL and PL were determined by gas chromatography with mass spectrometry (GC/MS) of the corresponding fatty acid methyl esters (FAME). Chromatographic separation was performed by Thermo Scientific FOCUS Gas Chromatograph on a TR-5 MS capillary column (30 m, 0.25 mm i.d.). For identification and quantification of FAME peaks authentic standards – SUPELCO FAME Mix C4-C24 and PUFA №3 from Menhaden oil (Sigma-Aldrich, Merck) were used.

Fat-soluble vitamins and carotenoids analysis

Analyses of the non-saponifiable lipids – vitamin A, D₃, E, cholesterol, astaxanthin and β-carotene were performed by following the method of Dobrova et al. [6]. Briefly, soft edible tissue was subjected to direct alkaline hydrolysis with methanolic potassium hydroxide. Consequently, analytes of interest were extracted with a mixture of hexane: dichloromethane and simultaneously analyzed by high performance liquid chromatography.

Nutrition quality indices (NQI)

Several indices and ratios were used to evaluate lipid quality of rapana meat: omega-6/omega-3 (n-6/n-3) and polyunsaturated fatty acids/saturated fatty acids (PUFA/SFA) ratios, indices of atherogenicity (AI) and thrombogenicity (TI), and cholesterolemic index (h/H).

Statistical analysis

Student's t-test was employed to estimate the significance of differences. Statistical significance was indicated at p<0.05.

RESULTS AND DISCUSSION*Total lipids and lipid classes composition*

The results for total lipids (TL), neutral lipids (NL) and polar lipids (PL) are presented in Table 1. *Rapana venosa* was characterized by very low lipid content, which is in agreement with previously published data [7-10].

Table 1. Total lipids (TL), neutral lipids (NL) and polar lipids (PL) content in *Rapana venosa* meat

	Spring	Summer
Mean water temperature, °C	9.4	25.3
Mean length, cm	6.27±0.9	
TL, g.100g-1 ww	0.51±0.02	0.48±0.05
NL, % of TL	31.9±0.8*	60.0±0.8*
PL, % of TL	68.0±0.4*	40.0±1.1*

*Statistical differences, p<0.05

TL content in *Rapana venosa* edible meat is very low and no significant differences between seasons were observed. Sea snails edible meat (also called “foot”) is not considered as lipid storage organ, therefore its lipid content is usually low and not affect by seasonal changes [11,12]. On the other hand, large differences were observed in the distribution of lipid classes. PL were higher than NL content in spring, while summer samples showed the opposite trend (NL>PL). The observed variations are probably related to different roles of the lipid classes during the reproductive cycle of rapana.

Fatty acids composition

Studies on fatty acid composition of marine species provide important information for the sources of fatty acids, especially very long-chain PUFA, which exhibit physiological and structural benefits for organisms. There are numerous studies devoted to biochemical composition of marine invertebrates, but studies on lipid components of Black Sea mollusks are scarce. Fatty acids composition of total lipids and lipid classes of spring and summer *Rapana venosa* are presented in Table 2.

Fatty acids composition of marine invertebrates is usually affected by the environmental factors such as dietary sources, season, salinity, pollution, sun radiation, etc. [13]. PUFA was the most abundant FA group in both spring and summer samples, followed by SFA and MUFA. Same pattern was observed for total lipids and lipid classes in both seasons PUFA>SFA>MUFA. In previous studies [7-9] authors reported same distribution of FA groups for Black Sea *Rapana venosa* lipids. On the other hand, autumn samples of raw and cooked *Rapana venosa* showed slightly higher amounts of SFA, compared to PUFA in total lipids [14].

The results of the present study revealed that polar lipids and neutral lipids of rapana contained predominantly C16:0 (13.56%-20.10%), C18:0 (7.00%-12.84%), C20:5n3 (24.15%-33.84%), C22:6n3 (10.79%-16.31%) and C22:5n3 (1.20%-15.06%), while C8:0, C10:0, C12:0, C15:0, C17:0, C20:0, C24:0, C14:1, C22:1, C24:1, C18:4n3, C18:3n6, C18:3n3, C20:3n3 and C20:2n6 were minor components of mollusks lipids. Palmitic acid (C16:0) was the most abundant FA in SFA group, palmitoleic acid (C16:1n7) in MUFA, and eicosapentaenoic acid (C20:5 n3, EPA) in PUFA group in all lipid fractions for both seasons.

Table 2. FA (as relative %) composition of TL, NL and PL in spring and summer *Rapana venosa*

FA, % of TFA	TL		NL		PL	
	Spring	Summer	Spring	Summer	Spring	Summer
8:0	0.06±0.01	0.03±0.01	0.01±0.0	0.06±0.01	0.02±0.0	0.09±0.01
10:0	0.11±0.01	0.02±0.0	0.02±0.0	0.12±0.01	0.02±0.0	0.06±0.0
12:0	0.21±0.01	0.04±0.0	0.03±0.0	0.12±0.01	0.09±0.01	0.06±0.0
14:0	2.54±0.23	2.01±0.21	3.84±0.3	0.85±0.09	1.58±0.14	2.10±0.23
15:0	nd	0.03±0.0	0.07±0.01	0.16±0.01	0.04±0.0	0.99±0.1
16:0	15.6±0.9	13.56±0.9*	20.10±1.7	16.89±1.1*	18.91±1.3	15.70±1.0*
17:0	nd	0.15±0.01	nd	0.20±0.01	nd	1.03±0.1
18:0	7.6±0.7	9.89±0.9	7.00±0.7	11.39±0.9	8.42±0.9	12.8±0.9
20:0	0.68±0.7	0.40±0.03	0.05±0.0	0.48±0.04	0.14±0.01	0.37±0.03
22:0	1.65±0.16	1.03±0.1	0.50±0.05	0.38±0.03	1.56±0.14	1.61±0.15
24:0	0.72±0.07	0.74±0.07	0.36±0.04	0.79±0.08	0.28±0.02	0.65±0.07
SFA	29.26	27.90*	32.00	31.33	31.07	35.50*
14:1	0.42±0.04	0.14±0.01	0.48±0.04	0.26±0.02	0.20±0.01	0.06±0.0
16:1	6.67±0.6	4.51±0.43*	6.35±0.6	1.05±0.1*	4.58±0.43	2.22±0.21*
18:1	3.08±0.3	3.95±0.4	3.17±0.3	1.00±0.1*	2.41±0.23	1.27±0.11*
20:1	0.41±0.04	1.18±0.11	0.61±0.05	0.26±0.02	1.24±0.11	0.60±0.06
22:1	0.38±0.04	0.15±0.01	0.42±0.04	0.21±0.02	0.53±0.04	0.11±0.01
24:1	0.60±0.05	0.20±0.01	0.24±0.02	0.40±0.04	0.23±0.02	0.39±0.03
MUFA	11.57	10.35	11.26	3.11*	9.19	4.73*
18:4n3	0.68±0.06	0.39±0.03	0.25±0.02	0.74±0.07	0.80±0.07	0.31±0.03
18:3n6	0.16±0.01	0.08±0.01	0.15±0.01	nd	0.10±0.01	0.08±0.01
18:3n3	0.14±0.01	0.14±0.01	0.56±0.05	0.20±0.01	0.12±0.01	0.22±0.02
18:2n6	1.37±0.1	0.80±0.07*	1.27±0.1	0.74±0.07*	2.00±0.2	0.90±0.07*
20:5n3	24.5±2.3	28.7±2.6*	24.1±2.3	33.8±3.1*	25.7±2.3	32.7±3.2*
20:4n6	4.17±0.4	2.37±0.2*	3.60±0.3	2.20±0.2*	4.17±0.4	3.31±0.3*
20:3n6	1.99±0.2	1.54±0.2	0.34±0.3	0.78±0.07	2.01±0.2	2.36±0.2
20:3n3	0.80±0.07	0.40±0.04	0.07±0.0	0.70±0.07	0.22±0.01	0.63±0.07
20:2n6	0.44±0.04	0.36±0.04	0.24±0.01	0.36±0.02	1.00±0.1	0.30±0.02
22:2n6	2.03±0.2	1.15±0.1	0.21±0.01	2.39±0.2	1.69±0.2	0.55±0.04
22:6n3	16.31±1.5	10.79±0.9*	14.05±1.3	13.15±1.2	11.63±1.2	12.04±1.2
22:5n3	6.60±0.6	15.06±1.5*	8.10±0.7	8.67±0.8	8.71±0.8	1.20±0.1*
22:4n3	nd	0.40±0.04	3.55±0.3	1.64±0.2	1.55±0.1	0.63±0.06
PUFA	59.17	61.91	56.54	65.40*	59.74	59.79

Statistical differences, p<0.05 (Spring vs Summer)

The amount of palmitic acid decreased significantly from spring to summer. Koral and Kiran [9] reported same tendency for C16:0 in *Rapana venosa* from several sites of the Black Sea. SFA increased significantly in PL due to the increase of the amount of C18:0 in summer. Total SFA content decreased in total lipid and neutral fractions during the summer season, while MUFA content decreased significantly in both NL and PL. One possible reason could be that the sea snails metabolize NL and TL in colder seasons and stores

them in hotter seasons, especially for reproductive purposes. In the Black Sea the observed reproductive period of *Rapana venosa* is from July to September [15]. The decrease in MUFA was mainly due to the content of C16:1n7 and C18:1n9. The latter fatty acid promotes membrane fluidity in colder seasons, thus there is inverse correlation between MUFA content and environmental temperatures. Summer samples showed higher content of PUFA in TL and NL fractions and no change in the PL class. Ekin *et al.* [13] reported similar changes for fatty acid

profiles of TL, NL and PL classes of the freshwater snail *Melanopsis praemorsa*. However, in this study sea snail *Rapana venosa* lipids presented significantly higher PUFA content, compared to the freshwater snail.

Marine invertebrates are characterized by higher content of essential very long chain n-3 PUFA, namely EPA, docosahexaenoic acid (C22:6 n3, DHA) and docosapentaenoic acid (C22:5n3, DPA). Together, these three FA constitute almost half of the total FAs in spring and more than half of TFA in summer season. There was an increase in TL and NL PUFAs in the summer period, while PL PUFA did not change. Generally, PL fractions of marine mollusks show less seasonal variation compared to the NL fractions, because they play major role in maintaining cellular integrity [16]. The most abundant PUFAs in the present study were EPA, DHA, DPA and arachidonic acid (C20:4n6, AA). The sum of EPA and DHA represented 69% of PUFA in TL in spring and 63.8% – in summer. The amount of EPA increased significantly in all lipid fractions in summer period. On the other hand, DHA content showed the opposite trend in TL and NL, and only a slight increase was observed in the PL fraction. The amount of DPA in the present study increased significantly in the TL and decreased in the PL fractions from spring to summer. Koral and Kiran [9] reported different variations for EPA and DHA in the TL of *Rapana venosa* from several locations along the eastern Black Sea coast. In their study, authors found that AA was the most abundant in the PUFA group. Same pattern was observed for total lipids of the black mussel *Mytilus galloprovincialis* from the northern part of the Bulgarian Black Sea coast [17]. The black mussel comprises the main food source for rapana [1]. Marine invertebrates are good alternative sources of very long chain omega-3 fatty acids, especially EPA and DHA. Together with DPA, they are important membrane lipids with well recognized health benefits. The fact that significant amounts of these fatty acids are bound to PL increases their bioavailability and can therefore be important for achieving the corresponding healthy effects.

Fat-soluble vitamins and carotenoids and cholesterol

The results for the fat soluble vitamins, carotenoids and cholesterol, expressed as mean and standard deviation (mean \pm SD) are presented in table 3. The results are expressed as microgram per 100 grams wet weight ($\mu\text{g}\cdot 100^{-1}$ g ww) for vitamin A, D₃, astaxanthin and β -carotene and milligram per 100 grams wet weight ($\text{mg}\cdot 100^{-1}$ g ww) for cholesterol and vitamin E.

Table 3. Fat-soluble vitamins, carotenoids and cholesterol contents in spring and summer *Rapana venosa*

	Spring	Summer
Astaxanthin	20.5 \pm 1.7	19.7 \pm 1.5
β -carotene	216.9 \pm 19	180.2 \pm 15*
Vitamin A	49.35 \pm 3.8	37.03 \pm 2.5*
Vitamin D ₃	15.40 \pm 1.5	17.60 \pm 1.5
Vitamin E, mg.100g ⁻¹ ww	2.71 \pm 0.5	2.82 \pm 0.6
Cholesterol, mg.100g ⁻¹ ww	23.1 \pm 1.8	25.4 \pm 1.9

*Statistical differences, p<0.05

Fat-soluble vitamins, especially vitamin D₃ are present in high concentration in marine organisms. Their concentrations show seasonal variations related to spawning cycle, environmental conditions and food availability [18]. In this study, β -carotene and vitamin A content decreased significantly from spring to summer. There was no change in astaxanthin amount related to the season. Vitamin E and cholesterol content increased in summer, but the observed change was not significant. Vitamin E and carotenoids (beta-carotene and astaxanthin) are fat-soluble components with high antioxidant activity. One of the main roles of vitamin E is the protection of n-3 PUFA against oxidation [19]. In this study, there was a correlation between vitamin E content and PUFA content in rapana lipids. Higher vitamin E and higher PUFA were found in summer. In our previous study *Rapana venosa* showed significantly higher amounts of the fat-soluble vitamins D₃ and E, carotenoids and cholesterol and lower for vitamin A [14]. There is inverse correlation between the levels of β -carotene and temperature. Lower water temperature is related to higher β -carotene content [14,20]. Same variation is observed in the present study.

Nutrition quality indices (NQI)

There are two fatty acids ratios that are common indicators for the relative nutritional values of dietary lipids. In this study the PUFA/SFA ratio was found to be higher than the recommended 0.4 and n-6/n-3 – lower than 4.0 in both seasons [21]. The PUFA/SFA ratio increased, while n-6/n-3 ratio decreased significantly in summer, corresponding to higher PUFA and higher n-3 content (Table 4).

The ratio n-6/n-3 decreased two fold in the summer – from 0.21 to 0.11. Popova *et al.* [8] reported higher n-6/n-3 ratios (0.42-0.56) and lower PUFA/SFA (1.16-1.63) for summer and autumn *Rapana venosa* harvested in the Black Sea. Koral and Kiran [9] also found higher n-6/n-3 ratios and lower PUFA/SFA in the TL of *Rapana venosa* from several locations along the eastern Black Sea coast. The differences are mainly due to the higher content of some SFA (C18:0) and n-6 PUFA (C20:4n6) reported by the authors.

Table 4. Fatty acid contents, FA ratios, nutrition quality indices in spring and summer *Rapana venosa*

	Spring	Summer
n-6/n-3	0.21	0.11*
PUFA/SFA	2.02	2.22
AI*	0.37	0.30
TI*	0.16	0.14
h/H*	2.37	2.22

*AI= [C12:0+ (4×C14:0) +C16:0]/ (n6PUFA+ n3PUFA+ MUFA);

*TI = (C14:0+C16:0+C18:0)/[(0.5MUFA) + (0.5n6PUFA) + (3n3PUFA) + (n3PUFA/ n6PUFA)] *h/H= (C18:1n9+C18:2n6 +C18:3n3 +C20:4n6+ C20:5n3+ C22:6n3)/ (C14:0 +C16:0)

*Statistical differences, p<0.05

The functional properties of *Rapana venosa* total body lipids were also assessed by the following indices: index of atherogenicity (AI), thrombogenicity (TI), and cholesterolemic index (h/H). Their values decreased slightly in the summer, but there were no significant differences between the values of nutrition quality indices among the two seasons. The results showed very low AI (< 1) and TI (<< 1) values and higher h/H (> 1) levels in the mollusks lipids in both seasons. Anti-atherogenic and anti-thrombogenic indexes of both spring and summer samples were found lower than those presented by Popova *et al* [8]. These results confirm the good anti-atherogenic, anti-thrombogenic and hypocholesterolaemic properties (AI, TI < 1 and h/H > 1) of *Rapana venosa* lipids, which could classify the gastropod meat as beneficial for human consumptions.

CONCLUSIONS

The present study analyzed seasonal changes in biologically active lipid composition in the muscle tissue of the edible sea snail *Rapana venosa* from the Black Sea. Regardless of the observed seasonal fluctuations, *R. venosa* showed very low lipid content, comprising mainly of polar lipids, which increases the bioavailability of the fatty acids. There were significant differences between the lipid classes distribution in the two seasons. The main PUFAs in the present study were EPA and DHA, together representing more than half of total PUFA in *Rapana venosa* TL in both seasons. Although characterized by very low lipid content, Black Sea *Rapana venosa* remains significant source of PUFA, especially those bonded to polar lipids, vitamin D₃ and carotenoids. These results of the present study also confirm the good anti-atherogenic, anti-thrombogenic and hypocholesterolaemic properties of *Rapana venosa* meat. In conclusion, the studied rapana harvested from Bulgarian Black Sea coast presents preferable lipid quality in terms of human health protection. Further investigation is required to determine the biological potential of rapana lipids during the year and changes occurring in the

antioxidants during various cooking processes and prolonged storage.

Acknowledgements: The authors would like to thank to National Science Fund of Bulgaria for the financial support by the project #DM 09/2 from 15 Dec 2016 for young scientists.

REFERENCES

1. S. Stoykov and E. Petrova, *Izvestiya na sayuza na uchenite – Varna, Seriya “Morski nauki”*, 78 (2010).
2. P. Vernocchi, M. Mafei, R. Lanciotti, G. Suzzi, F. Gardini, *Food Control*, **18**, 1575 (2007).
3. N.Ş. Özdemir, F. Caf, A.M. Feyzioğlu, İ. Yildiz, *Turk J Fish Aquat Sci*, **17**, 301 (2017)
4. E. Bligh, W.J. Dyer, *Canad. J. Biochem and Phys*, **37**, 913 (1959)
5. BDS EN ISO 12966-2:2017. Animal and vegetable fats and oils - Gas chromatography of fatty acid methyl esters - Part 2: Preparation of methyl esters of fatty acids. 37 pp.
6. D.A. Dobрева, V. Panayotova, R. Stancheva, M. Stancheva, *Bulg Chem Commun*, **49(G)**, 112 (2017)
7. A. Merdzhanova, D.A. Dobрева, L. Makedonski, *Ovidius Univ. Annals Chem.*, **25**, 15 (2014)
8. T. Popova, D. Stratev, I. Vashin, G. Zhelyazkov, E. Valkova and L. Dospataliev, *Turkish J. Agric. Natural Sci.*, **4**, 277 (2017)
9. S. Koral, A. Kiran, *Ege J. Fisheries Aquatic Sci.*, **34**, 47 (2017)
10. M. Y. Celik, S. T. Culha, M. Culha, H. Yildiz, S. Acarli, I. Celik, P. Celik. *Indian J Geomarine Sci* **43**, 601 (2014)
11. B. Bayrakli, S. Ozdemir, H.A. Duyar, *Alinteri J. Agric. Sci.*, **31**, 72 (2016)
12. J. Bi, Q. Li, H. Yu, Zh. Zhang, Y. Lian, R. Wang, T. Wang, *Mar Bio Res*, **12**, 177 (2016)
13. I. Ekin, M. Bashan and R. Sesen, *Turk J Zool*, **35(6)**, 837 (2011)
14. A. Merdzhanova, V. Panayotova, D.A. Dobрева, R. Stancheva, K. Peycheva, *Ovidius Univ. Annals Chem.*, **29**, 48 (2018)
15. ICES. 2004. In: Alien Species Alert: *Rapana Venosa* (veined whelk), R. Mann, A. Occhipinti and J.M. Harding (eds), ICES Cooperative Research Report No. 264. 14 pp.
16. S. Kaçar, M. Başhan, S.A. Oymak, *J Food Sci Technol*, **53**, 2913 (2016)
17. A. Merdzhanova, D.A. Dobрева, V. Panayotova, (2018) In: Biological Resources of Water, S. Ray (Ed), Available from: <https://www.intechopen.com/books/biological-resources-of-water> (accessed: 1.10.2018)
18. Z.E. Sikorski (1990) In: Seafood: Resources, Nutritional Composition, and Preservation, CRC Press, 256 pp.
19. N.Ş. Özdemir, F. Caf, A.M. Feyzioğlu, İ. Yildiz, *Turk J Fish Aquat Sc*, **17**, 301 (2017)
20. A.V. Borodina, T. Maoka, A.A. Soldatov, *J Evol Biochem Physiol*, **49**, 283 (2013)
21. Department of Health 1994. Nutritional aspects of cardiovascular disease: Health and social subjects (Report No 46) HMSO, London, 187 p.

Effect of thermal stress on the biologically active lipids of *Mytilus galloprovincialis*

A. Merdzhanova*, V. Panayotova, D. A. Dobрева, R. Stancheva

Medical University of Varna, Department of Chemistry, Faculty of Pharmacy,
84 Tzar Osvoboditel St., 9002 Varna, Bulgaria

Received November 5, 2018; Revised January 4, 2019

Black mussels (*Mytilus galloprovincialis*) are the most important marine aquaculture species in Bulgaria. They are widely traded and consumed fresh and frozen. To our knowledge, there is limited information in the scientific literature about changes in lipid composition of Black Sea mussel after cooking and prolonged storage. The aim of the present study was to investigate the changes in total lipids, lipid classes, fatty acid composition, fat-soluble vitamins (A, D₃ and E), carotenoids and cholesterol of *Mytilus galloprovincialis* following culinary treatment (steaming) and three month-storage at -20 °C. Lipids were extracted by the method of Bligh & Dyer and subsequently separated by column and thin-layer chromatography. Fat-soluble vitamins and cholesterol were determined by RP-HPLC/UV/FL. Fatty acid methyl esters were analyzed by GC/MS. There were significant differences in the amounts of total lipids and moisture between raw and steamed mussels, but no changes occurred after the period of freezer storage. Mussel lipids were characterized by higher contents of polar lipids (PL) than neutral lipids (NL). The most abundant FAs in the polyunsaturated FA group were eicosapentaenoic acid (C20:5n-3, EPA) and docosahexaenoic acid (C22:6n-6, DHA). The amounts of astaxanthin, α -tocopherol and cholesterol did not change after cooking, but decreased significantly after storage. Vitamin D₃ increased after thermal treatment but decreased twofold in the freezer. Vitamin A and β -carotene were most affected by temperature changes. Despite the changes observed, the present study confirmed that steamed and frozen *Mytilus galloprovincialis* from the Black Sea is a good natural source of high quality nutritional lipids.

Keywords: *Mytilus galloprovincialis*, lipid classes, fat-soluble vitamins, carotenoids, cooking, freezing

INTRODUCTION

In recent years, marine molluscs have attracted much attention as inexpensive food, low in calories but high in nutrients. The health-beneficial effect of seafood consumption depends on the lipid content, lipid classes and fatty acid composition. Other essential components such as fat-soluble vitamins, carotenoids and cholesterol, complemented and enhanced the marine lipids quality. Black mussels (*Mytilus galloprovincialis*) are the most important marine aquaculture species in Bulgaria. They are widely traded and consumed fresh and frozen. One of the preferable cooking methods for healthier diet is steaming. Other widely used method for food long storage is freezing. This method makes able to preserve the nutrition quality of stored food. Moreover, mussel meat is an easy perishable food that strongly depends on the storage conditions during distribution and commercialization. During frozen storage and cooking process, the mussel tissue is subjected to different physicochemical qualitative changes [1]. Among other tissue constituents, lipids are the major labile components which are significantly affected after steaming and freezing processes. The rate of lipid changes depends on the degree of fatty acid saturation,

storage time and temperature treatment. To our knowledge there is limited or scattered information in the scientific literature about changes in lipid composition of Black Sea mussel after cooking and prolonged storage. In relation to the foregoing, the aim of the present study is to investigate the changes in total lipids, lipid classes, fatty acid composition, fat-soluble vitamins (A, D₃, D₂ and E), carotenoids and cholesterol of *Mytilus galloprovincialis* following culinary treatment (steaming) and three months-storage at -20 °C.

EXPERIMENTAL

Sample preparation

Mussel samples were purchased alive from a mussel farm located along the northern Black Sea coast in November 2017. One hundred animals were chosen randomly to determine the sample mean. Specimens were divided into three groups: first group (n=35) – raw samples; second group (n=32) – steamed mussels (at 90 °C for 6 min); third group (n=34) – frozen samples (at -20 °C for 3 months). At each group sampling, mussels of similar size class were selected (Table 1). The moisture content was determined by drying in an oven for 3 h at 105 °C until constant weight [2].

* To whom all correspondence should be sent.

E-mail: a.merdzhanova@gmail.com

Extraction of total lipids (TL)

Three replicate samples of raw, cooked and frozen meat homogenates (2.000±0.001 g) were extracted following the Bligh and Dyer procedure [3]. Lipid content was determined gravimetrically and the results were expressed as g per 100 g wet weight.

Separation of lipid classes

Total lipids were separated into different classes by column chromatography. The applied procedure for lipid separation was described in details by Merdzhanova et al. (2018) [4].

Preparation of fatty acids methyl esters (FAME) and GS-MS analysis

The dry residues of each fraction were methylated using 2% H₂SO₄ in methanol and n-hexane [5]. FAMES were separated by gas chromatograph Thermo Scientific FOCUS with TR-5 MS capillary column (30 m, 0.25 mm i.d.) and MS detector (Polaris Q). For peaks identification two parameters were used: mass spectra of FAME mixed standard (SUPELCO 37 F.A.M.E. Mix C4 - C24) and internal data base (Thermo Sciences Mass Library, USA). Results for total lipid fraction were calculated using conversion factor for molluscs and for the individual lipid classes – as a percentage of each FA with respect to the total FAs. [6].

Saponification, extraction of vitamins, pigments, cholesterol and HPLC analysis

Alkaline saponification was used to analyse β-carotene, astaxanthin, cholesterol, all-*trans*-retinol, alpha-tocopherol, ergocalciferol, and cholecalciferol content in mussel tissue. All-*trans*-retinol, ergocalciferol, cholecalciferol, alpha-tocopherol, β-carotene, astaxanthin and cholesterol were determined simultaneously using high performance liquid chromatography (HPLC). Sample preparation procedure and HPLC analysis were performed following the method of Dobрева et al. [7].

RESULTS AND DISCUSSION

Total lipids, lipid classes and moisture content

The results for biometric characteristic, total lipids (TL), neutral lipids (NL), phospholipids (PL) and moisture content are presented in Table 1. Black Sea mussels were characterized by low lipid contents, regardless of the thermal treatment.

Table 1. Biometric characteristic, total lipids (TL), neutral lipids (NL), phospholipids (PL) and moisture content in raw, steamed and 3 month-stored Black Sea mussel edible tissues

	Raw	Steamed	3 Month-stored
Length (cm)		4.55±0.15	
TL, g 100 g ⁻¹ ww	1.20±0.03	2.92±0.10 ^a	1.87±0.05 ^b
NL, % of TL	41.20±0.4	43.20±0.4	32.9±0.2 ^b
PL, % of TL	58.80±0.5	56.80±0.1	67.1±0.8 ^b
Moisture, %	83.30±0.8	74.80±0.5 ^a	75.38±0.4 ^b

^a p<0.001(Raw vs Steamed); ^b p<0.001(Raw vs Stored); ^c p<0.001(Steamed vs Stored)

Significant differences were observed in the moisture content of raw, cooked and frozen samples. The water content was reduced by approximately 11-12% after cooking and storage processes. According to Fokina et al. (2018) cellular dehydration occurring in freezing, provokes reduction of cell volume in this way securing tolerance to ice formations of bivalve molluscs' tissues [8]. Moreover, higher levels of PL in mussel tissues probably perform a protective role against freezing. In our research, the amounts of TLs and PL increased significantly after heat treatment (140%) and freezing (56%), while the NL levels decreased up to 20% (after storage). Observed results for increase of PL levels during low-temperature storage confirm the suggestion of Fokina et al. Other possible explanation of noted PL increase after 3 months of storage is elevation of extractability of PL due to the protein denaturation occurring during prolonged frozen storage [9]. Zhou et al. (2014) reported a similar increase of PL levels after steaming and high-pressure treated New Zealand Greenshell mussel (*Perna canaliculus*) [10]. The same author supposed that the activity of the main enzyme which catalyzes ester bonds hydrolysis (lipase) in lipids during mussel storage may be protected or enhanced by temperature treatments. However, the lipid class distributions (PL>NL) in all analysed mussel samples remained unchanged.

Fatty acids composition of total lipids and lipid classes

The FA alignment of analyzed mussel samples was dominated by PUFA, followed by SFA and MUFA in all lipid fractions, regardless of the temperature treatment. FA composition of TL, NL and PL fractions of raw, steamed and 3 month-stored molluscs are presented in Table 2.

Table 2. Fatty acid composition of total lipids (TL), neutral lipids (NL), phospholipids (PL) in raw, cooked and 3 month-stored Black Sea mussel edible tissues

Fatty Acid	Raw			Steamed			3 months-stored		
	TL	NL	PL	TL	NL	PL	TL	NL	PL
C 8:0	0.03±0.01	0.02±0.01	0.02±0.01	0.03±0.01	0.07±0.01	0.12±0.01	0.02±0.01	Nd	0.02±0.01
C 10:0	0.02±0.01	0.03±0.01	0.07±0.05	0.17±0.02	0.18±0.02	Nd	Nd	0.01±0.01	0.05±0.01
C 12:0	0.61±0.02	0.20±0.05	1.82±0.10	0.37±0.03	0.11±0.01	0.06±0.01 ^a	Nd	Nd	0.01±0.01 ^b
C 14:0	1.07±0.08	1.10±0.03	1.16±0.04	1.03±0.05	2.26±0.10 ^a	1.54±0.30	0.94±0.07	1.39±0.07	0.92±0.04 ^a
C 16:0	16.28±1.05	17.40±1.10	19.40±1.25	15.53±0.50	21.71±2.05 ^a	19.85±1.5	18.25±0.56	25.28±1.10	20.61±1.25 ^a
C 18:0	4.20±0.35	3.85±0.30	7.95±0.56	3.17±0.30 ^a	3.62±0.15	7.89±0.50	6.90±0.16	10.13±0.30	7.14±0.56 ^a
C 20:0	0.04±0.01	0.01±0.01	Nd	0.06±0.01	0.02±0.01	Nd	0.04±0.01	0.12±0.01	0.05±0.01
C 21:0	Nd	Nd	Nd	0.05±0.01	Nd	Nd	Nd	Nd	Nd
C 22:0	0.20±0.01	0.06±0.01	0.10±0.02	0.06±0.01	1.10±0.20	Nd	0.42±0.01	2.29±0.01	1.49±0.02
C 23:0	Nd	Nd	Nd	0.04±0.01	0.07±0.03	Nd	0.03±0.02	0.27±0.02	0.01±0.01
C 24:0	0.24±0.02	0.15±0.02	0.38±0.05	0.64±0.08	1.51±0.10	1.63±0.15	0.60±0.24	0.76±0.02	0.53±0.01
SFA	22.69±0.90	22.60±0.65	29.97±0.65	21.47±0.85	30.65±3.10 ^a	31.59±2.25 ^a	28.77±0.43	41.51±1.65	32.60±1.68
C 14:1 n 5	0.10±0.01	0.08±0.01	0.17±0.03	0.10±0.01	0.08±0.01	0.24±0.02	0.09±0.04	0.02±0.01	0.05±0.03
C 16:1 n 7	3.81±0.58	3.40±0.15	1.98±0.12	4.60±0.20	5.34±0.15 ^a	1.65±0.04 ^a	2.62±0.09 ^c	6.97±0.15 ^b	1.86±0.12 ^b
C 18:1 n 9	2.62±0.47	2.19±0.10	1.33±0.05	3.65±0.15	2.72±0.10	0.97±0.01	2.19±0.47 ^c	3.67±0.10 ^{b,c}	0.90±0.05 ^b
C 20:1 n 9	0.54±0.02	0.77±0.03	0.67±0.08	0.98±0.08	2.19±0.05	0.62±0.02	0.54±0.02	0.65±0.03	0.08±0.08 ^b
C 22:1 n 9	0.35±0.01	0.21±0.01	0.15±0.01	0.63±0.05	0.23±0.02	0.16±0.03	0.35±0.01	0.07±0.01	0.17±0.01
C 24:1 n 9	0.21±0.01	0.43±0.01	0.38±0.01	0.41±0.03	1.72±0.10	0.25±0.01	0.21±0.01	0.59±0.01	0.45±0.01 ^b
MUFA	7.60±0.85	7.05±0.18	4.66±0.20	10.36±0.60	12.29±0.40	3.89±0.05	6.88±0.15	12.0±0.36	3.57±0.20
C 18:4 n 3	0.11±0.01	0.36±0.02	0.14±0.01	0.09±0.02	Nd	0.29±0.02	0.26±0.09	Nd	0.16±0.01
C 18:3 n 6	Nd	Nd	Nd	0.13±0.03	0.57±0.03	Nd	0.09	Nd	Nd
C 18:2 n 6	2.06±0.15	2.21±0.15	1.63±0.05	1.22±0.06 ^a	1.68±0.10 ^a	2.10±0.10 ^a	0.42±0.04 ^b	1.00±0.07 ^b	0.56±0.02 ^{b,c}
C 18:3 n 3	1.10±0.08	1.59±0.40	1.00±0.05	0.58±0.04	0.70±0.04	0.21±0.02 ^a	0.92±0.08	1.57±0.40	1.06±0.05 ^c
C 20:3 n 3	0.62±0.01	1.05±0.18	0.90±0.02	1.00±0.10	0.40±0.03	0.12±0.01	1.66±0.01	0.17±0.18	0.11±0.01
C 20:3 n 6	1.44±0.01	0.38±0.02	1.62±0.04	2.61±0.14	1.59±0.10	0.77±0.03	5.60±0.01	1.13±0.02	0.69±0.04
C 20:2 n 6	0.94±0.05	0.61±0.02	0.58±0.02	0.90±0.07	0.56±0.05	0.53±0.03	0.94±0.05	1.22±0.02	0.43±0.02
C 20:4 n 6	6.24±0.25	7.64±0.25	4.38±0.20	5.06±0.40	7.90±0.65	8.50±0.15	7.41±0.25	2.27±0.25	0.91±0.04
C 20:5 n 3	31.70±2.28	27.59±1.30	13.21±0.50	35.04±2.80 ^a	16.84±1.20 ^a	19.44±1.28 ^a	16.49±0.76 ^{b,c}	4.92±1.30 ^{b,c}	22.19±0.50 ^{b,c}
C 22:6 n 3	26.85±2.56	31.04±1.45	42.78±2.5	21.70±1.75 ^a	25.03±1.65 ^a	32.96±2.8 ^a	23.24±1.56	34.24±1.45 ^{b,c}	37.28±2.56 ^{b,c}
C 22:2 n 9	0.82±0.01	0.63±0.03	0.90±0.07	1.14±0.83	3.48±0.60	2.00±0.30 ^a	0.62±0.04	0.25±0.03	0.39±0.02
PUFA	69.71±3.55	70.35±3.40	65.37±2.50	68.16±3.40	57.07±3.50 ^a	64.53±3.30	64.35±0.55 ^b	46.79±2.40 ^{b,c}	63.83±1.94
Σ n 3	60.38	61.63	58.03	57.78	42.97	53.03	42.66	40.9	60.80
Σ n 6	9.33	8.72	7.34	10.38	14.1	11.5	21.69	5.89	3.03
N 6/n 3	0.15	0.14	0.13	0.18	0.33	0.22	0.51	0.15	0.10
PUFA/SFA	3.07	3.11	2.18	3.17	1.86	2.04	2.24	1.13	1.93
(EPA+DHA)/C16:0	3.62	3.37	2.88	3.65	1.97	2.64	2.18	1.55	2.88

^a - p<0.001(Raw vs Steamed); ^b - p<0.001(Raw vs Stored); ^c - p<0.001(Steamed vs Stored)

Saturated fatty acids (SFA), monounsaturated fatty acids (MUFA) and polyunsaturated fatty acids (PUFA) underwent statistically significant changes during the observed thermal treatments. The levels of SFA groups in NL and PL fractions increased after steaming (up to 35% for NL class) and freezing (up to 80% in NL class), which resulted in elevated content of palmitic acid (C16:0). Among the FA groups, palmitic acid was the most abundant FA in SFA group, palmitoleic acid (C16:1 n7) in MUFA, and eicosapentaenoic acid (C20:5 n3, EPA) and docosahexaenoic acid (C22:6 n3, DHA) in PUFA group. Three SFAs (C16:0>C18:0>C14:0), accounted for 95-98% of the total SFAs in raw samples and decreased up to 87% of total saturates in PL fractions after 3 months of freezing. The major MUFAs (C16:1n7>C18:1n9) showed significant decrease especially in NL fractions after cooking process ($p<0.01$), while storage conditions preserved the levels of these FAs.

Biji et al. (2015) also reported higher C16:1N7 compared to C18:1n9 values in New Zealand green mussel tissues and insignificant changes in these FAs after thermal processing [11]. According to Bastias et al. (2017) some of the principal changes that occur during thermal processed tissues are due to oxidation [12]. The thermal labile unsaturated C₂₀ and C₂₂ PUFAs are considered highly unstable and susceptible to oxidation during cooking and freezing storage. Observed results confirm these findings, because the PUFA levels show significant decrease in NL and PL classes after steaming (4%) and especially after 3 months of storage. The major differences were found in NL polyunsaturated FAs (33.5%, $P<0.01$) due to significantly decrease of long chain C₂₀ as EPA (80%, $p<0.01$). Opposite trends were observed for C₂₂ n-3 PUFAs, where DHA increased in NL (10%). There were a limited information for FA changes in lipid classes of mussel tissues after cooking and especially after storage. Biji et al., (2015) reported significant changes in PUFA contents of TLs for green mussel tissue after thermal processing.

According to Joseph (1982), marine molluscs are characterized by high levels of essential omega-3 (n3) PUFAs, mainly EPA and DHA, which accounted half of the total FAs [13]. Our results for Black Sea mussels confirm this statement and showed that both EPA+DHA constitute approximately from 40% up to 59% of total FAs in different lipid classes. Sum of these n3 PUFAs in TL and NL fractions decreased after steaming (30%) and especially after 3 months of storage (34%, $p<0.01$), whereas PL levels

increased after storage (5%, $p<0.05$), compared to raw samples. Given the relative importance of essential n3 PUFAs as key dietary markers, these findings suggest that both methods can retain these biologically active FAs throughout steaming and storage at -20 °C processes. The favourable lipid quality of Black mussel tissues was well illustrated by the high values of n3 long chain PUFAs. Nevertheless, thermal processed n3 PUFAs showed 40.9% to 61.63% of total FAs in both lipid classes, whereas omega 6 (n6) PUFAs displayed significantly lower levels (3.03%-21.69%). Moreover, observed increase of n3 PUFA values in PL fractions after storage compared to NL classes, confirm that 3 months of storage can preserve the high bioavailability of these FAs in mussel tissues.

The analyzed samples were assessed from a nutrition quality perspective by two traditionally used FA ratios— n6/ n3 and PUFA/SFA. Depending of the applied treatment, these ratios significantly varied between thermal processed samples (Table 2). According to Simopolous, (2013) the beneficial n6/n3 ratio for the human health is below one [14]. Presented results ranged from 0.1 to 0.5 and confirmed the high quality of Black Sea mussel lipids regardless of treatment. PUFA/SFA ratio described the FA balance in mussel lipids well. In this study PUFA/SFA ratios ranged from 1.13 to 3.17 and were several times higher than recommended from Department of Health (1994) values (should be higher than 0.45) [15]. Based on reported results we may conclude that steaming and 3 months of storage can preserve well-balanced and beneficial lipid class levels, and human-health improved FA profile.

The polyene index (EPA+DHA/16:0) is determined as a valuable indicator of tissue degradations, respective lipid oxidations, during cooking or storage processes [16]. In this study its value ranged from 2.88 (PL) to 3.62 (TL) for raw samples and showed significant reductions in NL fraction after cooking (42%, $p<0.01$) and freezing (56%), whereas in PL fractions it remained unchanged. Due to these findings we can suppose that 3 months of storage at -20°C affects mostly lipid stability of mussel tissue, especially at NL fraction, compared to PL fraction. One possible reason for the observed changes is that oxidation mechanisms are active during frozen storage and PL fractions are more stable in these conditions. No comparable information is found in scientific literature for this index for steamed and stored Black Sea mussels from the Bulgarian Black Sea coast.

A.Merdzhanova et al.: Effect of thermal stress on the biologically active lipids of *Mytilus galloprovincialis*
Table 3. Fat-soluble vitamins, cholesterol and carotenoid contents in raw, steamed and 3 month-stored Black Sea mussel edible tissues

	Raw	Steamed	3 Months of storage
Vitamin A, $\mu\text{g } 100 \text{ g}^{-1} \text{ w.w.}$	113.4 \pm 10.2	32.8 \pm 4.5 ^a	31.88 \pm 3.8 ^b
Vitamin D ₂ , $\mu\text{g } 100 \text{ g}^{-1} \text{ w.w.}$	7.93 \pm 0.6	7.87 \pm 0.5	6.10 \pm 0.55
Vitamin D ₃ , $\mu\text{g } 100 \text{ g}^{-1} \text{ w.w.}$	17.12 \pm 0.8	25.20 \pm 0.65 ^a	12.74 \pm 0.5 ^b
Vitamin E, $\mu\text{g } 100 \text{ g}^{-1} \text{ w.w.}$	5120.89 \pm 45.0	5064.3 \pm 55.0	1463.46 \pm 23.8 ^{b,c}
Cholesterol, $\text{mg } 100 \text{ g}^{-1} \text{ w.w.}$	37.64 \pm 0.60	40.68 \pm 0.50	20.20 \pm 0.15 ^{b,c}
β -Carotene, $\mu\text{g } 100 \text{ g}^{-1} \text{ w.w.}$	206.39 \pm 25.4	80.47 \pm 10.3 ^a	25.45 \pm 12.5 ^{b,c}
Astaxanthin, $\mu\text{g } 100 \text{ g}^{-1} \text{ w.w.}$	78.28 \pm 8.5	80.07 \pm 10.0	60.42 \pm 5.5 ^{b,c}

^a – $p < 0.001$ (Raw vs Steamed); ^b – $p < 0.001$ (Raw vs Stored); ^c – $p < 0.001$ (Steamed vs Stored)

Fat-soluble vitamins, carotenoids and cholesterol

The results for the fat-soluble vitamins, cholesterol and carotenoids contents are presented in Table 3. Vitamin A, D₃, astaxanthin and β -carotene are expressed as micrograms per 100 grams wet weight ($\mu\text{g } 100 \text{ g}^{-1} \text{ w.w.}$), vitamin E and cholesterol is expressed as milligrams per 100 grams wet weight ($\text{mg } 100 \text{ g}^{-1} \text{ w.w.}$)

All analysed components significantly decreased after 3 months of storage, as minor changes were observed for astaxanthin (22%), maximal – for vitamin E (70%). Most significant decrease was observed for vitamin A and β -carotene between raw and cooked samples. Vitamin D₃ and cholesterol content was higher in cooked samples, vitamin D₃ was twofold higher than the recommended daily intake [17]. Thus, analysed Black Sea mussels can be classified as an excellent source of vitamin D₃, which increases its beneficial value. Merdzhanova et al. (2018) reported lower levels for all fat-soluble vitamins, especially for vitamin D₃ (only 3.1 $\mu\text{g}/100 \text{ g w.w.}$) and higher values for cholesterol and carotenoids for aquaculture mussels from the Northern part of Bulgarian Black Sea [18]. Similar increase of cholesterol and vitamin D₃ amounts and decrease of β -carotene and vitamin A were found in raw and cooked *Rapana venosa* TLs from the Bulgarian part of Black Sea [4]. There was no comparable information for changes of analysed fat-soluble components of black mussels from the Bulgarian part of Black Sea after freezing storage. Presented results confirmed that thermally processed Black Sea mussels preserve nutritionally beneficial quality with respect to bioactive lipids with antioxidant properties as β -carotene, astaxanthin, vitamin E compared to raw samples, although some nutrient loss was detected.

CONCLUSIONS

The health-beneficial value of mussels depends strongly on the TL content, lipid classes, FA composition, fat-soluble vitamins, carotenoids and cholesterol contents. The traditionally used

methods of processing and storage of black mussels caused different changes in their quality as food. Due to this fact, the evaluation of the lipid composition in steamed and 3 month-stored mussels helps to disclose the levels of resistance of analysed edible tissues to thermal stress processes. Observed changes of biologically active components give the opportunity to assess the food quality preservation during these commonly used methods. Both steaming and freezing methods affected mostly the FA profile of the NL fraction, especially after freezing, whereas FA content of PL fractions remained significantly stable. The similar trends for decrease of fat soluble vitamins, carotenoids and cholesterol contents after 3 months of storage showed that freezing affects more aggressively mussel tissues lipids components compared to steaming process. However, freezing as a commonly used method for mussel edible tissue preservation caused a minimal decrease in nutrition value and naturally occurring components, such as unsaturated n3 PUFAs, vitamin D₃ and antioxidants (vitamin E, β -carotene, and astaxanthin) were significantly retained. It would be important to study the effects of different cooking methods and storage time on biologically active lipids of black mussel tissue over a longer period of time. Regardless of the thermal processes, the analysed mussel samples from Bulgarian coast are well balanced and rich of biologically active lipids to meet the needs of consumers.

Acknowledgement: The study is a part of a project DM09/2 from 15 Dec 2016 “Seasonal variations in lipid profile and thermal stress effect on the lipid composition of Black sea *Mytilus galloprovincialis* and *Rapana venosa*”.

REFERENCES

1. M. Zymon, J. Strzetelski, H. Pustkowiak, E. Sosin, *Polish Journal of Food and Nutrition Sciences*, **57**(4C), 647 (2007).

2. AOAC 950.46, 2000, Moisture in meat and meat products. 17th edn., Association of Official Analytical Chemists, Gaithersburg, MD, USA, 2200P.
3. E.G. Bligh, W.J. Dyer, *Canadian Journal of Biochemistry and Physiology*, **37**(8), 911 (1959)
4. BDS EN ISO 12966-2:2017, Animal and vegetable fats and oils - Gas chromatography of fatty acid methyl esters - Part 2: Preparation of methyl esters of fatty acids. p. 37.
5. BDS EN ISO 12966-4:2015, Animal and vegetable fats and oils. Gas chromatography of fatty acid methyl esters. Part 4: Determination by capillary gas chromatography, p. 30.
6. D.A. Dobрева, V. Panayotova, R. Stancheva, M. Stancheva, *Bulgarian Chemical Communications*, **49**(G), 112 (2017).
7. N. Fokina, E. Storhaug, I. Bakhmet, N. Maximovich, M. Frantzen, J. Nahrgang, *Polar Biology*, **41** (10), 2103 (2018).
8. F. Yin, D. Zhou, Xi Meizhu, Qi Zhao, Z. Liu, D. Li, X. Dong, B. Zhu, *Journal of Food Processing and Preservation*, **40**, 10.1111/JFPP.12709 (2016).
9. M. Zhou, M. O. Balaban, S. Gupta, G. C. Fletcher, *Journal of Shellfish Research*, **33**(2), 473 (2014).
10. K. B. Biji, R.M Shamseer, C. O. Mohan, C. N. Ravishankar, S. Mathew, S. T. Gopal, *Journal of Food Science and Technology*, **52**(10), 6804 (2015).
11. J. M. Bastías, P. Balladares, S. Acuña, R. Quevedo, O. Muñoz, *PloS one*, **12**(7) e0180993 (2017).
12. J.D. Joseph, *Progress of Lipid Research*, **21**, 109 (1982).
13. A. Simopolous, *Nutrients*, **5**(8), 2901 (2013).
14. Department of Health (1994). Nutritional aspects of cardiovascular disease: Health and social subjects (Report No 46) HMSO, London, p. 187.
15. L. Meyer, H. Pethybridge, P.D. Nichols, C. Beckmann, B.D. Bruce, J.M. Werry, C. Huvneers, *Frontiers in Marine Science*, **4**, 369 (2017).
16. Ordinance №1/22.01.2018 on the physiological feeding of population, Ministry of Health, Bulgaria, (in Bulgarian).
17. A. Merdzhanova, D. A. Dobрева, V. Panayotova, Book Chapter 9 in Biological Resources of Water, Intech Open, DOI: 10.5772/intechopen.71909, 2018.
18. A. Merdzhanova, V. Panayotova, D. A. Dobрева, R. Stancheva, K. Peycheva, *Ovidius University Annals of Chemistry*, **29**(1), 49 (2018).

A comparative study on chemical and lipid composition of amaranth seeds with different origin

Zh. Y. Petkova*, G. A. Antova, M. I. Angelova-Romova, I. Ch. Vaseva

University of Plovdiv 'Paisii Hilendarski', Department of Chemical Technology,
24 Tzar Asen Street, Plovdiv 4000, Bulgaria

Received December 13, 2018; Revised January 4, 2019

A comparative study on chemical and lipid composition of amaranth seeds with different origin (Indian and Turkish) was performed. The amount of glyceride oil in the seeds was 6.2 and 6.6%, respectively. The content of proteins, total carbohydrates, fibers and ash was 19.4 – 20.0%, 60.5 – 61.4%, 1.8 – 5.3% and 2.0 – 2.4%, respectively. Starch consisted of 53.5 – 56.5% of all carbohydrates and the amount of the available sugars was 2.2 – 2.6%. The moisture of the samples varied between 10.6 and 10.9%. The main components in triacylglycerols of seed oil from India were oleic (38.7%) and palmitic acid (38.4%), while in that from Turkey – palmitic (33.1%), oleic (31.7%) and linoleic acid (22.6%). Total content of unsaponifiable substances in the oils was found to be 8.5 – 9.3%. The amount of sterols in the oils was 1.3 – 2.6% and the main component was β -sitosterol (38.1 – 41.9%), followed by stigmasterol (24.9 – 26.1%) and Δ^5 -avenasterol (20.1 – 23.5%). Total tocopherol content was 1015 - 1060 mg/kg and the main components were β -tocopherol (54.2 – 55.5%), δ -tocopherol (26.1 – 26.3%), and α -tocopherol (13.6 – 14.6%). The total content of phospholipids in the oils was 3.4 – 3.5%. The major representative in the oil from seeds with Indian origin was phosphatidylserine (21.5%), while in that with Turkish origin all identified phospholipid classes were present in similar quantities (10.1 – 14.9%). Overall, significant differences were observed in the fatty acid and phospholipid composition of the oils from Indian and Turkish amaranth seeds, as well as in their content of macro- and microelements.

Keywords: amaranth seeds, chemical composition, lipid composition, biologically active components

INTRODUCTION

Recently, many not sufficiently examined plants which are a source of valuable nutrients can successfully replace the already established plant species in the diverse diet. A similar plant is amaranth which belongs to the family Amaranthaceae. It is an annual plant that has some agronomic advantages, including rapid growth, ability to adapt to unfavorable growing conditions such as low-nutrient soils, sand, heat resistance and irradiation. Its tolerance to different conditions is of interest for its potential use as a nutritious cereal crop in many geographic areas [1].

Chemical composition of amaranth seeds has been the subject of a number of studies and it has been found that the content of the major chemical components varies in a great extent depending on the species, variety, climatic conditions and the way the plant has been grown. The moisture content of the seeds was found to be between 7.5 (in *A. caudatus*) and 11.4% (in *A. hypochondriacus*) [2 - 4]. This is one of the indicators for the shelf-life of food products and shows how long products can be stored without development of molding processes [5, 6]. Amaranth seeds have a high nutritional value that is even higher than those of some cereals. The protein content in them reaches 13 – 18% [3, 7-

11], which is comparable to corn (12%), wheat (12 – 14%) and rice (7 – 10%) [9, 11]. The oil content of the seeds is relatively low (from 4.9 to 10.0%) [3, 10-12] with predominantly unsaturated fatty acids (61.0 – 87.3%), mainly oleic (20.2 – 32.9%) and linoleic acid (37.0 – 47.8%). The content of saturated fatty acids ranges from 20.1 to 30.9%, and palmitic (12.3 – 25.9%) and stearic acid (2.7 – 4.7%) are the main representatives [3, 13-16]. Linolenic, arachidic and behenic acids are found in smaller amounts (from 0.11 to 1.54%). The lipid fraction also contains a number of biologically active substances (tocopherols, sterols and phospholipids) that define this oil as a valuable source of useful compounds for the human body [9, 16].

Although some previous studies on chemical and lipid composition of amaranth seeds and oils were performed, there was not observed results about the influences of the origin of the seeds on their proximate composition. Therefore, the aim of the present research was to be carried out a comparative study on chemical and lipid composition of amaranth seeds with different origin (from India and Turkey), and to be established the differences in the composition of the seeds that were in result of their origin.

* To whom all correspondence should be sent.

EXPERIMENTAL

Determination of phospholipids

Samples

Amaranth seeds with Indian and Turkish origin were purchased from the local market. The seeds were stored at room temperature and after that were analyzed.

Chemical composition

Protein was calculated from the nitrogen content by Kjeldahl method using factor 6.25 [17]. The carbohydrate content was calculated by the following formula: $100 - (\text{weight in grams [protein + lipids + water + ash] in 100g of dry seeds})$ [18]. The soluble carbohydrates and the starch content were identified by using BS 7169:89 [19] and BS 13488:76 [20]. Crude fiber, ash content and moisture were determined according to AOAC (2016) [17].

Determination of macro- and microelements

The method is based on decomposition of the samples at 180 – 200°C in a Milestone ETHOS labstation microwave oven with a high pressure HPR1000/10S segmented rotor in the presence of nitric acid and hydrogen peroxide. The element content is determined by atomic absorption spectroscopy. Multivariate standard solution with concentration of 1000 mg/dm³ is used to prepare dilute working standard calibration solutions. The content of elements was calculated using standard curves of these solutions [21].

Isolation of glyceride oil and determination of oil content

The oil was extracted from grounded seeds using hexane in a Soxhlet apparatus [22].

Fatty acid composition

Fatty acid composition of triacylglycerols was determined by gas chromatography (GC) [23]. Fatty acid methyl esters (FAMES) were prepared by pre-esterification of the triacylglycerols with sulfuric acid in methanol [24]. Determination of FAMES was performed on HP 5890 gas chromatograph equipped with a 75 m × 0.18 mm × 25 µm (film thickness) capillary Supelco column and a flame ionization detector. The column temperature was programmed from 140°C (hold 5 min), at 4°C/min to 240°C (hold 3 min); the injector and detector temperatures were set at 250°C. Identification was performed by comparison of the retention times with those of a standard mixture of FAME (Supelco, USA 37 comp. FAME mix) subjected to GC under identical experimental conditions.

Ground seeds were subjected to Folch extraction [25]. Individual phospholipid classes were isolated by two-dimensional thin-layer chromatography (TLC) [26]. Identification was performed by comparing the respective R_f values with those of authentic standards. The quantification was carried out spectrophotometrically at 700 nm after scrapping the phospholipid spot and mineralization of the substance with a mixture of perchloric and sulphuric acid, 1:1 (v/v) [27].

Determination of sterols

Unsaponifiables were determined after saponification of the glycerides oil and extraction with hexane [28]. Quantification of sterols was carried out spectrophotometrically (at 597 nm), after isolation of sterols from other unsaponifiable matter by TLC [29].

Sterol composition was determined on HP 5890 gas chromatograph equipped with 25 m × 0.25 mm DB – 5 capillary column and flame ionization detector. Temperature gradient from 90°C (hold 3 min) up to 290°C at a rate of change 15°C/min and then up to 310°C a rate of 4°C/min (hold 10 min); detector temperature – 320°C; injector temperature – 300°C and carrier gas was hydrogen. Identification was confirmed by comparison of retention times with those of a standard mixture of sterols [30].

Determination of tocopherols

Determination of tocopherols was carried out by high performance liquid chromatography on 250 mm × 4 mm Nucleosil Si 50-5 column and fluorescent detection at 295 nm excitement and 330 nm emission. The operating conditions were mobile phase of hexane: dioxane, 96:4 (v/v) and flow rate 1 mL/min [31].

RESULTS AND DISCUSSION

The main chemical composition of amaranth seeds is presented in Table 1.

Table 1. Chemical composition of amaranth seeds with different origin

Chemical composition, %	Amaranth (India)	Amaranth (Turkey)
Oil content	6.2±0.2	6.6±0.3
Proteins	19.4±0.5	20.0±0.5
Carbohydrates	61.4±1.1	60.5±0.9
- starch	53.5±0.8	56.5±0.7
- available sugars	2.6±0.1	2.2±0.1
Fibers	5.3±0.3	1.8±0.1
Ash	2.4±0.1	2.0±0.1
Moisture	10.6±0.2	10.9±0.3

Amaranth seeds with different origin had relatively low oil content (6.2 and 6.6%), which was in agreement with the results from previous studies, according to which the oil content ranged from 4.9 to 10.0% [3, 10, 11, 12]. It was found that the amount of oil in amaranth seeds was higher than that of maize (4.5%) [11]. Despite the low oil content, the seeds were characterized with high protein content (19.4 and 20.0%, respectively). This depicts that they are products with rather high protein content. The content of total carbohydrates was relatively high (61.4 and 60.5%, respectively). Great part of the latter was starch content (53.5 and 56.5%), while the available sugars were in relatively low amount (2.2 and 2.6%) in the seeds, which content was lower than the results reported by Colmenares de Ruiz and Bressani (1990) (7.7 – 10.6, 8.0 and 8.7%) [2]. The ash content ranged from 2.0 to 2.4% and the moisture was 10.6 and 10.9%, respectively for the seeds from India and Turkey, which was higher than the results by Paredes-Lopez and Mora-Escobedo (1989) (7.5%) [4]. The most significant differences were observed in the content of fibers, which percent was much higher in the seeds from India (5.3%) than in the seeds from Turkey (1.8%). These results are in agreement with previous studies where the content of fibers is from 2.2 to 5.8% [9, 11, 32], but they are lower than the results reported by Pedersen *et al.* (1987) (8.0%) [10]. The results about the content of protein, carbohydrate, starch and ash in amaranth seeds was in agreement with these from some previous studies: protein (13 - 18%) [3, 7, 8, 9, 10, 11]; carbohydrates (57.0-72.7%) [8, 11,13]; starch (49.5 - 64.0%) [7, 10, 13]; ash (1.8-4.1%) [3, 10, 11].

Table 2. Element concentrations in amaranth seeds with different origin

Elements, mg/kg	Amaranth (India)	Amaranth (Turkey)
Ca	2422	1792
Mg	2069	2013
K	1658	1934
Na	12.8	4.7
Ba	2.4	1.8
Al	9.3	3.6
Zn	15.7	22.5
Mn	18.2	22.9
Pb	0.2	0.0
Fe	77.5	72.0
Cu	2.3	1.0
Ni	0.1	0.2

The content of macro- and microelements in the amaranth seeds is shown in Table 2.

Significant differences were observed between the concentrations of micro- and macroelements in both examined seeds. Calcium (2422 mg/kg) was in the highest amount in Indian seeds, followed by Mg (2069 mg/kg), while in the seeds from Turkey the latter macroelement predominated (2013 mg/kg), followed by K (1934 mg/kg). The concentration of Na in both seeds is rather low – 12.8 and 4.7 mg/kg, respectively. Iron was the most abundant microelements in the amaranth seeds (77.5 and 72.0 mg/kg), followed by Mn (18.2 and 22.9 mg/kg) and Zn (15.7 and 22.5 mg/kg). Lead is non-essential toxic metal [33, 34] but its content in the amaranth seeds with Indian origin is rather low (0.2 mg/kg) and is absent in these from Turkey.

The results about the content of biologically active substances in amaranth seeds and glyceride oils with different origin are presented in Table 3.

Table 3. Content of biologically active components of amaranth seed oils with different origin

Biologically active components	Amaranth (India)	Amaranth (Turkey)
Unsaponifiable matter, %		
- in the oil	8.5±0.2	9.3±0.2
- in the seeds	0.5±0.01	0.6±0.01
Sterols, %		
- in unsaponifiable matter	15.7±1.2	27.9±2.1
- in the oil	1.3±0.1	2.6±0.2
- in the seeds	0.08±0.01	0.17±0.01
Tocopherols, mg/kg		
- in the oil	1015±52	1060±49
- in the seeds	62.9±3.2	70.0±3.2
Phospholipids, %		
- in the oil	3.4±0.3	3.5±0.5
- in the seeds	0.2±0.02	0.2±0.03

Total content of unsaponifiable matters in both amaranth seed oils was similar (8.5 and 9.3%). Considerable differences were observed in total sterols of the oils with Indian and Turkish origin. Their content was two times higher in the oil from Turkey (2.6%), while in the oil from Indian seeds they were 1.3%. The latter result was in agreement with that reported by previous study about the sterol content of some common used vegetable oils (from 0.1 to 1.3%) [35]. Both oils contained relatively high amount of total tocopherols (1015 and 1060 mg/kg in the oils and 62.9 and 70.0 mg/kg in the seeds) and this was in agreement with the results reported by Bruni *et al.* (2001) [14] (51.81 and 116.02 mg/kg total tocopherols in the seeds). On the other hand, this content was much higher than those by Tang *et al.* (2016) (7.28 – 27.90 µg/g in the seeds) [16]. Total phospholipid

Zh.Y. Petkova et al.: A comparative study on chemical and lipid composition of amaranth seeds with different origin content in the oils ranged from 3.4 to 3.5%, which was lower than the results by Gamel et al. (2007) (9.1 – 10.2%) [12].

Fatty acid composition of amaranth seed oils with different origin is presented in Table 4.

Table 4. Fatty acid composition of triacylglycerols of amaranth seed oils with different origin

Fatty acids, %	Amaranth (India)	Amaranth (Turkey)
Caprylic (C _{8:0})	0.2±0.02	0.1±0.02
Capric (C _{10:0})	0.1±0.03	-*
Myristic (C _{14:0})	0.1±0.01	0.1±0.03
Pentadecanoic (C _{15:0})	0.2±0.03	-
Palmitic (C _{16:0})	38.4±0.2	33.1±0.1
Palmitoleic (C _{16:1})	0.9±0.05	0.7±0.1
Margaric (C _{17:0})	0.2±0.02	0.2±0.03
Stearic (C _{18:0})	8.6±0.1	6.3±0.1
Oleic (C _{18:1})	38.7±0.4	31.7±0.3
Linoleic (C _{18:2})	6.8±0.1	22.6±0.2
Trans Linoleic (C _{18:2})	0.7±0.1	0.5±0.1
Linolenic (C _{18:3})	0.4±0.1	0.5±0.1
Arachidic (C _{20:0})	1.8±0.1	1.2±0.1
Gadoleic (C _{20:1})	0.2±0.03	0.2±0.02
Eicosadienoic (C _{20:2})	0.1±0.01	0.1±0.02
Behenic (C _{22:0})	0.6±0.1	0.5±0.1
Eicosatrienoic (C _{20:3})	-	0.3±0.02
Arachidonic (C _{20:4})	0.4±0.1	0.1±0.01
Tricosylic (C _{23:0})	-	0.1±0.02
Lignoceric (C _{24:0})	1.1±0.1	1.1±0.1
Eicosapentaenoic (C _{20:5})	0.5±0.1	0.6±0.2

* - Not identified

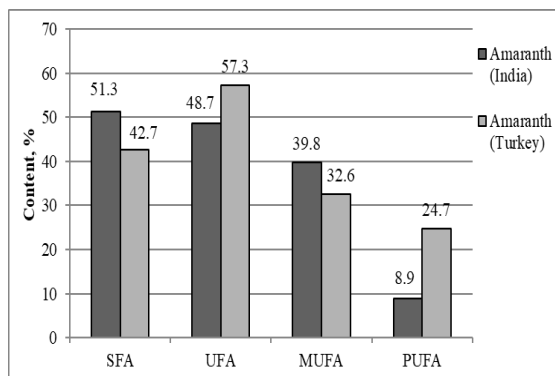


Figure 1. Content of saturated (SFA), unsaturated (UFA), mono- (MUFA) and polyunsaturated (PUFA) fatty acids in amaranth seed oils.

Nineteen fatty acids were identified in the oils. Oleic (38.7%) and palmitic (38.4%) acids predominated in the oil from Indian seeds, while in the oil from Turkey the main fatty acids were palmitic (33.1%) and oleic (31.7%). Stearic (8.6%) and linoleic (6.8%) acids were observed in lower amount in the oil from India. The most significant difference was observed in the quantity of linoleic

acid which amount was much higher in the oil from Turkish seeds (22.6%).

The obtained results about the fatty acid composition of amaranth seed oils distinguished from the data from previous authors where the main fatty acid was linoleic and its amount varies from 37.0 to 47.8%, followed by oleic acid (20.2 – 32.9%). On the other hand, the content of palmitic acid (12.3 - 25.9%) [3, 13-16] were much lower than those found in the present study (38.4%).

The content of saturated (SFA), unsaturated (UFA), monounsaturated (MUFA) and polyunsaturated (PUFA) fatty acids in the amaranth seed oils is shown on Figure 1.

The oil from Turkish seeds contained higher amount of unsaturated fatty acids (57.3%), while in the oil from Indian seeds predominated saturated fatty acids (51.3%). Monounsaturated fatty acids (39.8 and 32.6%) were in higher quantity than polyunsaturated fatty acids (8.9 and 24.7%) in both oils. On the other hand, the content of the latter were much higher in the oil from Turkish seeds.

The differences in the fatty acid composition of the examined seeds were probably due to the different geographical areas where the plants had been grown. Triacylglycerols which contain predominantly unsaturated fatty acids are synthesized in the oil-bearing plants that have been grown in countries with moderate and cool climates (e. g. the northern part of Turkey), while triacylglycerols containing saturated fatty acids are mostly synthesized in countries with warm climate [36]. This is most likely the reason why the oil from Turkish seeds is richer in unsaturated fatty acids (57.3%).

The results about individual sterol composition of amaranth seed oils are shown in Table 5.

Table 5. Individual sterol composition of amaranth seed oils with different origin

Sterols, %	Amaranth (India)	Amaranth (Turkey)
Cholesterol	0.3±0.01	0.2±0.02
Campesterol	2.8±0.2	2.0±0.1
Stigmasterol	26.1±1.2	24.9±1.0
β-Sitosterol	38.1±1.3	41.9±1.2
Fucosterol	1.2±0.02	0.3±0.02
Δ ⁵ -Avenasterol	23.5±0.7	20.1±0.5
Δ ⁷ -Stigmasterol	7.7±0.1	10.3±0.2
Δ ⁷ -Avenasterol	0.3±0.01	0.3±0.01

No considerable differences were observed in the sterol composition of the examined oils. The main component was β-sitosterol (38.1 and 41.9%),

followed by stigmasterol (26.1 and 24.9%) and Δ^5 -avenasterol (23.5 and 20.1%). Δ^7 -Stigmasterol (7.7 and 10.3%) and campesterol (2.8 and 2.0%) were also detected in relatively high amounts. The results about the sterol composition of the examined seeds were completely different from the data reported in a previous study [3]. Tocopherol composition of amaranth seed oils is presented in Table 6.

Table 6. Tocopherol composition of amaranth seed oils with different origin.

Tocopherols, %	Amaranth (India)	Amaranth (Turkey)
α -Tocopherol	14.6±0.2	13.6±0.5
β -Tocopherol	54.2±1.5	55.5±1.0
γ -Tocopherol	5.2±0.4	4.7±0.6
δ -Tocopherol	26.1±0.8	26.3±1.1

β -Tocopherol predominated in the tocopherol fraction of both oils (54.2 and 55.5%), followed by δ -tocopherol (26.1 and 26.3%) and α -tocopherol (13.6 and 14.6%). The amount of γ -tocopherol was significantly low (4.7 and 5.2%). These results were in agreement with the reported by Ogradowska *et al.* (2014) [3], who also found that the main tocopherol was β -tocopherol (38.4%), followed by δ -tocopherol (31.4%). Bruni *et al.* (2001) [14] also reported that β -tocopherol (43.0-61.0%) was in the highest quantity, but the amount of α -tocopherol was considerably higher (29.8-42.7%) than in the examined amaranth seed oils.

The results about phospholipid composition of the investigated amaranth seed oils are shown in Figure 2.

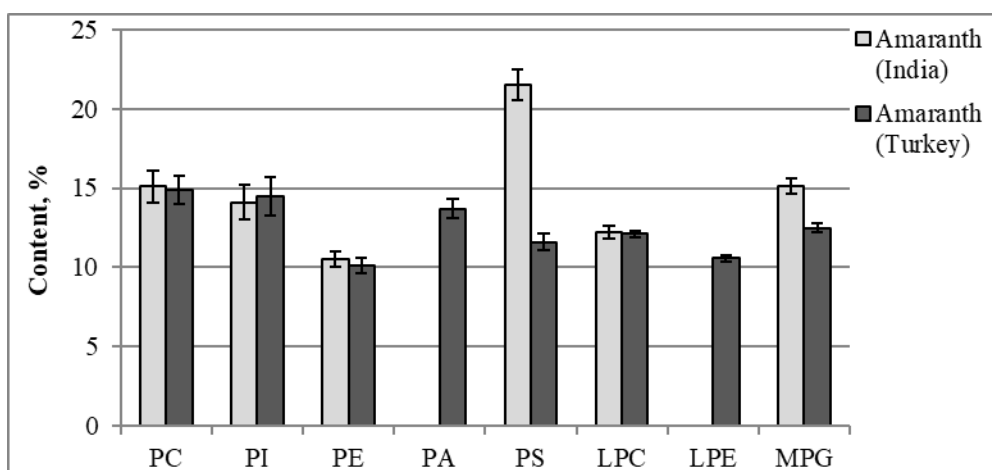


Figure 2. Phospholipid composition of amaranth seed oils with different origin. PC – Phosphatidylcholine; PI – Phosphatidylinositol; PE – Phosphatidylethanolamine; PA – Phosphatidic acids; PS – Phosphatidylserine; LPC – Lysophosphatidylcholine; LPE – Lysophosphatidylethanolamine; MPG – Monophosphatidylglycerol

Phosphatidylserine (21.5%) was the main component in the phospholipid fraction of the oil from Indian seeds, followed by phosphatidylcholine (15.1%) and monophosphatidylglycerol (15.1%), while the phospholipid classes of the oil with Turkish origin were present in similar quantities from 10.1 to 14.9%. Phosphatidic acids and lysophosphatidylethanolamine were identified only in the oil from Indian seeds (13.7 and 10.6%, respectively).

CONCLUSIONS

Detailed examinations on the chemical and lipid composition of amaranth seeds and seed oils with different origins (Indian and Turkish) were performed for the first time. No significant differences were observed in the chemical composition of the two examined seeds. The seeds were characterized with low oil content, but were abundant in proteins and carbohydrates. No

considerable differences were observed in the tocopherol and sterol composition of the two examined seed oils. They were characterized with relatively higher sterol and tocopherol content than other common seed oils (sunflower, soybean, sesame, etc.). β -Tocopherol predominated in the oils, while β -sitosterol – in the sterol fraction. Significant differences were observed in the fatty acid and phospholipid composition of the oils from Indian and Turkish amaranth seeds. Finally, it can be concluded that the origin of the plants has the greatest impact on fatty acid and phospholipid composition of their seed oils as well as on the content of macro- and microelements of the seeds. Overall, despite the different chemical and lipid composition of the amaranth seeds with Indian and Turkish origin, they both are a source of valuable nutrients and can fully participate in the diverse human nutrition.

Acknowledgements: The investigations were carried out with the partial financial support of the Science Research Department to University of Plovdiv "Paisii Hilendarski", SII7 FC013 and supported by National Program "Young Scientists and Postdoctoral Students", Bulgaria.

REFERENCES

1. G. J. H. Grubben, *Amaranthus cruentus* L, in: Plant resources of tropical Africa 2. Vegetables, Grubben G.J.H., Denton OA (eds.), Backhuys Publishers, Wageningen, 2004, p. 67.
2. A. S. Colmenares De Ruiz, R. Bressani, *Cereal Chem.*, **67** (6), 519 (1990).
3. D. Ogrodowska, R. Zadernowski, S. Czaplicki, D. Derewiaka, B. Wronowska, *Pol. J. Food Nutr. Sci.*, **64** (3), 165 (2014).
4. O. Paredes-Lopez, R. Mora-Escobedo, *J. Food Sci.*, **54** (3), 761 (1989).
5. P. J. Fellows, *Food processing technology: Principles and Practice* (2nd edn.), Woodhead Publishing Limited and CRC Press LLC, Cambridge, England, 2000.
6. M. Ivanova, P. Papazov., L. Dospatliev, N. Katrandzhiev, *Chemistry*, **27** (4), 615 (2018).
7. T. H. Gamel, J. P. Linssen, A. S. Mesallam, A. A. Damir, L. A. Shekib, *Journal of the Science of Food and Agriculture*, **85**, 319 (2005).
8. O. A. López-Mejía, A. López-Malo, E. Palou, *Industrial Crops and Products*, **53**, 55 (2014).
9. D. Orona-Tamayo, O. Paredes-López, Chapter 15 – Amaranth, Part 1 – Sustainable crop for the 21st century: Food Properties and nutraceuticals for improving human health, *Sustainable Protein Sources*, 2017, p. 239.
10. B. Pedersen, L. S. Kalinowski, B. O. Eggum, *Plant Food Hum. Nutr.*, **36** (4), 309 (1987).
11. M. Segura-Nieto, A. Barba De La Rosa, O. Paredes-López, Biochemistry of amaranth proteinsin. In: *Amaranth: Biology, chemistry and technology*, Paredes-López O. (ed.), Boca Raton, FL: CRC Press, 1994, p. 75.
12. T. H. Gamel, A. S. Mesallam, A. A. Damir, L. A. Shekib, J. P. Linssen, *J. Food Lipids*, **14**, 323 (2007).
13. L. Alvarez-Jubete, E. K. Arendt, E. Gallagher, *Trends in Food Science & Technology*, **21** (2), 106 (2010).
14. R. Bruni, A. Medici, A. Guerrini, S. Scalia, F. Poli, M. Muzzoli, G. Sacchetti, *J. Agric. Food Chem.*, **49**, 5455 (2001).
15. P. Kraujalis, P. R. Venskutonis, A. Pukalskas, R. Kazernaviciute, *LWT - Food Science and Technology*, **54**, 528 (2013).
16. Y. Tang, X. Li, P. X. Chen, B. Zhang, R. Liu, M. Hernandez, J. Draves, M. F. Marccone, R. Tsao, *J. Agric. Food Chem.*, **64** (5), 1103 (2016).
17. AOAC - Association of Official Analytical Chemist (2016). *Official methods of analysis*, 20th edn. Washington, DC.
18. Food and Agriculture Organization of the United Nations.(2003). *Food energy —Methods of analysis and conversion factors* (FAO Food and Nutrition Paper, Report of a Technical Workshop, vol. 77). Rome: Author. ISSN 0254-4725.
19. BS 7169:1989. Products of processed fruit and vegetables. Determination of sugar content.
20. BS 13488:1976. Grain. Method for determining the starch content.
21. ISO 14082:2003. Foodstuffs, Determination of trace elements by atomic absorption spectrometry (AAS) after ashing.
22. ISO 659:2014. Oilseeds. Determination of oil content (Reference method).
23. ISO 12966-1:2014. Animal and vegetable fats and oils. Gas chromatography of fatty acid methyl esters – Part 1: Guidelines on modern gas chromatography of fatty acid methyl esters.
24. ISO 12966-2:2011. Animal and vegetable fat and oils. Gas chromatography of fatty acid methyl esters – Part 2: Preparation of methyl esters of fatty acids.
25. J. Folch, M. Lees, G. H. Sloane-Stanley, *J. Biol. Chem.*, **226**, 497 (1957).
26. R. Schneiter, G. Daum, Analysis of yeast lipids, in: *Yeast Protocol: 2nd edn. Methods in Molecular Biology*, Xiao, W. (ed.), Humana Press Inc., Totowa, NJ, 2006, p. 75.
27. ISO 10540-1:2014. Animal and vegetable fats and oils. Determination of phosphorus content. Part 1: Colorimetric method.
28. ISO 18609:2000. Animal and vegetable fats and oils. Determination of unsaponifiable matter. Method using hexane extraction.
29. S. Ivanov, P. Bitcheva, B. Konova, *Rev. Franc. Corps Gras*, **19**, 177 (1972).
30. ISO 12228-1:2014. Part 1: Animal and vegetable fats and oils. Determination of individual and total sterols contents. Gas chromatographic method.
31. ISO 9936:2016. Animal and vegetable fats and oils. Determination of tocopherol and tocotrienol contents by high-performance liquid chromatography.
32. P. R. Venskutonis, P. Kraujalis, *Comprehensive Reviews in Food Science and Food Safety*, **12**, 381 (2013).
33. L. Dospatliev, M. Ivanova, *CR Acad. Bulg. Sci.*, **70**, 795 (2017).
34. L. Dospatliev, M. Ivanova, *Oxid. Commun.*, **40**, 993 (2017).
35. Codex Stan 210 - 1999. Codex standard for named vegetable oils. Revisions 2001, 2003, 2009. Amendments 2005, 2011.
36. A. Stoyanova, M. Perifanova-Nemska, E. Georgiev, *Raw Material Science about glyceride and essential oils*, Agency 7D Publishing, Plovdiv, 2006.

Lipid composition of watermelon seed oil

M. Y. Angelova-Romova*, Zh. B. Simeonova, Zh. Y. Petkova, G. A. Antova, O. T. Teneva

*University of Plovdiv 'Paisii Hilendarski', Department of Chemical Technology,
24 Tzar Asen Street, 4000 Plovdiv, Bulgaria*

Received November 13, 2018; Revised January 4, 2019

Lipid composition of watermelon seed oils with Bulgarian and Greek origin was examined. The oil content was found to be 25.2 and 24.0%, respectively. The main fatty acids in triacylglycerols were linoleic (58.7 – 63.6%), oleic (18.3 – 18.8%) and palmitic (14.0 – 15.0%). Total phospholipid content varied between 3.1 and 6.3%, and the main representatives were phosphatidylcholine (42.2%) in the seeds from Bulgarian origin and phosphatidylserine (26.9%) in those with Greek origin. The main components in the sterol fraction (0.6 – 0.9%) were β -sitosterol (53.5 – 58.9%) and Δ^5 -avenasterol (35.9 – 37.4 %). Fatty acid composition of the phospholipids differed from those of triacylglycerols. Saturated fatty acids prevailed in phospholipid fraction, while unsaturated fatty acids – in triacylglycerols. Fatty acid composition of phosphatidylcholine in Bulgarian seed oil was the only exception where unsaturated fatty acids (59.0%) were in a higher amount than saturated (41.0%). Total tocopherol content was established to be 962 – 1010 mg/kg and the main component was γ -tocopherol (92.3 – 97.0%).

Keywords: watermelon seeds, lipid composition, tocopherols, sterols, phospholipids

INTRODUCTION

Watermelon is an annual plant from Cucurbitaceae family. It is widely distributed and cultivated in Africa and the Middle East, but can also be grown in Europe [1 - 3]. The fruit is rich of carbohydrates, carotenoids and lycopene and it is well-known for its high water content [4]. Watermelon is grown in almost every region in Bulgaria, apart from the mountain areas.

Many authors report that watermelon seeds are waste products from the fruit and can be eaten as a roasted snack or used in cooking [1 - 4]. They are abundant in lipids and proteins. The oil content of the seeds is considerably high (27.1 – 57.26%) [1 - 7]. Linoleic acid is the main fatty acid (56.8 – 62.1%), followed by oleic (11.0 – 14.6%), palmitic (10.6 – 15.0%) and stearic acids (8.3 – 16.0%) [2, 6, 8].

The content of unsaponifiable matters ranges from 0.56 to 0.80% and depends on the specific watermelon species [3, 7] and total sterols are 1.12 – 8.1%. The main components in the sterol fraction are $\Delta^{7,22,25}$ – stigmastatrienol (31.6%), $\Delta^{7,25}$ – stigmastadienol (29.7%) and $\Delta^{7,22}$ – stigmastadienol (26.5%) [1, 9].

Total tocopherol content is 131 – 369 mg/kg [3, 7] and according to Raziq *et al.* (2012) [7] the main representative is α -tocopherol (73.8 – 94.1%). On the other hand, Mariod *et al.* (2009) [3] reported that the main tocopherol is γ -tocopherol (97.3%). The information about the total phospholipid

content and their individual composition is rather scarce and El-Adawy and Taha (2001) [1] established that total phospholipid content of watermelon seed oil is 0.96%.

Watermelon seed oil can be considered as an alternative source to traditional oil produced in Bulgaria (e.g. sunflower, soybean and rapeseed oil). For now no studies have been conducted on the use of watermelon seeds as an oilseed feedstock for food and industrial purposes in the country.

Therefore, the aim of the present study is to examine the fatty acid composition of watermelon seed oils with different origin (Bulgarian and Greek), as well as the determination of the main biologically active components (phospholipids, sterols and tocopherols).

EXPERIMENTAL

Samples

Two kinds of watermelon seeds with different origin (from Bulgaria and Greece) were used for the analysis.

Isolation of glyceride oil and determination of oil content

The oil was extracted from ground seeds using hexane in a Soxhlet apparatus for 8 h. The solvent was partly removed in a rotary vacuum evaporator, the residue was transferred in a pre-weighed glass vessel and the rest of the solvent was removed under stream of nitrogen to a constant weight to determine the oil content [10].

* To whom all correspondence should be sent.

E-mail: maioan@uni-plovdiv.bg

Fatty acid composition

Fatty acid composition of triacylglycerols (TAG) was determined by gas chromatography (GC) [11]. Fatty acid methyl esters (FAMES) were prepared by pre-esterification of the triacylglycerols with sulfuric acid in methanol [12]. Determination of FAMES was performed on HP 5890 gas chromatograph equipped with a 60 m × 0.25 mm × 25 µm capillary DB-23 column and a flame ionization detector. The column temperature was programmed from 130 °C (hold 1 min), at 6.5 °C/min to 170 °C, at 3 °C/min to 215 °C (hold 9 min), at 40 °C/min to 230 °C (hold 1 min); the injector and detector temperature was 250 °C. Hydrogen was the carrier gas at a flow rate of 0.8 mL/min. Identification was performed by comparison of the retention times with those of a standard mixture of FAME (Supelco, USA 37 comp. FAME mix) subjected to GC under identical experimental conditions.

Determination of phospholipids

Ground seeds were subjected to Folch extraction [13]. Individual phospholipid classes were isolated by two-dimensional thin-layer chromatography (TLC) [14]. Identification was performed by comparing the respective R_f values with those of authentic standards. The quantification was carried out spectrophotometrically at 700 nm after scraping the phospholipid spot and mineralization of the substance with a mixture of perchloric and sulphuric acid, 1:1 (v/v) [15].

Determination of sterols

Unsaponifiables were determined after saponification of the glyceride oil and extraction with hexane [16]. Quantification of sterols was carried out spectrophotometrically (at 597 nm), after isolation of sterols from other unsaponifiable matter by TLC on silica gel 60 G in the mobile phase diethyl ether: hexane (1:1 (v/v)) [17].

Sterol composition was determined on HP 5890 gas chromatograph equipped with 25 m × 0.25 mm DB-5 capillary column and flame ionization detector. Temperature gradient from 90 °C (hold 3 min) up to 290 °C at a rate of change 15 °C/min and then up to 310 °C a rate of 4 °C/min (hold 10 min); detector temperature – 320 °C; injector temperature – 300 °C and carrier gas was hydrogen. Identification was confirmed by comparison of retention times with those of a standard mixture of sterols [18].

Determination of tocopherols

Determination of tocopherols was carried out by high performance liquid chromatography [19] on 250 mm × 4 mm Nucleosil Si 50-5 column and

fluorescence detection at 295 nm excitement and 330 nm emission. The operating conditions were mobile phase of hexane:dioxane, 96:4 (v/v) and flow rate of 1 mL/min.

RESULTS AND DISCUSSION

Lipid composition of watermelon seed oils, as well as the content of biologically active components are shown in Table 1.

Table 1. Lipid composition of watermelon seeds

Compounds	Origin	
	Bulgaria	Greece
Oil content, %	25.2 ± 0.3	24.0 ± 0.2
Phospholipids, %		
- in the oil	6.3 ± 0.1	3.1 ± 0.1
- in the seeds	1.6 ± 0.03	0.8 ± 0.03
Unsaponifiable matter, %		
- in the oil	4.9 ± 0.2	5.1 ± 0.2
- in the seeds	0.3 ± 0.01	0.3 ± 0.01
Sterol content, %		
- in the oil	0.9 ± 0.1	0.6 ± 0.1
- in the seeds	0.06 ± 0.01	0.04 ± 0.01
Tocopherols, mg/kg		
- in the oil	1010 ± 15	962 ± 8
- in the seeds	255 ± 4	231 ± 2

The oil content did not differ in the seeds with Bulgarian and Greek origin (25.2 and 24.0%, respectively). These results were lower than those observed in previous studies where the oil content of watermelon seeds was from 28.5 to 57.2% [1, 2, 4 - 7].

Total phospholipid content of the oil obtained from Bulgarian seeds was two times higher (6.3%) than the content of the Greek seed oil (3.1%). Despite that, these results were much higher than the reported by El-Adawy and Taha (2001) (0.96%) [1].

The content of unsaponifiable matters in the seed oils was 4.9 – 5.1%, which was considerably higher than the data by Raziq *et al.* (2012) [7] and Mariod *et al.* (2009) [3] (0.56 – 0.82%). Total sterol content of the oils was from 0.6 to 0.9%, which was lower than the results reported by El-Adawy and Taha (2001) [1] and Oelschlägel *et al.* (2012) [9] (1.12 – 8.10%).

Total tocopherol content was 1010 and 962 mg/kg, respectively, for the Bulgarian and Greek seed oils, which was much higher than the results from previous studies (131 – 369 mg/kg) [3, 7].

Fatty acid composition of the examined seed oils is presented in Table 2.

The main fatty acid was linoleic acid (63.6 and 58.7 %), followed by oleic (18.8 and 18.3 %) and palmitic (15.0 and 14.0%). The quantity of stearic acid in the oil from Greek seeds was much higher

(6.5%) than in the Bulgarian one (1.3%). This was at the expense of the content of linoleic acid in the same oil. The amount of the other fatty acids ranged from 0.1 to 0.8%. The obtained results were in agreement with these from previous studies [2, 6, 8].

Table 2. Fatty acid composition of triacylglycerols of watermelon seed oils

Fatty acids, %	Origin	
	Bulgaria	Greece
C 10:0 ^a	*	0.8 ± 0.2
C 12:0	-	0.4 ± 0.1
C 14:0	0.3 ± 0.05	0.4 ± 0.1
C 14:1	-	0.1 ± 0.02
C 15:0	0.1 ± 0.02	-
C 16:0	15.0 ± 0.2	14.0 ± 0.1
C 16:1	0.1 ± 0.05	0.1 ± 0.02
C 17:0	0.1 ± 0.01	0.2 ± 0.02
C 18:0	1.3 ± 0.04	6.5 ± 0.1
C 18:1	18.8 ± 0.2	18.3 ± 0.2
C 18:2	63.6 ± 0.3	58.7 ± 0.2
C 18:3	0.1 ± 0.02	-
C 20:0	0.3 ± 0.02	0.2 ± 0.01
C 20:1	0.2 ± 0.02	0.1 ± 0.01
C 22:0	0.1 ± 0.01	0.2 ± 0.01

*- Not identified

^a- C_{10:0}- Capric acid; C_{12:0}- Lauric acid; C_{14:0}- Myristic acid; C_{14:1}- Myristoleic acid; C_{15:0}- Pentadecanoic acid; C_{16:0}- Palmitic acid; C_{16:1}- Palmitoleic acid; C_{17:0}- Margaric acid; C_{18:0}- Stearic acid; C_{18:1}- Oleic acid; C_{18:2}- Linoleic acid; C_{18:3}- Linolenic acid; C_{20:0}- Arachidic acid; C_{20:1}- Eicosenoic acid (gadoleic); C_{22:0}- Behenic acid

The content of saturated (SFA), unsaturated (UFA), mono- (MUFA) and polyunsaturated (PUFA) fatty acids of watermelon seed oils is shown in Figure 1.

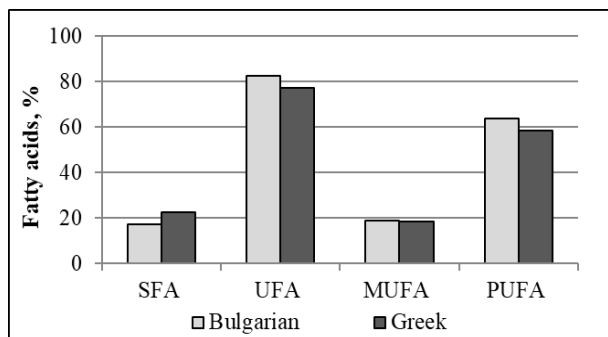


Figure 1. Content of saturated (SFA), unsaturated (UFA), mono- (MUFA) and polyunsaturated (PUFA) fatty acids of watermelon seed oils

UFA predominated in both oils (77.3 – 82.8%) and the share of the PUFA was bigger (58.7 – 63.7%) than MUFA (18.6 – 19.1%). The content of SFA ranged from 17.2 to 22.7% and it was higher in the oil from Greek seeds.

The individual sterol composition of the examined seed oils is shown in Table 3.

Table 3. Individual sterol composition of watermelon seed oils

Sterols, %	Origin	
	Bulgaria	Greece
Cholesterol	0.7 ± 0.1	0.4 ± 0.05
Campesterol	0.6 ± 0.1	0.5 ± 0.06
Δ ⁷ – Campesterol	2.1 ± 0.1	1.6 ± 0.1
Stigmasterol	2.5 ± 0.05	0.7 ± 0.05
β – Sitosterol	53.5 ± 0.5	58.9 ± 0.4
Δ ⁵ – Avenasterol	37.4 ± 0.4	35.9 ± 0.2
Δ ⁷ – Stigmasterol	2.5 ± 0.05	1.6 ± 0.1
Δ ⁷ – Avenasterol	0.7 ± 0.02	0.4 ± 0.02

The main component in both oils was β – sitosterol (53.5 – 58.9%), followed by Δ⁵ – avenasterol (35.9 – 37.4%). The other sterols were presented in quantities from 0.4 to 2.5%. The sterol composition of the oil from Bulgarian seeds did not differ from that of Greek origin. On the other hand, the results were completely different from these reported by Oelschlägel *et al.* (2012) [9], where the main sterol was Δ^{7,22,25} – stigmastatrienol (31.6%), followed by Δ^{7,25} – stigmastadienol (29.7%) and Δ^{7,22} – stigmastadienol (26.5%).

Individual tocopherol composition of the watermelon seed oils is presented in Table 4.

Table 4. Tocopherol composition of watermelon seed oils

Tocopherols, %	Origin	
	Bulgaria	Greece
α-Tocopherol	5.4 ± 0.2	2.0 ± 0.1
γ-Tocopherol	92.3 ± 0.6	97.0 ± 0.5
δ-Tocopherol	2.3 ± 0.1	1.0 ± 0.05

γ-Tocopherol (92.3 – 97.0%) predominated in the tocopherol fraction of the oils and considerable small amounts of α-tocopherol (5.4 – 2.0%) and δ-tocopherol (2.3 – 1.0%) were detected. The results were in agreement with these by Mariod *et al.* (2009) [3], who reported that γ-tocopherol was also the main tocopherol in watermelon seed oil (97.3%), but were different from the data by Raziq *et al.* (2012) [7], who established that α-tocopherol predominated (73.8 – 94.1%).

Phospholipid composition of the examined oils is shown in Table 5.

Table 5. Phospholipid composition of watermelon seeds oils

Phospholipids, %	Origin	
	Bulgaria	Greece
Phosphatidylcholine	42.2 ± 1.1	22.8 ± 0.1
Phosphatidylinositol	22.0 ± 0.9	16.2 ± 0.4
Phosphatidylethanolamine	10.6 ± 0.5	17.6 ± 0.1
Phosphatidic acids	16.8 ± 0.3	16.5 ± 0.1
Phosphatidylserine	8.4 ± 0.2	26.9 ± 0.4

As could be seen, phospholipid composition of the oils differed a lot. While the main component of the oil from Bulgarian seeds was phosphatidylcholine (42.2%), followed by phosphatidylinositol (22.0%), all phospholipid classes in the oil from Greek seeds were present in almost similar amounts – from 16.2% (phosphatidylinositol) to 26.9% (phosphatidylserine). The content of phosphatidylethanolamine and phosphatidylserine was higher in the Greek oil (17.6 and 26.9%, respectively), while the amount of phosphatidic acids was almost the same in both oils (16.5 – 16.8%). These differences could also be explained by the agro-meteorological conditions and geographic regions where the seeds had been grown.

The major fatty acids of the main phospholipid classes are presented in Figure 2.

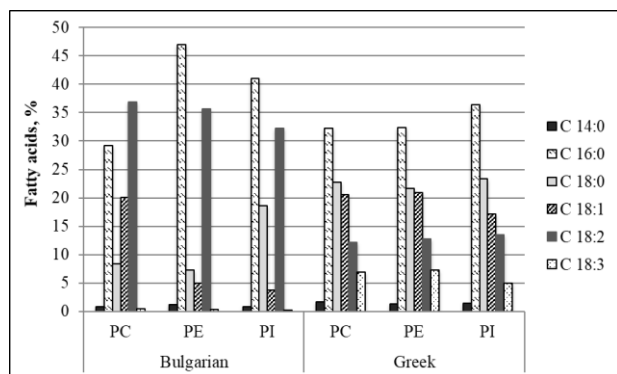


Figure 2. Fatty acid composition of the main phospholipids in watermelon seed oils.

C_{14:0}- Myristic acid; C_{16:0}- Palmitic acid; C_{18:0}- Stearic acid; C_{18:1}- Oleic acid; C_{18:2}- Linoleic acid; C_{18:3}- Linolenic acid; PC- Phosphatidylcholine; PE- Phosphatidylethanolamine; PI- Phosphatidylinositol

The fatty acid composition of the main phospholipid classes (phosphatidylcholine, phosphatidylethanolamine and phosphatidylinositol) of watermelon seed oils was examined for the first time. It was observed that the fatty acid composition of the major phospholipid classes of the examined seed oils differed a lot.

Palmitic acid (32.3 – 47.0%) was the main fatty acid in the phospholipids from both examined watermelon seed oils, except in phosphatidylcholine in the Bulgarian oilseed (29.2%). The main fatty acid in the latter was linoleic acid (36.9%). The content of stearic acid in the phospholipids from seeds with Greek origin ranged from 21.6 to 23.3% and it was higher than those of the same fatty acid in the phospholipids from Bulgarian seed oil (7.3 – 18.6%). On the other hand, the amount of linoleic fatty acid in the main phospholipids of the oil from Bulgaria (32.3 – 36.9%) was much higher than these with Greek origin (12.1 – 13.5%). The content of linolenic acid was lower in the phospholipids from Bulgarian seed oil (0.2 – 0.5%), while their quantity in the phospholipids from Greek seed oil ranged from 5.0 (in phosphatidylinositol) to 7.3% (in phosphatidylethanolamine).

The content of saturated (SFA), mono- (MUFA) and polyunsaturated (PUFA) fatty acids of the main phospholipid classes of watermelon seed oils is shown in Figure 3.

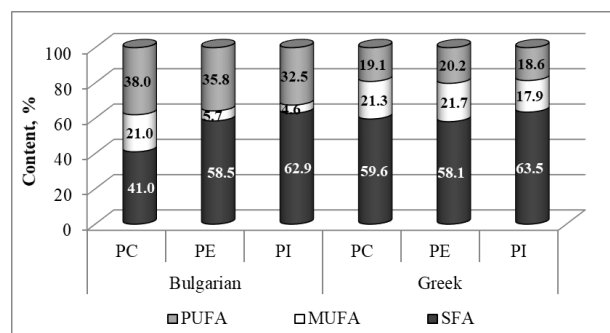


Figure 3. Content of saturated (SFA), mono- (MUFA) and polyunsaturated (PUFA) fatty acids of the main phospholipid classes of watermelon seed oils.

PC- Phosphatidylcholine; PE- Phosphatidylethanolamine; PI- Phosphatidylinositol

The contents of SFA, MUFA and PUFA in the main phospholipids of the watermelon seed oil from Bulgaria differed from those from Greece. SFA predominated in all phospholipids of the examined oils (58.1 – 63.5%) except in the phosphatidylcholine from Bulgarian oil (41.0%), where the main fatty acids were UFA (59.0%). PUFA were found in much higher amount in the phospholipids of Bulgarian seed oil (32.5 – 38%) than in the Greek one (18.6 – 20.2%). On the other hand, the content of MUFA was much lower in phosphatidylethanolamine and phosphatidylinositol of the Bulgarian oil (5.7 and 4.6%, respectively). Overall, fatty acid composition of the main phospholipids of the examined oils was completely different from those of triacylglycerols. While the

SFA predominated in the first ones, the content of UFA was higher in the triacylglycerols.

CONCLUSIONS

The examined watermelon seeds are relatively rich in glyceride oil, which contains a high amount of biologically active substances. There are some differences in the total sterol content and individual phospholipid composition in the watermelon seed oils due to their different origin, climatic and agrometeorological conditions. In conclusion, due to the lipid composition of the examined watermelon seed oils they can be successfully used as an alternative source of glyceride oil and potentially used in the food industry and cosmetics.

REFERENCES

1. T. A. El-Adawy, K. M. Taha, *J. Agric. Food Chem.*, **49**, 1253 (2001).
2. E. A. Essien, U. M. Eduok, *Elixir Org. Chem.*, **54**, 12700 (2013).
3. A. Mariod, Y. M. Ahmed, B. Matthäus, G. Khaleel, A. Siddig, A. M. Gabra, S. I. Abdelwahab, *J. Am. Oil Chem. Soc.*, **86**, 1181 (2009).
4. G. O. Oyeleke, E. O. Olagunju, A. Ojo, *IOSR Journal of Applied Chemistry (IOSR-JAC)*, **2** (2), 29 (2012).
5. B. A. Anhwange, B. A. Ikyenge, D. T. Nyiatagher, J. T. Ageh, *Journal of Applied Sciences Research*, **6** (3), 265 (2010).
6. M. K. Sabahelkhier, K. E. A. Ishag, A. K. Sabir Ali, *British Journal of Science*, **1** (2), 76 (2011).
7. S. Raziq, F. Anwar, Z. Mahmood, S. A. Shahid, R. Nadeem, *Grasas y aceites*, **63** (4), 365 (2012).
8. O. M. Oluba, Y. R. Ogunlowo, G. C. Ojeh, K. E. Adebisi, G. O. Eidangbe, I. O. Isiosio, *Journal of Biological Sciences*, **8** (4), 814 (2008).
9. S. Oelschlägel, C. Menzel, K. Speer, *Lipid Technology*, **24** (8), 181 (2012)
10. ISO 659:2014. Oilseeds. Determination of oil content (Reference method).
11. ISO 12966-1:2014. Animal and vegetable fats and oils. Gas chromatography of fatty acid methyl esters – Part 1: Guidelines on modern gas chromatography of fatty acid methyl esters.
12. ISO 12966-2:2011. Animal and vegetable fats and oils. Gas chromatography of fatty acid methyl esters – Part 2: Preparation of methyl esters of fatty acids.
13. J. Folch, M. Lees, G. H. Sloane-Stanley, *J. Biol. Chem.*, **226**, 497 (1957).
14. R. Schneiter, G. Daum, Analysis of yeast lipids, in: *Yeast Protocol: 2nd edn. Methods in Molecular Biology*, Xiao, W. (ed.), Humana Press Inc., Totowa, NJ, 2006, p. 75.
15. ISO 10540-1:2014. Animal and vegetable fats and oils. Determination of phosphorus content. Part 1: Colorimetric method.
16. ISO 18609:2000. Animal and vegetable fats and oils. Determination of unsaponifiable matter. Method using hexane extraction.
17. S. Ivanov, P. Bitcheva, B. Konova, *Rev. Franc. Corps Gras*, **19**, 177 (1972).
18. ISO 12228-1:2014. Part 1: Animal and vegetable fats and oils. Determination of individual and total sterols contents. Gas chromatographic method.
19. ISO 9936:2016. Animal and vegetable fats and oils. Determination of tocopherol and tocotrienol contents by high-performance liquid chromatography.

Composition of residual lipids isolated from *salinomycin*

Bl. S. Chuchkov*, G. A. Antova

University of Plovdiv "Paisii Hilendarski", Department of Chemical Technology,
24 Tzar Asen Str., 4000 Plovdiv, Bulgaria

Received November 15, 2018; Revised January 4, 2019

Salinomycin is an antimicrobial polyether ionophore antibiotic that is synthesized by microbiological pathway, and vegetable oils (mainly rapeseed oil) are used as a nutrient medium. Some of the lipids remain in the final product and affect its quality (fluidity). The composition of residual lipids isolated from three *salinomycin* samples of different fluidity (with good fluidity (80%), with bad fluidity (<80%) and imported sample with good fluidity (>80%)) was studied. The general lipid composition of rapeseed oil used for the nutrient medium in the preparation of *salinomycin* is: triglycerides - 96.0%, unsaponifiables - 1.7%, free fatty acids - 0.5%, phospholipids and other polar compounds - 1.2%. The lipid content of the *salinomycin* samples is 30.2%, 40.5% and 21.6% respectively and they have the following composition: monoglycerides - from 5.1 to 12.7%, diglycerides - from 8.3 to 14.8%, triglycerides - from 10.4 to 25.2%, free fatty acids - from 1.4 to 14.7%, polar compounds - from 45.9 to 62.2%. Significant changes in fatty acid composition were observed during the biosynthesis process. The amount of unsaturated fatty acids (oleic and linoleic) in the oils isolated from the samples with good viscosity decreased significantly at the expense of the increased content of saturated fatty acids - stearic, palmitic and especially capric acid (from 0.1% to 2.9 - 14.1%). It can be concluded that in the process of *salinomycin* biosynthesis, the lipids undergo significant transformations - triacylglycerols are hydrolyzed and the long-chain unsaturated fatty acids are degraded to medium-chain saturated fatty acids.

Keywords: salinomycin, lipids, fatty acid composition

INTRODUCTION

The antibiotic *salinomycin* is an antibacterial and coccidiostat ionophore therapeutic drug. *Salinomycin* exhibits high antimicrobial activity against Gram-positive bacteria and is used in birds and other animals. The "Biovet" Peshtera produces two products based on *salinomycin* with the market brand Sacox - Sacox®120 microgranulate and Sacox®200 microgranulate. They are anticoccidial feed additives for the prophylactic control of coccidiosis in chickens for fattening and chickens reared for laying. Sacox 120 and Sacox 200 microgranulate contain 12% and 20% of *salinomycin*, sodium and calcium carbonate and silicon dioxide as carriers. These components are produced by means of microgranulation, which are inseparably combined and this lead to improving the activity of the product. This production process results in a uniform microgranulate with excellent flow characteristics.

The production of *salinomycin* was carried out by fermentation in a known manner [1-3], wherein vegetable oils such as soybean oil, sesame oil, rapeseed oil, safflower oil, olive oil, methyl oleate, methyl myristate and methyl linoleate are used as carbon sources and as defoaming agents. The formed agglomerates with polyether antibiotics include glyceride fats, free fatty acids, and phospholipids such as lecithin. *Salinomycin* from

"Biovet" Peshtera is produced by using mainly rapeseed and soybean oil as culture medium. The final product contains a residual amount of lipids that affect its fluidity, so it is necessary to determine their composition.

The purpose of this work is to determine the composition of the residual lipids isolated from *salinomycin* with different fluidity.

EXPERIMENTAL

Samples

Three *salinomycin* samples with different fluidity (with good fluidity (80%), with bad fluidity (<80%) and imported sample with very good fluidity (>80%)) were studied. The first two were manufactured by "Biovet" Peshtera and the third was imported from China.

Methods

Isolation and quantification of lipid classes by thin-layer chromatography (TLC)

The residual lipids were extracted with hexane in a Soxhlet apparatus for 8 h [4]. After that the solvent was removed by a rotary evaporator and the residue was weighed to determine the oil content of each sample. The main lipid classes were identified by applying 1 mL of the residual lipids solution in hexane on a 20 cm × 20 cm glass plate with ca. 1 mm thick silica gel 60 G layer and developed with hexane-acetone, 100:8 (v/v). The mixture of lipid

* To whom all correspondence should be sent.
E-mail: blago_chuchkov@abv.bg

classes containing equal parts of docosane-, cholesterol oleate-, triolein-, cholesterol-, 1,3-diolein-, 1-monooleinrac-glycerol and oleic acid were used as references. Triacylglycerols, sterols, diacylglycerols, monoacylglycerols, free fatty acids and polar lipids (eluted in this order) were unambiguously identified and isolated by elution with diethyl ether. The solvent was evaporated under a stream of nitrogen and the residues were weighed in small glass containers to constant weight [5].

Gas chromatography of fatty acid methyl esters

The fatty acid composition of lipids was determined by gas chromatography (GC) after transmethylation of the respective sample with 2% H₂SO₄ in CH₃OH at 50°C [6]. Fatty acid methyl esters (FAME) were purified by TLC. GC was performed on an HP 5890 series II gas chromatograph unit equipped with a 60 m × 0.25 mm (I.D.) × 25 μm (film thickness) capillary Supelco column and a flame ionization detector. The column temperature was programmed from 140°C (5 min), at 4 °C/min to 240°C (10 min); injector and detector temperatures are kept at 250°C. Identification of fatty acids was performed by comparison of retention times with those of a standard mixture of fatty acids subjected to GC under identical experimental conditions [7]. The analytical standard of fatty acid methyl esters was purchased from Sigma-Aldrich Chemical Co. All solvents and reagents were of analytical grade from Merck and were used without additional purification.

Determination of salinomycin by HPLC

Antibiotic content in the products was determined by high performance liquid chromatography. Chromatographic system is Shimadzu, equipped with a chromatographic column-Chromolith RP-18 100×4.6 mm. Mobile phase contained a mixture of methanol, water and acetic acid – 90:10:0.1 (v/v/v). Chromatographic conditions were: flow of the mobile phase 0.850 mL/min, flow of the derivatizing solution 0.900 mL/min, analysis temperature 98°C and wavelength 520 nm [8].

Table 2. Lipid composition of residual lipids isolated from *salinomycin* with different fluidity

Component, %	Product Sacox		
	Good fluidity	Bad fluidity	Very good fluidity
Monoglycerides	5.1	12.7	6.6
Diglycerides	8.3	14.8	8.7
Triacylglycerols	10.4	25.2	14.9
Free fatty acids	14.0	1.4	14.7
Polar compounds	62.2	45.9	55.1

RESULTS AND DISCUSSION

General characteristics of the oil and residual lipids

The content of antibiotic and residual lipids, isolated from Sacox with different fluidity is shown in Table 1. The sample with bad fluidity has the greatest oil content while the sample with very good fluidity has the smallest quantity of the oil. It was found that the antibiotic *salinomycin* was present in an amount from 11.9 to 18.8% in the tested samples. The results about antibiotic content in the examined samples are in agreement with the quality certificate for *salinomycin* content in the marked products. The level of antibiotic content is lower than that of samples with very good fluidity. The general lipid composition of rapeseed oil used for the nutrient medium in the preparation of *salinomycin* is: triglycerides - 96.0%, unsaponifiables - 1.7%, phospholipids and other polar compounds - 1.2%, free fatty acids - 0.5% and small amounts of mono- and diacylglycerols (about 0.5%).

Table 1. Content of antibiotic and residual lipids, isolated from Sacox with different fluidity

Samples	Residual lipids from Sacox, %	Antibiotic content, %
Good fluidity (80%)	30.2	18.8
Bad fluidity (<80%)	40.5	18.6
Very good fluidity (>80%)	21.6	11.9

The general lipid composition of residual lipids isolated from *salinomycin* with different fluidity is shown in Table 2. The significant changes in lipid composition between the initial rapeseed oil and the isolated lipids from the tested samples have been observed during the biosynthesis process. The content of triacylglycerols significantly reduces during the process while this of mono-, diglycerides and free fatty acids increases. The residual lipids from samples of the *salinomycin* with good and very good fluidity have the higher quantities of polar compounds and free fatty acids.

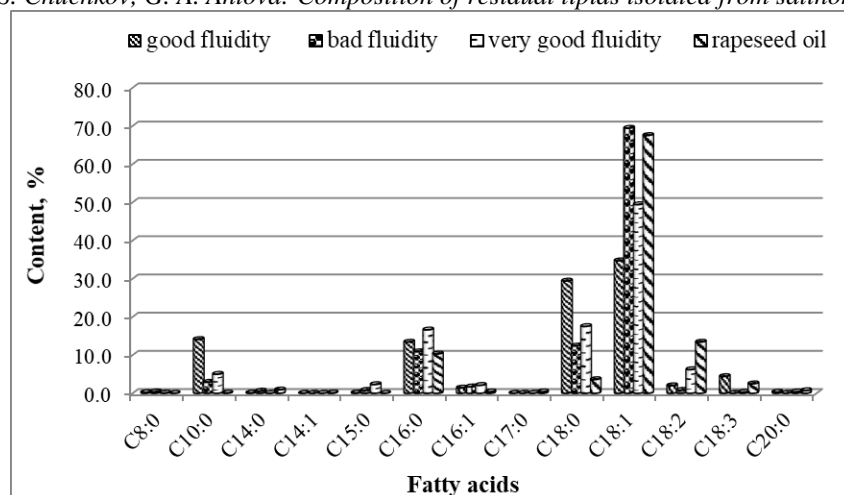


Figure 1. Fatty acids composition of rapeseed oil and residual lipids isolated from *salinomycin* with different fluidity:

*C_{8:0} – caprylic, C_{10:0} – capric, C_{14:0} – myristic, C_{14:1} – myristoleic, C_{15:0} – pentadecanoic, C_{16:0} – palmitic, C_{16:1} – palmitoleic, C_{17:0} – margaric, C_{18:0} – stearic, C_{18:1} – oleic, C_{18:2} – linoleic, C_{18:3} – linolenic, C_{20:0} – arachidic acid

The changes in the fatty acid composition of rapeseed oil and residual lipids isolated from *salinomycin* with different fluidity have also been investigated (Figure 1). Oleic acid (67.5%) and linoleic acid (13.4%), followed by palmitic acid (10.3%) and stearic acid (3.6%), were found to predominate in the fatty acid composition of the rapeseed oil.

Oleic acid is in the highest amount in all samples (in the sample with good fluidity it is 34.7%, with very good fluidity - 49.4% and with bad fluidity - 69.4%, respectively). The residual lipids from the different samples contain palmitic acid between 10.9% (with bad fluidity) and 16.6% (with very good fluidity) and a significantly high amount of stearic acid - between 12.4% (with bad fluidity) and 29.4% (with good fluidity). The amount of unsaturated fatty acids (oleic and linoleic) in the oils isolated from the samples with good viscosity decreased significantly at the expense of increasing of the content of saturated fatty acids - stearic, palmitic and especially capric acid (from 0.1% (rapeseed oil) to 2.9 - 14.1% (with good fluidity)).

Figure 2 shows the ratio of unsaturated and saturated fatty acids in rapeseed oil and residual lipids isolated from *salinomycin*. In the composition of rapeseed oil used as a nutrient medium, unsaturated fatty acids predominate (83.9%). In the process of synthesizing *salinomycin*, their amount decreases significantly. In the residual lipids isolated from *salinomycin* with good and very good fluidity the amount of unsaturated fatty acids is 42.5% (good fluidity) and 58.0% (very good fluidity), respectively. The quantity of saturated fatty acids increases from 16.1% to 42.0% and 57.5% (with good fluidity). The ratio of saturated:

unsaturated fatty acids in rapeseed oil and isolated lipids from the sample with poor fluidity is 16.1:83.9, i. e. 1:5.2 and 28.0:72.0, i. e. 1:2.6, respectively, while in the lipids of the sample with very good fluidity it is much lower 42.0:58.0, i. e. 1:1.4. Lower content of unsaturated (42.5%) and respectively higher content of saturated fatty acids (57.5%) is found in the lipids isolated from the sample with good fluidity (1:0.7).

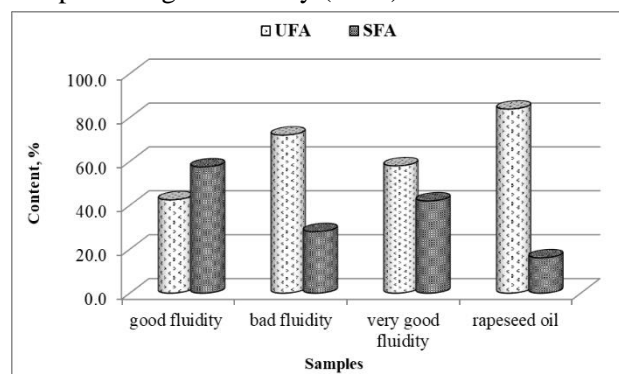


Figure 2. Ratio between unsaturated (UFA) and saturated (SFA) fatty acids in rapeseed oil and in residual lipids isolated from *salinomycin* with different fluidity

CONCLUSIONS

The lipids undergo significant transformations in the process of *salinomycin* biosynthesis - triacylglycerols are hydrolysed and the long-chain unsaturated fatty acids are degraded to medium-chain saturated fatty acids.

In conclusion, the use of vegetable oils with a higher content of saturated fatty acids (palmitic and stearic fatty acid) is recommended in the process of *salinomycin* biosynthesis, which ensures higher fluidity and quality of the final product.

Acknowledgement: We are grateful to “Biovet” Peshtera for the provided samples for carrying out this study.

REFERENCES

1. Y. Miyazaki, M. Shibuya, H. Sugawara, O. Kawaguchi, Ch. Hirose, J. Nagatsu, S. Esumi, *Journal of Antibiotics* (Tokyo), **27**, 814 (1974).
2. H. Kinashi, N. Otake, H. Yonehara, *Tetrahedron Letters*, **49**, 4955 (1973).
3. H. Kinashi, N. Otake, *Agr. Biol. Chem.* **40**, 1625 (1976).
4. Company standard “Biovet” Peshtera QCD-FPC-0878-09. Determination of crude fat content.
5. M. Kates, *Techniques of lipidology: Isolation, analysis and identification of lipids*, North-Holland Pub. Co., American Elsevier Publishing Co., Inc.-New York, 1972.
6. ISO 12966-2:2011. Animal and vegetable fats and oils. Gas chromatography of fatty acid methyl esters Part 2: Preparation of methyl esters of fatty acids.
7. ISO 12966-1:2014. Animal and vegetable fats and oils. Gas chromatography of fatty acid methyl esters. Part 1: Guidelines on modern gas chromatography of fatty acid methyl esters.
8. Company standard “Biovet” Ltd. Peshtera QCD-FPC-0878-03. Determination of the contents and impurities of salinomycin by HPLC.

BULGARIAN CHEMICAL COMMUNICATIONS

Instructions about Preparation of Manuscripts

General remarks: Manuscripts are submitted in English by e-mail or by mail (in duplicate). The text must be typed double-spaced, on A4 format paper using Times New Roman font size 12, normal character spacing. The manuscript should not exceed 15 pages (about 3500 words), including photographs, tables, drawings, formulae, etc. Authors are requested to use margins of 3 cm on all sides. For mail submission hard copies, made by a clearly legible duplication process, are requested. Manuscripts should be subdivided into labelled sections, e.g. **Introduction, Experimental, Results and Discussion, etc.**

The title page comprises headline, author's names and affiliations, abstract and key words.

Attention is drawn to the following:

a) **The title** of the manuscript should reflect concisely the purpose and findings of the work. Abbreviations, symbols, chemical formulas, references and footnotes should be avoided. If indispensable, abbreviations and formulas should be given in parentheses immediately after the respective full form.

b) **The author's** first and middle name initials, and family name in full should be given, followed by the address (or addresses) of the contributing laboratory (laboratories). **The affiliation** of the author(s) should be listed in detail (no abbreviations!). The author to whom correspondence and/or inquiries should be sent should be indicated by asterisk (*).

The abstract should be self-explanatory and intelligible without any references to the text and containing not more than 250 words. It should be followed by key words (not more than six).

References should be numbered sequentially in the order, in which they are cited in the text. The numbers in the text should be enclosed in brackets [2], [5, 6], [9–12], etc., set on the text line. References, typed with double spacing, are to be listed in numerical order on a separate sheet. All references are to be given in Latin letters. The names of the authors are given without inversion. Titles of journals must be abbreviated according to Chemical Abstracts and given in italics, the volume is typed in bold, the initial page is given and the year in parentheses. Attention is drawn to the following conventions:

a) The names of all authors of a certain publications should be given. The use of "*et al.*" in

the list of references is not acceptable.

b) Only the initials of the first and middle names should be given.

In the manuscripts, the reference to author(s) of cited works should be made without giving initials, e.g. "Bush and Smith [7] pioneered...". If the reference carries the names of three or more authors it should be quoted as "Bush *et al.* [7]", if Bush is the first author, or as "Bush and co-workers [7]", if Bush is the senior author.

Footnotes should be reduced to a minimum. Each footnote should be typed double-spaced at the bottom of the page, on which its subject is first mentioned.

Tables are numbered with Arabic numerals on the left-hand top. Each table should be referred to in the text. Column headings should be as short as possible but they must define units unambiguously. The units are to be separated from the preceding symbols by a comma or brackets.

Note: The following format should be used when figures, equations, *etc.* are referred to the text (followed by the respective numbers): Fig., Eqns., Table, Scheme.

Schemes and figures. Each manuscript (hard copy) should contain or be accompanied by the respective illustrative material as well as by the respective figure captions in a separate file (sheet). As far as presentation of units is concerned, SI units are to be used. However, some non-SI units are also acceptable, such as °C, ml, l, etc.

The author(s) name(s), the title of the manuscript, the number of drawings, photographs, diagrams, etc., should be written in black pencil on the back of the illustrative material (hard copies) in accordance with the list enclosed. Avoid using more than 6 (12 for reviews, respectively) figures in the manuscript. Since most of the illustrative materials are to be presented as 8-cm wide pictures, attention should be paid that all axis titles, numerals, legend(s) and texts are legible.

The authors are asked to submit **the final text** (after the manuscript has been accepted for publication) in electronic form either by e-mail or mail on a 3.5" diskette (CD) using a PC Word-processor. The main text, list of references, tables and figure captions should be saved in separate files (as *.rtf or *.doc) with clearly identifiable file names. It is essential that the name and version of

the word-processing program and the format of the text files is clearly indicated. It is recommended that the pictures are presented in *.tif, *.jpg, *.cdr or *.bmp format, the equations are written using "Equation Editor" and chemical reaction schemes are written using ISIS Draw or ChemDraw programme.

The authors are required to submit the final text with a list of three individuals and their e-mail addresses that can be considered by the Editors as potential reviewers. Please, note that the reviewers should be outside the authors' own institution or organization. The Editorial Board of the journal is not obliged to accept these proposals.

EXAMPLES FOR PRESENTATION OF REFERENCES

REFERENCES

1. D. S. Newsome, *Catal. Rev.–Sci. Eng.*, **21**, 275 (1980).
2. C.-H. Lin, C.-Y. Hsu, *J. Chem. Soc. Chem. Commun.*, 1479 (1992).
3. R. G. Parr, W. Yang, *Density Functional Theory of Atoms and Molecules*, Oxford Univ. Press, New York, 1989.
4. V. Ponec, G. C. Bond, *Catalysis by Metals and Alloys* (Stud. Surf. Sci. Catal., vol. 95), Elsevier, Amsterdam, 1995.
5. G. Kadinov, S. Todorova, A. Palazov, in: *New Frontiers in Catalysis* (Proc. 10th Int. Congr. Catal., Budapest, 1992), L. Guzzi, F. Solymosi, P. Tetenyi (eds.), Akademiai Kiado, Budapest, 1993, Part C, p. 2817.
6. G. L. C. Maire, F. Garin, in: *Catalysis. Science and Technology*, J. R. Anderson, M. Boudart (eds), vol. 6, Springer-Verlag, Berlin, 1984, p. 161.
7. D. Pocknell, *GB Patent 2 207 355* (1949).
8. G. Angelov, PhD Thesis, UCTM, Sofia, 2001.
9. JCPDS International Center for Diffraction Data, Power Diffraction File, Swarthmore, PA, 1991.
10. *CA* **127**, 184 762q (1998).
11. P. Hou, H. Wise, *J. Catal.*, in press.
12. M. Sinev, private communication.
13. <http://www.chemweb.com/alchem/articles/1051611477211.html>.

CONTENTS

Preface

<i>K.T. Stojnova, V. V. Divarova, P. V. Racheva, K. G. Bozhinova, V. D. Lekova</i> , Complex formation and liquid-liquid extraction of the ion-pair of molybdenum(VI) with 3,5-dinitrocatechol and 3-(4,5-dimethylthiazol-2-yl)-2,5-diphenyl-2H-tetrazolium bromide.....	3
<i>P. E. Marinova, S. H. Tsoneva, S. A. Nikolova, I. I. Ivanov</i> , Novel complexes of N-substituted-4,5-dimethoxy-phenylethyl-2-arylketamides with metal ions.....	8
<i>P. Paunović, G. Načevski, A. Petrovski, A. Tomova, A. Grozdanov, A. T. Dimitrov</i> , Kinetic analysis of ultrasound leaching of nickel laterite ore.....	12
<i>E. Cherneva, R. Buyukliev, A. Bakalova</i> , Palladium complexes containing dithiocycloheptane-spiro-5'-hydantoin ligand. Synthesis, characterization, theoretical analysis and cytotoxic activity.....	19
<i>Kr. Nikolova, G. Gentscheva, S. Minkova, Ch. Tzvetkova</i> , Elemental composition and some optical characteristics of Bulgarian beers.....	24
<i>I. A. Shanin, E. A. Zvereva, A. V. Zherdev, T. Godjevargova, S.A. Eremin</i> , Chemical reagents for immunodetection of fluoroquinolones with determinable specificity.....	27
<i>I. D. Ivanov, S. S. Stoykova, N. T. Burdzhiev, I. N. Pantcheva, V. N. Atanasov</i> , Analytically confirmed synthetic cannabinoid 5F-ADB sprayed on “herbal mixture.....	32
<i>A. Grozdanov, A. Petrovski, M. Avella, P. Paunović, M. E. Errico, R. Avolio, G. Gentile, F. De Falco, A. T. Dimitrov</i> , Spectroscopic study of nanocomposites based on PANI and carbon nanostructures for pH sensors.....	36
<i>Z. A. Mustafa, R. S. Milina</i> , A static headspace GC-FID method for trace analysis of volatile organic compounds (VOCs) in waters.....	42
<i>E. S. Belyaev, S. V. Andreev, A. O. Ivanova, A. A. Ischenko</i> , Determination of brodifacoum, bromadiolone and difenacoum in commercial rodenticides by using high-performance liquid chromatography with UV detection.....	47
<i>D. M. Davcheva, G. K. Kirova, T. Z. Tsvetkova, D. D. Terzieva, M. T. Kiryakova, V. J. Kmetov</i> , Sample preparation and calibration optimization for ICP-MS analysis of copper, zinc, selenium, rubidium, strontium, magnesium, iron, molybdenum and barium in human serum.....	52
<i>M. T. Kiryakova, E. K. Varbanova, K. K. Simitchiev, V. J. Kmetov</i> , Nanoparticles assisted MSIS-MP-AES hydride generation determination of As and Sb.....	58
<i>V. Y. Markova, K. K. Simitchiev</i> , Assessment of different approaches for background correction in microwave plasma atomic emission spectrometry – case study for analysis of Cd, Cr, Cu, Ni, Pb and Zn in treated bio-waste.....	64
<i>E. K. Varbanova, V. M. Stefanova</i> , Determination of silver in cosmetic products by microwave plasma - atomic emission spectrometry.....	71
<i>V. M. Stefanova, L. I. Kaynarova, D. L. Georgieva</i> , General characteristics of silver nanoparticles analysis by single particle inductively coupled plasma mass spectrometry.....	77
<i>D. Georgieva, A. Ivancheva, Ts. Lazarova, V. Stefanova</i> , Magnetic assisted solid phase extraction of trace elements by APDC impregnated silica coated manganese-ferrite nanoparticles.....	85
<i>L. Dospatliev, V. Lozanov, M. Ivanova, P. Papazov, P. Sugareva</i> , Amino acids in edible wild mushroom from the Batak mountain, Bulgaria.....	92
<i>V. A. Hadjimitova, N. G. Hristova-Avakumova, B. I. Nikolova-Mladenova, E. Valcheva</i> , Suppressive effect of salicylaldehyde benzoylhydrazone derivatives on ferrous iron-induced oxidative molecular damage – evaluation of the structure-protection activity relationship via Raman spectral analysis....	97
<i>P. I. Bozov, P. N. Penchev</i> , Neo-Clerodane Diterpenoids from <i>Scutellaria velenovskyi</i> Rech. fil.....	103
<i>N. S. Todorov</i> , Surface coatings based on glycerol phase and waste polyethylene terephthalate.....	107
<i>M. H. Docheva, D. M. Kirkova, Y. G. Kochev, A. B. Stoilova</i> , Determination of carbonyl compounds in tobacco smoke and factors influence of their composition.....	113
<i>Y. Georgieva, M. Katsarova, K. Gercheva, P. Bozov, S. Dimitrova</i> , HPLC analysis of flavonoids from <i>Scutellaria altissima</i>	119
<i>Y. Stremski, D. Kirkova, S. Statkova-Abeghe, P. Angelov, I. Ivanov</i> , Multicomponent reactions for the synthesis of bis-heterocyclic pyrrole derivatives.....	124
<i>R. Khattak, I. I. Naqvi</i> , Study of the effect of structure on the kinetics and mechanism of the redox reactions of Fe(III)/Fe(II) complexes.....	129

I. A. Hayrullina, E. A. Boruleva, I. A. Nagovitsyn, T. F. Sheshko, A. G. Cherednichenko, E. A. Sarycheva, G. K. Chudinova, The effect of bovine myoglobin on ultraviolet fluorescence of gadolinium-doped zinc oxide films.....	135
V. V. Kost, T. A. Kryuchkova, V. D. Zimina, T. F. Sheshko, A. G. Cherednichenko, V. V. Kurilkin, M. G. Safronenko, L. V. Yafarova, Catalytic performance of LnFeO ₃ complex oxides for dry reforming of methane to synthesis gas.....	138
A. A. Sharaeva, T. F. Sheshko, T. A. Kryuchkova, L. V. Yafarova, I. A. Zvereva, Effect of substitution Fe by Mn in GdFeO ₃ perovskite catalyst for CO hydrogenation.....	143
K. V. Kamarska, N. D. Dimcheva, Electrooxidation and bioelectrooxidation of L- and D-ascorbic acids	149
A. Terziyski, S. Tenev, V. Jeliaskov, N. Kochev, G. Dimitrov, N. Jeliaskova, L. Iliev, Ch. Angelov, I. Kalapov, T. Arsov, Balloon-borne measurements in the upper troposphere and lower stratosphere above Bulgaria (N41-43° E24-26°).....	153
V. V. Ivanova-Kolcheva, M. K. Stoyanova, Catalytic activation of PMS by Co ₃ O ₄ modified g-C ₃ N ₄ for oxidative degradation of the azo dye Acid Orange 7 dye in aqueous solutions.....	158
N. T. Kochev, V. H. Paskaleva, N. Jeliaskova, Automatic generation of molecular zwitterionic forms with ambit-zwitterion.....	165
N. S. Yantcheva, D. B. Karashanova, B. C. Georgieva, I. N. Vasileva, A. S. Stoyanova, P. N. Denev, R. H. Dinkova, M. H. Ognyanov, A. M. Slavov, Characterization and application of spent brewer's yeast for silver nanoparticles synthesis.....	173
N. S. Yantcheva, I. N. Vasileva, P. N. Denev, H. N. Fidan, R. S. Denkova, A. M. Slavov, Utilization of essential oil industry chamomile wastes as source of polyphenols.....	178
A. P. Hambarliiska, V. T. Dobрева, H. N. Strinska, B. Y. Zhekova, G. T. Dobrev, Isolation and purification of lipase produced from <i>Rhizopus arrhizus</i> in solid state fermentation by fractional precipitation.....	184
A. Shulga, E. A. Boruleva, T. F. Sheshko, I. A. Nagovitsyn, A. G. Cherednichenko, G. K. Chudinova, Luminescent properties of cerium (IV) -doped zinc oxide films.....	189
Y. L. Lazarova, T. M. Dodevska, A. M. Slavov, D. B. Karashanova, B. C. Georgieva, Biosynthesized silver nanoparticles: electrochemical application.....	192
G. P. Peeva, B. N. Midyurova, V. A. Nenov, Innovative treatment of livestock manure by a single – compartment microbial fuel cell with air-breathing cathode.....	198
T. M. Dodevska, I. G. Shterev, Y. L. Lazarova, Carbonaceous materials modified with iridium oxide as an electrochemical sensing platform.....	203
S. T. Tasheva, T. A. Ivanova, V. T. Popova, I. Z. Iliev, S. S. Stankov, H. N. Fidan, N. N. Mazova, A. S. Stoyanova, Coefficient of diffusion of tannins in extracts from physalis leaves (<i>Physalis peruviana</i> L.).....	209
M. D. Dimov, K. Z. Dobрева, A. S. Stoyanova, Chemical composition of the dill essential oils (<i>Anethum graveolens</i> L.) from Bulgaria.....	214
G. Uzunova, M. Perifanova-Nemaska, Zh. Petkova, St. Minkova, Kr. Nikolova, Physicochemical characteristic of chia seed oil from Peru.....	217
L. Dospatliev, M. Ivanova, P. Papazov, Fatty acids, phospholipids, health risk index and daily intake of metals in edible wild mushroom (<i>Tricholoma equestre</i>) from the Batak mountain, Bulgaria...	221
S. K. Georgieva, M. Stancheva, Zl. Peteva, Residual levels and tissue distribution of polychlorinated biphenyls (PCBs) in fish from the Danube River, Bulgaria.....	227
Z. V. Peteva, G. N. Kalinova, B. Krock, M. D. Stancheva, St. K. Georgieva, Evaluation of paralytic shellfish poisoning toxin profile of mussels from Bulgarian North Black Sea coast by HPLC-FID with post and pre-column derivatization.....	233
K. Peycheva, V. Panayotova, A. Merdzhanova, R. Stancheva, Estimation of THQ and potential health risk for metals by consumption of some black sea marine fishes and mussels in Bulgaria.....	241
D. A. Dobрева, A. Merdzhanova, V. Panayotova, Quality-related changes of biologically active lipids in bluefish muscle tissue after cooking.....	247
V. Z. Panayotova, A. V. Merdzhanova, D. A. Dobрева, R. S. Stancheva, K. Peycheva, Seasonal variation in fat-soluble vitamins, cholesterol and fatty acid profile of lipid classes of <i>Rapana venosa</i>	251
A. Merdzhanova, V. Panayotova, D. A. Dobрева, R. Stancheva, Effect of thermal stress on the biologically active lipids of <i>Mytilus galloprovincialis</i>	256
Zh. Y. Petkova, G. A. Antova, M. I. Angelova-Romova, I. Ch. Vaseva, A comparative study on chemical and lipid composition of amaranth seeds with different origin.....	262

<i>M. Y. Angelova-Romova, Zh. B. Simeonova, Zh. Y. Petkova, G. A. Antova, O. T. Teneva, Lipid composition of watermelon seed oil.....</i>	268
<i>Bl. S. Chuchkov, G. A. Antova, Composition of residual lipids isolated from salinomycin.....</i>	273
<i>Instruction about preparation of manuscripts.....</i>	277

